THE UNIVERSITY
of ADELAIDE

THE ISOTOPIC EVOLUTION OF THE NORTHERN EAST AFRICAN OROGEN

MORGAN L. BLADES

Earth Sciences
School of Physical Sciences
University of Adelaide

This thesis is submitted in fulfilment of the requirements for the degree of Doctor of Philosophy

February, 2018

TABLE OF CONTENTS

TABLE OF CONTENTS

ABSTRACT

The Neoproterozoic era saw some of the most important events in the evolution of the planet. These events notably include the emergence of complex life and climatic extremes that involved widespread, possibly global glaciation. This era also saw the demise of the supercontinent Rodinia and formation of the supercontinent Gondwana, which likely played a fundamental role in the recorded events. Thus, to better understand these events there is a need to have rigorous models that describe the plate reconfiguration occurring during the Neoproterozoic. The East African Orogen (EAO) is a Neoproterozoic to early Cambrian mobile belt that reflects the collision between India and the African continents. It is the major collisional orogeny that formed as central Gondwana coalesced and the Mozambique Ocean closed. The evolution of the northern East African Orogen is well documented in the Arabian Nubian Shield (ANS). However, much less is known about the development of the orogen to the west (Chad, Sudan, Ethiopia) and east (Oman) of the ANS. This thesis provides new evidence from a number of Mesoproterozoic to Neoproterozoic basement exposures from western Ethiopia, Sudan, Chad and Oman to further constrain the evolution of the northern East African Orogen and subsequent effects on surrounding terranes.

The Western Ethiopian Shield (WES) sits within the transition between the Arabian Nubian Shield and the Mozambique Belt. The shield is defined by three main phases of magmatism ca. 850–810 Ma, 780–700 Ma and 620–550 Ma, with no evidence for pre-Neoproterozoic crust. The rocks have a supra-subduction related geochemical signature suggesting formation from fractional crystallisation and assimilation of mantle derived parental magmas. Post tectonic magmatism within the Western Ethiopian Shield occurs at ca. 572 Ma, defining the cessation of subduction within the area. To the west of the WES lies the Sahara Metacraton, a tract of pre-Neoproterozoic continental crust that is bound by suture zones. The effects of the collisional events that create these suture zones, can be seen in the form of deformation, emplacement of igneous bodies (ca. 1000–1100 Ma and 600–560 Ma), as well as localised episodes of crust formation due to rifting. Butana to the east of the Sahara Metacraton, preserves three main phases of magmatism and deformation at; ca. 987 Ma, 862 Ma and 764 Ma. The youngest pulse at ca. 764 Ma has been interpreted to represent the collision or accretion of Butana onto the Sahara Metacraton, therefore constraining the timing of terrane amalgamation in Sudan. In Oman, a small number of basement exposures offer an insight into its relationship to the Arabian Nubian Shield. Geochronological data suggest that the basement rocks of Oman formed between ca. 1000–750 Ma. The cessation of magmatism occurred by ca. 700 Ma, this was followed by the deposition of passive margin sequences. Lu–Hf isotope data suggest the progressive development of arc rocks away from a continental source, starting from the older eastern exposures to the more juvenile exposures in west Oman. Detrital data suggest that the Omani basement accreted on the margin of Neoproterozoic NW India, sourcing Palaeoproterozoic–Neoarchaean zircons, possibly from the Kabul Block.

These data help to further constrain present reconstruction models for the Neoproterozoic, elucidating the continual remobilization of the Sahara Metacraton as a result of the Neoproterozoic orogenesis. These data can be used to place the terranes of the Arabian Nubian Shield in context with the rest of Gondwana and emphasise the importance of the migration of India towards the amalgams of Africa.

DECLARATION

I, Morgan Blades, certify that this work contains no material, which has been accepted for award of any other degree or diploma in my name, in any university or other tertiary institution and, to the best of my knowledge and belief, contains no material previously published or written by another person, except where due reference has been made in the text. In addition, I certify that no part of this work will, in the future, be used in a submission in my name, for any other degree or diploma in any university or other tertiary institute without the prior approval of the University of Adelaide and where applicable, any partner institution responsible for the joint-award of this degree.

I give consent to this copy of my thesis when deposited in the University Library, being made available for load and photocopying, subject to the provisions of the Copyright Act 1968.

The author acknowledges that copyright of published works contained within the thesis resides with copyright holder(s) of those works.

I also give permission for the digital version of my thesis to be made available on the web, via the University's digital research repository, the Library Search and also through web search engines unless permission has been granted by the University to restrict access for a period of time.

MORGAN BLADES   DATE

ACKNOWLEDGEMENTS

CHAPTER 1

Introduction and Thesis Outline

INTRODUCTION

The Neoproterozoic (1000–541 Ma) was a dynamic period in Earth's evolution, with rapid and enigmatic changes to the environment and biota (Stern, 1994b). The demise of Rodina and the amalgamation of Gondwana took place during a time of major climatic extremes, including glaciations, the appearance of multicellular life and the accumulation of economic mineral and petroleum deposits (Collins and Pisarevsky, 2005b; Evans, 2000; Hoffman et al., 1998). Therefore, understanding the distribution of the continents, mountain ranges and oceanic basins during the Neoproterozoic, is exceedingly important. Hindering this are difficulties in constraining the location of oceanic plates during the Neoproterozoic, as no in situ ocean crust exists from prior to ca. 250 Ma. Our understanding of this unique period in Earth's history relies solely on palaeomagnetic data and the geological products of past plate interactions, such as collisional zones (e.g. Himalayas), rifts (e.g. East African Rift) and subduction zones (e.g. Pacific Ring of Fire). The products of arcs that form in subduction zones have been used to provide isotopic proxies for oceanic crust. These arc products are interrogated using a multi-disciplinary approach to determine their age and geochemical nature, to understand the environment in which they formed.

There are three main foci in the following research and thesis. First, understanding the timing of Gondwana's amalgamation: The East African Orogen contains many terranes that formed and accreted to each other and to the growing Gondwana throughout the Neoproterozoic (Fritz et al., 2013a; Johnson, 2014; Johnson et al., 2011b). Second is to constrain the configuration of the cratons within Rodinia and how the plate margins represented by the East African Orogen terranes evolved through the Neoproterozoic.

One of the primary questions in this aspect of the research is if the East African Orogen represents the site of a major Rodinia break-up rift, or it represents a long lived accretionary margin through the late Mesoproterozoic to the Cambrian. Third, what is the origin and history of the building blocks of the East African Orogen. To address this the terranes within the orogen have been examined. These three foci combine to build a picture of the tectonic geography of the orogen, and therefore of the plate tectonic geography of this area during the Neoproterozoic (Merdith et al. 2017).

GEOLOGICAL BACKGROUND

The continents that constituted eastern Gondwana (Australia, India and East Antarctica), came together with the constituent blocks that now make up Africa and South America to form the supercontinent Gondwana (Collins and Pisarevsky, 2005b; Du Toit, 1937; Meert, 2003a; Stern, 2002a; Stern, 1994b). The East African Orogen was an extensive Himalayan-scale accretionary orogenic belt (>5000 km) that formed as a result of subduction of the Mozambique Ocean, which separated Neoproterozoic India from the blocks that made up Africa (Collins and Pisarevsky, 2005a; Fritz et al., 2013b; Johnson et al., 2011a; Meert, 2003b; Meert and Lieberman, 2008; Merdith et al., 2017). The timing and duration of arc formation along the length of this major Gondwana forming collisional zone is still only slowly being unravelled, with focus primarily on the southern arc terranes. Originally the East African Orogen was interpreted as being the product of the collision between two Neoproterozoic continental masses East and West Gondwana (Stern, 1994a). However, it was later suggested that the bimodality in zircon age distribution did not simply reflect a single collision. Considerable work has shown that Gondwana existed as smaller amalgams
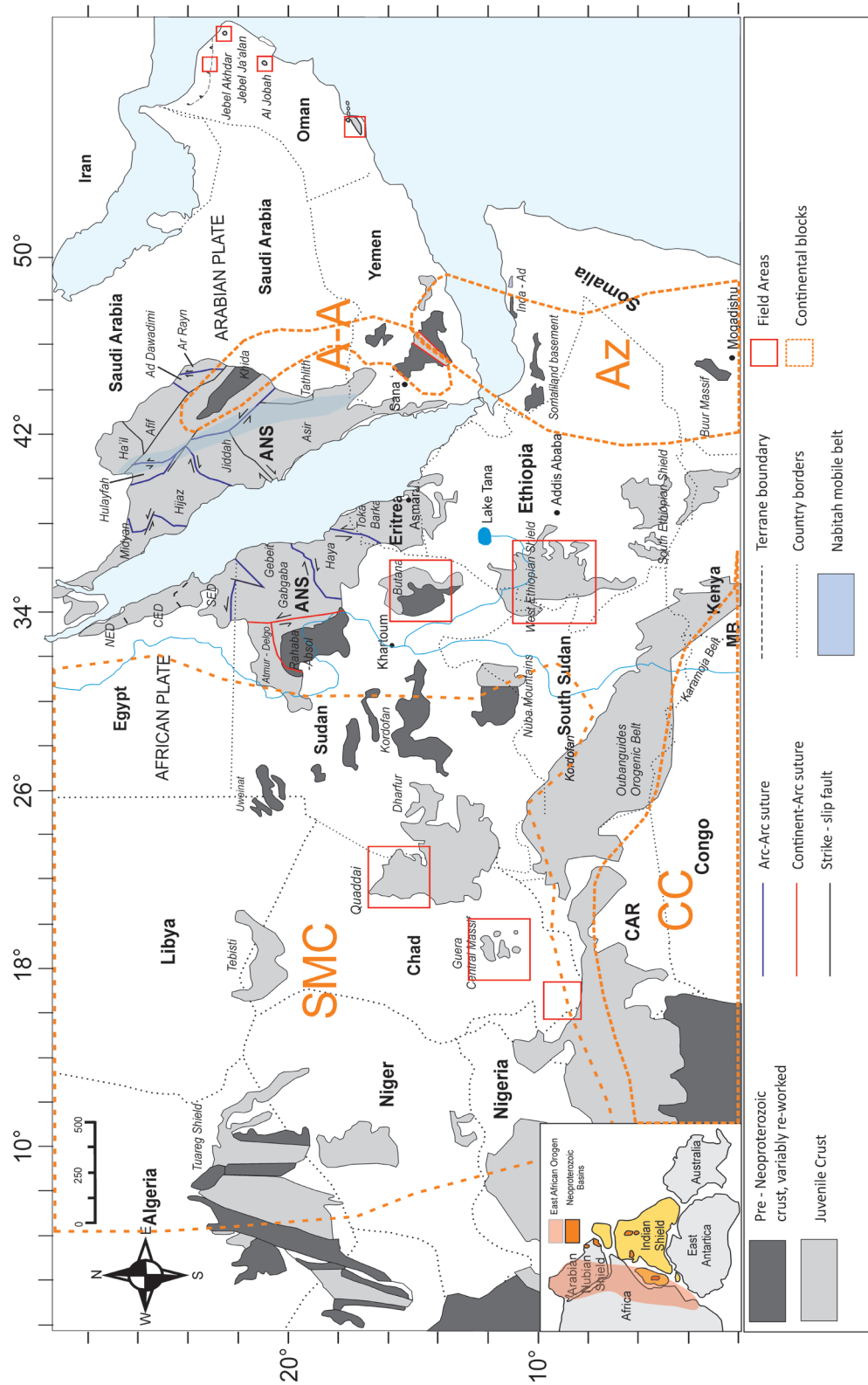
Figure 1: Location map and distribution of crustal domains in the East African Orogen. SMC, Sahara Meta-craton; ANS, Arabian Nubian Shield. MB, Mozambique Belt; CC, Congo Craton; AZ, Azania; A-A, Afif-Abas . The red boxes represent the study areas wihtin this thesis. Adapted from Johnson et al. (2011) and Blades et al. (2015).

of continents that came together during the Neoproterozoic and into the early Cambrian (Boger et al., 2006; Cawood and Buchan, 2007; Collins, 2003; Fitzsimons, 2000; Ganade de Araujo et al., 2014; McGee et al., 2014a; McGee et al., 2014b; Meert, 2003b; Pisarevsky et al., 2008; Trindade et al., 2006). A micro-continent was proposed by Collins and Windley (2002) and is interpreted to be preserved within the terranes of Madagascar, Somalia, eastern Ethiopia and Arabia. This ribbon of continental crust, named Azania after the ancient name of the East African coast (Collins and Pisarevsky, 2005), inferred to have collided with Congo/ Tanzania/Bangweulu Block and the western arc terranes of the Arabian Nubian Shield at ca. 650–630 Ma. A younger orogeny (ca. 570–520 Ma), representing the collision between Azania and Neoproterozoic India are preserved in east Madagascar and southern India (Collins and Pisarevsky, 2005a; Robinson et al., 2014; Stern, 2002b).

The East African Orogen is composed of a collage of oceanic domains and continental fragments between the Sahara-Congo-Kalahari Cratons in the west and Neoproterozoic India in the east (Collins et al., 2003; Fritz et al., 2013b; Johnson et al., 2011a; Küster et al., 2008; Meert, 2003a; Stern, 2002a; Stern, 1994b). The northern part of the orogen, the Arabian Nubian Shield, is made up of a juvenile crust that was formed in several arc terranes that began accreting at ca. 880 Ma and that coalesced thereafter (Abdelsalam and Stern, 1996a; Allen and Tadesse, 2003; Cox et al., 2012; Fritz et al., 2013b; Johnson, 2014; Kröner et al., 1991; Robinson et al., 2014; Shackleton, 1996; Stern, 1994a; Stern and Johnson, 2010). A broad band of Archaean to Palaeoproterozoic crust (2900–2000 Ma), is evident in the eastern terranes of the Arabian Nubian Shield. Despite this there is little evidence to suggest pre-Neoproterozoic

crust beneath the shield. To the south is a tract of largely older continental crust, which was extensively deformed and metamorphosed in the Neoproterozoic/Cambrian. This is known as the Mozambique Belt (Meert, 2003b; Woldemichael and Kimura, 2008; Woldemichael et al., 2010; Yibas et al., 2003a).

To the west of the northern segment of the East African Orogen is the enigmatic Sahara Metacraton, which occupies ~500,000 km^2 and extends from the Arabian Nubian Shield in the east to the Tuareg Shield to the west (Abdelsalam et al., 2002). The term 'metacraton' is used to describe a craton that has been remobilized during an orogenic event, yet is still recognisable through geochronological and isotopic characteristics (Abdelsalam et al., 2003; Abdelsalam et al., 2002; Abdelsalam and Stern, 1996b). The Neoproterozoic remobilisation of the Sahara Metacraton is prevalent in forms of deformation, metamorphism, and emplacement of igneous bodies and interpreted to be the result of partial destabilisation due to collisional related deformation (Abdelsalam et al., 2011). Details about interior regions of the Saharan Metacraton are poorly known, with much of it covered by Phanerozoic cover. The Sahara Metacraton is bounded to the east, west, and south by lithospheric scale suture zones resulting from collisional events during the Neoproterozoic and is treated as a coherent continental block in many Neoproterozoic reconstructions (e.g. Collins and Pisarevsky, 2005; Pisarevsky et al. 2006; Li et al. 2008; Merdith et al. 2017).

The terranes examined within this thesis (western Ethiopia, Chad, Sudan and Oman) provide a window into the timing and nature of Mesoproterozoic and Neoproterozoic magmatism within northern Africa and Arabia, as well as helping to further elucidate the

relationship between the Sahara Metacraton, Arabian Nubian Shield and north-west India as Gondwana coalesced.

The Western Ethiopian Shield is situated in a key transitional location between the Arabian Nubian Shield and Mozambique Belt, adjacent, and to the east of, the 'Eastern Saharan Metacraton' (Abdelsalam and Stern, 1996a). The rocks found within western Ethiopia are made up of a range of supracrustal and plutonic rocks that formed in an arc environment (Alemu, 2005; Allen and Tadesse, 2003; Ayalew et al., 1990; Ayalew and Peccerillo, 1998; Blades et al., 2015; Braathen et al., 2001; Grenne et al., 2003; Johnson et al., 2004; Kebede et al., 2001a; Kebede and Koeberl, 2003; Kebede et al., 1999; Kebede et al., 2001b; Mogessie et al., 2000; Teklay et al., 1998b; Woldemichael and Kimura, 2008; Woldemichael et al., 2010; Yibas et al., 2003b; Yibas et al., 2002). Largely, the Western Ethiopian Shield consists of high-grade gneisses, low-grade metavolcanic and metasedimentary rocks with associated mafic–ultramafic intrusions and syn- to post-tectonic gabbroic to granitic intrusions. Original work done in the area (Abraham, 1989; Ayalew et al., 1990; Wolde and Team, 1996) interpreted the eastern extension of the Sahara Metacraton to extend into the western most terranes of Ethiopia, however to date little modern geological work has been conducted in the western-most regions to confirm this.

To the north of the Western Ethiopian Shield are the exposures of Butana, 250 km south east of Khartoum. Butana forms one of the few exposures of Precambrian basement in Central Sudan and has been previously suggested to sit close to the suture zone between the juvenile Arabian Nubian Shield and the enigmatic Sahara Metacraton. However, due to the inaccessibility of the region, little geological work has been done. Not only is understanding the location of the boundary between the metacraton and the Arabian Nubian Shield important, but understanding the orogenic effects that the west (Dahomenides), the south (Oubanguides) and the east (East African Orogeny) collisional zones had on the metacraton. These orogenic events resulted in deformation, the emplacement of igneous bodies, as well as localised episodes of crust formation due to rifting, within the Sahara Metacraton. However, details about interior regions of the Saharan Metacraton are extremely poorly known, with much of it covered by Phanerozoic cover. Geochronological and isotopic data from the Sahara Metacraton are highly variable as exemplified by the wide range of ages (3100–500 Ma) (Abdelsalam et al., 2002; Küster and Harms, 1998; Küster and Liégeois, 2001; Küster et al., 2008; Liégeois et al., 1994; Stern, 1994a; Sultan et al., 1994). Within the centre of the Sahara Metacraton, there are five distinct Precambrian massifs that outcrop in Chad, Libya and Sudan; the Mayo Kebbi, the Tibesti, the Ouaddaï, the Guera and the Yade. These outcrops form a significant portion of the Sahara Metacraton, and provide some insight into the remobilisation of the craton during the Neoproterozoic amalgamation of Gondwana.

Moving to the east of the arc terranes of the Arabian Nubian Shield is the basement exposures of Oman. These basement exposures sit below the Huqf Supergroup, host to some of the oldest known petroleum source rocks, and provide a complex record of the basin's development. While the geology and nature of the Arabian Nubian Shield is relatively well known, the basement to the east is far less understood. Towards the Gulf States and Oman, sedimentary cover increases and much of Oman's basement is extensively overlain by Late Neoproterozoic to Phanerozoic

sedimentary and volcanic rocks. Many authors note the possibility that Oman represents an eastern extension of the Arabian Nubian Shield (Bowring et al., 2007; Gass et al., 1990; Immenhauser et al., 2000; Worthing, 2005), which was described by Johnson et al. (2011a) as a collage of Neoproterozoic juvenile arcs, younger sedimentary and volcanic basins, granitoid intrusions and enclaves of pre-Neoproterozoic crust. However, the absence of pre-Phanerozoic outcrop between Oman and the Arabian Nubian Shield impede any direct connection between the regions (Alessio et al., 2017; Collins and Pisarevsky, 2005b; Merdith et al., 2017; Rantakokko et al., 2014; Stern and Johnson, 2010; Worthing, 2005). It has been shown that arc accretion during the Tonian (1000-850 Ma) and early Cryogenian (Alessio et al., 2017; Allen, 2007; Allen and Leather, 2006; Bowring et al., 2007; Mercolli et al., 2006; Rantakokko et al., 2014; Rieu et al., 2007; Stern and Johnson, 2010; Whitehouse et al., 2016; Worthing, 2005), created the terranes that make up Oman. The relationship between the Omani basement and the Arabian Nubian Shield has been addressed by several authors and recent studies concluded that the Omani basement represents its own tectonic domain separate to the Arabian Nubian Shield (Alessio et al., 2017; Merdith et al., 2017; Rantakokko et al., 2014; Whitehouse et al., 2016). However, where Oman sits in the reconstruction of Gondwana is still being determined.

These basement exposures in Ethiopia, Chad, Sudan and Oman offer an opportunity to provide insight into the palaeogeography of the region during Neoproterozoic time; a period of plate reorganisation, glacial episodes and the explosion of Ediacaran fauna (Allen, 2007; Hoffman et al., 1998; Meert and Lieberman, 2008; Merdith et al., 2017).

THESIS OUTLINE

The central aim of this thesis is to develop a temporal and isotopic framework for the evolution of the northern East African Orogen, with particular focus on the terranes of western Ethiopia, Chad, Sudan and Oman. Zircon ($ZrSiO_4$) is a common accessory mineral in nature, occurring in a wide variety of sedimentary, igneous, and metamorphic rocks. Zircon can incorporate an assortment of minor and trace elements and has the ability to retain substantial chemical and isotopic information over a range of lithospheric temperatures and pressures (Corfu et al., 2003; Hanchar and Hoskin, 2003; Hoskin and Black, 2000; Hoskin and Schaltegger, 2003; Kinny and Maas, 2003). Using zircon derived from the arcs of Neoproterozoic subduction zones it is possible to further constrain: 1) the timing and location of oceanic-crust subduction; 2) whether the subduction zones involved the consumption of old continental crust or the formation of new continental crust; and 3) whether the subduction-zone magmas incorporated surface-derived rocks. These data can be integrated into the picture of the tectonic geography of the East African Orogen, and therefore of this Neoproterozoic hemisphere. This thesis has been written as a series of individual manuscripts addressing specific terranes within the East African Orogen, this leads to some repetition in the methodology sections and the interpretations.

Chapter 2

Chapter 2a is published in Precambrian Research as:

Blades, M. L., Collins, A. S., Foden, J., Payne, J. L., Xu, X., Alemu, T., Woldetinsae, G., Clark, C. & Taylor, R. J. 2015. Age and hafnium isotopic evolution of the Didesa and Kemashi Domains, western Ethiopia. Precambrian Research 270, 267-84.

Chapter 2b is written for submission to Earth Science Reviews as:

Blades, M. L., Collins, A. S., Foden, J., Payne, J. L., Holden. P., Glorie, S., Alemu, T., Woldetinsae, G. The East African Orogenic Missing Link: Age, Hafnium and Oxygen Isotopic Evolution of the Western Ethiopian Shield.

This chapter focus on the evolution of the Western Ethiopian Shield, a large tract of crust that sits in the transitional zone between the Arabian Nubian Shield and the Mozambique Belt. The aim of this chapter is to develop a temporal and isotopic framework (U–Pb, Hf and O) for the evolution of the eastern section of the Western Ethiopian Shield. These studies provide the only examination of in-situ zircon Hf and O isotopes in western Ethiopia, which is used to unravel the degree of mantle involvement in the source magmas for the Western Ethiopian Shield. Part 2a focusses on igneous and metasedimentary rocks from the eastern terranes of the Western Ethiopia Shield and provides high precision U–Pb (SHRIMP) and Hf isotopic data for the region. Part 2b is a regional, systematic study of plutonic rocks from the whole Western Ethiopian Shield, with the aim of providing constraints on magmatism and determining whether Western Ethiopia contained Palaeoproterozoic–Archaean crust as previously thought (Abraham, 1989; Ayalew et al., 1990; Wolde and Team, 1996).

Chapter 3
Chapter 3 is published in the Geological Magazine as:

Blades, M. L., Foden, J., Collins, A. S., Alemu, T., Woldetinsae, G. The Origin of Ultramafic rocks of the Tulu Dimtu Belt, western Ethiopia–Do they represent remnants of the Mozambique Ocean? Geological Magazine (In press).

Chapter 3 uses mineral geochemistry to determine the origin of ultramafic rocks found within western Ethiopia. These ultramafic bodies are of equivocal origin and sit within the Tulu Dimtu shear belt, within the Barka–Tulu Dimtu zone in western Ethiopia. Identifying the petrogenetic origin of these enigmatic rocks provides evidence for the geodynamic significance of these shear zones. Due the altered state of these ultramafic rock, their well-preserved chrome spinels and olivine provide the only reliable evidence for their source and tectonic affiliation.

Chapter 4
Chapter 4 is written for submission to Gondwana Research as:

Blades, M. L., Foden, J., Collins, A. S., Glorie, S., Alemu, T., Woldetinsae, G. The geochemical evolution of the Neoproterozoic Western Ethiopian Shield.

Chapter 4 provides a comprehensive study on the trace element and isotope geochemistry from a range of plutonic samples from the Western Ethiopian Shield to determine the palaeotectonic setting from which these rocks were formed. The Western Ethiopian Shield (WES) is made up of a range of supra-crustal and plutonic rocks that formed in Tonian volcanic arc environments, that are a representation of much of the orogen's development (Alemu, 2005; Ayalew et al., 1990; Ayalew and Peccerillo, 1998; Blades et al., 2015; Braathen et al., 2001; de Wit and Aguma, 1977; Grenne et al., 2003; Jackson, 2006; Johnson et al., 2004; Kebede et al., 2001a; Kebede and Koeberl, 2003; Kebede et al., 1999; Kebede et al., 2001b; Tadesse and Allen, 2004, 2005; Teklay et al., 1998a; Woldemichael and Kimura, 2008; Woldemichael et al., 2010). Despite being well exposed and accessible, a comprehensive study of the WES is lacking and the datasets available

mostly deal with a single suite (Ayalew et al., 1990; Grenne et al., 2003; Kebede et al., 1999). This chapter is a complimentary dataset to Chapter 2, providing further insight into the plutonic samples that were dated from western Ethiopia.

Chapter 5

Chapter 5 is written for submission to Geoscience Frontiers as:

Blades, M. L., Foden, J., Collins, A. S., Payne, J. L., Stüwe, K., Glorie, S., Abu-Alam., T.S., Hassan, M. The Age and Hafnium Isotope Evolution of Butana and Chad–Does Butana Represent the Eastern Margin of the Sahara Metacraton.

Chapter 5 examines the terranes of Butana and Chad, with the main goal to examine the nature of this extensive enigmatic region. This chapter provides some of the first U–Pb data and the only in-situ zircon Hf isotope data for the central parts of the Sahara Metacraton, Butana in Sudan, and the central and southern parts of Chad. These provide a window into the timing and nature of Mesoproterozoic and Neoproterozoic magmatism within the central regions of the Sahara Metacraton, as well as helping to further elucidate the relationship between the Sahara Metacraton and the Arabian Nubian Shield as Gondwana coalesced.

Chapter 6

Chapter 6 is written for submission to Journal of the Geological Society of (London) as:

Blades, M.L., Alessio, B.L., Collins, A.S., Foden, J., Payne, J.L., Holden, P., Glorie, S., Thorpe, B., Al-Khirbash, S. Unravelling the Neoproterozoic accretionary history of Oman, using an array of isotopic systems in zircon.

Chapter 6 characterises the basement exposures of Oman, using U–Pb, Hf and O isotopes in zircon. The position of Oman during the Neoproterozoic is still relatively unconstrained. Yet, understanding it is critical to understanding the tectonic geographic link between the Arabian Nubian Shield and Neoproterozoic India. This chapters provides some of the first Lu–Hf and O isotope data from Oman, by using these geochemical fingerprints, together with previously published data, we constrain the nature of the basement rocks in Oman. These findings are used to further understand the geological evolution of Oman during a period of major tectonic plate reorganisation, and to further elucidate its location in the Neoproterozoic Gondwanan.

Chapter 7

Chapter 7 provides a summary for the findings within this study. To provide a clear overview, a G-plates model, made in collaboration with Andrew Merdith (EarthByte group, University of Sydney), was created to demonstrate how these data combine to provide information on the evolution of the northern East African Orogen. The model presented in this study expands upon the reconstruction proposed by Merdith et al. (2017) .

REFERENCES:

Abdelsalam, M., Stern, R., 1996a. Sutures and shear zones in the Arabian-Nubian Shield. Journal of African Earth Sciences 23, 289-310.

Abdelsalam, M.G., Abdel-Rahman, E., -S.M., El-Faki, E.-F.M., Al-Hur, B., El-Bashier, F.-R.M., Stern, R.J., Thurmond, A.K., 2003. Neoproterozoic deformation in the northeastern part of the Saharan Metacraton, northern Sudan. Precambrian Research 123, 203-221.

Abdelsalam, M.G., Gao, S.S., Liégeois, J.-P., 2011. Upper mantle structure of the Saharan Metacraton. Journal of African Earth Sciences 60, 328-336.

Abdelsalam, M.G., Liégeois, J.P., Stern, R.J.,

2002. The Saharan Metacraton. Journal of African Earth Sciences 34, 119-136.

Abdelsalam, M.G., Stern, R.J., 1996b. Sutures and shear zones in the Arabian-Nubian Shield. Journal Of African Earth Sciences 23, 289-310.

Abraham, A., 1989. Tectonic history of the Pan-African low-grade belt of western Ethiopia. Ethiopian Institute of Geological Survey.

Alemu, T., 2005. Discussion of "Geological setting and tectonic subdivision of the Neoproterozoic Orogenic Belt of Tuludimtu, Western Ethiopia"[Journal of African Earth Sciences 36 (2003) 329–343]. Journal of African Earth Sciences 41, 329-332.

Alessio, B.L., Blades, M.L., Murray, G., Thorpe, B., Collins, A.S., Kelsey, D.E., Foden, J.F., Payne, J.L., Al-Khirbash, S., Jourdan, F., 2017. Origin and tectonic evolution of the NE basement of Oman: a window into the Neoproterozoic accretionary growth of India? Geological Magazine, 1-25.

Allen, A., Tadesse, G., 2003. Geological setting and tectonic subdivision of the Neoproterozoic orogenic belt of Tuludimtu, western Ethiopia. Journal of African Earth Sciences 36, 329-343.

Allen, P.A., 2007. The Huqf Supergroup of Oman: Basin development and context for Neoproterozoic glaciation. Earth Science Reviews 84, 139-185.

Allen, P.A., Leather, J., 2006. Post-Marinoan marine siliciclastic sedimentation: the Masirah bay formation, Neoproterozoic Huqf supergroup of Oman. Precambrian Research 144, 167-198.

Ayalew, T., Bell, K., Moore, J.M., Parrish, R.R., 1990. U-Pb and Rb-Sr geochronology of the western Ethiopian shield. Geological Society of America Bulletin 102, 1309-1316.

Ayalew, T., Peccerillo, A., 1998. Petrology and geochemistry of the Gore-Gambella plutonic rocks: implications for magma genesis and the tectonic setting of the Pan-African Orogenic Belt of western Ethiopia. Journal of African Earth Sciences 27, 397-416.

Blades, M.L., Collins, A.S., Foden, J., Payne, J.L., Xu, X., Alemu, T., Woldetinsae, G., Clark, C.,

Taylor, R.J., 2015. Age and hafnium isotopic evolution of the Didesa and Kemashi Domains, western Ethiopia. Precambrian Research 270, 267-284.

Boger, S.D., Wilson, C.J.L., Fanning, C.M., 2006. An Archaean province in the southern Prince Charles Mountains, East Antarctica: U-Pb zircon evidence for c.3170 Ma granite plutonism and c.2780 Ma partial melting and orogenesis. Precambrian Research 145, 207-228.

Bowring, S.A., Grotzinger, J.P., Condon, D.J., Ramezani, J., Newall, M.J., Allen, P.A., 2007. Geochronologic constraints on the chronostratigraphic framework of the Neoproterozoic Huqf Supergroup, Sultanate of Oman. American Journal of Science 307, 1097-1145.

Braathen, A., Grenne, T., Selassie, M., Worku, T., 2001. Juxtaposition of Neoproterozoic units along the Baruda–Tulu Dimtu shear-belt in the East African Orogen of western Ethiopia. Precambrian Research 107, 215-234.

Cawood, P.A., Buchan, C., 2007. Linking accretionary orogenesis with supercontinent assembly. Earth-Science Reviews 82, 217-256.

Collins, A., Fitzsimons, I., Hulscher, B., Razakamanana, T., 2003. Structure of the eastern margin of the East African Orogen in central Madagascar. Precambrian Research 123, 111-133.

Collins, A., Pisarevsky, S., 2005a. Amalgamating eastern Gondwana: The evolution of the Circum-Indian Orogens. Earth-Science Reviews 71, 229-270.

Collins, A., Pisarevsky, S., 2005b. Amalgamating eastern Gondwana: the evolution of the Circum-Indian Orogens. Earth-Science Reviews 71, 229-270.

Collins, A.S., 2003. Structure and age of the northern Leeuwin Complex, Western Australia: constraints from field mapping and U–Pb isotopic analysis. Australian Journal of Earth Sciences 50, 585-599.

Collins, A.S., Windley, B.F., 2002. The tectonic evolution of central and northern Madagascar

and its place in the final assembly of Gondwana. Journal of Geology 110, 325-339.

Corfu, F., Hanchar, J.M., Hoskin, P.W.O., Kinny, P.D., 2003. Atlas of zircon textures, in: Hanchar, J.M., Hoskin, P.W.O. (Eds.), Zircon. Mineralogical Society of America, Reviews in Mineralogy and Geochemistry, Washington, D.C., pp. 468-500.

Cox, G.M., Lewis, C.J., Collins, A.S., Halverson, G.P., Jourdan, F., Foden, J., Nettle, D., Kattan, F., 2012. Ediacaran terrane accretion within the Arabian-Nubian Shield. Gondwana Research 21, 341-352.

Du Toit, A.L., 1937. Our Wandering Continents. Oliver and Boyd, Edinburgh.

Evans, D.A.D., 2000. Stratigraphic, geochronological, and paleomagnetic constraints upon the Neoproterozoic climatic paradox. American Journal of Science 300, 347-433.

Fitzsimons, I.C.W., 2000. A review of tectonic events in the East Antarctic Shield and their implications for Gondwana and earlier supercontinents. Journal of African Earth Sciences 31, 3-23.

Fritz, H., Abdelsalam, M., Ali, K.A., Bingen, B., Collins, A.S., Fowler, A.R., Ghebreab, W., Hauzenberger, C.A., Johnson, P., Kusky, T., Macey, P., Muhongo, S., Stern, R.J., Viola, G., 2013a. Orogen styles in the East Africa Orogens: A review of the Neoproterozoic to Cambrian Tectonic Evolution. Journal of African Earth Sciences 86, 65-106.

Fritz, H., Abdelsalam, M., Ali, K.A., Bingen, B., Collins, A.S., Fowler, A.R., Ghebreab, W., Hauzenberger, C.A., Johnson, P.R., Kusky, T.M., Macey, P., Muhongo, S., Stern, R.J., Viola, G., 2013b. Orogen styles in the East African Orogen: A review of the Neoproterozoic to Cambrian tectonic evolution. Journal of African Earth Sciences.

Ganade de Araujo, C.E., Weinberg, R.F., Cordani, U.G., 2014. Extruding the Borborema Province (NE-Brazil): a two-stage Neoproterozoic collision process. Terra Nova 26, 157-168.

Gass, I.G., Ries, A.C., Shackleton, R.M., Smewing, J.D., 1990. Tectonics, geochronology and geochemistry of the Precambrian rocks of Oman, in: Robertson, A.H.F., Searle, M.P., Ries, A.C. (Eds.), The Geology and Tectonics of the Oman Region, pp. 585-599.

Grenne, T., Pedersen, R., Bjerkgård, T., Braathen, A., Selassie, M., Worku, T., 2003. Neoproterozoic evolution of Western Ethiopia: igneous geochemistry, isotope systematics and U–Pb ages. Geological magazine 140, 373-395.

Hanchar, J.M., Hoskin, P.W.O., 2003. Zircon. Mineralogical Society of America, Washington, D.C., p. 500.

Hoffman, P.F., Kaufman, A.J., Halverson, G.P., Schrag, D.P., 1998. A Neoproterozoic Snowball Earth. Science 281, 1342-1346.

Hoskin, P., Black, L., 2000. Metamorphic zircon formation by solid-state recrystallization of protolith igneous zircon. Journal of metamorphic Geology 18, 423-439.

Hoskin, P.W.O., Schaltegger, U., 2003. The composition of zircon and igneous and metamorphic petrogenesis, in: Hanchar, J.M., Hoskin, P.W.O. (Eds.), Zircon. Mineralogical Society of America, Reviews in Mineralogy & Geochemistry, Volume 53, Washington, D.C., pp. 27-62.

Immenhauser, A., Schreurs, G., Gnos, E., Oterdoom, H.W., Hartmann, B., 2000. Late Palaeozoic to Neogene geodynamic evolution of the northeastern Oman margin. Geological Magazine 137, 1-18.

Johnson, P., Andresen, A., Collins, A.S., Fowler, A., Fritz, H., Ghebreab, W., Kusky, T., Stern, R., 2011a. Late Cryogenian–Ediacaran history of the Arabian–Nubian Shield: A review of depositional, plutonic, structural, and tectonic events in the closing stages of the northern East African Orogen. Journal of African Earth Sciences 61, 167-232.

Johnson, P.R., 2014. An Expanding Arabian-Nubian Shield Geochronologic and Isotopic Dataset: Defining Limits and Confirming the Tectonic Setting of a Neoproterozoic Accretionary Orogen. Open Geology Journal 8, 3-33.

Johnson, P.R., Andresen, A., Collins, A.S., Fowler,

A.R., Fritz, H., Ghebreab, W., Kusky, T., Stern, R.J., 2011b. Late Cryogenian-Ediacaran history of the Arabian-Nubian Shield: A review of depositional, plutonic, structural, and tectonic events in the closing stages of the northern East African Orogen. Journal of African Earth Sciences 61, 167-232.

Johnson, T.E., Ayalew, T., Mogessie, A., Kruger, F.J., Poujol, M., 2004. Constraints on the tectonometamorphic evolution of the Western Ethiopian Shield. Precambrian Research 133, 305-327.

Kebede, T., Kloetzli, U., Koeberl, C., 2001a. U/Pb and Pb/Pb zircon ages from granitoid rocks of Wallagga area: constraints on magmatic and tectonic evolution of Precambrian rocks of western Ethiopia. Mineralogy and Petrology 71, 251-271.

Kebede, T., Koeberl, C., 2003. Petrogenesis of A-type granitoids from the Wallagga area, western Ethiopia: constraints from mineralogy, bulk-rock chemistry, Nd and Sr isotopic compositions. Precambrian Research 121, 1-24.

Kebede, T., Koeberl, C., Koller, F., 1999. Geology, geochemistry and petrogenesis of intrusive rocks of the Wallagga area, western Ethiopia. Journal of African Earth Sciences 29, 715-734.

Kebede, T., Koeberl, C., Koller, F., 2001b. Magmatic evolution of the Suqii-Wagga garnet-bearing two-mica granite, Wallagga area, western Ethiopia. Journal of African Earth Sciences 32, 193-221.

Kinny, P.D., Maas, R., 2003. Lu-Hf and Sm-Nd isotope systems in zircon, in: Hanchar, J.M., Hoskin, P.W.O. (Eds.), Zircon. Mineralogical Society of America, Reviews in Mineralogy & Geochemistry, Volume 53, Washington, D.C., pp. 327-341.

Kröner, A., Linnebacher, P., Stern, R., Reischmann, T., Manton, W., Hussein, I., 1991. Evolution of Pan-African island arc assemblages in the southern Red Sea Hills, Sudan, and in southwestern Arabia as exemplified by geochemistry and geochronology. Precambrian Research 53, 99-118.

Küster, D., Liégeois, J.-P., Matukov, D., Sergeev, S., Lucassen, F., 2008. Zircon geochronology and Sr, Nd, Pb isotope geochemistry of granitoids from Bayuda Desert and Sabaloka (Sudan): Evidence for a Bayudian event (920–900Ma) preceding the Pan-African orogenic cycle (860–590Ma) at the eastern boundary of the Saharan Metacraton. Precambrian Research 164, 16-39.

McGee, B., Collins, A.S., Trindade, R.I.F., 2014a. Age and Provenance of the Cyrogenian to Cambrian passive margin to foreland basin sequence of the northern Paraguay Belt, Brazil. Geological Society of America, Bulletin in press.

McGee, B., Collins, A.S., Trindade, R.I.F., Jourdan, F., 2014b. Tracking glaciation, orogenic exhumation and foreland basin evolution: Sedimentology and 40Ar/39Ar detrital muscovite provenance in the Paraguay Belt, Brazil. Sedimentology in press.

Meert, J.G., 2003a. A synopsis of events related to the assembly of eastern Gondwana. Tectonophysics 362, 1-40.

Meert, J.G., 2003b. A synopsis of events related to the assembly of eastern Gondwana. Tectonophysics 362, 1-40.

Meert, J.G., Lieberman, B.S., 2008. The Neoproterozoic assembly of Gondwana and its relationship to the Ediacaran–Cambrian radiation. Gondwana Research 14, 5-21.

Mercolli, I., Briner, A.P., Frei, R., Schönberg, R., Nägler, T.F., Kramers, J., Peters, T., 2006. Lithostratigraphy and geochronology of the Neoproterozoic crystalline basement of Salalah, Dhofar, Sultanate of Oman. Precambrian Research 145, 182-206.

Merdith, A.S., Collins, A.S., Williams, S.E., Pisarevsky, S., Foden, J.F., Archibald, D.A., Blades, M.L., Alessio, B.L., Armistead, S., Plavsa, D., Clark, C., D.R, M., 2017. A Full PLate Global Reconstruction of the Neoproterzoic Gondwana Research.

Mogessie, A., Belete, K., Hoinkes, G., 2000. Yubdo-Tulu Dimtu mafic-ultramafic belt, Alaskan-type intrusions in western Ethiopia: Its implication to the Arabian-Nubian Shield and tectonics of the Mozambique Belt. Journal of African Earth

Sciences 30, 62.

Pisarevsky, S.A., Murphy, J.B., Cawood, P.A., Collins, A.S., 2008. Late Neoproterozoic and Early Cambrian palaeogeography: models and problems. Geological Society, London, Special Publications 294, 9-31.

Rantakokko, N.E., Whitehouse, M.J., Pease, V., Windley, B.F., 2014. Neoproterozoic evolution of the eastern Arabian basement based on a refined geochronology of the Marbat region, Sultanate of Oman. Geological Society, London, Special Publications 392, 107-127.

Rieu, R., Allen, P.A., Cozzi, A., Kosler, J., Bussy, F., 2007. A composite stratigraphy for the Neoproterozoic Huqf Supergroup of Oman: integrating new litho-, chemo-and chronostratigraphic data of the Mirbat area, southern Oman. Journal of the Geological Society 164, 997-1009.

Robinson, F., Foden, J., Collins, A., Payne, J., 2014. Arabian Shield magmatic cycles and their relationship with Gondwana assembly: Insights from zircon U–Pb and Hf isotopes. Earth and Planetary Science Letters 408, 207-225.

Shackleton, R., 1996. The final collision zone between East and West Gondwana: where is it? Journal of African Earth Sciences 23, 271-287.

Stern, R.A., 2002a. Crustal evolution in the East African Orogen: a neodymian isotopic perspective. Journal Of African Earth Sciences 34, 109-117.

Stern, R.J., 1994a. Arc-Assembly and Continental Collision in the Neoproterozoic African Orogen: Implications for the Consolidation of Gondwanaland. Annual Review of Earth and Planetary Sciences 22, 319-351.

Stern, R.J., 1994b. Arc Assembly and continental collision in the Neoproterozoic East African orogeny - implications for the consolidation of Gondwana. Annual Review of Earth and Planetary Sciences 22, 319-351.

Stern, R.J., 2002b. Crustal evolution in the East African Orogen: a neodymium isotopic perspective. Journal of African Earth

Sciences 34, 109-117.

Stern, R.J., Johnson, P., 2010. Continental lithosphere of the Arabian Plate: a geologic, petrologic, and geophysical synthesis. Earth-Science Reviews 101, 29-67.

Teklay, M., Kröner, A., Mezger, K., Oberhänsli, R., 1998. Geochemistry, Pb-Pb single zircon ages and Nd-Sr isotope composition of Precambrian rocks from southern and eastern Ethiopia: implications for crustal evolution in East Africa. Journal of African Earth Sciences 26, 207-227.

Trindade, R.I., D'Agrella-Filho, M.S., Epof, I., Brito Neves, B.B., 2006. Paleomagnetism of Early Cambrian Itabaiana mafic dikes (NE Brazil) and the final assembly of Gondwana. Earth and Planetary Science Letters 244, 361-377.

Whitehouse, M.J., Pease, V., Al-Khirbash, S., 2016. Neoproterozoic crustal growth at the margin of the East Gondwana continent– age and isotopic constraints from the easternmost inliers of Oman. International Geology Review 58, 2046-2064.

Wolde, B., Team, G.-G.G., 1996. Tonalite-trondhjemite-granite genesis by partial melting of newly underplated basaltic crust: an example from the Neoproterozoic Birbir magmatic arc, western Ethiopia. Precambrian Research 76, 3-14.

Woldemichael, B.W., Kimura, J.-I., 2008. Petrogenesis of the Neoproterozoic Bikilal-Ghimbi gabbro, Western Ethiopia. Journal of mineralogical and petrological sciences 103, 23-46.

Woldemichael, B.W., Kimura, J.-I., Dunkley, D.J., Tani, K., Ohira, H., 2010. SHRIMP U–Pb zircon geochronology and Sr–Nd isotopic systematic of the Neoproterozoic Ghimbi-Nedjo mafic to intermediate intrusions of Western Ethiopia: a record of passive margin magmatism at 855 Ma? International Journal of Earth Sciences 99,

1773-1790.

Worthing, M., 2005. Petrology and geochronology of a Neoproterozoic dyke swarm from Marbat, South Oman. Journal of African Earth Sciences 41, 248-265.

Yibas, B., Reimold, W., Anhaeusser, C., Koeberl, C., 2003a. Geochemistry of the mafic rocks of the ophiolitic fold and thrust belts of southern Ethiopia: constraints on the tectonic regime during the Neoproterozoic (900–700 Ma). Precambrian Research 121, 157-183.

Yibas, B., Reimold, W.U., Anhaeusser, C.R., Koeberl, C., 2003b. Geochemistry of the mafic rocks of the ophiolitic fold and thrust belts of southern Ethiopia: constraints on the tectonic regime during the Neoproterozoic (900-700 Ma). Precambrian Research 121, 157-183.

Yibas, B., Reimold, W.U., Armstrong, R., Koeberl, C., Anhaeusser, C.R., Phillips, D., 2002. The tectonostratigraphy, granitoid geochronology and geological evolution of the Precambrian of southern Ethiopia. Journal Of African Earth Sciences 34, 57-84.

CHAPTER 2

Part A of this chapter has been published in *Precambrian Research* as:
Blades, M. L., Collins, A. S., Foden, J., Payne, J. L., Xu, X., Alemu, T., Woldetinsae,
G., Clark, C. & Taylor, R. J. 2015. Age and hafnium isotopic evolution of the Didesa
and Kemashi Domains, western Ethiopia. Precambrian Research 270, 267-84.

Part B of this chapter is written for sumbission to Earth Science Reviews as:
Blades, M. L., Collins, A. S., Foden, J., Payne, J. L., Holden. P., Glorie, S., Alemu, T.,
Woldetinsae, G. The East African Orogenic Missing Link: Age, Hafnium and Oxygen
Isotopic Evolution of the Western Ethiopian Shield.

Statement of Authorship

Title of Paper	Age and hafnium isotopic evolution of the Didesa and Kemashi Domains, western Ethiopia.
Publication Status	☑ Published ☐ Accepted for Publication ☐ Submitted for Publication ☐ Unpublished and Unsubmitted work written in manuscript style
Publication Details	Clark, C. & Taylor, R. J. 2015. Age and hafnium isotopic evolution of the Didesa and Kemashi Domains, western Ethiopia. Precambrian Research 270, 267-84.

Principal Author

Name of Principal Author (Candidate)	Morgan Blades		
Contribution to the Paper	Project fieldwork, sample preparation, data collection, processing and interpretation, manuscript design and composition, creation of figures		
Overall percentage (%)	80		
Certification:	This paper reports on original research I conducted during the period of my Higher Degree by Research candidature and is not subject to any obligations or contractual agreements with a third party that would constrain its inclusion in this thesis. I am the primary author of this paper.		
Signature		Date	06/09/201

Co-Author Contributions

By signing the Statement of Authorship, each author certifies that:

i. the candidate's stated contribution to the publication is accurate (as detailed above);

ii. permission is granted for the candidate in include the publication in the thesis; and

iii. the sum of all co-author contributions is equal to 100% less the candidate's stated contribution.

Name of Co-Author	Professor Alan Collins		
Contribution to the Paper	Guidance in fieldwork, sample preparation, data interpretation and manuscript review.		
Signature		Date	06/09/2017

Name of Co-Author	Emeritus Professor John Foden		
Contribution to the Paper	Guidance in fieldwork, sample preparation, data interpretation and manuscript review.		
Signature		Date	06/09/2017
Name of Co-Author	Dr Justin Payne		

Contribution to the Paper	Guidance in sample preparation, data collection and interpretation (Lu-Hf isotopes) and manuscript review.
Signature		Date	06/09/2017

Name of Co-Author	Xiaochen Xu
Contribution to the Paper	Collection of some U/Pb data
Signature		Date	06/09/2017

Name of Co-Author	Tadesse Alemu
Contribution to the Paper	Guidance in the field and logistics in Ethiopia
Signature		Date	06/09/2017

Name of Co-Author	Dr Girma Woldetinsae
Contribution to the Paper	Guidance in the field and logistics in Ethiopia
Signature		Date	06/09/2017

Name of Co-Author	Associate Professor Chris Clark
Contribution to the Paper	SHRIMP data collection at Curtin University, manuscript review
Signature		Date	06/09/2017

Name of Co-Author	Dr Richard Taylor
Contribution to the Paper	SHRIMP data collection at Curtin University, manuscript review
Signature		Date	06/09/2017

Please cut and paste additional co-author panels here as required.

Statement of Authorship

Title of Paper	The East African Orogenic Missing Link: Age, Hafnium and Oxygen Isotopic Evolution of the Western Ethiopian Shield. .
Publication Status	☐ Published ☐ Accepted for Publication ☐ Submitted for Publication ☑ Unpublished and Unsubmitted work written in manuscript style
Publication Details	For submission to Earth Science Reviews as: Blades, M. L., Collins, A. S., Foden, J., Payne, J. L., Holden. P., Glorie, S., Alemu, T., Woldetinsae, G. The East African Orogenic Missing Link: Age, Hafnium and Oxygen Isotopic Evolution of the Western Ethiopian Shield.

Principal Author

Name of Principal Author (Candidate)	Morgan Blades
Contribution to the Paper	Project fieldwork, sample preparation, data collection, processing and interpretation, manuscript design and composition, creation of figures
Overall percentage (%)	80
Certification:	This paper reports on original research I conducted during the period of my Higher Degree by Research candidature and is not subject to any obligations or contractual agreements with a third party that would constrain its inclusion in this thesis. I am the primary author of this paper.
Signature		Date	06/09/2017

Co-Author Contributions

By signing the Statement of Authorship, each author certifies that:

     i.   the candidate's stated contribution to the publication is accurate (as detailed above);

     ii.   permission is granted for the candidate in include the publication in the thesis; and

     iii.   the sum of all co-author contributions is equal to 100% less the candidate's stated contribution.

Name of Co-Author	Professor Alan Collins
Contribution to the Paper	Guidance in fieldwork, sample preparation, data interpretation and manuscript review.
Signature		Date	06/09/2017

Name of Co-Author	Emeritus Professor John Foden
Contribution to the Paper	Guidance in fieldwork, sample preparation, data interpretation and manuscript review.
Signature		Date	06/09/2017

Name of Co-Author	Dr Justin Payne		
Contribution to the Paper	Guidance in sample preparation, data collection and interpretation (Lu-Hf isotopes) and manuscript review.		
Signature		Date	06/09/2017

Name of Co-Author	Dr Peter Holden		
Contribution to the Paper	SHRIMP O isotope data collection and manuscript review		
Signature		Date	06/09/2017

Name of Co-Author	Dr Stijn Glorie		
Contribution to the Paper	Guidance in sample preparation, data interpretation and manuscript review.		
Signature		Date	06/09/2017

Name of Co-Author	Tadesse Alemu		
Contribution to the Paper	Guidance in the field and logistics in Ethiopia		
Signature		Date	06/09/2017

Name of Co-Author	Dr Girma Woldetinsae		
Contribution to the Paper	Guidance in the field and logistics in Ethiopia		
Signature		Date	06/09/2017

Please cut and paste additional co-author panels here as required.

ABSTRACT

The Western Ethiopian Shield (WES) forms a vast, underexplored, region of the East African Orogen. Lying towards the west of the orogen and between the dominantly juvenile Arabian Nubian Shield in the north and the high-grade Mozambique Belt to its south, it holds a key position; vital in understanding the role of the East African Orogen in Gondwana formation. The WES is made up of a range of supra-crustal and plutonic rocks that formed in Tonian volcanic arc environments. The relative timing and duration of arc formation within the East African Orogen is still slowly being unravelled and we present new U–Pb and Hf isotopic data from zircons that help to define the maximum depositional age and provenance of the protoliths to meta-sedimentary units, as well as constrain the age of igneous intrusions located within the WES. Detrital zircons, obtained from a meta-sandstone, yield provenance age peaks at 2.8–2.4 Ga, ca. 1.8 Ga and 1.15–0.84 Ga and a maximum depositional age of 838 ± 13 Ma. Hafnium isotopes from the same zircons demonstrate that both the oldest and youngest populations have broadly juvenile Hf isotopic values. However, the ca. 1.8 Ga population shows significantly evolved Hf isotopic values. Sensitive High Resolution Ion MicroProbe (SHRIMP) U–Pb ages from two granites and a felsic granite and hornblende + biotite tonalite in the Nekempt–Ghimbi region of the Western Ethiopian Shield (Didesa and Kemashi Domains) indicate two pulses of magmatism at 850–840 Ma and 780–760 Ma. Partial melting and deformation in the Didesa Terrane occurred at ca. 660 Ma. Further west, the post-tectonic Ganjii granite yielded a $^{206}Pb/^{238}U$ age of 584 ± 10 Ma, constraining pervasive deformation in the area. Age constraints on orogenesis in the Western Ethiopian Shield (ca. 660 Ma) are similar to those in NE Uganda (ca. 690–660 Ma), but are older than the Ediacaran peak orogenesis reported from the Southern Ethiopian Shield, Eritrea and northern Ethiopia and from SE Kenya. This suggests that closure of the western Mozambique Ocean involved progressive volcanic-arc accretion to the active margin of Cryogenian–Ediacaran Africa.

INTRODUCTION

The East African Orogen (EAO) is a Neoproterozoic to early Cambrian mobile belt that reflects the collision between Neoproterozoic India and the African Neoproterozoic continents——it is the major collisional orogeny that formed as central Gondwana coalesced (Collins and Pisarevsky, 2005; Fritz et al., 2013; Jacobs and Thomas, 2004; Johnson et al., 2011; Meert, 2003). The EAO provides a complex record of magmatic and tectonothermal events that mark the closure of a major ocean basin (the Mozambique Ocean). The orogen encompasses vast tracts of juvenile Neoproterozoic crust (Stern, 2002) that represent volcanic arc magmatism that formed by subduction of the Mozambique

Ocean. Despite the extent of this magmatism, the timing and duration of arc formation is only slowly being resolved, with most work so far focused in the north of the orogen (Saudi Arabia, Egypt; summarized by Johnson et al. 2011), or in its southern extent (Madagascar, Tanzania; summarized in Fritz et al. 2013). The Western Ethiopian Shield (WES) is one of the largest continuous outcrop tracts in the EAO and lies between these better studied north and south regions. It fact it forms an interface between the lower crustal rocks found in the southern East African Orogen (known as the Mozambique Belt), and upper crustal rocks of the northern Arabian Nubian Shield (Fritz et al., 2013; Johnson et al., 2011; Robinson et al., in press; Robinson et al., 2014; Stern, 1994)

(Fig. 1). The WES contains poorly dated and geochemically characterised tectonic blocks that host significant ore systems (Mogessie et al., 2000; Tadesse and Allen, 2004, 2005; Yibas et al., 2003).

The aim of this study is to develop a temporal and isotopic framework for the evolution of the eastern section of the extensive WES that can help relate the WES to the Arabian Nubian Shield, the Mozambique Belt and/or the enigmatic Sahara metacraton (Figs. 1 & 2)

and better elucidate the nature and evolution of Neoproterozoic ocean plate tectonics within the Mozambique Ocean. To do this, we use in-situ U–Pb zircon geochronology to a) date the protolith crystallization and metamorphism of upper amphibolite meta-igneous rocks in the Didesa Domain (Fig. 2), b) better constrain the maximum depositional age and provenance of metasedimentary from the Kemashi Domain (Fig. 2), and, c) constrain the termination of orogenesis by dating the crystallization of
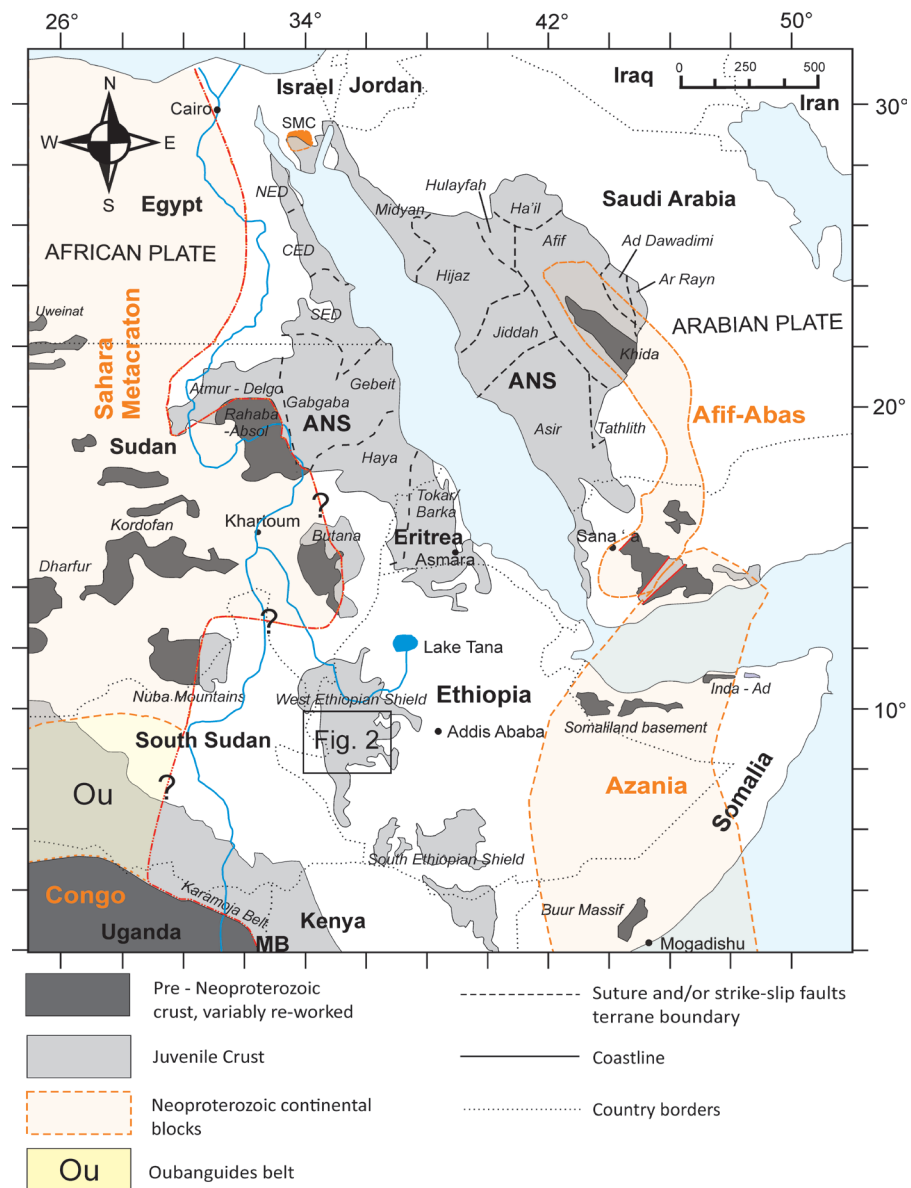
Figure 1: Location map and distribution of crustal domains in the East African Orogen. SM, Sahara Metacraton; ANS, Arabian Nubian Shield. MB, Mozambique Belt. The black box represents the map area in figure 2. Adapted from Johnson et al. (2011) and Blades et al. (2015).

the post-tectonic Ganjii Granite. This study provides the only in-situ zircon Hf isotope study in western Ethiopia, which is used to unravel the degree of mantle involvement in the source magmas of both the metaigneous and metasedimentary zircons. Combined, these help to further constrain the Neoproterozoic evolution of the WES.

GEOLOGICAL BACKGROUND
East African Orogen
The East African Orogen (Stern, 1994) preserves a complex history of intra-oceanic and continental margin, magmatic and tectonothermal events. Many of the rocks found in the orogen formed in volcanic arcs during the Neoproterozoic subduction of the Mozambique Ocean (Collins and Pisarevsky, 2005; Fritz et al., 2013; Johnson et al., 2011; Meert, 2003; Meert and Lieberman, 2008), which separated Neoproterozoic India from the Neoproterozoic continents that formed Gondwanan Africa (Collins and Pisarevsky, 2005; Fritz et al., 2013; Johnson et al., 2011; Meert, 2003; Meert and Lieberman, 2008). However, the timing and duration of arc formation along the >5000 km strike length of the orogen is only slowly being unraveled. Orogenesis was originally interpreted by Stern (1994) to be the product of collision between two Neoproterozoic continental masses, East Gondwana (India–Australia–Antarctica) and West Gondwana (Africa–South America). However, Meert and Van Der Voo (1997) suggested that a single collision model was too simple as they identified bimodality in the zircon age distribution within the orogeny. At the same time, considerable work across Gondwana suggested that East and West Gondwana did not exist as Neoproterozoic continents, but represent amalgams of smaller, Australia-sized, continents, which came together during the Neoproterozoic and into the early Cambrian

(Boger et al., 2006; Cawood and Buchan, 2007; Collins, 2003; Fitzsimons, 2000; Ganade de Araujo et al., 2014; McGee et al., 2014a; McGee et al., 2014b; Meert, 2003; Pisarevsky et al., 2008; Trindade et al., 2006). Collins and Windley (2002) proposed the existence of a Neoproterozoic continent, which was called Azania by Collins and Pisarevsky (2005), to explain the bimodality of East African Orogen ages. Azania is interpreted to be preserved within the East African Orogen of Madagascar, Somalia, eastern Ethiopia and Arabia and was suggested to have collided with the Congo/Tanzania/Bangweulu Block, and with the previously amalgamated western Arabian-Nubian Shield, at ca.650–630 Ma to form the East African Orogeny (Collins and Pisarevsky, 2005; Robinson et al., 2014; Stern, 2002). A younger (ca. 570-520 Ma) orogeny was also proposed to result from collision of Azania/Africa with Neoproterozoic India (Collins and Pisarevsky, 2005), and its effects were focused to the east of the East African Orogen, in east Madagascar and southern India (Clark et al., 2009; Collins et al., 2014; Collins et al., 2007; Plavsa et al., 2012; Plavsa et al., 2014).

The East African Orogen is subdivided into two terrains based on lithological and metamorphic differences. To the north lies the broadly juvenile Arabian Nubian Shield (Johnson et al., 2011), which is dominated by low grade volcano-sedimentary rocks in association with plutons and ophiolitic remnants (Abdelsalam and Stern, 1996; Allen and Tadesse, 2003; Cox et al., 2012; Kröner et al., 1991; Robinson et al., 2014; Shackleton, 1996; Stern, 1994). To the south is the Mozambique Belt, which is a tract of largely older continental crust that was extensively deformed and metamorphosed in the Neoproterozoic/Cambrian (Meert, 2003; Woldemichael and Kimura, 2008; Woldemichael et al., 2010; Yibas et al., 2003). The WES is situated in a key location, close
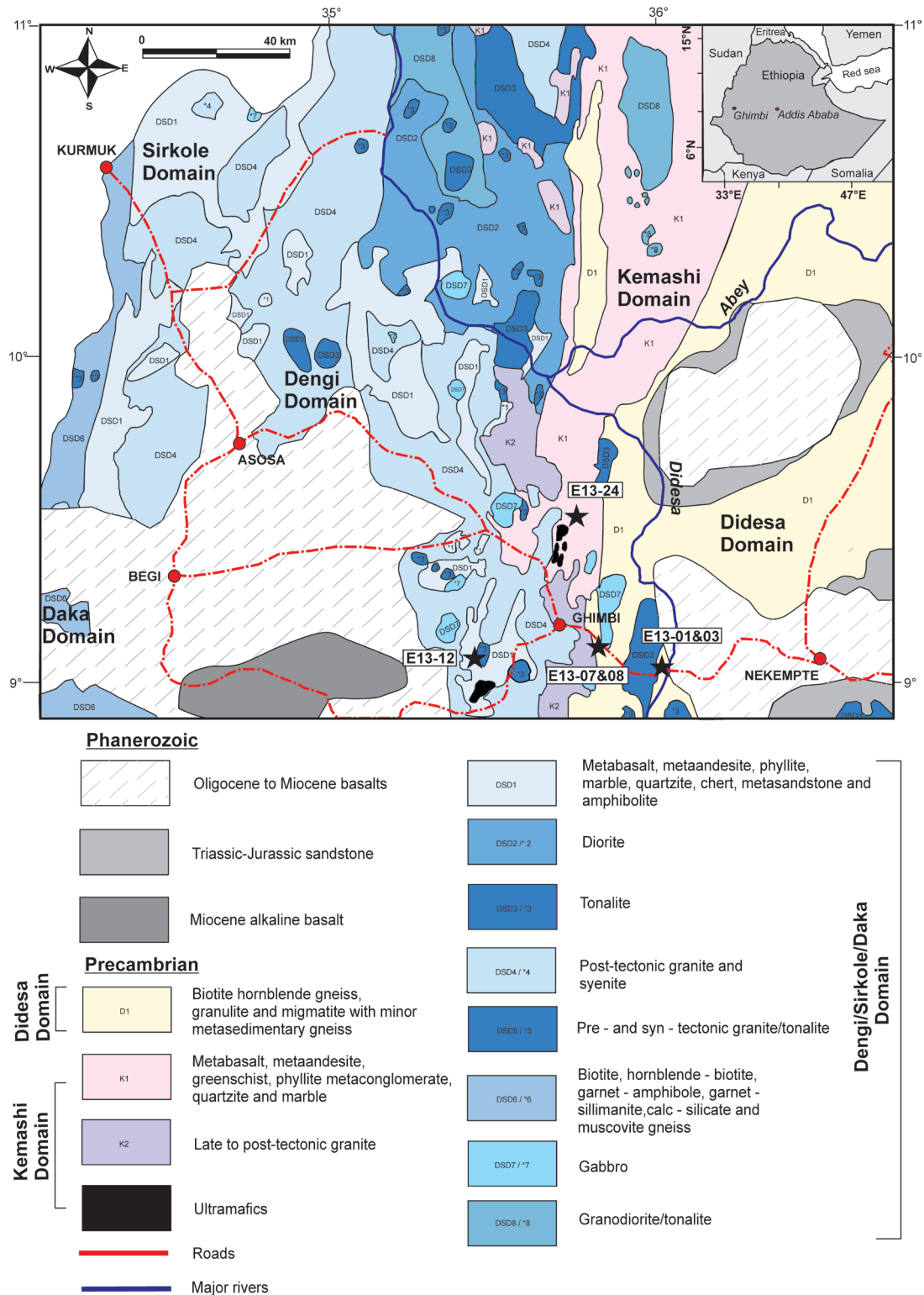
Figure 2: Simplified geological map of the area of study in western Ethiopia. Adapted from geological map of western Ethiopia (2nd edition), scale 1:2 000,000, published by the Geological Survey of Ethiopia(1996). The Dengi, Sirkole and Daka domains are separated either by a tectonic contact or are isolated by Phanerozoic cover.

to the transition between the Arabian Nubian Shield and Mozambique Belt, adjacent, and east of the 'Eastern Saharan Meta-craton' (Abdelsalam and Stern, 1996).

Western Ethiopia

Western Ethiopia is a metamorphic terrane, which consists of high-grade gneisses, low-grade metavolcanic and metasedimentary rocks with associated mafic–ultramafic intrusions and syn- to post-tectonic gabbroic to granitic intrusions. Many lithotectonic subdivisions have been proposed for the region (see Alemu 2005 for a summary). Here we use the division of Allen and Tadesse (2003), which is based largely on domains of shared lithological assemblages and geological histories. Allen and Tadesse (2003) defined the rocks of the WES the Tuludimtu Orogenic Belt (here shortened to the non-genetic 'Tuludimtu Belt'), the central region of which they subdivided into five litho-tectonic domains, interpreted to have formed during the amalgamation of western Gondwana before the final closure of the Mozambique Ocean (Allen and Tadesse, 2003). These five domains occur within the study area and include; the Didesa, Kemashi, Dengi, Sirkole and Daka Domains (Fig. 2). The Didesa Domain forms the eastern boundary of the study area. It consists of amphibolite-facies paragneiss and orthogneiss, intruded by Neoproterozoic intrusive rocks. The Didesa Domain was interpreted by Allen and Tadesse (2003) to represent the eastern foreland of the Tuludimtu Belt. To the west of the Didesa Domain, the Kemashi Domain forms a narrow N–S strip that is 10–15 km wide (Fig. 2). This domain is characterised by a sequence of metasedimentary rocks whose protoliths are interpreted to have a marine origin, including pelagic sediments, cherts, and quartzites, interlayered with abundant mafic to ultramafic volcanic material, all metamorphosed to upper

greenschist/epidote–amphibolite facies. Ultra mafic/mafic plutonic rocks within the Kemashi Domain have been interpreted to represent an ophiolite sequence (Abdelsalam and Stern, 1996; Allen and Tadesse, 2003; Ayalew et al., 1990; Stern, 2002; Tadesse and Allen, 2005), named the Tuludimtu Ophiolite by Tadesse and Allen (2005) (Fig. 2). However, others have suggested that there is a lack of geochemical evidence to support the presence of ophiolites in the Western Ethiopian Shield (Alemu, 2005; Braathen et al., 2001; Grenne et al., 2003; Mogessie et al., 2000; Woldemichael and Kimura, 2008; Woldemichael et al., 2010) and have instead suggested that the ultra mafic bodies represent Alaskan-type, concentrically zoned intrusions, which were emplaced into an extensional arc or back arc environment (Braathen et al., 2001; Grenne et al., 2003; Mogessie et al., 2000). The Dengi Domain to the west of the Kemashi Domain (Fig. 2) is ~120 km wide and is characterized by a deformed and metamorphosed volcano–sedimentary sequence and the Jamoa-Ganti orthogneiss. There are a number of intrusive bodies incorporated in this domain. Allen and Tadesse (2003) interpreted the Dengi Domain to represent a volcanic arc sequence related to closure of the ocean represented by the Tuludimtu Ophiolite to the east. The Sirkole Domain occupies the northwestern portion of the study area, west of Asosa (Fig. 2) and extends into Sudan. This region is composed of gneissic and volcano-sedimentary rocks, intruded by granites. Allen and Tadesse (2003) interpreted this suite to represent a series of interleaved N–S striking sheets. The Daka Domain lies in the southwest corner of the region. The relationship between the Daka Domain and the Sirkole and Dengi Domains is unclear as it is separated from these by Cenozoic cover (Allen and Tadesse, 2003). The Daka Domain was interpreted by Allen and Tadesse (2003) to

represent the western basement margin to the Tuludimtu Belt, which they suggested consisted of pre-Neoproterozoic basement gneisses.

SAMPLE DESCRIPTIONS
E13.01: K-feldspar-rich granite,
E13.03: Quartzo–feldspathic Gneiss
(Didesa River, N 9 01.865 E36 09.304)
Both samples are located in the Didesa River,

located approximately 240 km west of Addis Ababa.

Sample E13.01 is from a finely crystalline, homogeneous, K-feldspar-rich granite. The granite is the structurally youngest rock type sampled from this location (Fig. 3 b–c). Both a granitic pegmatite and micro-granite crosscut this rock type as seen in figure 3c. K-feldspar rich granite (Fig 4 a–b) is holocrystalline
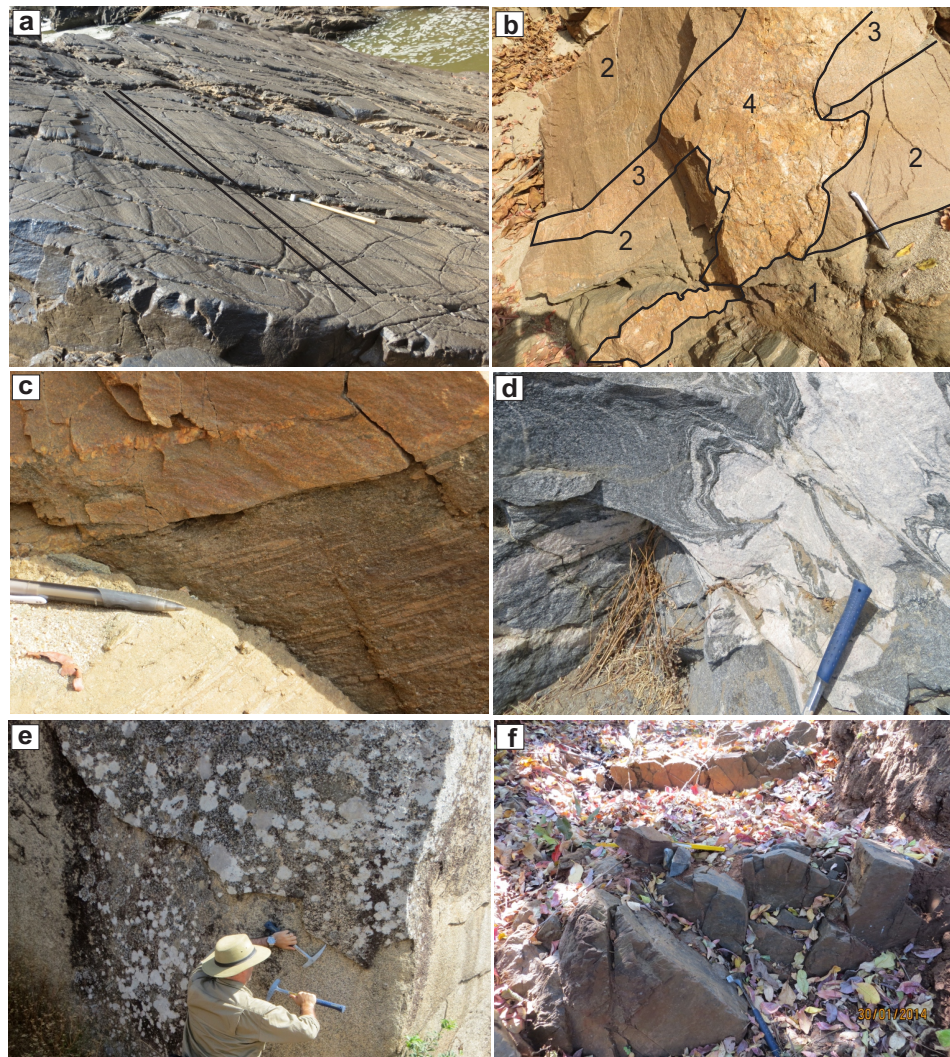
Figure 3: Field photos of each sample analysed. a–c) photos demonstrating the field relationships at the Didesa River outcrop. (a) Foliated gneiss, the structurally oldest unit at the outcrop. The prominent mineral aggregate lineation is marked by the black lines. Numbers used in (b) indicate the relative timing of each crosscutting relationship, as seen in the field. 2: homogeneous K feldspar rich granite (E13.01), 3 :fine grained granite dyke that cross cuts the homogeneous K-feldspar rich granite and 4: late course grained granite dyke, which cross cuts all lithologies. c) Cross cutting relationship between the foliated gneiss and the macroscopically younger homogeneous K-feldspar rich granite. (d) Rocks in the Ethiopian Road Authority Quarry showing medium grained felsic granite intermingling with the hornblende biotite rich tonalite. (e) The post tectonic Ganjii granite. (f) Meta-quartz arenite from Tere Dimtu village .

and phaneritic with subhedral grain shapes. Mineralogically it has biotite (without a preferred orientation), opaque minerals (mainly pyrite), K-feldspar (sanidine and orthoclase) and Na-plagioclase and quartz.

Quartzo-feldspathic Gneiss (E13.03) is the oldest rock structurally and is foliated with a distinct mineral aggregate banding and alignment of the quartz and feldspars (Fig. 3a–c). Foliation strikes approximately E-W and is cut by late N–S striking faults. In outcrop, this S-L tectonite is seen cut by the homogenous microgranite represented by sample E13.01 (Fig. 3). In thin section (Fig. 4 c–d) the sample is holocrystalline with subhedral, phaneritic grains. Dominant minerals are quartz, feldspar and biotite (distinct alignment/foliation); in comparison to the above section there is a higher abundance of biotite and a higher proportion of plagioclase rather than K-rich feldspar.

E13.07 and E13.08: Hornblende, biotite Tonalite and Felsic Granite
(Ethiopian Road Authority Quarry, N9 09.939 E35 37.500)
Samples E13.07 and 08 were taken from the same outcrop and are examples of pre- syn-tectonic magmatism, at the Ethiopian Road Authority Quarry, located about 20 km west of Didesa River. Field observations suggest that the outcrop represents a felsic magmatic pluton with entrained schlieran (Fig. 3d). Samples were taken from both the felsic magma and the hornblende + biotite tonalite, to determine any age difference. Petrography of E13.07 (Fig. 4 e–f) shows that the section is holocrystalline with phaneritic, subhedral grains and confirms that the darker bands are rich in biotite, amphibole (hornblende), epidote and both plagioclase and K-feldspar and the minor amounts of sphene. Sample E13.08 is holocrystalline, phaneritic and contains large amounts of quartz, feldspars (both plagioclase and alkali feldspars). There

are minor amounts of biotite present, which do not have a preferred orientation (Fig. 4 g–h).

E13.12: Post Tectonic Ganjii Granite
(N8 56.746 E35 27.240)
Sample E13.12 was collected from the undeformed Ganjii granitoid, is representative of the post-tectonic phase. This is primarily a monzogranite, with subordinate monzodiorite. The monzogranite is porphyritic, with K-feldspar megacrysts. The granitoid is cut by NE-striking sub-vertical fractures and joints. These joints are often filled by micro-granite dykes. The Ganjii monzogranite is generally composed of plagioclase, K-feldspar, quartz, biotite, and hornblende. K-feldspar is perthitic microcline, often poikilitic (Fig. 4 i–j).

E13.24a: Meta-quartz arenite
(Doro Dimtu, N9 26 12.1 E35 42.42.1)
Sample E13.24a was sourced from a meta-quartz arenite located near the Doro Dimtu Village. These meta-sedimentary rocks are located in the major Tulu-Dimtu shear zone. To date there has been little to no work done on the meta-sedimentary units of the Western Ethiopian Shield and therefore gaining any understanding into the provenance and maximum depositional environment of this area is of importance. This sample contains sub-rounded, sand-sized grains, with minimal feldspar and lithic fragments. The sample displays dark, heavy mineral banding, and contains minor amounts of pyrite.

ANALYTICAL TECHNIQUES
U–Pb zircon geochronology
Zircon grains were extracted from crushed rocks using standard magnetic and heavy liquid techniques. Mineral separates were hand-picked and mounted in epoxy resin. The mounts were polished to expose the minerals; carbon coated and imaged using a cathodoluminescence (CL)
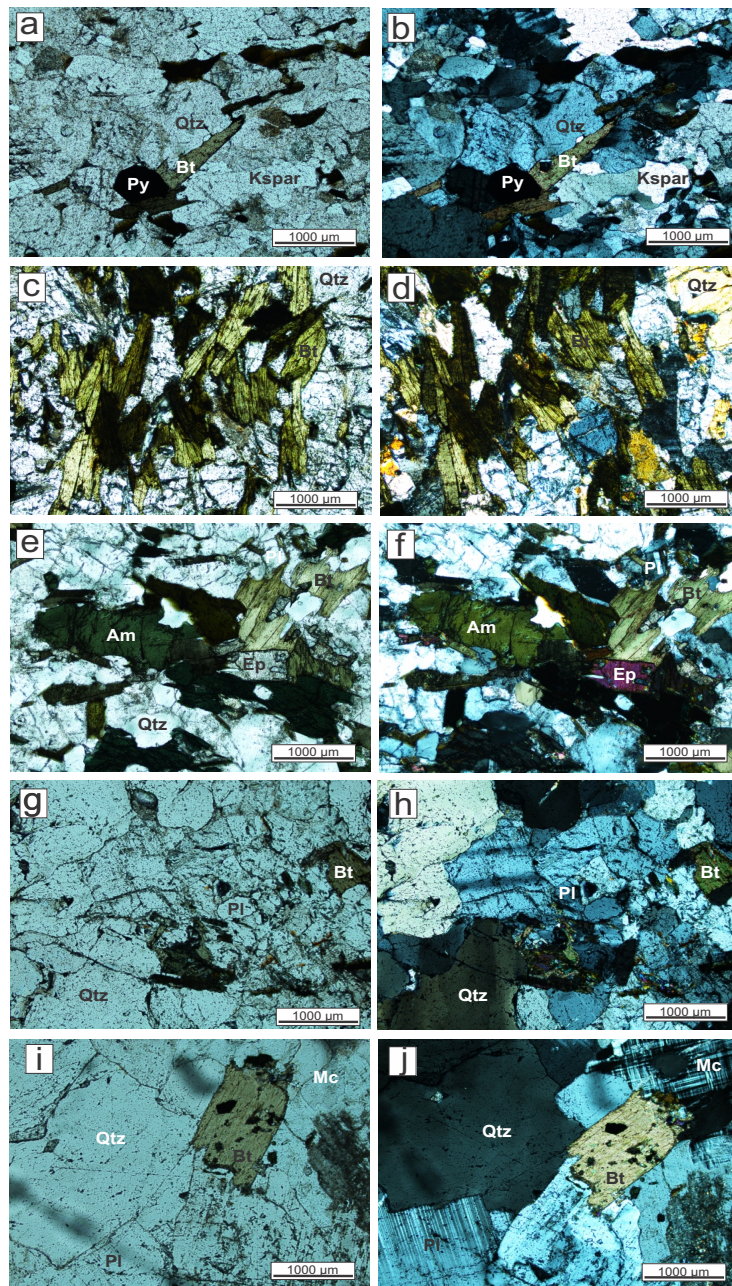
Figure 4: Thin sections of the igneous samples collected in the eastern section of the Western Ethiopian Shield. (a–b) Sections from homogeneous K-feldspar rich granite (E13.01); (a) plane polarised light, (b) cross polarised light. Mineralogically this granite is made up of K-feldspar (Kspar), quartz (Qtz), plagioclase (Plag) with minor amounts of opaque minerals. These have been interpreted as pyrite (py) using hand specimen. (c–d) Section from the foliated gneiss (E13.03); (c) plane polarised light, (d) crossed polarised light. The foliated gneiss has distinct bands of biotite that have been aligned, plagioclase (plag), K-feldspar (Kspar), quartz (Qtz) are also dominant minerals. (e–f) Hornblende, biotite tonalite (E13.07); (e) plane polarised light (f)crossed polarised light. It is recrystallised, holocrystalline, phaneritic and composed of biotite (bt), amphibole (hornblende, Am), epidote (Ep), quartz (Qtz), K-feldspar (Kspar), plagioclase (Pl) and sphene. (g-h) Felsic granite (E13.08); (g) plane polarised light,(h) crossed polarised light. The sample is holocrystalline and phaneritic composed of quartz (Qtz), K-feldspar (Kspar), plagioclase (Pl) and biotite (Bt). (i ─j) Ganjii granite, holocrystalline and phaneritic and composed of plagioclase (Pl), K-feldspar (Kfs), quartz (Qtz), biotite (Bt), and hornblende (Hbl). K-feldspar is perthitic microcline, often poikilitic.

detector on a scanning electron microscope at Curtin University, Perth, to identify compositional domains that were suitable for analysis. U–Th–Pb isotopic data were collected from domains interpreted to be magmatic or new metamorphic growth using a Sensitive High Resolution Ion Micro-Probe (SHRIMP II) at the John de Laeter Centre of Mass Spectrometry, Perth, Western Australia. The sensitivity for Pb isotopes in zircon using SHRIMP II was 20 cps/ppm/nA, the primary beam current was 2.5–3.0 nA and mass resolution was ca. 5000. Correction of measured isotopic ratios for common Pb was based on the measured ^{204}Pb in each sample and typically represented a <1% correction to the ^{206}Pb counts. Pb/U isotopic ratios were corrected for instrumental discrimination using the observed co-variation between Pb^+/U^+ and UO^+/U^+ (Hinthorne et al., 1979; Compston et al., 1984) determined from interspersed analyses of the primary zircon standard BR266, a zircon megacryst from Sri Lanka with an age of 559 ± 0.3 Ma, a ^{206}Pb/^{238}U ratio of 0.09059, and U and Th contents of 909 ppm and 201 ppm respectively (Stern, 2002). The secondary zircon standard used was Temora, which yielded a mean ^{206}Pb/^{238}U mean age of 413.8 ± 5.9 Ma, with a MSWD of 1.5. This is compared to 416.75 ± 0.24 Ma that was determined by Black et al. (2003). Data were reduced using SQUID2 and Isoplot 4.1 (Ludwig, 2001, 2003).

Zircon Lu–Hf Isotope analysis

Analytical methods for zircon Lu–Hf isotope analysis follow Payne et al. (2013). Analyses were undertaken using a New Wave UP-193 ArF excimer laser attached to a Thermo-Scientific Neptune Multi-Collector ICP-MS at the University of Adelaide. The bulk of analyses were carried out using a beam diameter of 50 μm for large and a minimum of ~25 μm for smaller grains. Typical ablation times were 40–

100 s using a 5 Hz repetition rate, a 4 ns pulse rate, and an intensity of ca. 10 J/cm^2. Zircons were ablated in a helium atmosphere, which was then mixed with argon upstream of the ablation cell.

Reduction of zircon data was undertaken using a macro-driven Hf isotope data reduction Excel spreadsheet, HfTRAX (Payne et al., 2013). The data were normalised to ^{179}Hf/^{177}Hf = 0.7325, using an exponential correction for mass bias. Yb and Lu isobaric interferences on ^{176}Hf were corrected for following the methods of Woodhead et al. (2004).

The accuracy of the Yb and Lu corrections has been demonstrated by repeated analysis of standard zircons with a range in ^{176}Yb/^{177}Hf and ^{176}Lu/^{177}Hf (Griffin et al., 2006). Before and during the analysis of unknowns, standards were analysed to check instrument performance and stability. The primary zircon standard used was Plešovice, which yielded a mean ^{176}Hf/^{177}Hf ratio of 0.282470 ± 0.000015. This compares to the published value of 0.282482 ± 0.000013 (2SD) by Sláma et al. (2008). Values for ε_{Hf}(t), and TDMc were calculated using ^{176}Lu decay constant after Scherer et al. (2001). TDM crustal was calculated using the methods of Griffin et al. (2002) with an average crustal composition of ^{176}Lu/^{177}Hf = 0.015 (Griffin et al., 2002).

RESULTS
Zircon U–Pb geochronology

SHRIMP analytical data are presented in supplementary material. All results are plotted as 204 – corrected ages (Ludwig et al., 2004), in which analyses have been categorised into their broadly identified internal structure based on CL imaging and grains used for concordia age calculations (Fig. 6). Data are presented using inverse concordia diagrams (^{207}Pb / ^{206}Pb v. ^{238}U/^{206}Pb, Fig. 7). All age uncertainties are quoted at the two sigma level and MSWDs are
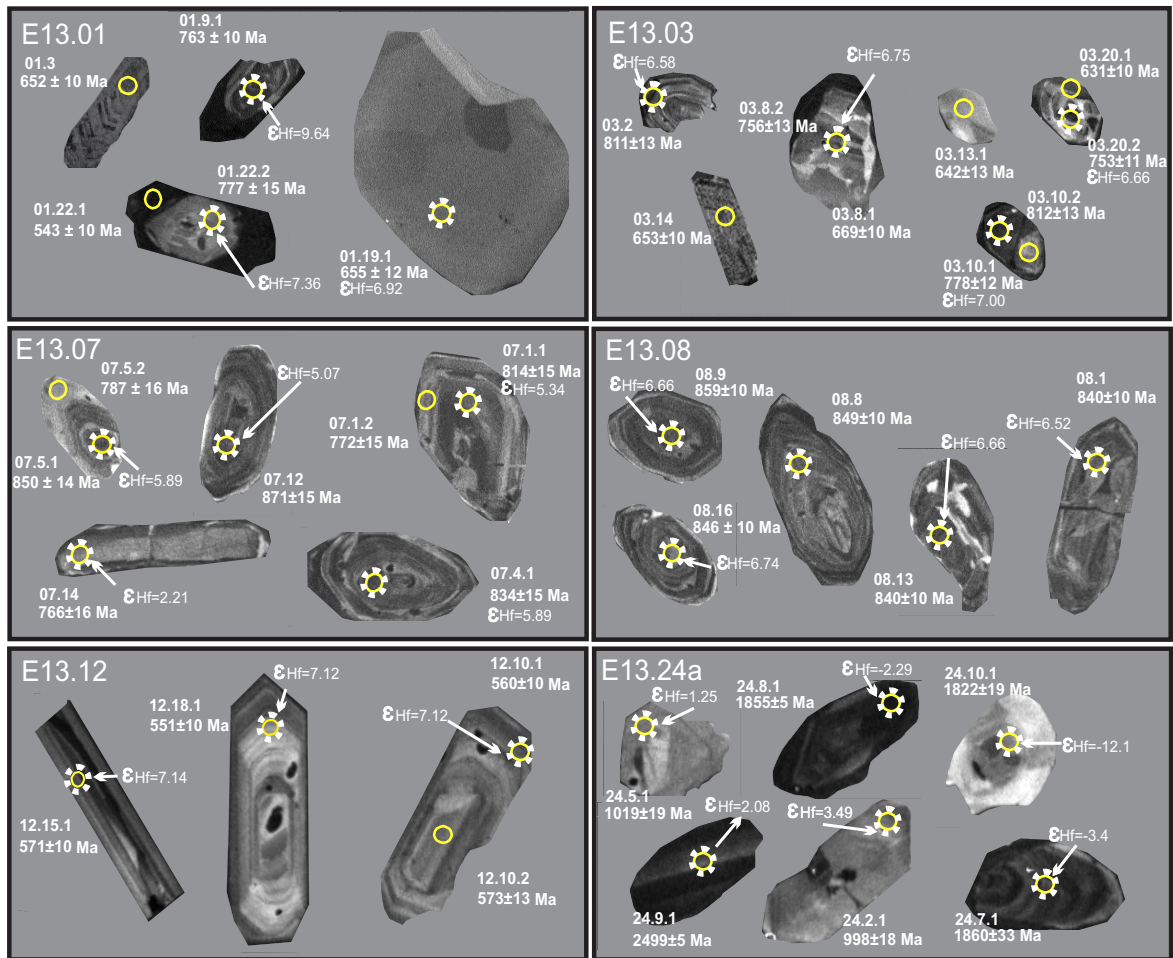
Figure 5: CL images showing both SHRIMP and Hf spots with corresponding data. CL images for E13.01 and 03, a quartz-feldspathic gneiss and K-feldspar rich granite, E13.07 and 08, felsic granite and hornblende, biotite tonalite, and E13.12 the post tectonic Ganjii granite, Western Ethiopia. Zircon morphology is varied with pronounced prismatic and acicular shapes, typical of igneous zircons. The low response (dark) suggests higher trace element content. Some zircons show oscillatory zonation patterns typical of formation in a magma chamber. However, recrystallization transgressive zones, fronts and minor convolution are present. Xenocryst cores with a metamorphic overgrowth are characteristic in E13.01, 03 and 07. E13.24a CL images for E13.24a, a meta-quartz-arenite, taken from Western Ethiopia. E13.24a has a typical irregular and partially rounded detrital shape. The low response (dark) suggesting a higher uranium content. Apatite and titanite are abundant within this sample.

quoted for each calculated age.

E13.03: Quartzo-feldspathic Gneiss (Didesa River, N 9 01.865 E36 09.304)

Zircons in sample E13.03 generally have a light brown hue; however, in some cases they display a pale pink colour. Crystal lengths range from c. 80μm–200μm. and zircon aspect ratios vary from a stubby (1:1) to elongated prismatic (4:1). Some of the zircons occur as

fragments of the original grain (Fig. 5b). They can be divided into two broad morphological groups. Group 1 is dominated by prismatic zircon with well-developed pyramidal crystal faces and an aspect ratio of ca. 4:1. Most grains are poorly luminescent under CL and have faint luminescent bands, similar to features that develop as a result of solid-state recrystallisation (Hoskin and Black, 2000). This faint zoning is interpreted to reflect trace

element geochemical variations in the original zircon that have been partially preserved after subsequent recrystallization (Fig 5b). Group 2 contains zircons of varying morphology, from elliptical to prismatic, with aspect ratios between 1:1 and 4:1. These grains are brightly luminescent and preserve distinct oscillatory zonation. Dark luminescent rims are seen mantling some of these grains (Fig. 5b).

Twenty eight zircons were analysed, targeting both the darkly luminescent rims and some cores. Fourteen analyses were <10% discordant and show a range of $^{206}Pb/^{238}U$ ages between 800–630 Ma. Two distinct age groups are present with ages between ca. 669–630 Ma and 812–742 Ma. On the 204 - $^{206}Pb/^{238}U$ corrected age plot there are two defined plateaus suggesting that the younger age is not related to Pb-loss. This contrasts the 6 younger analyses with apparently younger ages that are interpreted to represent some Pb-loss (Fig. 6). The older grains exhibit well-defined zoning characteristic of zircon grown from a melt (Hoskin and Black, 2000). Using all near concordant analyses yields a $^{206}Pb/^{238}U$ age of 767±22 Ma (MSWD = 5.3). The relatively large MSWD suggests that the analyses do not form a single age and define an array along the concordia line between 811–740 Ma. This spread is interpreted to be the result of post-formation lead loss, with these zircons defining a discordia indistinguishable from the concordia curve (Fig. 7a). We therefore use the four oldest grains, which are interpreted as best representing their time of formation and which statistically define a good population. These analyses yield a $^{206}Pb/^{238}U$ age of 794±30 Ma (MSWD = 2.2). To confirm the $^{206}Pb/^{238}U$ age the mean was recalculated using all concordant $^{206}Pb/^{207}Pb$ ages, this yielded an age of 782±33 Ma (MSWD = 1.6). This age is used as the best estimate for the time of formation of these zircons due to the lower MSWD. The

younger analyses (669–630 Ma) were taken from dark rims mantling the grains and from non-luminescent, faintly-zoned zircons, are interpreted to represent recrystallisation during to metamorphism. Connelly (2001) has documented very subtle metamorphic recrystallization, which has led to a gradual but homogeneous fading of original growth zoning and these observations have been correlated to the younger population. These yield a weighted average $^{206}Pb/^{238}U$ age of 660±8 Ma (MSWD = 0.8) as well as a $^{206}Pb/^{207}Pb$ age of 664±18 (MSWD = 1.2). The interpretation that the younger 660 Ma age is related to a metamorphic event is supported by the presence of a core–rim relationship seen in Fig. 5 and by the presence of sub-rounded, resorbed zircon, which has a slightly discordant $^{206}Pb/^{238}U$ age of 642±13 Ma. Thorium is less compatible in zircon than uranium (Hoskin and Black, 2000) and therefore can be used as a broad indicator of metamorphic recrystallization as thorium is often preferentially expelled from zircon with respect to uranium. The older analyses have a marginally higher Th/U ratio and uranium concentration, supporting the interpretation that the younger zircon grains have expelled thorium, some uranium (and presumably lead) during recrystallisation (Fig. 7). The CL appearance, Th/U ratio and U concentration suggests that the older grains denote the protolith crystallisation age (782 ±33 Ma), whilst the younger grains represent the partial recrystallisation of the zircon during metamorphism at 660±8 Ma.

E13.01: K feldspar rich granite (Didesa River, N 9 01.865 E36 09.304)

Zircon grains in sample E13.01 vary in colour from a pale yellow/pink hue to clear and colourless. Crystal lengths range from ca. 90 µm–180 µm, with the dominant aspect ratio being ca. 4:1 with some more equant, rounded,
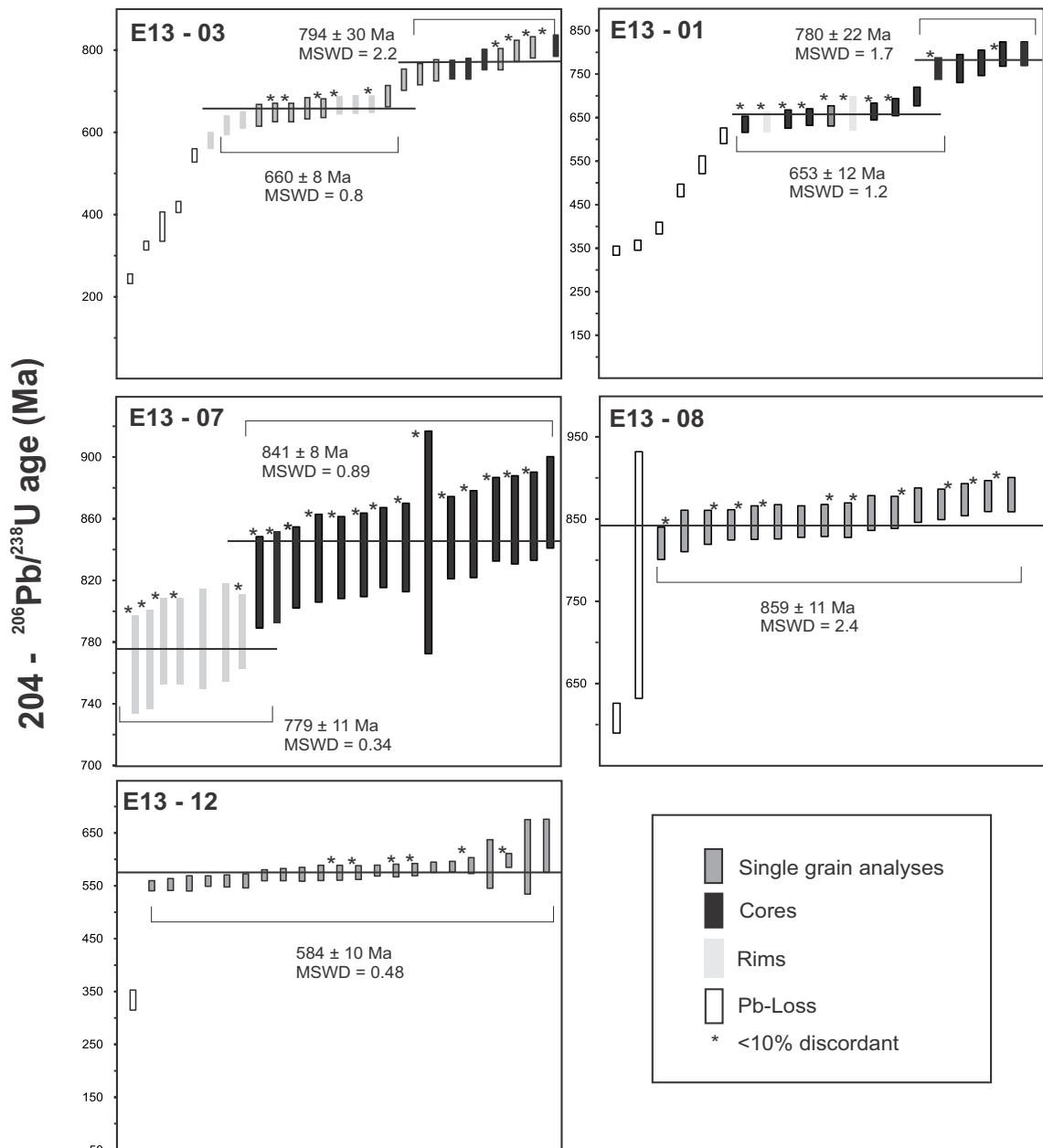
Figure 6: Age plots of individual zircon analyses (with 2s error bars) shown in order of increasing apparent age. Black-shaded error bars represent zircon core/fragments or inner overgrowths on inherited grains; light grey age bars represent rims/overgrowths. Dark grey age bars with a black outline represent zircons that either have oscillatory zonation or do not have a defined rim or core. Unfilled age bars are ages that are interpreted as resulting from lead loss. Calculated ages are quoted with 2 sigma errors.

grains present. The zircon grains can be divided into three groups. Group 1 is composed of zircons with well-developed pyramidal crystal faces with an aspect ratio of ca. 4:1. Most of the grains are poorly luminescent under CL with faint luminescent bands displaying oscillatory zonation. These make up the majority of the zircon grains. Group 2 is composed of zircon grains with differing morphologies. These grains typically have prismatic crystal forms with aspect ratios of ca. 4:1 and have brightly luminescent cores that commonly preserve traces of oscillatory zoning. Dark rims are seen mantling some of these grains that in some cases appear to have replaced the original zircon rather than precipitated onto a core.

Lastly, Group 3 zircons are generally rounded and ovoid in morphology and are featureless in CL (Fig. 5a).

The cumulative 204–corrected $^{206}Pb/^{238}U$ age plot of all analyses highlights two distinct age groups, marked by the plateaus, with zircon that experienced Pb-loss making up the other analyses (Fig. 6). Of the twenty analyses, ten are <10% discordant. These show a range of $^{206}Pb/^{238}U$ ages between 800 and 630 Ma, with two distinct groups between ca. 799–763 Ma and 675–630 Ma respectively. The older population includes only two <10% discordant grains and consists of luminescent cores surrounded by weakly luminescent rims. The two grains yield $^{206}Pb/^{238}U$ ages of 797±14 Ma and 763±12 Ma, but when combined with the less concordant members of the population yield a weighted mean age of 780±22 Ma (MSWD = 1.7). The slight discordance of these other analyses is interpreted to be due to minor, incompletely resolved, common Pb. Crystals with ages between 675 Ma and 630 Ma mainly have low luminescence and form dark rims in CL, which in some cases surround the inherited zircons. One large multifaceted sector zoned zircon also yielded this age (Group 3; Fig. 5). Analysis of these younger grains gives a weighted mean $^{206}Pb/^{238}U$ age of 653±12 Ma with an MSWD of 1.2 and a weighted mean $^{206}Pb/^{207}Pb$ age of 664±16 Ma (MSWD = 1.2). The homogeneous K-feldspar-rich granite cuts the gneiss at the Didesa River outcrop (Fig 3c) and we interpret the granite to have crystallised at 653±12 Ma. The older grains are interpreted to be xenocrysts, inherited from the host gneiss.

E13.07: Hornblende + biotite tonalite (Ethiopian Road Authority Quarry, N9 09.939 E35 37.500)
Zircon grains from sample E13.07 are typically light orange in colour with the presence of some with a light pink hue, with aspect ratios of ca. 2:1. Some elongated grains have aspect ratios up to 5:1. The low aspect ratio zircon grains have well preserved prismatic and pyramidal crystal faces. Grains are brightly luminescent and preserve well-defined oscillatory zoning. However, in some cases, convolute boundaries between rims and cores are present (Fig. 5). Rims appear to have replaced the original zircon and represent a recrystallisation front in some grains (Hoskin and Black, 2000). Zircon grains typically have thin bright rims.

Twenty one analyses of 18 zircon grains are within 10% of concordance (including both cores and rims). Ages spread broadly along the concordia between ca. 860 and 760 (Fig. 7). On the 204–corrected $^{206}Pb/^{238}U$ age plot two distinct plateaus can be isolated (Fig. 6), suggesting two distinct periods of zircon formation. The older analyses are dominantly grains with well-defined oscillatory luminescence zoning and yielded a $^{206}Pb/^{238}U$ weighted mean age of 841±8 Ma (MSWD = 0.89). Six rims (four of which are <10% discordant; 776±14 Ma, MSWD = 0.52) define an equilibrium plateau and yield a younger age of 779±11 Ma (MSWD = 0.34). Including all near concordant zircons provides the best estimate with a lower MSWD. The rims are shown by lobes and patches that overprint the pre-existing textures (Fig. 5), suggesting metamorphic recrystallization at ca. 779 Ma.

E13.08: Felsic granite (Ethiopian Road Authority Quarry, N9 09.939 E35 37.500)
Zircon grains from sample E13.08 are typically light orange in colour with a few light pink exceptions and typically have an aspect ratio of ca. 2:1; the presence of elongated grains with aspect ratios >5:1 is not as common as the other sample collected from this outcrop (E13.07). Grains are brightly luminescent with well-defined oscillatory zoning. They contain cores that have patchy, complex zoning
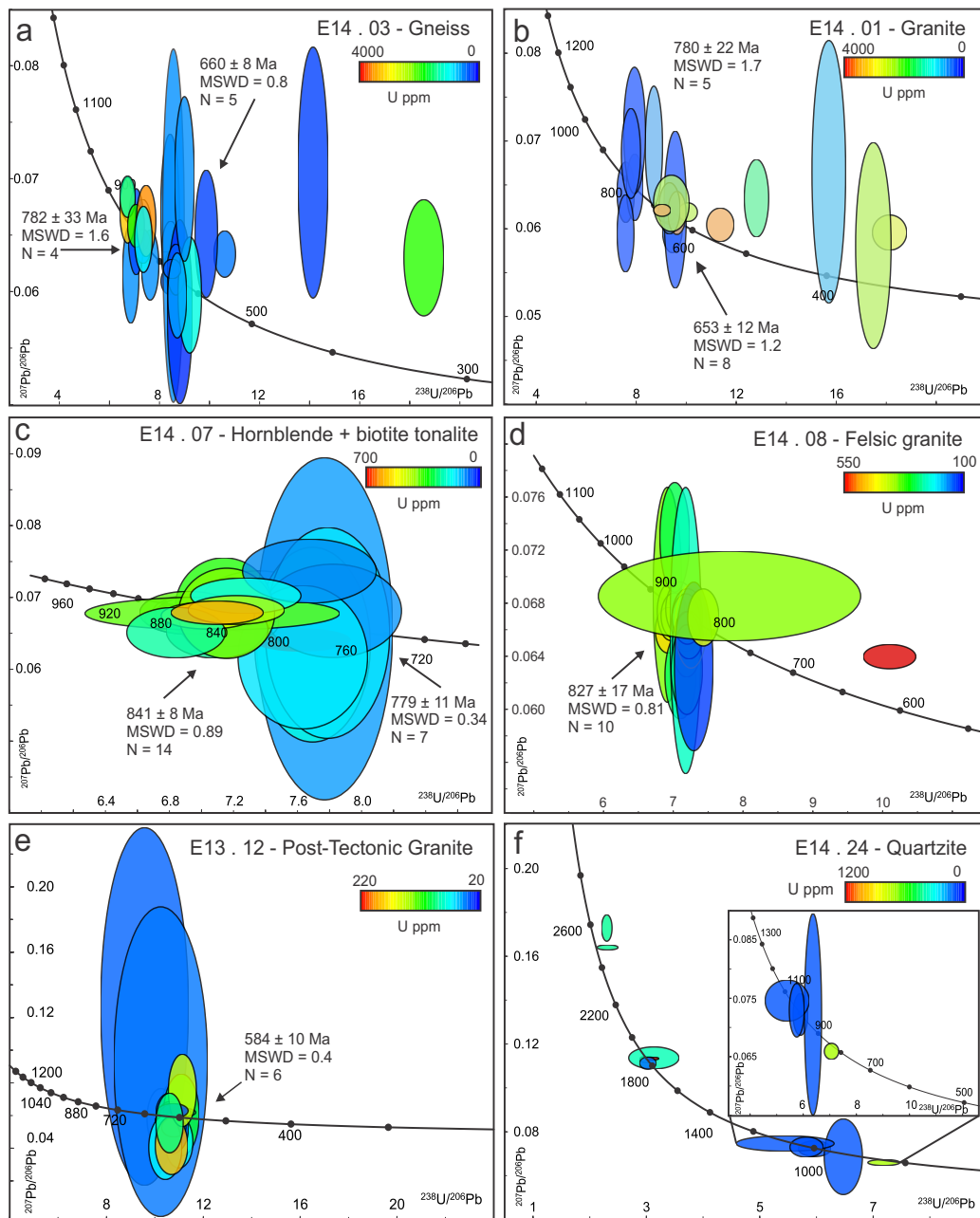
Figure 7: U—Pb Tera-Wasserburg concordia diagram constructed with a 2 sigma data point error ellipses. a: U—Pb Concordia of all zircons (n=31), which were sourced from a quartzo-feldspathic gneiss at the Didesa River cut (E13.03) uranium concentrations range between 91—5486. b: K-feldspar granite (E13.01) with a cross cutting relationship to the Didesa river gneiss (n=26), the uranium concentration range is 115—3837 ppm. c:Hornblende, biotite tonalite (E13.07, n=34), the uranium concentration has a range of 89—606 ppm, d:Felsic granite (E13.08, n=18), the uranium concentrations for zircons vary between 134—5310, e:Ganjii monzogranite (E13.12, n=23), uranium concentration has a range of 29—205 ppm a) U—Pb Concordia of all zircons (n=13), which were sourced from a meta-quartz arenite (E13.24a).The inset shows that there are rocks in the source region with ages at ca. 820 Ma and ca. 1000—1100 Ma. There is a population of detrital zircons at ca.1850. $^{206}Pb/^{207}Pb$ ages are used when ages are over 1 Ga. $^{206}Pb/^{238}U$ ages are used when the age is less than ca.1 Ga. There are three detrital zircon populations at ca. 2499 Ma, ca.1855 Ma and between 1100—800 Ma.

surrounded by oscillatory zonation.

Of the twenty analyses that were conducted, fifteen are <10% discordant data. The cores were mainly targeted and these define a range of $^{206}Pb/^{238}U$ ages between 880 and 820 Ma (Fig. 7). On the cumulative 204–corrected $^{206}Pb/^{238}U$ age plot of individual analyses, the youngest age is attributed to lead loss and therefore has been excluded from the concordia age calculation. A weighted mean of these ages yields one distinct group with a mean age of 859±11 Ma (MSWD = 2.4). The $^{206}Pb/^{207}Pb$ age gives a weighted average of 827±17 Ma with a MSWD of 0.81. This lies within error of the crystallisation age of the hornblende + biotite tonalite and together with the field observations shows that these magmas were coeval.

E13.12: Post Tectonic Ganjii Granite (N8 56.746 E35 27.240)

E13.12 contains zircons that are yellow to orange in colour, dominated by prismatic and pyramidal crystal forms, with some highly elongate prismatic grains present. The grains have aspect ratios between 2:1 and 5:1 and vary from 90 μm to 200 μm in length. The grains have well-defined oscillatory zonation. Cores in some grains have patchy zonation and inclusions are common.

Twenty two analyses of 19 zircon grains mostly represent zircon rims and the few core analyses showed no discernible age difference (Fig. 7). Of the twenty two analyses, only five lie within 10% concordance. The cumulative 204–corrected $^{206}Pb/^{238}U$ age plot of individual analyses displays a defined equilibrium plateau, suggesting a single population, however, one young grain has been interpreted to have been affected by Pb-loss. A weighted mean $^{206}Pb/^{238}U$ age of all the analyses yields an age of 584±10 Ma with a MSWD of 0.5. A previously reported $^{207}Pb–^{206}Pb$ zircon age of

622±7 Ma was interpreted to reflect the age of crystallisation of this intrusion (Kebede et al., 2001a), however, the data presented here suggests that the Ganjii Granite crystallised ca. 40 Ma later. We suggest that the older age either dated an unrecognised older phase in the intrusion, or dated xenocrysts within the rock.

E13-24a: Meta-quartz arenite (Doro Dimtu, N9 26 12.1 E35 42.42.1)

E13.24a is composed of angular to sub-rounded grains with aspect ratios of 2:1–3:1. Crystal lengths are between 30 μm–90 μm. Grains commonly preserve traces of oscillatory zonation and are poorly luminescent under CL. Grains that are angular give a CL bright response and contain inclusions. These grains have both oscillatory and sector zonation.

Only thirteen zircons were recovered from this sample. The U–Pb concordia and probability density plots (Fig. 7) demonstrate the presence of detrital zircons at ca. 2499 Ma, ca. 1855 Ma and between 1100–800 Ma (Fig. 7). The limited number of zircons available are too few to statistically characterise the source region (Vermeesch, 2004), yet the data reflect ages present in the source region of the sandstone protolith. The population at ca. 2499 Ma is slightly discordant, whereas the four ca. 1855 Ma zircons yield a weighted mean $^{207}Pb/^{206}Pb$ age of 1852±8 Ma with an MSWD of 0.35, suggesting that these come from the same-aged source. The youngest near concordant zircon has a $^{206}Pb/^{238}U$ age of 841±14 Ma (4% discordant), which we interpret as the maximum depositional age of the protolith of this meta-quartz-arenite.

Zircon Hafnium Isotopic Analysis

The Lu–Hf isotope system can be used to track the history of chemical differentiation of the silicate Earth (crust and mantle) as fractionation of Lu from Hf occurs during magma genesis
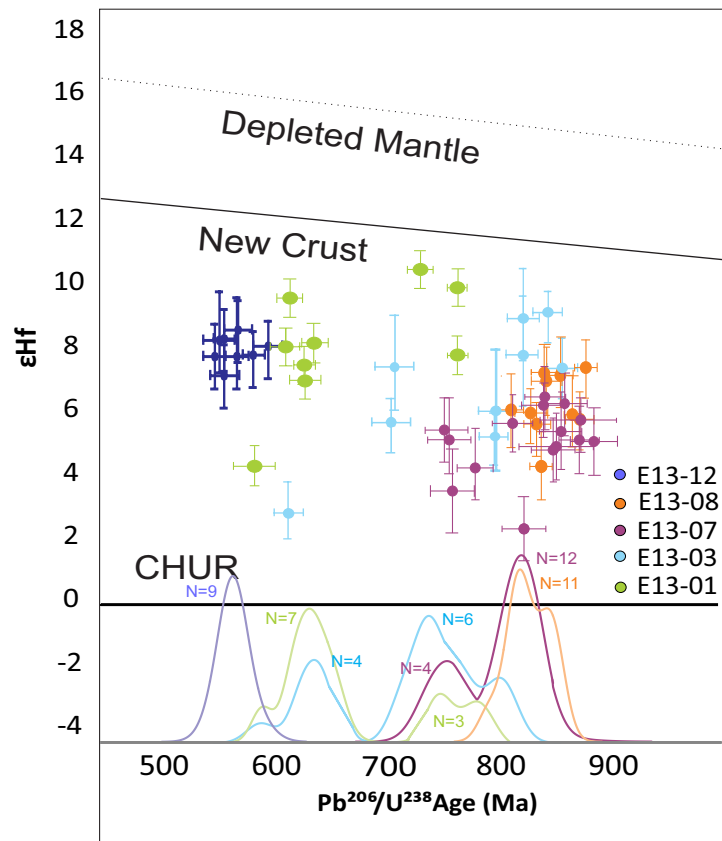
Figure 8: ε_{Hf}(t) versus age plot for all igneous samples. Plots show that all samples are juvenile with continental crust input being minimal. Peaks show the relative number of zircons in each sample. Both horizontal and vertical error bars plotted at the one sigma error level.
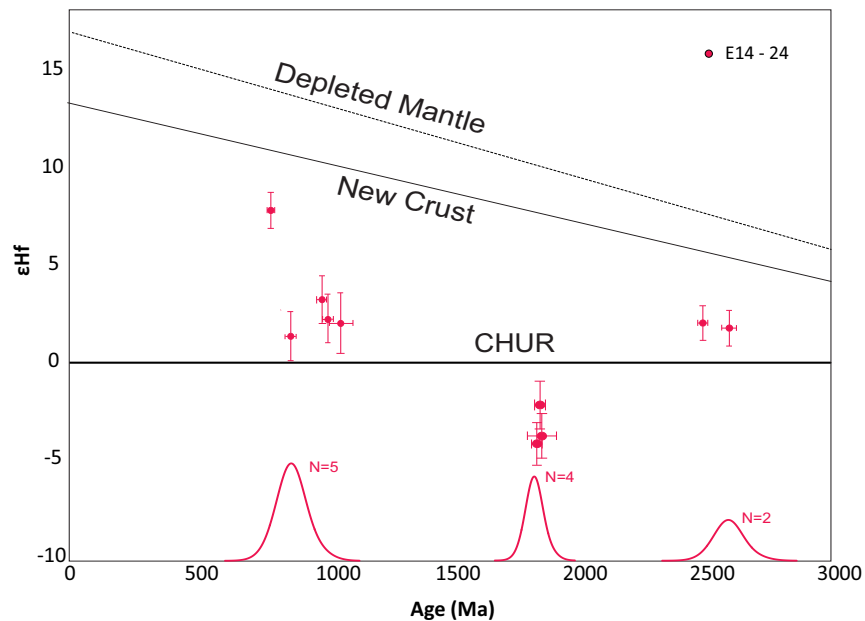
Figure 9: ε_{Hf}(t) versus age plot for metasedimentary sample, meta quartz-arenite (E13.24a). This shows three distinct populations the oldest and youngest being of juvenile nature. The population at ca. 1800 Ma is more evolved suggesting that addition of a continental influence. Peaks show the relative number of zircons in each sample. Both horizontal and vertical error bars show two sigma error.

(Hawkesworth and Kemp, 2006). Zircon effectively preserves the initial $^{176}Hf/^{177}Hf$ ratio of the magma from which it grew, providing an enduring record of the Hf isotopic composition of the source environment at the time of crystallization. Hafnium isotope analyses were obtained by overlapping the pre-existing U–Pb analytical spots (Fig. 5). These data are plotted on an $\varepsilon_{Hf}(t)$ vs. time plot (Fig. 8 and Fig. 9)

E13.03: Quartzo-feldspathic Gneiss
Hafnium isotope analysis was conducted on eleven zircon grains from the quartzofeldspathic gneiss, Didesa River outcrop. $\varepsilon_{Hf}(t)$ values ranging between +2.5 to +8.0 and suggests relatively juvenile sources, with minimal continental crust involvement.

E13 .01: Homogeneous K-feldspar-rich granite
Eleven zircons from the K-feldspar-rich granite at the Didesa River outcrop were analysed for hafnium isotopes. $\varepsilon_{Hf}(t)$ values range between +4.1 and +9.6 (Fig. 8), again demonstrating the relatively juvenile nature of these rocks.
E13. 07: Hornblende + biotite tonalite
The analysis of 15 zircons for hafnium isotopes yielded $\varepsilon_{Hf}(t)$ values of +3.4 to +6.1 (Fig. 8).

E13.08: Felsic granite
The analysis of 11 zircons for hafnium yielded $\varepsilon_{Hf}(t)$ values between +3.8 to +6.9 (Fig. 8).
E13.12 Post tectonic Ganjii Granite
Hafnium data collected from this sample yielded positive $\varepsilon_{Hf}(t)$ values that range from +6.7 to +7.9 (Fig. 8).

E13.24a Meta-Quartz Arenite
The Hf isotopic data for detrital zircons from this sample yielded positive $\varepsilon_{Hf}(t)$ values ranging from +1.79 to +2.08 for the ca. 2499 Ma grains. Conversely, zircons at ca. 1855 Ma, have negative $\varepsilon_{Hf}(t)$ values ranging from -2.3 to -12.4 (Fig. 9), suggesting that they are not

juvenile; the magma from which the zircons grew contained a significant component of older continental crustal. Lastly, the population between 1100–800 Ma yields positive $\varepsilon_{Hf}(t)$ values ranging from +1.25 to +7.84.

DISCUSSION
Timing and Nature of Pre- Syn-tectonic Magmatism and Deformation in the Didesa Domain
The oldest ages obtained in this study are from well-defined oscillatory-zoned zircon grains extracted from the hornblende + biotite tonalite (841±8 Ma) and zircons within the coeval felsic granite (827±17 Ma). Evidence of metamorphism is seen by the rims and recrystallisation of zircon in the tonalite; however, this is not the case in the felsic granite. A possibility is that the tonalite's bulk composition remained more reactive due to excess water, meaning that the propensity to grow zircon was higher in the tonalite than in the felsic environment. The epidote within the hornblende + biotite tonalite is an important mineral in low-grade regional metamorphism, where it marks the beginning of the epidote-amphibolite facies. It can form from the breakdown of chlorite, however, in this case it is interpreted to result from the saussuritization of plagioclase feldspar and from the breakdown of amphibole due to a late stage hydrothermal alteration. The older zircons yield $\varepsilon_{Hf}(t)$ values between + 2 and +7, demonstrating their juvenile, mantle-derived origin. Zircon rims yield an age of 779±11 Ma, which is coeval with the oldest ages derived from the Didesa River gneisses (E13-03 protolith crystallisation age interpreted to be 782±33 Ma). These late Tonian zircons also yield positive $\varepsilon_{Hf}(t)$ values (+2 to +10) suggesting a similar juvenile origin compatible with magma generated within an oceanic setting. Younger zircon from the Didesa river gneiss (660±8 Ma) is interpreted
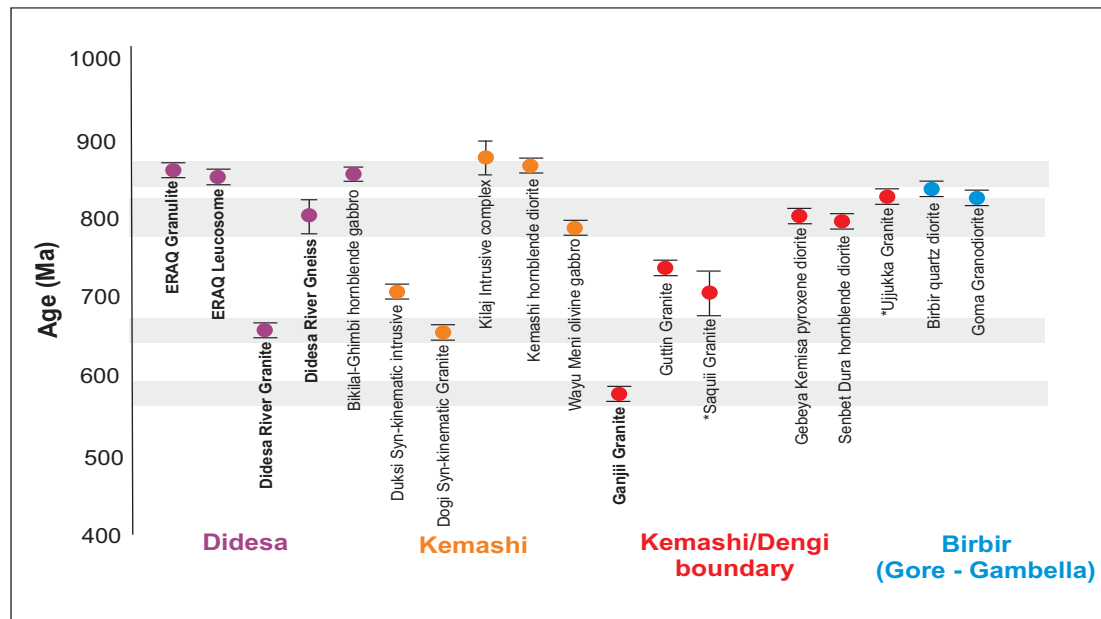
Figure 10: Comparative table between published crystallisation ages and newly interpreted ages, in the Western Ethiopian Shield. Samples highlighted in bold represent the data presented in this paper. '*' Zircons analysed by using lead–lead evaporation. (Ayalew et al., 1990; Grenne et al., 2003; Johnson et al., 2004; Kazmin, 1972; Kebede et al., 2001; Kebede and Koeberl, 2003; Kebede et al., 1999; Teklay et al., 1998; Woldemichael et al., 2010; Yibas et al., 2002).

as dating the tectono-thermal event in which the pervasive L-S fabric was imposed on the rock. This age is coeval with the interpreted crystallisation age of a cross-cutting granite (653±12 Ma). Field relationships between the gneiss and the granite demonstrate that the granite post-dates the gneiss fabric, suggesting that granite intruded after deformation, but within error of the ages obtained. The difference between the two samples is seen when plotted together on an $\varepsilon_{Hf}(t)$ versus age plot, the younger Didesa River zircons stretch to more positive values than the older analyses, suggesting that ca. 650 Ma magmatism may involve a further input of mantle-derived magma and that it is not exclusively composed of melts derived from the ca. 850–780 Ma basement.

The three tectono-thermal events the Didesa Domain—ca. 845 Ma, ca. 790–780 Ma and ca. 660–655 Ma—are broadly supported by previously published ages from elsewhere in the WES that suggested three phases of

magmatism at ca. 850–810 Ma, 780–700 Ma and 620–550 Ma (Ayalew et al., 1990; Ayalew and Peccerillo, 1998; Kebede et al., 2001a; Kebede et al., 1999; Kebede et al., 2001b). These have been suggested to represent pre-, syn- and post-tectonic environments respectively (Woldemichael and Kimura, 2008; Woldemichael et al., 2010). The data presented in this study better reveal the timing of these tectonothermal events and also illustrate that the pre-, syn- and post- tectonic history is complicated by metamorphism/deformation occurring both at ca. 790–780 Ma and at ca. 660–655 Ma.

Time of Crystallisation and Hf Isotopic Value of Post-Tectonic Magmatism

The Ganjii Granite is the only truly post-tectonic intrusion dated and it crosscuts rocks of the Kemashi and Dengi Domains. The crystallisation age for this monzogranite (Kebede and Koeberl, 2003) is 584±10 Ma, ca. 40 Myr
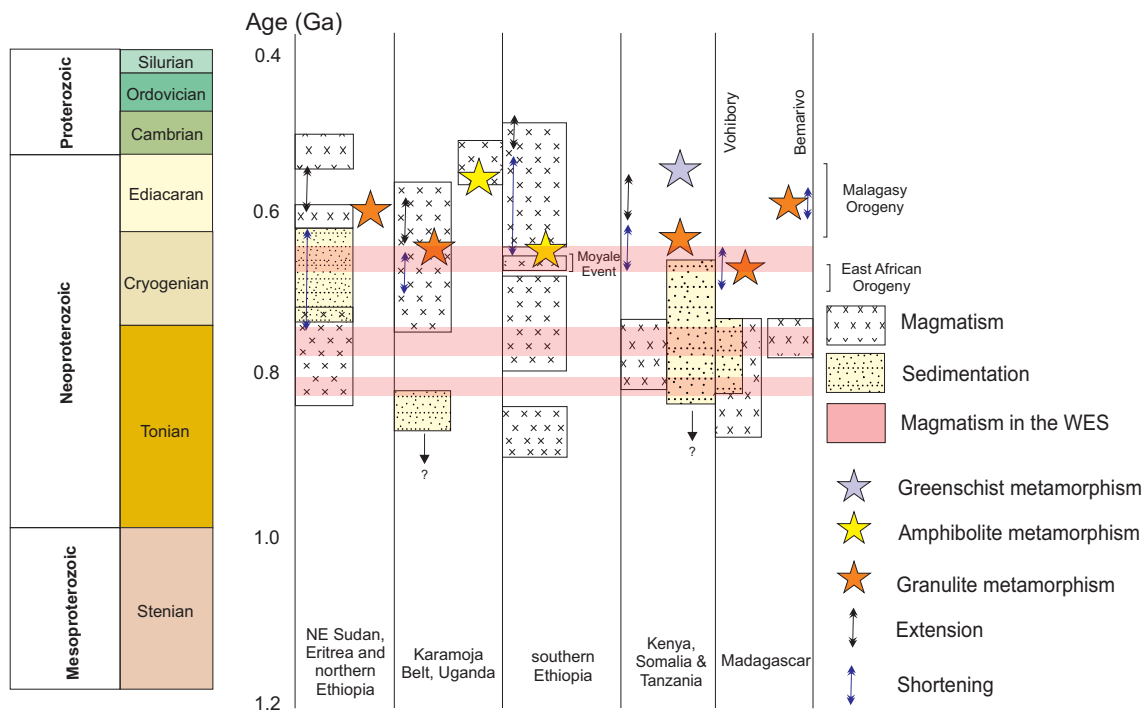
Figure 11: : A condensed geological time space plot for major geological events in the East African Orogen. ANS: Arabian Nubian Shield. Adapted from Fritz et al. (2013).

younger than previously interpreted. It shows chemical and mineralogical characteristics of intra-plate granite, generated and emplaced in an extensional tectonic environment (Kebede and Koeberl, 2003). Zircons from the Ganjii Granite have positive $\varepsilon_{Hf}(t)$ values that range from +6.8 to +8 (Fig. 8). The $\varepsilon_{Hf}(t)$ versus age plot (Fig. 8) suggests that the Ganjii Granite has an isotopic composition consistent with being derived by the melting of the early Neoproterozoic basement, with hafnium isotopic values similar to those obtained from the Didesa Domain samples.

Age and Provenance Significance of Metasedimentary Rocks in the Western Ethiopian Shield

Detrital zircons from a meta-quartz-arenite found in the Kemashi Domain, are sourced from Neoarchaean-Palaeoproterzoic (ca. 2.8–2.4 Ga), late Palaeoproterozoic (ca. 1.8 Ga) and Stenian-Tonian (ca. 1.15–0.84 Ga) rocks. The maximum depositional age of the protolith to this metasedimentary rock is 841±14 Ma based on the age of the youngest near concordant zircon grain. These source age populations can all be found in rocks from further west in pre-Neoproterozoic Africa, but also similar ages are present to the east within the East African Orogen itself. Evidence of Tonian - Stenian magmatism and metamorphism have been found in the granitoids and gneisses in the north-central Bayunda Desert in Sudan (Küster et al., 2008) and Stenian intrusions have been described from the Dharfur region of west Sudan and east Chad (de Wit and Linol, 2015; de Wit and Senbeto, 1981). In addition, similar ages have recently been described from within the East African Orogen in the Sinai Peninsula of Egypt (Be'eri-Shlevin et al., 2012; Bentor, 1985; Johnson and Woldehaimanot, 2003) albeit a considerable distance to the north. This peak (ca. 1.15–0.84 Ga) defines the largest and youngest population of zircons.
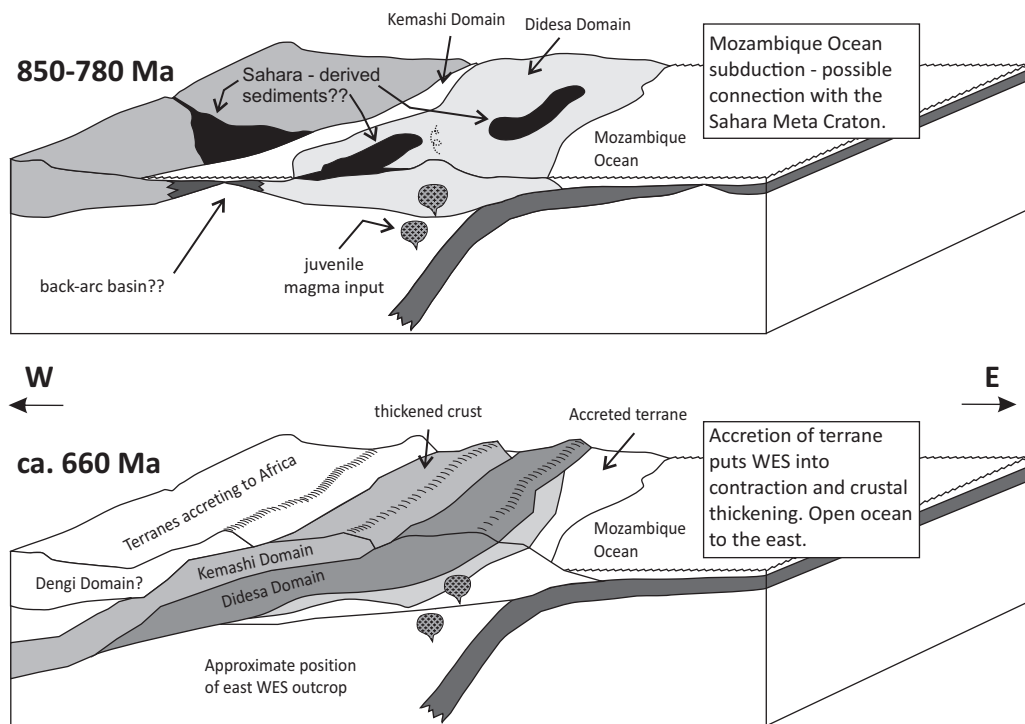
Figure 12: Schematic illustration of stages of development in the Western Ethiopian Shield. There are two main phases. 850 Ma–780 Ma: subduction and intra oceanic arc magmatism followed by deformation and further magmatism and 660: orogenic thickening and crustal melting followed by the emplacement of post tectonic sequences.

The positive $\varepsilon_{Hf}(t)$ of these zircons suggest that the source rocks were juvenile. The late Palaeoproterozoic zircons (ca. 1820 Ma) yield negative $\varepsilon_{Hf}(t)$ values (Fig. 9), suggesting that the source intrusions contained a component of pre-existing continental crust. Similar-aged crust exists to the south, in Uganda, Kenya and Tanzania, where it makes up part of the foreland to the East African Orogen (Abdelsalam et al., 2002; Leggo, 1974; Reddy et al., 2003). Within the Arabian Nubian Shield, similar-aged crust is found within the tract of pre-Neoproterozoic crust of Somaliland and far east Ethiopia (Kröner and Sassi, 1996; Teklay et al., 1998), interpreted by Collins and Windley (2002) and Collins and Pisarevsky (2005) as a part of a pre-Neoproterozoic continent named Azania. Neoarchaean to earliest Palaeoproterozoic rocks are common in cratonic Africa, (Muhongo et al., 2001) and also make up much of the basement of Azania

(Collins and Windley, 2002).

Consequently, possible sources for these detrital zircons occur both to the west (towards the closest foreland of the East African Orogen) and to the east within the orogen itself. U–Pb data is only now becoming available from this part of Africa and there is very little comparable Hf isotopic data presently available to try and distinguish sources. However, it is clear that at the time of deposition of the protolith of the meta-quartz-arenite in the Kemashi Domain ($<841 \pm 14$ Ma) the region was either depositionally connected to continental crust, or at least to crust with sedimentary rocks that had previously been sourced from an older continent. Mapping demonstrates that these rocks unconformably overlie gabbros, tectonic mélanges and serpentinites that have been interpreted as representing a suture zone (de Wit and Aguma, 1977; de Wit and Senbeto, 1981). We therefore tentatively suggest that the

protolith sedimentary rock to this sample was deposited after suturing of a Tonian-Cryogenian arc to a tectonic amalgam that was attached to pre-Neoproterozoic continental crust. This continent could be Azania (i.e. to the east), or the Sahara metacraton (to the west).

Tectonic Setting of the Didesa and Kemashi Domains

No evidence yet exists that any of the WES existed before the Neoproterozoic. The oldest rocks known in the area date back to ca. 850 Ma and show no evidence of being contaminated by any pre-Neoproterozoic crust. We interpret these rocks to have formed in an intra-oceanic setting, above a subduction zone. Later deformation and intrusion at 790–780 Ma is interpreted as evidence of further mantle-derived magmatism, and these rocks are also interpreted as the products of intra-oceanic arc magmatism (Fig. 12). However, subsequent magmatism at 660–655 Ma and ca. 584 Ma is interpreted as only involving melting of earlier Neoproterozoic crust and may represent orogenic thickening and crustal melting. Post ca. 840 Ma siliciclastic deposition is interpreted to seal terrane amalgamation between the Kemashi, Didesa and Dengi Domains and ends the intra-oceanic history of this region as it shows clear derivation from pre-Neoproterozoic continental crust.

Correlation with elsewhere in the East African Orogen

The three pre-/syntectonic deformation and magmatic phases recorded in the Didesa Domain, and suggested by the available data from elsewhere in the WES, reflect major tectonic reorganisations seen throughout the East African Orogen, in both the Arabian-Nubian Shield to the north and the Mozambique Belt to the south. Figure 11 shows a summary of tectonic and magmatic events within

parts of the East African Orogen during the Neoproterozoic. Below, we briefly discuss the geology of these areas and how they link to the WES.

The Northern Mozambique Belt

There is a gap in basement outcrop south of the WES until at latitude ~3° North where rocks of the Neoproterozoic Karamoja Belt of NE Uganda/NW Kenya are encountered (Fig. 1). This belt consists of Neoproterozoic metasedimentary rocks of the Karasuk Supergroup (Vail, 1983; Westerhof et al., 2014) and metaigneous rocks that crystallised between ca. 0.74 and 0.68 Ga (Mänttäri et al., 2011; Westerhof et al., 2014). The terrane is cut by post-tectonic granitoids with U-Pb crystallisation ages of ca. 0.66 Ga (Mänttäri et al., 2011) similar to the age of the late granite at the Didesa River. This terrane was thrust eastward over the NE edge of the Congo craton. The next major region of basement outcrop east along latitude 2–3° N is the Southern Ethiopian Shield (Fig. 1). Here four magmatic events have been identified as between 890–840 Ma, 790–700 Ma, ca. 660 Ma and 630–500 Ma (Stern et al., 2012; Teklay et al., 1998; Yibas et al., 2002). The first two events broadly match those from the WES. The ca. 660 Ma event in the Southern Ethiopian Shield has been termed the 'Moyale Event' (Teklay et al., 1998) and occurs at approximately the same time as the late magmatism in the Didesa Terrane (Fig. 10) and the post-tectonic granites in the Karamoja Belt (Mänttäri et al., 2011). A significant difference between the Southern Ethiopian Shield and both the Karamoja Belt and the WES is that major orogenesis in the former occurred between 630–550 Ma (Stern et al., 2012). In the WES, this is the time of post-orogenic magmatism, and little evidence for tectonothermal events occur in the Karamoja Belt at this time.

To the south, in Kenya, southern Somalia and Tanzania, the East African Orogen is marked by dominantly high-grade gneisses of the Mozambique Belt (see Fritz et al. 2013 for a recent review). The eastern part of the Mozambique Belt consists of a tract of largely pre-Neoproterozoic continental crust, strongly deformed, partially melted and metamorphosed in the Ediacaran/Cambrian (ca. 600 and 530 Ma, (Küster et al., 1990; Lenoir et al., 1994)). These rocks occur in southern Somalia, in a region known as the Buur Massif. Passing west, basement rocks crop out next in southern Kenya, in the Taita Hills/Galana River area, where recent studies have identified a Neoproterozoic suture separating crust with Palaeoproterozoic–Archaean Nd model ages in the east from juvenile crust further west (Bauernhofer et al., 2009; Hauzenberger et al., 2007). These juvenile Neoproterozoic rocks continue south, along strike, into the Umba Steppe, Pare Mountains and Usumbara Mountains region of NE Tanzania (Maboko and Nakamura, 2002) and may link with the Vohibory Complex in SW Madagascar (Collins et al., 2012; Jöns and Schenk, 2008). Further west, lies extensive tectonothermally reworked pre-Neoproterozoic crust that rings the Neoarchaean Tanzanian craton (Collins et al., 2004; Johnson et al., 2003; Muhongo et al., 2001; Reddy et al., 2003; Tenczer et al., 2012). Metamorphic zircons date near peak granulite-grade metamorphism along the western part of this belt at ca. 640 Ma (Appel et al., 1998; Coolen et al., 1982; Muhongo, 1994; Muhongo et al., 2001), considerably younger than the post-tectonic granites seen further north in Uganda and described above. Hauzenberger et al. (2007) also pointed out that the age of metamorphism further east, in the Galana River area, was considerably younger (580–530 Ma) overlapping the age of the 'Malagasy Orogeny' of Collins & Pisarevsky (2005). This Ediacaran-Cambrian deformation and metamorphism is not yet identified in the WES, and appears to be a feature of the southern and eastern East African Orogen.

The Southern Arabian Nubian Shield
The Sudanese Butana Block of the southern Arabian-Nubian Shield lies directly north of the WES at ~15° N (Fig. 1). Little data is available from here, however, to the east of the Butana Block lies extensive outcrop of the southern Arabian-Nubian Shield in NE Sudan, Eritrea and northern Ethiopia. The two main terranes here are known as the Haya and Tokar/Barka Terranes (Drury and de Souza Filho, 1998; Johnson et al., 2011). In the composite Tokar/Barka Terrane (which consists of the high-grade Barka, Arag and Ghedem terranes of Eritrea that lie either side of the low grade Hagar, Adhoba-Abi, Nacfa of Eritrea and the Tsaliet Group of northern Ethiopia; (Andersson et al., 2006; Avigad et al., 2007) juvenile arc magmatism occurred between ca. 850–740 Ma (Andersson et al., 2006; Teklay et al., 2003) and is followed in the low-grade terranes by deposition of the Cryogenian Tambien Group. This group is intruded by the post-tectonic Mereb granites at 640–600 Ma (Avigad et al., 2007). Upper amphibolie facies metamorphism occurred in the surrounding high-grade terranes at ca. 590 Ma and is interpreted to relate to final continental collision in the area (Andersson et al., 2006). These terranes correlate broadly with the Asir and Jiddah Terranes of Arabia (Johnson et al., 2011) and the early history compares well with the WES as presented in this paper, where arc-related magmatism occurred at ca. 850–840 Ma and ca. 780–760 Ma. However, high-temperature deformation and magmatism also occur in the Didesa Terrane at ca. 660 Ma, earlier than the ages suggested for the area to the north.

CONCLUSIONS

New data from the Didesa and Kemashi Domains of the Western Ethiopian Shield demonstrate that there were three pulses of syn-tectonic magmatism at 850–840 Ma, 790–780 Ma and ca. 660 Ma. Hafnium isotopic analysis indicates that the early Cryogenian magmas were generated from juvenile Neoproterozoic mantle sources with little involvement of the pre-Neoproterozoic continental crust. The hafnium isotopic data from the ca. 660 Ma granitoid is consistent with it being, at least partially, generated by melting of the older Tonian-Cryogenian rocks. Widespread deformation and metamorphism was over before intrusion of the post-tectonic 585± 8Ma Ganjii Granite.

Metasedimentary rocks preserve zircons that help to constrain protolith deposition to after 838 ± 13 Ma. Limited detrital zircons illustrate three distinct age populations at ca. 2.8–2.4 Ga, ca. 1.8 Ga and 1.15–0.84 Ga. Hafnium isotopes reveal that the ca. 1.8 Ga source involved evolved crust, whereas the other sources were broadly juvenile.

These data help constrain the tectonic evolution of the region and document consumption and closure of the western Mozambique Ocean. When compared to available constraints from the southern Arabian Nubian Shield (directly north of the WES) and the northern Mozambique Belt (directly south of the WES), it is clear that the timing of orogenesis youngs to the east. In the WES, and the Karamoja Belt of Uganda, peak metamorphism and deformation occurs at ca. 680–660 Ma, whereas to the east and southeast of the WES peak orogenesis occurs at 630–550 Ma (South Ethiopian Shield), 580–530 Ma (Galana River, Kenya), ca. 590 Ma (Eritrea and northern Ethiopia).

ACKNOWLEDGEMENTS

REFERENCES

Abdelsalam, M., Stern, R., 1996. Sutures and shear zones in the Arabian-Nubian Shield. Journal of African Earth Sciences 23, 289-310.

Abdelsalam, M.G., Liegeois, J.P., Stern, R.J., 2002. The Saharan Metacraton. Journal of African Earth Sciences 34, 119-136.

Alemu, T., 2005. Discussion of "Geological setting and tectonic subdivision of the Neoproterozoic Orogenic Belt of Tuludimtu, Western Ethiopia"[Journal of African Earth Sciences 36 (2003) 329–343]. Journal of African Earth Sciences 41, 329-332.

Allen, A., Tadesse, G., 2003. Geological setting and tectonic subdivision of the Neoproterozoic orogenic belt of Tuludimtu, western Ethiopia. Journal of African Earth Sciences 36, 329-343.

Andersson, U.B., Ghebreab, W., Teklay, M., 2006. Crustal evolution and metamorphism in east-central Eritrea, south-east Arabian-Nubian Shield. Journal of African Earth Sciences 44, 45-65.

Appel, P., Möller, P., Schenk, V., 1998. High-pressure granulite facies metamorphism in the Pan-African belt of eastern Tanzania: P-T-t evidence against granulite formation by continent collision. Journal of Metamorphic

Geology 16, 491-509.

Avigad, D., Stern, R., Beyth, M., Miller, N., McWilliams, M., 2007. Detrital zircon U–Pb geochronology of Cryogenian diamictites and Lower Paleozoic sandstone in Ethiopia (Tigrai): age constraints on Neoproterozoic glaciation and crustal evolution of the southern Arabian–Nubian Shield. Precambrian Research 154, 88-106.

Ayalew, T., Bell, K., Moore, J.M., Parrish, R.R., 1990. U-Pb and Rb-Sr geochronology of the western Ethiopian shield. Geological Society of America Bulletin 102, 1309-1316.

Ayalew, T., Peccerillo, A., 1998. Petrology and geochemistry of the Gore-Gambella plutonic rocks: implications for magma genesis and the tectonic setting of the Pan-African Orogenic Belt of western Ethiopia. Journal of African Earth Sciences 27, 397-416.

Bauernhofer, A., Hauzenberger, C., Wallbrecher, E., Muhongo, S., Hoinkes, G., Mogessie, A., Opiyo-Akech, N., Tenczer, V., 2009. Geochemistry of basement rocks from SE Kenya and NE Tanzania: indications for rifting and early Pan-African subduction. International Journal of Earth Sciences 98, 1809-1834.

Be'eri-Shlevin, Y., Eyal, M., Eyal, Y., Whitehouse, M.J., Litvinovsky, B., 2012. The Sa'al volcano-sedimentary complex (Sinai, Egypt): A latest Mesoproterozoic volcanic arc in the northern Arabian Nubian Shield. Geology 40, 403-406.

Bentor, Y., 1985. The crustal evolution of the Arabo-Nubian Massif with special reference to the Sinai Peninsula. Precambrian Research 28, 1-74.

Black, L.P., Kamo, S.L., Allen, C.M., Aleinikoff, J.N., Davis, D.W., Korsch, R.J., Foudoulis, C., 2003. TEMORA 1: a new zircon standard for Phanerozoic U–Pb geochronology. Chemical Geology 200, 155-170.

Boger, S.D., Wilson, C.J.L., Fanning, C.M., 2006. An Archaean province in the southern Prince Charles Mountains, East Antarctica: U-Pb zircon evidence for c. 3170 Ma granite plutonism and c. 2780 Ma partial melting and orogenesis. Precambrian Research 145, 207-228.

Braathen, A., Grenne, T., Selassie, M., Worku, T., 2001. Juxtaposition of Neoproterozoic units along the Baruda–Tulu Dimtu shear-belt in the East African Orogen of western Ethiopia. Precambrian Research 107, 215-234.

Cawood, P.A., Buchan, C., 2007. Linking accretionary orogenesis with supercontinent assembly. Earth-Science Reviews 82, 217-256.

Clark, C., Collins, A.S., Timms, N.E., Kinny, P.D., Chetty, T.R.K., Santosh, M., 2009. SHRIMP U–Pb age constraints on magmatism and high-grade metamorphism in the Salem Block, southern India. Gondwana Research 16, 27-36.

Collins, A., Reddy, S., Buchan, C., Mruma, A., 2004. Temporal constraints on Palaeoproterozoic eclogite formation and exhumation (Usagaran Orogen, Tanzania). Earth and Planetary Science Letters 224, 175-192.

Collins, A.S., 2003. Structure and age of the northern Leeuwin Complex, Western Australia: constraints from field mapping and U–Pb isotopic analysis. Australian Journal of Earth Sciences 50, 585-599.

Collins, A.S., Clark, C., Plavsa, D., 2014. Peninsular India in Gondwana: The tectonothermal evolution of the Southern Granulite Terrain and its Gondwanan counterparts. Gondwana Research 25, 190-203.

Collins, A.S., Clark, C., Sajeev, K., Santosh,

M., Kelsey, D.E., Hand, M., 2007. Passage through India: the Mozambique Ocean suture, high-pressure granulites and the Palghat-Cauvery shear zone system. Terra Nova 19, 141-147.

Collins, A.S., Kinny, P.D., Razakamanana, T., 2012. Depositional Age, Provenance and Metamorphic Age of Metasedimentary Rocks from Southern Madagascar. Gondwana Research. 21, 353-361.

Collins, A.S., Pisarevsky, S.A., 2005. Amalgamating eastern Gondwana: the evolution of the Circum-Indian Orogens. Earth-Science Reviews 71, 229-270.

Collins, A.S., Windley, B.F., 2002. The tectonic evolution of central and northern Madagascar and its place in the final assembly of Gondwana. Journal of Geology 110, 325-339.

Coolen, J.J.M.M., Priem, H.N.A., Verdurmen, E.A.T., Versuchure, R.H., 1982. Possible zircon U-Pb evidence for Pan-African granulite-facies metamorphism in the Mozambique belt of southern Tanzania. Precambrian Research 17, 31-40.

Cox, G.M., Lewis, C.J., Collins, A.S., Halverson, G.P., Jourdan, F., Foden, J., Nettle, D., Kattan, F., 2012. Ediacaran terrane accretion within the Arabian-Nubian Shield. Gondwana Research 21, 341-352.

de Wit, M., Aguma, A., 1977. Geology of the ultramafic and associated rocks of Tulu Dimtu, Welega. Ethiopian Institute of Geological Surveys Report, 26.

de Wit, M.J., Linol, B., 2015. Precambrian Basement of the Congo Basin and Its Flanking Terrains, Geology and Resource Potential of the Congo Basin. Springer, pp. 19-37.

de Wit, M.J., Senbeto, C., 1981. Plate tectonic evolution of Ethiopia and the origin of its mineral deposits: an overview, in: Senbeto, C., de Wit, M.J. (Eds.), Plate Tectonics

and Metallogenesis: Some Guidelines to Ethiopian Mineral Deposits. Ethiopian Institute of Geological Survey, Abbis Ababa, pp. 115-129.

Drury, S., de Souza Filho, C., 1998. Neoproterozoic terrane assemblages in Eritrea: review and prospects. Journal of African Earth Sciences 27, 331-348.

Fitzsimons, I.C.W., 2000. A review of tectonic events in the East Antarctic Shield and their implications for Gondwana and earlier supercontinents. Journal of African Earth Sciences 31, 3-23.

Fritz, H., Abdelsalam, M., Ali, K.A., Bingen, B., Collins, A.S., Fowler, A.R., Ghebreab, W., Hauzenberger, C.A., Johnson, P.R., Kusky, T.M., Macey, P., Muhongo, S., Stern, R.J., Viola, G., 2013. Orogen styles in the East African Orogen: A review of the Neoproterozoic to Cambrian tectonic evolution. Journal of African Earth Sciences.

Ganade de Araujo, C.E., Weinberg, R.F., Cordani, U.G., 2014. Extruding the Borborema Province (NE-Brazil): a two-stage Neoproterozoic collision process. Terra Nova 26, 157-168.

Grenne, T., Pedersen, R., Bjerkgård, T., Braathen, A., Selassie, M., Worku, T., 2003. Neoproterozoic evolution of Western Ethiopia: igneous geochemistry, isotope systematics and U–Pb ages. Geological magazine 140, 373-395.

Griffin, W., Pearson, N., Belousova, E., Saeed, A., 2006. Comment: Hf-isotope heterogeneity in zircon 91500. Chemical Geology 233, 358-363.

Griffin, W., Wang, X., Jackson, S., Pearson, N., O'Reilly, S.Y., Xu, X., Zhou, X., 2002. Zircon chemistry and magma mixing, SE China: in-situ analysis of Hf isotopes, Tonglu and Pingtan igneous complexes. Lithos 61, 237-269.

Hauzenberger, C.A., Sommer, H., Fritz, H.,

Bauernhofer, A., Kröner, A., Hoinkes, G., Wallbrecher, E., Thöni, M., 2007. SHRIMP U-Pb zircon and Sm-Nd garnet ages from the granulite facies basement of SE-Kenya: evidence for Neoproterozoic polycyclic assembly of the Mozambique Belt. Journal of the Geological Society, London 164, 189-201.

Hawkesworth, C.J., Kemp, A.I.S., 2006. Using hafnium and oxygen isotopes in zircons to unravel the record of crustal evolution. Chemical Geology 226, 144-162.

Hoskin, P., Black, L., 2000. Metamorphic zircon formation by solid-state recrystallization of protolith igneous zircon. Journal of metamorphic Geology 18, 423-439.

Jacobs, J., Thomas, R.J., 2004. Himalayan-type indenter-escape tectonics model for the southern part of the late Neoproterozoic-early Palaeozoic East African-Antarctic orogen. Geology 32, 721-724.

Johnson, P., Andresen, A., Collins, A.S., Fowler, A., Fritz, H., Ghebreab, W., Kusky, T., Stern, R., 2011. Late Cryogenian–Ediacaran history of the Arabian–Nubian Shield: A review of depositional, plutonic, structural, and tectonic events in the closing stages of the northern East African Orogen. Journal of African Earth Sciences 61, 167-232.

Johnson, P.R., Woldehaimanot, B., 2003. Development of the Arabian-Nubian Shield: perspectives on accretion and deformation in the northern East African Orogen and the assembly of Gondwana, in: Yoshida, M., Windley, B.F., Dasgupta, S. (Eds.), Proterozoic East Gondwana: Supercontinent Assembly and Breakup. Geological Society, London, Special Publication 206, pp. 289-325.

Johnson, S.P., Cutten, H.N.C., Muhongo, S., De Waele, B., 2003. Neoarchean magmatism and metamorphism of the western granulites in the central domain of the Mozambique belt, Tanzania: U-Pb SHRIMP geochronology and PT estimates. Tectonophysics 375, 125-145.

Jöns, N., Schenk, V., 2008. Relics of the Mozambique Ocean in the central East African Orogen: evidence from the Vohibory Block of southern Madagascar. Journal of Metamorphic Geology 26, 17-28.

Kebede, T., Kloetzli, U., Koeberl, C., 2001a. U/Pb and Pb/Pb zircon ages from granitoid rocks of Wallagga area: constraints on magmatic and tectonic evolution of Precambrian rocks of western Ethiopia. Mineralogy and Petrology 71, 251-271.

Kebede, T., Koeberl, C., 2003. Petrogenesis of A-type granitoids from the Wallagga area, western Ethiopia: constraints from mineralogy, bulk-rock chemistry, Nd and Sr isotopic compositions. Precambrian Research 121, 1-24.

Kebede, T., Koeberl, C., Koller, F., 1999. Geology, geochemistry and petrogenesis of intrusive rocks of the Wallagga area, western Ethiopia. Journal of African Earth Sciences 29, 715-734.

Kebede, T., Koeberl, C., Koller, F., 2001b. Magmatic evolution of the Suqii-Wagga garnet-bearing two-mica granite, Wallagga area, western Ethiopia. Journal of African Earth Sciences 32, 193-221.

Kröner, A., Linnebacher, P., Stern, R., Reischmann, T., Manton, W., Hussein, I., 1991. Evolution of Pan-African island arc assemblages in the southern Red Sea Hills, Sudan, and in southwestern Arabia as exemplified by geochemistry and geochronology. Precambrian Research 53, 99-118.

Kröner, A., Sassi, F.P., 1996. Evolution of the northern Somali basement: new constraints from zircon ages. Journal of African Earth Sciences 22, 1-15.

Küster, D., Liégeois, J.-P., Matukov, D., Sergeev, S., Lucassen, F., 2008. Zircon geochronology and Sr, Nd, Pb isotope geochemistry of granitoids from Bayuda Desert and Sabaloka (Sudan): Evidence for a Bayudian event (920–900Ma) preceding the Pan-African orogenic cycle (860–590Ma) at the eastern boundary of the Saharan Metacraton. Precambrian Research 164, 16-39.

Küster, D., Utke, A., Leupolt, L., Lenoir, J.L., Haider, A., 1990. Pan-African Granitoid Magmatism in northeastern and southern Somalia. Berliner Geowissenschaftliche Abhandlungen 120, 519-536.

Leggo, P.M., 1974. A geochronological study of the basement complex of Uganda. Journal of the Geological Society, London 130, 263-277.

Lenoir, J.-L., Küster, D., Liégeois, J.-P., Utke, A., Haider, A., Matheis, G., 1994. Origin and regional significance of late Precambrian and early Palaeozoic granitoids in the Pan-African belt of Somalia. Geologische Rundschau 83, 624-641.

Ludwig, W., Strunk, O., Westram, R., Richter, L., Meier, H., Buchner, A., Lai, T., Steppi, S., Jobb, G., Förster, W., 2004. ARB: a software environment for sequence data. Nucleic acids research 32, 1363-1371.

Maboko, M., Nakamura, E., 2002. Isotopic dating of Neoproterozoic crustal growth in the Usambara Mountains of Northeastern Tanzania: evidence for coeval crust formation in the Mozambique Belt and the Arabian–Nubian Shield. Precambrian Research 113, 227-242.

Mänttäri, I., Kigereigu, F., Huhma, H., De Kock, G., Koistinen, T., Kuosmanen, E., Lahaye, Y., Lehtonen, M., Mäkitie, H., Manninen, T., 2011. New Precambrian rock ages from Uganda, 23rd Colloquium of African Geology (CAG23), University of Johannesburg, Republic of South Africa, Abstract Volume, p. 260.

McGee, B., Collins, A.S., Trindade, R.I.F., 2014a. Age and Provenance of the Cyrogenian to Cambrian passive margin to foreland basin sequence of the northern Paraguay Belt, Brazil. Geological Society of America, Bulletin in press.

McGee, B., Collins, A.S., Trindade, R.I.F., Jourdan, F., 2014b. Tracking glaciation, orogenic exhumation and foreland basin evolution: Sedimentology and 40Ar/39Ar detrital muscovite provenance in the Paraguay Belt, Brazil. Sedimentology in press.

Meert, J.G., 2003. A synopsis of events related to the assembly of eastern Gondwana. Tectonophysics 362, 1-40.

Meert, J.G., Lieberman, B.S., 2008. The Neoproterozoic assembly of Gondwana and its relationship to the Ediacaran–Cambrian radiation. Gondwana Research 14, 5-21.

Meert, J.G., Van Der Voo, R., 1997. The assembly of Gondwana 800-550 Ma. Journal of Geodynamics 23, 223-235.

Mogessie, A., Belete, K., Hoinkes, G., 2000. Yubdo-Tulu Dimtu mafic-ultramafic belt, Alaskan-type intrusions in western Ethiopia: Its implication to the Arabian-Nubian Shield and tectonics of the Mozambique Belt. Journal of African Earth Sciences 30, 62.

Muhongo, S., 1994. Neoproterozoic Collision Tectonics In the Mozambique Belt Of East- Africa - Evidence From the Uluguru Mountains, Tanzania. Journal Of African Earth Sciences 19, 153-168.

Muhongo, S., Kröner, A., Nemchin, A., 2001. Single zircon evaporation and SHRIMP ages for granulite-facies rocks in the Mozambique belt of Tanzania. The Journal of Geology 109, 171-189.

Payne, J.L., Pearson, N.J., Grant, K.H., G.P, 2013. Reassessment of relative oxide

formation rates and molecular interferences on in-situ Lutetium-Hafnium analysis with Laser Ablation MC-ICP-MS. . Journal of Analytical Atomic Spectrometry 28, 1068-1079.

Pisarevsky, S.A., Murphy, J.B., Cawood, P.A., Collins, A.S., 2008. Late Neoproterozoic and Early Cambrian palaeogeography: models and problems. Geological Society, London, Special Publications 294, 9-31.

Plavsa, D., Collins, A.S., Foden, J.F., Kropinski, L., Santosh, M., Chetty, T., Clark, C., 2012. Delineating crustal domains in Peninsular India: Age and chemistry of orthopyroxene-bearing felsic gneisses in the Madurai Block. Precambrian Research 198, 77-93.

Plavsa, D., Collins, A.S., Payne, J.L., Foden, J.D., Clark, C., Santosh, M., 2014. Detrital zircons in basement metasedimentary protoliths unveil the origins of southern India. Geological Society of America Bulletin 126, 791-811.

Reddy, S.M., Collins, A.S., Mruma, A., 2003. Complex high-strain deformation in the Usagaran Orogen, Tanzania: structural setting of Palaeoproterozoic eclogites. Tectonophysics 375, 101-123.

Robinson, F., Foden, J., Collins, A., in press. Geochemical and isotopic constraints on island arc, synorogenic, post-orogenic and anorogenic granitoids in the Arabian Shield, Saudi Arabia. . Lithos.

Robinson, F., Foden, J., Collins, A., Payne, J., 2014. Arabian Shield magmatic cycles and their relationship with Gondwana assembly: Insights from zircon U–Pb and Hf isotopes. Earth and Planetary Science Letters 408, 207-225.

Scherer, E., Münker, C., Mezger, K., 2001. Calibration of the lutetium-hafnium clock. Science 293, 683-687.

Shackleton, R., 1996. The final collision zone between East and West Gondwana: where

is it? Journal of African Earth Sciences 23, 271-287.

Sláma, J., Kosler, J., Condon, D.J., Crowley, J.L., Gerdes, A., Hanchar, J.M., Horstwood, M.S.A., Morris, G.A., Nasdala, L., Norberg, N., Schaltegger, U., Schoene, B., Tubrett, M.N., Whitehouse, M.J., 2008. Plesovice zircon - A new natural reference material for U-Pb and Hf isotopic microanalysis. . Chemical Geology 249, 1-35.

Stern, R., Ali, K.A., Abdelsalam, M.G., Wilde, S.A., Zhou, Q., 2012. U–Pb zircon geochronology of the eastern part of the Southern Ethiopian Shield. Precambrian Research 206, 159-167.

Stern, R.J., 1994. Arc-Assembly and Continental Collision in the Neoproterozoic African Orogen: Implications for the Consolidation of Gondwanaland. Annual Review of Earth and Planetary Sciences 22, 319-351.

Stern, R.J., 2002. Crustal evolution in the East African Orogen: a neodymium isotopic perspective. Journal of African Earth Sciences 34, 109-117.

Tadesse, G., Allen, A., 2004. Geochemistry of metavolcanics from the Neoproterozoic Tuludimtu orogenic belt, Western Ethiopia. Journal of African Earth Sciences 39, 177-185.

Tadesse, G., Allen, A., 2005. Geology and geochemistry of the Neoproterozoic Tuludimtu Ophiolite suite, western Ethiopia. Journal of African Earth Sciences 41, 192-211.

Teklay, M., Haile, T., Kröner, A., Asmerom, Y., Watson, J., 2003. A back-arc palaeotectonic setting for the Augaro Neoproterozoic magmatic rocks of western Eritrea. Gondwana Research 6, 629-640.

Teklay, M., Kröner, A., Mezger, K., Oberhänsli, R., 1998. Geochemistry, Pb-Pb single zircon ages and Nd-Sr isotope composition

of Precambrian rocks from southern and eastern Ethiopia: implications for crustal evolution in East Africa. Journal of African Earth Sciences 26, 207-227.

Tenczer, V., Hauzenberger, C., Fritz, H., Hoinkes, G., Muhongo, S., Klötzli, U., 2012. Crustal age domains and metamorphic reworking of the deep crust in Northern-Central Tanzania: a U/Pb zircon and monazite age study. Mineralogy and Petrology.

Trindade, R.I., D'Agrella-Filho, M.S., Epof, I., Brito Neves, B.B., 2006. Paleomagnetism of Early Cambrian Itabaiana mafic dikes (NE Brazil) and the final assembly of Gondwana. Earth and Planetary Science Letters 244, 361-377.

Vail, J.R., 1983. Pan-African crustal accretion in north-east Africa. Journal of African Earth Sciences (1983) 1, 285-294.

Vermeesch, P., 2004. How many grains are needed for a provenance study? Earth and Planetary Science Letters 224, 441-451.

Westerhof, A., Haermae, P., Isabirye, E., Katto, E., Koistinen, T., Kuosmanen, E., Lehto, T., Lehtonen, M., Maekitie, H., Manninen, T., 2014. Geology and geodynamic development of Uganda with explanation of the 1: 1,000,000: scale geological map. Geol Surv Finland, Special Paper 55.

Woldemichael, B.W., Kimura, J.-I., 2008. Petrogenesis of the Neoproterozoic Bikilal-Ghimbi gabbro, Western Ethiopia. Journal of mineralogical and petrological sciences 103, 23-46.

Woldemichael, B.W., Kimura, J.-I., Dunkley, D.J., Tani, K., Ohira, H., 2010. SHRIMP U–Pb zircon geochronology and Sr–Nd isotopic systematic of the Neoproterozoic Ghimbi-Nedjo mafic to intermediate intrusions of Western Ethiopia: a record of passive margin magmatism at 855 Ma? International Journal of Earth Sciences 99, 1773-1790.

Woodhead, J.D., Hergt, J.M., Shelley, M., Eggins, S., Kemp, R., 2004. Zircon Hf-isotope analysis with an Excimer laser, depth profiling, ablation of complex geometries, and concomitant age estimation. . Chemical Geology 209, 121-135.

Yibas, B., Reimold, W., Anhaeusser, C., Koeberl, C., 2003. Geochemistry of the mafic rocks of the ophiolitic fold and thrust belts of southern Ethiopia: constraints on the tectonic regime during the Neoproterozoic (900–700 Ma). Precambrian Research 121, 157-183.

Yibas, B., Reimold, W.U., Armstrong, R., Koeberl, C., Anhaeusser, C.R., Phillips, D., 2002. The tectonostratigraphy, granitoid geochronology and geological evolution of the Precambrian of southern Ethiopia. Journal Of African Earth Sciences 34, 57-84.

ABSTRACT

The East African Orogen (EAO) is a Neoproterozoic to early Cambrian mobile belt that reflects the collision between Neoproterozoic India and the African Neoproterozoic continents—it is the major collisional orogeny that formed as central Gondwana coalesced. The Western Ethiopian Shield (WES) is made up of a range of supra-crustal and plutonic rocks that formed in Tonian volcanic arc environments, it holds a key position, between the juvenile Arabian Nubian Shield in the north and the southern high-grade Mozambique Belt. The relative timing and duration of arc formation within the East African Orogen is still being unravelled and we present new U–Pb, Hf and O isotopic data from zircons that further constrain the magmatism within the WES. Data suggest that the main tectono-thermal events occur at ca. 854–835 Ma, ca. 810–770 Ma and ca. 660–600 Ma and are broadly supported by previously published ages from elsewhere in the WES. Hafnium isotopic analysis of the WES indicates that the Tonian magmas were generated from juvenile Neoproterozoic mantle sources (ε_{Hf}(t) values of +11.91 to +1.94) that stretch to lower ε_{Hf}(t) than elsewhere in the EAO, suggesting some involvement of early Tonian, or pre-Neoproterozoic crust. Oxygen isotopes support the relatively juvenile nature ($\delta^{18}O$ ratios of 8.84–5.99‰) of the magma from which the zircons grew. The data presented in this study better reveal the timing and nature of these tectonothermal events within the WES. Comparative data analyses from elsewhere in the northern East African Orogen suggests that closure of the western Mozambique Ocean involved progressive volcanic-arc accretion to the active margin of Cryogenian–Ediacaran Africa.

INTRODUCTION

The East African Orogen (EAO) is the world's largest Neoproterozoic to Cambrian orogenic complex and preserves a complex history of intra-oceanic and continental margin, magmatic and tectonothermal events (see Fritz et al 2013 and Johnson et al. 2011 for recent reviews). The rocks that are found in the orogen formed in a series of volcanic arcs during the consumption of the Mozambique Ocean, as Neoproterozoic India collided with the continents that formed Africa (Archibald et al., 2016; Archibald et al., 2017b; Blades et al., 2015; Collins and Pisarevsky, 2005a; Fritz et al., 2013; Johnson et al., 2011a; Meert, 2003; Meert and Lieberman, 2008; Robinson et al., 2015; Robinson et al., 2014). Traditionally, the East African Orogen is divided into the Arabian Nubian Shield (ANS) in the north, composed of largely juvenile Neoproterozoic crust, and the Mozambique Belt in the south, comprising mostly pre-Neoproterozoic crust, with a strong Neoproterozoic–early Cambrian

tectono-thermal overprint (Fig. 1). This general interpreted arrangement of crustal ages/types has been modified recently with reports of juvenile, Neoproterozoic crust in Antarctica (Jacobs and Thomas, 2004) and Madagascar (Archibald et al., 2017a; Collins et al., 2012; Jöns and Schenk, 2008, 2011; Jöns et al., 2005a, 2006; Jöns et al., 2005b). The Western Ethiopian Shield (WES) is one of the largest continuous outcrop tracts in the EAO (Fig. 2) and forms the interface between the dominantly juvenile Arabian Nubian Shield in the north and the high-grade Mozambique Belt to its south. This geographical location implies the WES is the site of Neoproterozoic crustal growth meaning it may provide an excellent record of the nature of crustal growth on a craton margin.

The WES is composed of a range of supracrustal and plutonic rocks that formed in Tonian volcanic arc environments (Alemu, 2005; Ayalew et al., 1990; Ayalew and Peccerillo, 1998; Blades et al., 2015; Braathen et al.,

2001; de Wit and Aguma, 1977; Grenne et al., 2003; Jackson, 2006; Johnson et al., 2004; Kebede et al., 2001a; Kebede and Koeberl, 2003; Kebede et al., 1999; Kebede et al., 2001b; Tadesse and Allen, 2004, 2005; Teklay et al., 1998a; Woldemichael and Kimura, 2008; Woldemichael et al., 2010). The aim of this study is to use these rocks to develop a temporal and isotopic framework (U–Pb, Hf, O) for the evolution of the eastern section of the extensive WES. This study provides the only in-situ zircon Hf and O isotope study in western Ethiopia, which is used to unravel the degree of mantle involvement in the source magmas. Combined, the data help relate the WES to the Arabian Nubian Shield and the Mozambique Belt (Figs. 1 & 2) and better elucidate the nature and evolution of Neoproterozoic ocean plate tectonics.

GEOLOGICAL SETTING
East African Orogen
The East African Orogen, in a reconstructed Gondwana, extends from Turkey and the Levant, in the north, to Mozambique, Madagascar, Sri Lanka and East Antarctica in the south. It is the world's largest Neoproterozoic to Cambrian orogenic complex and preserves a complex history of intra-oceanic and continental margin, magmatic and tectonothermal events. Many of the rocks found in the orogen formed in volcanic arcs during the Neoproterozoic subduction of the Mozambique Ocean (Archibald et al., 2016; Archibald et al., 2017b; Blades et al., 2015; Collins and Pisarevsky, 2005a; Fritz et al., 2013; Johnson et al., 2011a; Meert, 2003; Meert and Lieberman, 2008; Robinson et al., 2015; Robinson et al., 2014). This ocean separated Neoproterozoic India from the Neoproterozoic continents that formed Gondwanan Africa (Collins and Pisarevsky, 2005a; Fritz et al., 2013; Johnson et al., 2011a; Meert, 2003; Meert and Lieberman, 2008;

Merdith et al., 2017). Stern (1994) interpreted the orogen to be a product of the collision between East Gondwana (India–Australia–Antarctica) and West Gondwana (Africa–South America). However, it was later recognized that both East and West Gondwana did not exist as coherent Neoproterozoic continents, but rather, represent amalgams of smaller continents, which came together during the Neoproterozoic to early Cambrian (Boger et al., 2006; Cawood and Buchan, 2007; Collins, 2003; Fitzsimons, 2000; Ganade de Araujo et al., 2014; McGee et al., 2014a; McGee et al., 2014b; Meert, 2003; Pisarevsky et al., 2008; Trindade et al., 2006).

A broad band of Archaean and Palaeoproterozoic crust (2900–2000 Ma) within the East African Orogen was identified by (Collins and Windley, 2002b) as an extensive Neoproterozoic ribbon or micro-continent that is now preserved in rocks from southern India, Madagascar, Somalia, eastern Ethiopia to Arabia (Afif Terrane). Collins and Pisarevsky (2005a) named this palaeo-continent Azania, after the ancient name of the East African coast, and suggested that it collided with the Congo/Tanzania/Bangweulu Block and previously amalgamated western Arabian Nubian Shield, at ca. 650–630 Ma as represented by the East African Orogen (Collins and Pisarevsky, 2005a; Robinson et al., 2014; Stern, 2002). The existence of Azania was used to explain the bimodality in the ages from the East African Orogen (Collins and Pisarevsky, 2005b; Meert et al., 1997). A younger orogeny (ca. 570–520 Ma) was interpreted to be the result of the collision between India and the already amalgamated Congo and Azania terranes. Collins and Pisarevsky (2005) named this tectono-thermal event the Malagasy Orogeny.

The northern East African Orogen is known as the Arabian Nubian Shield (ANS), and is largely composed of juvenile Neoproterozoic
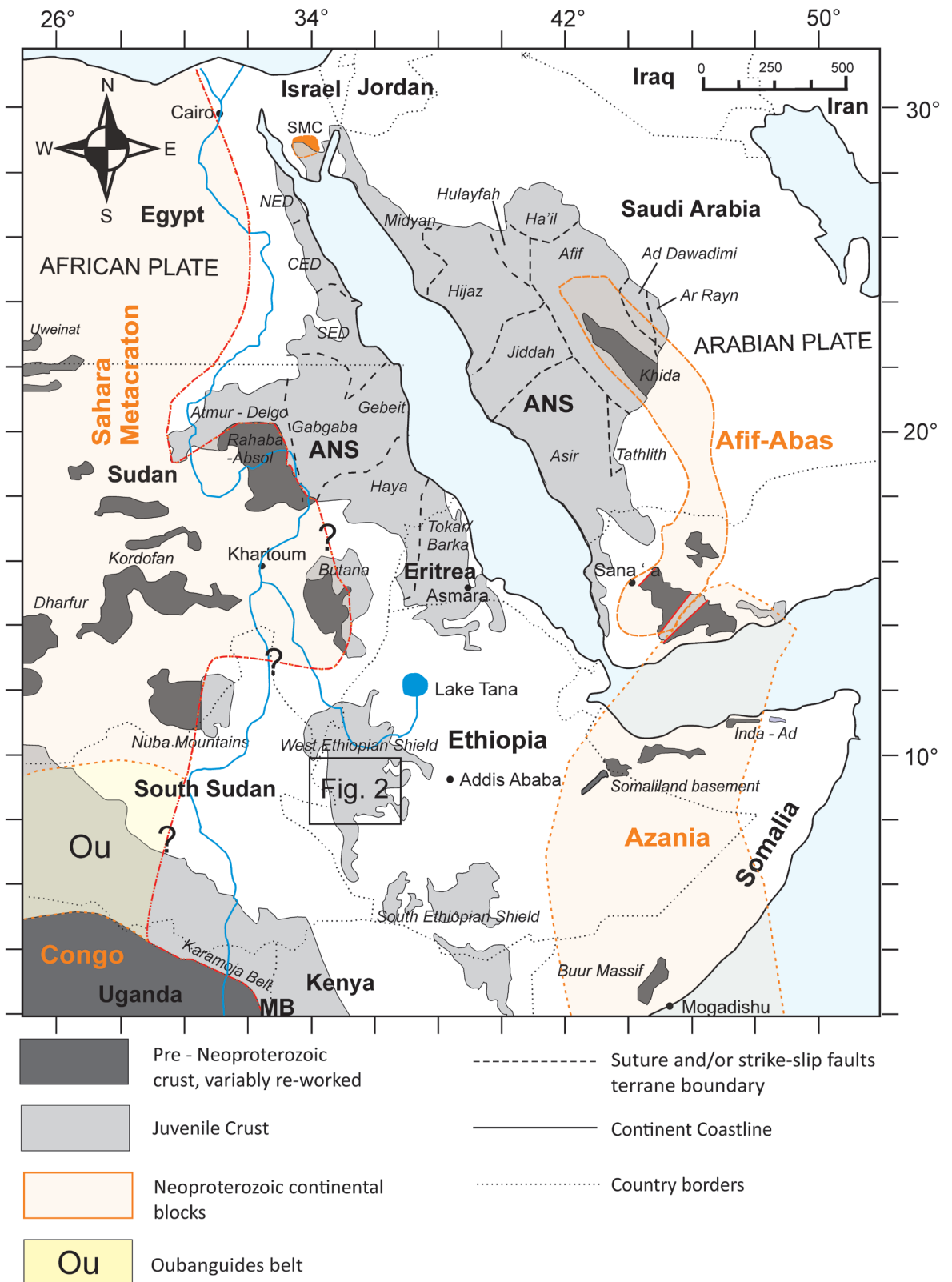
Figure 1: Location map and distribution of crustal domains in the East African Orogen. SM, Sahara Metacraton; ANS, Arabian Nubian Shield. MB, Mozambique Belt. The black box represents the map area in figure 2. Adapted from Johnson et al., (2014) and Blades et al., (2015).

crust (Johnson et al., 2011b; Johnson and Woldehaimanot, 2003; Stern, 1994, 2002). This is dominated by low grade volcano-sedimentary rocks in association with plutons and ophiolitic remnants (Abdelsalam and Stern, 1996; Allen and Tadesse, 2003; Cox et al., 2012b; Kröner et al., 1991; Robinson et al., 2014; Shackleton, 1996; Stern, 1994). To the south is a tract of largely older continental crust, which was extensively deformed and metamorphosed in the Neoproterozoic/Cambrian. This is known as the Mozambique Belt (Meert, 2003; Woldemichael and Kimura, 2008; Woldemichael et al., 2010; Yibas et al., 2003a). The Western Ethiopian Shield is situated in a key transitional location between the Arabian Nubian Shield and Mozambique Belt, adjacent, and to the east of, the 'Eastern Saharan Metacraton' (Abdelsalam and Stern, 1996).

The Western Ethiopian Shield

Western Ethiopia is comprised of a range of supracrustal and plutonic rocks that formed in a Tonian volcanic arc system (Alemu, 2005; Allen and Tadesse, 2003; Ayalew et al., 1990; Ayalew and Peccerillo, 1998; Blades et al., 2015; Braathen et al., 2001; Grenne et al., 2003; Johnson et al., 2004; Kebede et al., 2001a; Kebede and Koeberl, 2003; Kebede et al., 1999; Kebede et al., 2001b; Mogessie et al., 2000; Teklay et al., 1998b; Woldemichael and Kimura, 2008; Woldemichael et al., 2010; Yibas et al., 2003b; Yibas et al., 2002). The WES consists of high-grade gneisses, low-grade metavolcanic and metasedimentary rocks with associated mafic—ultramafic intrusions and syn-to post-tectonic gabbroic to granitic intrusions. Allen and Tadesse (2003) divided the WES into domains of shared lithological assemblages and geological histories and though there have been many other lithotectonic divisions proposed for the region (see Alemu 2005 for a summary).

Allen and Tadesse (2003) defined the rocks of the WES as the Tuludimtu Orogenic Belt (here shortened to the non-genetic 'Tuludimtu Belt'), the central region of which they subdivided into five litho-tectonic domains, interpreted to have formed during the amalgamation of this part of Gondwana before the final closure of the Mozambique Ocean (Allen and Tadesse, 2003). The five domains are named the Didesa, Kemashi, Dengi, Sirkole and Daka Domains and are all found within the study area (Fig. 2).

Didesa Domain

The Didesa Domain forms the eastern boundary of the study area and consists of amphibolite-facies paragneiss and orthogneiss, intruded by Neoproterozoic intrusive rocks. The Didesa Domain was interpreted by Allen and Tadesse (2003) to represent the eastern foreland of the Tuludimtu Belt. Broad age constraints on magmatism have been previously reported from the Didesa Domain, where a hornblende + biotite tonalite (841 ± 8 Ma) and a coeval felsic granite (827 ± 17 Ma) yielded Tonian ages of formation (Blades et al. 2015). U–Pb analysis of zircon grain rims from this tonalite yielded an age of 779 ± 11 Ma and is interpreted to represent metamorphism in the area (Blades et al., 2015). Ages coeval with the rims in the hornblende + biotite tonalite were reported from the Didesa River gneisses (782 ± 33 Ma). These data suggest that ca. 780 Ma represents magmatism and metamorphism in the Didesa Domain. Zircon rims on these grains yielded an age of 660 ± 8 Ma, dating the tectono-thermal event in which a pervasive L/S fabric was imposed on the rock. A granite cross-cutting the Didesa River yielded an age of 653 ± 12 Ma. These zircons also yield positive $\varepsilon_{Hf}(t)$ values (+2 to +10), suggesting a mantle-dominated origin compatible with magma generated within an oceanic setting (Blades et al. 2015).
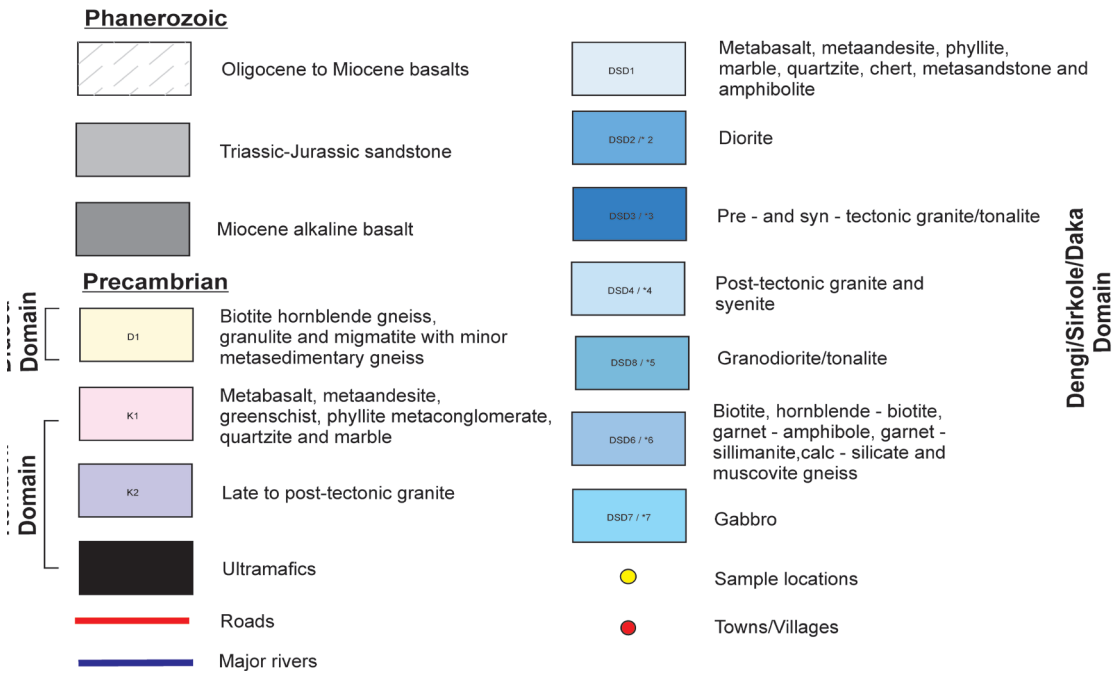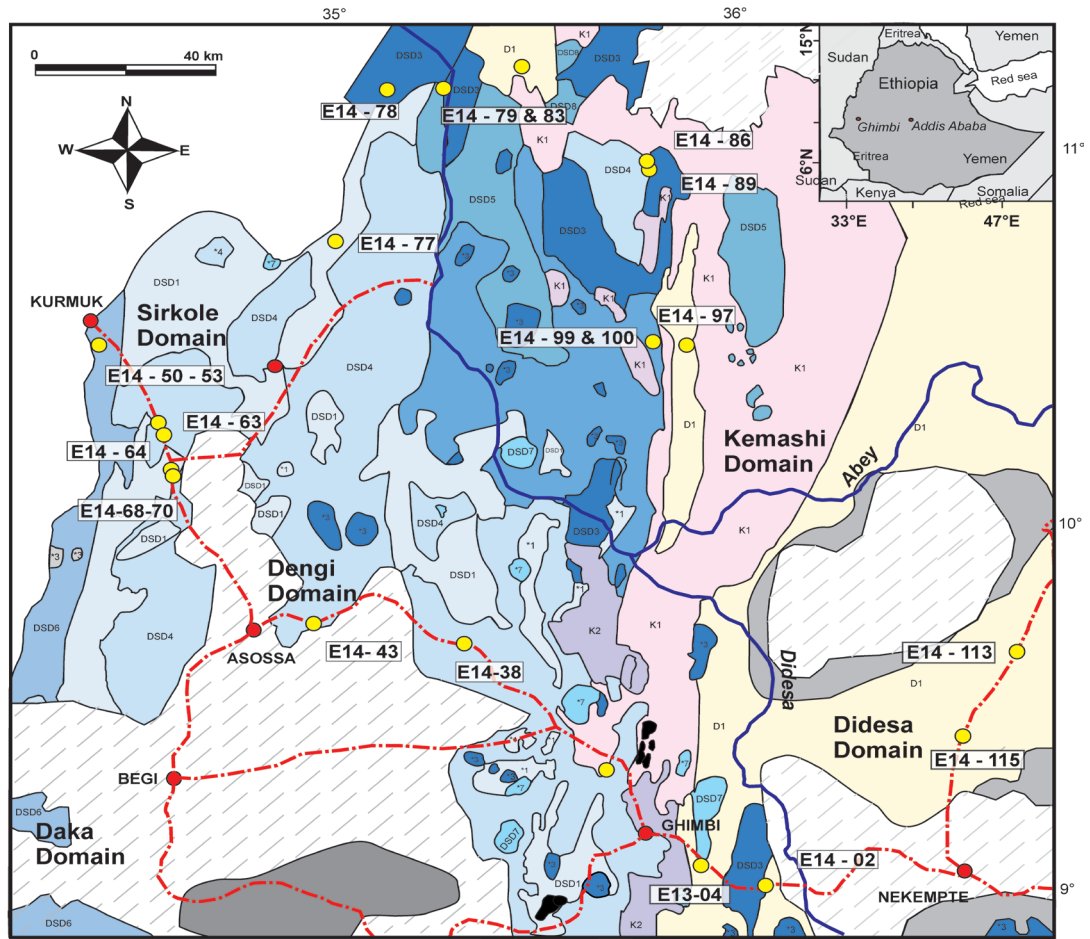
Figure 2: Simplified geological map of the area of study in western Ethiopia. Adapted from geological map of western Ethiopia (2nd edition), scale 1:2 000,000, published by the Geological Survey of Ethiopia (1996). The Dengi, Sirkole and Daka domains are separated either by a tectonic contact or are isolated by Phanerozoic cover.

Kemashi Domain

To the west of the Didesa Domain, the Kemashi Domain forms a narrow N–S strip that is 10–15 km wide (Fig. 2). This domain is characterised by a sequence of metasedimentary rocks whose protoliths are interpreted to have a marine origin. The metasedimentary sequence is characterised by cherts, and quartzites, interlayered with abundant mafic to ultramafic material, all metamorphosed to upper greenschist/epidote-amphibolite facies ((Johnson et al., 2004; Kebede et al., 2001a; Kebede and Koeberl, 2003; Kebede et al., 2001b). Recent detrital geochronological studies, from a single quartzite sample, show provenance age peaks at 2.8–2.4 Ga, ca. 1.8 Ga and 1.15–0.84 Ga and a maximum depositional age of 838 ± 13 Ma (Blades et al., 2015). The Ganjii Granite, on the Dengi/Kemashi boundary, is the only truly post-tectonic intrusion dated within the WES (584 ± 10 Ma; Blades et al., 2015). Ultramafic/mafic plutonic rocks within the Kemashi Domain have been interpreted to represent an ophiolite sequence (Abdelsalam and Stern, 1996; Allen and Tadesse, 2003; Ayalew et al., 1990; Stern, 2002; Tadesse and Allen, 2005), named the Tuludimtu Ophiolite by Tadesse and Allen (2005) (Fig. 2). However, others have suggested that there is a lack of geochemical evidence to support the presence of ophiolites in the Western Ethiopian Shield (Alemu, 2005; Braathen et al., 2001; Grenne et al., 2003; Mogessie et al., 2000; Woldemichael and Kimura, 2008; Woldemichael et al., 2010) and have instead suggested that the ultramafic bodies represent Alaskan-type, concentrically zoned intrusions, which were emplaced into an extensional arc or back arc environment (Braathen and Davidsen, 2000; Grenne et al., 2003; Jackson, 2006; Mogessie et al., 2000). Blades et al. (2017) used the chemistry of chrome spinels within a range of intrusions to suggest that both Alaskan-type intrusions and pods of ocean-lithosphere occur in the domain.

Dengi Domain

The Dengi Domain to the west of the Kemashi Domain (Fig. 2) is ca. 120 km wide and is characterized by a deformed and metamorphosed volcano-sedimentary sequence and the Jamoa-Ganti orthogneiss. There are also a number of intrusive bodies incorporated in this domain. Geochronological data have been suggested to represent three distinct generations of intrusions (Ayalew et al., 1990; Kebede et al., 2001a; Kebede et al., 2001b). In the Gore/Gambella region, intrusion ages for pre-kinematic Birbir quartz-diorite and Goma granodiorite of 828 ± 9 Ma and 814 ± 2 Ma, respectively (Ayalew et al., 1990). These pre-kinematic bodies have been previously interpreted to have a calc-alkaline affinity and a show evidence of mantle derivation (Ayalew and Peccerillo, 1998). Syn-tectonic granites from the region have ages between 783–730 Ma (Ayalew et al., 1990; Kebede et al., 2001a). These plutons have a metaluminous to peraluminous chemistry and trace-element signatures that have been interpreted to have been largely derived from the anataxis of crustal rocks (Ayalew and Peccerillo, 1998; Kebede et al., 2001a). Allen and Tadesse (2003) interpreted geochemical data from the Dengi Domain to represent a volcanic arc sequence related to closure of the ocean represented by the Tuludimtu Ophiolite to the east.

Sirkole and Daka Domain

The Sirkole Domain occupies the north-western portion of the study area, west of Asosa (Fig. 2) and extends into Sudan. This region is composed of gneissic and volcano-sedimentary rocks, intruded by granites. There

Figure 3: Thin section images of the igneous samples collected from the Western Ethiopian Shield, in cross po-larised light. Minerals present are labelled where: Qtz is quartz; Bt is biotite; Mu is muscovite; Am is amphibole mainly hornblende in these samples); Pl is plagioclase; Mc is microcline and Px is pyroxene.

Figure 3: Thin section images of the igneous samples collected from the Western Ethiopian Shield, in cross po-larised light. Minerals present are labelled where: Qtz is quartz; Bt is biotite; Mu is muscovite; Am is amphibole mainly hornblende in these samples); Pl is plagioclase; Mc is microcline and Px is pyroxene.

Figure 3: Thin section images of the igneous samples collected from the Western Ethiopian Shield, in cross po-larised light. Minerals present are labelled where: Qtz is quartz; Bt is biotite; Mu is muscovite; Am is amphibole mainly hornblende in these samples); Pl is plagioclase; Mc is microcline and Px is pyroxene.

has been little geochronological work done in this area, however, Allen and Tadesse (2003) interpreted this suite to represent a series of interleaved N–S striking thrust sheets. The Daka Domain lies in the southwest corner of the region. The relationship between the Daka Domain and the Sirkole Domains is unclear, as it is separated from these by Cenozoic cover (Allen and Tadesse, 2003). The Daka Domain

was interpreted by Allen and Tadesse (2003) to represent the western basement margin to the Tuludimtu Belt, which they suggested consisted of pre-Neoproterozoic basement gneisses.

METHODOLOGY
U–Pb zircon geochronology

Samples from metaigneous rocks were collected along a transect extending from Nekempte to

Kurmuk (see Fig. 2) located within the Western Ethiopian Shield. Zircon grains were extracted from crushed rocks using standard magnetic and heavy liquid techniques (Howard et al., 2009). Mineral separates were hand-picked and mounted in epoxy resin. The polished mounts were carbon coated and zircons imaged under cathodoluminescence (CL) on a Philips XL40 scanning electron microscope (SEM), operating in high-vacuum mode with a tungsten filament with attached Gatan CL at Adelaide Microscopy (The University of Adelaide). Zircon (U–Pb) analysis on twenty two plutonic samples was conducted on New Wave 213 nm Nd–YAG laser coupled with the Agilent 7500cs Inductively Coupled Plasma Mass Spectrometer (LA–ICP–MS) at the University of Adelaide. The 30 μm diameter spot size was used with a typical pit depth of 30–50μm. GEMOC GJ-1 zircon together with TIMS normalising data $^{207}Pb/^{206}Pb$ = 607.7 ± 4.3 Ma, $^{206}Pb/^{238}U$ = 600.7 ± 1.1 Ma and $^{207}Pb/^{235}U$ = 602.0 ± 1.0 Ma (Jackson et al., 2004) was used to correct for the U-Pb mass bias and laser induced fractionation. The Plešovice zircon standard (ID TIMS $^{206}Pb/^{238}U$ age = 337.13 ± 0.37 Ma, Sláma et al., 2008), was used to assess accuracy before and during the analysis of the unknowns. Plešovice analyses yield a weighted-mean $^{206}Pb/^{238}U$ age of 335.6 ± 1.5 Ma (2SD, n = 126).

Data were collected, corrected and filtered in the software package GLITTER version 3.0 (Van Achterbergh et al., 2001). Concordia diagrams and weighted averages were calculated using ISOPLOT 4.15 for Excel (Ludwig, 2009).

Zircon Lu–Hf Isotope analysis

Analytical methods for zircon Lu–Hf isotope analysis follows Payne et al. (2013). Analyses were undertaken using a New Wave UP-193 ArF excimer laser attached to a Thermo-Scientific Neptune Multi-Collector ICP-MS at the University of Adelaide. The bulk of analyses were carried out using a beam diameter of 50 μm for large and a minimum of ~25 μm for smaller grains. Typical ablation times were 40–100 s using a 5 Hz repetition rate, a 4 ns pulse rate, and an intensity of ~10J/cm². Zircons were ablated in a helium atmosphere, which was then mixed with argon and nitrogen upstream of the ablation cell.

Reduction of zircon data were undertaken using a macro-driven Hf isotope data reduction Excel spreadsheet, HfTRAX (Payne et al., 2013). The data were normalised to $^{179}Hf/^{177}Hf$ = 0.7325, using an exponential correction for mass bias. Yb and Lu isobaric interferences on ^{176}Hf were corrected following the methods of Woodhead et al. (2004). The accuracy of the Yb and Lu corrections has been demonstrated by repeated analysis of standard zircons with a range in $^{176}Yb/^{177}Hf$ and $^{176}Lu/^{177}Hf$ values (Griffin et al., 2006). Before and during the analysis of unknowns, standards were analysed to check instrument performance and stability. The primary zircon standard used was Plešovice, which yielded a mean $^{176}Hf/^{177}Hf$ ratio of 0.282470 ± 0.000015. This compares to the published value of 0.282482 ± 0.000013 (2SD) by Sláma et al. (2008). Values for $\varepsilon_{Hf}(t)$, and T_{DMc} were calculated using the ^{176}Lu decay constant after Scherer et al. (2001). T_{DMc} was calculated using the methods of Griffin et al. (2002) with an average crustal composition of $^{176}Lu/^{177}Hf$ = 0.015.

Zircon oxygen isotope analysis

Oxygen isotopes were collected from the same samples that were used for U–Pb geochronology. Zircon grain mounts were repolished and oxygen isotope analysis spots were placed on the same sites as those used in the Hf determination. Analyses were undertaken using the SHRIMP SI at the Research School of Earth Sciences in the Australian National University,

Table 1: Descriptions and locations for samples collected in Western Ethiopia.

Sample ID	Main Field Relationships	Locality description	GPS Location	Minerology	Analyses completed	Rock Type
E14.02	Foliated gneiss is cross-cut by K-feldspear rich granite. Field relationships similar to those seen at Didesa river (Blades et al., 2015).	5km west of the Didesa River Bridge next to Jogir river	N 09° 02' 15.4" E 36° 02' 07.4"	Holocrystalline, large grains, Qtz + Pl + Kfs	LA–IC–MS U–Pb, Hf	Granite Pegmatite
E14.04	No fabric present, outcrop forms in rounded boulders	Located on hillside above road, ~ 15km from Didesa River Bridge	N 09° 02' 15.4" E 36° 02' 07.4"	Holocrystalline, equi-granular, Qtz + Pl + kfs + Bt + Grt + Mc	LA–IC–MS U–Pb, Hf	Suqii-Wagga Granite
E14.38	Mafic dykes cross cut the granodiorite. Little to no deformation in the country rock and the presence of a chilled margin suggesting that they are co-magmatic.	Located in Gori Quarry, close to Gori Village.	N 09° 37' 18.9" E 35° 19' 16.4"	Seriate texture, large an-hedral, poikilitic grains Qtz + Kfs + Bt	LA–IC–MS U–Pb, Hf	Gabbroic Diorite
E14.43	Porphyritic texture with large K-feldspar crystals in a finer plagioclase and quartz matrix. No fabric	Located on the Mendi – Daleti Road	N 09° 57' 23.7" E 35° 09' 59.8"	Seriate texture, large anhedral, poikilitic grains Qtz + Kfs + Pl + Mc + Bt	LA–IC–MS U–Pb, Hf	K-feldspar Granite
E14.50	Not well foliated and cross cuts the well foliated granodiorite gneiss (E14.53).	Located 3 km South of Kurmuk in a river outcrop	N 10° 32' 28.1" E 34° 19' 06.2"	Holocrystalline, gran-ular, hypidiomorphic, quartz and feldspar have a poikilitic textures. Qtz + Pl + Bt + Kfs	LA–IC–MS U–Pb, Hf	Granite
E14.53	Gneissic texture and is being cross but by E14.50 (granite).	Located 3 km South of Kurmuk in a river outcrop	N 10° 32' 28.1" E 34° 19' 06.2"	Holocrystalline, equi-granular, subhedral, Pr, Kfs + Pl + Bt and Mu. Bt defines a fabric	LA–IC–MS U–Pb, Hf	Gneiss

GPS coordinates are based on the WGS84 datum.

Geochemical classification according to Streckeisen (1976).

For Geochemical data - Blades et al., in prep

Table 1: Descriptions and locations for samples collected in Western Ethiopia.

Sample ID	Main Field Relationships	Locality description	GPS Location	Minerology	Analyses completed	RockType
E14 . 58	Host rock is a chlorite, biotite phyllite. The foliated leucogranite shows a well-defined intrusive relationship with the greenschist phyllite.	Collected 3km East of Kutawark	N 10° 33' 48.3" E 34° 24' 48.6"	Larger grains have poikilitic texture giving it a sponge appearane Qtz + Pl + Kfs + Bt	LA–IC–MS U–Pb, Hf	Leucogranite
E14 . 63	Homogeneous, unfoliated granite	Road side outcrop located near Shula Village (Argubella)	N 10° 23' 42.7" E 34° 34' 43.6"	Holocrystalline, equigranular, subhedral Qtz + Pl + Kfs + Bt + Hbl	LA–IC–MS U–Pb, Hf	Granite
E14 . 64	Homogeneous, unfoliated granite	Shula Village, large road side outcrop near Shekula refugee camp	N 10° 20' 47.1" E 34° 37' 22.3"	Holocrystalline, equigranular, smaller grain size, Qtz + Pl + Kfs + Bt opaques	LA–IC–MS U–Pb, Hf	Foliated K -Feldspar granite
E14 . 68	Gradational boundary between the monzonite and the granite (E14.69). Intermingling textures present	Homosha Village. 5km from Shekula Refugee Camp towards Asosa	N 10° 16' 09.8" E 34° 37' 29.9"	Holocrystalline, seriate texture, large anhrdral, poikilitic grains Qtz + Kfs + Pl + Mc + Bt	LA–IC–MS U–Pb, Hf	Monzonite
E14 . 69	Psammitic xenoliths are seen, forming a chilled margin as a result of rapid cooling of the magma adjacent to the colder country rocks and xenoliths.	Homosha Village. 5km from Shekula Refugee Camp towards Asosa	N 10° 16' 09.8" E 34° 37' 29.9"	Holocrystalline, seriate texture, large anhrdral, Qtz + Kfs + Pl + Mc + Bt	LA–IC–MS U–Pb, Hf	Granite
E14 . 70	Epidote veins present, no foliation present	Homosha Village. 5km from Shekula Refugee Camp towards Asosa	N 10° 16' 09.8" E 34° 37' 29.9"	Holocrystalline, seriate texture, subhedral, Qtz + Pl + Kfs + Bt + Hbl	LA–IC–MS U–Pb, Hf	Granodiorite

GPS coordinates are based on the WGS84 datum.

Geochemical classification according to Streckeisen (1976).

For Geochemical data - Blades et al., in prep

Table 1: Descriptions and locations for samples collected in Western Ethiopia.

Sample ID	Main Field Relationships	Locality description	GPS Location	Minerology	Analyses completed	Rock Type
E14.77	No fabrics present, outcrop forms rounded boulders	75km East of Kurmuk, alongside the road.	N 10° 42' 52.1" E 34° 57' 11.6"	Holocrystalline, Qtz + Pl + Kfs + Bt + Hbl	LA–IC–MS U–Pb, Hf, O	Granodiorite
E14.78	Felsic granite, no fabric present	Located at the Nile River Dam, 20 km from Guba	N 11° 14' 18.5" E 35° 05' 44.4"	Holocrystalline, inequigranular, Qtz + Pl + Kfs + Bt + Mc + Px + opaques	LA–IC–MS U–Pb, Hf, O	Granite
E14.79	Coarse grained, very weak foliation.	Located 5 km from Guba along the side of the road	N 11° 15' 54.4" E 35° 18' 26.9"	Holocrystalline , equigranular, subhedral, Qtz + Pl + Kfs + Bt	LA–IC–MS U–Pb, Hf, O	Leucogranite
E14.83	No fabric present	Located in a creek 60 km SE of Guba, along the road	N 11° 19' 08.7" E 35° 38' 21.7"	Holocrystalline, seriate texture, subhedral, Qtz + Kfs + Pl + Mc + Bt + Px	LA–IC–MS U–Pb, Hf, O	Granite
E14.86	Very fine grained, strong foliation defined by thin bands of felsic minerals	Located under the Belesse River Bridge	N 11° 11' 57" E 36° 19' 33"	Holocrystalline, equigranular, subhedral, Qtz + Kfs + Pl + Bt. Bt defines a fabric	LA–IC–MS U–Pb, Hf, O	Granodiorite
E14.87	Foliated-biotite rich	Located under the Little Belesse River Bridge	N 11° 09' 56.9" E 36° 20' 16.4"	Holocrystalline + inequigranular, Qtz + Pl + Kfs + Bt + Mc + Px + opaques	LA–IC–MS U–Pb, Hf, O	Granite

GPS coordinates are based on the WGS84 datum.

Geochemical classification according to Streckeisen (1976).

For Geochemical data - Blades et al., in prep

Table 1: Descriptions and locations for samples collected in Western Ethiopia.

Sample ID	Main Field Relationships	Locality description	GPS Location	Minerology	Analyses completed	Rock Type
E14.97	No signs of deformation.	Located in the lower Mora metasediments	N 10° 31' 59.2" E 36° 02' 02.7"	Holocrystalline + equigranular, perthitic textures, Qtz + Pl + Kfs + Bt + Mc + Px	LA–IC–MS U–Pb, Hf, O	Granite
E14.99	Intruded by the granite (E14.100), no defined foliation	Located at the intersection of the road and Mata River.	N 10° 31' 51.9" E 35° 57' 34.3"	Holocrystalline + equigranular, Qtz + Pl + Kfs + Bt + Mc	LA–IC–MS U–Pb, Hf, O	Granodiorite
E14.100	Granite is intruding the granodiorite (E14.100), no defined foliation	Located at the intersection of the road and Mata River.	N 10° 31' 51.9" E 35° 57' 34.3"	Holocrystalline + equigranular, Qtz + Pl + Kfs + Bt + Mc	LA–IC–MS U–Pb, Hf, O	Granite
E14.113	The mafic biotite gneiss is inter-mingling with the felsic Guttin granite. Texturally the oldest rock unit.	On the road between Chagni and Nekempte (approximately 70km North), just after the Nile River Gorge pass. Near the village of Agnur	N 09° 42' 51.8" E 36° 37' 49.0"	Holocrystalline + equigranular, Qtz + Pl + Kfs + Bt + Mc + Px + Hbl Opaques + titanite	LA–IC–MS U–Pb, Hf, O	Gneiss
E14.115	Guttin Granite is texturally the youngest rock-type. Weakly foliated though becomes mylonitised closer to the Guttin shear-zone	Located 5km from Agnur Village on the road side	N 10° 16' 09.8" E 34° 37' 29.9"	Holocrystalline + seriate texture, Qtz + Pl + Kfs + Bt + Mc +Px, opaques + titanite	LA–IC–MS U–Pb, Hf, O	Guttin granite

GPS coordinates are based on the WGS84 datum.

Geochemical classification according to Streckeisen (1976).

For Geochemical data - Blades et al., in prep

Table 2: Description of zircon morphologies and cathodoluminescence (CL) interpretations for each sample in the Western Ethiopian Shield. Figure 3 shows the representative CL images.

Sample	Zircon Morphology	Cathodoluminescence (CL) interpretation
E14 . 02	Size: 100—400 µm Colour: Orange, pale brown Ratio: Majority of zircons are ca. 3:1 with some crystals having an aspect ratio of 2:1 Shape: Euhedral/Prismatic	Majority of the zircon cores are metamict and poorly luminescent. Some rims display faint oscillatory zonation, whilst others are featureless.
E14 . 04	Size: 100—200 µm Colour: Light pink - colourless Aspect Ratio: Varying from ca. 2:1—5:1 Shape: Euhedral/prismatic, with some subhedral grains	Brightly luminescent cores that commonly preserve traces of oscillatory zoning. Dark rims are seen mantling most of these grains.
E14 . 38	Size: 30—200 µm Colour: Pale yellow—pale pink Aspect Ratio: Low aspect ratio ca. 1:1—2:1 Shape: Subhedral fragmented crystals	Sector zonation present in some grains. Luminescent and preserve well-defined oscillatory zoning - in some grains. Some grains preserve convolute boundaries.
E14 . 44	Size: 50—200 µm Colour: Pale yellow - orange Aspect Ratio: ca. 2:1—5:1 Shape: euhedral. preserved prismatic and pyramidal crystal faces.	Most of the grains are poorly luminescent under CL with bands displaying oscillatory zonation. They contain cores that have patchy, complex zoning surrounded by oscillatory zonation. Some grains preserve convolute boundaries.
E14 . 50	Size: 50—300 µm Colour: Colourless to pale pink Aspect Ratio: Varied 1:1, 2:1, 3:1, 5:2 Shape: Subhedral grains, some zircon crystals exhibit moderate rounding of the crystal edges. Others have a prismatic euhedral shape.	Sector zonation present in some grains. Luminescent and preserve well-defined oscillatory zoning - in some grains. Some grains preserve convolute boundaries. There are strong variations in the relative development of zoned domains, where one large uniform central zone is succeeded by much finer oscillatory-zoned bands. Zircons have segments of homogeneously textured zircon appearing as transgressive (across all pre-existing textures) zircon patches and lobes.
E14 . 53	Size: 50—150 µm Colour: Light pink Aspect Ratio: ~ 1:1, Shape: Some zircon crystals exhibit moderate rounding of the crystal edges whereas in others the original crystal shape has been destroyed, and the final product being smoothly sub-rounded grains	Zircons have segments of homogeneously textured zircon appearing as transgressive (across all pre-existing textures) zircon patches and lobes. Areas of recrystallization occur dominantly at crystal terminations. There are a few zircons that display oscillatory zonation - varied frequencies with some relatively broad and others are defined by narrow zones.
E14 . 58	Size: 50—200 µm Colour: pale orange - brown Aspect Ratio: 1:1—2:1 Shape: Prismatic euhedral grains	Grains preserve oscillatory zoning. Dark rims are seen mantling most of these grains.
E14 . 63	Size: 20—300 µm Colour: Pale pink to colourless Aspect Ratio: ~2:1, 31 Shape: Some have a prismatic shape though most zircon crystals exhibit moderate rounding of the crystal edges whereas in others the original crystal shape has been destroyed, and the final product being smoothly sub-rounded grains	Oscillatory zonation present. Zircons have segments of homogeneously textured zircon appearing as transgressive (across all pre-existing textures) zircon patches and lobes. Areas of recrystallization occur dominantly at crystal terminations. Zircons contain cracks and inclusions.

Table 2: Description of zircon morphologies and cathodoluminescence (CL) interpretations for each sample in the Western Ethiopian Shield. Figure 3 shows the representative CL images.

Sample	Zircon Morphology	Cathodoluminescence (CL) interpretation
E14 . 64	Size: 30–200 μm Colour: Pale yellow - colourless Aspect Ratio: ~ 1.1, 2:1, 3:1, 5:2 Shape: euhedral - subhedral - preserved prismatic and pyramidal crystal faces. Some have rounding at the edges	Majority of the zircons have sector zonation. There is no defined oscillatory zonation. There are inclusions within the zircon
E14 . 68	Size: 50–400 μm Colour: Pale yellow Aspect Ratio: 1:1, 3:1 and 5:2 Shape: Subhedral grains - Some zircon crystals exhibit varying degrees of rounding of the crystal edges.	Majority of larger (400 μm) zircon cores are metamict and poorly luminescent. Rims display faint oscillatory zonation. Zircons have segments of homogeneously textured zircon appearing as transgressive (across all pre-existing textures) zircon patches and lobes. Varied frequencies of zonation are seen, with some relatively broad and others are defined by narrow zones. Grains contain cracks and inclusions
E14 . 69	Size: 50–200 μm Colour: Pale yellow - colourless Aspect Ratio: 2:1, 3:1 Shape: Subhedral grains - Some zircon crystals exhibit moderate rounding of the crystal edges. Others have a prismatic euhedral shape.	Poorly luminescent cores with progressively brighter rims. Commonly preserves oscillatory zoning. Many of the zircons contain inclusions and exhibit cracks
E14 . 70	Size: 100–400 μm Colour: Light pink Aspect Ratio: ~3:1 Shape: Varied grain shapes - euhedral and prismatic to subhedral crystals	In individual crystals there are strong variations in the relative development of zoned domains, where one large uniform central zone is succeeded by much finer oscillatory-zoned bands. Anhedral grains have varied zones with some relatively broad and others are defined by narrow zones.
E14 . 77	Size: 100–400 μm Colour: Pale yellow - brown Aspect Ratio: Majority of zircons are ca. 3:1 with some crystals having an aspect ratio of 2:1 Shape: Euhedral/Prismatic	Majority of the zircon cores are metamict and poorly luminescent. Some rims display faint oscillatory zonation, whilst others are featureless.
E14 . 78	Size: 100–200 μm Colour: Pale yellow - colourless Aspect Ratio: Varying from ca. 2:1–5:1 Shape: Euhedral/Prismatic, with some subhedral grains	Brightly luminescent cores that commonly preserve traces of oscillatory zoning. Dark rims are seen mantling most of these grains.
E14 . 79	Size: 40–200 μm Colour: Pale orange - colourless Aspect Ratio: Varying from ca. 2:1–5:1 Shape: Subhedral grains - Some zircon crystals exhibit moderate - well rounding of the crystal edges. Others have a prismatic euhedral shape.	Commonly preserve well defined oscillatory zoning and some sector zonation. Dark rims (various thicknesses) are seen mantling some of these grains. Lobes of recrystallised zircon are seen replacing the original texture.

Table 2: Description of zircon morphologies and cathodoluminescence (CL) interpretations for each sample in the Western Ethiopian Shield. Figure 3 shows the representative CL images.

Sample	Zircon Morphology	Cathodoluminescence (CL) interpretation
E14 . 83	Size: 30—200 μm Colour: Pale orange - pale brown Aspect Ratio: Low aspect ratio ca. 1:1—2:1 Shape: Subhedral fragmented crystals.	Sector zonation present in some grains. Luminescent and pre-serve well-defined oscillatory zoning - in some grains. Some grains preserve convolute boundaries.
E14 . 84	Size: 50—200 μm Colour: Pale orange - colourless Aspect Ratio: ca. 2:1—5:1 Shape: euhedral - preserved prismatic and pyra-midal crystal faces.	Most of the grains are poorly luminescent under CL with bands displaying oscillatory zonation. They contain cores that have patchy, complex zoning surrounded by oscillatory zona-tion. Some grains preserve convolute boundaries.
E14 . 86	Size: 50—300 μm Colour: Pale yellow - orange Aspect Ratio: Varied 1:1, 2:1, 3:1, 5:2, 6:1 Shape: Subhedral grains - some zircon crystals exhibit moderate rounding of the crystal edges. Others have a prismatic euhedral shape.	Sector zonation present in some grains. Luminescent and preserve well-defined oscillatory zoning - in some grains. Some grains preserve convolute boundaries. There are strong variations in the relative development of zoned domains, where one large uniform central zone is succeeded by much finer oscillatory-zoned bands. Zircons have segments of homo-geneously textured zircon appearing as transgressive (across all pre-existing textures) zircon patches and lobes.
E14 . 97	Size: 50—150 μm Colour: Colourless - pale brown Aspect Ratio: 1:1, 2:1, Shape: Some zircon crystals exhibit moderate rounding of the crystal edges whereas in others the original crystal shape has been destroyed, and the final product being smoothly sub-rounded grains	Zircons have segments of homogeneously textured zircon appearing as transgressive (across all pre-existing textures) zircon patches and lobes. Areas of recrystallization occur dominantly at crystal terminations. There are a few zircons that display oscillatory zonation - varied frequencies with some relatively broad and others are defined by narrow zones.
E14 . 99	Size: 50—200 μm Colour: Pale orange to brown Aspect Ratio: 1:1 - 2:1 , 4:1, 5:1 Shape: Prismatic euhedral grains	Grains preserve oscillatory zoning. Dark rims are seen man-tling most of these grains.
E14 . 100	Size: 50—500 μm Colour: Aspect Ratio: ~2:1, 1:1 Shape: Subhedral grains - some zircon crystals exhibit moderate rounding of the crystal edges. Others have a prismatic euhedral shape.	Dark rims are seen mantling one grain and in some cases os-cillatory zonation is discontinuous. In individual crystals there are strong variations in the relative development of zoned domains, where one large uniform central zone is succeeded by much finer oscillatory-zoned bands.
E14 . 113	Size: 50—200 μm Colour: Pale orange, colourless, light pink Aspect Ratio: Varied 1:1, 2:1, 3:1 Shape: Some zircon crystals exhibit slight rounding of the crystal edges whereas in others the original crystal shape has been destroyed, and the final product being smoothly sub-rounded to rounded grains	Brightly luminescent cores that commonly preserve traces of oscillatory zoning. Dark rims are seen mantling most of these grains. Zircons have segments of homogeneously textured zircon appearing as transgressive (across all pre-existing textures) zircon patches and lobes. These zones are very bright and are evidence for a metamorphic event. Many of the zircons contain inclusions
E14 . 115	Size: 70—200 μm Colour: Pale pink/colourless - pale orange Aspect Ratio: Varied 1:1, 2:1, 5:2 Shape: Euhedral/Prismatic, with some subhedral grains with smoothly sub - rounded to rounded edges	Well defined oscillatory zonation. Variations in the relative development of zoned domains, where one large uniform cen-tral zone is succeeded by much finer oscillatory-zoned bands. Some grains preserve convolute boundaries. Zircons have segments of homogeneously textured zircon appearing as a transgressive feathery texture (across all pre-existing textures)

Canberra. A 10 kV, ~3 nA Cs+ primary ion beam was focused to an ~30 μm diameter spot on an Al-coated sample. Each analysis consisted of a pre-burn of about 2 min to allow the secondary ion isotopic composition to stabilise and remove the Al-coat prior to the analysis, followed by 5, ~10 second measurements of the $^{18}O/^{16}O$ ratio. A standard (Temora II) was analysed first, then repeated after every 6 unknown samples. Sample $\delta^{18}O$(zircon) values were determined by difference relative to the mean $\delta^{18}O$(zircon) measured on standards following normalisation for long-term drift in its measured composition. The $\delta^{18}O$(zircon) values for the Temora II standard analysed in this study are 8.19 ± 0.20‰. These values are statistically equivalent to the published $\delta^{18}O$(zircon) value of 8.20 ± 0.01‰ (Valley et al., 2005).

RESULTS
Zircon U–Pb geochronology, oxygen and hafnium isotopic analyses

All petrology and sample descriptions are provided in Table 1. Some samples had very low zircon yield and hence produce ages that can only be considered as preliminary ages requiring further investigation at a later date. These ages are reported as they still provide important information in this relatively uncharacterised region. Analytical data are presented in Appendix 2.2. All results are plotted on weighted average diagrams (Ludwig et al., 2004), in which analyses have been categorised into their broadly identified internal structure based on CL imaging (Fig. 4) and grains used for concordia age calculations. Data are presented using concordia diagrams ($^{207}Pb/^{206}Pb$ v. $^{206}Pb/^{238}U$ Appendix 2.2: Fig. 1 (a–w) and Fig. 5. All age uncertainties are quoted at the two sigma level and MSWDs are quoted for each calculated age (Supplementary Fig. 1(a–w)). All calculations are considered to

be statistically meaningful if the MSWD value falls within the range of acceptability calculated using the rule outlined in Wendt and Carl (1991) (as highlighted in Schoene (2014). Data are summarised on concordia diagrams in Fig. 5. Hafnium isotope analyses were conducted on all samples and these data are plotted on an ε_{Hf}(t) vs. time plot (Fig. 6). To give regional context, ε_{Hf}(t) values were plotted against longitude and an average ε_{Hf}(t) value were colour scaled (Fig. 7 (a–b)). Oxygen isotope analyses were conducted on ten representative samples (Fig. 8 (a–b)). The zircon $\delta^{18}O$ record is generally preserved even after rocks experience high-grade metamorphism or intense hydrothermal alteration when other minerals are reset (Valley, 2003).

E14.02 Granite pegmatite
(Didesa Domain N9° 02' 25.7"E36° 02' 12.3")
Thirty five zircons were analysed, mainly targeting rims and avoiding metamict cores. Seven analyses were <10% concordant and show a range of $^{206}Pb/^{238}U$ ages between 673–608 Ma. The $^{206}Pb/^{238}U$ weighted average age plot of analyses highlights that these do not form an equilibrium plateau (Appendix 2.2: Fig. 1a). Nevertheless, a weighted mean $^{206}Pb/^{238}U$ age of these grains yields an age of 643 ± 21 Ma with an MSWD of 7.3. Due to the nature of these zircons and the recognition that the $^{206}Pb/^{238}U$ age spread is broadly linear, suggesting radiogenic Pb loss, the mean of all <10% discordant zircons was recalculated using $^{207}Pb/^{206}Pb$ ages, this yielded an age of 664 ± 18 Ma (MSWD = 1.17). This age is used as the best estimate for the time of formation of these zircons due to the acceptable MSWD value. The sampled granite pegmatite cross cuts a foliated gneiss and hence provides a minimum age on the host gneiss and the deformation event. These phases are similar to those seen at the Didesa River outcrop (Blades et al., 2015)

Figure 4: Representative CL images for all igneous rocks sampled in Western Ethiopia. U–Pb laser, hafnium and oxygen spots are shown. Hafnium and oxygen analyses were conducted in the same pit. Generally grains are pyramidal or prismatic. Majority of the zircons display oscillatory zonation, with varied frequencies of zonation development. Each sample have zircons with segments of homogeneously textured zircon, appearing as transgressive (across all pre-existing textures) patches and lobes. Areas of recrystallization occur dominantly at crystal terminations. Where grains are larger than 400 µm, they appear to have metamict cores and poorly luminescent rims.

with the age within uncertainty of the youngest igneous phase record there.

Hafnium isotope analysis was conducted on six zircon grains from the granite pegmatite. $\varepsilon_{Hf}(t)$ values ranging between +5.58 to +7.76 suggesting juvenile sources, with minimal continental crust involvement (Fig. 6).

E14.04 Suqii-Wagga granite
(Didesa Domain N 09° 02' 15.4"E 36° 02' 07.4")
Fifty three analyses were undertaken, of which twenty one were <10% discordant and show a range of $^{206}Pb/^{238}U$ ages between 890–630 Ma. Two distinct plateaus are seen on the $^{206}Pb/^{238}U$ weighted average age plot (Appendix 2.2: Fig 1b), suggesting two distinct periods of zircon formation. The three youngest near concordant analyses are interpreted to reflect lead loss and therefore have been excluded from the concordia age calculation (Appendix 2.2: Fig 1b). The older population includes fifteen <10% discordant grains that are defined by luminescent oscillatory-zoned cores that yield a $^{206}Pb/^{238}U$ age of 853 ± 9 Ma (MSWD = 1.5). The younger population, made up of four <10% discordant zircons, yield a $^{206}Pb/^{238}U$ age of 699 ± 10 Ma with a MSWD of 0.47. The younger analyses were taken from dark rims mantling the grains and are interpreted to be related to a latter metamorphic event. A previously reported $^{207}Pb/^{206}Pb$ zircon age of 698 ± 27 Ma was interpreted to reflect the age of crystallisation of this intrusion (Kebede et al., 2001a). The data presented here, instead, suggest that the Suqii-Wagga Granite crystallised ca. 155 Ma earlier. The younger crystallisation age, which lies within error of the younger population analysed in this study, is likely due to the complex nature of these zircons and most likely reflects the age of metamorphism. Therefore, it is interpreted that the best estimate for crystallisation is 853 ± 9 Ma with metamorphism occurring at 699

± 10 Ma.
Eleven zircons from the Suqii-Wagga granite were analysed for hafnium isotopes. The $\varepsilon_{Hf}(t)$ values range between +1.94 and +9.71 (Fig. 6), demonstrating the relatively juvenile nature of these rocks. However, the weakly positive value of some of these zircons suggests that some older crust was involved in the source of the protolith magma.

E14.38 Gabbroic Diorite
(Dengi Domain N 09° 37' 18.9"E 35° 19' 16.4")
Thirty one analyses from this sample yielded twenty four analyses within 10% of concordance and show a range of $^{206}Pb/^{238}U$ ages from 881–785 Ma. A central, seemingly coherent population is defined within a $^{206}Pb/^{238}U$ cumulative probability plot but a weighted average calculation for these data yield a MSWD above the acceptable threshold (820 ± 10 Ma, MSWD = 3.4). The excessive spread of these data is interpreted to represent minor lead loss to create a continuum of ages. Because of this, the age was recalculated using $^{207}Pb/^{206}Pb$ ages, to account for limited Pb loss, which yielded an age of 843 ± 14 Ma (MSWD = 1.3). These ages are within error of each other and due to the lower MSWD, we suggest that ca. 843 ± 14 Ma provides the best estimate of crystallisation of this gabbroic diorite.
Eight zircons from this gabbroic diorite were analysed for hafnium isotopes. The $\varepsilon_{Hf}(t)$ values range between +6.48 and +9.34 (Fig. 6). This suggests that these samples were derived from juvenile sources, with negligible continental crust influence.

E14.43 K-feldspar granite
(Dengi Domain N 09° 57' 23.7"E 35° 09' 59.8")
Thirteen U–Pb analyses were conducted, with only five within 10% of concordance. The four older analyses show a range of $^{206}Pb/^{238}U$ ages from 788–729 Ma. The
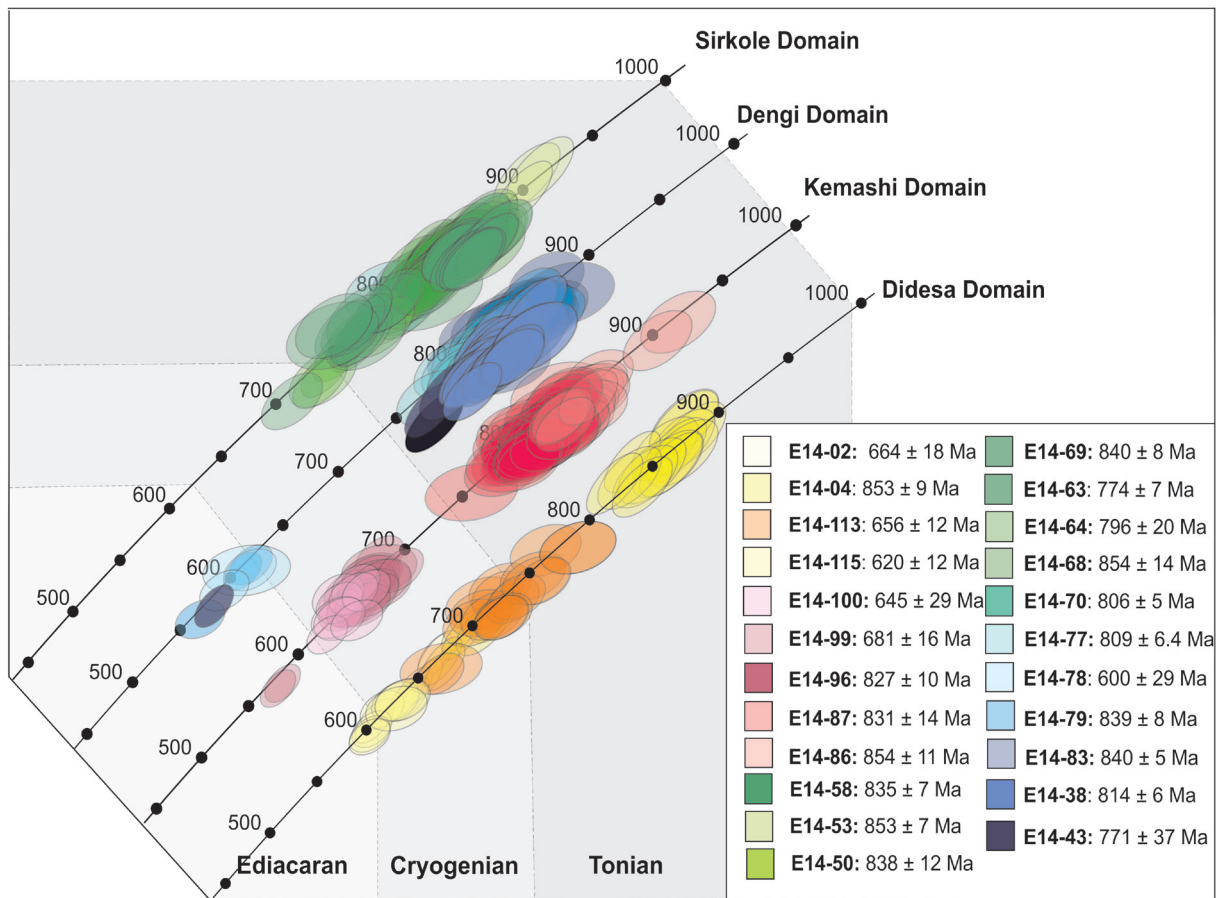
Figure 5: Samples are collated on a U-Pb Wetherill plots ($^{235}U/^{207}Pb$ v. $^{238}U/^{206}Pb$) and coloured by domain. This plot was constructed with a 2 sigma data point error ellipses, only analyses within 90% concordance are shown in this figure. Weighted average are included on the plot. Each Concordia and cumulative weighted average plot, are displayed in the supplementary material. Domains in the Western Ethiopia Shield show that there were three main phases of magmatism ca. 850–810 Ma, 780–700 Ma and 620–550 Ma. These are complicated by metamorphism and deformation. The late Cryogenian phase of magmatism seems to be absent in the Sirkole Domain.

youngest concordant grain is characterised by CL-bright, homogeneous features and yields an anomalously young age. The significance of this age cannot be determined and has therefore been omitted from the age calculations.   A $^{206}Pb/^{238}U$ weighted mean of these ages yields an age of 759 ± 40 Ma (n=4, MSWD = 5.4). Therefore, the age was recalculated using $^{207}Pb/^{206}Pb$ ages, to account for limited Pb loss, which yielded an age of 827 ± 60 Ma (MSWD = 1.8). This is interpreted as the best estimate for the age of crystallisation of this K-feldspar rich granite (Appendix 2.2: Fig 1d). Hafnium isotope analyses were conducted on

five zircons from this sample and yielded $\varepsilon_{Hf}(t)$ values between +9.97 and +7.89 (Fig. 6).

E14. 50 Granite
(Sirkole Domain N 10° 32' 28.1"E 34° 19' 06.2") Nineteen U–Pb analyses were completed on this sample. Thirteen are within 10% of concordance and show a range of $^{206}Pb/^{238}U$ ages from 844–792 Ma. On a $^{206}Pb/^{238}U$ weighted average age plot (Appendix 2.2: Fig. 1e) the three youngest analyses are interpreted to represent minor Pb-loss and are therefore excluded from the $^{206}Pb/^{238}U$ age calculation. All other analyses define a single statistically

valid population and yield a $^{206}Pb/^{238}U$ age of 838 $\pm$ 12 Ma (MSWD = 1.6). This age was recalculated using $^{207}Pb/^{206}Pb$ ages and yielded an age of 868 $\pm$ 16 Ma (MSWD = 1.17). These ages are within uncertainty of each other and due to the lower MSWD and recognition of a lead loss trend, we suggest that 868 $\pm$ 16 Ma provides the best estimate of crystallisation of this granite (Appendix 2.2: Fig. 1e).

Hafnium isotope analysis was conducted on eight zircons from the granite (E14.50). The $\varepsilon_{Hf}(t)$ values range between +6.48 and +9.34 (Fig. 6), demonstrating the juvenile nature of these zircons.

E14. 53 Gneiss

(Sirkole Domain N 10° 32' 28.1"E 34° 19' 06.2")
Twenty four U–Pb analyses were undertaken on zircons from this sample. Of these, sixteen were <10% discordant and show a range of $^{206}Pb/^{238}U$ ages between 917–781 Ma. Two distinct plateaux are evident on the cumulative $^{206}Pb/^{238}U$ age plot (Appendix 2.2: Fig 1f), suggesting more than one population. The three youngest ages have been attributed to lead loss using the cumulative plots and CL images and have therefore been excluded from the age calculation (Appendix 2b: Fig 1f). The older population includes three <10% discordant grains that demonstrate a low CL response, have rounded edges and yield a weighted average $^{206}Pb/^{238}U$ age of 919 $\pm$ 14 Ma (MSWD = 0.71). The younger population, made up of eleven <10% discordant zircons, yield a $^{206}Pb/^{238}U$ age of 853 $\pm$ 7 Ma with a MSWD of 0.72. Therefore the younger population is interpreted to provide the best estimate for the age of crystallisation at 853 $\pm$ 7 Ma with the inheritance of older zircons at 919 $\pm$ 14 Ma.

E14. 58 Leucogranite

(Sirkole Domain N 10° 33' 48.3"E 34° 24' 48.6")
Thirty U–Pb analyses were undertaken on

this sample. Thirteen analyses were <10% discordant and show a range of $^{206}Pb/^{238}U$ ages between 1028–825 Ma. The cumulative $^{206}Pb/^{238}U$ age plot shows two distinct plateaux (Appendix 2.2: Fig 1g), suggesting more than one population of zircon ages. The older population includes three <10% discordant grains that are defined by highly luminescent cores. These grains yield a $^{206}Pb/^{238}U$ age of 1014 $\pm$ 12 Ma (MSWD = 1.4). The younger population (n=10) is characterised by well-defined oscillatory-zoned zircons and yields a weighted average $^{206}Pb/^{238}U$ age of 835 $\pm$ 7 Ma with a MSWD of 0.72. Therefore, we suggest that the younger population provides the best estimate for the age of crystallisation at 835 $\pm$ 7 Ma with the inheritance of older zircons at 1014 $\pm$ 12 Ma.

E14. 63 Granite

(Dengi Domain N 10° 23' 42.7"E 34° 34' 43.6")
Thirty zircon grains were analysed in this sample. Analysis locations mostly represent zircon rims and the few core analyses undertaken show no discernible age difference. Twelve analyses were <10% discordant and show a range of $^{206}Pb/^{238}U$ ages between 797–702 Ma. Using the cumulative $^{206}Pb/^{238}U$ age plot of individual analyses and CL images, the youngest age is attributed to lead loss and therefore has been excluded from the age calculation (Appendix 2.2: Fig 1h). A weighted mean of the remaining $^{206}Pb/^{238}U$ analyses yields an age of 774 $\pm$ 7 Ma (MSWD = 1.14). This age is therefore used to represent the age of crystallisation of the granite.

Ten zircons from this sample were analysed for Hf isotope data. The $\varepsilon_{Hf}(t)$ values range between +3.43 and +6.70 (Fig. 6), suggesting there was minimal crustal input.

E14. 64 Foliated K-feldspar granite

(Dengi Domain N 10° 20' 47.1"E 34° 37' 22.3")

Thirty five analyses were undertaken for this sample with 15 that are <10% discordant. The <10% discordant analyses show a range of ^{206}Pb/^{238}U ages between 782 and 701 Ma. A weighted mean of these ^{206}Pb/^{238}U ages yields an age of 737 ± 13 Ma (MSWD = 4.7). The relatively large MSWD indicates that the analyses do not form a single age which is consistent with the suggestion of both a common Pb and Pb-loss trend amongst discordant data. The cumulative ^{206}Pb/^{238}U age plot of <10% discordant analyses also highlights a distinct Pb-loss trend (Appendix 2.2: Fig 1i). This spread is interpreted to be the result of post-formation lead loss, with these zircons defining a discordia indistinguishable from the concordia curve. In this case, a weighted average ^{207}Pb/^{206}Pb age of 796 ± 20 Ma (MSWD = 0.45) is considered to provide an adequate representation of the age of crystallisation of the granite.

The analyses of hafnium isotopes was conducted on nine zircons from the foliated granite (E14. 64). The ε_{Hf}(t) values range between +6.94 and +9.97 (Fig. 6), suggesting that these zircons were derived from depleted mantle sources.

E14. 68 Monzonite
(Dengi Domain N 10° 16' 09.8"E 34° 37' 29.9")
Thirty zircons were analysed for this sample with the analysed spots mostly located on zircon rims. Analyses within the zircon cores showed no discernible age difference to the rims. Twenty nine analyses were <10% discordant and show a range of ^{206}Pb/^{238}U ages between 870–805 Ma. The cumulative ^{206}Pb/^{238}U age plot of individual analyses shows a slight trend attributed to minor radiogenic lead loss. A ^{206}Pb/^{238}U weighted mean of these analyses yields an age of 835 ± 6 Ma (MSWD = 1.9). The ^{207}Pb/^{206}Pb age gives a weighted average of 854 ± 14 Ma with a MSWD of 1.3. These ages lie within error of each other and therefore the ^{207}Pb/^{206}Pb is used to represent

the age of crystallisation the granite, due to the better MSWD (Appendix 2b: Fig 1j).
Hafnium isotope analyses were conducted on twelve zircons from this monzonite (E14.68), these yield juvenile ε_{Hf}(t) values between +9.97 and +7.89 (Fig. 6).

E14. 69 Granite
(Dengi Domain N 10° 16' 09.8"E 34° 37' 29.9")
The cumulative ^{206}Pb/^{238}U age plot of all analyses shows a distinct trend that is attributed to Pb-loss (Appendix 2.2: Fig 1k). The youngest two analyses have been excluded from the age calculation. Of the twenty eight analyses, sixteen are <10% discordant and show a range of ^{206}Pb/^{238}U ages between 859 and 790 Ma respectively. A weighted mean of these ^{206}Pb/^{238}U ages yields an age of 840 ± 8 Ma (MSWD = 1.4), which is used as the best estimate for the age of crystallisation of the granodiorite.

Twelve zircons from sample E14.69 were analysed for hafnium isotopes. The ε_{Hf}(t) values range between + 6.99 and +10.4 (Fig. 6), suggesting juvenile sources, with minimal continental crust input.

E14. 70 Granodiorite
(Dengi Domain N 10° 16' 09.8"E 34° 37' 29.9")
Thirty one zircons were analysed. Analyses mostly represent zircon rims with two core analyses showing no discernible age difference. All analyses were <10% discordant and yield a range of ^{206}Pb/^{238}U ages between 830–777 Ma. A ^{206}Pb/^{238}U weighted average of these ages yields one distinct group with a mean age of 806 ± 5 Ma (MSWD = 1.5). This age is interpreted to represent the crystallisation age for the granodiorite.

Hafnium isotope analysis was conducted on five zircon grains from sample E14.70. The ε_{Hf}(t) values range between +5.0 and +7.25 (Fig. 6), suggesting relatively juvenile sources,

with minimal continental crust involvement.

E14. 77 Granodiorite
(Dengi Domain N 11° 42' 52.1"E 34° 57' 11.6")
Forty five zircon U–Pb analyses were undertaken on this sample. Of these, twenty three are <10% discordant and show a range of $^{206}Pb/^{238}U$ ages between 834 and 768 Ma. The cumulative $^{206}Pb/^{238}U$ age plot of all analyses shows a distinct Pb-loss trend (Appendix 2.2: Fig 1m). The youngest analysis is considerably lead loss affected, and therefore has been excluded from the age calculation. Of the twenty two analyses remaining, a $^{206}Pb/^{238}U$ weighted mean was calculated and yielded an age of 807 ± 6 Ma (MSWD = 1.7). Due to the distinct lead loss trend the age was recalculated using the $^{207}Pb/^{206}Pb$ age, which gives a weighted average of 841 ± 13 Ma with a MSWD of 0.97. This age is slightly older, however, and we interpret it to represent the most accurate age of crystallisation of this granodiorite due to the nature of these zircons and the recognition that the $^{206}Pb/^{238}U$ age spread is broadly linear, suggesting radiogenic Pb-loss (Appendix 2.2: Fig 1j).
Oxygen isotope analyses on zircons from sample E14.77 have $\delta^{18}O$ ratios between +6.63 and +7.55‰ with an average of +7.13‰ (Fig. 8a). Hafnium isotope analyses were conducted on twelve zircons from this granodiorite, these yield juvenile values between + 8.79 and + 5.93 (Fig. 6).

E14. 78 Granite
(Dengi Domain N 11° 14' 18.5"E 35° 05' 44.4")
Twenty four U–Pb zircon analyses were undertaken from this sample, mostly from zircon rims. The few core analyses showed no discernible age difference. Of those twenty four analyses, only four were <10% discordant and show a cluster of three 206Pb/238U ages at 600 ± 29 Ma (MSWD = 1.8) with

a fourth analysis at ca. 475 Ma. The mean of the three older <10% discordant analyses was recalculated using $^{207}Pb/^{206}Pb$ ages, this yielded an age of 608 ± 9.8 Ma (MSWD = 1.5), which is interpreted as the best estimate for the time of formation of these zircons.
Oxygen isotope analyses on zircons from sample E14.78 have $\delta^{18}O$ ratios between +8.12 and +8.33 ‰ with an average of +8.21‰ (Fig.8a). Hafnium isotope analysis was conducted on five zircon grains from sample E14.78. The $\varepsilon_{Hf}(t)$ values range between +4.4 and +7.61 and suggests relatively juvenile sources, with minimal continental crust involvement (Fig. 6).

E14.79 Coarse grained felsic granite
(Dengi Domain N 11° 15' 54.4"E 35° 18' 26.9")
Thirty eight zircons were analysed, with analyses spots targeted at zircon rims. Seventeen analyses were <10% discordant and show a range of $^{206}Pb/^{238}U$ ages between 862–560 Ma. The cumulative $^{206}Pb/^{238}U$ age plot of individual analyses shows that two analyses are distinctly younger than the others. The youngest grains have $^{206}Pb/^{238}U$ ages of 612 ± 8 Ma and 606 ± 7 Ma respectively, likely representing a recrystallisation event. A weighted mean of the main group of analyses yields a $^{206}Pb/^{238}U$ age of 839 ± 8 Ma (MSWD = 1.7). The MSWD is within the realm of acceptability for the number of analyses and therefore 839 ± 8 Ma is used to represent the age of crystallisation of this rock (Appendix 2.2: Fig 1o).
Oxygen isotope analyses on zircons from sample E14. 79 have $\delta^{18}O$ ratios between +7.63 and +8.02 ‰ with an average of +7.77 ‰ (Fig. 8a). Hafnium isotope analyses were conducted on five zircon grains from sample E14.79 $\varepsilon_{Hf}(t)$ values range between +5.95 to +7.88, which suggests relatively juvenile sources, with minimal continental crust involvement (Fig. 6).
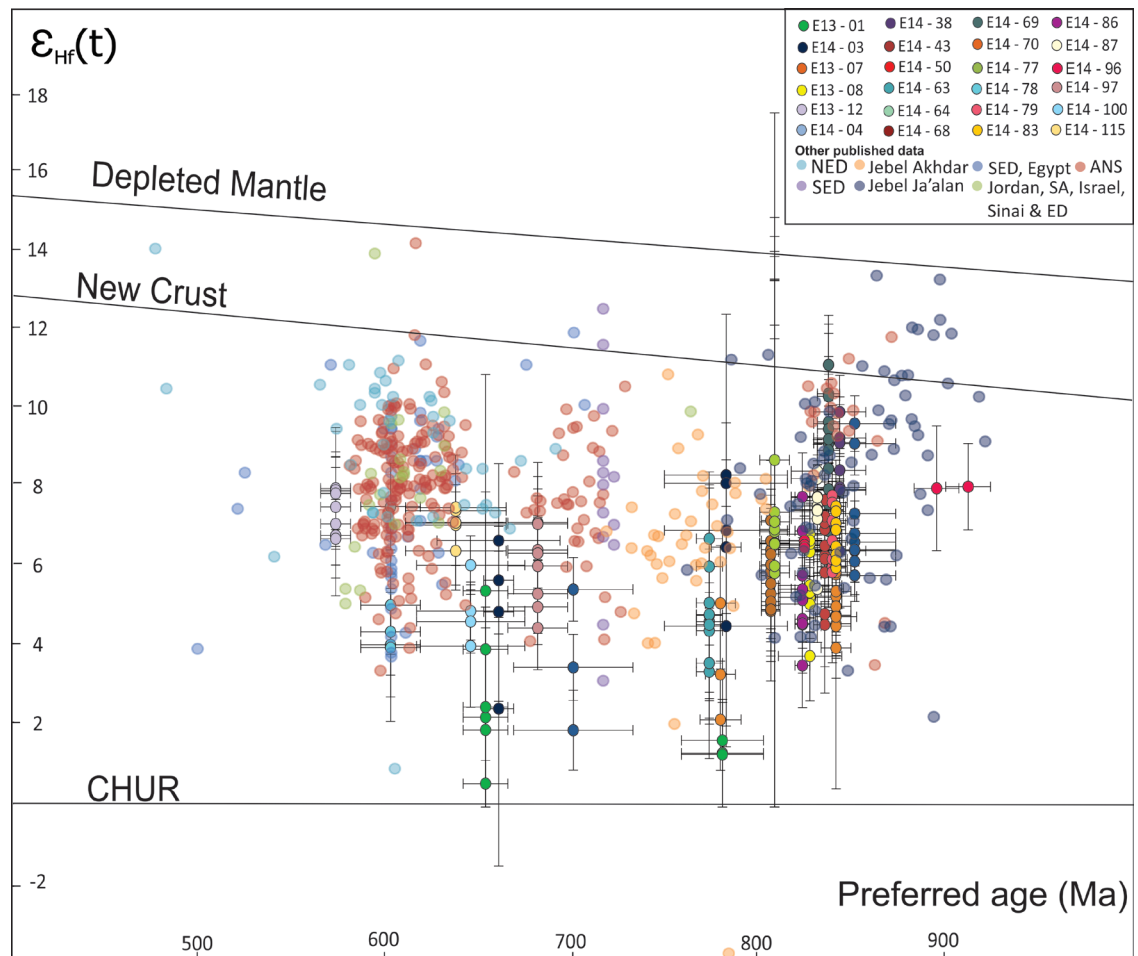
Figure 6: ε_{Hf}(t)versus preferred age plot for all igneous samples in the Western Ethiopian Shield. Plots show that all samples are juvenile, with negligible old, continental crust input although Neoproterozoic crustal additions cannot be excluded. Both horizontal and vertical error bars show 2σ error. New Crust line represents the best estimate for present-day compostion (ε_{Hf}(t)=13.2±1.1), calculated by the weighted average o the means of 13 modern island arcs world wide. Other data collated from the Arabian Nubian Shield and Oman are also displayed and show the same 'U' shaped trend as seen in Western Ethiopia (Alessio et al., 2017; Ali et al., 2013; Ali et al., 2016; Be'eri-Shlevin et al., 2010; Blades et al., 2015; Robinson et al., 2015; Robinson et al., 2014).

E14.83 Granite
(Kamashi Domain N 11° 19' 02.1" E 35° 31' 41.3")
Fifty zircons were analysed from this sample. Analyses mostly targeted zircon rims and the few core analyses showed no discernible age difference. Of the fifty analyses, thirty five were <10% discordant and show a range of $^{206}Pb/^{238}U$ ages between 876–790 Ma. The $^{206}Pb/^{238}U$ age plot of individual analyses highlights that the youngest four ages are significantly younger, which is attributed to lead loss and therefore these have been

excluded from the age calculation. A weighted mean of the remaining $^{206}Pb/^{238}U$ ages yields an age of 840 ± 5 Ma (MSWD = 1.5). The mean of all <10% zircons was recalculated using $^{207}Pb/^{206}Pb$ ages, this yielded an age of 860 ± 13 Ma (MSWD = 0.53), which we suggest is the best estimate for the time of the crystallisation of this granite (Appendix 2.2: Fig 1p)
Nine zircons from sample E14.83 were analysed for hafnium isotopes. The ε_{Hf}(t) values give juvenile values between + 6.48 and + 9.34 (Fig. 6).
E14.86 Belesse River granodiorite

(Kemashi Domain N 11° 11' 57"E 36° 19' 33")
Forty four zircons were analysed from this sample. Analyses mostly targeted zircon rims and the few core analyses showed no discernible age difference. Of the fifty analyses, forty five were <10% discordant and show a range of $^{206}Pb/^{238}U$ ages between 860–787 Ma. The $^{206}Pb/^{238}U$ age plot of individual analyses shows a slight lead loss trend with the youngest two ages excluded from the age calculation. A weighted mean of the remaining $^{206}Pb/^{238}U$ ages yields an age of 823 ± 5 Ma (MSWD = 2.2). The relatively large MSWD is outside of the range of acceptability, suggesting that the analyses do not form a single population. This spread is therefore interpreted to be the result of post-formation lead loss. A weighted mean $^{207}Pb/^{206}Pb$ age was calculated, which yielded a value of 854 ± 11 Ma with a MSWD of 0.63, which is used as the best estimate for the age of crystallisation of the Belesse River Granodiorite (Appendix 2.2: Fig 1q).
Oxygen isotope analyses on zircons from sample E14.86 have $\delta^{18}O$ ratios between +6.98 and +9.38 ‰ with an average of +8.72 ‰ (Fig. 8a). Nine zircons from sample E14.86 were analysed for hafnium isotopes. The $\varepsilon_{Hf}(t)$ values range between +6.48 and +9.34 (Fig. 6) and this suggests that these zircons were derived from relatively juvenile sources.

E14.87 Little Belesse granite
(Kemashi Domain N 11° 09' 56.9"E 36° 20' 18.4")
The cumulative $^{206}Pb/^{238}U$ age plot of all analyses shows a distinct trend that is attributed to radiogenic Pb-loss (Appendix 2.2: Fig 1r), the youngest two analyses are excluded from the concordia age calculation. Of the fifty analyses, thirty seven are <10% discordant and show a range of $^{206}Pb/^{238}U$ ages between 844 and 753 Ma. A weighted mean of these $^{206}Pb/^{238}U$ ages yields an age of 804 ± 6 Ma (MSWD=3). The relatively large MSWD suggests that the

analyses do not form a single age and define an array along the concordia line between 844–775 Ma. Most of the zircons show convolute CL patterns with rims appearing to replace original zircon, with recrystallisation fronts interpreted to be preserved in some grains (Hoskin and Black, 2000). These are shown by lobes and patches that overprint the pre-existing textures. This spread is interpreted to be the result of post-formation lead loss, with these zircons defining a discordia indistinguishable from the concordia curve. Therefore the $^{207}Pb/^{206}Pb$ age is used here, which gives a weighted average of 831 ± 14 Ma with a MSWD of 0.41 and is used as the best estimate for the age of crystallisation of the Little Belesse Granite.
Oxygen isotope analyses on zircons from sample E14. 87 have ratios between +5.73 and +6.30 with an average of +5.99 ‰ (Fig. 8a). Nine zircons from the granite were analysed for hafnium isotopes. $\varepsilon_{Hf}(t)$ values range from +5.52 to +8.50 (Fig. 6), demonstrating the juvenile nature of this rock.

E14.96 Mora Granite
(Kemashi Domain N 10° 31' 59.2"E 36° 02' 02.7")
Eighteen zircons from this sample were analysed, seven were <10% discordant and show a range of $^{206}Pb/^{238}U$ ages between 911–806 Ma. On the cumulative $^{206}Pb/^{238}U$ age plot, two distinct plateaus can be isolated (Appendix 2.2: Fig. 1s), suggesting two distinct periods of zircon formation. Two older <10% discordant grains, yield $^{206}Pb/^{238}U$ ages of 912 ± 12 Ma and 895 ± 11 Ma. These grains have been interpreted to represent inheritance due to the rounded nature of the zircon as seen in CL images. The younger population, made up of five <10% discordant zircons, is characterised by well-defined oscillatory zoned zircons and yields a mean $^{206}Pb/^{238}U$ age of 827 ± 10 Ma with a MSWD of 1.05. We interpret the younger population as the best estimate for
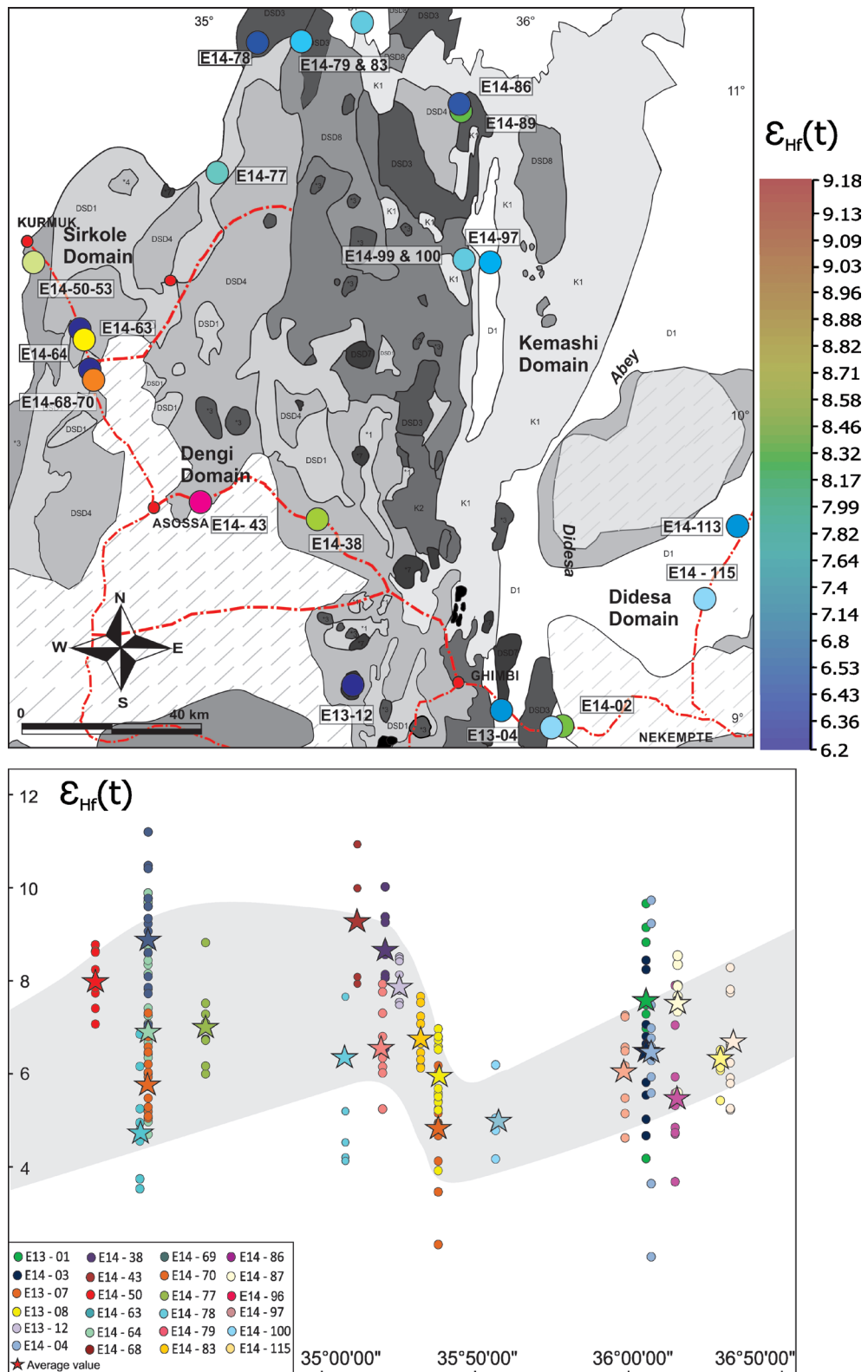
Figure 7: a) Samples are plotted geographically and coloured by their respective $\varepsilon_{Hf}(t)$ values. $\varepsilon_{Hf}(t)$ values range between +1.94 and +10 across the shield. The plots (Fig. 6 and Fig. 7) show that all samples are juvenile, with negligible old, continental crust input although recent crustal additions cannot be excluded. b) $\varepsilon_{Hf}(t)$ is plotted against longitude to show the variation from east to west, as well as the spread of sample compositions in a single area. Stars represent the average value for each sample.

the age of crystallisation at 827 ± 10 Ma with inheritance of older zircon.

Oxygen isotope analyses on zircons from sample E14.96 have $\delta^{18}O$ ratios between +8.12 and +8.33 ‰ with an average of +8.21‰ (Fig. 8a).

Hf isotopic data for zircons from this sample (four zircons) yielded positive $\varepsilon_{Hf}(t)$ values ranging from + 6.57 to + 6.73 for the ca. 827 Ma grains. Hafnium isotope analysis of the two older grains give $\varepsilon_{Hf}(t)$ values of + 8.07 and + 8.11 and suggests relatively juvenile sources, with minimal continental crust involvement (Fig. 6).

E14.99 Mata River Granodiorite
(Kemashi Domain N 10° 31' 51.9"E 35° 57' 34.3")
The cumulative $^{206}Pb/^{238}U$ age plot of all analyses highlights a distinct trend that is attributed to radiogenic Pb-loss. The youngest two ages may represent more extreme lead loss, or possibly hydrothermal zircon growth. They have been excluded from further age calculation. Of the forty five analyses, twenty six are <10% discordant and show a range of $^{206}Pb/^{238}U$ ages between 691 and 567 Ma. A weighted mean of these $^{206}Pb/^{238}U$ ages yields an age of 660 ± 6 Ma (MSWD = 2.3). The MSWD is quite large. This is interpreted to be the result of post-formation lead loss and therefore a $^{207}Pb/^{206}Pb$ age was calculated that gave a weighted average of 681 ± 16 Ma with a MSWD of 0.73 and is used as the best estimate for the age of crystallisation of the Mata River Granodiorite (Appendix 2.2: Fig. 1t).
Oxygen isotope analyses on zircons from sample E14.99 have $\delta^{18}O$ ratios between +5.98 and +7.19 ‰ with an average of +6.60 ‰ (Fig. 8a). Nine zircons from the Mata River Granodiorite were analysed for hafnium isotopes. $\varepsilon_{Hf}(t)$ values range between +4.53 and +7.17 (Fig. 6), demonstrating the relative juvenile nature of these rocks.

E14.100 Mata River Granite
(Kemashi Domain N 10° 31' 51.9" E 35° 57' 34.3")
Twelve zircons were analysed that mostly represent zircon rims, with the few core analyses showing no discernible age difference. Ten analyses were <10% discordant and showed a range of 206Pb/238U ages between 665–619 Ma. On the cumulative $^{206}Pb/^{238}U$ age plot of individual analyses a lead loss trend is evident, with the analyses not forming a distinct plateau. A weighted mean of these ages yields a mean $^{206}Pb/^{238}U$ age of 645 ± 16 Ma (MSWD =4.7). The large MSWD suggests that the analyses do not form a single age and define an array along the concordia line between 665–619 Ma. This spread is interpreted to be the result of post-formation lead loss and therefore a $^{207}Pb/^{206}Pb$ age was calculated to give a weighted average of 645 ± 29 Ma with a MSWD of 0.44. The granite is the structurally youngest rock type sampled from this location, cross cutting E14. 99, which yielded and older mean age, but both interpreted crystallisation ages overlap at the 2 sigma error level (681 ± 16 Ma for E14.99 and 645 ± 29 Ma for E14.100; Supplementary Fig. 1u).
Oxygen isotope analyses on zircons from sample E14. 100 have $\delta^{18}O$ ratios between +8.00 and +8.71 ‰ with an average of +8.84 ‰ (Fig. 8a). The $\varepsilon_{Hf}(t)$ values (n=4) range between +4.07 and +6.12 (Fig. 6).

E14.113 Gneiss
(Didesa Domain N 09° 42' 51.8"E 35° 57' 34.3")
Nineteen analyses from thirty zircon grains are within 10% of concordance (including both cores and rims). Ages spread broadly along the concordia between ca. 774 and 654 Ma. On the $^{206}Pb/^{238}U$ age plot three distinct plateaus can be isolated, suggesting three distinct periods of zircon formation (Appendix 2.2: Fig. 1v). The
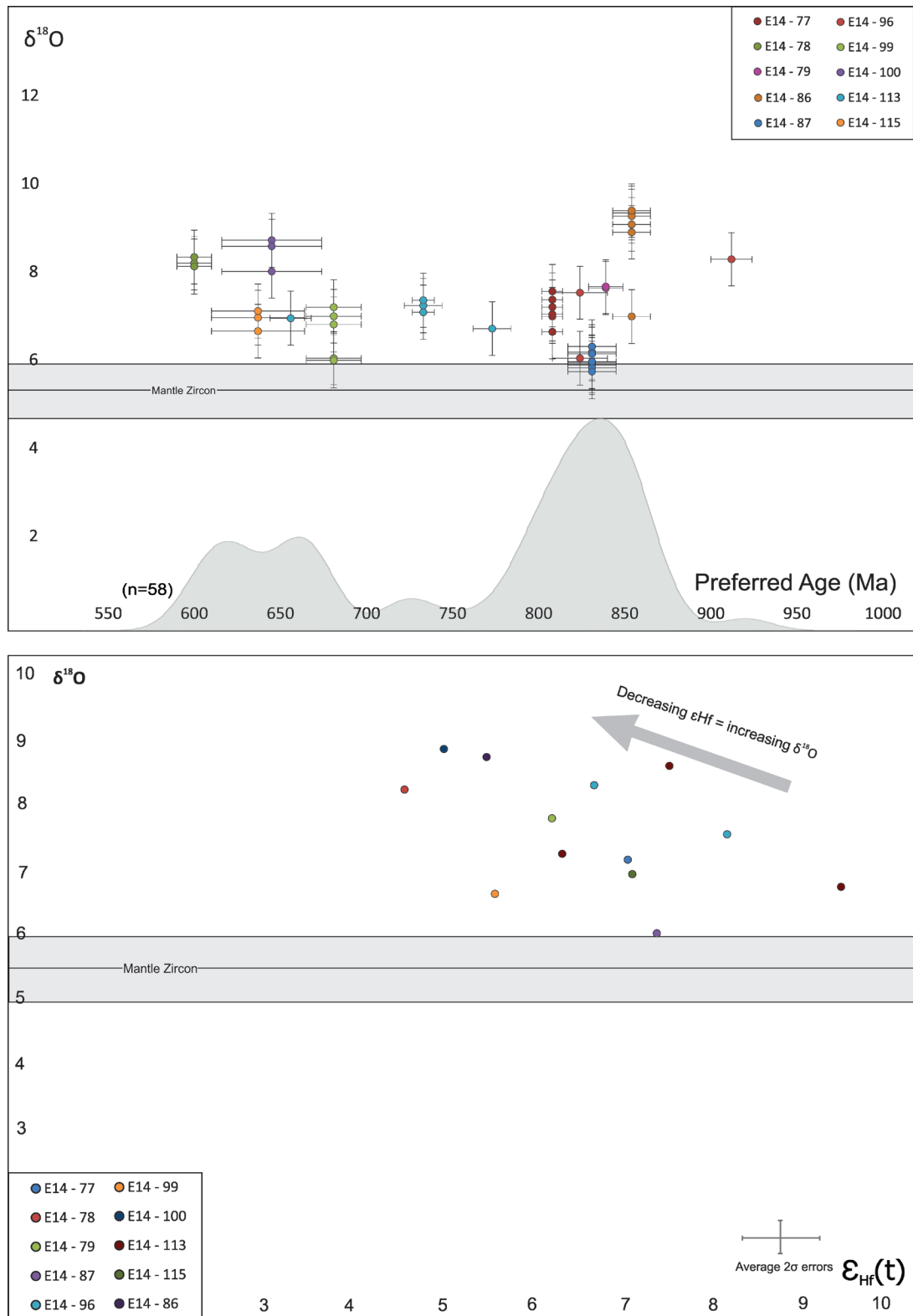
Figure 8: Plot of a) $\delta^{18}O$ plotted against the interpreted crystallisation age for zircons analysed in this study. Error bars are 2σ. Range of mantle derived $\delta^{18}O$ (zircon) values are 5.3 ± 0.6‰ (Valley, 2005). b) $\delta^{18}O$ plotted against $\epsilon_{Hf}(t)$ with patterns showing a relative decrease in $\epsilon_{Hf}(t)$ and an increase in $\delta^{18}O$. This suggests either an input of supra-crustal material or the re-melting of previously formed juvenile crust.

older analyses are grains with rounded edges, well-defined oscillatory luminescence zoning, and yield a $^{206}Pb/^{238}U$ weighted mean age of 773 ± 11 Ma (MSWD = 0.23). These grains are interpreted to represent inherited zircon. The second distinct age group is defined by fourteen analyses and show a lead loss trend in the cumulative weighted average plot. These grains yield a $^{206}Pb/^{238}U$ weighted mean age of 722 ± 9 Ma (MSWD = 2.7). A $^{207}Pb/^{206}Pb$ age was calculated using all 14 values in this plateau and gave an age of 754 ± 26 Ma (MSWD 1.19), within error of the $^{206}Pb/^{238}U$ weighted mean. We interpret the $^{207}Pb/^{206}Pb$ weighted mean to provide the best representative crystallisation age for the gneiss due to the better MSWD value.   The two youngest near-concordant analyses (Th/U <0.2) are from rims, shown by lobes and patches that overprint the pre-existing textures (Fig. 4), and yield a $^{206}Pb/^{238}U$ weighted mean age of 656 ± 12 Ma (MSWD = 0.14).   This is interpreted to represent metamorphic recrystallisation.

Oxygen isotope analyses on zircons from sample E14. 113 have $\delta^{18}O$ ratios between +6.71 and +7.35 ‰ with an average of +7.06 ‰ (Fig. 8a). Hafnium isotopic data for zircons from this sample (N=9) yielded positive $\varepsilon_{Hf}(t)$ values ranging from +9.38 to +6.28 for the ca. 733 Ma grains. Hafnium isotope analysis on the younger grains (ca. 656 Ma) give $\varepsilon_{Hf}(t)$ values of +6.26, which suggests relatively juvenile sources, with minimal continental crust involvement (Fig. 6).

E14.115 Gutin Granite
(Didesa Domain N 09° 30' 49.6.8" E 36° 34' 05.8")
Forty four zircons were analysed from this sample for U–Pb isotopes, seven were <10% discordant and show a range of $^{206}Pb/^{238}U$ ages between 593–629 Ma. On the cumulative

$^{206}Pb/^{238}U$ age plot two distinct plateaus defined (Appendix 2.2: Fig. 1w). The three youngest grains are defined by featureless cores and have been interpreted to represent Pb-loss. A weighted mean of all the ages, excluding the last three grains, yields a $^{206}Pb/^{238}U$ age of 620 ± 12 Ma (MSWD = 2.1). Using all data points a $^{207}Pb/^{206}Pb$ age was calculated to give a weighted average of 637 ± 27 Ma with a MSWD of 0.22. This age is agreement with the $^{206}Pb/^{238}U$ calculated age therefore we use 620 ± 12 Ma to represent the age of crystallisation of the granite.

Oxygen isotope analyses on zircons from sample E14.115 have $\delta^{18}O$ ratios between +6.65 and +7.1 ‰ with an average of +6.90 ‰ (Fig. 8a). The analysis of hafnium isotopes was conducted on six zircons from sample E14.115. $\varepsilon_{Hf}(t)$ values are all juvenile and range between +6.64 and +7.10 (Fig. 6).

DISCUSSION
Timing and Nature of Magmatism and Deformation in the Didesa Domain
The Didesa Domain forms the eastern region of the study area. It consists of amphibolite-facies paragneiss and orthogneiss, intruded by Neoproterozoic intrusive rocks. Three tectonothermal events occur in the Didesa Domain; two of these are Tonian ca. 853–827 Ma, ca. 790–733 Ma, with a younger Cryogenian magmatic phase dated at ca. 699–655 Ma (Figs. 5 and 9). The oldest ages obtained in this area are from well-defined oscillatory-zoned zircon grains extracted from the Suqii-Wagga Granite (E14.02: 853 ± 9 Ma). Evidence of metamorphism is seen by the rims and recrystallisation of zircon in the granite (ca. 660 Ma). Previously published ages from this area are from the hornblende + biotite tonalite (841 ± 8 Ma) and zircons within the coeval felsic granite (827 ± 17 Ma;
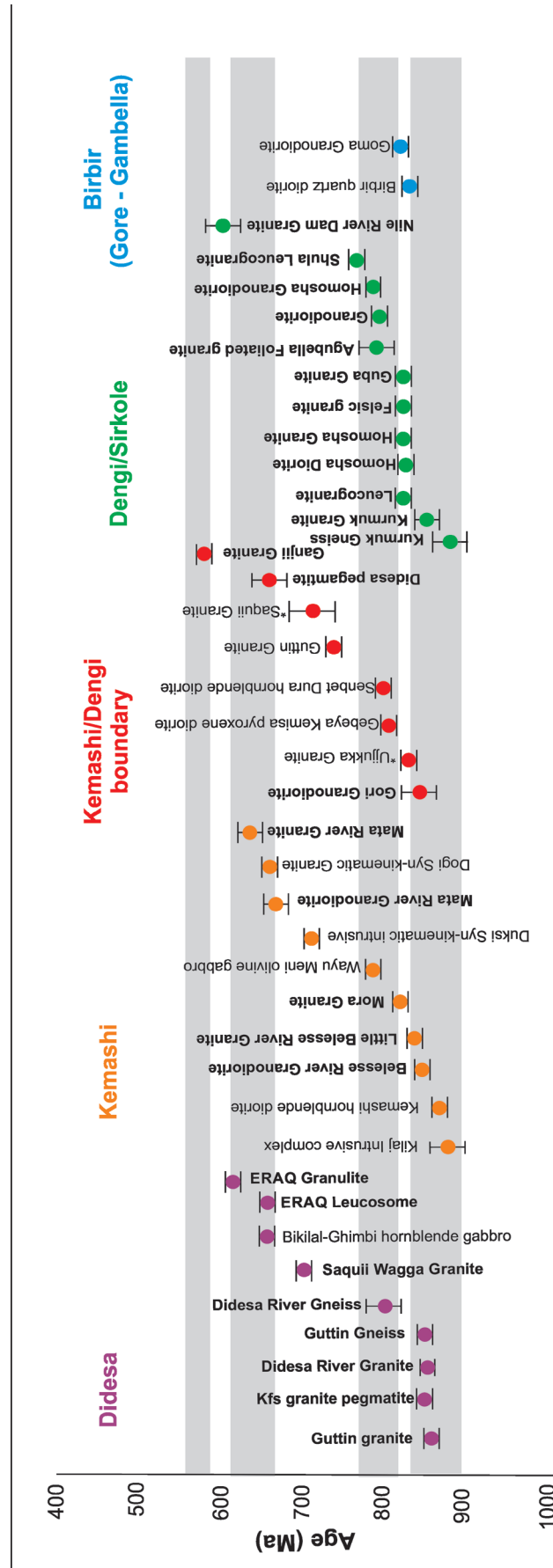
Figure 9: Comparative table between published igneous crystallisation ages and newly interpreted ages, in the Western Ethiopian Shield. Samples highlighted in bold represent the data presented in this paper. '*' Zircons analysed by using lead – lead evaporation. The grey boxes highlight the main interpreted phases of magmatism in the WES.

Blades et al. 2015). Zircon grain rims yield an age of 779 ± 11 Ma. Other magmatism north of these samples, in the gneiss (E14.113), yields a crystallisation age of 733 ± 6.4 Ma. This is similar to magmatism seen at the previously published Didesa River Gneiss (782 ± 33 Ma: Blades et al. 2015). Younger zircon from the Didesa River gneiss (660 ± 8 Ma) as well as the metamorphic recrystallization of zircon seen in the Suqii-Wagga Granite and Bt-gneiss at 699 ± 10 Ma and 656 ± 12 Ma respectively, further constrains the timing of magmatism and metamorphism in the Didesa Domain.

Zircons in equilibrium with pristine mantle-derived melts have $\delta^{18}O$ values of 5.3‰ ± 0.6‰; (Valley et al., 2005). It has been inferred that zircons with $\delta^{18}O$ of less than 6.5‰ formed from melts that contained a minor to negligible sedimentary component (Valley et al., 2005). The Didesa Domain has an average $\delta^{18}O$ value of 6.98 ‰, suggesting that sedimentary input is minimal. The zircons from the oldest phase of magmatism (ca. 854 Ma) yield $\varepsilon_{Hf}(t)$ values between +1.94 and +9.71. The maximum values for these zircons approach the composition of the depleted mantle for this time period and a number fall above the New Crust model of Dhuime et al. (2012). This highlights a mantle derived source for many of the magmas. The lower values indicate that although there was almost certainly a crustal component to the magmas, when combined with relatively low $\delta^{18}O$ values, it is likely that this crustal component was derived from the mantle a relatively short time period before generation of the recorded intrusions. This suggests the igneous complex was not built upon an evolved continental margin and instead an ocean island arc setting seems most appropriate. The late Tonian zircons also yield positive $\varepsilon_{Hf}(t)$ values (+5.5 to +9.4), suggesting a similar juvenile origin compatible with magma generated within an oceanic setting.

Timing and Nature of Magmatism and Deformation in the Kemashi Domain

To the west of the Didesa Domain, the Kemashi Domain forms a narrow, 10–15 km wide, N-S belt (Fig. 2) that is characterised by a sequence of metasedimentary rocks whose protoliths are interpreted to have a marine origin, including cherts and quartzites, interlayered with abundant mafic to ultramafic volcanic material, all metamorphosed to upper greenschist/epidote–amphibolite facies (Tadesse and Allen, 2005). There are a number of intrusive bodies incorporated in this domain and broadly these correlate to three pulses of magmatism at ca. 854–824 Ma, ca. 780 Ma (zircon rims from a hornblende-biotite gneiss; Blades et al., 2015) and ca. 684–645 Ma (E14.86, 87, 96, 99 and 100; Fig. 5). The granite (E14.87) has an average $\delta^{18}O$ value of 5.99 ‰ suggesting melts that were mantle derived, with negligible crustal input. However, higher $\delta^{18}O$ values are seen in other samples (e.g. E14.86). The elevated $\delta^{18}O$ values seen in some zircons from this domain are, therefore, interpreted to either reflect a component of ^{18}O-enriched, supracrustal, material or pre-existing igneous crust, incorporated into the magma from which the zircon precipitated. These oxygen values are mirrored by the hafnium isotopes: The 854–824 Ma zircons yield $\varepsilon_{Hf}(t)$ values between +4 and +9, whilst the younger magmatic phase (684–645 Ma) yields similar $\varepsilon_{Hf}(t)$ values of between +4 and +7 (Figs. 6, 7a and b). This shows that these magmas were derived from relatively juvenile magma, with some crustal input (shown by decreasing $\varepsilon_{Hf}(t)$ and increasing $\delta^{18}O$).

Timing and Nature of Magmatism and Deformation in the Dengi Domain

The Dengi Domain to the west of the Kemashi Domain is characterised by a deformed and metamorphosed volcano-sedimentary sequence and the Jamoa-Ganti orthogneiss (Tadesse and Allen, 2005). There are a number of intrusive bodies incorporated in this domain and broadly these correlate to two pulses of magmatism at ca. 840 Ma and ca. 812–780 Ma (Fig. 5). The oldest ages obtained in this domain are obtained from well-defined oscillatory-zoned zircon grains extracted from a granite near Guba (E14.68: 854 ± 14 Ma). Similar ages were obtained from a coarse grained leucogranite further east (E14.79 and 38: 839 ± 8 Ma and 843 ± 14 respectively). Magmatism is recorded at ca. 774 Ma in a K-feldspar granite (E14.63: 774 ± 7 Ma) near Mendi. Younger Cryogenian ages (E14.78) are recorded by four grains in a granite, with grains yielding an age of ca. 608 Ma. Oxygen isotope analyses were only obtained from the ca. 840 zircons and these average $\delta^{18}O$ ratios of + 7.77 ‰ (Fig. 8 a–b), which suggest that the parent magma incorporated some supracrustal material. Nevertheless, these ca. 840 Ma zircons (E14.79 and 83) yield $\varepsilon_{Hf}(t)$ values between +5.95 and +9.34, which suggest that any incorporated supracrustal material is likely to have been derived from juvenile sources extracted from the mantle a short time beforehand.

Timing and Nature of Magmatism and Deformation in the Sirkole Domain

The Sirkole Domain occupies the north-western portion of the study area, west of Asosa (Fig. 2), and extends into Sudan. This region is composed of gneissic and volcano-sedimentary rocks, intruded by granites. The oldest ages obtained in this area are from small zircon grains extracted from a gneiss close to the border town of Kurmuk (853 ± 7 Ma) and a granodiorite (854 ± 14 Ma). Outcrop just east of Kurmuk shows the granodiorite (854 ± 14 Ma) being cut by younger intrusions; one at ca. 840 Ma and a second at ca. 806 Ma. Magmatism occurs at 835 ± 7 Ma in a granite just east of Kurmuk, providing a lower constraint for the first pulse magmatism in the Sirkole Domain (Fig. 5). Oxygen isotope analyses on zircons from the ca. 806 Ma zircons have average $\delta^{18}O$ ratios of + 7.13 ‰ (Fig. 8 a–b), suggesting a sedimentary input from upper crustal rocks giving heavier oxygen isotope values than that of the mantle. Zircons from ca. 850–835 Ma intrusions (E14.53, 58, 68, 69) yield $\varepsilon_{Hf}(t)$ values between +6.99 and +10 demonstrating their extremely juvenile, mantle-derived, origin. The later Tonian zircons (810–770 Ma) also yield positive $\varepsilon_{Hf}(t)$ values (+5 and +9.7) suggesting a similar juvenile origin. Cryogenian magmatism is again absent from this region.

Correlation with elsewhere in the East African Orogen

Tectonic reorganisations seen throughout the East African Orogen are reflected in the terranes of the WES. Figure 10 is a summary of tectonic and magmatic events within parts of the East African Orogen during the Neoproterozoic. Basement exposure in the northern East African Orogen is scarce and it is important to understand how these exposures correlate to the WES.

A detailed summary of the Mozambique Belt (Southern Ethiopia, Kenya, southern Somalia and Tanzania) is found in Blades et al. (2015), however, we will briefly cover these basement outcrops here. The closest basement outcrop to the WES is in southern Ethiopia. Four magmatic events have been defined (890–840 Ma, 790–700 Ma, ca. 660 Ma and 630–500 Ma). The ca. 660 Ma event in the Southern Ethiopian Shield, termed the 'Moyale Event' (Teklay et al.,
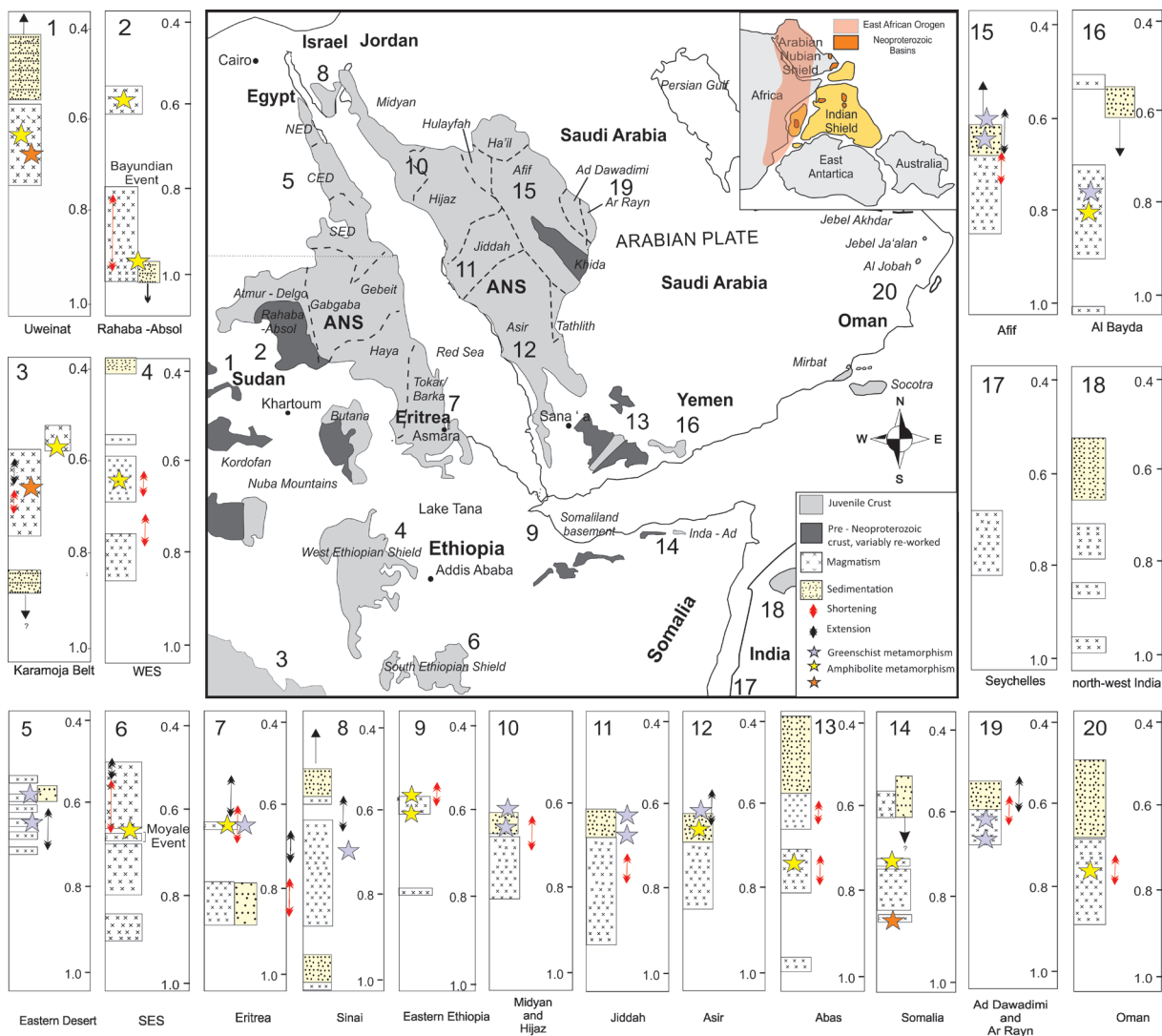
Figure 10: A condensed geological time space plot for major geological events in the East African Orogen. ANS: Arabian Nubian Shield. Adapted from Blades et al (2015) and Johnson et al (2011, 2014). (Abdelsalam and Stern, 1996; Abdelsalem and Stern, 1996; Alessio et al., 2017; Ali et al., 2013; Ali et al., 2016; Allen, 2007; Allen and Leather, 2006; Andersson et al., 2006; Avigad et al., 2007; Be'eri-Shlevin et al., 2012; Be'eri-Shlevin et al., 2010; Bowring et al., 2007; Cox et al., 2012; Cozzi et al., 2012; Denèle et al., 2013; Hargrove et al., 2006; Johnson et al., 2011; Johnson, 2014; Johnson and Woldehaimanot, 2003; Küster et al., 2008; Le Mée et al., 2004; Mercolli et al., 2006; Merdith et al., 2017; Morag et al., 2011; Rantakokko et al., 2014; Rieu et al., 2007; Robinson et al., 2015; Robinson et al., 2014; Robinson et al., 2017; Stern et al., 2004; Whitehouse et al., 2016; Whitehouse et al., 1998; Whitehouse et al., 2001; Windley et al., 1996; Worthing, 2005; Yeshanew et al., 2015)

1998b), occurs at approximately the same time as the late magmatism in the eastern WES (Figs. 9 and 10). Also relatively close to the WES is the Karamoja Belt of NE Uganda. Rocks here are dominated by the Karasuk Supergroup (Vail, 1983; Westerhof et al., 2014), metaigneous rocks that crystallised between ca. 740 Ma and 680 Ma (Mänttäri et al., 2011; Westerhof et al., 2014) and post-tectonic granitoids with U–Pb crystallisation ages of ca. 660 Ma (Mänttäri et al., 2011). Similar timing in magmatism is seen within the WES, however, there is a notable

difference between the Southern Ethiopian Shield and the Karamoja Belt. New U–Pb geochronological data from Yeshanew et al. (2016) have identified Tonian (c. 790 Ma) and Ediacaran granitic magmatism (600–560 Ma) in the Dire Dawa basement in eastern Ethiopia. The older magmatic event agrees somewhat with the earlier single zircon evaporation ages from the region by Teklay et al. (1998a), who reported Neoproterozoic magmatic episodes at ca. 845, 782 and ca. 650 Ma. However, the Ediacaran ages extend known magmatic events in the region to much younger ages than previously reported. Two of the granitoid samples dated at ca. 600 and ca. 585 Ma are not deformed, whereas the younger gneisses at ca. 568 and 560 Ma are strongly deformed. These were interpreted to represent a low-strain domain during orogenesis (Yeshanew et al., 2016) and suturing between two lithospheric blocks (WES and Eastern Ethiopia). These mid-late Ediacaran ages are much younger than any evidence for tectonism found in the WES, and any suggested ocean closure from the ANS west of the Saudi Arabian Afif Terrane (Johnson et al. 2011), so rather than representing suturing between the WES and eastern Ethiopia, we suggest that the post ca. 560 Ma deformation may reflect late intra-continental deformation, seen elsewhere in the ANS, rather than terrane suturing.

To the south, in Kenya, southern Somalia and Tanzania, the East African Orogen is dominated by high-grade gneisses of the Mozambique Belt (see Fritz et al. 2013 for a recent review). The eastern part of the Mozambique Belt (Burr Massif, Somalia) consists of a tract of largely pre-Neoproterozoic continental crust, strongly deformed, partially melted and metamorphosed in the Ediacaran/Cambrian (ca. 600 and 530 Ma, (Küster et al., 1990; Lenoir et al., 1994). Extensive tectonothermally reworked pre-Neoproterozoic crust lies further west in the

Neoarchaean Tanzanian craton (Johnson et al., 2003; Muhongo et al., 2001; Reddy et al., 2003; Tenczer et al., 2012). Near peak, granulite-grade metamorphism along the western part of this belt (ca. 640 Ma), has been dated by metamorphic zircons (Appel et al., 1998; Coolen et al., 1982; Muhongo, 1994; Muhongo et al., 2001). Hauzenberger et al. (2007) identified that the age of metamorphism further east, in the Galana River area, is considerably younger (580–530 Ma) overlapping the age of the 'Malagasy Orogeny' of Collins and Pisarevsky (2005b). Ediacaran-Cambrian deformation and metamorphism is not yet identified in the WES, though it appears to be prominent in the southern and eastern parts of the East African Orogen.

The Southern Arabian Nubian Shield

The extensive outcrop of the southern Arabian-Nubian Shield in NE Sudan, Eritrea and northern Ethiopia lies to the north of the WES. The two main terranes here are known as the Haya and Tokar/Barka Terranes (Drury and de Souza Filho, 1998; Johnson et al., 2011a). The Tokar/Barka Terrane consists of the high-grade Barka, Arag and Ghedem terranes that lie either side of the low-grade Hagar, Adhoba-Abi, Nacfa terrane of Eritrea and the Tsaliet Group of northern Ethiopia; (Andersson et al., 2006; Avigad et al., 2007). Juvenile arc magmatism occurred between ca. 850–740 Ma (Andersson et al., 2006; Teklay et al., 2003), which is followed in the low-grade terranes by deposition of the Tonian-Cryogenian Tsalkiet and Tambien Groups (post ca. 820 Ma; Swanson-Hysell et al. (2015)). This group is intruded by the post-tectonic Mereb granites at 640–600 Ma (Avigad et al., 2007). Upper amphibolite-facies metamorphism occurred in the surrounding high-grade terranes at ca. 590 Ma and is interpreted to relate to final continental collision in the area (Andersson et
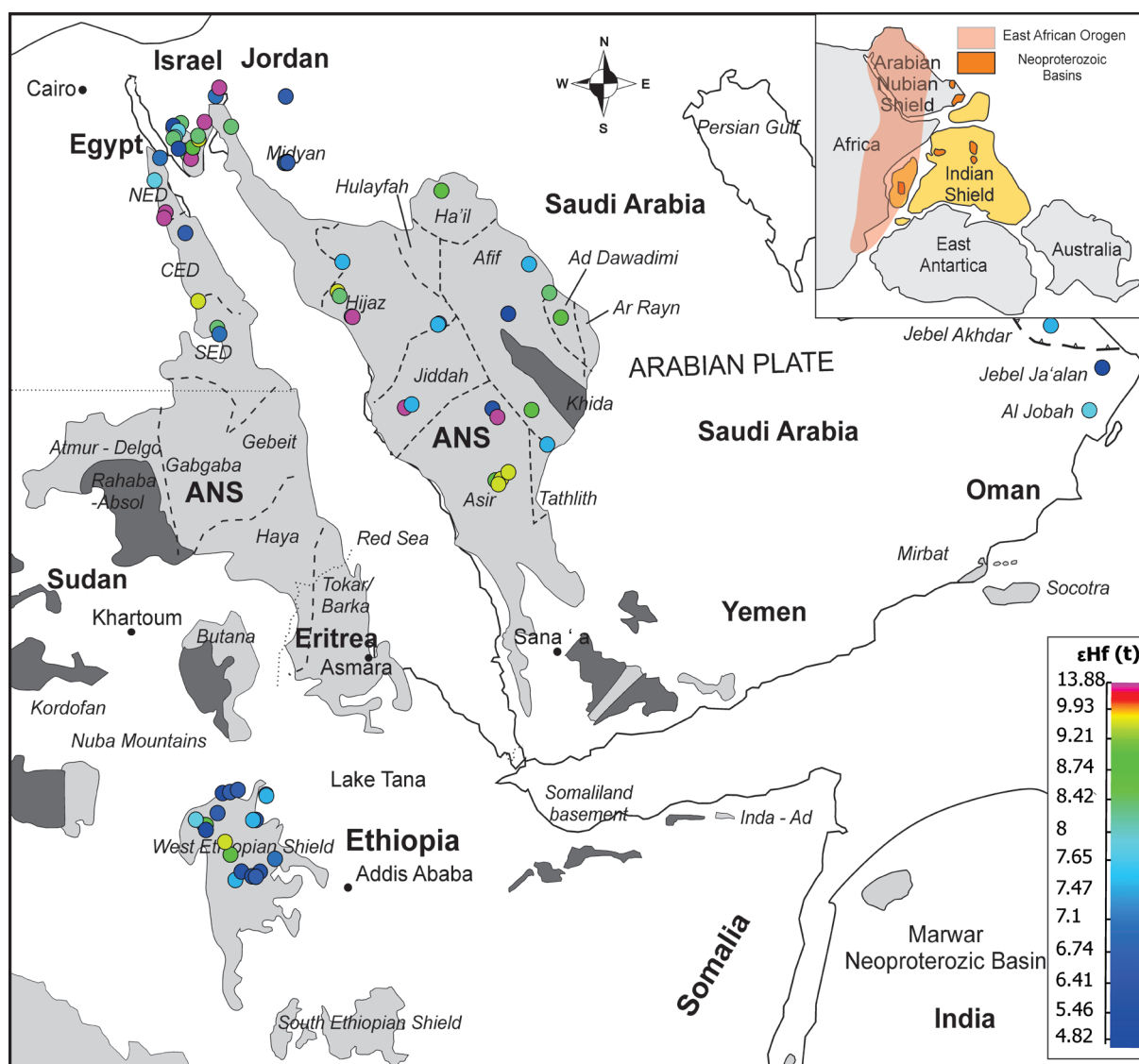
Figure 11: Location map showing distribution of crustal domains in the East African Orogen. SM, Sahara Metacraton; ANS, Arabian Nubian Shield. MB, Mozambique Belt. Previously published $\varepsilon_{Hf}(t)$ values (Alessio et al., 2017; Ali et al., 2013; Ali et al., 2016; Be'eri-Shlevin et al., 2010; Blades et al., 2015; Robinson et al., 2015; Robinson et al., 2014), have been collated with data from this study and are scaled by colour. Data shows that the ANS has on average more juvenile material than the Western Ethiopian Shield. Adapted from Blades et al., (2015).

al., 2006). These terranes correlate broadly with the Asir and Jiddah Terranes of Arabia (Johnson et al., 2011a) and the early history compares well with the WES as presented in this paper, where arc-related magmatism occurred at ca. 850–840 Ma and ca. 780–760 Ma. However, high-temperature deformation and magmatism also occur in the Didesa Terrane at ca. 660 Ma, considerably earlier than the ages suggested for these areas to the north.

The Northern Arabian Nubian Shield

The Egyptian Eastern Desert is part of the Neoproterozoic Arabian Nubian Shield (Fig. 10). The Precambrian rocks exposed in the Eastern Desert are traditionally subdivided into two tiers. The structurally lower unit, tier 1, is dominated by amphibolite facies gneisses. It is separated by a low angle shear zone from the overlying tier 2, which is dominated by greenschist facies volcanic and sedimentary
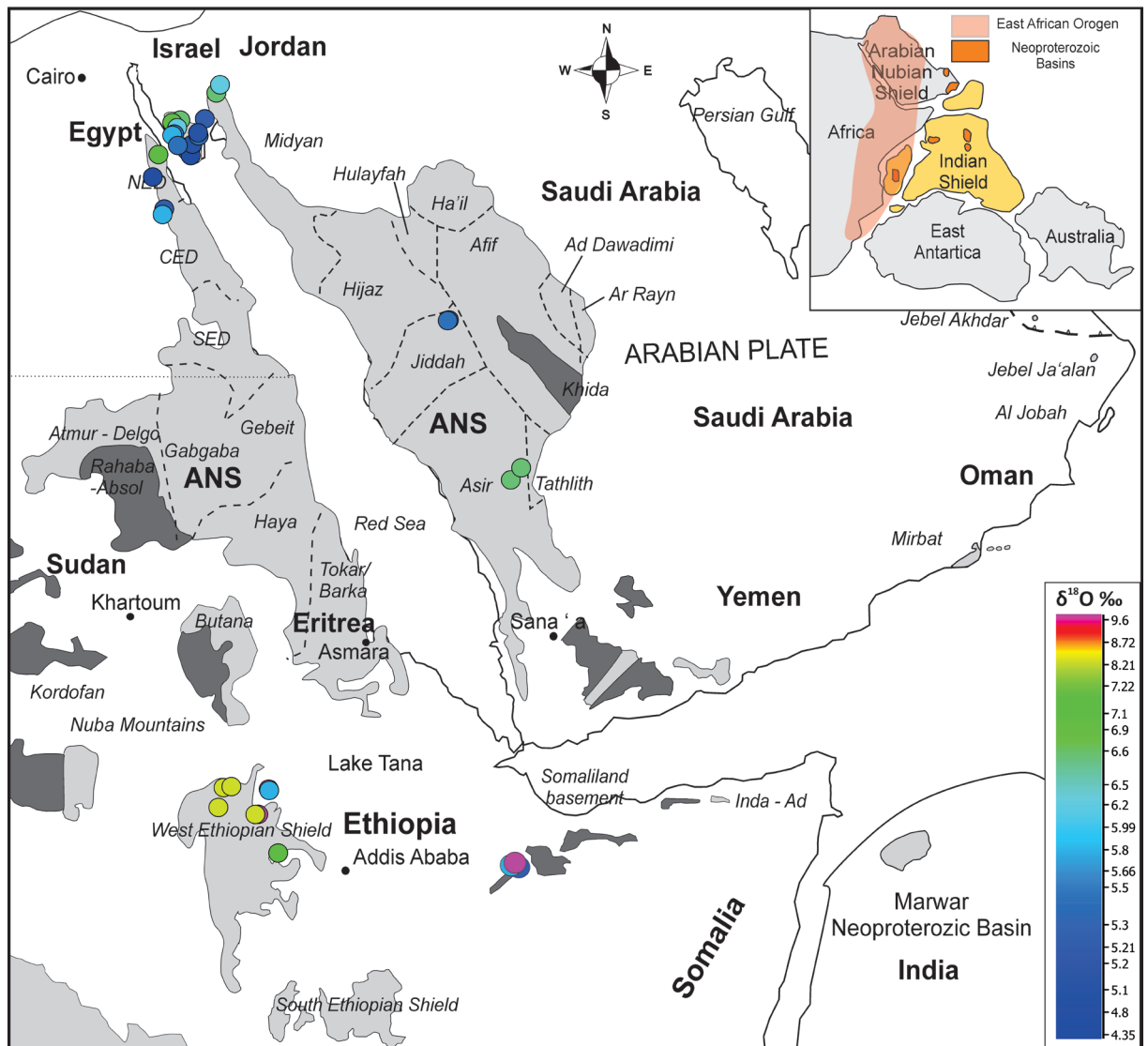
Figure 12: Location map showing distribution of crustal domains in the East African Orogen. SM, Sahara Metacraton; ANS, Arabian Nubian Shield. MB, Mozambique Belt. Previously published $\delta^{18}O$ values (Ali et al., 2015; Ali et al., 2013; Ali et al., 2016; Be'eri-Shlevin et al., 2012)have been collated with data from this study and are scaled by colour. Data shows that the Western Ethiopian shield has higher $\delta^{18}O$ values, with blue representing more mantle-like signatures. These higher values may suggest that these data formed as a result of the incorporation of newly formed crust and/or supra-crustal material. Adapted from Blades et al., (2015).

rocks. Both tiers are intruded by granitoid plutons, some deformed, others undeformed (Bennett and Mosley, 1987; Greiling et al., 1994). The collective data from variably deformed granitoids in the central Eastern Desert, along with the data from Hafafit migmatite in the South Eastern Desert and gneiss complexes, indicate that there are six pulses of magmatic/metamorphic events, but all are Cryogenian or younger. The oldest

ca. 705–680 Ma magmatic pulse is linked to migmatites in the structurally deepest part of the Hafafit gneiss complex (tier 1), and to gneisses in the El Sibai area (Augland et al., 2012), the undeformed El Sukkari pluton (Lundmark et al., 2012) and the Wadi Nabi intrusive complex (Pease et al., 2010) in the deep-water allochthon (tier 2). The second pulse is defined by one age from a migmatite (ca. 654 Ma) in the Hafafit area, (Shalaby et al.,
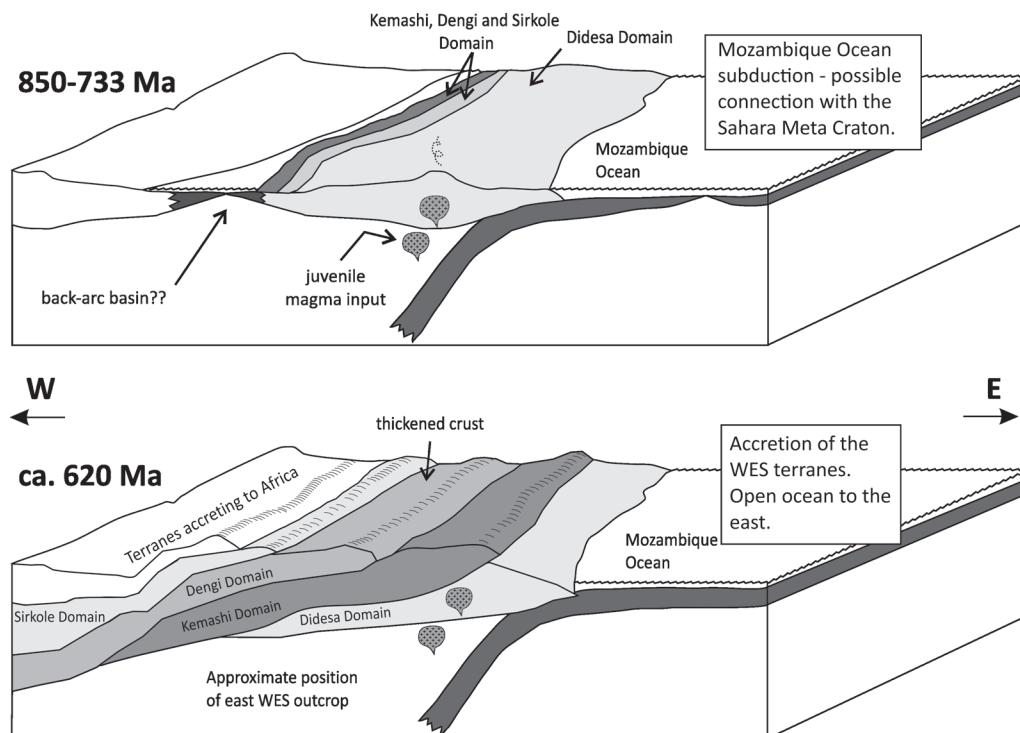
Figure 13: Schematic illustration of the stages of development in the Western Ethiopian Shield. There are two main phases. 850–733 Ma subduction and intra oceanic arc magmatism followed by deformation and further magmatism. Ca. 620 Ma represents the final stages of syn-tectonic magmatism and the transition to post tectonic phases at ca. 572 Ma. This depicts the final closure of the Mozambique Ocean and the amalgamation of Gondwana. Adapted from Blades et al. (2015).

2005) and it is suggested that that the age is likely belongs to the older pulse as a result of reverse discordance (Lundmark et al., 2012). The third pulse at ca. 630 Ma includes the Tier 1 gneiss in the Meatiq gneiss complex (Andresen et al., 2010), anatexis and deformation of the gneiss in the Hafafit gneiss complex and the protolith ages for other plutons in the area. The fourth pulse at ca. 610–604 Ma is defined by minor syn-tectonic plutons in the Meatiq area, along with hydrothermal activity related to magmatism related to movements on both the EDSZ and Meatiq area (Andresen et al., 2010) and the related Nugrus Shear Zone in the Hafafit area. The fifth pulse is defined by 600–590 Ma granites in the Meatiq area (Andresen et al., 2010), the Nugrus biotite granite and a metamorphic age defined by titanites in migmatite in the Hafafit area. The magmatism associated with the final ca. 540 Ma

pulse is only seen in the El Sibai area (Augland et al., 2012). Though synchronous with the latest phase of syn-tectonic magmatism (ca. 660–655 Ma) in the WES, magmatism in the Egyptian Desert continues until ca. 540 Ma, considerably later than seen in the WES, where ca. 584 Ma denotes post-tectonic orogenic thickening (Blades et al., 2015).

The Sa'al Metamorphic Complex is exposed at the northernmost limit of the exposed ANS, in Sinai. This is one of four metasedimentary, metavolcanic, and gneissic assemblages that developed early in the geologic history of the northern ANS. Until recently, the Sa'al Metamorphic Complex was believed to be Cryogenian, with an age of between ca. 820–740 Ma, but new U–Pb zircon age data suggest that it is instead latest Mesoproterozoic (ca. 1100–1000 Ma), with post-collisional calc-alkaline (ca. 635–590 Ma) and alkaline (ca.

608–580 Ma) granitic plutons (Be'eri-Shlevin et al., 2012; Johnson, 2014).

The eastern Arabian Nubian Shield

The Khida Terrane of central Saudi Arabia is a Palaeoproterozoic (ca. 1800–1670 Ma) terrane that has previously been identified as part of the proposed pre-Neoproterozoic continent Azania (Collins and Windley, 2002a). Apart from the Khida Terrane, there is no evidence of any intact pre-Neoproterozoic rocks exposed in, or in the crust beneath, this eastern part of the shield. From 950–640 Ma the generation of a chain of juvenile island arcs, formed the key elements of the western Arabian Shield (Midyan, Hijaz and Asir Terranes).   It is suggested that the ca. 845 Ma Makkah Suite (Jeddah Terrane) represents the initiation of western island arc magmatism (Johnson et al., 2011a; Johnson, 2014; Robinson et al., 2014). Syn-collisional magmatism in the northern Shield at ca. 736–709 Ma (Shufayyah and Jar-Salajah Complexes) stitched the Midyan and Hijaz Terranes together. The granitoids of the northern Abas Terrane record an older episode of granitic magmatism that occurred at ca. 790–730 Ma, followed by post-tectonic granite genesis at 625–590 Ma shown by the appearance of the ca. 611 Ma Ar-Ruwaydah Suite and ca. 607 Ma Najirah granitoid along the Halaban Suture (Ad Dawadimi Terrane). Post-tectonic calc-alkaline and alkaline magmatism were synchronous at ca. 605 Ma, followed by younger alkaline magmatism at ca. 590 Ma shown by the generation of the Al Bad (ca. 597 Ma), Al Hawiyah (ca. 591 Ma) and Abanat (ca. 585 Ma) Suites. This indicates that the period from 605 Ma onwards was dominated by alkaline magmatism, presumably in an extensional setting. These phases of magmatism overlap with those seen in the WES with greenschist metamorphism in the east ANS at 650 − 605 Ma (Johnson et al., 2011, Fig. 10) and post tectonic magmatism occurring from 605 Ma onwards (Cox et al., 2012a; Cox et al., 2012b; Doebrich et al., 2007; Doebrich et al., 2004; Johnson, 2014; Johnson et al., 2011c; Robinson et al., 2015; Robinson et al., 2014) (Robinson et al 2015a; b; 2017).

Hafnium and oxygen isotopes in the Arabian Nubian Shield

Widespread acceptance of the juvenile character of the ANS has come about in the past decade, although consensus is not universal (Johnson, 2014). To date, one of the most widely adopted approaches is using Sm-Nd isotope data, however hafnium and oxygen isotopes in zircon are increasingly being used as tools to determine the magma sources and the extent of crustal recycling. Below we review previously published hafnium and oxygen isotope data from the ANS.

It has been proposed that four discrete magmatic events exist in the eastern Arabian Nubian Shield; island arc (ca. 845 Ma), syn-collisional (ca. 710 Ma), post-tectonic (ca. 620 Ma) and anorogenic (ca. 525 Ma) (Robinson et al., 2014). These are defined by juvenile magmas ($\varepsilon_{Hf}(t)$ values of +4.5 to +10) regardless of their intrusive ages or spatial relationship (Morag et al., 2011, Ali et al., 2013, Ali et al., 2014, Robinson et al. 2014, 2015a, 2015b, 2017 and Ali et al., 2015). Not included in this approach to suite classification, is the recognition that in the eastern ANS some magmatism is pre-orogenic and represents ocean floor magmatism prior to ophiolite obduction (Cox et al. 2012). Recent zircon oxygen isotopic work has been reported from eastern Ethiopia in the Precambrian exposures of the Dire Dawa (Fig. 12). The slightly higher than pristine mantle $\delta^{18}O$ values of the Ediacaran eastern Ethiopian granitoids indicate the presence of a minor amount of supracrustal ^{18}O-enriched material at the source. The highly elevated $\delta^{18}O$ values (7.8–9.6‰) of the older

granitoids (ca. 630 Ma), suggest that these have formed by melting of a metasedimentary source, consistent with the S-type features of rocks of this age in the region (Yeshanew et al., 2016). Oxygen isotope data are sparse in the ANS, however, oxygen isotopes from post collisional A-type granitoids (Habd adh Dayeen) in the central - eastern ANS, yield $\delta^{18}O$ values of +3.2‰ to +6.4‰, suggesting crystallization of zircon from magma derived from magmatic rocks altered by meteoric water in a magma chamber caldera system (Ali et al., 2013). In the southern portion of the ANS, in the Asir Terrane, oxygen isotopes from the Jabal Al-Hassir ring complex have $\delta^{18}O$ values of +5.8‰ to +7.4‰ consistent with melting of a relatively juvenile crustal protolith that was formed during the Neoproterozoic assembly of the Arabian Nubian Shield (Ali et al., 2015).

Moving to the northernmost ANS in southwest Jordan, the northern part of Saudi Arabia, southern Israel, Sinai (Egypt), and the northern part of the Eastern Desert in Egypt. The rocks in Sinai have an average $\delta^{18}O$ values of 5.7-5.8‰ indicating a dominance of mantle-like $\delta^{18}O$ sources with higher values in north-western Sinai (6.9-8.2‰). Hafnium isotopes, complementary with oxygen isotopes, also reveal a gradual transition from lower $\varepsilon_{Hf}(t)$ values in the north-western regions (+5.5 to +5.9) to slightly higher values in the south-east (+9.2 to +13.9), reflecting more supracrustal and older crust involvement in magmatism in the northwest Sinai (Be'eri — Shlevin et al., 2012). The syn-collisional granites of the North Eastern Desert yield correspondingly high $\varepsilon_{Hf}(t)$ values (+ 9.1 to + 11.2) and mantle $\delta^{18}O$ values (mean = + 5.12‰). However, the post-collisional granites of the NED show slightly higher $\delta^{18}O$ values (+ 5.15 to 6.70) and slightly lower $\varepsilon_{Hf}(t)$ values (+ 6.3 to + 10.6), which have been interpreted to reflect melting

of a juvenile Neoproterozoic mantle source that assimilated slightly older Neoproterozoic crustal material during magma mixing (Ali et al, 2016).

Figure 12 shows that, on average, the terranes of the northern and eastern ANS have higher $\varepsilon_{Hf}(t)$ and lower $\delta^{18}O$ values than the Western Ethiopian shield (+1.94 − +9.97 and +5.99 − +10, respectively). The deviations of $\delta^{18}O$ from the mantle values seen in the zircons from some samples in the western Ethiopia are interpreted as the direct or indirect result of intra-crustal recycling, the magma interaction with supra-crustal materials that ultimately derived their evolved $\delta^{18}O$ from low temperature processes on or near the surface of the Earth where oxygen isotope fractionations are large. The relative juvenile nature of these rocks suggests the remelting of a juvenile crustal protolith.

Tectonic Setting of the WES

The data presented in this study reveal the timing of tectonothermal events throughout the Western Ethiopia Shield. Previous studies in the WES show that there were three main phases of magmatism ca. 850–810 Ma, 780–700 Ma and 620–550 Ma (Ayalew et al., 1990; Ayalew and Peccerillo, 1998; Blades et al., 2015; Kebede et al., 2001a; Kebede et al., 1999; Kebede et al., 2001b). These magmatic pulses been previously assigned to pre-, syn- and post-tectonic environments, respectively (Woldemichael and Kimura, 2008; Woldemichael et al., 2010). Here we demonstrate that this pre-, syn- and post-tectonic assignment is complicated by metamorphism/deformation occurring both at ca. 770 Ma and at ca. 690–660 Ma.

All phases of magmatism show minimal evidence of being contaminated by any pre-Neoproterozoic crust (Figs. 6 and 7 a–b). This contrasts with recent maps of the WES that designate high-grade regions as Archaean (Berhe, 1990; Kazmin and Berhe, 1978). We

see no direct evidence of pre-Neoproterozoic crust in the WES, the oldest rocks in the area date back to ca. 855 Ma. However, more evolved Hf isotopes in the Didesa Domain suggest that some older Neoproterozoic crust was incorporated into the protolith magma. Despite this caveat, we interpret all these rocks to have formed in an intra-oceanic setting, above a subduction zone (Chapter 3 and 4). The Didesa Domain may incorporate a kernel of pre-Neoproterozoic or early Tonian rock, or even hide a metasedimentary core derived from erosion of an unknown older terrane. Later deformation and intrusion at 810–770 Ma is interpreted as evidence of further mantle-derived magmatism and the remelting of juvenile Neoproterozoic rocks (as shown by the broad Hf evolution band in Fig. 7a and b). Subsequent syn- tectonic magmatism (660–655 Ma) in the Didesa domain, is coeval with the tectonothermal event only preserved in the rocks in the east of the Western Ethiopian Shield and ca. 584 Ma is interpreted as representing post-tectonic magmatism (Blades et al., 2015).

The tectonic organisation of the Western Ethiopian Shield and the Arabian Nubian Shield during the Neoproterozoic Below is a summary of two time slices that reflect re-organisation in the Western Ethiopian Shield and the ANS (Fig. 13) and a brief summary of tectonic and magmatic events within parts of the northern East African Orogen during the Neoproterozoic.

850 Ma to 630 Ma
Juvenile magmatism in seen in Butana at ca. 987 Ma, north Sudan ca. 920–900 Ma and amphibolite metamorphism is recorded south of the Keraf Suture at this time. Slightly younger oceanic arc magmatism is occurring at this time in the WES at ca. 854–760 Ma. The Dire Dawa area records granites that are ca.

790 Ma (Yeshanew et al., 2016). The terranes that form the Arabian shield, were accreted as a chain of juvenile island arcs. It has been suggested that the ca. 845 Ma Makkah Suite (Jeddah Terrane) represents the initiation of island arc magmatism emplaced in the upper plate above the eastward subduction formed in the preliminary phase of the closure of the Mozambique ocean (Cox et al., 2012; Evuk et al., 2014; Küster and Liégeois, 2001; Merdith et al., 2017; Robinson et al., 2015; Robinson et al., 2014). Periods of magmatism, metamorphism and deformation are recorded in northern Uganda, southern Ethiopia, the WES and Sudan between ca. 750–600 Ma (Appel et al., 2004; Leggo, 1974; Mänttäri et al., 2011; Stern et al., 2012; Westerhof et al., 2014; Yibas et al., 2003; Yibas et al., 2002; Yihunie, 2002). By 650 Ma most of the crust of the ANS had been formed (Fritz et al., 2013; Johnson et al., 2011; Johnson, 2014; Johnson and Woldehaimanot, 2003). These island arc terranes collided with the Afif Abas between 680–640 Ma to form the Nabitah Suture (Johnson et al., 2011a). The ca. 630 Ma A-type granites have been interpreted to constrain the final accretion of the eastward migrating terranes (Robinson et al., 2017). By 630 Ma the core terranes of the ANS had already been amalgamated and the Abt formation was being deposited on the flank of the ANS with the Al Amar arc forming what remained of the Mozambique Ocean (Johnson et al 2014). This terrane assembly occurred east of, but not in contact with the Sahara Metacraton, though convergence was occurring along the Keraf Suture (650–580 Ma) (Cox et al., 2012; Evuk et al., 2014; Johnson et al., 2011a; Johnson, 2014; Johnson and Woldehaimanot, 2003; Küster and Liégeois, 2001; Merdith et al., 2017; Robinson et al., 2015; Robinson et al., 2014).

Ca. 620 Ma

East of the Afif Terrane, westward-dipping subduction magmatism was still occurring until ca. 600 Ma in the Ar Ryan Terrane (Cox et al., 2012). The Ad Dawadimi Terrane, lies between the Ar Rayn and Afif Terranes and largely consists of a ca. 615 Ma fore-arc sedimentary basin represented by the Abt Schist (Cox et al., 2012b). Upper amphibolite-facies metamorphism seen in the surrounding high-grade terranes in NE Sudan, Eritrea and northern Ethiopia (600–590 Ma) are interpreted to relate to final continental collision in the area (Andersson et al., 2006; Collins and Pisarevsky, 2005; Cox et al., 2012; Evuk et al., 2014; Johnson et al., 2011; Johnson, 2014; Johnson and Woldehaimanot, 2003; Küster and Liégeois, 2001; Merdith et al., 2017; Robinson et al., 2015; Robinson et al., 2014). Ediacaran granitic magmatism (600–560 Ma) occurs in Dire Dawa Basement, in eastern Ethiopia, however these terranes record a younger phase of deformation and metamorphism (ca. 580–545 Ma). Yeshanew et al. (2016) interpreted these younger ages to represent the collision between eastern Ethiopia and the terranes of the western Arabian Nubian Shield (Yeshanew et al., 2016).

Geochronology and geochemistry in the northern extent of the East African Orogen demonstrate that these terranes were formed by a multiphase accretion of a number of crustal blocks The existence of the East African Orogen as a continuous tectonic event has been previously disputed, with Collins and Piservesky (2005) pointing out that the EAO seems to bifurcate south of Tanzania/Madagascar with one arm heading west to the Zambezi and the other heading into India. The complexity of the East African Orogen, and in particular the northern extent does not reflect a simple Wilson cycle of oceanic opening and closing, but instead reflects more than 400 Ma of subduction accretion.

CONCLUSIONS

Data presented here help constrain the tectonic evolution of the region and document consumption and closure of the western Mozambique Ocean. New data from the Western Ethiopian Shield demonstrate that there were three broad pulses of syn-tectonic magmatism at ca. 854–835 Ma, ca. 810–770 Ma and ca. 660–600 Ma. These are complicated by metamorphism and deformation at ca. 660–690 Ma and ca. 770 in the Didesa and Kemashi Domains. Importantly, Cryogenian magmatism and metamorphism is only seen in the eastern domains of the shield. Hafnium isotopic analysis indicates that the early Cryogenian magmas were generated from juvenile Neoproterozoic mantle sources with little involvement of the pre-Neoproterozoic continental crust. The hafnium isotopic data from the ca. 810–770 Ma and ca. 660–600 Ma rocks are consistent with them being, at least partially, generated by melting of the older Tonian–Cryogenian rocks. The deviation of $\delta^{18}O$ values from mantle values seen in the zircons from some samples in the western Ethiopia are likely the result of magma interaction with supra-crustal materials, though some are undoubtedly derived from mantle sources. The magmatic phases within the eastern Arabian Nubian Shield (ca. 845 Ma, 710 Ma, 620 Ma and 525 Ma) are defined by juvenile magmas ($\varepsilon_{Hf}(t)$ values of +4.5 to +10), similar to the juvenile magmatism seen in the WES. Age constraints on orogenesis in the eastern most part of the Western Ethiopian Shield (ca. 660 Ma) are similar to those in NE Uganda (ca. 690–660 Ma), but are older than the Ediacaran peak orogenesis reported from the Southern Ethiopian Shield, Eritrea and northern Ethiopia and from SE Kenya. These younger syn-tectonothermal events are likely

to be related to the progressive closure of the Mozambique Ocean and amalgamation of terranes onto the active margin of Africa.

REFERENCES

Abdelsalam, M., Stern, R., 1996. Sutures and shear zones in the Arabian-Nubian Shield. Journal of African Earth Sciences 23, 289-310.

Alemu, T., 2005. Discussion of "Geological setting and tectonic subdivision of the Neoproterozoic Orogenic Belt of Tuludimtu, Western Ethiopia" Journal of African Earth Sciences 41, 329-332.

Allen, A., Tadesse, G., 2003. Geological setting and tectonic subdivision of the Neoproterozoic orogenic belt of Tuludimtu, western Ethiopia. Journal of African Earth Sciences 36, 329-343.

Andersson, U.B., Ghebreab, W., Teklay, M., 2006. Crustal evolution and metamorphism in east-central Eritrea, south-east Arabian-Nubian Shield. Journal of African Earth Sciences 44, 45-65.

Andresen, A., Augland, L., Boghdady, G., Lundmark, A., Elnady, O., Hassan, M., El-Rus, M.A., 2010. Structural constraints on the evolution of the Meatiq Gneiss Dome (Egypt), East-African Orogen. Journal of African Earth Sciences 57, 413-422.

Appel, P., Möller, P., Schenk, V., 1998. High-pressure granulite facies metamorphism in the Pan-African belt of eastern Tanzania: P-T-t evidence against granulite formation by continent collision. Journal of Metamorphic Geology 16, 491-509.

Archibald, D.B., Collins, A.S., Foden, J.D., Payne, J.L., Holden, P., Razakamanana, T., De Waele, B., Thomas, R.J., Pitfield, P.E., 2016. Genesis of the Tonian Imorona-Itsindro Magmatic Suite in central Madagascar: Insights from U-Pb, oxygen and hafnium isotopes in zircon. Precambrian Research.

Archibald, D.B., Collins, A.S., Foden, J.D., Payne, J.L., Macey, P., Holden, P., Razakamanana, T., 2017a. Stenian–Tonian arc magmatism in west central Madagascar: Genesis of the Dabolava Suite. Journal of the Geological society, London

Archibald, D.B., Collins, A.S., Foden, J.D., Razakamanana, T., 2017b. Tonian Arc Magmatism in Central Madagascar: The Petrogenesis of the Imorona-Itsindro Suite. The Journal of Geology 125, 271-297.

Augland, L.E., Andresen, A., Boghdady, G.Y., 2012. U–Pb ID-TIMS dating of igneous and metaigneous rocks from the El-Sibai area: time constraints on the tectonic evolution of the Central Eastern Desert, Egypt. International Journal of Earth Sciences 101, 25-37.

Avigad, D., Stern, R., Beyth, M., Miller, N., McWilliams, M., 2007. Detrital zircon U–Pb geochronology of Cryogenian diamictites and Lower Paleozoic sandstone in Ethiopia (Tigrai): age constraints on Neoproterozoic glaciation and crustal evolution of the southern Arabian–Nubian Shield. Precambrian Research 154, 88-106.

Ayalew, T., Bell, K., Moore, J.M., Parrish, R.R., 1990. U-Pb and Rb-Sr geochronology of the western Ethiopian shield. Geological Society of America Bulletin 102, 1309-

1316.

Ayalew, T., Peccerillo, A., 1998. Petrology and geochemistry of the Gore-Gambella plutonic rocks: implications for magma genesis and the tectonic setting of the Pan-African Orogenic Belt of western Ethiopia. Journal of African Earth Sciences 27, 397-416.

Be'eri-Shlevin, Y., Eyal, M., Eyal, Y., Whitehouse, M.J., Litvinovsky, B., 2012. The Sa'al volcano-sedimentary complex (Sinai, Egypt): a latest Mesoproterozoic volcanic arc in the northern Arabian Nubian Shield. Geology 40, 403-406.

Bennett, J., Mosley, P., 1987. Tiered-tectonics and evolution, Eastern Desert and Sinai, Egypt, Colloquium on african geology. 14, pp. 79-82.

Berhe, S.M., 1990. Ophiolites in Northeast and East Africa: implications for Proterozoic crustal growth. Journal of the Geological Society, London 147, 41-57.

Blades, M.L., Collins, A.S., Foden, J., Payne, J.L., Xu, X., Alemu, T., Woldetinsae, G., Clark, C., Taylor, R.J., 2015. Age and hafnium isotopic evolution of the Didesa and Kemashi Domains, western Ethiopia. Precambrian Research 270, 267-284.

Boger, S.D., Wilson, C.J.L., Fanning, C.M., 2006. An Archaean province in the southern Prince Charles Mountains, East Antarctica: U-Pb zircon evidence for c.3170 Ma granite plutonism and c.2780 Ma partial melting and orogenesis. Precambrian Research 145, 207-228.

Braathen, A., Davidsen, B., 2000. Structure and stratigraphy of the Palaeoproterozoic Karasjok Greenstone Belt, north Norway - regional implications. Norsk Geologisk Tidsskrift 80, 33-50.

Braathen, A., Grenne, T., Selassie, M., Worku, T., 2001. Juxtaposition of Neoproterozoic units along the Baruda–Tulu Dimtu shear-belt in the East African Orogen of western Ethiopia. Precambrian Research 107, 215-234.

Cawood, P.A., Buchan, C., 2007. Linking accretionary orogenesis with supercontinent assembly. Earth-Science Reviews 82, 217-256.

Collins, A., Pisarevsky, S., 2005a. Amalgamating eastern Gondwana: the evolution of the Circum-Indian Orogens. Earth-Science Reviews 71, 229-270.

Collins, A., Pisarevsky, S., 2005b. Amalgamating eastern Gondwana: The evolution of the Circum-Indian Orogens. Earth-Science Reviews 71, 229-270.

Collins, A., Windley, B., 2002a. The tectonic evolution of central and northern Madagascar and its place in the final assembly of Gondwana. Journal of Geology 110, 325-339.

Collins, A.S., 2003. Structure and age of the northern Leeuwin Complex, Western Australia: constraints from field mapping and U–Pb isotopic analysis. Australian Journal of Earth Sciences 50, 585-599.

Collins, A.S., Kinny, P.D., Razakamanana, T., 2012. Depositional age, provenance and metamorphic age of metasedimentary rocks from southern Madagascar. Gondwana Research 21, 353-361.

Collins, A.S., Windley, B.F., 2002b. The tectonic evolution of central and northern Madagascar and its place in the final assembly of Gondwana. Journal of Geology 110, 325-339.

Coolen, J.J.M.M., Priem, H.N.A., Verdurmen, E.A.T., Versuchure, R.H., 1982. Possible zircon U-Pb evidence for Pan-African granulite-facies metamorphism in the Mozambique belt of southern Tanzania. Precambrian Research 17, 31-40.

Cox, G.M., Lewis, C.J., Collins, A.S., Halverson, G.P., Jourdan, F., Foden, J.,

Nettle, D., Kattan, F., 2012a. Ediacaran Terrane Accretion in the Arabian-Nubian Shield. Gondwana Research 21, 341-352.

Cox, G.M., Lewis, C.J., Collins, A.S., Halverson, G.P., Jourdan, F., Foden, J., Nettle, D., Kattan, F., 2012b. Ediacaran terrane accretion within the Arabian-Nubian Shield. Gondwana Research 21, 341-352.

de Wit, M., Aguma, A., 1977. Geology of the ultramafic and associated rocks of Tulu Dimtu, Welega. Ethiopian Institute of Geological Surveys Report, 26.

Dhuime, B., Hawkesworth, C.J., Cawood, P.A., Storey, C.D., 2012. A change in the geodynamics of continental growth 3 billion years ago. Science 335, 1334-1336.

Doebrich, J.L., Al-Jehani, A.M., Siddiqui, A.A., Hayes, T.S., Wooden, J.L., Johnson, P.R., 2007. Geology and metalogeny of the Ar Rayn terrane, eastern Arabian shield: Evolution of a Neoproterozoic continental-margin arc during assembly of Gondwana within the East African orogen. Precambrian Research 158, 17-50.

Doebrich, J.L., Zahony, S.G., Leavitt, J.D., Portacio, J.S., Siddiqui, A.A., Wooden, J.L., Fleck, R.J., Stein, H.J., 2004. Ad Duwayhi, Saudi Arabia: geology and geochronology of a Neoproterozoic intrusion-related gold system in the Arabian Shield. Economic Geology 99, 713-741.

Drury, S., de Souza Filho, C., 1998. Neoproterozoic terrane assemblages in Eritrea: review and prospects. Journal of African Earth Sciences 27, 331-348.

Evuk, D., Franz, G., Frei, D., Lucassen, F., 2014. The Neoproterozoic evolution of the central-eastern Bayuda Desert (Sudan). Precambrian Research 240, 108-125.

Fitzsimons, I.C.W., 2000. A review of tectonic events in the East Antarctic Shield and their implications for Gondwana and earlier supercontinents. Journal of African Earth Sciences 31, 3-23.

Fritz, H., Abdelsalam, M., Ali, K.A., Bingen, B., Collins, A.S., Fowler, A.R., Ghebreab, W., Hauzenberger, C.A., Johnson, P.R., Kusky, T.M., Macey, P., Muhongo, S., Stern, R.J., Viola, G., 2013. Orogen styles in the East African Orogen: A review of the Neoproterozoic to Cambrian tectonic evolution. Journal of African Earth Sciences.

Ganade de Araujo, C.E., Weinberg, R.F., Cordani, U.G., 2014. Extruding the Borborema Province (NE-Brazil): a two-stage Neoproterozoic collision process. Terra Nova 26, 157-168.

Greiling, R., Abdeen, M., Dardir, A., El Akhal, H., El Ramly, M., Kamal, G.E.D., Osman, A., Rashwan, A., Rice, A., Sadek, M., 1994. A structural synthesis of the Proterozoic Arabian-Nubian Shield in Egypt. Geologische Rundschau 83, 484-501.

Grenne, T., Pedersen, R., Bjerkgård, T., Braathen, A., Selassie, M., Worku, T., 2003. Neoproterozoic evolution of Western Ethiopia: igneous geochemistry, isotope systematics and U–Pb ages. Geological magazine 140, 373-395.

Griffin, W., Pearson, N., Belousova, E., Saeed, A., 2006. Comment: Hf-isotope heterogeneity in zircon 91500. Chemical Geology 233, 358-363.

Griffin, W., Wang, X., Jackson, S., Pearson, N., O'Reilly, S.Y., Xu, X., Zhou, X., 2002. Zircon chemistry and magma mixing, SE China: in-situ analysis of Hf isotopes, Tonglu and Pingtan igneous complexes. Lithos 61, 237-269.

Hauzenberger, C.A., Sommer, H., Fritz, H., Bauernhofer, A., Kröner, A., Hoinkes, G., Wallbrecher, E., Thöni, M., 2007. SHRIMP U-Pb zircon and Sm-Nd garnet ages from the granulite facies basement of SE-Kenya: evidence for Neoproterozoic polycyclic assembly of the Mozambique Belt. Journal

of the Geological Society, London 164, 189-201.

Hoskin, P., Black, L., 2000. Metamorphic zircon formation by solid-state recrystallization of protolith igneous zircon. Journal of metamorphic Geology 18, 423-439.

Howard, K.E., Hand, M., Barovich, K.M., Reid, A., Wade, B.P., Belousova, E.A., 2009. Detrital zircon ages: Improving interpretation via Nd and Hf isotopic data. Chemical Geology 262, 277-292.

Jackson, M., 2006. Lithogeochemistry and spinel compositions in the ultramafic complexes of Western Ethiopia: criteria for the identification of Alaskan-type intrusions. Cardiff University.

Jackson, S.E., Pearson, N.J., Griffin, W.L., Belousova, E.A., 2004. The application of laser ablation-inductively coupled plasma-mass spectrometry to in-situ U/Pb zircon geochronology. Chemical Geology 211, 47-69.

Jacobs, J., Thomas, R.J., 2004. Himalayan-type indenter-escape tectonics model for the southern part of the late Neoproterozoic–early Paleozoic East African–Antarctic orogen. Geology 32, 721-724.

Johnson, P., Andresen, A., Collins, A.S., Fowler, A., Fritz, H., Ghebreab, W., Kusky, T., Stern, R., 2011a. Late Cryogenian–Ediacaran history of the Arabian–Nubian Shield: A review of depositional, plutonic, structural, and tectonic events in the closing stages of the northern East African Orogen. Journal of African Earth Sciences 61, 167-232.

Johnson, P.R., 2014. An Expanding Arabian-Nubian Shield Geochronologic and Isotopic Dataset: Defining Limits and Confirming the Tectonic Setting of a Neoproterozoic Accretionary Orogen. Open Geology Journal 8, 3-33.

Johnson, P.R., Andresen, A., Collins, A.S.,

Fowler, A.R., Fritz, H., Ghebreab, W., Kusky, T., Stern, R.J., 2011b. Late Cryogenian-Ediacaran history of the Arabian-Nubian Shield: A review of depositional, plutonic, structural, and tectonic events in the closing stages of the northern East African Orogen. Journal of African Earth Sciences 61, 167-232.

Johnson, P.R., Andresen, A., Collins, A.S., Fowler, A.R., Fritz, H., Ghebreab, W., Kusky, T., Stern, R.J., 2011c. Late Cryogenian-Ediacaran history of the Arabian-Nubian Shield: A review of depositional, plutonic, structural, and tectonic events in the closing stages of the northern East African Orogen. Journal of African Earth Sciences 61, 167-232.

Johnson, P.R., Woldehaimanot, B., 2003. Development of the Arabian-Nubian Shield: perspectives on accretion and deformation in the northern East African Orogen and the assembly of Gondwana, in: Yoshida, M., Windley, B.F., Dasgupta, S. (Eds.), Proterozoic East Gondwana: Supercontinent Assembly and Breakup. Geological Society, London, Special Publication 206, pp. 289-325.

Johnson, S.P., Cutten, H.N.C., Muhongo, S., De Waele, B., 2003. Neoarchean magmatism and metamorphism of the western granulites in the central domain of the Mozambique belt, Tanzania: U-Pb SHRIMP geochronology and PT estimates. Tectonophysics 375, 125-145.

Johnson, T.E., Ayalew, T., Mogessie, A., Kruger, F.J., Poujol, M., 2004. Constraints on the tectonometamorphic evolution of the Western Ethiopian Shield. Precambrian Research 133, 305-327.

Jöns, N., Schenk, V., 2008. Relics of the Mozambique Ocean in the central East African Orogen: evidence from the Vohibory Block of southern Madagascar. Journal of

Metamorphic Geology 26, 17-28.

Jöns, N., Schenk, V., 2011. The ultrahigh temperature granulites of southern Madagascar in a polymetamorphic context: implications for the amalgamation of the Gondwana supercontinent. European Journal of Mineralogy 23, 127-156.

Jöns, N., Schenk, V., Appel, P., Razakamanana, T., 2005a. P-T evolution of the Bemarivo Belt (nothern Madagascar): the final assembly of Gondwana, in: Wingate, M.T.D., Pisarevsky, S.A. (Eds.), Supercontinents and Earth Evolution. Geological Society of Australia, Abstracts, No. 81, Fremantle, p. 103.

Jöns, N., Schenk, V., Appel, P., Razakamanana, T., 2006. Two-stage metamorphic evolution of the Bemarivo Belt of northern Madagascar: constraints from reaction textures and in situ monazite dating. Journal of Metamophic Geology 24, 329-347.

Jöns, N., Schenk, V., John, T., Razakamanana, T., 2005b. Relics of the Mozambique Ocean: geochemistry of the Vohibory Block (Madagascar), in: Wingate, M.T.D., Pisarevsky, S.A. (Eds.), Supercontinents and Earth Evolution. Geological Society of Australia, Abstracts, No. 81, Fremantle, p. 133.

Kazmin, V., Berhe, S., 1978. Geology and development of the Nazareth area. Ethiopian Institute of Geological Survey, Addis Ababa, Ethiopia.

Kebede, T., Kloetzli, U., Koeberl, C., 2001a. U/Pb and Pb/Pb zircon ages from granitoid rocks of Wallagga area: constraints on magmatic and tectonic evolution of Precambrian rocks of western Ethiopia. Mineralogy and Petrology 71, 251-271.

Kebede, T., Koeberl, C., 2003. Petrogenesis of A-type granitoids from the Wallagga area, western Ethiopia: constraints from mineralogy, bulk-rock chemistry, Nd and Sr isotopic compositions. Precambrian

Research 121, 1-24.

Kebede, T., Koeberl, C., Koller, F., 1999. Geology, geochemistry and petrogenesis of intrusive rocks of the Wallagga area, western Ethiopia. Journal of African Earth Sciences 29, 715-734.

Kebede, T., Koeberl, C., Koller, F., 2001b. Magmatic evolution of the Suqii-Wagga garnet-bearing two-mica granite, Wallagga area, western Ethiopia. Journal of African Earth Sciences 32, 193-221.

Kröner, A., Linnebacher, P., Stern, R., Reischmann, T., Manton, W., Hussein, I., 1991. Evolution of Pan-African island arc assemblages in the southern Red Sea Hills, Sudan, and in southwestern Arabia as exemplified by geochemistry and geochronology. Precambrian Research 53, 99-118.

Küster, D., Liégeois, 2001. Sr, Nd isotopes and geochemistry of the Bayuda Desert high-grade metamorphic basement (Sudan): an early Pan-African oceanic convergent margin, not the edge of the East Saharan ghost craton? Precambrian Research 109, 1-23.

Küster, D., Utke, A., Leupolt, L., Lenoir, J.L., Haider, A., 1990. Pan-African Granitoid Magmatism in northeastern and southern Somalia. Berliner Geowissenschaftliche Abhandlungen 120, 519-536.

Lenoir, J.-L., Küster, D., Liégeois, J.-P., Utke, A., Haider, A., Matheis, G., 1994. Origin and regional significance of late Precambrian and early Palaeozoic granitoids in the Pan-African belt of Somalia. Geologische Rundschau 83, 624-641.

Ludwig, W., Strunk, O., Westram, R., Richter, L., Meier, H., Buchner, A., Lai, T., Steppi, S., Jobb, G., Förster, W., 2004. ARB: a software environment for sequence data. Nucleic acids research 32, 1363-1371.

Lundmark, A.M., Andresen, A., Hassan, M.A.,

Augland, L.E., Boghdady, G.Y., 2012. Repeated magmatic pulses in the East African Orogen in the Eastern Desert, Egypt: an old idea supported by new evidence. Gondwana Research 22, 227-237.

Mänttäri, I., Kigereigu, F., Huhma, H., De Kock, G., Koistinen, T., Kuosmanen, E., Lahaye, Y., Lehtonen, M., Mäkitie, H., Manninen, T., 2011. New Precambrian rock ages from Uganda, 23rd Colloquium of African Geology (CAG23), University of Johannesburg, Republic of South Africa, Abstract Volume, p. 260.

McGee, B., Collins, A.S., Trindade, R.I.F., 2014a. Age and Provenance of the Cyrogenian to Cambrian passive margin to foreland basin sequence of the northern Paraguay Belt, Brazil. Geological Society of America, Bulletin in press.

McGee, B., Collins, A.S., Trindade, R.I.F., Jourdan, F., 2014b. Tracking glaciation, orogenic exhumation and foreland basin evolution: Sedimentology and 40Ar/39Ar detrital muscovite provenance in the Paraguay Belt, Brazil. Sedimentology in press.

Meert, J., Torsvik, T.H., Eide, E.A., Nédélec, A., 1997. A paleomagnetic review of Gondwana assembly including preliminary paleomagnetic results from Madagascar, in: Cox, R., Ashwal, L.D. (Eds.), Proceedings of the UNESCO-IUGS-IGCP 348/368 International Field Workshop on Proterozoic Geology of Madagascar, 5 ed, p. 52.

Meert, J.G., 2003. A synopsis of events related to the assembly of eastern Gondwana. Tectonophysics 362, 1-40.

Meert, J.G., Lieberman, B.S., 2008. The Neoproterozoic assembly of Gondwana and its relationship to the Ediacaran–Cambrian radiation. Gondwana Research 14, 5-21.

Merdith, A.S., Collins, A.S., Williams, S.E., Pisarevsky, S., Foden, J.F., Archibald, D.A.,

Blades, M.L., Alessio, B.L., Armistead, S., Plavsa, D., Clark, C., D.R, M., 2017. A Full PLate Global Reconstruction of the Neoproterzoic Gondwana Research.

Mogessie, A., Belete, K., Hoinkes, G., 2000. Yubdo-Tulu Dimtu mafic-ultramafic belt, Alaskan-type intrusions in western Ethiopia: Its implication to the Arabian-Nubian Shield and tectonics of the Mozambique Belt. Journal of African Earth Sciences 30, 62.

Muhongo, S., 1994. Neoproterozoic Collision Tectonics In the Mozambique Belt Of East- Africa - Evidence From the Uluguru Mountains, Tanzania. Journal Of African Earth Sciences 19, 153-168.

Muhongo, S., Kröner, A., Nemchin, A., 2001. Single zircon evaporation and SHRIMP ages for granulite-facies rocks in the Mozambique belt of Tanzania. The Journal of Geology 109, 171-189.

Payne, J.L., Pearson, N.J., Grant, K., Halverson, G.P., 2013. Reassessment of relative oxide formation rates and molecular interferences on in-situ Lutetium-Hafnium analysis with Laser Ablation MC-ICP-MS. . Journal of Analytical Atomic Spectrometry 28, 1068-1079.

Pease, V., Shalaby, E., Axelsson, E., Whitehouse, M., Om, M., 2010. Neoproterozoic Wadi Nabi intrusive complex, Central Eastern Desert. Saudi Geological Survey, Technical Report SGS-TR-2010 2, 56-60.

Pisarevsky, S.A., Murphy, J.B., Cawood, P.A., Collins, A.S., 2008. Late Neoproterozoic and Early Cambrian palaeogeography: models and problems. Geological Society, London, Special Publications 294, 9-31.

Reddy, S.M., Collins, A.S., Mruma, A., 2003. Complex high-strain deformation in the Usagaran Orogen, Tanzania: structural setting of Palaeoproterozoic eclogites. Tectonophysics 375, 101-123.

Robinson, F., Foden, J., Collins, A., 2015.

Geochemical and isotopic constraints on island arc, synorogenic, post-orogenic and anorogenic granitoids in the Arabian Shield, Saudi Arabia. Lithos 220, 97-115.

Robinson, F., Foden, J., Collins, A., Payne, J., 2014. Arabian Shield magmatic cycles and their relationship with Gondwana assembly: Insights from zircon U–Pb and Hf isotopes. Earth and Planetary Science Letters 408, 207-225.

Robinson, F.A., Bonin, B., Pease, V., Anderson, J., 2017. A discussion on the tectonic implications of Ediacaran late-to post-orogenic A-type granite in the northeastern Arabian Shield, Saudi Arabia. Tectonics 36, 582-600.

Scherer, E., Münker, C., Mezger, K., 2001. Calibration of the lutetium-hafnium clock. Science 293, 683-687.

Schoene, B., 2014. 4.10-U–Th–Pb Geochronology. Treatise on Geochemistry 4, 341-378.

Shackleton, R., 1996. The final collision zone between East and West Gondwana: where is it? Journal of African Earth Sciences 23, 271-287.

Shalaby, A., Stüwe, K., Makroum, F., Fritz, H., Kebede, T., Klötzli, U., 2005. The Wadi Mubarak belt, Eastern Desert of Egypt: a Neoproterozoic conjugate shear system in the Arabian–Nubian Shield. Precambrian Research 136, 27-50.

Sláma, J., Kosler, J., Condon, D.J., Crowley, J.L., Gerdes, A., Hanchar, J.M., Horstwood, M.S.A., Morris, G.A., Nasdala, L., Norberg, N., Schaltegger, U., Schoene, B., Tubrett, M.N., Whitehouse, M.J., 2008. Plesovice zircon - A new natural reference material for U-Pb and Hf isotopic microanalysis. . Chemical Geology 249, 1-35.

Stern, R.J., 1994. Arc-Assembly and Continental Collision in the Neoproterozoic African Orogen: Implications for the Consolidation of Gondwanaland. Annual Review of Earth and Planetary Sciences 22, 319-351.

Stern, R.J., 2002. Crustal evolution in the East African Orogen: a neodymium isotopic perspective. Journal of African Earth Sciences 34, 109-117.

Swanson-Hysell, N.L., Maloof, A.C., Condon, D.J., Jenkin, G.R., Alene, M., Tremblay, M.M., Tesema, T., Rooney, A.D., Haileab, B., 2015. Stratigraphy and geochronology of the Tambien Group, Ethiopia: Evidence for globally synchronous carbon isotope change in the Neoproterozoic. Geology 43, 323-326.

Tadesse, G., Allen, A., 2004. Geochemistry of metavolcanics from the Neoproterozoic Tuludimtu orogenic belt, Western Ethiopia. Journal of African Earth Sciences 39, 177-185.

Tadesse, G., Allen, A., 2005. Geology and geochemistry of the Neoproterozoic Tuludimtu Ophiolite suite, western Ethiopia. Journal of African Earth Sciences 41, 192-211.

Teklay, M., Haile, T., Kröner, A., Asmerom, Y., Watson, J., 2003. A back-arc palaeotectonic setting for the Augaro Neoproterozoic magmatic rocks of western Eritrea. Gondwana Research 6, 629-640.

Teklay, M., Kröner, A., Mezger, K., Oberhänsli, R., 1998a. Geochemistry, Pb-Pb single zircon ages and Nd-Sr isotope composition of Precambrian rocks from southern and eastern Ethiopia: implications for crustal evolution in East Africa. Journal of African Earth Sciences 26, 207-227.

Teklay, M., Kröner, A., Mezger, K., Oberhänsli, R., 1998b. Geochemistry, Pb-Pb single zircon ages and Nd-Sr isotope composition of Precambrian rocks from southern and eastern Ethiopia: implications for crustal evolution in East Africa. Journal of African

Earth Sciences 26, 207-227.

Tenczer, V., Hauzenberger, C., Fritz, H., Hoinkes, G., Muhongo, S., Klötzli, U., 2012. Crustal age domains and metamorphic reworking of the deep crust in Northern-Central Tanzania: a U/Pb zircon and monazite age study. Mineralogy and Petrology.

Trindade, R.I., D'Agrella-Filho, M.S., Epof, I., Brito Neves, B.B., 2006. Paleomagnetism of Early Cambrian Itabaiana mafic dikes (NE Brazil) and the final assembly of Gondwana. Earth and Planetary Science Letters 244, 361-377.

Vail, J.R., 1983. Pan-African crustal accretion in north-east Africa. Journal of African Earth Sciences (1983) 1, 285-294.

Westerhof, A., Haermae, P., Isabirye, E., Katto, E., Koistinen, T., Kuosmanen, E., Lehto, T., Lehtonen, M., Maekitie, H., Manninen, T., 2014. Geology and geodynamic development of Uganda with explanation of the 1: 1,000,000: scale geological map. Geol Surv Finland, Special Paper 55.

Woldemichael, B.W., Kimura, J.-I., 2008. Petrogenesis of the Neoproterozoic Bikilal-Ghimbi gabbro, Western Ethiopia. Journal of mineralogical and petrological sciences 103, 23-46.

Woldemichael, B.W., Kimura, J.-I., Dunkley, D.J., Tani, K., Ohira, H., 2010. SHRIMP U–Pb zircon geochronology and Sr–Nd isotopic systematic of the Neoproterozoic Ghimbi-Nedjo mafic to intermediate intrusions of Western Ethiopia: a record of passive margin magmatism at 855 Ma? International Journal of Earth Sciences 99, 1773-1790.

Woodhead, J.D., Hergt, J.M., Shelley, M., Eggins, S., Kemp, R., 2004. Zircon Hf-isotope analysis with an Excimer laser, depth profiling, ablation of complex geometries, and concomitant age estimation. . Chemical

Geology 209, 121-135.

Yeshanew, F.G., Pease, V., Abdelsalam, M.G., Whitehouse, M.J., 2016. Zircon U–Pb ages, $\delta^{18}O$ and whole-rock Nd isotopic compositions of the Dire Dawa Precambrian basement, eastern Ethiopia: implications for the assembly of Gondwana. Journal of the Geological Society, jgs2016-2017.

Yibas, B., Reimold, W., Anhaeusser, C., Koeberl, C., 2003a. Geochemistry of the mafic rocks of the ophiolitic fold and thrust belts of southern Ethiopia: constraints on the tectonic regime during the Neoproterozoic (900–700 Ma). Precambrian Research 121, 157-183.

Yibas, B., Reimold, W.U., Anhaeusser, C.R., Koeberl, C., 2003b. Geochemistry of the mafic rocks of the ophiolitic fold and thrust belts of southern Ethiopia: constraints on the tectonic regime during the Neoproterozoic (900-700 Ma). Precambrian Research 121, 157-183.

Yibas, B., Reimold, W.U., Armstrong, R., Koeberl, C., Anhaeusser, C.R., Phillips, D., 2002. The tectonostratigraphy, granitoid geochronology and geological evolution of the Precambrian of southern Ethiopia. Journal Of African Earth Sciences 34, 57-84.

Appel, P.W.U., Schenk, V., Schumann, A., 2004. P-T conditions and metamorphic ages of pelitic schists at Murchison Falls (NW Uganda): evidence for a Pan-African event within the cratonic crust of Uganda, 20th Colloquium of African Geology. BRGM, Orléans, France, p. 49.

Ayalew, T., Bell, K., Moore, J.M., Parrish, R.R., 1990. U-Pb and Rb-Sr geochronology of the western Ethiopian shield. Geological Society of America Bulletin 102, 1309-1316.

Ayalew, T., Peccerillo, A., 1998. Petrology and geochemistry of the Gore-Gambella

plutonic rocks: implications for magma genesis and the tectonic setting of the Pan-African Orogenic Belt of western Ethiopia. Journal of African Earth Sciences 27, 397-416.

Blades, M.L., Collins, A.S., Foden, J., Payne, J.L., Xu, X., Alemu, T., Woldetinsae, G., Clark, C., Taylor, R.J., 2015. Age and hafnium isotopic evolution of the Didesa and Kemashi Domains, western Ethiopia. Precambrian Research 270, 267-284.

Fritz, H., Abdelsalam, M., Ali, K.A., Bingen, B., Collins, A.S., Fowler, A.R., Ghebreab, W., Hauzenberger, C.A., Johnson, P.R., Kusky, T.M., Macey, P., Muhongo, S., Stern, R.J., Viola, G., 2013. Orogen styles in the East African Orogen: A review of the Neoproterozoic to Cambrian tectonic evolution. Journal of African Earth Sciences.

Johnson, P., Andresen, A., Collins, A.S., Fowler, A., Fritz, H., Ghebreab, W., Kusky, T., Stern, R., 2011. Late Cryogenian–Ediacaran history of the Arabian–Nubian Shield: A review of depositional, plutonic, structural, and tectonic events in the closing stages of the northern East African Orogen. Journal of African Earth Sciences 61, 167-232.

Johnson, P.R., 2014. An Expanding Arabian-Nubian Shield Geochronologic and Isotopic Dataset: Defining Limits and Confirming the Tectonic Setting of a Neoproterozoic Accretionary Orogen. Open Geology Journal 8, 3-33.

Johnson, P.R., Woldehaimanot, B., 2003. Development of the Arabian-Nubian Shield: perspectives on accretion and deformation in the northern East African Orogen and the assembly of Gondwana, in: Yoshida, M., Windley, B.F., Dasgupta, S. (Eds.), Proterozoic East Gondwana: Supercontinent Assembly and Breakup. Geological Society, London, Special Publication 206, pp. 289-

325.

Johnson, T.E., Ayalew, T., Mogessie, A., Kruger, F.J., Poujol, M., 2004. Constraints on the tectonometamorphic evolution of the Western Ethiopian Shield. Precambrian Research 133, 305-327.

Kebede, T., Kloetzli, U., Koeberl, C., 2001a. U/Pb and Pb/Pb zircon ages from granitoid rocks of Wallagga area: constraints on magmatic and tectonic evolution of Precambrian rocks of western Ethiopia. Mineralogy and Petrology 71, 251-271.

Kebede, T., Koeberl, C., 2003. Petrogenesis of A-type granitoids from the Wallagga area, western Ethiopia: constraints from mineralogy, bulk-rock chemistry, Nd and Sr isotopic compositions. Precambrian Research 121, 1-24.

Kebede, T., Koeberl, C., Koller, F., 2001b. Magmatic evolution of the Suqii-Wagga garnet-bearing two-mica granite, Wallagga area, western Ethiopia. Journal of African Earth Sciences 32, 193-221.

Leggo, P.M., 1974. A geochronological study of the basement complex of Uganda. Journal of the Geological Society, London 130, 263-277.

Mänttäri, I., Kigereigu, F., Huhma, H., De Kock, G., Koistinen, T., Kuosmanen, E., Lahaye, Y., Lehtonen, M., Mäkitie, H., Manninen, T., 2011. New Precambrian rock ages from Uganda, 23rd Colloquium of African Geology (CAG23), University of Johannesburg, Republic of South Africa, Abstract Volume, p. 260.

Stern, R., Ali, K.A., Abdelsalam, M.G., Wilde, S.A., Zhou, Q., 2012. U–Pb zircon geochronology of the eastern part of the Southern Ethiopian Shield. Precambrian Research 206, 159-167.

Westerhof, A., Haermae, P., Isabirye, E., Katto, E., Koistinen, T., Kuosmanen, E., Lehto, T., Lehtonen, M., Maekitie, H., Manninen,

T., 2014. Geology and geodynamic development of Uganda with explanation of the 1: 1,000,000: scale geological map. Geol Surv Finland, Special Paper 55.

Yeshanew, F.G., Pease, V., Abdelsalam, M.G., Whitehouse, M.J., 2016. Zircon U–Pb ages, $\delta^{18}O$ and whole-rock Nd isotopic compositions of the Dire Dawa Precambrian basement, eastern Ethiopia: implications for the assembly of Gondwana. Journal of the Geological Society, jgs2016-2017.

Yibas, B., Reimold, W., Anhaeusser, C., Koeberl, C., 2003. Geochemistry of the mafic rocks of the ophiolitic fold and thrust belts of southern Ethiopia: constraints on the tectonic regime during the Neoproterozoic (900–700 Ma). Precambrian Research 121, 157-183.

Yibas, B., Reimold, W.U., Armstrong, R., Koeberl, C., Anhaeusser, C.R., Phillips, D., 2002. The tectonostratigraphy, granitoid geochronology and geological evolution of the Precambrian of southern Ethiopia. Journal Of African Earth Sciences 34, 57-84.

Yihunie, T., 2002. Pan-African deformations in the basement of the Negele area, southern Ethiopia. International Journal of Earth Sciences 91, 922-933.

CHAPTER 3

Statement of Authorship

Title of Paper	The Origin of Ultramafic rocks of the Tulu Dimtu Belt, western Ethiopia – Do they represent remnants of the Mozambique Ocean?
Publication Status	☐ Published ☑ Accepted for Publication ☐ Submitted for Publication ☐ Unpublished and Unsubmitted work written in manuscript style
Publication Details	Blades, M. L., Foden, J., Collins, A. S., Alemu, T., Woldetinsae, G. The Origin of Ultramafic rocks of the Tulu Dimtu Belt, western Ethiopia – Do they represent remnants of the Mozambique Ocean? Geological Magazine (In press).

Principal Author

Name of Principal Author (Candidate)	Morgan Blades		
Contribution to the Paper	Project fieldwork, sample preparation, data collection, processing and interpretation, manuscript design and composition, creation of figures		
Overall percentage (%)	80		
Certification:	This paper reports on original research I conducted during the period of my Higher Degree by Research candidature and is not subject to any obligations or contractual agreements with a third party that would constrain its inclusion in this thesis. I am the primary author of this paper.		
Signature		Date	06/09/2017

Co-Author Contributions

By signing the Statement of Authorship, each author certifies that:

i. the candidate's stated contribution to the publication is accurate (as detailed above);

ii. permission is granted for the candidate in include the publication in the thesis; and

iii. the sum of all co-author contributions is equal to 100% less the candidate's stated contribution.

Name of Co-Author	Professor Alan Collins		
Contribution to the Paper	Guidance in fieldwork, sample preparation, data interpretation and manuscript review.		
Signature		Date	06/09/2017

Name of Co-Author	Emeritus Professor John Foden		
Contribution to the Paper	Guidance in fieldwork, sample preparation, data interpretation and manuscript review.		
Signature		Date	06/09/2017

Name of Co-Author	Tadesse Alemu
Contribution to the Paper	Guidance in the field and logistics in Ethiopia

Signature		Date	06/09/2017

Name of Co-Author	Dr Girma Woldetinsae
Contribution to the Paper	Guidance in the field and logistics in Ethiopia

Signature		Date	06/09/2017

Please cut and paste additional co-author panels here as required.

ABSTRACT

The East African Orogen (EAO) contains a series of high strain zones that formed as Gondwana amalgamated. The Tulu Dimtu shear belt is one of these N–S structures within the Barka–Tulu Dimtu zone in western Ethiopia, and contains ultramafic bodies of equivocal origin. Identifying the petrogenetic origin of these enigmatic rocks provides evidence for the geodynamic significance of these shear zones. Due to their altered state, these ultramafic rock's well-preserved chrome spinels provide the only reliable evidence for their source and tectonic affiliation. Chrome spinels have high Cr_2O_3 (30.04 wt % - 68.76 wt %), while recalculated Fe_2O_3 (<2%) and TiO_2 (0.01-0.51%) values are low. The Cr# (molar $Cr^{3+}/Cr^{3+}+Al^{2+}$) and Mg# ($Mg^{2+}/Mg^{2+}+Fe^{2+}$) have averages of 0.88 and 0.22 respectively. Based on olivine-spinel equilibria, the calculated fO_2 values (FMQ +3.03) for the dunites, reveal a highly oxidised environment. This spinel chemistry (high Cr#>0.6 and low–Ti) supports a supra subduction origin, with an oxidised mantle source more refractory than depleted MORB mantle (DMM). These spinel compositions indicate that some ultramafic bodies in western Ethiopia, including those from Daleti, Tulu and Dimtu, are serpentinised peridotites emplaced as obducted ophiolite complexes. By contrast, the ultramafic rocks from the Yubdo locality have a different spinel chemistry, with strong affiliation with igneous spinels formed in Alaskan-style mafic intrusions. These collective results suggest that regardless of their origin as supra-subduction ophiolites or as Alaskan-type intrusions, these spinels were formed on a convergent-subduction margin.

INTRODUCTION

Ultramafic and mafic complexes are seen in shear zones throughout the East African Orogen (Kazmin, 1976; Berhe, 1990; Stern, 1994b; Abdelsalam and Stern, 1996; Helmy and Mogessie, 2001; Helmy and El Mahallawi, 2003; Stern et al., 2004; Stern, 2005; Farahat and Helmy, 2006; El-Rahman et al., 2012; Helmy et al., 2014; Helmy et al., 2015; Abdel-Karim et al., 2016). These shear zones provide a record of the amalgamation of central Gondwana. The Western Ethiopian Shield (WES) lies in an important position within the East African Orogen, between the predominately gneissic Mozambique Belt in the south, and the greenschist-facies volcanic-arc complexes of the Arabian Nubian Shield in the north and east. Within the WES, the Kemashi Domain is characterised by a sequence of metasedimentary rocks, interlayered with abundant mafic to ultramafic material. The ultramafic/mafic plutonic rocks within the Kemashi Domain were initially interpreted to represent an ophiolite sequence (Berhe, 1990; Tadesse and Allen, 2004; Tadesse and Allen, 2005); however, others have suggested that there is a lack of geochemical evidence to support the presence of ophiolites in the Western Ethiopian Shield (Mogessie et al., 2000; Braathen et al., 2001; Grenne et al., 2003).

The composition of spinel is both useful as a petrogenetic recorder of mafic magma evolution, and as a discriminator of the geotectonic source of mafic to ultramafic rocks (Irvine, 1965; Irvine, 1967; Dick and Bullen, 1984a). Spinel crystallises over a wide range of conditions from mafic and ultramafic magmas and Cr-rich spinel is the liquidus phase of a broad range of mafic magmas over wide pressure ranges. Spinel is relatively refractory and resistant to alteration, particularly when compared to other high temperature igneous silicates such as olivine, making it particularly

useful as a source indicator in altered rocks. A large database of spinel compositions from a wide range of mafic and ultramafic rock types is available from the published literature (Barnes and Roeder, 2001), providing a sound comparative discrimination tool to establish the tectonic setting of mafic and ultramafic rocks (Kamenetsky et al., 2001).

Microprobe data from chrome spinels, as well as from rare relict fresh olivine, are used here to test the two main theories for the formation of the WES ultramafic complexes; either that the complexes are oceanic ophiolites, remnants of the Mozambique Ocean, or that they form in a supra subduction environment as Alaskan-type ultramafic to mafic intrusions. These data help to further constrain and understand the enigmatic Kemashi Domain as well as further develop the tectonic model for the Neoproterozoic evolution of the WES.

THE ULTRAMAFIC QUANDARY

A significant aspect of the Arabian-Nubian Shield is the recognition of the N-S oriented regional shear zones. The Baruda-Tulu Dimtu zone stretches through Ethiopia and connects with the Barka zone in Eritrea (Stern, 1994a; Braathen et al., 2001; Tadesse and Allen, 2004; Tadesse and Allen, 2005). These regional shear-zones have often been interpreted as ophiolite decorated sutures, representing the major boundaries that separate arc terranes that accreted during amalgamation of eastern and western Gondwana (Stern, 1994a; Tadesse and Allen, 2004; Tadesse and Allen, 2005). Braathen et al. (2001) questioned this interpretation, and pointed out that the components essential to the identification of ophiolites such as, tectonised mantle harzburgite, sheeted dyke complexes, or basaltic pillow lavas with associated pelagic sediments, had not been recognised in Ethiopia (de Wit and Aguma, 1977; Braathen et al., 2001; Alemu and Abebe,

2002; Allen and Tadesse, 2003; Grenne et al., 2003; Woldemichael and Kimura, 2008; Woldemichael et al., 2010). Alternatively, Braathen et al. (2001) proposed that the zoned mafic and ultramafic as well as isolated bodies along the shear zone, were originally intruded as magma chambers preserving mafic and ultramafic cumulate layering equivalent to so-called 'Alaskan-Type intrusions' (Mogessie, Belete and Hoinkes, 2000). These intrusions were interpreted to be a result of limited dilation of back-arc basins without the development of extended oceanic crust (Braathen et al., 2001; Grenne et al., 2003). This paper outlines the application of chrome spinel compositions to test the two main theories for the formation of the WES ultramafic complexes; either that the complexes are structurally emplaced ophiolite sheets, remnants of the Mozambique Ocean or that they formed as Alaskan-type mafic intrusions above subduction zones.

Alaskan-type intrusions

Alaskan-type zoned mafic-ultramafic complexes are characterized by a concentric arrangement of rock types including dunite, pyroxenite, hornblendite and gabbro. Examples of these complexes have been described from Alaska, the Urals of Russia, eastern Australia, British Columbia, and Columbia, as well as the Eastern Desert of Egypt (Dick and Bullen, 1984a; Himmelberg and Loney, 1995; Barnes and Roeder, 2001; Helmy and Mogessie, 2001; Helmy and El Mahallawi, 2003; Farahat and Helmy, 2006). Alaskan-type intrusions are small (ranging from a few meters, up to ~10 km) in size, elliptical or rounded in shape and located along crustal lineaments. Alaskan-type intrusions are distinguished by; 1) the gradation from dunite to gabbros, 2) Fe^{3+} - Ti-rich spinels, 3) depletion of CaO in olivine, and 5) evidence of crystal accumulation such as scarce graded layers (Dick and Bullen,

1984a; Himmelberg and Loney, 1995; Helmy and Mogessie, 2001; Helmy and El Mahallawi, 2003; Farahat and Helmy, 2006). The chemical composition of chromium spinel, in particular its elevated Fe_2O_3 content, is another typical feature of Alaskan-type intrusions (Irvine, 1967; Findlay, 1969; Taylor Jr and Noble, 1969; Himmelberg et al., 1986; Himmelberg and Loney, 1995; Chashchukhin et al., 2002; Krause et al., 2007). This has been ascribed to high total iron contents in the parental melt (Taylor Jr and Noble, 1969), fractionation of olivine and clinopyroxene (Findlay, 1969; Krause, Brügmann and Pushkarev, 2007) or an elevated oxygen fugacity (Himmelberg and Loney, 1995; Chashchukhin et al., 2002). Alaskan-type intrusions are confined to subduction-related magmatic arcs (deBari and Coleman, 1989; Himmelberg and Loney, 1995; Krause, Brügmann and Pushkarev, 2007; Helmy et al., 2014)

Ophiolites

Although the basic definition has evolved somewhat in recent years (Dilek and Furnes, 2014), the classical definition of an ophiolite is that of a stratified complex of mafic and ultramafic rocks emplaced by over thrusting (obduction) onto the passive margin of an ocean in the process of closure, as a result of subduction. The ensemble of mafic and ultra-mafic igneous rocks are formed by magmatic processes at a mid ocean ridge and/or beneath an oceanic volcanic arc. Although the latter supra-subduction type is probably most common, the numerous examples of ophiolite complexes that adorn the closed Tethyan suture illustrate that many have combined supra-subduction and mid ocean ridge characteristics (Dilek and Furnes, 2011; Whattam and Stern, 2011).

Many studies have shown that peridotites in Mid Oceanic Ridge ophiolite complexes have chromite with Cr# of < 0.70 (Dick and Sinton, 1979; Dick and Bullen, 1984b; Stern et al., 2004) whereas supra-subduction peridotites have Cr# values > 75 (Pearce et al., 1984; Augé, 1987; Ahmed and Arai, 2002; Arai et al., 2004; Stern et al., 2004; Abdel-Karim et al., 2016).

The Samail ophiolite in Oman is an example of a complex with both mid ocean ridge and supra-subduction components. Dunites from the northern mantle section of this complex have spinels with Cr# < 0.6 (Le Mée et al., 2004), similar to those of a fast spreading ridge (Niu and Hekinian, 1997; Arai et al., 2011). By contrast from peridotite in the more southern part of the same ophiolite, Tamura and Arai (2006) reported spinels with supra subduction affinity with Cr# >0.6 and from discordant dunites spinel with Cr# ranging from 0.4 – 0.8 and TiO_2 < 0.3 wt% (Arai et al., 2006). Ophiolitic peridotites that have spinel Cr# that exceed 0.55 and low TiO_2 values (< 0.3), suggest derivation from highly depleted mantle peridotite. They imply mantle source depletion due to partial melting and melt extraction beyond the exhaustion of clinopyroxene, leaving a harzburgite residue. This extensive melting is attributed to the role of hydrous subduction-derived fluids (Dick and Bullen, 1984a). Many Tethyan ophiolite complexes, including the Semail ophiolite in Oman, have complex histories whereby initially oceanic upper mantle ophiolite have a supra-subduction history imposed prior to obduction onto the adjacent continental passive margin. As in the Semail ophiolite (Shervais, 2001) this may lead to a complex spinel geochemical record. (Leblanc and Nicolas, 1992; Zhou and Bai, 1992; Zhou et al., 1994; Zhou and Robinson, 1997; Proenza et al., 1999; Rollinson, 2008; Uysal et al., 2009; Escayola et al., 2011).
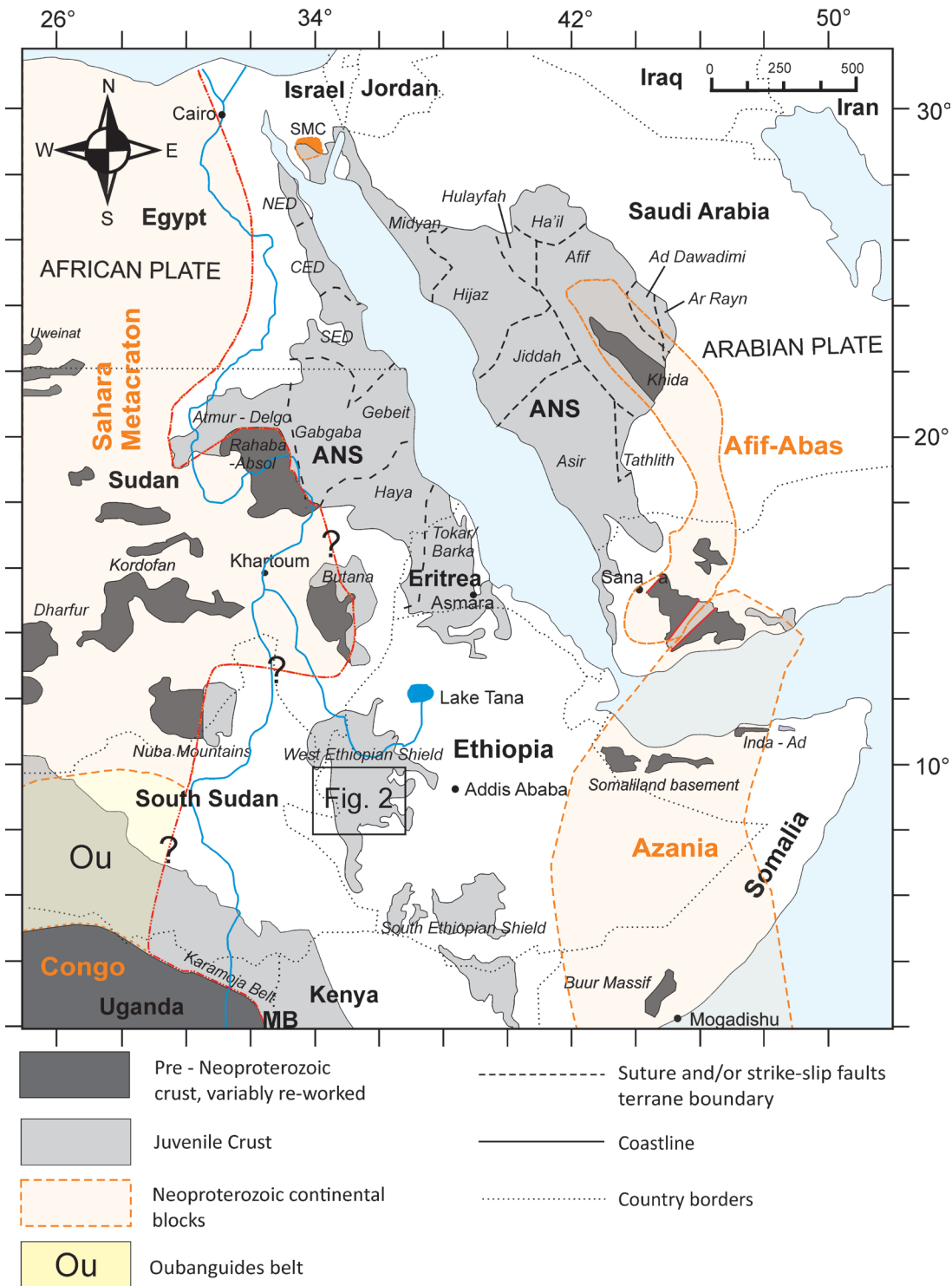
Figure 1: Location map and distribution of crustal domains in the East African Orogen. SM, Sahara Metacraton; ANS, Arabian Nubian Shield. MB, Mozambique Belt. The black box represents the map area in figure 2. Adapted from Johnson et al. (2011) and Blades et al. (2015).

GEOLOGICAL BACKGROUND

The East African Orogen (EAO) is the world's largest Neoproterozoic to Cambrian orogenic belt. It preserves a complex history of intra-oceanic and continental margin, magmatic and tectonothermal events. Traditionally, the East African Orogen is divided into the Arabian Nubian Shield (ANS) in the north, composed of
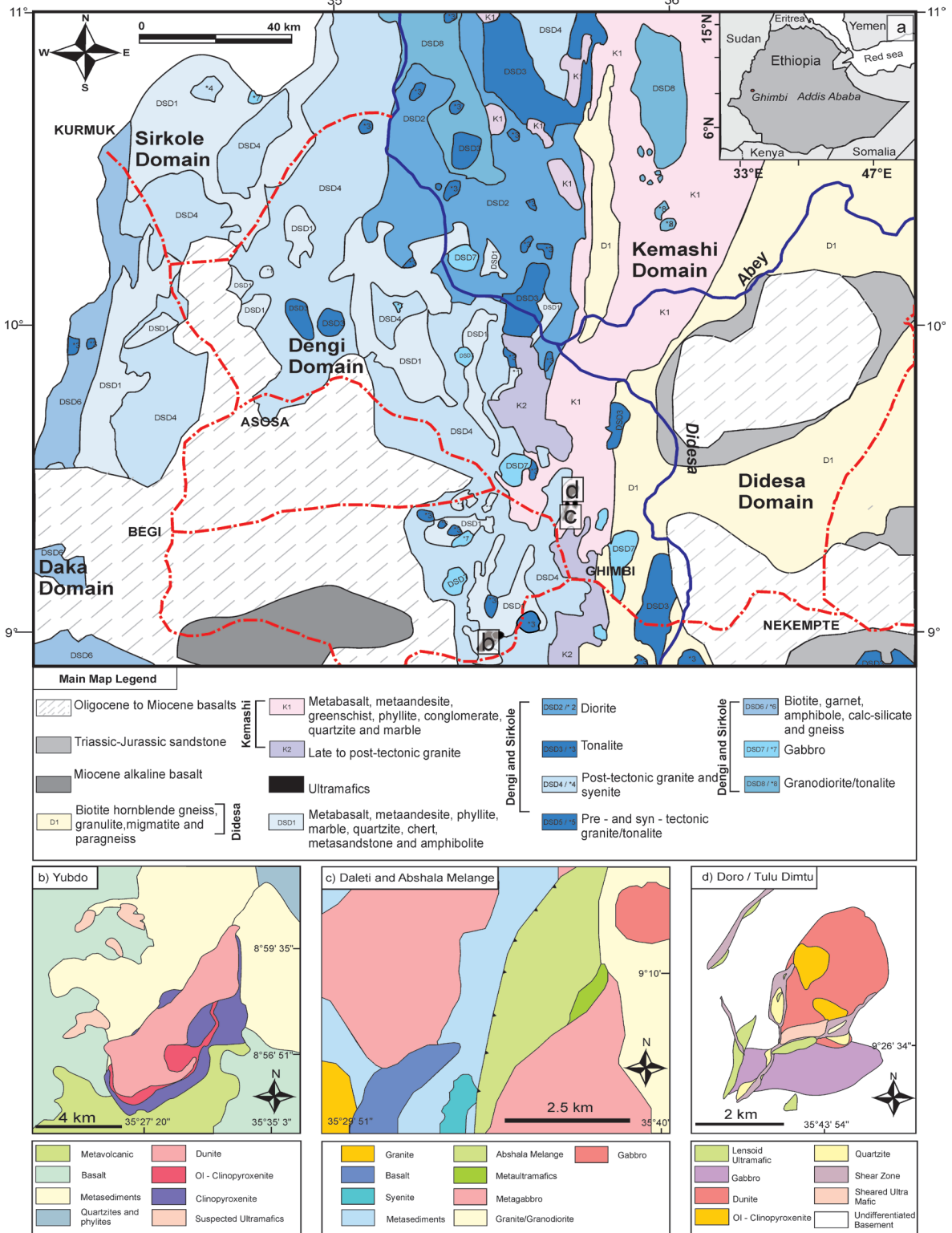
Figure 1: Simplified geological maps of the study regions. a) Simplified geological map of the area of study in western Ethiopia. Adapted from geological map of western Ethiopia (2nd edition), scale 1:2 000,000, published by the Geological Survey (1996) and Blades et al. (2015). b – d) Simplified geological maps of b) Yubdo, c) Daleti d) Tulu Dimtu respectively. Adapted from geological maps from an unpublished thesis (Jackson et al., 2006) and Alemu and Abebe (2000).

largely juvenile Neoproterozoic crust, and the Mozambique Belt (MB) in the south comprising of mostly pre-Neoproterozoic crust with a Neoproterozoic – early Cambrian overprint. Many of the rocks found in the orogen formed in volcanic arcs during the Neoproterozoic subduction of the Mozambique Ocean (Meert, 2003; Collins and Pisarevsky, 2005; Meert and Lieberman, 2008; Johnson et al., 2011; Fritz et al., 2013), which separated Neoproterozoic India from the Neoproterozoic continents that formed Gondwanan Africa (Meert, 2003; Johnson et al., 2004; Collins and Pisarevsky, 2005; Meert and Lieberman, 2008; Johnson et al., 2011; Fritz et al., 2013; Merdith et al., 2017). The Western Ethiopian Shield (Fig. 1) is situated in a key transitional location between the Arabian Nubian Shield and Mozambique Belt, adjacent to, and east of, the 'Eastern Saharan Metacraton' (Abdelsalam and Stern, 1996).

The Western Ethiopian Shield comprises high-grade gneisses, low-grade metavolcanic and meta-sedimentary rocks with associated mafic–ultramafic intrusions and syn- to post-tectonic gabbroic to granitic intrusions. In this paper we use the lithotectonic division outlined by Allen and Tadesse (2003), based on domains of shared lithological assemblages and geological histories (see Allen and Tadesse; 2003 for a summary). The area is divided into five domains, interpreted to have formed during the final closure of the Mozambique Ocean (Allen and Tadesse, 2003), these include; the Didesa, Kemashi, Dengi, Sirkole and Daka Domains (Fig. 2). The Kemashi Domain forms a narrow ~N–S strip that is 10–15 km wide (Fig. 2) and lies towards the west of the Didesa Domain (illustrated in Alemu and Abebe (2000)). Within this domain, there is a prominent expression of the regional Baruda–Tulu Dimtu shear/suture zone (Abdelsalam

and Stern, 1996), sometimes referred to as the Sekerr–Yubdo–Barka suture/shear zone (Berhe, 1990). This domain is characterised by a sequence of metasedimentary rocks, informally referred to as the Mora metasediments, made up of cherts and quartzites, interlayered with abundant mafic to ultramafic volcanic material, all metamorphosed to upper greenschist/epidote-amphibolite facies (Johnson et al., 2004). Identical lithologies exist to the west of the shear-belt, although they are generally more deformed and intercalated with tectonic slivers of metavolcanic rocks (Tefera, 1991; Braathen et al., 2001). Published geochronology data suggest three phases of magmatism at ca. 850–810 Ma, 780–700 Ma and 620–550 Ma (Ayalew et al., 1990; Ayalew and Peccerillo, 1998; Kebede et al., 1999; Kebede et al., 2001a; Kebede et al., 2001b). These have been interpreted to represent pre-, syn- and post-tectonic environments, respectively (Woldemichael and Kimura, 2008; Woldemichael et al., 2010). Recent studies have suggested that these are complicated by metamorphism/deformation occurring both at ca. 790–780 Ma and at ca. 660–655 Ma. Hafnium isotopic analysis indicates that the magmas were generated from juvenile Neoproterozoic mantle sources with little involvement of the pre-Neoproterozoic continental crust (Blades et al., 2015). Post-tectonic magmatism is recorded in the Ganjii granite (^{206}Pb/^{238}U age of 584 ± 10 Ma), constraining pervasive deformation in the Western Ethiopian Shield (Blades et al., 2015). Ultramafic/mafic plutonic rocks within the Western Ethiopian Shield, where little metamorphism and deformation have occurred, allows for the identification of primary structures (Braathen et al., 2001). These structures do not contradict an oceanic crust origin. However, others have suggested that there is a lack of geochemical evidence to

ID number	E14-10	E13-11	E14 - 19	E13 - 20	E13 - 22	E13-26
SiO_2	0.08	0.01	<0.01	0.02	0.01	0.01
TiO_2	0.38	0.01	0.01	<0.01	0.38	0.01
$Al2O_3$	9.65	1.66	6.99	10.54	10.84	5.22
Cr_2O_3	42.45	37.65	65.72	60.25	53.02	64.90
Fe_2O_3	17.56	29.15	0.00	0.00	3.54	0.00
FeO	21.65	27.57	22.71	20.72	27.44	24.67
MnO	0.52	2.76	0.34	7.90	0.57	0.54
MgO	7.40	0.60	3.85	0.36	3.65	4.40
ZnO	0.28	0.18	0.29	0.20	0.47	0.15
CaO	<0.01	0.01	0.02	<0.01	0.01	0.01
Na_2O	<0.02	0.03	0.04	<0.02	<0.02	0.04
K_2O	0.00	0.00	0.00	0.00	0.00	0.00
NiO	0.03	0.37	0.05	<0.03	0.07	0.04
Cations to 32 oxygens						
Si	0.00	0.00	0.00	0.00	0.00	0.00
Ti	0.01	0.00	0.00	0.00	0.01	0.00
Al	0.39	0.07	0.29	0.44	0.44	0.22
Cr	1.14	1.11	1.82	1.69	1.45	1.80
Fe^{3+}	0.45	0.82	0.00	0.00	0.09	0.00
Fe^{2+}	0.61	0.86	0.67	0.61	0.79	0.72
Mn^{2+}	0.02	0.09	0.01	0.24	0.02	0.02
Mg	0.37	0.03	0.20	0.02	0.19	0.23
Zn	0.01	0.01	0.01	0.01	0.01	0.00
Ca	0.00	0.00	0.00	0.00	0.00	0.00
Na	0.00	0.00	0.00	0.00	0.00	0.00
K	0.00	0.00	0.00	0.00	0.00	0.00
Ni	0.00	0.01	0.00	0.00	0.00	0.00
Mg #	0.38	0.04	0.23	0.03	0.19	0.24
Fe #	0.62	0.96	0.77	0.97	0.81	0.76
Cr #	0.58	0.55	0.86	0.79	0.73	0.89
Fe#	0.23	0.41	0.00	0.00	0.05	0.00
Avg Co-existing Ol						
Ca	0.00	0.00	-	-	-	-
Ni	0.00	0.01	-	-	-	-
Xmg (mg/(fe+mg))	0.90	0.93	-	-	-	-
Temperature (K)	1427	951	-	-	-	-
$\Delta fO_{2\ (FMQ)}$	3.03	4.81	-	-	-	-

Table 1: Representative chrome spinel and co-existing olivine microprobe analyses from ultramafic rocks of the Western Ethiopian Shield.

support the presence of ophiolites in the Western Ethiopian Shield and although the ultramafic complexes are concentrated along the Baruda-Tulu Dimtu shear belt, their existence outside this zone is has been considered problematic to an ophiolite suture model (Braathen et al., 2001). The alternate theory proposed by Braathen et al. (2001), suggested that these represent solitary intrusions, which have been tectonically modified and partly aligned along the shear-belt in response to penetrative D1 deformation. It has been suggested that they represent Alaskan-type, concentrically zoned intrusions, which were emplaced into an extensional arc or back arc environment (Mogessie, Belete and Hoinkes, 2000; Braathen et al., 2001; Grenne et al., 2003). These small elliptical bodies are common in the northern parts of the Arabian Nubian Shield in the Eastern Desert of Egypt; Gabbro Akarem (Helmy and El Mahallawi, 2003; El-Rahman et al., 2012), Genina Gharbia (Helmy et al., 2014), Abu Hamamid (Helmy et al., 2015) and Dahanib (Khedr and Arai, 2016).

ANALYTICAL METHODS
Microprobe Mineral Chemistry
The chemical compositions of the chrome spinels and olivine were determined using an Electron Microprobe Cameca SX51 at Adelaide Microscopy, the University of Adelaide. Spot analyses were conducted using a beam current of 20 nA and an accelerating voltage of 15 kV, with a defocused beam of 5 microns. Representative spinel and olivine are given in Table 1. All analyses and calculations are in Appendix 3: Tables 1–4. Calibration was made based on natural and synthetic mineral standards.

RESULTS
Petrography of Ultramafic Samples
The petrography of the ultramafic rocks from the WES was investigated using an optical microscope, with emphasis on the occurrence, relationships and textures of spinel (Fig. 3). The geology of Gimbi and accompanied geological map compiled by Alemu and Abebe (2000) was used to understand the geology of the area. Map features of each the complexes are shown in Figure 2 and were taken and adapted from an unpublished thesis from Cardiff University. (Jackson, 2006)

Daleti Quarry E13.11
(09° 09' 56.4"N, 35° 37' 30.0"E)
Daleti covers an area approximately 5 km2 and primarily consists of dunite, with no discernible concentric outcrop patterns (Fig. 2). Sample E13 - 11 was collected from the Daleti Quarry, where the exposure are dominated by serpentinised dunite, with minor intercalations of talc schist, talc carbonate schist. The chrome spinel and magnetite are seen disseminated throughout the outcrop, with pervasive serpentinite veins cross cutting the main lithology.
The Daleti dunite (Fig. 3a–b) shows extensive alteration to mesh-textured serpentine, with isolated fresh remnants of the original olivine grains. The primary mineralogy consists of olivine and Cr spinel. The chrome spinels occur as large 1–2 mm euhedral to subhedral grains (Fig. 3a-b).

Abshala Melange E14.19
(09° 23' 16 .0"N 035° 43' 15.9"E)
The Abshala Mélange is internally complex, containing rocks of disparate histories (Alemu and Abebe, 2000). It comprises tectonically mixed rock types; metabasalt/amphibolite, peridotite and quartzite/chert. This is interpreted to represent an accretionary melange at a convergent plate boundary/subduction zone (Chapter 4).
Sample E14 − 19 was taken from a serpentinised
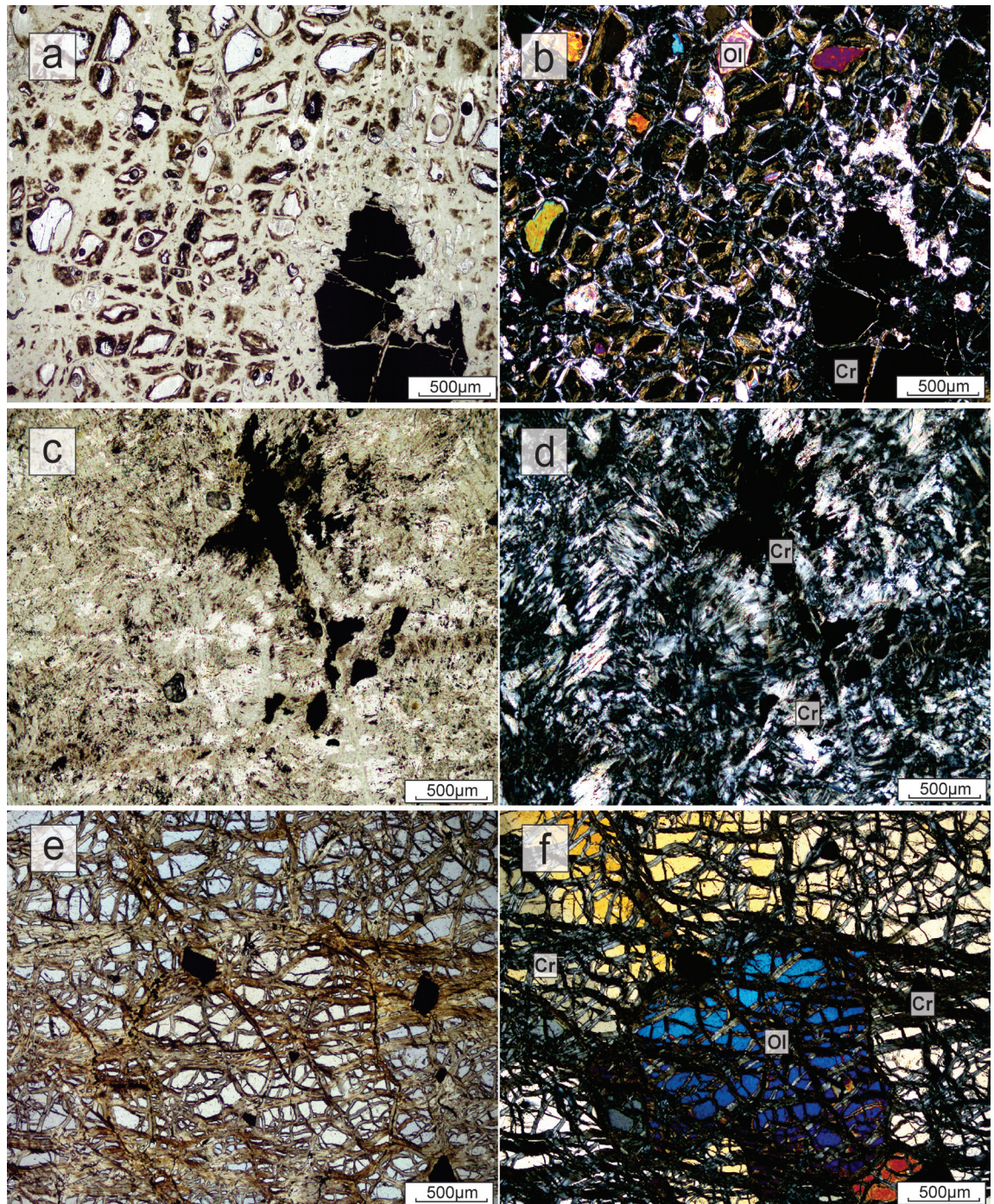
Figure 3: Thin sections of the ultramafic samples collected from the Western Ethiopian Shield (WES). a – b sections from Daleti Quarry (E13–11) a) is plane polar and b) is in cross polar. The primary mineralogy consists of olivine and Cr spinel. Extensive alteration, serpentine forms a mesh texture, resembling a fisherman's net, where the rim of the net is serpentine and the empty space in the mesh centre is occupied by fresh (relict) olivine. c–d) – representative section of Abshala melange and Tulu Dimtu Hill (E13–19, 20, 22 and 26). c) is plane polar and d) is in cross polar. These samples have been more extensively altered with no relict/fresh olivines seen within this sample. The dunite contains chrome spinels with euhedral to subhedral shapes. All silicate minerals within the sample have been altered by serpentine. e–f) – Sample was taken from Yubdo (E13–10) e) is plane polar and f) is in cross polar. The spinels are subhedral spinels and occur in serpentine filled cracks. The olivine are fresh with little evidence for serpentinisation other than in the cracks between these minerals

peridotite clast. This serpentinised sample contains euhedral and anhedral chrome spinel grains (~1mm) and no preserved relict olivine (Fig. 3c-d).

Doro Dimtu E13. 20, 22 and 26
(9° 27' 60.9"N 35° 44' 19.8"E)
There are three main intrusions in the Tulu Dimtu area: the main intrusion, sheared ultramafics and lensoid ultramafics. The lithologies of the main intrusion include dunite, olivine – clinopyroxenite and clinopyroxenite.

The sheared ultramafics are highly deformed and are found at the edge of the main intrusion. The map features show that there are multiple shear zones and these are associated with talc and chlorite with one of the shear zones enveloping quartzite bodies.

The samples were collected from a previously mapped dunite body (Jackson, 2006). However, in thin section they are extensively altered with no relict/fresh olivine. They contain chrome spinels (0.2 – 2 mm) with euhedral to subhedral shapes. All silicate minerals within
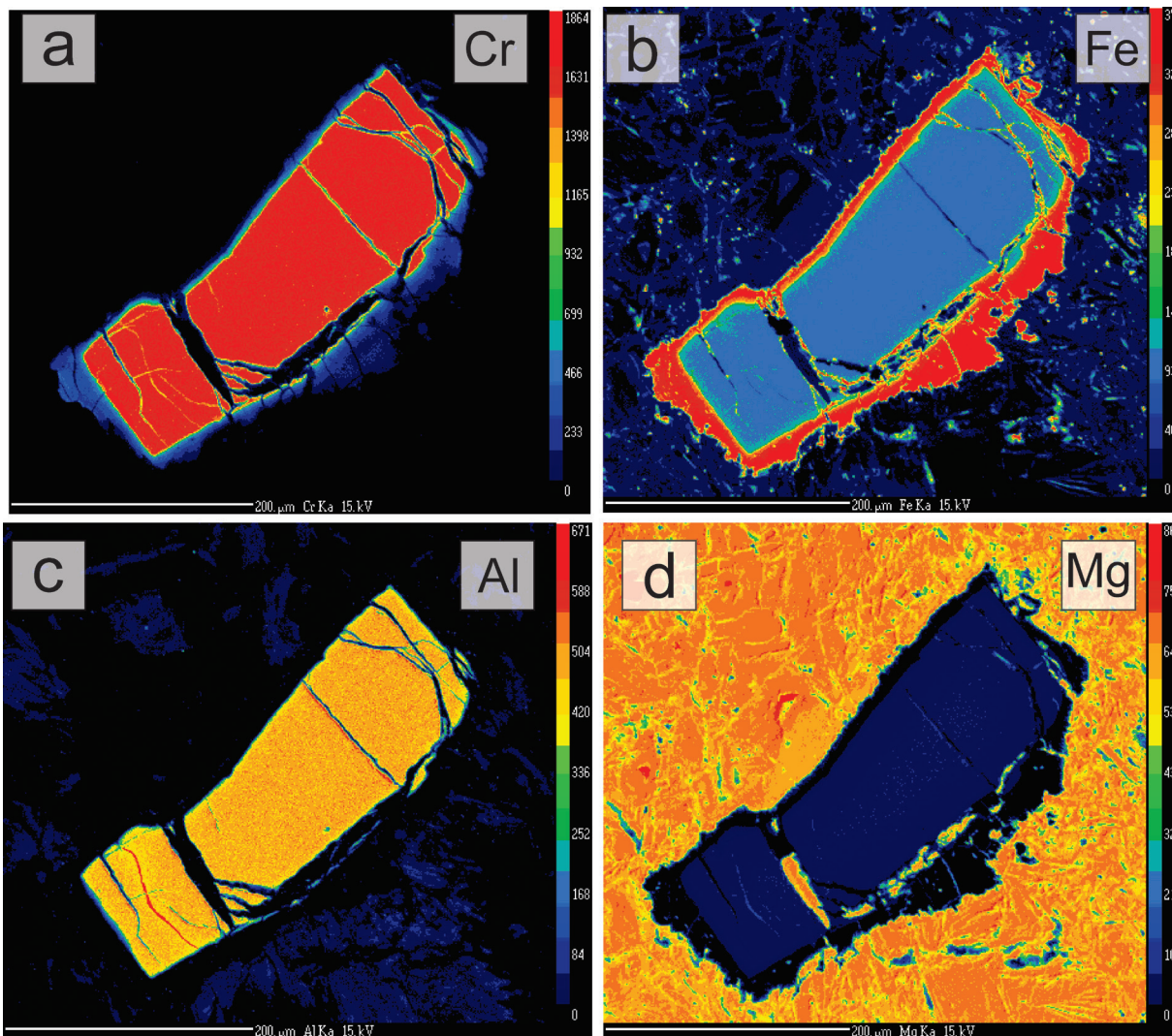
Figure 4: Elemental maps for a representative chrome spinel grain at Tulu Dimtu Hill. a) The chromium concentration across the given grain, shows lower concentrations at the rim. b) Depicts the Fe concentrations showing magnetite (high Fe) rims surrounding a chromite core (low Fe). c) Al concentration showing moderately high homogeneous concentrations across the grain. d) Mg concentrations across the grain, relatively low concentrations. Rims show very low concentrations.

the sample have been replaced by serpentine. In some cases the chrome spinel grains have been affected by alteration shown by ferrichromite rims (Fig. 4). Also, in some cases spinel crystals preserve a pull apart texture.

Yubdo E14.10
(8° 57'37.4"N, 35° 27' 18.2"E)
The Yubdo body (Fig. 2) is zoned with dunite at its core, surrounded by pyroxenite and hornblende-clinopyroxenite. This elliptical outcrop, 30 km² in area, preserves fresh rock under the alteration crust. These features are characteristic features of Alaskan — type intrusions, where orthopyroxene and plagioclase are extremely rare; in Yubdo they are not seen. Yubdo shows a "birbirite" alteration cap over the dunites, which consists essentially of secondary silicates and limonite, and is

derived from the dunites through alteration and concentration (Molly, 1959).

In thin section subhedral spinels (1 − 2 mm) occur in serpentine-filled cracks between fresh olivine and pyroxene. Although these do not form nests or schlieran of chromite, such as are found in Alaskan-type intrusions in the Urals (Molly, 1959). In comparison to other ultramafic outcrops in the Western Ethiopian Shield, Yubdo has not experience the same alteration; the olivines are fresh with little evidence for serpentinisation other than in the cracks between these minerals (Fig. 3e-f).

Chrome Spinel and Olivine Composition
Chromite and olivine are the only minerals from the original ultramafic rock that routinely retain their original igneous composition. Electron microprobe analyses have been undertaken
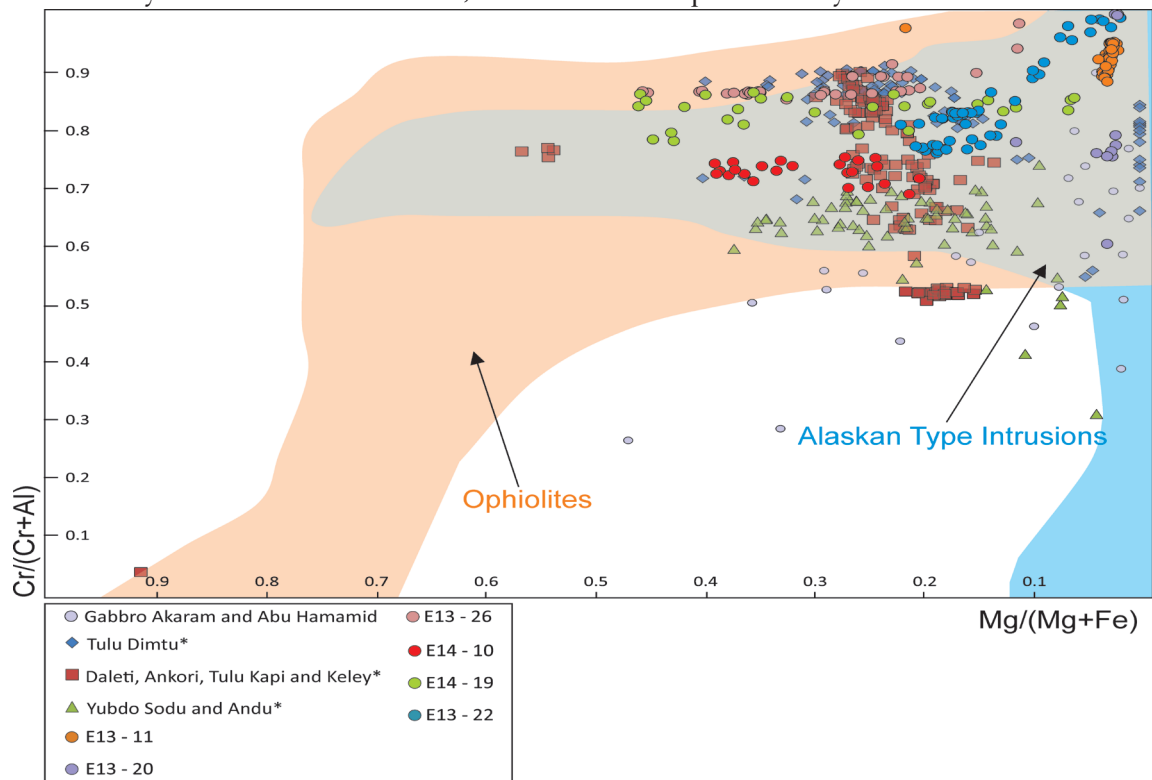
Figure 5: Cr# (Cr/Cr + Al) vs. Mg# (Mg/Mg + Fe^{2+}) from chrome spinels analysed within the WES (Dick and Bullen, 1984b). Other data from the ultra-mafic rocks in the WES (*) was taken from an unpublished Ph.D. thesis. Gabbro Akaram and Abu Hamamid Alaskan type intrusions, Egypt used as a comparison for other Alaskan Type intrusions in the Arabian Nubian Shield (Farahat and Helmy, 2006). Data predominately plots in a similar field to Alaskan type intrusions. Alteration is evident with a decrease in Cr# seen in E13−11 and E13−20.
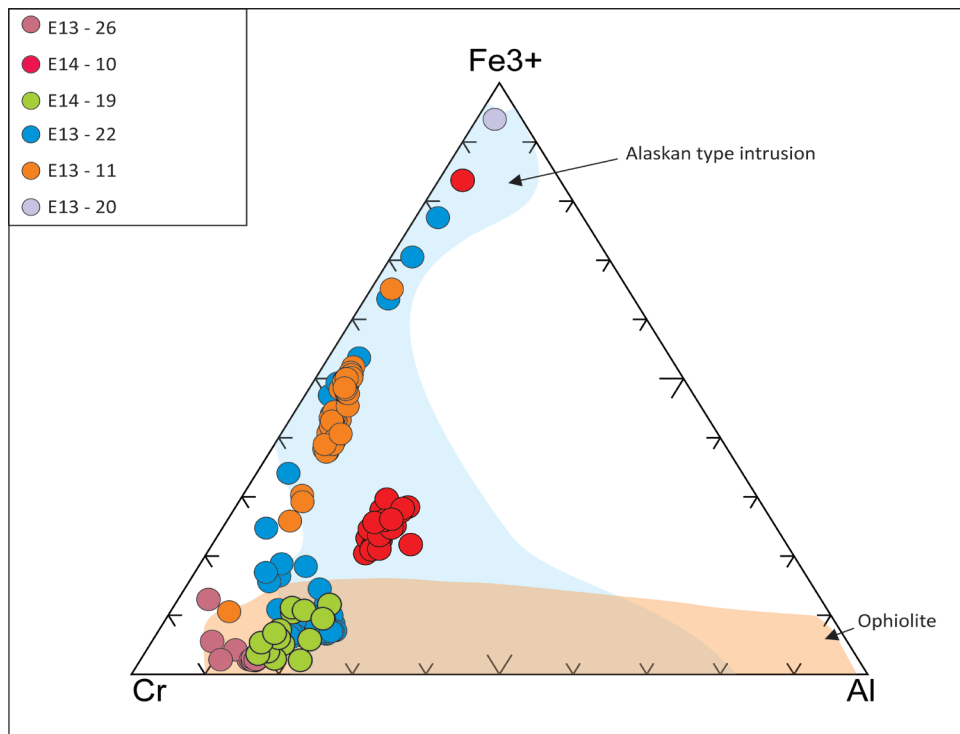
Figure 6: Trivalent cation ratios of chrome spinel in ultramafic and related rocks from previously published ophiolites and Alaskan type intrusions (Barnes and Roeder, 2001). Samples E13—11 and E13—20 taken from Daleti and Tulu Dimtu display a Fe^{3+} enrichment most likely due to alteration of the chrome spinels, showing a similar pattern to layered intrusions and Alaskan type intrusions.
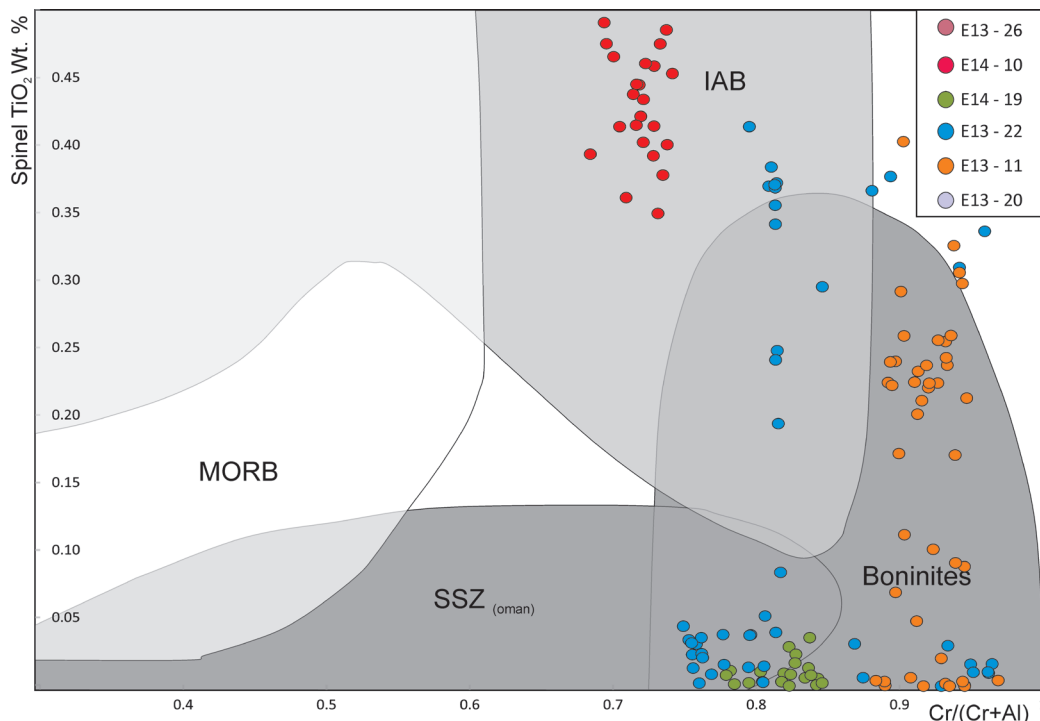
Figure 7: TiO2 content versus Cr# in spinel from ultramafic rocks of the Western Ethiopian Shield. Spinel compositions of MORB, island arc basalts (IAB) and boninites are from Arai (1992), Kelemen et al. (1995) and Dick and Natland (1996). SSZ peridotites from Oman were taken from Arai et al. (2006). Chrome spinels are seen in a number of fields but predominately in boninite, SSZ (Oman) and IAB.

on chrome spinels from ultramafics at Daleti, Abshala Melange, Yubdo and Doro Dimtu (Fig. 1). Representative analyses of chrome spinel and olivine are listed in Tables 1 (full dataset in Appendix 3: Tables 1 and 2). The Barnes and Roeder (2001) database, comprising of more than 26 000 analyses of spinels from igneous and meta-igneous rocks, is used here to define and differentiate compositional fields for spinels for various tectonic settings and magma compositions. Data collected previously in the area, in an unpublished in a PhD thesis, have also been used (Jackson, 2006).

The chrome spinels are characterised by generally high Cr_2O_3, but with a large range (30.04 wt %–68.76 wt %), low TiO_2 content (0.01–0.51) and have Cr# (molar Cr^{3+}/ $Cr^{3+}+Al^{3+}$) in the range of 0.607 to 0.99. The average Cr# is 0.86 (Fig. 5 and Appendix 3: Table 1) and have Mg# (Mg# = Mg^{2+}/ $Mg^{2+}+Fe^{2+}$) ranging from 0.22 to 0.46 (Fig. 5). These data overlap both the Alaskan – type intrusions and oceanic ophiolite fields (Barnes and Roeder, 2001). In many samples the Cr-rich chromite is rimmed by Fe-rich spinel (Fig. 4). These Fe-rich rims are probably a result of Fe replacement during serpentinisation of olivine (Barnes, 2000). On the Cr–A–Fe^{3+} ternary diagram, the chrome spinels are clustered at relatively low Fe^{3+} , high Cr contents, sitting on the Cr–Fe join indicating chromite–magnetite solid solution (Fig. 6) with low spinel (ss) substitution. Chromite is less susceptible to trapped liquid reaction effects when the proportion of chromite to liquid in the rock is high (Barnes and Roeder, 2001). As already observed the presence of these populations of high-Cr#, lower-Al_2O_3, low-TiO_2 spinels (Figs. 5, 6 and 7) are indicative of precipitation from primitive subduction related arc magmas including boninites (Barnes and Roeder, 2001). Olivine is the most common primary mineral

in ultramafic terranes and can be used in association with chrome spinel as a petrogenetic indicator (Dick and Bullen, 1984b). Fresh olivine is only observed from the bodies at Yubdo (E14 −10) and Daleti (E13−11). Olivine from the Yubdo body is of uniform composition (Fo_{90}, Appendix 3: Table 2) with CaO (wt %) and MnO (wt %) values between 0.23–0.12 and 0.18–0.07 respectively. These CaO and MnO values are like those from olivines of the Alaskan-type complexes (Irvine, 1974; Snoke et al., 1981). Also, like Alaskan intrusions, where cumulate olivine is formed during early stage fractionation of primitive mafic magmas, these olivines have an average of 0.11 wt% NiO (895ppm), significantly lower than refractory mantle peridotite olivine. By contrast the olivine from the Daleti complex is much more magnesian, with a mean composition of $Fo_{93.5}$. Also compared with the Yubdo olivines, these are MnO- and particularly CaO–poor (CaO average = 0.007 wt%) and have very high (mantle-like) Ni concentrations (2990 ppm average) (Bodinier and Godard, 2003).

The olivine – spinel mantle array was proposed by Arai (1987, 1990) as a residual mantle peridotite trend, defined by the forsterite content of olivine and the Cr# of spinel. The sample from Daleti plots above the OSMA (Fig. 8), with high Cr# and Fo. Sub-solidus formation of another aluminous phase could be responsible for this shift in the spinel chemistry (Arai, 1994), or possibility the result of metasomatic or metamorphic alteration. Samples from Yubdo (Fig. 8) plot on the edge of, or to the right of, the olivine - spinel mantle array (OSMA)(Arai, 1994). Arai (1994) argues that the OSMA is a residual peridotite array and that cumulates on this plot trend to the right. If this is the case, Yubdo can be inferred to be of cumulate origin, plotting towards the most primitive end of the Alaskan cumulate
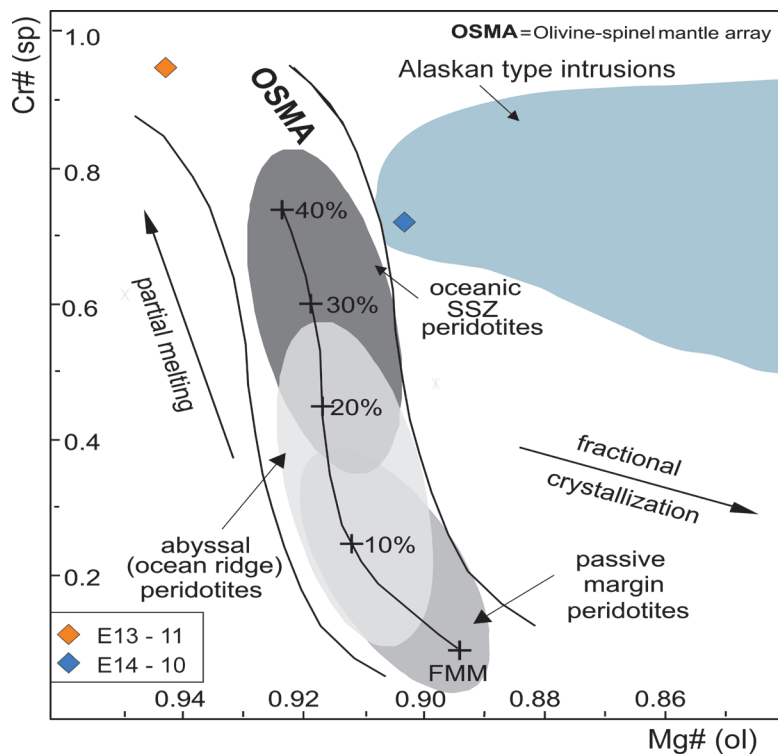
Figure 8: Average Mg# of olivine and Cr# of spinel in ultramafic rocks of the WES. The olivine-spinel mantle array (OSMA) is shown by the two black lines, with supra-subduction field (top grey ellipse), abyssal peridotites (middle grey ellipse) and passive margin peridotites (bottom light grey) (Dick and Bullen, 1984b; Dick, 1989; Arai, 1994; Pearce et al., 2000) and boninites (Metcalf and Shervais, 2008). Pressure curves give approximate values on the depth of melting of the peridotites. 5 and 10 kbar curves are from Sobolev and Batanova (1995) and 15 kbar from Jaques and Green (1980). E14 -10 plots to the right of the OSMA suggesting that these have a cumulate origin (Arai, 1994).
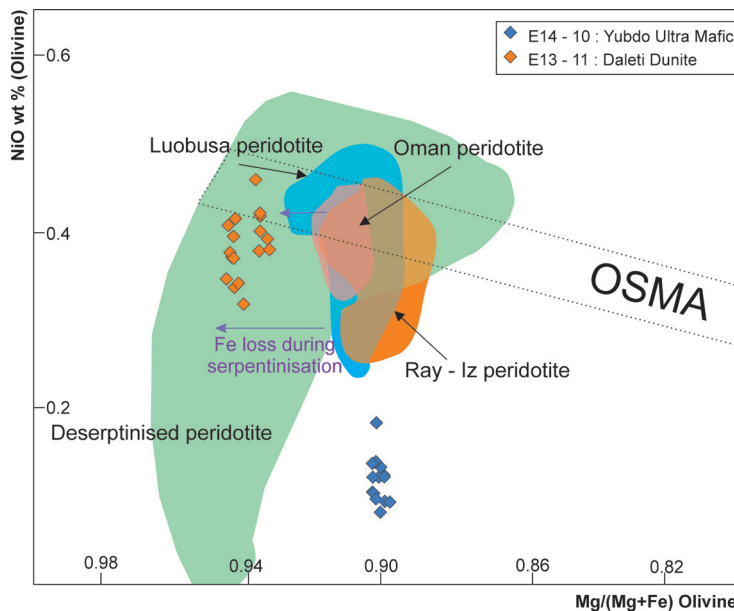
Figure 9: Fo vs. NiO relationship of olivine in chrome spinels between Yubdo and Daleti. Olivine mantle array is the field for olivines in residual mantle peridotites (Takahashi et al., 1987). Fields were taken from (Arai and Miura, 2016). Olivines from peridotites are mostly high in Fo but low in NiO. The relatively low NiO content differentiates these from other MORB related peridotites.

field (Fig. 8). The relatively low NiO content differentiates these from other MORB related peridotites (Fig. 9). The high Cr# and Fo values (Fig. 8 and 9) of these peridotites are consistent with a supra-subduction zone origin (Dick and Bullen, 1984a; Bonatti and Michael, 1989). Where the Ethiopian data fall in the fields for boninites (Fig. 7), this suggests the rocks have been formed from a hydrous melt characteristic of subduction environments (Beccaluva and Serri, 1988).

Oxygen Fugacity of Yubdo and Daleti Peridotite*s*

The oxygen fugacity of mafic and ultramafic rocks is generally calculated using the olivine-spinel equilibria calibrated by Ballhaus et al. (1991) and Ballhaus et al. (1994) who also standardized the olivine-spinel FeMg-1 exchange thermometer. Based on these calibrations, peridotite from abyssal- and DMM (MORB-source) mantle has been shown to have $\Delta \log fO_2$(FMQ) values in the range 0 to -2.5, whereas supra-subduction zone lithospheric mantle peridotite has values in the range +0.5 to +2 (Parkinson and Arculus, 1999). Basalts from different mantle sources also reflect these oxidation differences. Evans et al. (2012), also quote the MORB tends to have $\Delta \log fO_2$(FMQ) values close to 0 (Aldanmaz et al., 2009), while subduction magmas range from +0.5 to +3.5.

The results of Fe–Mg exchange thermometry between olivine and chromite using the corrected equation from Ballhaus, Berry and Green (1991) and Ballhaus, Berry and Green (1994) gives an average temperature of 1154°C and 678 °C for Yubdo (E14–10) and Daleti (E13-11) respectively (Appendix 3: Table 3). Arai–et al. (2001) has recorded the average temperatures for spinels in ophiolite or abyssal peridotites as 681 ± 44°C, whereas, by comparison, Yubdo exhibits higher temperatures than expected for arc related peridotites, and those from Daleti sit within error of previously published ophiolite data.

The Fo contents of olivine coexisting with chromite varies from 0.90 (Yubdo, E14–10) to 0.94 (Daleti, E13–11) and increases with decreasing temperature, indicating that the more magnesian olivines may have lost iron as they re-equilibrated during cooling and probably do not represent primary compositions (Rollinson and Adetunji, 2015b). These high equilibrium temperatures, especially in equilibration with Fo_{90} olivines, further confirm that the chrome-spinel compositions for Yubdo are relics of the original igneous cooling stage, and have not been reset during subsequent metamorphism or alteration. However, the relatively low temperatures of spinels in the case of equilibration with Fo_{94} olivines, which is apparently below the expected liquidus temperature of mantle peridotites, indicates sub-solidus re-equilibration (Mg–Fe exchange) between chrome-spinel and olivine (Faharat 2008, Roeder and Campbell, 1985; Scowen et al., 1991). The $\Delta \log fO_2$(FMQ) values (Table 1 and Appendix 3: Table 4) for the Yubdo (E14 -10) samples average fO_2(FMQ) +3.03 (Fig. 10a). These are significantly more oxidized than abyssal peridotite values and much more like typical arc related peridotites (Parkinson and Arculus, 1999; Arai and Ishimaru, 2008). The Yubdo spinels are oxidized relative to oceanic ophiolites and have similar values to other Alaskan-type intrusions (Fig. 10) (Himmelberg and Loney, 1995; Parkinson and Arculus, 1999; Garuti et al., 2003; Chen et al., 2009). The spinels from Daleti (E13–11) have a $\Delta \log fO_2$ (FMQ) average value of +4.8 (Table 1 and Appendix 3: Table 4), this is unusually high, further supporting that these may have been effected by possible metasomatic (Mellini et al., 2005; Frost and Beard, 2007; Iyer et al., 2008) overprint by subsequent serpentinisation.
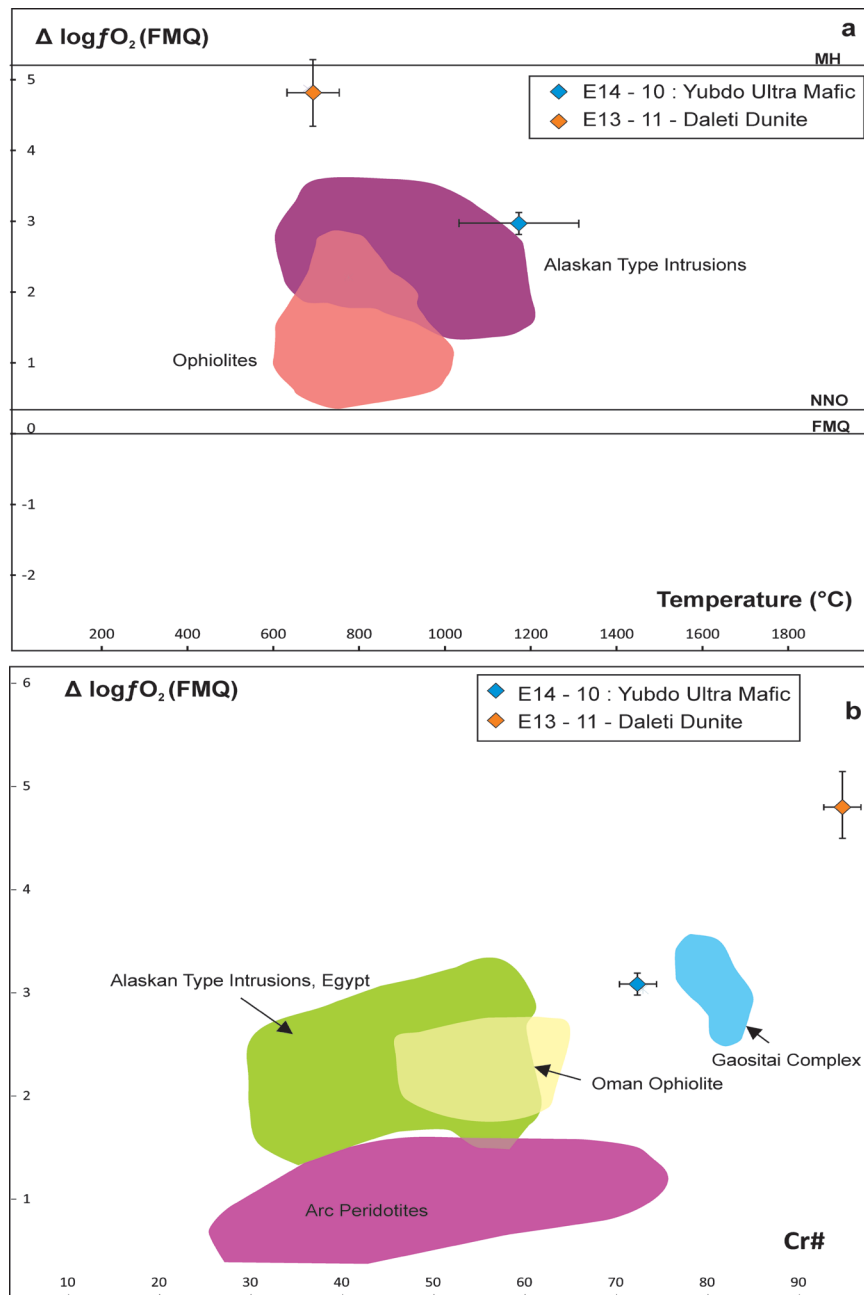
Figure 10: The plots shows that interaction trends involve increases in both oxygen fugacity and Cr# of spinel. The oxygen fugacity was calculated using the method outlined in Ballhaus, Berry and Green (1991) and Ballhaus, Berry and Green (1994) Fe—Mg exchange thermometry and a nominal 1 GPa was used as the best representation of pressure and temperature (Ballhaus, Berry and Green, 1991). a) Plot of Δ fO$_2$ (FMQ) vs temperature. Δ fO$_2$ (FMQ) refers to the deviation from the FMQ buffer in log units. The sample collected from Yubdo lies in the range of FMQ-+3.03. Sample E13–11 from Daleti has a Δ log fO2(FMQ) average value of +4.8. Examples of both arc peridotites and Alaskan type intrusions have been plotted showing that Yubdo are oxidized relative to ophiolites, and seem to be similar to the Alaskan type intrusions (Parkinson and Arculus, 1999; Chen et al., 2009). b) Δ fO2 (FMQ) values are plotted against spinel Cr# (molar Cr/(Cr+Al)) (Parkinson and Arculus, 1999; Garuti et al., 2002; Garuti et al., 2003; Rollinson, 2008; Chen et al., 2009; Khedr and Arai, 2013; Rollinson and Adetunji, 2015b; Rollinson and Adetunji, 2015a). Yubdo and Daleti have high Cr# and a highly oxidised nature, typical of supra-subduction zone settings. Yubdo (E14—10) plots close to the field of Alaskan-type intrusions.

Samples in which fresh olivine and spinel coexist and thus permit the calculation of the ΔfO_2 (FMQ), are very rare. In the data set there are single samples from each of the interpreted Alaskan (Yubdo) and ophiolite –type (Daleti) peridotites and both yield highly oxidized values (ΔfO_2 (FMQ) >3), significantly more oxidized than DMM MORB source mantle. The high Cr# and highly oxidised nature of both these samples are more characteristic of supra-subduction zone settings, and Yubdo, in particular, tends to have values closer to those of known Alaskan Type intrusions (Fig 10a and b).

DISCUSSION

How do the spinels compare to those elsewhere in the East African Orogen?

The Neoproterozoic ophiolites and associated ultramafic–mafic intrusions in the Eastern Desert of Egypt have been suggested to be 890-690 Ma (Stern et al., 2004; Azer and Stern, 2007; Abdel-Karim et al., 2016). The northern Arabian Nubian Shield is made up of both ophiolitic mafic–ultramafic rocks (Stern et al., 2004; Ahmed, 2013; Khedr and Arai, 2016) and Alaskan-type ultramafic–mafic rocks (Helmy and Mogessie, 2001; Helmy and El Mahallawi, 2003; Farahat and Helmy, 2006; El-Rahman et al., 2012; Khedr and Arai, 2016).

Ophiolitic complexes are usually aligned along the NW trending Najd shear zones in the northern ANS or along N–S trending shear zones, though these interpretations are complicated by variably dismembered and deformed outcrops. It has generally been recognised that these are generated in supra-subduction zones (Bakor et al., 1976; Pallister et al., 1988; Stern et al., 2004). Within northern parts of the ANS (Egyptian Desert) most authors have inferred a back-arc setting for the Egyptian ophiolites (El Bahariya and Abd El-Wahed, 2003; Farahat et al., 2004; Ahmed,

2013); sea floor spreading and production of ophiolites can also occur in a fore arc, during early stages of subduction initiation, though this idea is relatively new (Stern et al., 2004; Azer and Stern, 2007). Stern et al. (2004) suggested that majority of the ophiolitic ultramafics are harzburgitic, containing magnesian rich olivines and spinels Cr# > 0.6 (Azer and Stern, 2007). Similar spinel chemistry are also seen in the ophiolites in NW Sudan (Cr#, 0.69–0.84), though these have been thought to not be a part of the Arabian Nubian Shield (Rahman et al., 1990). The Onib ophiolite shows bimodal chromite populations both Cr-rich (Cr# 0.62–0.65) and Al-rich (~64%), the chemistry of these are very different to those seen in the Western Ethiopian Shield. Alaskan-type intrusions in the Eastern Desert typically have Cr# ranges between, 0.31–0.90 and Fe^{3+}#s between 75–55. The spinels are characteristically Al–Mg poor, similar to those seen in Yubdo (Helmy and Mogessie, 2001; Helmy and El Mahallawi, 2003; Farahat and Helmy, 2006; El-Rahman et al., 2012; Khedr and Arai, 2016).

The olivines in the WES (Fo_{90-94}), have higher average Fo contents than that of the olivines in Abu Hamamid (Fo_{74-81}), Gabbro-Akarem (Fo_{69-87}) and Genina Gharbia (Fo_{80-86}) Alaskan-type complexes, but are comparable to those of the Dahanib Complex (Fo_{83-92}) (Helmy and Mogessie, 2001; Farahat and Helmy, 2006; Helmy et al., 2014; Abdel-Karim et al., 2016). Forsterite contents from olivines in rocks from interpreted ophiolites (Abu Daher area (Khudeir, 1995), Um Khariga (Khalil and Azer, 2007) have a wide variation and range from $Fo_{(91.3 - 93.0)}$. These higher Fo values, like the ones seen in Daleti, are much more like peridotites found at Cape Vogel in Papua New Guinea (Kamenetsky et al., 2002). Similar compositions also occur among the dunites and harzburgites from the Izu–Bonin–Mariana

forearc (Ishii, 1992; Yamamoto et al., 1992; Parkinson and Pearce, 1998). The olivines from the Onib Complex, Sudan have lower olivine forsterite contents of Fo(88) and do not seem to overlap with olivine compositions from the Western Ethiopian Shield (Hussein et al., 2004).

Petrogenesis of the ultramafic rocks of the WES

The ultramafic rocks in the Western Ethiopian Shield are generally comprised of dunite, olivine–clinopyroxenite and clinopyroxenites in association with metasediments, whose protoliths are interpreted to have a marine origin, including pelagic sediments, cherts, and quartzites that have all been metamorphosed to upper greenschist/epidote-amphibolite facies (Johnson et al., 2004). Most of these ultramafic bodies show disparate histories and have been serpentinised and therefore the identification of primary structures and features make it difficult to determine their origin (Daleti, Abashala Melange and Tulu Dimtu). The ultramafic complexes are concentrated generally along the Baruda–Tulu Dimtu shear belt (suture zone), however, their occurrence outside this zone has been suggested to be problematic for the ophiolite-decorated suture model (Braathen et al., 2001). In some instances, the ultramafics are enclosed in the Mora metasedimentary rocks and this could suggest that they represent solitary intrusions that have been modified and aligned along the shear- belt in response to deformation, rather than being fragments of oceanic crust caught up in a suture zone (Braathen et al., 2001). However, the Yubdo ultramafic body does not seem to show the same disparate history or alteration (Fig. 3) and has been shown to have concentric zoning typical of Alaskan-type intrusions (Fig. 2), with dunites at the core, surrounded by pyroxenite and hornblende-clinopyroxenite; similar to the

Neoproterozoic Alaskan-type complexes in Egypt (Helmy and Mogessie, 2001; Helmy and El Mahallawi, 2003; Farahat and Helmy, 2006; El-Rahman et al., 2012; Khedr and Arai, 2016). The chrome spinels from the Western Ethiopian Shield are characterised by generally high but varied Cr_2O_3 (30.04 wt %–68.76 wt %), low TiO^2 (0.01–0.51), Cr#s in the range of 0.607 to 0.99. and have Mg# ranging from 0.22 to 0.46 (Fig. 5). These data fall in overlapping fields of known Alaskan-type intrusions and ophiolites (Barnes and Roeder, 2001), however clearly differentiate Daleti (E13–11) . In general these spinels have high-Cr#, lower-Al_2O_3, low-TiO_2 spinels (Figs. 5, 6 and 7) are these plots show that these are characteristic of supra-subduction peridotites formed from melting of hydrated crust. (Barnes and Roeder, 2001). The samples (Daleti and Tulu Dimtu) demonstrate clear alteration trends (Figs. 6 and 7), sitting along the Cr^{3+} and Fe^{3+} join. The spinel chemistry reported here supports the subduction-related (island-arc) environment, from sources that are enriched in the slab component in the presence of a hydrous melt. The spinels have a boninitic affinity (Fig. 7), defining a field of high Cr# and low TiO_2 lavas, formed in a supra-subduction zone (Barnes and Roeder, 2001) as a result of the modification of mantle compositions from the percolating of melts or fluids within a subduction setting (Barnes and Roeder, 2001; Arai et al., 2006). Fresh olivine chemistry could only be obtained from Yubdo (E14–10) and Daleti (E13–11), with forsterite contents ranging between $Fo_{90} - Fo_{93.5}$. There is a clear differentiation in olivine chemistry, the Daleti olivine is much more magnesian, MnO- and particularly CaO-poor and have very high Ni concentrations. Arai (1994) defines the 'OSMA' array as a reflection of the composition of residual, refractory peridotite, while spinels that trend to the right of the array are typically cumulate.

If this is the case, the Yubdo samples analysed here can be inferred to be of cumulate origin. The position of Yubdo in the mantle array show that the ultramafics of the WES carry a supra-subduction zone signature and sit within the know field of Alaskan-type intrusions (Fig. 8). The oxygen fugacity of the magma producing the peridotites (FMQ +3.03) is significantly higher than previously reported MORB values, however, falls within arc range. These values are comparable to oxygen fugacity values for peridotites from the Dahanib Complex Δ log $f O_2$ varying from 2.4 to 3.3 (Khedr and Arai, 2016). Figure 10a shows that $f O_2$ (FMQ) of ophiolites and arc related peridotites, even from SSZ environments, are more reduced that the values obtained from the Yubdo peridotite (Parkinson and Arculus, 1999). However, it should be noted that metasomatic (Mellini, Rumori and Viti, 2005; Frost and Beard, 2007; Iyer et al., 2008) or metamorphic overprinting (Springer, 1974; Frost, 1975; Pinsent and Hirst, 1977; Kimball, 1990) may cause an enrichment of iron in spinel and may also increase the Fe^{3+}/Δ Fe ratio leading to the calculation of elevated oxygen fugacity and can be used to explain the anomalously high values for Daleti (Δ log $f O_2$ +4). Metamorphosed chromite is substantially more iron rich than igneous precursors, as a result of the Mg-Fe exchange with silicates and carbonates. The relative proportions of the trivalent cations Cr^{3+}, Al^{3+} and Fe^{3+} are not greatly modified, although Fe^{3+} depletion occurs during the talc – carbonate alteration at low temperatures. Metamorphism can have a substantial effect on the Mg#, tending to lower values (Daleti, Fig. 5), as a consequence of the exchange between Mg^{2+} and Fe^{2+} between chromite and co-existing silicates. The equilibrium constant for the reaction between Mg(spinel) and Fe^{2+} (olivine) is dependent on temperature, changing in a way that the olivine becomes more Mg rich and the spinel more Fe-rich with falling temperature (Daleti, Fig. 4 and Fig. 5). This can explain the uncharacteristic values for Daleti and why it plots to the left of the OSMA (Fig. 8), with elevated oxygen fugacity (Fig 10a and b).

Previously published geochemical data from Yubdo show relatively high values of Pt, Pd and Rh, characteristic of Alaskan-type intrusions (Belete et al., 2000; Mogessie, Belete and Hoinkes, 2000). Together with the concentric nature of this body and chemistry of the spinels (Figs. 5-7), it is interpreted that Yubdo does represent a solitary intrusion, comparable to other intrusions in the Arabian Nubian Shield. However, samples from Tulu Dimtu, Daleti and Yubdo have chrome spinel chemistry with considerably lower TiO_2 than typical Alaskan-type intrusions and therefore alternate theories still exist for origin of the Daleti and Tulu Dimtu bodies (Supplementary Table 1). (Dick and Bullen, 1984a; Himmelberg and Loney, 1995; Barnes and Roeder, 2001; Helmy and Mogessie, 2001; Kamenetsky, Crawford and Meffre, 2001; Helmy and El Mahallawi, 2003; Farahat and Helmy, 2006; Proenza et al., 2007). The chemical differences between the Yubdo and Daleti bodies have therefore been interpreted to suggest that the Western Ethiopian Shield has examples of both solitary intrusions (Yubdo) and supra subduction ophiolitic remnants (Daleti, Tulu Dimtu and Abshala).

Tectonic evolution of the WES

The ultramafic rocks of the Western Ethiopian Shield have previously been interpreted to have represented a slice of oceanic crust, though there have been dissenting opinions (Kazmin, 1976; de Wit and Aguma, 1977; Abraham, 1989; Stern, 1994a; Alemu and Abebe, 2000; Belete et al., 2000; Mogessie, Belete and Hoinkes, 2000; Braathen et al., 2001; Alemu and Abebe, 2002;
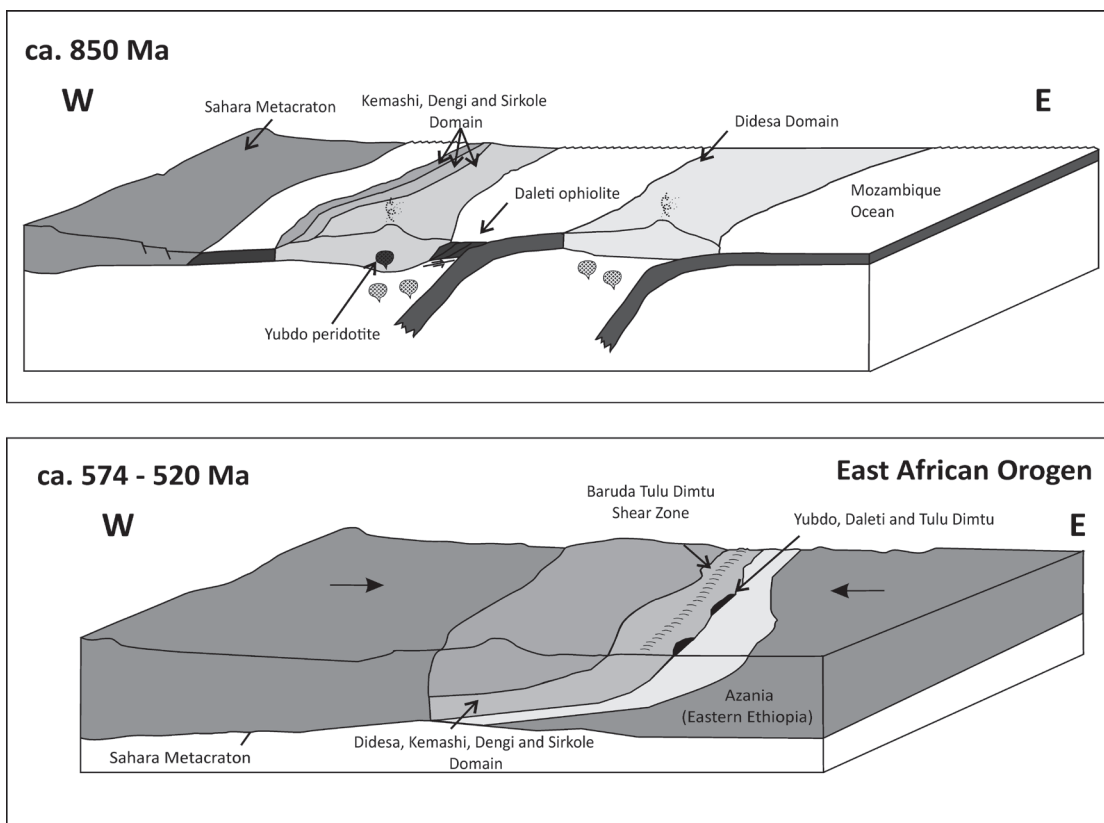
Figure 11: Schematic illustration of the development of Daleti, Tulu Dimtu, Abshala and Yubdo in the Western Ethiopian Shield. Subduction and intra-oceanic arc magmatism is initiated at 854 Ma followed by deformation and further magmatism between 750 and 660 Ma. Closure of the Mozambique Ocean and amalgamation of terranes in the northern East African Orogen is completed by 520 Ma.

Alemu, 2004; Tadesse and Allen, 2004; Tadesse and Allen, 2005; Alemu and Abebe, 2007). The parental melts to the ultramafic rocks of the WES are not typical MORB, these are more oxidized and have equilibrated at higher fO_2. The range in the composition of the spinels is wide though; they have a boninitic parentage (of arc origin) and are hydrous, supporting their interaction with a subduction zone. Using all, available evidence clearly suggests that regardless of being obducted or intruded, these spinels were formed on a convergent margin, above a subduction zone. The chemistry of the spinels in Yubdo and the presence of these bodies outside of these interpreted suture zones, though no analyses have been done on these samples, suggest that these bodies are intrusions (Fig. 11) formed in a similar supra-subduction zone to those seen in elsewhere in

the ANS (Helmy and Mogessie, 2001; Helmy and El Mahallawi, 2003; Farahat and Helmy, 2006; El-Rahman et al., 2012; Khedr and Arai, 2016), rather than far-travelled obducted remnants of the Mozambique Oceanic crust (Stern et al., 2004; Ahmed, 2013; Khedr and Arai, 2016). However, the ultramafic rocks at Daleti and Tulu Dimtu have a refractory nature, chemically different to that of Yubdo and have been interpreted to be oceanic crust obducted in a fore or back arc setting, though the geochemical differences between these settings are subtle. Fore-arc assemblages are more likely to become entrapped in orogens, in contrast to back-arc basin lithosphere, which is reconsumed by subduction following collision of the retreating forearc (Dilek and Flower, 2003) and therefore fore-arc settings are favoured in this model (Fig. 11) for Daleti,

Tulu Dimtu and Abshala. The oldest rocks known in the area date back to ca. 850 Ma, with magmatism, metamorphism and deformation occurring until ca. 630 Ma (Blades et al., 2015). These granites have been previously interpreted to have formed in an intra-oceanic setting; above a subduction zone. Post tectonic granites are seen in the WES at ca. 574 Ma (Blades et al. 2015), therefore suggesting that these ultramafic bodies were emplaced sometime before post tectonic magmatism began. Yubdo, being a subduction related intrusion, would have an age broadly synonymous with the oldest phase of magmatism in the area (~854 Ma). Neoproterozoic ophiolites and associated ultramafic–mafic intrusions in the Eastern Desert and Sudan, have been suggested to be 890-690 Ma (Stern et al., 2004; Azer and Stern, 2007; Abdel-Karim et al., 2016). These ages are coeval with the formation of the Western Ethiopian Shield and therefore we interpret the Daleti, Tulu Dimtu and Abshala peridotites to be of a similar age. What this paper unequivocally shows is that these ultramafic bodies were emplaced in a supra-subduction zone (island-arc) environment, from sources that are enriched in the slab component in the presence of a hydrous melt, further supporting the formation of the Western Ethiopian Shield in a supra-subduction environment (Berhe, 1990; Stern, 1994b; Braathen et al., 2001; Kebede, Koeberl and Koller, 2001b; Allen and Tadesse, 2003; Grenne et al., 2003; Stern et al., 2004; Tadesse and Allen, 2004; Tadesse and Allen, 2005; Woldemichael et al., 2010; Blades et al., 2015).

CONCLUSION

New chrome spinel and olivine data from the Western Ethiopian Shield combined with previous data demonstrate that ultramafic rocks of Tulu Dimtu, Daleti and Yubdo are derived from a subduction - related (island-arc)

environment, from sources that are enriched in the slab component in the presence of a hydrous melt.

A common feature of the WES spinels is their high Cr# (from 33 to 99), lower Mg# (0.117 - 0.464) and a trend towards Fe^{3+}- rich compositions, which is a typical arc trend. The high Cr (>0.6) and low Ti character of the primary spinels in peridotite and chromite suggest a supra – subduction zone environment that agrees with discrimination diagrams, that show data plotting within an intrusion-related field. What the spinel chemistry highlights is that there is a difference in chemistry between the Yubdo body and the Daleti, Tulu Dimtu and Abshala Melange. This differentiation is also seen in the olivine chemistry (Yubdo Fo_{90} and Daleti $Fo_{93.5}$) demonstrating that the Daleti olivine is much more magnesian, MnO- and particularly CaO-poor and have very high Ni concentrations. The oxygen fugacity of the peridotites from Yubdo are highly oxidised (FMQ +2.71−+3.6) from the FMQ buffer, suggesting that these higher values are related to the parental magma composition and emplacement within an oxidised environment. These values are within the arc range and significantly greater than MORB, plotting closer to other known Alaskan type intrusions. Together with the concentric nature of this body and chemistry of the spinels (Figs. 5-7), it is interpreted that Yubdo does represent a solitary intrusion, comparable to other intrusions in the Arabian Nubian Shield (particularly Dahanib Alaskan – type intrusion).

The oldest rocks known in the area date back to ca. 850 Ma. There are three broad pre-/syntectonic deformation and magmatic phases recorded in the Western Ethiopian Shield, a period that defines major tectonic reorganisation throughout the East African Orogen (Merdith et al., 2017). We suggest that the ultramafic bodies of Daleti, Tulu Dimtu,

Abshala Melange and Yubdo were formed close to the initiation of supra-subduction and the beginning of known magmatism in the Western Ethiopian Shield. Therefore, we conclude that these ultramafic complexes, are indeed remnants of the Mozambique Ocean. They originated as new ocean crust and intrusions formed during the break up of Rodinia and onset of subduction, and were fortuitously preserved by emplacement in shear zones in the East African Orogen during the final assembly of Gondwana.

REFERENCES

Abdel-Karim, A.-a. M., Ali, S., Helmy, H. M. & El-Shafei, S. A. 2016. A fore-arc setting of the Gerf ophiolite, Eastern Desert, Egypt: Evidence from mineral chemistry and geochemistry of ultramafites. Lithos 263, 52-65.

Abdelsalam, M. & Stern, R. 1996. Sutures and shear zones in the Arabian-Nubian Shield. Journal of African Earth Sciences 23(3), 289-310.

Abraham, A. 1989. Tectonic history of the Pan-African low-grade belt of western Ethiopia. Ethiopian Institute of Geological Survey.

Ahmed, A. & Arai, S. 2002. Unexpectedly high-PGE chromitite from the deeper mantle section of the northern Oman ophiolite and its tectonic implications. Contributions to Mineralogy and Petrology 143(3), 263-78.

Ahmed, A. H. 2013. Highly depleted harzburgite–dunite–chromitite complexes from the Neoproterozoic ophiolite, south Eastern Desert, Egypt: a possible recycled upper mantle lithosphere. Precambrian Research 233, 173-92.

Aldanmaz, E., Schmidt, M., Gourgaud, A. & Meisel, T. 2009. Mid-ocean ridge and supra-subduction geochemical signatures in spinel–peridotites from the Neotethyan ophiolites in SW Turkey: implications for upper mantle melting processes. Lithos 113(3), 691-708.

Alemu, T. 2004. Structural evolution of the Pan-African Tulu Dimtu Belt, western Ethiopia. In Proceedings of the 4th Ethiopian Geoscience and Mineral Engineering Association (EGMEA) (ed A. Asrat). pp. 188-94.

Alemu, T. & Abebe, T. 2007. Geology and Tectonic Evolution of the Pan-African Tulu Dimtu Belt, Western Ethiopia. Online Journal of Earth Sciences 1(1), 24-42.

Alemu, T. & Abebe, T. 2002. Geology and tectonic evolution of the Pan-African Tulu Dimtu Belt, Western Ethiopia. . p. 45. Unpublished report Geological Survey of Ethiopia.

Alemu, T. & Abebe, T. 2000. Geology of the Gimbi Area. Geological Survey of Ethiopia.

Allen, A. & Tadesse, G. 2003. Geological setting and tectonic subdivision of the Neoproterozoic orogenic belt of Tuludimtu, western Ethiopia. Journal of African Earth Sciences 36(4), 329-43.

Arai, S. 1994. Characterization of spinel peridotites by olivine-spinel compositional relationships: review and interpretation. Chemical Geology 113(3), 191-204.

Arai, S. 1992. Chemistry of chromian spinel in volcanic rocks as a potential guide to magma chemistry. Mineralogical Magazine 56(383), 173-84.

Arai, S. & Ishimaru, S. 2008. Insights into

petrological characteristics of the lithosphere of mantle wedge beneath arcs through peridotite xenoliths: a review. Journal of Petrology 49(4), 665-95.

Arai, S. & Miura, M. 2016. Formation and modification of chromitites in the mantle. Lithos 264, 277-95.

Arai, S., Okamura, H., Kadoshima, K., Tanaka, C., Suzuki, K. & Ishimaru, S. 2011. Chemical characteristics of chromian spinel in plutonic rocks: Implications for deep magma processes and discrimination of tectonic setting. Island Arc 20(1), 125-37.

Arai, S., Shimizu, Y., Ismail, S. & Ahmed, A. 2006. Low-T formation of high-Cr spinel with apparently primary chemical characteristics within podiform chromitite from Rayat, northeastern Iraq. Mineralogical Magazine 70(5), 499-508.

Arai, S., Takada, S., Michibayashi, K. & Kida, M. 2004. Petrology of peridotite xenoliths from Iraya volcano, Philippines, and its implication for dynamic mantle-wedge processes. Journal of Petrology 45(2), 369-89.

Augé, T. 1987. Chromite deposits in the northern Oman ophiolite: mineralogical constraints. Mineralium Deposita 22(1), 1-10.

Ayalew, T., Bell, K., Moore, J. M. & Parrish, R. R. 1990. U-Pb and Rb-Sr geochronology of the western Ethiopian shield. Geological Society of America Bulletin 102(9), 1309-16.

Ayalew, T. & Peccerillo, A. 1998. Petrology and geochemistry of the Gore-Gambella plutonic rocks: implications for magma genesis and the tectonic setting of the Pan-African Orogenic Belt of western Ethiopia. Journal of African Earth Sciences 27(3), 397-416.

Azer, M. K. & Stern, R. J. 2007. Neoproterozoic (835–720 Ma) serpentinites in the Eastern Desert, Egypt: fragments of forearc mantle. The Journal of Geology 115(4), 457-72.

Bakor, A. R., Gass, I. G. & Neary, C. R. 1976. Jabal al Wask NW Saudi Arabia: an Eocambrian back arc ophiolite. Earth and Planetary Sciences 30, 1-9.

Ballhaus, C., Berry, R. & Green, D. 1994. High-pressure experimental calibration of the olivine-orthopyroxene-spinel oxygen geobarometer: implications for the oxidation state of the upper mantle. Contributions to Mineralogy and Petrology 118(1), 109-09.

Ballhaus, C., Berry, R. & Green, D. 1991. High pressure experimental calibration of the olivine-orthopyroxene-spinel oxygen geobarometer: implications for the oxidation state of the upper mantle. Contributions to Mineralogy and Petrology 107(1), 27-40.

Barnes, S. J. 2000. Chromite in komatiites, II. Modification during greenschist to mid-amphibolite facies metamorphism. Journal of Petrology 41(3), 387-409.

Barnes, S. J. & Roeder, P. L. 2001. The range of spinel compositions in terrestrial mafic and ultramafic rocks. Journal of Petrology 42(12), 2279-302.

Beccaluva, L. & Serri, G. 1988. Boninitic and low-Ti subduction-related lavas from intraoceanic arc-backarc systems and low-Ti ophiolites: a reappraisal of their petrogenesis and original tectonic setting. Tectonophysics 146(1), 291-315.

Belete, K., Mogessie, A., Hoinkes, G. & Ettinger, K. 2000. Platinum group minerals and chrome spinels in the Yubdo ultramafic rocks, western Ethiopia. Journal of African Earth Sciences 30(4), 10-10.

Berhe, S. M. 1990. Ophiolites in Northeast and East Africa: implications for Proterozoic crustal growth. Journal of the Geological society, London 147, 41-57.

Blades, M. L., Collins, A. S., Foden, J., Payne, J. L., Xu, X., Alemu, T., Woldetinsae, G., Clark, C. & Taylor, R. J. 2015. Age and hafnium isotopic evolution of the Didesa and Kemashi Domains, western Ethiopia. Precambrian Research 270, 267-84.

Bodinier, J.-L. & Godard, M. 2003. Orogenic, ophiolitic, and abyssal peridotites. Treatise on geochemistry 2, 568.

Bonatti, E. & Michael, P. J. 1989. Mantle peridotites from continental rifts to ocean basins to subduction zones. Earth Planet. Sci. Lett. 91,

297-311.

Braathen, A., Grenne, T., Selassie, M. & Worku, T. 2001. Juxtaposition of Neoproterozoic units along the Baruda–Tulu Dimtu shear-belt in the East African Orogen of western Ethiopia. Precambrian Research 107(3), 215-34.

Chashchukhin, I., Votyakov, S., Pushkarev, E., Anikina, E., Mironov, A. & Uimin, S. 2002. Oxithermobarometry of ultramafic rocks from the Ural Platinum Belt. Geochemistry International 40(8), 762-78.

Chen, B., Suzuki, K., Tian, W., Jahn, B. & Ireland, T. 2009. Geochemistry and Os–Nd–Sr isotopes of the Gaositai Alaskan-type ultramafic complex from the northern North China craton: implications for mantle–crust interaction. Contributions to Mineralogy and Petrology 158(5), 683-702.

Collins, A. & Pisarevsky, S. 2005. Amalgamating eastern Gondwana: the evolution of the Circum-Indian Orogens. Earth-Science Reviews 71(3), 229-70.

De Wit, M. & Aguma, A. 1977. Geology of the ultramafic and associated rocks of Tulu Dimtu, Welega. Ethiopian Institute of Geological Surveys Report, 26.

Debari, S. M. & Coleman, R. G. 1989. Examination of the deep levels of an island arc: evidence from the Tonsina ultramafic-mafic assemblage, Tonsina, Alaska. J. Geophys. Res. 94, 4373-91.

Dick, H. J. & Bullen, T. 1984a. Chromian spinel as a petrogenetic indicator in abyssal and alpine-type peridotites and spatially associated lavas. Contributions to Mineralogy and Petrology 86(1), 54-76.

Dick, H. J. & Natland, J. H. 1996. Late-stage melt evolution and transport in the shallow mantle beneath the East Pacific Rise. In Proceedings-Ocean Drilling Program Scientific Results pp. 103-34. National Science Foundation.

Dick, H. J. B. 1989. Abyssal peridotites, very slow spreading ridges and ocean ridge magmatism. Magmatism in the Ocean Basins 42, 71-105.

Dick, H. J. B. & Bullen, T. 1984b. Chromian spinel as a petrogenetic indicator in abyssal and alpine-type peridotites and spatially associated lavas.

Contrib. Mineral. Petrol. 86, 54-76.

Dick, H. J. B. & Sinton, J. M. 1979. Compositional layering in alpine peridotites: evidence for pressure solution creep in the mantle. J. Geol. 87, 403-16.

Dilek, Y. & Flower, M. F. 2003. Arc-trench rollback and forearc accretion: 2. A model template for ophiolites in Albania, Cyprus, and Oman. Geological Society, London, Special Publications 218(1), 43-68.

Dilek, Y. & Furnes, H. 2011. Ophiolite genesis and global tectonics: geochemical and tectonic fingerprinting of ancient oceanic lithosphere. Geological Society of America Bulletin 123(3-4), 387-411.

El-Rahman, Y. A., Helmy, H. M., Shibata, T., Yoshikawa, M., Arai, S. & Tamura, A. 2012. Mineral chemistry of the Neoproterozoic Alaskan-type Akarem Intrusion with special emphasis on amphibole: Implications for the pluton origin and evolution of subduction-related magma. Lithos 155, 410-25.

El Bahariya, G. & Abd El-Wahed, M. 2003. Petrology, mineral chemistry and tectonic evolution of the northern part of Wadi Hafafit area, Eastern Desert, Egypt. In The third international Conference on the Geology of Africa, Assiut University, Assiut (7-9 December 2003), Egypt pp. 201-31.

Escayola, M., Garuti, G., Zaccarini, F., Proenza, J. A., Bédard, J. H. & Van Staal, C. 2011. Chromitite and platinum-group-element mineralization at middle Arm Brook, central Advocate ophiolite complex, Baie Verte peninsula, Newfoundland, Canada. The Canadian Mineralogist 49(6), 1523-47.

Evans, K., Elburg, M. & Kamenetsky, V. 2012. Oxidation state of subarc mantle. Geology 40(9), 783-86.

Farahat, E., El Mahalawi, M., Hoinkes, G. & Abdel Aal, A. 2004. Continental back-arc basin origin of some ophiolites from the Eastern Desert of Egypt. Mineralogy and Petrology 82(1), 81-104.

Farahat, E. & Helmy, H. 2006. Abu hamamid neoproterozoic alaskan-type complex, south

Eastern Desert, Egypt. Journal of African Earth Sciences 45(2), 187-97.

Findlay, D. 1969. Origin of the Tulameen ultramafic-gabbro complex, southern British Columbia. Canadian Journal of Earth Sciences 6(3), 399-425.

Fritz, H., Abdelsalam, M., Ali, K. A., Bingen, B., Collins, A. S., Fowler, A. R., Ghebreab, W., Hauzenberger, C. A., Johnson, P. R., Kusky, T. M., Macey, P., Muhongo, S., Stern, R. J. & Viola, G. 2013. Orogen styles in the East African Orogen: A review of the Neoproterozoic to Cambrian tectonic evolution. Journal of African Earth Sciences (0).

Frost, B. R. 1975. Contact metamorphism of serpentinite, chloritic blackwall and rodingite at Paddy-Go-Easy Pass, Central Cascades, Washington. Journal of Petrology 16(1), 272-313.

Frost, B. R. & Beard, J. S. 2007. On silica activity and serpentinization. Journal of Petrology 48(7), 1351-68.

Garuti, G., Pushkarev, E. V. & Zaccarini, F. 2002. Composition and paragenesis of Pt alloys from chromitites of the Uralian–Alaskan-type Kytlym and Uktus complexes, northern and central Urals, Russia. The Canadian Mineralogist 40(2), 357-76.

Garuti, G., Pushkarev, E. V., Zaccarini, F., Cabella, R. & Anikina, E. 2003. Chromite composition and platinum-group mineral assemblage in the Uktus Uralian-Alaskan-type complex (Central Urals, Russia). Mineralium Deposita 38(3), 312-26.

Grenne, T., Pedersen, R., Bjerkgård, T., Braathen, A., Selassie, M. & Worku, T. 2003. Neoproterozoic evolution of Western Ethiopia: igneous geochemistry, isotope systematics and U–Pb ages. Geological magazine 140(04), 373-95.

Helmy, H. & El Mahallawi, M. 2003. Gabbro Akarem mafic-ultramafic complex, Eastern Desert, Egypt: a Late Precambrian analogue of Alaskan-type complexes. Mineralogy and Petrology 77(1-2), 85-108.

Helmy, H. M., El-Rahman, Y. M. A., Yoshikawa, M., Shibata, T., Arai, S., Tamura, A. & Kagami, H. 2014. Petrology and Sm–Nd dating of the Genina Gharbia Alaskan-type complex (Egypt): insights into deep levels of Neoproterozoic island arcs. Lithos 198, 263-80.

Helmy, H. M. & Mogessie, A. 2001. Gabbro Akarem, Eastern Desert, Egypt: Cu–Ni–PGE mineralization in a concentrically zoned mafic–ultramafic complex. Mineralium Deposita 36(1), 58-71.

Helmy, H. M., Yoshikawa, M., Shibata, T., Arai, S. & Kagami, H. 2015. Sm–Nd and Rb–Sr isotope geochemistry and petrology of Abu Hamamid intrusion, Eastern Desert, Egypt: An Alaskan-type complex in a backarc setting. Precambrian Research 258, 234-46.

Himmelberg, G. R. & Loney, R. A. 1995. Characteristics and petrogenesis of Alaskan-type ultramafic-mafic intrusions, southeastern Alaska. US Government Printing Office.

Himmelberg, G. R., Loney, R. A. & Craig, J. T. 1986. Petrogenesis of the ultramafic complex at the Blashke Islands, southeastern Alaska. Department of the Interior, US Geological Survey.

Hussein, I., Kröner, A. & Reischmann, T. 2004. The Wadi Onib mafic-ultramafic complex: a Neoproterozoic supra-subduction zone ophiolite in the northern Red Sea hills of the Sudan. Developments in Precambrian Geology 13, 163-206.

Irvine, T. 1965. Chromian spinel as a petrogenetic indicator: Part 1. Theory. Canadian Journal of Earth Sciences 2(6), 648-72.

Irvine, T. 1967. Chromian spinel as a petrogenetic indicator: Part 2. Petrologic applications. Canadian Journal of Earth Sciences 4(1), 71-103.

Irvine, T. N. 1974. Petrology of the Duke Island ultramafic complex southeastern Alaska. Geological Society of America Memoirs 138, 1-244.

Ishii, K. 1992. Partitioning of non-coaxiality in deforming layered rock masses. Tectonophysics 210(1-2), 33-43.

Iyer, K., Austrheim, H., John, T. & Jamtveit, B. 2008.

Serpentinization of the oceanic lithosphere and some geochemical consequences: constraints from the Leka Ophiolite Complex, Norway. Chemical Geology 249(1), 66-90.

Jackson, M. 2006. Lithogeochemistry and spinel compositions in the ultramafic complexes of Western Ethiopia: criteria for the identification of Alaskan-type intrusions. Cardiff University.

Jaques, A. & Green, D. 1980. Anhydrous melting of peridotite at 0–15 kb pressure and the genesis of tholeiitic basalts. Contributions to Mineralogy and Petrology 73(3), 287-310.

Johnson, P., Andresen, A., Collins, A. S., Fowler, A., Fritz, H., Ghebreab, W., Kusky, T. & Stern, R. 2011. Late Cryogenian–Ediacaran history of the Arabian–Nubian Shield: A review of depositional, plutonic, structural, and tectonic events in the closing stages of the northern East African Orogen. Journal of African Earth Sciences 61(3), 167-232.

Johnson, T. E., Ayalew, T., Mogessie, A., Kruger, F. J. & Poujol, M. 2004. Constraints on the tectonometamorphic evolution of the Western Ethiopian Shield. Precambrian Research 133(3), 305-27.

Kamenetsky, V. S., Crawford, A. J. & Meffre, S. 2001. Factors controlling chemistry of magmatic spinel: an empirical study of associated olivine, Cr-spinel and melt inclusions from primitive rocks. Journal of Petrology 42(4), 655-71.

Kamenetsky, V. S., Sobolev, A. V., Eggins, S., Crawford, A. J. & Arculus, R. 2002. Olivine-enriched melt inclusions in chromites from low-Ca boninites, Cape Vogel, Papua New Guinea: evidence for ultramafic primary magma, refractory mantle source and enriched components. Chemical Geology 183(1), 287-303.

Kazmin, V. 1976. Ophiolites in the Ethiopian basement. Ethiopian Inst. Geol. Surv., Note 35, 16.

Kebede, T., Kloetzli, U. & Koeberl, C. 2001a. U/Pb and Pb/Pb zircon ages from granitoid rocks of Wallagga area: constraints on magmatic and tectonic evolution of Precambrian rocks of western Ethiopia. Mineralogy and Petrology 71(3-4), 251-71.

Kebede, T., Koeberl, C. & Koller, F. 1999. Geology, geochemistry and petrogenesis of intrusive rocks of the Wallagga area, western Ethiopia. Journal of African Earth Sciences 29(4), 715-34.

Kebede, T., Koeberl, C. & Koller, F. 2001b. Magmatic evolution of the Suqii-Wagga garnet-bearing two-mica granite, Wallagga area, western Ethiopia. Journal of African Earth Sciences 32(2), 193-221.

Kelemen, P. B., Whitehead, J., Aharonov, E. & Jordahl, K. A. 1995. Experiments on flow focusing in soluble porous media, with applications to melt extraction from the mantle. Journal of Geophysical Research: Solid Earth 100(B1), 475-96.

Khalil, A. & Azer, M. 2007. Supra-subduction affinity in the Neoproterozoic serpentinites in the Eastern Desert, Egypt: evidence from mineral composition. Journal of African Earth Sciences 49(4), 136-52.

Khedr, M. Z. & Arai, S. 2013. Origin of Neoproterozoic ophiolitic peridotites in south Eastern Desert, Egypt, constrained from primary mantle mineral chemistry. Mineralogy and Petrology 107(5), 807-28.

Khedr, M. Z. & Arai, S. 2016. Petrology of a Neoproterozoic Alaskan-type complex from the Eastern Desert of Egypt: Implications for mantle heterogeneity. Lithos 263, 15-32.

Khudeir, A. 1995. Chromian spinel-silicate chemistry in peridotite and orthopyroxenite relicts from ophiolitic serpentinites, Eastern Desert, Egypt. Bull. Fac. Sci. Assiut Univ 24, 221-61.

Kimball, K. L. 1990. Effects of hydrothermal alteration on the compositions of chromian spinels. Contributions to Mineralogy and Petrology 105(3), 337-46.

Krause, J., Brügmann, G. E. & Pushkarev, E. V. 2007. Accessory and rock forming minerals monitoring the evolution of zoned mafic–ultramafic complexes in the Central Ural Mountains. Lithos 95(1), 19-42.

Le Mée, L., Girardeau, J. & Monnier, C. 2004.

Mantle segmentation along the Oman ophiolite fossil mid-ocean ridge. Nature 432(7014), 167-72.

Leblanc, M. & Nicolas, A. 1992. Ophiolitic chromitites. International Geology Review 34(7), 653-86.

Meert, J. G. 2003. A synopsis of events related to the assembly of eastern Gondwana. Tectonophysics 362(1), 1-40.

Meert, J. G. & Lieberman, B. S. 2008. The Neoproterozoic assembly of Gondwana and its relationship to the Ediacaran–Cambrian radiation. Gondwana Research 14(1–2), 5-21.

Mellini, M., Rumori, C. & Viti, C. 2005. Hydrothermally reset magmatic spinels in retrograde serpentinites: formation of "ferritchromit" rims and chlorite aureoles. Contributions to Mineralogy and Petrology 149(3), 266-75.

Merdith, A. S., Collins, A. S., Williams, S. E., Pisarevsky, S., Foden, J. F., Archibald, D. A., Blades, M. L., Alessio, B. L., Armistead, S., Plavsa, D., Clark, C. & D.R, M. 2017. A Full PLate Global Reconstruction of the Neoproterzoic Gondwana Research.

Metcalf, R. V. & Shervais, J. W. 2008. Suprasubduction-zone ophiolites: Is there really an ophiolite conundrum? Geological Society of America Special Papers 438, 191-222.

Mogessie, A., Belete, K. & Hoinkes, G. 2000. Yubdo-Tulu Dimtu mafic-ultramafic belt, Alaskan-type intrusions in western Ethiopia: Its implication to the Arabian-Nubian Shield and tectonics of the Mozambique Belt. Journal of African Earth Sciences 30(4), 62.

Molly, E. 1959. Platinum deposits of Ethiopia. Economic Geology 54(3), 467-77.

Niu, Y. & Hekinian, R. 1997. Spreading-rate dependence of the extent of mantle melting beneath ocean ridges. Nature 385(6614), 326.

Pallister, J. S., Stacey, J. S., Fischer, L. B. & Premo, W. R. 1988. Precambrian ophiolites of Arabia: Geologic settings, U/Pb geochronology, Pb-isotope characteristics, and implications for continental accretion. Precambrian Research 38(1), 1-54.

Parkinson, I. J. & Arculus, R. J. 1999. The redox state of subduction zones: insights from arc-peridotites. Chemical Geology 160(4), 409-23.

Parkinson, I. J. & Pearce, J. A. 1998. Peridotites from the Izu–Bonin–Mariana forearc (ODP Leg 125): evidence for mantle melting and melt–mantle interaction in a supra-subduction zone setting. Journal of Petrology 39(9), 1577-618.

Pearce, J. A., Barker, P., Edwards, S., Parkinson, I. & Leat, P. 2000. Geochemistry and tectonic significance of peridotites from the South Sandwich arc–basin system, South Atlantic. Contributions to Mineralogy and Petrology 139(1), 36-53.

Pearce, J. A., Lippard, S. & Roberts, S. 1984. Characteristics and tectonic significance of supra-subduction zone ophiolites. Geological Society, London, Special Publications 16(1), 77-94.

Pinsent, R. & Hirst, D. 1977. The metamorphism of the Blue River ultramafic body, Cassiar, British Columbia, Canada. Journal of Petrology 18(4), 567-94.

Proenza, J., Gervilla, F., Melgarejo, J. & Bodinier, J.-L. 1999. Al-and Cr-rich chromitites from the Mayari-Baracoa ophiolitic belt (eastern Cuba); consequence of interaction between volatile-rich melts and peridotites in suprasubduction mantle. Economic Geology 94(4), 547-66.

Proenza, J. A., Zaccarini, F., Lewis, J. F., Longo, F. & Garuti, G. 2007. Chromian spinel composition and the platinum-group minerals of the PGE-rich Loma Peguera chromitites, Loma Caribe peridotite, Dominican Republic. The Canadian Mineralogist 45(3), 631-48.

Rahman, E. A., Harms, U., Schandelmeier, H., Franz, G., Darbyshire, D., Horn, P. & Muller–Sohnius, D. 1990. A new ophiolite occurrence in NW Sudan; constraints on late Proterozoic tectonism. Terra Nova 2(4), 363-76.

Rollinson, H. 2008. The geochemistry of mantle chromitites from the northern part of the Oman ophiolite: inferred parental melt compositions. Contributions to Mineralogy and Petrology 156(3), 273-88.

Rollinson, H. & Adetunji, J. 2015a. Chromite in

the mantle section of the Oman Ophiolite: implications for the tectonic evolution of the Oman ophiolite. Acta Geologica Sinica (English Edition) 89(s2), 73-76.

Rollinson, H. & Adetunji, J. 2015b. The geochemistry and oxidation state of podiform chromitites from the mantle section of the Oman ophiolite: a review. Gondwana Research 27(2), 543-54.

Shervais, J.W. 2001. Birth, death, and resurrection: The life cycle of suprasubduction zone ophiolites. Geochemistry, Geophysics, Geosystems 2(1).

Snoke, A.W., Quick, J. E. & Bowman, H. R. 1981. Bear Mountain Igneous Complex, Klamath Mountains, California: an ultrabasic to silicic cale-alkaline suite. Journal of Petrology 22(4), 501-52.

Sobolev, A. T. & Batanova, V. 1995. Matnle Lherzolites of the Troodos Ophiolite Complex, Cyprus-Clinopyroxene Geochemistry Petrology 3(5), 440-48.

Springer, R. K. 1974. Contact metamorphosed ultramafic rocks in the western Sierra Nevada foothills, California. Journal of Petrology 15(1), 160-95.

Stern, R. 2005. Evidence from ophiolites, blueschists, and ultrahigh-pressure metamorphic terranes that the modern episode of subduction tectonics began in Neoproterozoic time. Geology 33, 557-60.

Stern, R. J. 1994a. Arc-Assembly and Continental Collision in the Neoproterozoic African Orogen: Implications for the Consolidation of Gondwanaland. Annual Review of Earth and Planetary Sciences 22, 319-51.

Stern, R. J. 1994b. Arc Assembly and continental collision in the Neoproterozoic East African orogeny - implications for the consolidation of Gondwana. Annual Review of Earth and Planetary Sciences 22, 319-51.

Stern, R. J., Johnson, P. R., Kröner, A. & Yibas, B. 2004. Neoproterozoic ophiolites of the Arabian-Nubian shield. Developments in Precambrian Geology 13, 95-128.

Tadesse, G. & Allen, A. 2004. Geochemistry of metavolcanics from the Neoproterozoic Tuludimtu orogenic belt, Western Ethiopia. Journal of African Earth Sciences 39(3), 177-85.

Tadesse, G. & Allen, A. 2005. Geology and geochemistry of the Neoproterozoic Tuludimtu Ophiolite suite, western Ethiopia. Journal of African Earth Sciences 41(3), 192-211.

Tamura, A. & Arai, S. 2006. Harzburgite–dunite–orthopyroxenite suite as a record of supra-subduction zone setting for the Oman ophiolite mantle. Lithos 90(1), 43-56.

Taylor Jr, H. P. & Noble, J. A. 1969. Origin of magnetite in the zoned ultramafic complexes of southeastern Alaska. Magmatic ore deposits 4, 209-30.

Tefera, M. 1991. Geology of the Kurmuk and Asosa area. Ethiopian Institute of Geological Survey draft Rep 109.

Uysal, I., Tarkian, M., Sadiklar, M. B., Zaccarini, F., Meisel, T., Garuti, G. & Heidrich, S. 2009. Petrology of Al-and Cr-rich ophiolitic chromitites from the Mugla, SW Turkey: implications from composition of chromite, solid inclusions of platinum-group mineral, silicate, and base-metal mineral, and Os-isotope geochemistry. Contributions to Mineralogy and Petrology 158(5), 659-74.

Whattam, S. A. & Stern, R. J. 2011. The 'subduction initiation rule': a key for linking ophiolites, intra-oceanic forearcs, and subduction initiation. Contributions to Mineralogy and Petrology 162(5), 1031-45.

Woldemichael, B. W. & Kimura, J.-I. 2008. Petrogenesis of the Neoproterozoic Bikilal-Ghimbi gabbro, Western Ethiopia. Journal of mineralogical and petrological sciences 103(1), 23-46.

Woldemichael, B. W., Kimura, J.-I., Dunkley, D. J., Tani, K. & Ohira, H. 2010. SHRIMP U–Pb zircon geochronology and Sr–Nd isotopic systematic of the Neoproterozoic Ghimbi-Nedjo mafic to intermediate intrusions of Western Ethiopia: a record of passive margin magmatism at 855 Ma? International Journal of Earth Sciences 99(8), 1773-90.

Yamamoto, K., Masutani, Y., Nakamura, N. & Ishii,

T. 1992. REE characteristics of mafic rocks from a fore-arc seamount in the Izu-Ogasawara region, western Pacific. Geochemical Journal 26(6), 411-23.

Zhou, M.-F. & Bai, W.-J. 1992. Chromite deposits in China and their origin. Mineralium Deposita 27(3), 192-99.

Zhou, M.-F., Robinson, P. & Bai, W. 1994. Formation of podiform chromitites by melt/rock interaction in the upper mantle. Mineralium Deposita 29(1), 98-101.

Zhou, M.-F. & Robinson, P. T. 1997. Origin and tectonic environment of podiform chromite deposits. Economic Geology 92(2), 259-62.

CHAPTER 4

This chapter is written for submission to *Gondwana Research* as:

Blades, M. L., Foden, J., Collins, A. S., Glorie, S., Alemu, T., Woldetinsae, G. The Geochemical Evolution of the Neoproterozoic Western Ethiopian Shield

Statement of Authorship

Title of Paper	The geochemical evolution of the Neoproterozoic Western Ethiopian Shield.
Publication Status	☐ Published ☐ Accepted for Publication ☐ Submitted for Publication ☑ Unpublished and Unsubmitted work written in manuscript style
Publication Details	Written for submission to Gondwana Research as: Blades, M. L., Foden, J., Collins, A. S., Glorie, S., Alemu, T., Woldetinsae, G. The geochemical evolution of the Neoproterozoic Western Ethiopian Shield.

Principal Author

Name of Principal Author (Candidate)	Morgan Blades		
Contribution to the Paper	Project fieldwork, sample preparation, data collection, processing and interpretation, manuscript design and composition, creation of figures		
Overall percentage (%)	80		
Certification:	This paper reports on original research I conducted during the period of my Higher Degree by Research candidature and is not subject to any obligations or contractual agreements with a third party that would constrain its inclusion in this thesis. I am the primary author of this paper.		
Signature		Date	06/09/2017

Co-Author Contributions

By signing the Statement of Authorship, each author certifies that:

    i.   the candidate's stated contribution to the publication is accurate (as detailed above);

    ii.   permission is granted for the candidate in include the publication in the thesis; and

    iii.   the sum of all co-author contributions is equal to 100% less the candidate's stated contribution.

Name of Co-Author	Professor Alan Collins		
Contribution to the Paper	Guidance in fieldwork, sample preparation, data interpretation and manuscript review.		
Signature		Date	06/09/2017

Name of Co-Author	Emeritus Professor John Foden		
Contribution to the Paper	Guidance in fieldwork, sample preparation, data interpretation and manuscript review.		
Signature		Date	06/09/2017

Name of Co-Author	Dr Stijn Glorie		
Contribution to the Paper	Guidance in sample preparation, data interpretation and manuscript review.		
Signature		Date	06/09/2017

Name of Co-Author	Tadesse Alemu		
Contribution to the Paper	Guidance in the field and logistics in Ethiopia		
Signature		Date	06/09/2017

Name of Co-Author	Dr Girma Woldetinsae		
Contribution to the Paper	Guidance in the field and logistics in Ethiopia		
Signature		Date	06/09/2017

Please cut and paste additional co-author panels here as required.

ABSTRACT

New geochemical and isotopic data indicate that igneous rocks in the Western Ethiopian Shield are predominantly calc-alkaline with characteristics consistent with emplacement within a volcanic or continental arc. Steeper rare earth element (REE) patterns and enrichment of incompatible trace elements are also consistent with subduction-related tectonic environments. The samples analysed show low high-field strength element (Ti, Zr, Nb and Y; HFSE) concentrations that are typical of sub-alkaline, island-arc volcanic rocks. Some samples have uncharacteristically high (>56 wt. %) SiO_2 (75–60. wt %), Al_2O_3 (> 15%), low MgO (0.6–0.1 wt %), low Y (5–3 ppm) and low heavy REE (e.g. Yb < 2 ppm) for volcanic arc rocks, indicating an adakite-like nature. High Sr/Y ratios are recorded and are interpreted to reflect melting from the deep lower crustal hot zone, rather than dehydration of the slab. These rocks formed from the fractional crystallization and assimilation of mantle derived parental magmas, as indicated by the isotopic data. The suites in western Ethiopia have variable but mostly high $^{87}Sr/^{86}Sr$ and high $^{143}Nd/^{144}Nd$ signatures, indicating some crustal involvement. These geochemical and isotopic data correlate with the other terranes in the Arabian Nubian Shield, but exhibit a stronger crustal isotopic signature. This indicates that the Western Ethiopian Shield terranes incorporated a kernel of pre-Neoproterozoic rocks and represents a transition from an oceanic arc to continental arc close to the Sahara Metacraton.

INTRODUCTION:

The East African Orogen is one of the largest Neoproterozoic to early Cambrian mobile belts that formed due to the closure of the Mozambique Ocean, as India collided with the continents that formed Gondwanan Africa (Collins and Pisarevsky, 2005c; Fritz et al., 2013a; Johnson et al., 2011c; Meert, 2003c; Stern, 2002a; Stern, 1994b). The East African Orogen is commonly divided into two along strike, with terranes of the Arabian Nubian Shield (ANS) in the north and Mozambique Belt in the South. The Arabian Nubian Shield is largely comprised of juvenile Neoproterozoic crust (Johnson et al., 2011b; Johnson and Woldehaimanot, 2003; Stern, 1994a, 2002b), dominated by low grade volcano-sedimentary rocks associated with plutonic rocks and ophiolitic remnants (Abdelsalam and Stern, 1996; Allen and Tadesse, 2003; Cox et al., 2012; Kröner et al., 1991; Robinson et al., 2014; Shackleton, 1996; Stern, 1994a). Older, Archaean and Palaeoproterozoic crust (2900–2000 Ma), is preserved in rocks from southern India, Madagascar, Somalia, eastern

Ethiopia to Arabia (Afif Terrane) and has been recognised as a microcontinent named Azania that collided with the Congo-Tanzania-Bangweulu Block at ca. 650–630 Ma (Collins and Pisarevsky, 2005a; Robinson et al., 2014; Stern, 2002b). In the south (Tanzania, Kenya, Madagascar) the East African Orogen is evident in a tract of older continental crust, with a Neoproterozoic to Cambrian metamorphic overprint (Collins and Pisarevsky, 2005b; Meert et al., 1997). A large, exposed, tract of outcrop exists in the transitional zone between the ANS and the Mozambique Belt named the Western Ethiopian Shield (WES) that provides important information on the tectonic evolution of northern Africa.

The WES is made up of a range of supra-crustal and plutonic rocks that formed in Tonian-aged volcanic arc environments, that are a representation of much of the East African Orogen's development (Alemu, 2005; Ayalew et al., 1990; Ayalew and Peccerillo, 1998; Blades et al., 2015; Braathen et al., 2001; de Wit and Aguma, 1977; Grenne et al., 2003;
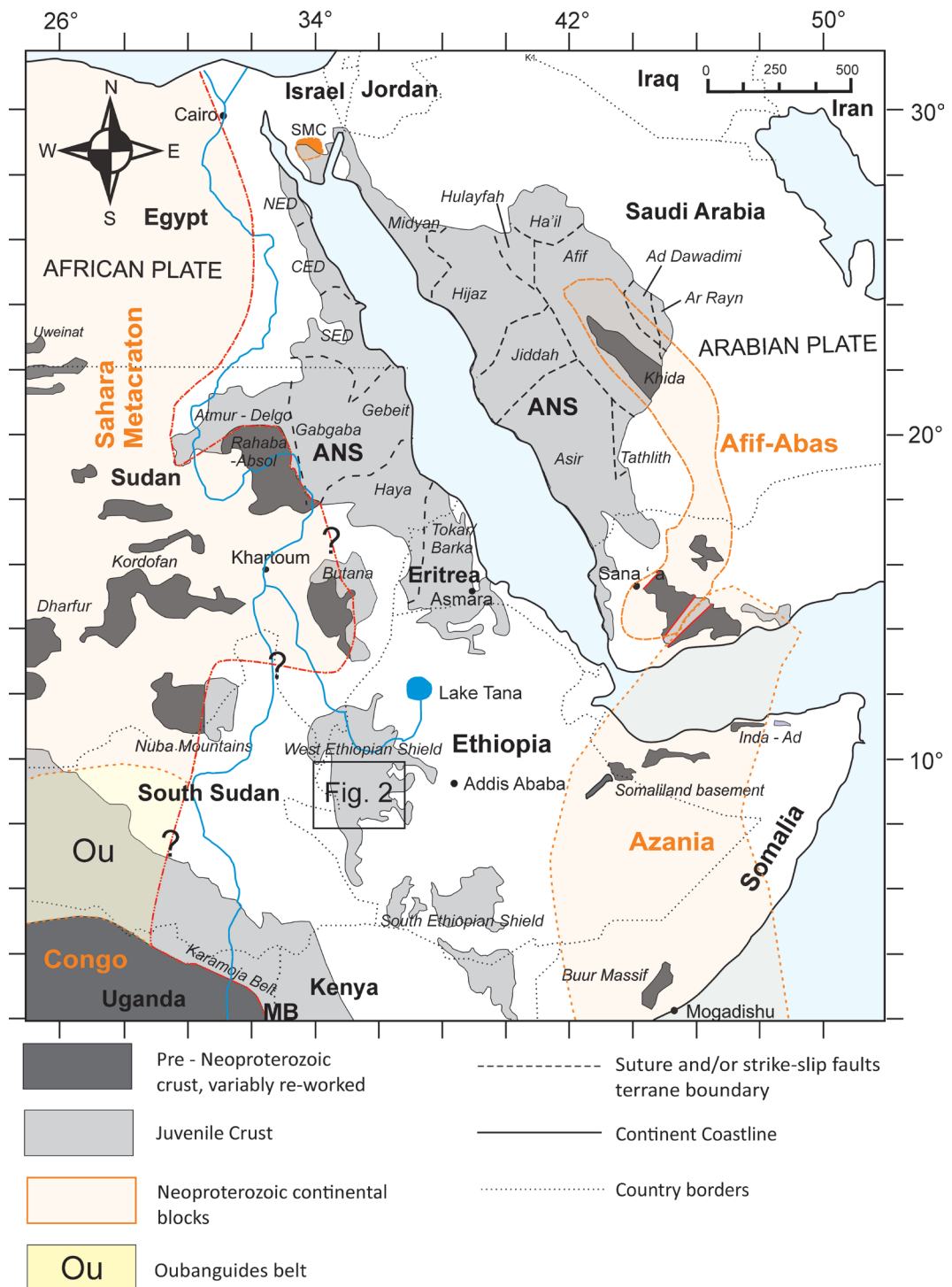
Figure 1: Location map and distribution of crustal domains in the East African Orogen. SM, Sahara Metacraton; ANS, Arabian Nubian Shield. MB, Mozambique Belt. The black box represents the map area in figure 2. Adapted from Johnson et al. (2011) and Blades et al. (2015).

Jackson, 2006; Johnson et al., 2004; Kebede et al., 2001a; Kebede and Koeberl, 2003; Kebede et al., 1999; Kebede et al., 2001b; Tadesse and Allen, 2004, 2005; Teklay et al., 1998; Woldemichael and Kimura, 2008; Woldemichael et al., 2010). Despite being well exposed and accessible, a comprehensive study of the WES has not been conducted and the

available datasets focus on a single suite (Ayalew et al., 1990; Grenne et al., 2003; Kebede et al., 1999). Here we present a comprehensive study of trace element and isotope geochemistry from a range of plutonic rock samples from the WES to determine the palaeotectonic setting and further elucidate the nature of arc magmatism during a time of major tectonic reorganisation.

GEOLOGICAL BACKGROUND
East African Orogen:
East Africa and Arabia represent fragments of the supercontinent Gondwana (Meert, 2003b; Stern, 1994b). The assembly of these fragments and their final configuration is relatively well documented (Collins and Pisarevsky, 2005a; Fritz et al., 2013b; Johnson et al., 2011a; Meert, 2003a; Meert and Lieberman, 2008). However, the sequence of events preceding Gondwana formation are complex and still being unravelled. The East African Orogen (EAO) is the largest Neoproterozoic to early Cambrian orogen that formed as the Mozambique Ocean closed and the amalgams of Neoproterozoic India and Africa collided (Collins and Pisarevsky, 2005a; Fritz et al., 2013b; Johnson et al., 2011a; Meert, 2003a; Meert and Lieberman, 2008). The products of volcanic arcs preserve a complex history of intra − oceanic and continental margin, magmatic and tectonothermal events (Collins and Pisarevsky, 2005a; Fritz et al., 2013b; Johnson et al., 2011a; Meert, 2003a; Meert and Lieberman, 2008). The East African Orogen can be divided into the Arabian Nubian shield (ANS) in the north (Fig. 1), composed of largely juvenile Neoproterozoic crust, and the Mozambique Belt in the south comprising mostly pre-Neoproterozoic crust with a Neoproterozoic–early Cambrian metamorphic overprint (Collins and Pisarevsky, 2005a; Fritz et al., 2013b; Johnson et al., 2011a; Meert, 2003a; Meert and Lieberman, 2008).

The Western Ethiopian Shield:
The Western Ethiopian Shield (Fig. 1) is located in the transitional zone between the Arabian Nubian Shield and Mozambique Belt (Abdelsalam and Stern, 1996). Lithologically and structurally there are several distinct domains that have been recognised in the Western Ethiopian Shield (Fig. 2). Here, we adopt the lithotectonic division outlined by Allen and Tadesse (2003), based on domains of shared lithological assemblages and geological histories (see Allen and Tadesse (2003) and Blades et al (2015) for a summary). The area is divided into five domains, interpreted to have formed during the amalgamation of western Gondwana before the final closure of the Mozambique Ocean (Allen and Tadesse, 2003) including the Didesa, Kemashi, Dengi, Sirkole and Daka Domains (Fig. 2). The basement is dominated by N–S striking structures, interpreted to be the result of E–W crustal shortening related to the amalgamation of the terranes of Gondwana (Stern, 1994b)

The Baruda–Tulu Dimtu zone (Fig. 2) stretches through Ethiopia and connects with the Barka zone in Eritrea (Braathen et al., 2001; Stern, 1994a; Tadesse and Allen, 2004, 2005). These regional shear zones were interpreted as ophiolitic sutures, representing the major boundaries that separate arc terranes that accreted during amalgamation of eastern and western Gondwana (Stern, 1994a; Tadesse and Allen, 2004, 2005). Recently published data from the ultramafic rocks of the Western Ethiopian Shield, show that a common feature of the chemistry of spinels in these ultramafic rocks, is their high Cr# (from 33 to 99), lower Mg# (0.117-0.464) and a trend towards Fe^{3+}- rich compositions that is typical of arc-related settings. The high Cr (>0.6) and low Ti character of the primary spinels in peridotite and chromite suggest a supra-subduction
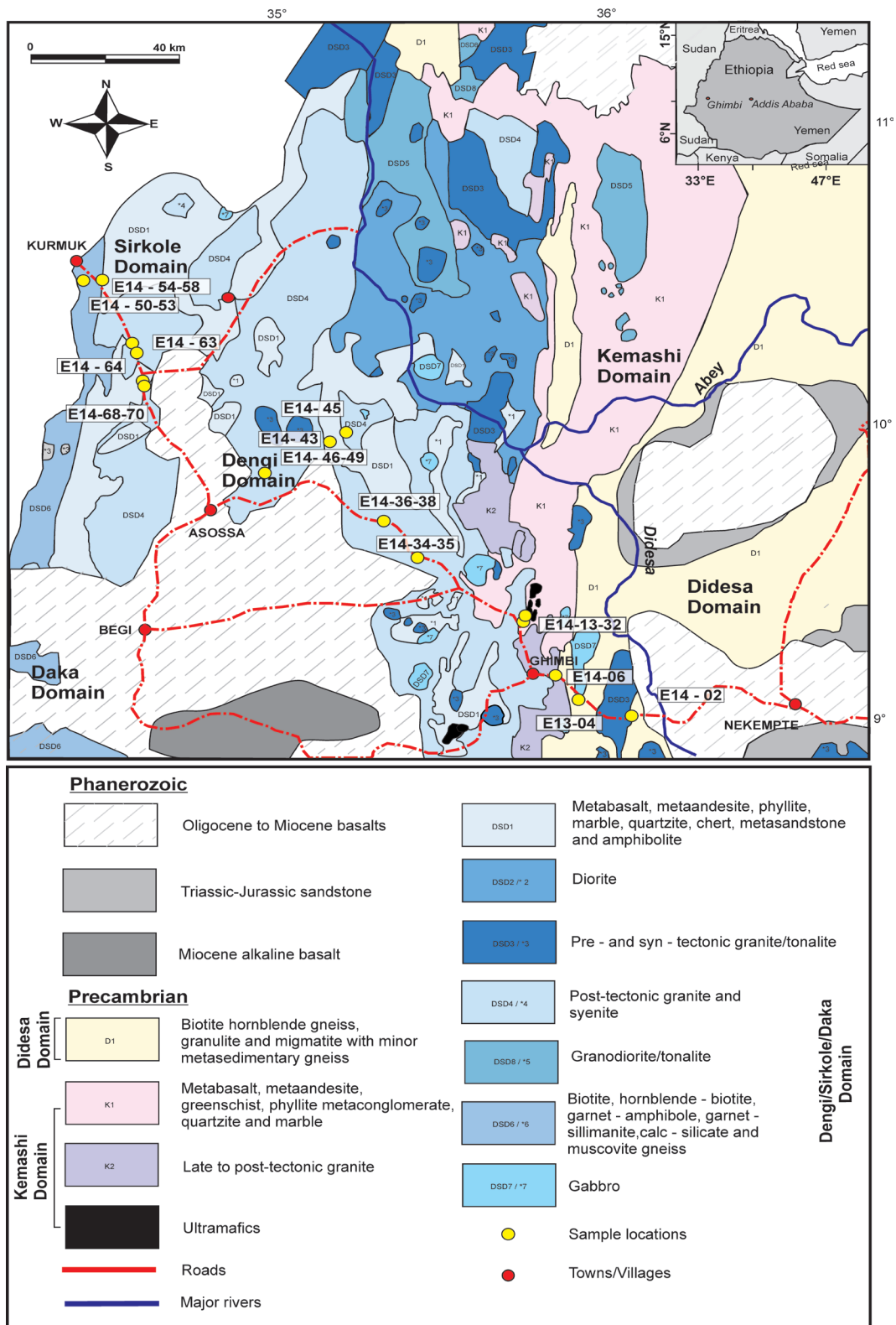
Figure 2: Simplified geological maps of the study regions. Simplified geological map of the area of study in western Ethiopia. Adapted from geological map of western Ethiopia (2nd edition), scale 1:2 000,000, published by the Geological Survey of Ethiopia (1996)

Table 1: Main field relationships and minerology of samples from the Western Ethiopian Shield. Available age data (Blades et al., in prep) has been quoted in the table.

Sample ID	Main Field Relationships	Locality description	GPS Location	Minerology	Analyses completed	Rock Type	Age (Ma)
E14 . 02	Foliated gneiss is cross-cut but by K-feldspar rich granite. Field relationships similar to those seen at Didesa river	5 km west of the Didesa River Bridge next to Jogir river	N 09° 02' 15.4" E 36° 02' 07.4"	Holocrystalline, large grains, Qtz + Pl + Kfs	LA-ICP-MS U/Pb, Hf	Granite Pegmatite	664 ± 18 Ma
E14 . 04	No fabric present, outcrop forms in rounded boulders	Located on hillside above road, ~ 15km from Didesa River Bridge	N 09° 02' 15.4" E 36° 02' 07.4"	Holocrystalline, equigranular, Qtz + Pl + kfs + Bt + Grt + Mc	LA-ICP-MS U/Pb, Hf	Suqii - Wagga Granite	853 ± 9 Ma
E14.06	No foliation present. Map features suggest that this is surrounded by a pre-tectonic gabbro. No field evidence for this.	10km west of Gimbi	N 09° 08' 06.8" E 35° 52' 53.6"	Holocrystalline, equigranular, coarse grained. Plag, Px. Late stage needle like mineral present (actinolite)	Nd-Sm, Rb-Sr and major and trace elements	Gabbro	
E14.13	Sitting in melange, little identifying field relationships. Taken from a dyke, hosted in talc-serpentinite-schist	Located in Abshala Melange	N 09° 23' 16" E 35° 43' 15.9"	Seriate, with Plg + Px and other minerals. Hard to determine due to large amounts of Hbl	Nd-Sm, Rb-Sr and major and trace elements	Abshala melange basalt	
E14.14	Sitting in melange, little identifying field relationships. Taken from a dyke, hosted in talc-serpentinite-schist	Located in Abshala Melange	N 09° 23' 16" E 35° 43' 15.9"	Fine grained, with coarse grains of amphibole.	Nd-Sm, Rb-Sr and major and trace elements	Abshala melange basalt	
E14.17	Sitting in melange, little identifying field relationships. Taken from a dyke, hosted in talc-serpentinite-schist	Located in Abshala Melange	N 09° 23' 16" E 35° 43' 15.9"	Holocrystalline, fine grained groundmass of pyroxene, feldspar (hard to determine) with larger grains of Am. Pockets of opaque minerals.	Nd-Sm, Rb-Sr and major and trace elements	Abshala melange basalt	

Table 1: Main field relationships and minerology of samples from the Western Ethiopian Shield. Available age data (Blades et al., in prep) has been quoted in the table.

Sample ID	Main Field Relationships	Locality description	GPS Location	Minerology	Analyses completed	Rock Type	Age (Ma)
E14.27	Ignimbrite/Dacite. Fine grained alignment of minerals	Sayi River Bridge	N 09° 26' 45.4" E 35° 47' 26"	Porphyritic. Fine grained ground mass (Qtz, Feldspar, opaques) with larger grains of Qtz and Ksp. Foliation defined by Mu	Nd-Sm, Rb-Sr and major and trace elements	Dacite	
E14.29	Basalt dyke intruding next to a marble. Dyke is folded	Located 200m W of Dere Dimtu Village	N 09° 26' 12.1" E 35° 42' 42.1"	Fine grained, plag + pyroxene	Nd-Sm, Rb-Sr and major and trace elements	Basalt	
E14.30	Basalt dyke sampled further upstream from E14.29. Dyke is folded	Located in a stream adjacent to Dere Dimtu Village	N 09° 26' 12.1" E 35° 42' 42.1"	Fine grained, plag + pyroxene	Nd-Sm, Rb-Sr and major and trace elements	Basalt	
E14.36	Sample is located with cross cutting felsic veins, seen in association with sample E14.38. No visible deformation	Located in Gori Quarry, close to Gori Village.	N 09° 37' 18.9" E 35° 19' 16.4	Holocrystalline, Intergranular. Plag, Opx, Ksp and small amounts of Qtz	Nd-Sm, Rb-Sr and major and trace elements	Gori Gabbro	
E14 . 38	Mafic dykes cross cut the granodiorite. Little to no deformation in the country rock and the presence of a chilled margin suggesting that they are co-magmatic.	Located in Gori Quarry, close to Gori Village.	N 09° 37' 18.9" E 35° 19' 16.4"	Seriate texture, large anhedral, poikilitic grains Qtz + Kfs + Bt	LA-ICP-MS U/Pb, Hf	Gabbroic Diorite	843 ± 14 Ma
E14.39	Basalt dykes are locally deformed. Dykes seem to be co-magmatic with other phases (granodiorite). The country rock is not deformed and the basalt dyke has a chilled margin	Located 5 Km from Gori Village	N 09° 38' 33.7" E 35° 19' 13.4"	Fine grained, plag + pyroxene	Nd-Sm, Rb-Sr and major and trace elements	Basalt	

Table 1: Main field relationships and minerology of samples from the Western Ethiopian Shield. Availiable age data (Blades et al., in prep) has been quoted in the table.

Sample ID	Main Field Relationships	Locality description	GPS Location	Minerology	Analyses completed	Rock Type	Age (Ma)
E14.41	Basalt dykes are locally deformed. Dykes seem to be co-magmatic with other phases (granodiorite). The country rock is not deformed and the basalt dyke has a chilled margin	Located 5 Km from Gori Village	N 09° 38' 33.7" E 35° 19' 13.4"	Holocrystalline, fine grained with Qtz, Opx and Am.	Nd-Sm, Rb-Sr and major and trace elements	Basalt	
E14.42	Massive Bt + Hbl granodiorite which is cross cut by fine mafic dykes that have been locally foliated. Granodiorite is undeformed. Likely co-magmatic.	Under bridge in Komis River, close to Gori.	N 09° 38' 33.7" E 35° 19' 13.4"	Holocrystalline, coarse grained, equigranular Am + Pl + Qtz + Px + Bt	Nd-Sm, Rb-Sr and major and trace elements	Granodiorite	
E14 . 43	Porphyritic texture with large K – feldspar crystals in a finer plagioclase and quartz matrix. No fabric	Located on the Mendi – Daleti Road	N 09° 57' 23.7" E 35° 09' 59.8"	Seriate texture, large anhedral, poikilitic grains Qtz + Kfs + Pl + Mc + Bt	LA-ICP-MS U/Pb, Hf	K - Feldspar Granite	771 ± 37 Ma
E14.44	Porphyritic texture with large K – feldspar crystals in a finer plagioclase and quartz matrix. Defined fabric.	Located 2km from Daleti	N 09° 57' 23" E 35° 09' 59"	Porphyritic. Qz + Ksp + Bt + Plag. Foliation present Ksp define the larger grains in the sample. Am present.	Nd-Sm, Rb-Sr and major and trace elements	Porphyritic granite	
E14.46	Green, medium grained. Locally strained	Koncho Village	N 10° 03' 35.6" E 35° 16' 42"	Acicular needles of Opx, feldspars exhibit undulose extinction, likely related to deformation and/or metamorphism	Nd-Sm, Rb-Sr and major and trace elements	Gabbro	

Table 1: Main field relationships and minerology of samples from the Western Ethiopian Shield. Availaible age data (Blades et al., in prep) has been quoted in the table.

Sample ID	Main Field Relationships	Locality description	GPS Location	Minerology	Analyses completed	Rock Type	Age (Ma)
E14.47	Outcrop adjacent to E14.46. Medium grained, though does not have the same level of deformation present	Koncho Village	N 10° 03' 35.6" E 35° 16' 42"	Holocrystalline, equigranular, med - coarse grains. Plag + Pyroxene	Nd-Sm, Rb-Sr and major and trace elements	Gabbro	
E14.50	Not well foliated and cross cuts the well foliated granodiorite gneiss (E14 – 53).	Located 3 km South of Kurmuk in a river outcrop	N 10° 32' 28.1" E 34° 19' 06.2"	Holocrystalline, granular, hypidiomorphic, quartz and feldspar have a poikilitic textures, Qtz + Pl + Bt + Kfs	LA-ICP-MS U/Pb, Hf	Granite	868 ± 16 Ma
E14.51	Felsic dyke cross cutting gneiss (E14.53)	Located 3 km South of Kurmuk in a river outcrop	N 10° 32' 28.1" E 34° 19' 06.2"	Holocrystalline, seriate texture, large anhrdral, poikilitic grains Qtz + Kfs + Pl + Mu + Bt	Nd-Sm, Rb-Sr and major and trace elements	Felsic dyke	
E14.53	Gneissic texture and is being cross but by E14 - 50 (granite).	Located 3 km South of Kurmuk in a river outcrop	N 10° 32' 28.1" E 34° 19' 06.2"	Holocrystalline, equigranular, subhedral, perthitic textures Qtz + Kfs + Pl + Bt and Mu. Bt defines a fabric	LA-ICP-MS U/Pb, Hf	Gneiss	853 ± 7 Ma
E14.53a	Samples located with E14.50 and 53. Sample seen mingling with E14.53.	Located Located 3 km South of Kurmuk in a river outcrop	N 10° 32' 28.1" E 34° 19' 06.2"	Holocrystalline, Seriate, medium, anhedral grains. Pyroxene, Plag, Am. The Pyroxene grains occur as larger grains in a finer groundmass.	Nd-Sm, Rb-Sr and major and trace elements	Amphibolite	

Table 1: Main field relationships and minerology of samples from the Western Ethiopian Shield. Available age data (Blades et al., in prep) has been quoted in the table.

Sample ID	Main Field Relationships	Locality description	GPS Location	Minerology	Analyses completed	Rock Type	Age (Ma)
E14.55	Chlorite - Bt phyllite host rocks Granitic phase (E14.56) cross cuts finer grained phyllite. Both units are deformed, with tension gashes present.	Located in a road cutting 3km East of Kutawark, at the base of an escarpment	N 10° 33' 48.3" E 34° 24' 44.6"	Holocrystalline, granular, Seriate very fine grained. Qtz + Bt + Plag.	Nd-Sm, Rb-Sr and major and trace elements	Chlorite -Bt - Phyllite	
E14.56	Phyllite (E14.55) is the host rocks Granitic phase cross cuts finer grained phyllite. Both units are deformed, with tension gashes present.	Located in a road cutting 3km East of Kutawark, at the base of an escarpment	N 10° 33' 48.3" E 34° 24' 44.6"	Holocrystalline, granular, fine grained. Foliation defined by Mu. Qtz + Pl and Ksp. Areas where deformation of the grains has not occurred. Though Qtz seems to be	Nd-Sm, Rb-Sr and major and trace elements	Granite	
E14 . 58	Host rock is a chlorite - biotite phyllite. The foliated leucogranite shows a well-defined intrusive relationship with the greenschist phyllite.	Collected 3km East of Kutawark	N 10° 33' 48.3" E 34° 24' 48.6"	Larger grains have poikilitic texture giving it a sponge appearance Qtz + Pl + Kfs + Bt	LA-ICP-MS U/Pb, Hf	Leucogranite	835 ± 7 Ma
E14 . 63	Homogeneous, unfoliated granite	Road side outcrop located near Shula Village (Argubella) Shula Village,	N 10° 23' 42.7" E 34° 34' 43.6"	Holocrystalline, equigranular, subhedral Qtz + Pl + Kfs + Bt + Hbl	LA-ICP-MS U/Pb, Hf	Granite	774 ± 7 Ma
E14 . 64	Homogeneous, unfoliated granite	large road side outcrop near Shekula refugee camp	N 10° 20' 47.1" E 34° 37' 22.3"	Holocrystalline, equigranular, smaller grain size, perthite textures, Qtz + Pl + Kfs + Bt opaques	LA-ICP-MS U/Pb, Hf	Foliated K - Feldspar granite	796 ± 20 Ma

Table 1: Main field relationships and minerology of samples from the Western Ethiopian Shield. Available age data (Blades et al., in prep) has been quoted in the table.

Sample ID	Main Field Relationships	Locality description	GPS Location	Minerology	Analyses completed	Rock Type	Age (Ma)
E14.65	Homogeneous, unfoliated granite. Relatively large Ksp grains and notable hornblende	2 km S of Homosha at the top of a hill with prominent exposure	N 10° 20' 47.1" E 34° 37' 22.3"	Holocrystalline, subhedral grains of Qtz + Mc + Plag + Ksp + Am	Nd-Sm, Rb-Sr and major and trace elements	Alkali Granite	
E14 . 68	Gradational boundary between the monzonite and the granite (E14 - 69). Intermingling textures present	Homosha Village. 5km from Shekula Refugee Camp towards Asosa	N 10° 16' 09.8" E 34° 37' 29.9"	Holocrystalline, seriate texture, large anhedral, poikilitic grains Qtz + Kfs + Pl + Mc + Bt	LA-ICP-MS U/Pb, Hf	Monzonite	854 ± 14 Ma
E14 . 69	Psammitic xenoliths are seen, forming a chilled margin as a result of rapid cooling of the magma adjacent to the colder country rocks and xenoliths.	Homosha Village. 5km from Shekula Refugee Camp towards Asosa	N 10° 16' 09.8" E 34° 37' 29.9"	Holocrystalline, seriate texture, large anhedral, perthitic textures Qtz + Kfs + Pl + Mc + Bt	LA-ICP-MS U/Pb, Hf	Granite	840 ± 8 Ma
E14 . 70	Epidote veins present, no foliation.	Homosha Village. 5km from Shekula Refugee Camp towards Asosa	N 10° 16' 09.8" E 34° 37' 29.9"	Holocrystalline, seriate texture, subhedral, perthitic textures Qtz + Pl + Kfs + Bt + Hbl	LA-ICP-MS U/Pb, Hf	Granodiorite	806 ± 5 Ma

zone tectonic setting (Blades et al., in press). Distinct chemical differences between the igneous plutons, namely Daleti and Yubdo, were interpreted to be examples of both solitary intrusions and refractory oceanic crust (Blades et al., in press). The spinel chemistry unequivocally shows that they were formed on a convergent margin, above a subduction zone (Blades et al., in press).

Geochronology and geochemistry within the WES.

The Western Ethiopian Shield experienced three main phases of magmatism at ca. 850–810 Ma, 780–700 Ma and 620–550 Ma (Ayalew et al., 1990; Ayalew and Peccerillo, 1998; Kebede et al., 2001a; Kebede et al., 1999; Kebede et al., 2001b). These magmatic episodes were interpreted to represent pre-, syn- and post-tectonic environments (Woldemichael and Kimura, 2008; Woldemichael et al., 2010). However, these have been shown to be complicated by metamorphism/deformation occurring both at ca. 790–780 Ma and at ca. 660–655 Ma. Recently published hafnium isotopic data indicates that these magmas were generated from juvenile Neoproterozoic mantle sources with little involvement of the pre-Neoproterozoic continental crust (Blades et al., 2015). The Ganjii granite pluton is a post-tectonic granite with an age of 584 ± 10 Ma and places a minimum constraint on pervasive deformation in the Western Ethiopian Shield (Blades et al., 2015).

Previous data indicates that pre- and syn-tectonic intrusions are calc-alkaline and arc-tholeiitic rocks that have been interpreted to have been formed from the fractional crystallization of mantle derived parental melts (Ayalew et al., 1990; Ayalew and Peccerillo, 1998; Belete et al., 2000; Braathen et al., 2001; Grenne et al., 2003; Kebede and Koeberl,

2003; Kebede et al., 1999; Kebede et al., 2001b). Volcanic rocks have been interpreted to be calc-alkaline and have low values of high-field strength elements such as Ti, Zr, Nb and Y, typical of sub-alkaline, island-arc volcanic rocks (Pearce, 1982; Woldemichael and Kimura, 2008; Woldemichael et al., 2010). MORB-normalised trace-element profiles for the basalt and basaltic andesite, as well as Zr-Nb relations in the more felsic rocks, suggest a high-K calc-alkaline affinity for the entire suite that is similar to rocks from mature oceanic arcs (Pearce, 1982). Grenne et al. (2003) suggested that the highly evolved, high-K to medium-K, calc-alkaline nature of the intermediate and felsic rocks of the Debesa metavolcanic rocks is typical of active continental margin magmatism. Mafic lavas have calc-alkaline and enriched MORB-like geochemical characteristics, a signature that is compatible with a continental back-arc or rifted-arc tectonic setting (Grenne et al., 2003; Johnson et al., 2004). The data presented by Green et al., (2003) has been compared to the geochemical characteristics recorded in arc rocks in New Zealand and rocks related to back-arc basin opening in the Japan Sea and the Banda Arc in Indonesia (Honthaas et al., 1998; Pouclet et al., 1994; Ujike and Tsuchiya, 1993). Stronger enrichment of highly incompatible trace elements epitomise arc extensional volcanic rocks of the Andean arc (Petford and Atherton, 1995).

Late to post-tectonic plutonic rocks are enriched relative to earlier intrusions and are characterised by incompatible trace element compositions that are between subduction-related and intraplate granites. Elemental variations suggest a shoshonitic chemical affinity for the post tectonic bodies and have been interpreted to be related to the melting and assimilation of calc-alkaline continental crust, followed by fractional crystallization
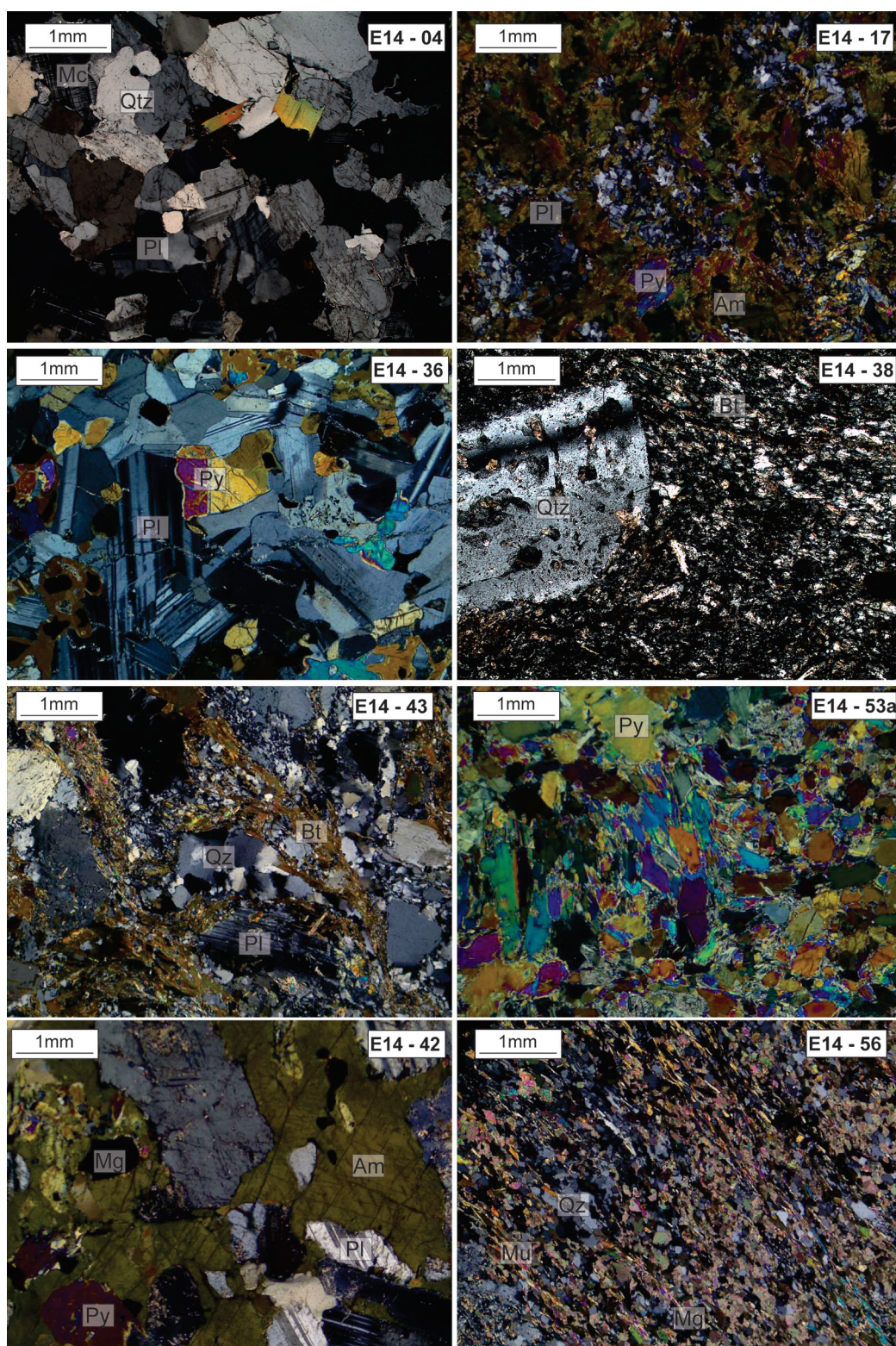
Figure 3: Representative thin section images in cross polarised light from samples collected in western Ethiopia. Minerals present are labelled where: Qtz is quartz; Bt is biotite; Pl is plagioclase; Mc is microcline and Ksp is K-feldspar, Am is amphibole, Py is pyroxene. E14-04: Suqii -Wagga Granite, E14-17: Abshala Melange Basalt, E14-36: Gori Gabbro, E14-38: Gabbroic Diorite, E14-43: K-Feldspar Granite, E14-53a: Amphibolite, E14-56: Granite. Sample descriptions can be found in Table 1.
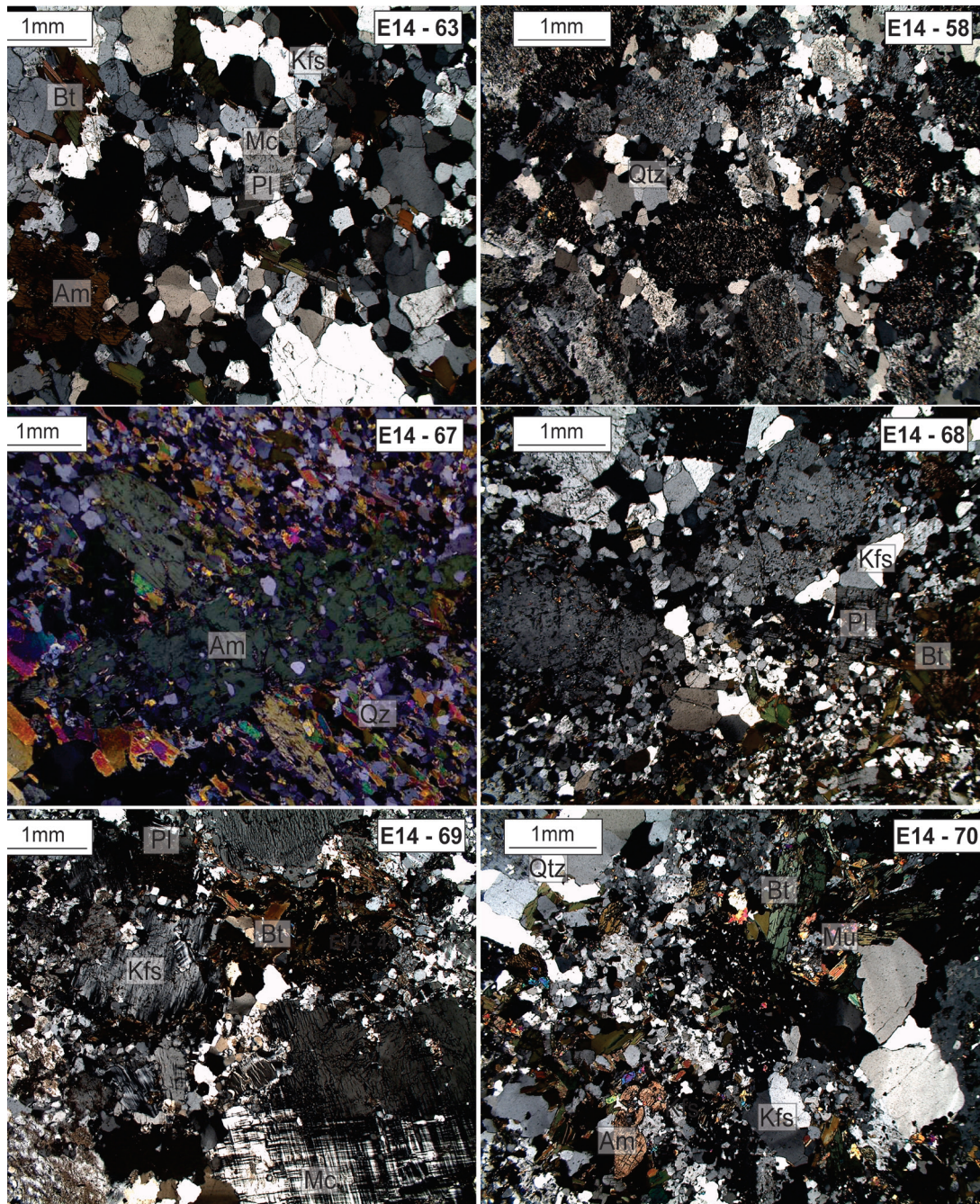
Figure 3: Representative thin section images in cross polarised light from samples collected in western Ethiopia. Minerals present are labelled where: Qtz is quartz; Bt is biotite; Pl is plagioclase; Mc is microcline and Ksp is K-feldspar, Am is amphibole, Py is pyroxene. E14-53: Gneiss, E14-58: Leucogranite, E14-63: Granite, E14-68: Monzonite, E14-69: Granite, E14-70: Granodiorite. Sample descriptions can be found in Table 1.

and continued assimilation (Morrison, 1980). Isotopic data collected from the Western Ethiopian Shield are sporadic, however, most rock samples have positive $\varepsilon_{Nd}(t)$ values between +0.4 and +8.6 (Grenne et al., 2003; Woldemichael and Kimura, 2008) and low initial 87Sr/86Sr ratios (0.7029 ± 0.0002)

(Woldemichael et al., 2010).

METHODS

A complete description of the methods employed in this study is available in the supplementary Appendix A. Thirty-four polished thin sections were examined under

transmitted and reflected light to determine mineralogy, textures. Fractions of the same samples were selected for whole-rock geochemical analyses for major, minor and trace elements at ACME Labs in Vancouver, Canada. In addition, twelve samples, five of which were dated by U–Pb geochronology (Blades et al., 2015) were analysed for Nd–Sm and Sr isotopic data. The Nd–Sm and Sr isotope analyses were done at the University of Adelaide and the complete methodology can be found in the supplementary material. The chosen samples are considered to represent the assortment of plutonic lithologies present in the Western Ethiopian Shield.

RESULTS
Petrography and field relationships
The Western Ethiopian Shield is made up of a series of amphibolite facies para- and ortho- gneissic rocks that are intruded by Neoproterozoic plutonic rocks (Fig. 2). These terranes are separated by the N–S trending Baruda–Tulu Dimtu shear zone (Fig. 2). The metasedimentary rocks are comprised of cherts and quartzites with associated mafic to ultramafic material. All of these rocks were metamorphosed to upper greenschist/ amphibolite facies during the Neoproterozoic. Within these terranes (especially the Kemashi), mélanges exist, containing rocks with distinct and disparate histories (Alemu and Abebe, 2000). Lithologically, these mélanges contain tectonically mixed rock-types; metabasalt/ amphibolite, peridotite and quartzite/chert. Representative samples were collected from these bodies and their field relationships and petrography (Fig. 3) can be found in Table 1.

Whole-rock geochemistry
Thirty four samples were selected for whole-rock geochemical analysis including four duplicate samples. All major and trace element

data are in Appendix 4: Table 1. Isotope data (Nd and Sr) are found in Table 1. The plutonic samples collected from Western Ethiopia, have a wide range of lithologies from ultramafic to granitic (Fig. 3), with SiO_2 concentrations ranging between 28 and 75 wt%. To determine the mobility of the major elements, these were plotted against the loss of ignition (LOI). Non-surprisingly ultramafic samples have a high LOI (>5%) and have therefore been excluded from Figure 4, due to alteration effects. No other definable patterns can be seen and therefore these have been interpreted to represent primary signatures.

Increasing silica content (Fig. 4) corresponds to depletions in MgO (0.04–42.75 wt%), CaO (0.01–12.3 wt%), MnO (0.01–0.74) and Fe_2O_3T ($FeO+Fe_2O_3$; 0.29–22.04). Increasing K_2O (0.01–4.81) and Na_2O (0.01–6.43) positive correlates with SiO_2. Inflected trends between TiO_2 (0.01–3.19) and P_2O_5 (0.01–0.63) indicate that fractional crystallisation was an important process (Chazen and Vogel, 1974). This inflected TiO_2 and P_2O_5 trend is likely due to the crystallisation of apatite (supported by the decreasing CaO trend) and Fe–Ti oxides. Other trace elements such as Y and Ce show inflection trends indicating a new crystallisation phase and the removal of these REE elements from the system. The positive correlation between Ca and Mg# indicates the co-precipitation of plagioclase and clinopyroxene.

Trace element geochemistry
Primitive mantle-normalised spider plots are lithologically subdivided based on petrographic data (Fig. 6). These samples have been divided based on lithology, with Figure 6 corresponding to granitic, basaltic and gabbroic, respectively. Samples (Fig. 6a; predominantly from the edge of the Dengi to Sirkole Domain) are characterised

by >56% SiO_2 (75–60 wt%), > 15% Al_2O_3, < 3% MgO (0.6–0.1 wt%), low Y (5.5–3.3 ppm) and low HREE (for example, Yb < 1.9 ppm respectively), high Sr, low HFSEs. They have Na_2O values between 3.53 and 5.72 wt% and Mg# ($Mg/Mg^{2+} + Fe^{2+}$) for these samples are between 23 and 47. The more felsic samples (Fig. 6a) show enrichment in the large-ion-lithophile-elements and depletions in high field strength elements (HFSE) such as Ta–Nb and Ti. Rock samples are characterised by a strong incompatible element enrichment and steep negative REE patterns (La_N/Yb_N ratios 0.82–70.4) and Eu/Eu* ratios between 0.44–1.52 (Appendix 4: Table 1). Basaltic rocks collected from mostly from the Abshala mélange, have a flat REE pattern and show strong depletions in K and Sr (Fig. 6b). They display incompatible element enrichment and steep REE patterns (La_N/Yb_N ratios 5.02–32.48). These basalts have negative anomalies for P, Ti and Eu (Fig. 6b). Lastly, gabbroic samples have relatively flat trace element patterns (Fig. 6c), with a slight enrichment in incompatible elements (La_N/Yb_N ratios between 0.89–15.64). The REE plot shows that these samples can be subdivided into two groups. One group has a flatter REE pattern and the other exhibiting a more defined negative slope. The Eu/Eu* ratios are between 0.88 and 1.13. REE and extended incompatible element patterns show enrichment in large-ion-lithophile-elements and relative depletion in heavy REE. All samples display marked negative HFSE (Nb, Ta and Ti) anomalies (Fig. 6c).

REE and extended incompatible element patterns (Fig. 6c) show a calc-alkaline trend (Tatsumi et al., 1986), enrichment in large-ion-lithophile-elements and relative depletion in heavy REE. These elements may be strongly controlled by the crystallization of individual minerals. For example, phosphorus concentrations are likely controlled by apatite crystallization and Ti and Nb by the precipitation of Ti-oxides (ilmenite, rutile or sphene). The Eu anomalies seen in all samples are related to the fractionation of plagioclase feldspar (Pearce, 1982; Pearce et al., 1984; Pearce and Norry, 1979). Depletion of Nb, Ta, Ti, Hf, and Zr compared to their neighbouring elements on spider plots (Pearce, 1982), are characteristic of convergent margin boundaries (Fig. 6), with negative Nb anomaly suggesting some involvement of continental crust. (Pearce, 1982). These signatures seen within the WES samples are supported by the incompatible element enrichment and steep REE patterns (La_N/Yb_N ratios 5.02–32.48), and are typical of calc-alkaline basalts that formed in an arc setting (Pearce, 1982; Pearce and Norry, 1979; Pearce and Peate, 1995). Together, with other geochemical data, these are typical of subduction related magmas (Pearce, 1982; Pearce and Norry, 1979; Pearce and Peate, 1995).

The Sr, Y and REE values correspond to Sr/Y > 40 and La/Yb > 20 that plot in the field tonalite-trondjemite-granodiorite rocks (TTGs) or adakites (Fig. 5c–f; Martin et al., 2005; Moyen, 2009; Rollinson and Tarney, 2005). Samples can be broadly subdivided into two groups based on concentrations of K with some samples exceeding 1000 ppm. Rb concentrations are between 10 and 100 ppm. K/Rb ratios (Fig. 5e) are near constant, plotting in the field of other known adakitic rocks (Rollinson and Tarney, 2005) and arc-related rocks. Th–U data (Fig. 5f) have a near constant ratios and define a trend similar to that defined by arc volcanic rocks (Hawkesworth et al., 1997; McDermott and Hawkesworth, 1991).

Nd–Sr Radiogenic Isotopes

Twelve samples, including one duplicate (13), were selected for Sm–Nd and Sr isotopic analyses
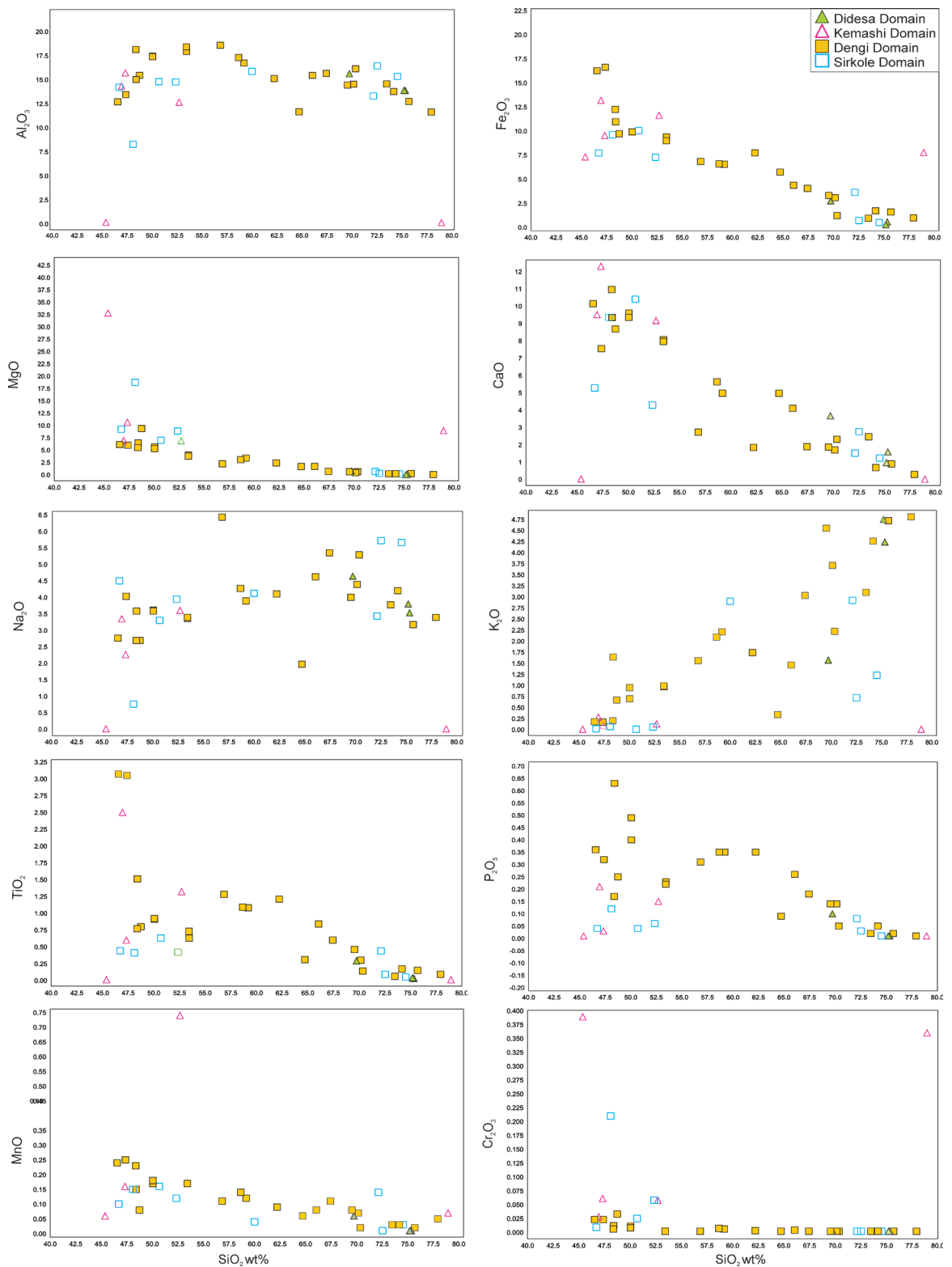
Figure 4: Harker major-element variation diagrams for major-element oxides, showing the extent of fractionation in the Western Ethiopian Shield. Samples are divided based on their respective Domain.

(Table 1). These samples are representative of the differing rock types in the WES. Samples have a $^{87}Sr/^{86}Sr_{(t)}$ ratios between 0.702015 and 0.714862. The $^{143}Nd/^{144}Nd_{(t)}$ ratios are between 0.511725 and 0.512353 and these correspond to positive $\varepsilon_{Nd}(t)$ values suggesting a more juvenile source material (Fig 7a; $\varepsilon_{Nd}(t)$ between 5.58–3.15), and the corresponding T_{DM} (depleted mantle) model ages are between 1287 and 906 Ma. These values suggest that these are largely juvenile, with minimal direct crustal input, these correspond to $\varepsilon_{Nd}(t)$ values for other rocks in the Arabian Nubian Shield (Fig. 9a). The $^{87}Sr/^{86}Sr(t)$ and $^{143}Nd/^{144}Nd(t)$ plot these samples in the high Rb–Sr, high Sm–Nd quadrant, similar to Andean arc values (Fig. 7b), indicating a proportion of crustal input these plot closer to known samples from Andean arcs, which perhaps suggest a proportion of crustal input (Fig. 7b) (Hawkesworth et al., 1993). The correlation between $^{144}Nd/^{143}Nd$ (t) and SiO_2 and Mg# (Fig. 5a and b; 0.07–0.89) suggest that the trace element and isotopic evolution in the magma chamber were affected simultaneously by fractional crystallisation and wall-rock assimilation (AFC).

DISCUSSION

What is the nature of magmatism in the Western Ethiopian Shield?

The Western Ethiopian Shield is made up of a range of supra-crustal and plutonic rocks that have been previously interpreted to be arc-related (Alemu, 2005; Ayalew et al., 1990; Ayalew and Peccerillo, 1998; Blades et al., 2015; Braathen et al., 2001; de Wit and Aguma, 1977; Grenne et al., 2003; Jackson, 2006; Johnson et al., 2004; Kebede et al., 2001a; Kebede and Koeberl, 2003; Kebede et al., 1999; Kebede et al., 2001b; Tadesse and Allen, 2004, 2005; Teklay et al., 1998; Woldemichael and Kimura, 2008; Woldemichael et al., 2010). Here we test the validity of these proposed

tectonic settings with a larger dataset from across the Western Ethiopian Shield. These interpretations are supported by the data presented here, which show deficiencies in Nb, Ta, Ti, Hf, and Zr (Fig. 6), enrichment in LILE and depletion in HREE. The steep REE patterns (La_N/Yb_N ratios 5.02–32.48) are typical of calc-alkaline rocks that formed in an arc setting (Pearce, 1982; Pearce and Norry, 1979; Pearce and Peate, 1995). Fig. 6a). Using initial $^{143}Nd/^{144}Nd(t)$ and Mg#, an apparent curvilinear trend is seen suggesting that both fractional crystallisation and assimilation (Fig. 5a and b)(DePaolo, 1981). This is supported by field evidence, which commonly shows magma mixing and mingling textures. Discrimination plots (Fig. 8a, b and c) show that majority of these data plot in the calc-alkaline field and have similar geochemistry to other data from the Arabian Nubian Shield. All of the data combined support that these rocks were formed in an arc environment, forming the basis for our tectonic model for the evolution of the Western Ethiopian Shield.

Some samples from the Western Ethiopian Shield have high Sr/Y (54.29–556.78) that are typical of adakite-type rocks (Moyen, 2009). Typically, the occurrence of adakitic rocks are the result of AFC and are observed in association with 'non-adakitic' rocks (from the same volcano). The adakitic-style samples within the Western Ethiopian Shield are highlighted on the classical discriminant diagrams (Fig. 5c and d; Sr/Y vs. Y and La/Yb vs. Yb) proposed by Defant and Drummond (1990), with Sr/Y ratios as high as 557 (Martin, 1999; Richards and Kerrich, 2007). Normal arc magma have significant overlap between "adakites" due to their high La/Yb and Sr/Y values (60-80), though their Yb_N (> 5) and Y (> 12 ppm) values are generally higher (Moyen, 2009). Both La/Yb and Sr/Y systems correlate, minimising
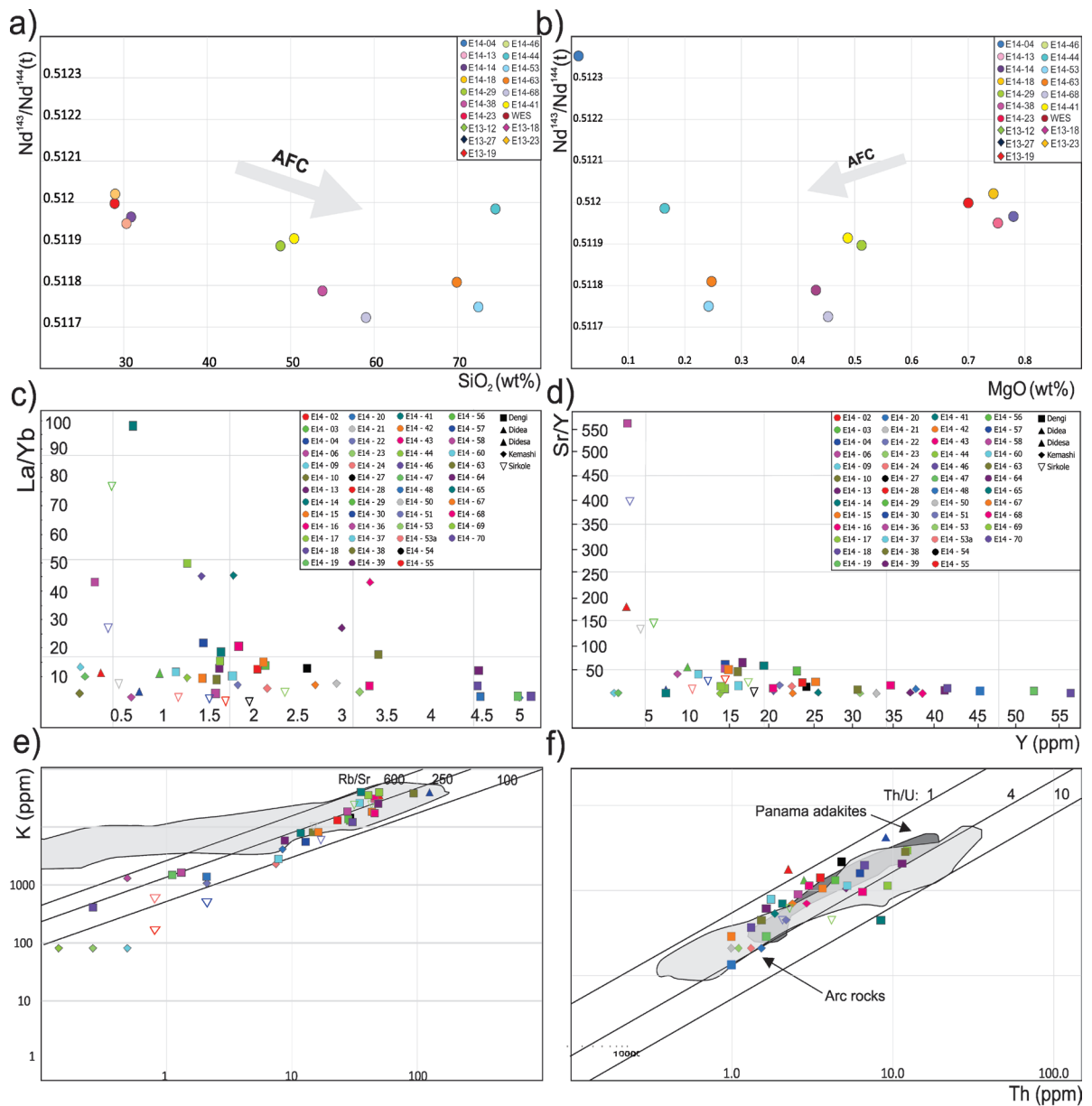
Figure 5: a-b) $^{143}Nd/^{144}Nd(t)$ vs SiO_2 MgO to determine effect of assimilation fractional crysallisation on samples from western Ethiopia. c) Yb (ppm) vs La/Yb d) Y (ppm) vs Sr/Y show the higher than average Sr/Y raitos in samples from Western Ethiopia e) K–Rb concentrations in adakites. The Austral Volcanic Zone (Stern and Kilian, 1996; Kay et al., 1993; Rogers et al., 1985; Puig et al., 1984), Ecuador (Beate et al., 2001; Bourdon et al., 2002), and Separation Point, New Zealand (Muir et al., 1995). Note higher K concentrations. f) Th vs U within rocks from western Ethiopia. Fields are data from Panama (Defant et al., 1991, 1992) compared with Th–U concentrations in arc volcanic rocks (McDermott and Hawkesworth, 1991).
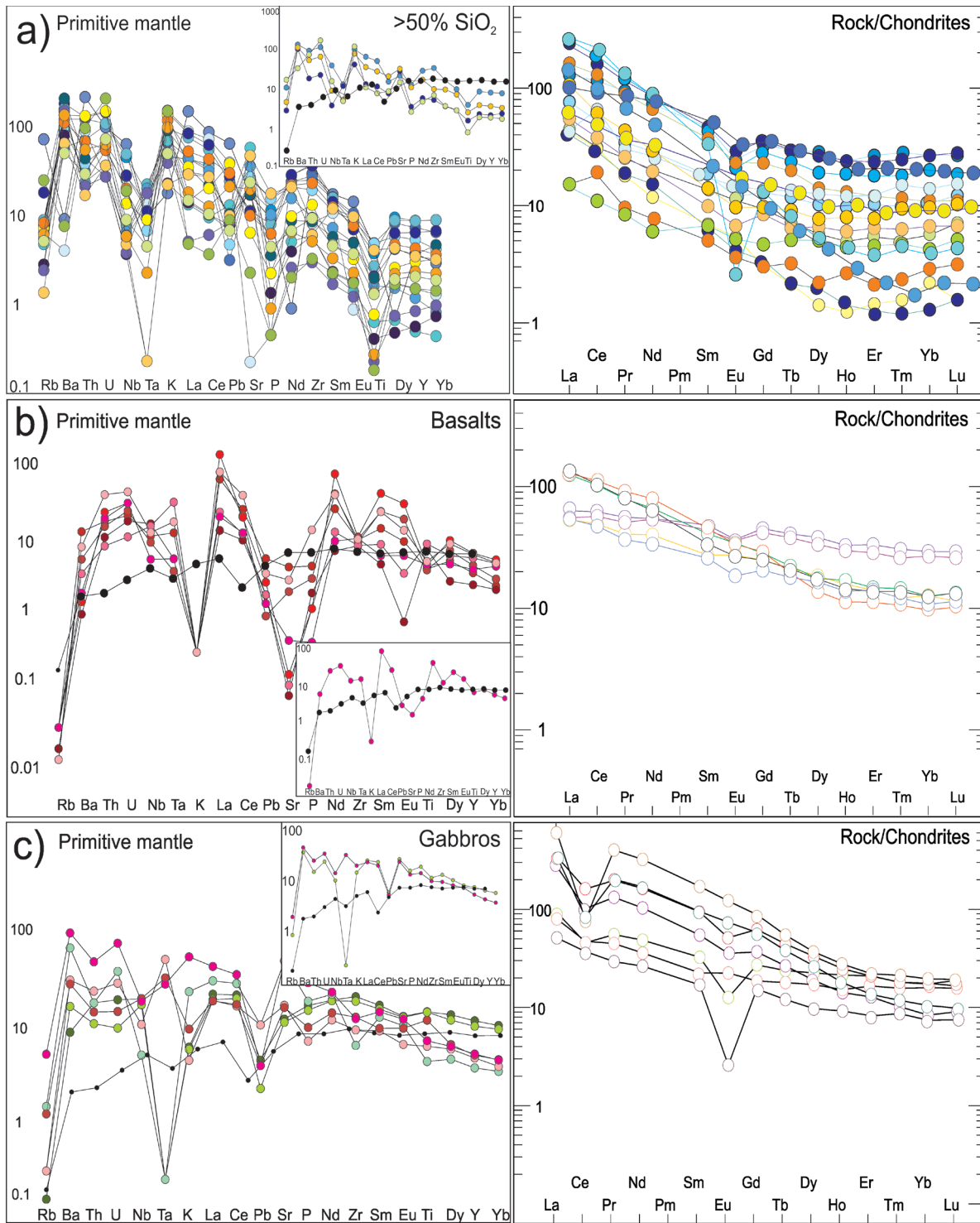
Figure 6: Plots on the right are Primitive Mantle-normalised incompatible element spider plots and the plots on the left are chondrite-normalised rare earth element diagrams. Inset shown, represent average patterns for these rocks. a) Displays samples >50wt% SiO$_2$. b) Basalts collected from Abshala Melange. c) Gabbros collected from the Dengi and Sirkole Domains. MORB on each plot is shown in black

the effect of low temperature alteration on the mobility of Sr. High Sr/Y ratios are commonly interpreted as reflecting melting from the deep lower crustal hot zone. As the pressure increase, plagioclase becomes unstable (therefore releasing Sr), whereas garnet becomes stable and an increasingly important phase, trapping Y. The result is a dramatic increase of the Sr/Y ratio with increasing pressure (Martin et al., 2005; Moyen, 2009). These high Sr/Y (> 40) and low HREE (Yb=1.8 ppm) suggest melting of the down going slab. Samples can be divided into two groups, based on their K concentrations (Fig. 5e) and are characterised by Rb concentrations between 10 and 100 ppm, where K/Rb ratios are near constant (Rollinson and Tarney, 2005). These rocks could have formed in the following ways: (1) partial melting of thickened and hydrous garnet amphibolite or amphibole eclogite lower arc crust (Chung et al., 2003; Hou et al., 2004; Petford and Atherton, 1996); (2) high-pressure fractional crystallization ($\pm$ assimilation) of hydrous basaltic magma (Castillo et al., 1999; Macpherson et al., 2006); (3) mixing of felsic magmas with basaltic magmas (Castillo et al., 1999; Streck et al., 2007); (4) partial melting of delaminated lower crust (Kay and Mahlburg Kay, 1993). Typically, adakites form where young, warm oceanic crust is being subducted (Defant and Kepezhinskas, 2001). It is likely that these samples from the Western Ethiopian Shield represent slab melts mixed with more normal arc magmas and/or melts of sediments from the subducting slab, have hybridised with the mantle wedge en-route to the surface and are the product of assimilation and fractional crystallisation processes (Kamber et al., 2002).

Samples collected from the WES in this study are relatively juvenile, with crustal input playing a minor role in this system. Using all available Nd data from the ANS (Fig. 9a), it highlights the relative juvenility of these known island arc terranes (Johnson et al., 2011a; Johnson, 2014; Johnson et al., 2011c), which broadly correlate to those seen in the WES. The apparent spread in Nd isotope ratios for volcanic arc rocks from the Mariana, South Sandwich and Kermandec arcs, are comparable to those seen in the WES (1.9 ε_{Nd}(t) units (Woodhead, 1989), 2.7 ε_{Nd}(t) units (Gamble et al., 1993) and ~4.3 ε_{Nd}(t)) units (Pearce et al., 1995) respectively. On Figure 9 ε_{Nd}(t) and recalculated ε_{Hf}(t) (Vervoort et al., 1999) data were used to create an isotopic map of the WES, these data highlight a definable trend, broadly following the Baruda–Tulu Dimtu shear zone, shown by the green (low ε_{Nd}(t) values) (Ayalew and Peccerillo, 1998; Blades et al., 2015; Braathen et al., 2001; Grenne et al., 2003; Kebede and Koeberl, 2003; Woldemichael et al., 2010). These data suggest that there is a slither of crustal input sitting within the proposed suture zone, bounded by juvenile material. The Hf isotopic analysis (in zircon) indicates that the magmas were generated from juvenile Neoproterozoic mantle sources (Fig. 9a) with little involvement of the pre-Neoproterozoic continental crust. However, it must me noted that a majority of these samples come from the Dengi and Sirkole Domains. The Hf isotopic data from the ca. 810–770 Ma and ca. 660–600 Ma rocks are consistent with them being, at least partially, generated by melting of the older Tonian–Cryogenian rocks (Ayalew et al., 1990; Ayalew and Peccerillo, 1998; Blades et al., 2015; Kebede et al., 2001a; Kebede et al., 1999; Kebede et al., 2001b). The deviation of $\delta^{18}O$ values from mantle values seen in the zircons from some samples in western Ethiopia are likely the result of magma interaction with supra-crustal materials, though some samples are undoubtedly derived from mantle sources (Blades et al., in prep). Previous interpretations by Grenne et al. (2003) suggest

Table 1: Sm-Nd and Rb-Sr data table for samples analysed in the Western Ethiopian Shield. Ages analysed in Blades et al., (in prep) have been included. *indicates uknown age.

Sample	Age (Ma)	Sm (ppm)	Nd (ppm)	^{147}Sm/^{144}Nd	^{143}Nd/^{144}Nd (t)	± 2σ (x10^{-6})	ε_{Nd}(0)	ε_{Nd}(t)	T_{DM} (Ma)	Sr (ppm)	Rb (ppm)	^{87}Sr/^{86}Sr	± 2σ
E14 - 68	854	1.08	0.24	0.13614	0.51172	0.000012	-2.9	3.7	1287	568.2	59.6	0.71486	1.7E-02
E14 - 63	835	0.72	0.12	0.10268	0.51181	0.000012	-5.2	4.9	1060	242.8	131.7	0.69392	8.5E-02
E14 - 53	853	3.42	0.80	0.14122	0.51175	0.000012	-1.9	4.1	1267	381.2	53.1	0.70247	3.7E-05
E14 - 44	700*	0.89	0.26	0.17650	0.51199	0.000012	3.1	4.9	1419	28	0.2	0.70393	3.4E-05
E14 - 41	700*	0.73	0.14	0.12009	0.51191	0.000012	-3.4	3.5	1104	1074.7	13.4	0.70454	3.2E-05
E14 - 38	814	2.15	0.48	0.13436	0.51179	0.000012	-2.6	3.9	1224	705.9	17.1	0.71265	4.2E-03
E14 - 29	700*	0.96	0.19	0.11967	0.51190	0.000012	-3.7	3.1	1131	1049.6	35	0.70556	2.9E-05
E14 - 23	700*	1.56	0.43	0.16601	0.51200	0.000012	2.4	5.1	1223	5.8	0.2	0.70552	5.7E-05
E14 - 18	700*	0.56	0.10	0.10785	0.51202	0.000012	-2.4	5.6	906	112.7	0.2	0.70755	3.4E-05
E14 - 14	700*	0.47	0.09	0.11206	0.51197	0.000012	-3.1	4.5	996	50.5	0.01	0.70832	3.5E-05
E14 - 13	700*	0.35	0.07	0.11620	0.51195	0.000012	-3.0	4.2	1033	73.8	0.01	0.71299	3.4E-05
E14 - 04	853	1.11	0.37	0.19963	0.51235	0.000012	16.2	15.9	-3323	49.1	181.6	0.81094	3.5E-05

*Sample has not been previously dated.
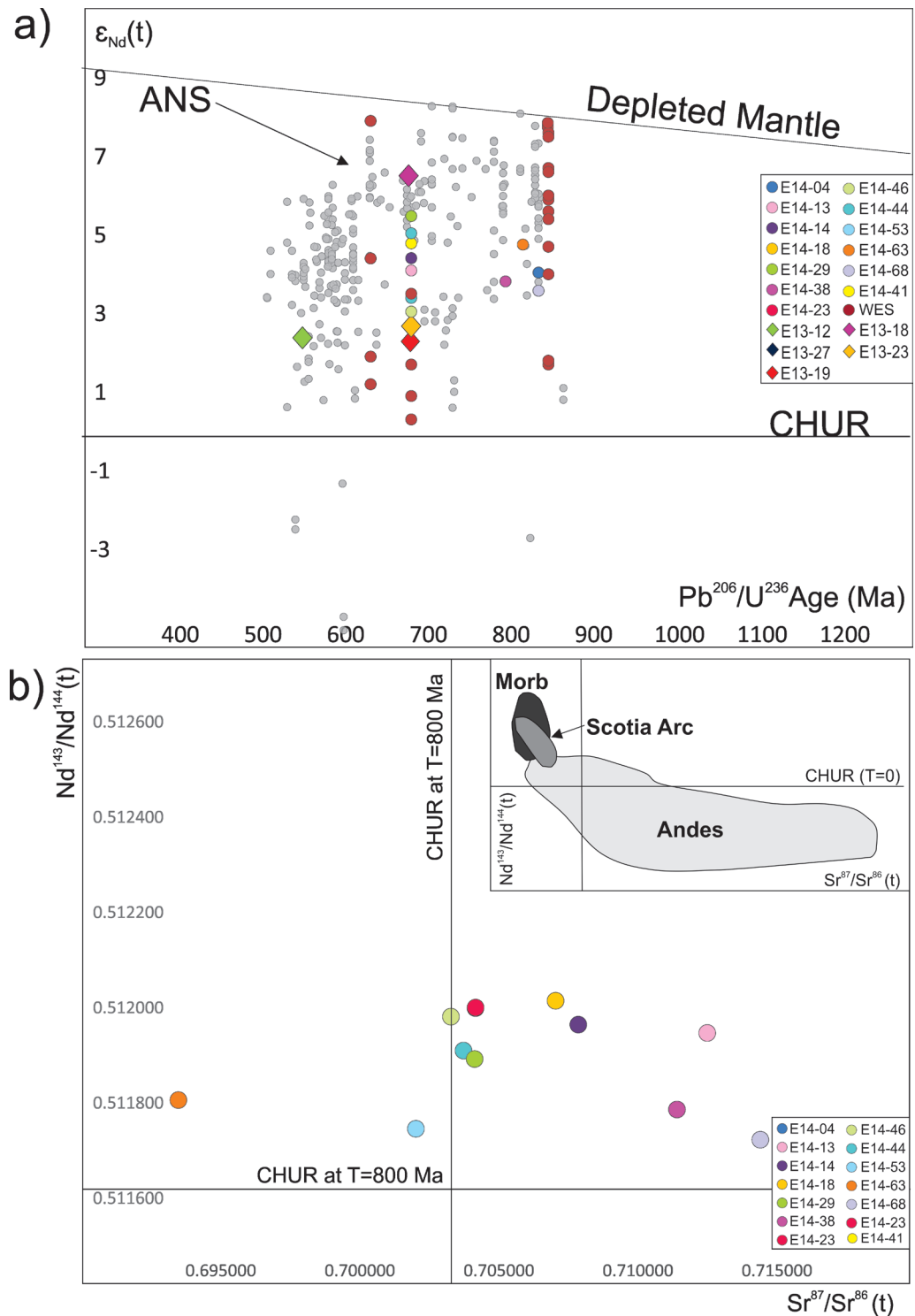
Figure 7: a) Age (Ma) vs $\varepsilon_{Nd}(t)$ data. Light grey data points are values from the Arabian Nubian Shield. Database expanded upon from Stern, (2002) (Ali et al., 2015; Be'eri-Shlevin et al., 2010; Blades et al., 2015; Rantakokko et al., 2014; Robinson et al., 2015; Robinson et al., 2017; Stern, 2002; Whitehouse et al., 2016; Woldemichael et al., 2010; Yeshanew et al., 2015). b) Sr/^{86}Sr(t) vs ^{143}Nd/^{144}Nd(t) with CHUR at 800 Ma. Inset shows present-day Andes, MORB (mid-ocean ridge basalt), and oceanic arc data referenced to CHUR (chondrite uniform reservoir). Andes and Scotian Arc data are from the GEOROC (Geochemistry of Rocks of the Oceans and Continents) database, and MORB data are from Saunders et al. (1988).
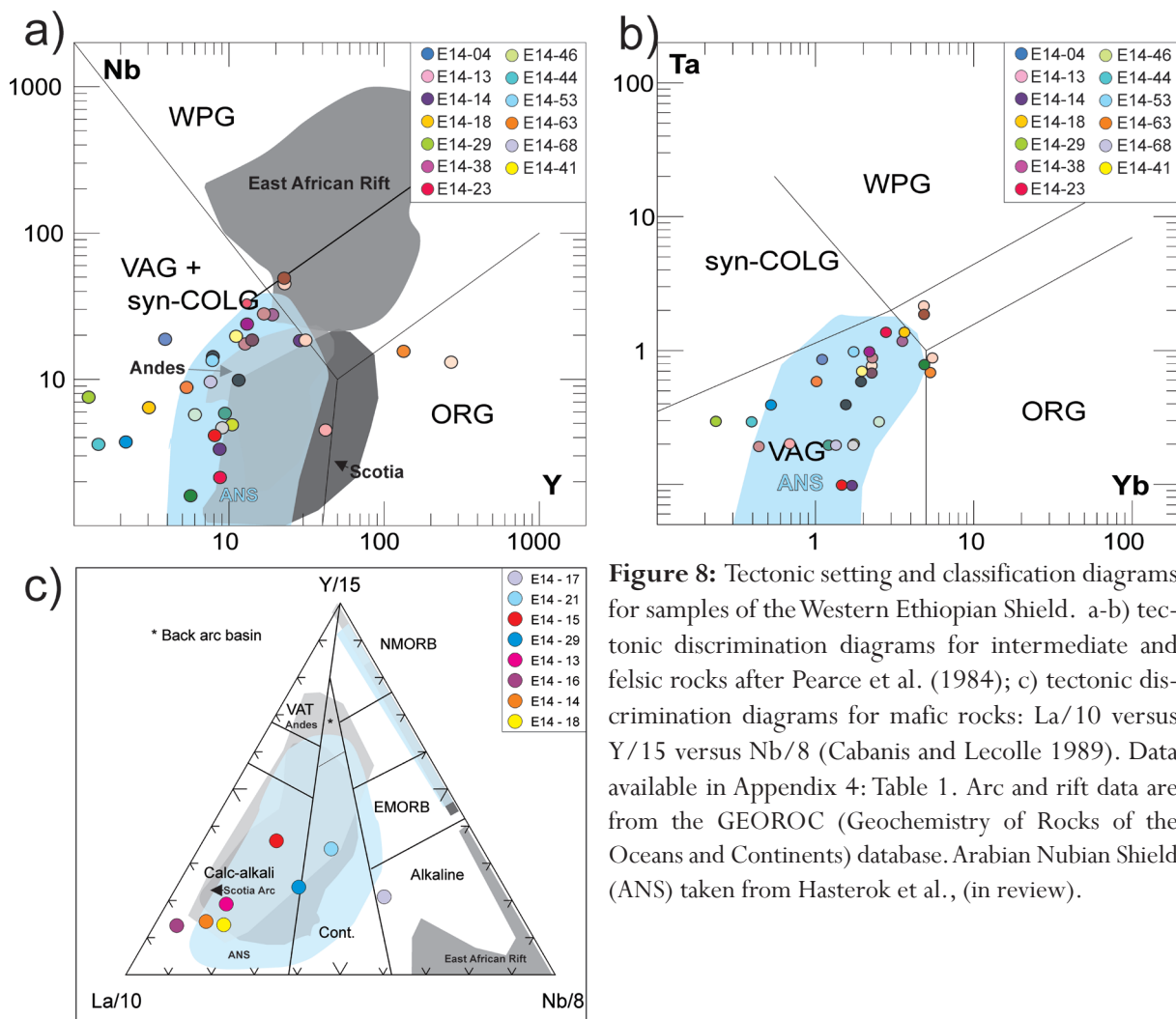
Figure 8: Tectonic setting and classification diagrams for samples of the Western Ethiopian Shield. a-b) tectonic discrimination diagrams for intermediate and felsic rocks after Pearce et al. (1984); c) tectonic discrimination diagrams for mafic rocks: La/10 versus Y/15 versus Nb/8 (Cabanis and Lecolle 1989). Data available in Appendix 4: Table 1. Arc and rift data are from the GEOROC (Geochemistry of Rocks of the Oceans and Continents) database. Arabian Nubian Shield (ANS) taken from Hasterok et al., (in review).

that the $\varepsilon_{Nd}(t)$ values are compatible with a model of arc development and rifting on a thin continental crust that had only a weak influence on the Nd isotope signatures. The $^{87}Sr/^{86}Sr_{(t)}$ vs $^{143}Nd/^{144}Nd_{(t)}$ diagram demonstrates that samples from western Ethiopia plot in the high Rb–Sr, high Sm–Nd quadrant, typical of Andean arcs (Hildreth and Moorbath, 1988). The low $\varepsilon_{Nd}(t)$ values illustrated in Fig. 9 and previously reported by Grenne et al. (2003), within the Kemashi Domain may represent siliciclastic deposition, sealing the terrane amalgamation between the Kemashi, Didesa and Dengi Domains.

Regional Significance:

Previous studies in the WES show that there were three main phases of magmatism ca. 850–810 Ma, 780–700 Ma and 620–550 Ma (Ayalew et al., 1990; Ayalew and Peccerillo, 1998; Blades et al., 2015; Kebede et al., 2001a; Kebede et al., 1999; Kebede et al., 2001b), complicated by metamorphism/deformation occurring both at ca. 810–770 Ma and at ca. 660–655 Ma. The magmatic phases during the Tonian are common to all domains, however the Cryogenian phase of magmatism seems to be absent west of the Kemashi Domain (Ayalew et al., 1990; Ayalew and Peccerillo, 1998; Blades et al., 2015; Kebede et al., 2001a; Kebede et al., 1999; Kebede et al., 2001b). The Kemashi Domain seems to be highlighted by $\varepsilon_{Nd}(t)$ values

(Fig. 9b) that suggest a crustal component, these are largely supported by previously published oxygen isotopes in zircon (Blades et al., in prep), which are most sensitive to sedimentary input (Valley et al., 2005). Data supports the formation of these rocks in an arc environment, with some of these rocks carrying adakite-like signatures, suggesting that these were formed from the deeper melting of the hydrous downgoing slab (Rollinson and Tarney, 2005). However, data seem to suggest that these may incorporate a kernel of pre-Neoproterozoic or early Tonian rocks. Unfortunately, little data exists from metasedimentary rocks in the Western Ethiopian Shield. However, detrital zircons from a meta-quartzarenite found in the Kemashi Domain, suggest derivation from Neoarchaean-Palaeoproterzoic (ca. 2.8–2.4Ga), late Palaeoproterozoic (ca. 1.8 Ga) and Stenian–Tonian (ca. 1.15–0.84 Ga) sources rock (Blades et al., 2015). The late Palaeoproterozoic zircons (ca. 1.82 Ga) yield negative $\varepsilon_{Hf}(t)$ values, suggesting that the source intrusions contained a component of pre-existing continental crust (Blades et al., 2015). Similar-aged crust exists to the south, in Uganda, Kenya and Tanzania, where it makes up part of the foreland to the East African Orogen (Abdelsalam et al., 2002; Leggo, 1974; Reddy et al., 2003) and the west in the Sahara Metacraton (Abdelsalam et al., 2003; Abdelsalam et al., 2002; Henry et al., 2009). These data show that the Western Ethiopian Shield was depositionally connected to older continental crust and we suggest that these have partially assimilated with the Mantle melts in the Kemashi Domain to produce this more evolved signature.

The Western Ethiopian Shield, as previously suggested by Grenne et al. (2003), may represent a terrane similar to modern analogues such as Kermadec Islands–Taupo Volcanic Zone (New Zealand) where there is a transition from an oceanic to continental arc. Deformation and magmatism is seen at 810–770 Ma and is interpreted as evidence of further mantle-derived magmatism and the re-melting of juvenile Neoproterozoic rocks. After ca. 840 Ma, siliciclastic deposition occurred on the eastern margin of the Dengi and Sirkole Domains, as these terranes amalgamated with the Didesa Domain. The last phase of syn-tectonic magmatism (660–655 Ma), whereby by the Western Ethiopian Shield transitioned into post-tectonic magmatism at ca. 584 Ma (Blades et al., 2015). The complexity of the East African Orogen, and in particular the northern extent, with multiple oceanic and continental arcs, does not seem to reflect a simple Wilson's cycle of oceanic opening and closing.

CONCLUSIONS

Data presented here help constrain the tectonic evolution of the region and document consumption and closure of the western Mozambique Ocean. The plutonic samples collected from western Ethiopia exhibit a wide range of lithologies from mafic to granitic, with SiO_2 ranging between 28–75 wt%. Increasing silica content show a depletion in MgO (0.04–42.75 wt%), CaO (0.01–12.3 wt%), MnO (0.01–0.74) and Fe_2O_3T ($FeO+Fe_2O_3$) and samples can be broadly subdivided into two groups based on K ppm. Trace element data suggest that the igneous rocks from western Ethiopia are predominately calc-alkaline, with low values of high-field strength elements such as Ti, Zr, Nb and Y, that is typical of sub-alkaline, arc volcanic rocks. Some samples have > 56% SiO_2 (75.2–60.00 wt%), > 15% Al_2O_3, < 3% MgO (0.6–0.12 wt%), low Y (5.5–3.3 ppm) and HREE relative (e.g. Yb < 1.9 ppm), suggesting an adakite-like nature. The high Sr/Y ratios reflect deeper melting of the subducting slab, rather than the dehydration.
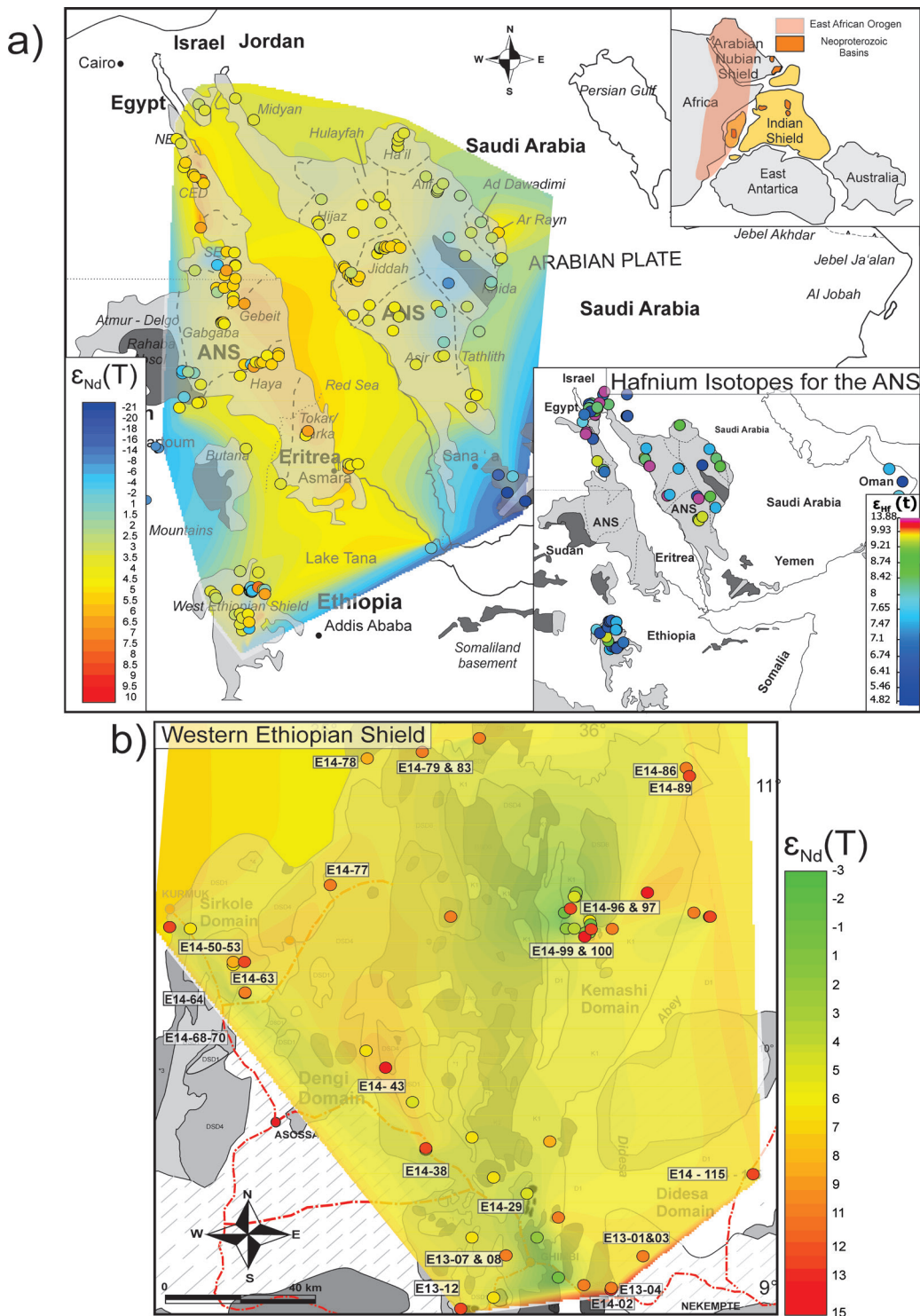
Figure 9: a) location map and distribution of crustal domains in the East African Orogen. SM, Sahara Meta-craton; ANS, Arabian Nubian Shield. MB, Mozambique Belt. Data scaled by colour to represent $\varepsilon_{Nd}(t)$ values from the ANS. Previously published $\varepsilon_{Nd}(t)$ values collated and expanded upon from Stern, (2002) (Ali et al., 2015; Be'eri-Shlevin et al., 2010; Blades et al., 2015; Rantakokko et al., 2014; Robinson et al., 2015; Robinson et al., 2017; Stern, 2002; Whitehouse et al., 2016; Woldemichael et al., 2010; Yeshanew et al., 2015). b) $\varepsilon_{Nd}(t)$ and recalculated $\varepsilon_{Hf}(t)$ data from the Western Ethiopia Shield. ArcGIS grid was created as a visual aid to highlight any crustal material. Zone of more evolved data shown in the Kemashi Domain (Grenne et al., 2003; Kebede and Koeberl, 2003; Kebede et al., 1999; Tadesse and Allen, 2004; Woldemichael et al., 2010).

The recognition of these adakite-like rocks suggests that this subduction zone experienced higher temperatures than normally expected, reflecting the interaction between slab-melt and mantle wedge peridotite at the initiation of subduction. The WES is characterised by three main phases of magmatism ca. 850–810 Ma, 780–700 Ma and 620–550 Ma, which are complicated by metamorphism/deformation occurring both at ca. 810–770 Ma and at ca. 660–655 Ma These phases of magmatism have variable but overall higher $^{87}Sr/^{86}Sr$ and high $^{143}Nd/^{144}Nd$ signatures ($\varepsilon_{Nd}(t)$ between 5.58–3.15), indicating some crustal involvement. A band of more evolved $\varepsilon_{Nd}(t)$ is highlighted in the Baruda-Tulu DImtu shear zone, suggesting re-melting of crustal rocks. Previously published detrital data show that the Kemashi Domain was connected to an older continental source explains the higher $^{87}Sr/^{86}Sr$ and lower $^{143}Nd/^{144}Nd$ ratios seen in these terranes. Though these data are synonymous with other isotopic data in the ANS, collated Nd and O isotopes indicate these terranes contain a crustal component, suggesting that palaeogeographically the WES may have sat close to or on a continental margin during the Neoproterozoic, adjacent to the Sahara Metacraton.

REFERENCES

Abdelsalam, M., Stern, R., 1996. Sutures and shear zones in the Arabian-Nubian Shield. Journal of African Earth Sciences 23, 289-310.

Abdelsalam, M.G., Abdel-Rahman, E.,-S.M., El-Faki, E.-F.M., Al-Hur, B., El-Bashier, F.-R.M., Stern, R.J., Thurmond, A.K., 2003. Neoproterozoic deformation in the northeastern part of the Saharan Metacraton, northern Sudan. Precambrian Research 123, 203-221.

Abdelsalam, M.G., Liégeois, J.P., Stern, R.J., 2002. The Saharan Metacraton. Journal of African Earth Sciences 34, 119-136.

Alemu, T., 2005. Discussion of "Geological setting and tectonic subdivision of the Neoproterozoic Orogenic Belt of Tuludimtu, Western Ethiopia"[Journal of African Earth Sciences 36 (2003) 329–343]. Journal of African Earth Sciences 41, 329-332.

Alemu, T., Abebe, T., 2000. Geology of the Gimbi Area, Memoir 15 ed. Geological Survey of Ethiopia.

Allen, A., Tadesse, G., 2003. Geological setting and tectonic subdivision of the Neoproterozoic orogenic belt of Tuludimtu, western Ethiopia. Journal of African Earth Sciences 36, 329-343.

Ayalew, T., Bell, K., Moore, J.M., Parrish, R.R., 1990. U-Pb and Rb-Sr geochronology of the western Ethiopian shield. Geological Society of America Bulletin 102, 1309-1316.

Ayalew, T., Peccerillo, A., 1998. Petrology and geochemistry of the Gore-Gambella plutonic rocks: implications for magma genesis and the tectonic setting of the Pan-African Orogenic Belt of western Ethiopia. Journal of African Earth Sciences 27, 397-416.

Belete, K., Mogessie, A., Hoinkes, G., Ettinger, K., 2000. Platinum group minerals and chrome spinels in the Yubdo ultramafic

rocks, western Ethiopia. Journal of African Earth Sciences 30, 10-10.

Blades, M.L., Collins, A.S., Foden, J., Payne, J.L., Xu, X., Alemu, T., Woldetinsae, G., Clark, C., Taylor, R.J., 2015. Age and hafnium isotopic evolution of the Didesa and Kemashi Domains, western Ethiopia. Precambrian Research 270, 267-284.

Braathen, A., Grenne, T., Selassie, M., Worku, T., 2001. Juxtaposition of Neoproterozoic units along the Baruda–Tulu Dimtu shear-belt in the East African Orogen of western Ethiopia. Precambrian Research 107, 215-234.

Chazen, S.I., Vogel, T.A., 1974. Distribution of Ti and P in oceanic basalts as a test of origin. Contributions to mineralogy and petrology 43, 307-316.

Collins, A., Pisarevsky, S., 2005a. Amalgamating eastern Gondwana: the evolution of the Circum-Indian Orogens. Earth-Science Reviews 71, 229-270.

Collins, A., Pisarevsky, S., 2005b. Amalgamating eastern Gondwana: The evolution of the Circum-Indian Orogens. Earth-Science Reviews 71, 229-270.

Collins, A.S., Pisarevsky, S.A., 2005c. Amalgamating eastern Gondwana: The evolution of the Circum-Indian Orogens. Earth Science Reviews 71, 229-270.

Cox, G.M., Lewis, C.J., Collins, A.S., Halverson, G.P., Jourdan, F., Foden, J., Nettle, D., Kattan, F., 2012. Ediacaran terrane accretion within the Arabian-Nubian Shield. Gondwana Research 21, 341-352.

de Wit, M., Aguma, A., 1977. Geology of the ultramafic and associated rocks of Tulu Dimtu, Welega. Ethiopian Institute of Geological Surveys Report, 26.

Defant, M.J., Drummond, M.S., 1990. Derivation of some modern arc magmas by melting of young subducted lithosphere. Nature 347, 662-665.

DePaolo, D., 1981. Trace element and isotopic effects of combined wallrock assimilation and fractional crystallisation. Earth Planet. Sci. Lett. 53, 189-202.

Fritz, H., Abdelsalam, M., Ali, K.A., Bingen, B., Collins, A.S., Fowler, A.R., Ghebreab, W., Hauzenberger, C.A., Johnson, P.R., Kusky, T.M., Macey, P., Muhongo, S., Stern, R.J., Viola, G., 2013a. Orogen styles in the East African Orogen: A review of the Neoproterozoic to Cambrian tectonic evolution. Journal of African Earth Sciences 86, 65-106.

Fritz, H., Abdelsalam, M., Ali, K.A., Bingen, B., Collins, A.S., Fowler, A.R., Ghebreab, W., Hauzenberger, C.A., Johnson, P.R., Kusky, T.M., Macey, P., Muhongo, S., Stern, R.J., Viola, G., 2013b. Orogen styles in the East African Orogen: A review of the Neoproterozoic to Cambrian tectonic evolution. Journal of African Earth Sciences.

Grenne, T., Pedersen, R., Bjerkgård, T., Braathen, A., Selassie, M., Worku, T., 2003. Neoproterozoic evolution of Western Ethiopia: igneous geochemistry, isotope systematics and U–Pb ages. Geological magazine 140, 373-395.

Hasterok, D., Gard, M., Webb, J., in review. On the radiogenic heat production of metamorphic, igneous, and sedimentary rocks. Geoscience Frontiers.

Hawkesworth, C., Turner, S., McDermott, F., Peate, D., Van Calsteren, P., 1997. U-Th isotopes in arc magmas: Implications for element transfer from the subducted crust. Science 276, 551-555.

Hawkesworth, C.J., Gallagher, K., Hergt, J.M., McDermott, F., 1993. Mantle and slab contributions in arc magmas. Annual Reviews of Earth and Planetary Science 21, 175-204.

Henry, B., Liégeois, J.-P., Nouar, O., Derder, M., Bayou, B., Bruguier, O., Ouabadi, A.,

Belhai, D., Amenna, M., Hemmi, A., 2009. Repeated granitoid intrusions during the Neoproterozoic along the western boundary of the Saharan metacraton, Eastern Hoggar, Tuareg shield, Algeria: an AMS and U–Pb zircon age study. Tectonophysics 474, 417-434.

Hildreth, W., Moorbath, S., 1988. Crustal contributions to arc magmatism in the Andes of central Chile. Contributions to mineralogy and petrology 98, 455-489.

Honthaas, C., Réhault, J.-P., Maury, R.C., Bellon, H., Hémond, C., Malod, J.-A., Cornée, J.-J., Villeneuve, M., Cotten, J., Burhanuddin, S., 1998. A Neogene back-arc origin for the Banda Sea basins: geochemical and geochronological constraints from the Banda ridges (East Indonesia). Tectonophysics 298, 297-317.

Jackson, M., 2006. Lithogeochemistry and spinel compositions in the ultramafic complexes of Western Ethiopia: criteria for the identification of Alaskan-type intrusions. Cardiff University.

Johnson, P., Andresen, A., Collins, A.S., Fowler, A., Fritz, H., Ghebreab, W., Kusky, T., Stern, R., 2011a. Late Cryogenian–Ediacaran history of the Arabian–Nubian Shield: A review of depositional, plutonic, structural, and tectonic events in the closing stages of the northern East African Orogen. Journal of African Earth Sciences 61, 167-232.

Johnson, P.R., 2014. An Expanding Arabian-Nubian Shield Geochronologic and Isotopic Dataset: Defining Limits and Confirming the Tectonic Setting of a Neoproterozoic Accretionary Orogen. Open Geology Journal 8, 3-33.

Johnson, P.R., Andresen, A., Collins, A.S., Fowler, A.R., Fritz, H., Ghebreab, W., Kusky, T., Stern, R.J., 2011b. Late Cryogenian-Ediacaran history of the Arabian-Nubian Shield: A review of depositional, plutonic, structural, and tectonic events in the closing stages of the northern East African Orogen. Journal of African Earth Sciences 61, 167-232.

Johnson, P.R., Andresen, A., Collins, A.S., Fowler, A.R., Fritz, H., Ghebreab, W., Kusky, T., Stern, R.J., 2011c. Late Cryogenian–Ediacaran history of the Arabian–Nubian Shield: A review of depositional, plutonic, structural, and tectonic events in the closing stages of the northern East African Orogen. Journal of African Earth Sciences 61, 167-232.

Johnson, P.R., Woldehaimanot, B., 2003. Development of the Arabian-Nubian Shield: perspectives on accretion and deformation in the northern East African Orogen and the assembly of Gondwana, in: Yoshida, M., Windley, B.F., Dasgupta, S. (Eds.), Proterozoic East Gondwana: Supercontinent Assembly and Breakup. Geological Society, London, Special Publication 206, pp. 289-325.

Johnson, T.E., Ayalew, T., Mogessie, A., Kruger, F.J., Poujol, M., 2004. Constraints on the tectonometamorphic evolution of the Western Ethiopian Shield. Precambrian Research 133, 305-327.

Kebede, T., Kloetzli, U., Koeberl, C., 2001a. U/Pb and Pb/Pb zircon ages from granitoid rocks of Wallagga area: constraints on magmatic and tectonic evolution of Precambrian rocks of western Ethiopia. Mineralogy and Petrology 71, 251-271.

Kebede, T., Koeberl, C., 2003. Petrogenesis of A-type granitoids from the Wallagga area, western Ethiopia: constraints from mineralogy, bulk-rock chemistry, Nd and Sr isotopic compositions. Precambrian Research 121, 1-24.

Kebede, T., Koeberl, C., Koller, F., 1999. Geology, geochemistry and petrogenesis of

intrusive rocks of the Wallagga area, western Ethiopia. Journal of African Earth Sciences 29, 715-734.

Kebede, T., Koeberl, C., Koller, F., 2001b. Magmatic evolution of the Suqii-Wagga garnet-bearing two-mica granite, Wallagga area, western Ethiopia. Journal of African Earth Sciences 32, 193-221.

Kröner, A., Linnebacher, P., Stern, R., Reischmann, T., Manton, W., Hussein, I., 1991. Evolution of Pan-African island arc assemblages in the southern Red Sea Hills, Sudan, and in southwestern Arabia as exemplified by geochemistry and geochronology. Precambrian Research 53, 99-118.

Martin, D.M., 1999. Depositional setting and implications of Paleoproterozoic glaciomarine sedimentation in the Hamersley Province, Western Australia. Geological Society of America Bulletin 111, 189-203.

Martin, H., Smithies, R., Rapp, R., Moyen, J.-F., Champion, D., 2005. An overview of adakite, tonalite–trondhjemite–granodiorite (TTG), and sanukitoid: relationships and some implications for crustal evolution. Lithos 79, 1-24.

McDermott, F., Hawkesworth, C., 1991. Th, Pb, and Sr isotope variations in young island arc volcanics and oceanic sediments. Earth and Planetary Science Letters 104, 1-15.

Meert, J., Torsvik, T.H., Eide, E.A., Nédélec, A., 1997. A paleomagnetic review of Gondwana assembly including preliminary paleomagnetic results from Madagascar, in: Cox, R., Ashwal, L.D. (Eds.), Proceedings of the UNESCO-IUGS-IGCP 348/368 International Field Workshop on Proterozoic Geology of Madagascar, 5 ed, p. 52.

Meert, J.G., 2003a. A synopsis of events related to the assembly of eastern Gondwana. Tectonophysics 362, 1-40.

Meert, J.G., 2003b. A synopsis of events related to the assembly of eastern Gondwana. Tectonophysics 362, 1-40.

Meert, J.G., 2003c. A synopsis of events related to the assembly of eastern Gondwana. Tectonophysics 362, 1-40.

Meert, J.G., Lieberman, B.S., 2008. The Neoproterozoic assembly of Gondwana and its relationship to the Ediacaran–Cambrian radiation. Gondwana Research 14, 5-21.

Morrison, G.W., 1980. Characteristics and tectonic setting of the shoshonite rock association. Lithos 13, 97-108.

Moyen, J.-F., 2009. High Sr/Y and La/Yb ratios: the meaning of the "adakitic signature". Lithos 112, 556-574.

Pearce, J.A., 1982. Trace element characteristics of lavas from destructive plate boundaries, in: Thorpe, R.S. (Ed.), Andesites. John Wiley & Sons.

Pearce, J.A., Harris, N.B.W., Tindle, A.G., 1984. Trace element discrimination diagrams for the tectonic interpretation of granitic rocks. Journal of Petrology 25, 956-983.

Pearce, J.A., Norry, M.J., 1979. Petrogenetic implications of Ti, Zr, Y, and Nb variations in volcanic rocks. Contrib. Mineral. Petrol. 69, 33-47.

Pearce, J.A., Peate, D.W., 1995. Tectonic implications of the composition of volcanic arc magmas. Annual Reviews of Earth and Planetary Science 23, 251-285.

Petford, N., Atherton, M.P., 1995. Crustal segmentation and the isotopic significance of the Abancay Deflection: Northern Central Andes (9-20° S). Andean Geology 22, 235-243.

Pouclet, A., Lee, J.-S., Vidal, P., Cousens, B., Bellon, H., 1994. Cretaceous to Cenozoic volcanism in South Korea and in the Sea of Japan: magmatic constraints on the opening of the back-arc basin. Geological Society,

London, Special Publications 81, 169-191.

Richards, J.P., Kerrich, R., 2007. Special paper: adakite-like rocks: their diverse origins and questionable role in metallogenesis. Economic geology 102, 537-576.

Robinson, F., Foden, J., Collins, A., Payne, J., 2014. Arabian Shield magmatic cycles and their relationship with Gondwana assembly: Insights from zircon U–Pb and Hf isotopes. Earth and Planetary Science Letters 408, 207-225.

Rollinson, H.R., Tarney, J., 2005. Adakites— the key to understanding LILE depletion in granulites. Lithos 79, 61-81.

Shackleton, R., 1996. The final collision zone between East and West Gondwana: where is it? Journal of African Earth Sciences 23, 271-287.

Stern, R.A., 2002a. Crustal evolution in the East African Orogen: a neodymian isotopic perspective. Journal Of African Earth Sciences 34, 109-117.

Stern, R.J., 1994a. Arc-Assembly and Continental Collision in the Neoproterozoic African Orogen: Implications for the Consolidation of Gondwanaland. Annual Review of Earth and Planetary Sciences 22, 319-351.

Stern, R.J., 1994b. Arc Assembly and continental collision in the Neoproterozoic East African orogeny - implications for the consolidation of Gondwana. Annual Review of Earth and Planetary Sciences 22, 319-351.

Stern, R.J., 2002b. Crustal evolution in the East African Orogen: a neodymium isotopic perspective. Journal of African Earth Sciences 34, 109-117.

Tadesse, G., Allen, A., 2004. Geochemistry of metavolcanics from the Neoproterozoic Tuludimtu orogenic belt, Western Ethiopia. Journal of African Earth Sciences 39, 177-185.

Tadesse, G., Allen, A., 2005. Geology and geochemistry of the Neoproterozoic Tuludimtu Ophiolite suite, western Ethiopia. Journal of African Earth Sciences 41, 192-211.

Tatsumi, Y., Hamilton, D., Nesbitt, R., 1986. Chemical characteristics of fluid phase released from a subducted lithosphere and origin of arc magmas: evidence from high-pressure experiments and natural rocks. Journal of Volcanology and Geothermal Research 29, 293-309.

Teklay, M., Kröner, A., Mezger, K., Oberhänsli, R., 1998. Geochemistry, Pb-Pb single zircon ages and Nd-Sr isotope composition of Precambrian rocks from southern and eastern Ethiopia: implications for crustal evolution in East Africa. Journal of African Earth Sciences 26, 207-227.

Ujike, O., Tsuchiya, N., 1993. Geochemistry of Miocene basaltic rocks temporally straddling the rifting of lithosphere at the Akita-Yamagata area, northeast Japan. Chemical Geology 104, 61-74.

Valley, J., Lackey, J., Cavosie, A., Clechenko, C., Spicuzza, M., Basei, M., Bindeman, I., Ferreira, V., Sial, A., King, E., 2005. 4.4 billion years of crustal maturation: oxygen isotope ratios of magmatic zircon. Contributions to Mineralogy and Petrology 150, 561-580.

Vervoort, J.D., Patchett, P.J., Blichert-Toft, J., Albarède, F., 1999. Relationships between Lu-Hf and Sm-Nd isotopic systems in the global sedimentary system. Earth & Planetary Science Letters 168, 79-99.

Wolde, B., Team, G.-G.G., 1996. Tonalite-trondhjemite-granite genesis by partial melting of newly underplated basaltic crust: an example from the Neoproterozoic Birbir magmatic arc, western Ethiopia. Precambrian Research 76, 3-14.

Woldemichael, B.W., Kimura, J.-I., 2008.

Petrogenesis of the Neoproterozoic Bikilal-Ghimbi gabbro, Western Ethiopia. Journal of mineralogical and petrological sciences 103, 23-46.

Woldemichael, B.W., Kimura, J.-I., Dunkley, D.J., Tani, K., Ohira, H., 2010. SHRIMP U–Pb zircon geochronology and Sr–Nd isotopic systematic of the Neoproterozoic Ghimbi-Nedjo mafic to intermediate intrusions of Western Ethiopia: a record of passive margin magmatism at 855 Ma? International Journal of Earth Sciences 99, 1773-1790.

CHAPTER 5

Blades, M. L., Foden, J., Collins, A. S., Payne, J. L., Stüwe, K., Glorie, S., Abu-Alam., T.S., Hassan, M. The Age and Hafnium Isotope Evolution of Butana and Chad – Does Butana Represent the Eastern Margin of the Sahara Metacraton.

Statement of Authorship

Title of Paper	The Age and Hafnium Isotope Evolution of Butana and Chad – Does Butana Represent the Eastern Margin of the Sahara Metacraton.
Publication Status	☐ Published ☐ Accepted for Publication ☐ Submitted for Publication ☑ Unpublished and Unsubmitted work written in manuscript style
Publication Details	For submission to Geoscience Frontiers as: Blades, M. L., Foden, J., Collins, A. S., Payne, J. L., Stüwe, K., Glorie, S., Abu-Alam., T.S., Hassan, M. The Age and Hafnium Isotope Evolution of Butana and Chad – Does Butana Represent the Eastern Margin of the Sahara Metacraton.

Principal Author

Name of Principal Author (Candidate)	Morgan Blades
Contribution to the Paper	Data collection, processing and interpretation, manuscript design and composition, creation of figures
Overall percentage (%)	80
Certification:	This paper reports on original research I conducted during the period of my Higher Degree by Research candidature and is not subject to any obligations or contractual agreements with a third party that would constrain its inclusion in this thesis. I am the primary author of this paper.
Signature		Date	06/09/2017

Co-Author Contributions

By signing the Statement of Authorship, each author certifies that:

i.   the candidate's stated contribution to the publication is accurate (as detailed above);

ii. permission is granted for the candidate in include the publication in the thesis; and

iii. the sum of all co-author contributions is equal to 100% less the candidate's stated contribution.

Name of Co-Author	Professor Alan Collins
Contribution to the Paper	Guidance in fieldwork, sample preparation, data interpretation and manuscript review.
Signature		Date	06/09/2017

Name of Co-Author	Emeritus Professor John Foden
Contribution to the Paper	Guidance in fieldwork, sample preparation, data interpretation and manuscript review.
Signature		Date	06/09/2017

Name of Co-Author	Dr Justin Payne		
Contribution to the Paper	Guidance in sample preparation, data collection and interpretation (Lu-Hf isotopes) and manuscript review.		
Signature		Date	06/09/2017

Name of Co-Author	Professor Kurt Stüwe		
Contribution to the Paper	Field work, sample preparation and manuscript review		
Signature		Date	06/09/2017

Name of Co-Author	Dr Stijn Glorie		
Contribution to the Paper	Guidance in sample preparation, data interpretation and manuscript review.		
Signature		Date	06/09/2017

Name of Co-Author	Dr Tamur Abu-Alam		
Contribution to the Paper	Geological mapping of Butana and manuscript review		
Signature		Date	06/09/2017

Name of Co-Author	Mahmoud Hassan		
Contribution to the Paper	Sample preparation and collection		
Signature		Date	06/09/2017

Please cut and paste additional co-author panels here as required.

ABSTRACT

The Sahara Metacraton is a poorly known tract of pre-Neoproterozoic continental crust that occupies the area between the juvenile Arabian Nubian Shield (ANS), in the east, and the Tuareg Shield to the west. Neoproterozoic orogenesis affects the west (Dahomenides), the south (Oubanguides) and the east (East African Orogeny) of the metacraton, which led to deformation, the emplacement of igneous bodies, and localised rifting, within the Sahara Metacraton. Details about interior regions of the Saharan Metacraton are extremely poorly known, with much of it covered by Phanerozoic cover. The basement outcrops in Sudan, Chad and Libya have been the subject of few, or no, modern geochronological studies. Here we present results from the first zircon geochronology and in-situ zircon hafnium isotope investigations from both the Sudanese Butana and central Chad.

The terranes in Butana, interpreted as accreted arc terranes, formed to the east of pre-Neoproterozoic continental crust of the Sahara Metacraton, with the oldest juvenile magmatism ($\varepsilon_{Hf}(t)$ of +4.89 to +7.89) at ca. 987 Ma and ca. 867 Ma followed by subsequent magmatism and recrystallisation at ca. 780 Ma, shown by zircon core–rim relationships. The ca. 780 Ma event (seen elsewhere in the East African Orogen) is believed to represent the terrane accreting onto the older crust of the Sahara Metacraton. The ca. 987 Ma magmatism is amongst the oldest known magmatism associated with the Arabian Nubian Shield and marks the initiation of subduction to the east of the Sahara Metacraton. The accretion of the Arabian Nubian Shield terranes in the Tonian (ca. 850 Ma), as a series of volcanic arcs, mark a period of voluminous magmatism throughout the East African Orogen.

The magmatic history of the Quaddai region in Chad begins in the late Mesoproterozoic, with localised rifting, resulting in the emplacement of juvenile granites (ca. 1040 Ma). The Cryogenian and Ediacaran in the Sahara Metacraton reveals a complicated history of magmatism and deformation; age data from Chad show the emplacement of granites (from melting of Mesoproterozoic crust: $\varepsilon_{Hf}(t)$ = +2.04 and -4.07) at ca. 665–654 Ma, coeval with the main East African Orogeny and accretion of the other ANS terranes to the Sahara Metacraton ca. 650–580 Ma. The youngest tectonothermal event within the Sahara Metacraton is recorded by emplacement of granites between 580–550 Ma ($\varepsilon_{Hf}(t)$ values of -17 to -31) in southern Chad.

INTRODUCTION:

North central Africa is one of the most poorly known geological regions on the planet. The ca. 500,000 km² area is largely covered by the Sahara Desert and older Phanerozoic cover. However, even where rocks crop out, little modern research has been undertaken due to their remoteness and difficulty of access in Algeria, Libya, Chad and Sudan. Conflicting geological, geochronological and isotopic observations have led to the region being referred to by many names; the Nile Craton (Kennedy, 1964; Rocci, 1965), Sahara–Congo Craton (Kröner, 1977), Eastern Saharan Craton, or Central Saharan Ghost Craton (Black and Liegeois, 1993). Abdelsalam et al. (2002) coined the name 'Sahara Metacraton' to best represent this enigmatic block, which remained a coherent rheological entity during the Neoproterozoic, rather than fully tectonically mobile as seen in the Arabian Nubian Shield to the east. The Neoproterozoic destabilisation of the region was first recognised by Kennedy (1964) who initially introduced the term Pan-African tectonothermal event. However, he was unable to distinguish the area

from other Neoproterozoic orogenic belts. The Sahara Metacraton (Fig 1a) is bounded to the east, west, and south by lithospheric – scale suture zones resulting from collisional events during the Neoproterozoic and has been treated as a coherent continental block in many Neoproterozoic reconstructions (e.g. Collins and Pisarevsky, 2005; Pisarevsky et al. 2006; Li et al. 2008; Merdith et al. 2017). To try and examine the nature of this extensive enigmatic region, we here provide some of the first U–Pb data and the only in-situ zircon Hf isotope data for the central parts of the Sahara Metacraton, Butana in Sudan, and the central and southern parts of Chad. These provide a window into the timing and nature of Mesoproterozoic and Neoproterozoic magmatism within the central regions of the Sahara Metacraton, as well as helping to further elucidate the relationship between the Sahara Metacraton and the Arabian Nubian Shield as Gondwana coalesced.

REGIONAL GEOLOGY
Sahara Metacraton

The Sahara Metacraton refers to pre-Neoproterozoic continental crust that occupies the north–central parts of Africa and extends to the Sahara Desert and Savannah Belt (Fig. 1a). This tract of continental crust occupies ca. 500,000 km^2 and extends from the Arabian Nubian Shield in the east, Tuareg Shield to the west (Abdelsalam et al., 2002). Recent work by Abdelsalam et al. (2011), show high S-wave velocity anomalies in the upper 100 km of the mantle, typical of a cratonic lithosphere. However, S-wave velocity anomalies (175–250 km) depth are lower than expected, which has been interpreted as being due to the loss of its cratonic root (Abdelsalam et al., 2011). The Neoproterozoic remobilisation of the Sahara Metacraton is prevalent in forms of deformation, metamorphism, and emplacement of igneous bodies and could be

the result of partial destabilisation as a result of collisional related deformation (Abdelsalam et al., 2011). The thin lithosphere was used to an extreme by De Wit and Linol (2015) to suggest that the whole region was simply floored with Neoproterozoic crust. Existing sparse geochronologic and isotopic data indicate, however, that the crust is heterogeneous (Abdelsalam et al., 2011) and contrasts with the Neoproterozoic juvenile crust of the Arabian Nubian Shield to the east and the Archaean continental crust of the Congo Craton in the south (de Wit and Linol, 2015).

The Sahara Metacraton is dominated by medium to high-grade gneisses, metasedimentary rocks, migmatites and smaller outcrops of granulites and low-grade volcano-sedimentary rocks. These Precambrian rocks are exposed as uplifted massifs within Cretaceous and younger cover rocks (Abdelsalam et al., 2002; Küster et al., 2008). There are two dominant structural trends within the Sahara Metacraton; an ENE–WSW and a younger N–S trend. The former has been documented in the Bayuda Desert, Nubian Desert, Kordofan and Darfur, Uweinat and Jebel El Asr inlier and has been referred to as the Zalingei folded zone (Abdelsalam et al., 2003; Abdelsalam et al., 2002; Abdelsalem and Stern, 1996; Schandelmeier et al., 1987; Schandelmeier et al., 1994; Stern, 1994a; Sultan et al., 1994; Toteu et al., 1987; Toteu et al., 1994; Vail, 1973, 1983; Vail and Rex, 1971). The latter N–S trending structures in the north–east are parallel to the Keraf-Kabus-Sekerr shear zone (Küster and Liégeois, 2001) and is interpreted to be the result of an arc–continental suture separating the Sahara Metacraton from the Arabian Nubian Shield, which represents the northern extension of the East African Orogen (Abdelsalam et al., 2003; Abdelsalam et al., 2002; Abdelsalam and Stern, 1996b; Küster and Liégeois, 2001).

Geochronological and isotopic data from
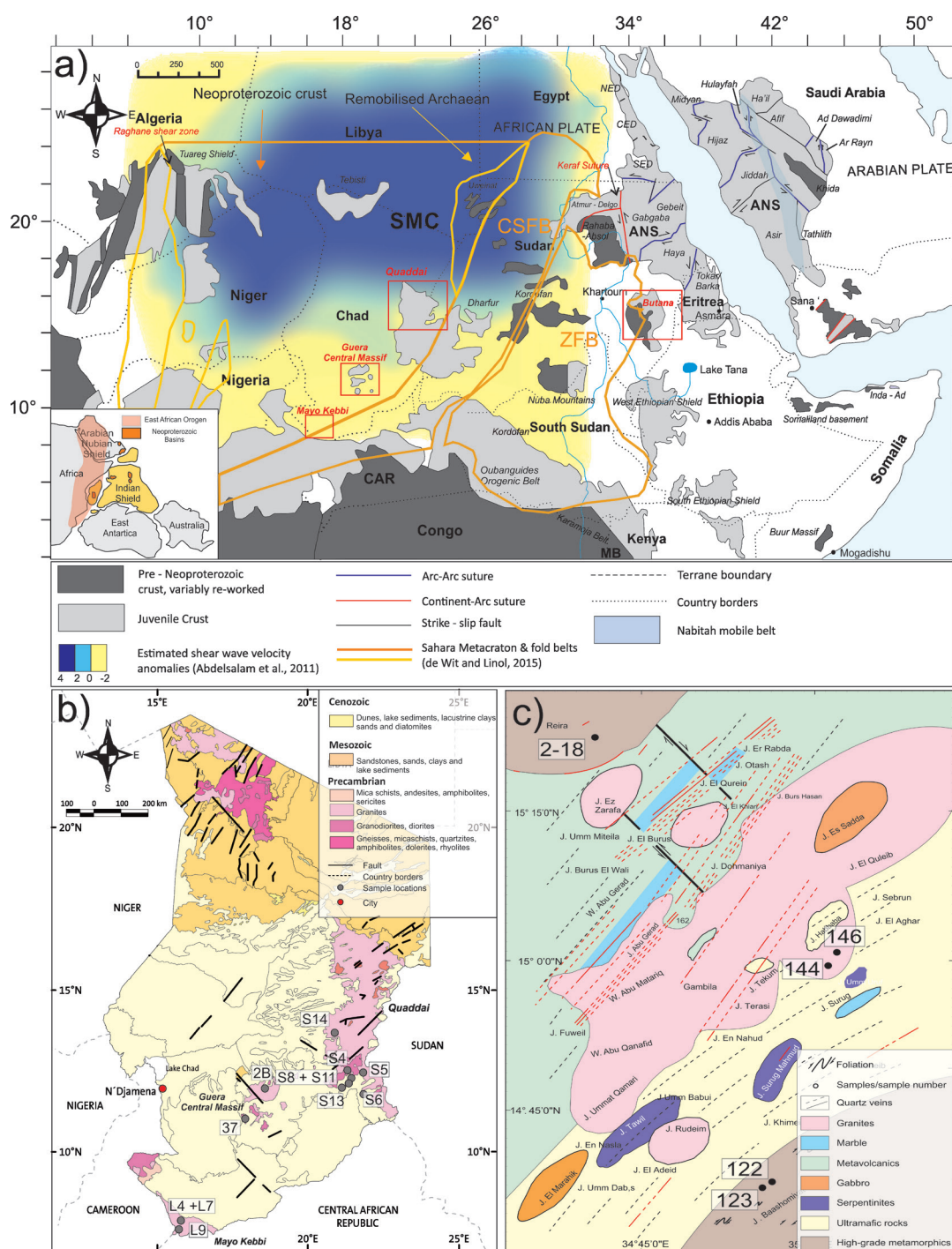
Figure 1: a) Location map of the Sahara Metacraton (SMC). The red boxes indicate the areas where Mesoproterozoic and Neoproterozoic basement samples were taken for this study (adapted from Blades et al. (2015); Johnson et al., (2014) and Abdelsalam et al. (2002). The previously suggested extents of Sahara Metacraton outlined by Abdelsalam et al., (2011) and de Wit and Linol (2015) have been shows on the map by the orange and yellow outlines. CSFB: Central Saharan Fold Belt. ZFB: Zalingai Fold Belt. A representation of the shear wave velocity anomalies underneath the Sahara Metacraton at 0–100 km. The colour indicates the percentage difference of S-wave velocity relatively to the Preliminary Reference Earth Model (PREM) taken from Abdelsalam et al. (2011). b) Geological map of Chad, showing the samples collected from the Precambrian exposures. Taken and modified after Saleh, 1994. c) First geological map of Butana constructed by Abu-Alam., T.S.

the Sahara Metacraton are highly variable as exemplified by the wide range of ages (3100–500 Ma). Archaean–Palaeoproterozoic ages within the metacraton have been reported for gneissic and granulitic rocks, using Rb–Sr and U–Pb zircon geochronology (Pin and Poidevin, 1987; Stern, 1994b; Sultan et al., 1994). Recent work, reported by de Wit and Linol (2015), has suggested that the southern parts of the metacraton are composed of mainly late Mesoproterozoic crust. In the east of the metacraton, existing geochronology (U–Pb, Rb–Sr) suggests ages between 2629–1922 Ma (Liégeois et al., 1994; Stern, 1994a; Sultan et al., 1994). These are intruded by early Neoproterozoic–late Mesoproterozoic granites (ca. 1100–1000 Ma), which were deformed during the Neoproterozoic. Post-collisional 600–560 Ma granites are abundant in the entire north-eastern Saharan Metacraton, with exception of the Uweynat massif (Abdelsalam et al., 2002; Küster and Harms, 1998; Stern, 1994b).

Within the centre of the Sahara Metacraton, there are five distinct Precambrian massifs that outcrop in Chad, Libya and Sudan (Fig. 1b); the Tibesti, the Ouaddaï, the Guera (Central Massif), the Yade and the Mayo Kebbi. These outcrops form a significant portion of the Sahara Metacraton, yet there has been little geological work done in the area.

The Precambrian exposures in the Tibesti are comprised of two distinct assemblages separated by an angular unconformity. The lower assemblage (north east) is made up of amphibolites, pyroxenites, quartzites, marbles, gneiss, leptynites and mica-schists. Within the upper assemblages there are a series of metasedimentary units interlayered with metavolcanic rocks. These are cross cut by the Super Tibestian magmatic series and the Ben Ghnema batholith (600–550 Ma), interpreted

to be related to westward subduction beneath the eastern margin of the basement of the Murzuk Basin (El Makkrouf, 1988; Ghuma and Rogers, 1978; Suayah et al., 2006). Post tectonic granites suggest deformation ended sometime before ca. 558 Ma (Suayah et al., 2006).

The Guera (Central Massif), located in the centre of the Lake Chad Basin, encompasses three main massifs — Abou Telfan, Kengas and Melfi, as well as numerous second order massifs and inselbergs (Fig. 1b). Lithologically, the Central Massif consists of granitoids and foliated metamorphic rocks that enclose volcano-sedimentary rocks equivalent to the Proterozoic rocks found in Quaddai region. The assemblages are intruded by Precambrian alkaline granites, monzonites and syenites. At the periphery, the Massif disappears under the formations of the Lake Chad Basin, from which inselbergs and exhumed antiforms of granites emerge (Schneider and Wolf, 1992).

The Ouaddai region occupies much of the eastern margin of the country towards the border with Sudan (Fig. 1b). The basement consists of a batholith that has been extensively eroded and is composed of granitoids, migmatites and gneisses. Volcanosedimentary rocks occur as septa between the granitoids in the northern part (Goz Beida Group) and as more massive belts in the south (Lele Series). The Northern Ouaddai host-rocks are made up of a series of quartzites, schists and amphibolites and in the Southern Quaddai region, are primarily quartzites, schists, conglomerates, marbles, amphibolites and gneisses. The batholith is made up of two distinct intrusive series: 1) calc-alkaline rocks consisting of two mica-bearing porphyritic and pegmatitic granites. 2) Alkaline rocks characterised by biotite bearing granites, syenites, monzo-gabbros and gabbros. Both

of these suites are associated with network of fine grained granites, diorites, pegmatites and northeast–southwest trending veins (Schneider and Wolf, 1992).

The Mayo Kebbi region in south west Chad is a part of the Neoproterozoic Central African Fold Belt (Fig. 1b). It is comprised of three calc – alkaline suites emplaced into metavolcanic–metasedimentary sequences. (Penaye et al., 2006). Most of the basement is covered by Phanerozoic platform sediments. The region is dominated by the Mayo Kebbi tonalitic batholith, emplaced into a medium to high-grade gneiss–amphibolite complex (ca. 737–723 Ma gabbro-diorites and meta-diorites) (Penaye et al., 2006; Schneider and Wolf, 1992) as several magmatic pulses between ca. 665 and 640 Ma. All these units are intruded by post-tectonic granitoids (Zabili granite, monzodiorite and porphyritic granite) at ca 570 Ma (Penaye et al., 2006; Schneider and Wolf, 1992).

Terranes surrounding the Sahara Metacraton

Oubanguides

The Oubanguides sit at the southern extent of the Sahara Metacraton and broadly consist of Paleoproterozoic basement thrust over the Congo Craton, with granulite facies metamorphism following collision (Toteu et al., 2004). The region has been divided into three tectonic units separated by shear zones. These are, from south to north, the schistose and gneissic Yaoundé domain, which contains extensive nappes thrust over the Congo Craton (Owona et al., 2011); the reworked Paleoproterozoic Adamawa-Yadé domain, intruded by numerous syn- to late- tectonic ca. 630–570 Ma granitoids; and the volcano-sedimentary schistose and gneissic Western Cameroon domain, which was intruded by

calc-alkaline granites between 660–580 Ma (Toteu et al., 2001). Dating of metagabbro rocks in the northern Yaoundé domain, show the earliest intrusions to be 660±22 Ma (Toteu et al., 2006), likely due to extension in response to subduction further south, facilitating the deposition within the Yaoundé Basin (Toteu et al., 2006). Deformation and metamorphism is constrained to ca. 660–600 Ma (Nkoumbou et al., 2014; Owona et al., 2011; Toteu et al., 2006).

Arabian Nubian Shield

To the east of the Sahara Metacraton is the expression of the northern East African Orogen, which encompasses the Arabian Nubian Shield and is characterised by Neoproterozoic crust that formed in a series of volcanic arcs (Johnson et al., 2011b; Johnson and Woldehaimanot, 2003; Stern, 1994a, 2002), dominated by low grade volcano-sedimentary rocks in association with plutons and ophiolitic remnants (Abdelsalam and Stern, 1996a; Allen and Tadesse, 2003; Cox et al., 2012; Kröner et al., 1991; Robinson et al., 2014; Shackleton, 1996; Stern, 1994a)(Blades et al. 2015; in press). Widespread acceptance of the juvenile character of the Arabian Nubian Shield has come about in the past decade, although consensus is not universal (Johnson, 2014). The juvenile rocks in the Bayuda Desert reported by Küster and Liégeois (2001) have been interpreted to represent the eastern margin of the Sahara Metacraton, known as the Keraf Suture. Recent ^{40}Ar–^{39}Ar dating on biotite and hornblende, from deformed granites in Bayuda suggest that the deformation along the shear zone ended by ca. 580 Ma (Küster and Liégeois, 2001). It is interpreted that the Keraf Suture represents a sinstral transgressive tectonic regime, as a result of the closing of the Mozambique Ocean (Abdelsalam et al., 1998; Merdith et al., 2017). To the east of the Keraf

Suture are the terranes of the Arabian Nubian Shield. The terranes of the eastern Arabian Nubian Shield are exposed in north east Sudan, Eritrea, Ethiopia, Egyptian Eastern Desert and Sinai. Rocks of the Western Ethiopian Shield show no evidence of pre-Neoproterozoic crust, with the oldest rocks in the area ca. 855 Ma (Blades et al., 2015). These rocks have been interpreted to have formed in an intra-oceanic setting, above a subduction zone. Magmatism (re-melting of juvenile crust) and deformation is seen at 810–770 Ma and at 660–655 Ma in the Western Ethiopian Shield, with post tectonic magmatism at ca. 584 Ma (Blades et al., 2015 and in preparation). All the rocks in the Western Ethiopian Shield have juvenile $\varepsilon_{Hf}(t)$ values of +4.5 to +10, suggesting that the influence of continental crust was minimal. Further north, in Eritrea, the Tonka/Barka terrane preserves juvenile arc magmatism that occurred between ca. 850–740 Ma (Andersson et al., 2006; Teklay et al., 2003), followed by deposition of the Cryogenian Tambien Group. This group is intruded by the post-tectonic Mereb granites at 640–600 Ma (Avigad et al., 2007). Upper amphibolite-facies metamorphism occurred in the surrounding high-grade terranes at ca. 590 Ma and is interpreted to relate to final continental collision in the area (Andersson et al., 2006). The Precambrian rocks of the Egyptian Eastern Desert have been suggested to represent six main pulses of magmatism at 1) 705–680 Ma 2) 654 Ma 3) ca. 630 Ma 4) 610–604 Ma, 5) 600–590 and lastly 6) ca. 540 Ma (Andresen et al., 2010; Augland et al., 2012; Lundmark et al., 2012; Shalaby et al., 2005; Stern and Hedge, 1985). These pulses of magmatism are associated with metamorphism and deformation in the area. Hafnium and oxygen isotopes in the North Eastern Desert show $\delta^{18}O$ values (+5.15 to 6.70) and $\varepsilon_{Hf}(t)$ values (+6.3 to +10.6), which were interpreted to reflect melting of a juvenile Neoproterozoic

mantle source that assimilated slightly older Neoproterozoic crustal material during magma mixing (Ali et al, 2016). The northern most extent of the Arabian Nubian Shield is defined by the Sa'al Metamorphic complex in Sinai. Until recently, the Sa'al Metamorphic Complex was believed to be Cryogenian, with an age of between 820–740 Ma, but new U–Pb zircon age data suggest that it is instead latest Mesoproterozoic (ca. 1100–1000 Ma), with post-collisional calc-alkaline (ca. 635–590 Ma) and alkaline (ca. 60–580 Ma) granitic plutons (Be'eri-Shlevin et al., 2012; Johnson, 2014). The rocks in Sinai have an average $\delta^{18}O$ values of 5.7 to 5.8‰ indicating a dominance of mantle-like $\delta^{18}O$ sources with higher values in north-western Sinai (6.9–8.2‰). Hafnium isotopes, synonymous with oxygen isotopes, also reveal a gradual transition from lower $\varepsilon_{Hf}(t)$ values in the north-western regions (+5.5 to +5.9) to slightly higher in south-eastern region (+9.2 to +13.9)(Be'eri-Shlevin et al., 2012).

The Butana region lies 250 km south east of Khartoum and is one of the few exposures of Precambrian basement in Central Sudan (Fig. 1c). Butana is thought to be located close to the transition between the juvenile Arabian Nubian Shield and the enigmatic Sahara Metacraton. Little geological work has been done in the region, therefore samples collected from this region provide valuable insight into the relationship between the Sahara Metacraton and the Arabian Nubian Shield. The region is characterized by flat lying topography with isolated basement exposures. Recent field studies conducted indicate that the terrane consists of low-grade metavolcanic rocks, pre- and syn-tectonic granitic intrusions, serpentinites, ophiolitic metagabbro and high-grade metamorphic rocks. The main metamorphic foliation trend in the low-grade rocks is northeast–southwest

Table 1: Location, sample description of zircon morphologies and cathodoluminescence (CL) interpretations for each sample in Chad. Figure 3 shows the representative CL images.

Sample	GPS Coordinates	Area	Rock Type	Minerology	Zircon Textures
L4 + L7	7°42'N 15°59'E	Chad	Monzogranite	Mc, K-Spar in medium grained Qz, Plag, Bt and Oxides	**Colour:** Pale orange - orange **Size:** 250 - 300 µm **Aspect Ratio:** Majority is 7:1 and 7:2, with some 3:1. **Morphologies and textures:** Dominated by {101} and {100} forms. Large cracks present and many are fragmented. Grains have faint oscillatory zonation or sector zoning, with darker rims mantling some grains. There are strong variations in the relative development of zoned domains, where one large uniform central zone is succeeded by much finer oscillatory-zoned bands.
L9	7°38'N 15°51'E	Chad	Mylonitized granite	Coarse grained perthitic K-spar and plag in fine to medium grained Qz. Well foliated Bt and fine grained Hbl. Zr, Ap and oxides are accessories. Ep present	**Colour:** Pale orange - orange **Size:** 200 - 350 µm **Aspect Ratio:** Majority is 7:2 and 7:1, with some 3:2 and 2:1. **Morphologies and textures:** Dominated by {101} and {211} forms. Large cracks present and many are fragmented. Grains have faint oscillatory zonation or sector zoning. Convolute boundaries and metamict textures are seen. Areas of homogeneously textured zircon appearing as transgressive (across all pre-existing textures) zircon patches and lobes. Areas of recrystallization occur dominantly at crystal terminations.
2B	12°10'N 18°40'E	Chad	Syenogranite	Megacrysts of perthicic K-spar in medium grained Qz and Pl. 10% Bt (highly chloritised). Oxides are present	**Colour:** Pale yellow-orange **Size:** 100 - 200 µm **Aspect Ratio:** Dominant aspect ratio of 7:1 and 3:1. **Morphologies and textures:** Dominated by {101} and {100/211} forms. Grains have faint oscillatory zonation or sector zoning. Convolute and disjointed boundaries between textures. Areas of homogeneously textured zircon appearing as transgressive (across all pre-existing textures) zircon patches and lobes.
37	11°05'N 17°48'E	Chad	Monzogranite	Qz , Perthite, Mc, K-spar, Pl. Bt (chloritised). Brittle	**Colour:** Pale yellow - orange **Size:** 150 - 200 µm **Aspect Ratio:** **Dominant** aspect ratio of 5:1 and 2:1. **Morphologies and textures:** Dominated by {101} pyramidal crystal forms. Crystal terminations have been rounded and grains are cracked. Xenocrystic cores differentiated from their rims by irregular surfaces that truncate internal zoning. Grains have faint oscillatory zonation or sector zoning. Areas of homogeneously textured zircon appearing as transgressive (across all pre-existing textures) zircon patches and lobes.

Table 1: Location, sample description of zircon morphologies and cathodoluminescence (CL) interpretations for each sample in Chad. Figure 3 shows the representative CL images.

Sample	GPS Coordinates		Area	Rock Type	Minerology	Zircon Textures
S4	12°38'N	21°20'E	Darsila	Gneiss	Well foliated Ms with Qz, Pl, Oxides. Crd.	**Colour:** Yellow **Size:** 100 - 200 μm **Aspect Ratio:** Dominant aspect ratio of 4:3, 2:1 and 1:1 **Morphologies and textures:** 2 main groups of zircons. Group 1 is defined by {100} and {110} forms. Some grains have well developed oscillatory zonation. The relative development in zonation varies across the group. Group 2 is defined by rounded grains. Oscillatory and patchy zonation exists in all. In both groups areas of homogeneously textured zircon appearing as transgressive (across all pre-existing textures) zircon patches and lobes. Fragments of homogeneous zircon are present.
S13	12°25'N	21°26'E	Darsila	Monzogranite	Qz + Mc + Pl + Bt, Sphene and Oxides are accessories. Deformed and partially altered.	**Colour:** light pink - yellow **Size:** 60 - 150 μm **Aspect Ratio:** Dominant aspect ratio of 4:3, 7:1 and 2:1. **Morphologies and textures:** Dominated by {100} and {101} forms. Grains can be divided into two groups. Elongate pyramidal grains some with well-defined zonation, a few are homogeneous, with no definable features. Group 2 - rounded grains, with both oscillatory and patchy zonation. Convolute and disjointed boundaries exist between textures in both groups. Dark rims are seen mantling a homogeneous core. Recrystallisation fronts seen in grains from both groups.
S14	13°46'N	20°50'E	Darsila	Monzogranite	Qz + Mc + Pl + Bt, Sphene and Oxides are accessories. Deformed and partially altered.	**Colour:** Orange –pale brown **Size:** 150 - 300 μm **Aspect Ratio:** Dominant aspect ratio of 4:1, 3:1 and 2:1. **Morphologies and textures:** Dominated by {110} and {101} forms. Grains have faint oscillatory zonation, which is either convolute or disjointed boundaries between textures. Areas of homogeneously textured zircon appearing as transgressive (across all pre-existing textures) zircon patches and lobes. Defined thin rims mantling some grains. Relative development of zoned domains vary, where one large uniform central zone is succeeded by much finer oscillatory-zoned bands. Some grains are cracked/fragmented and preserve metamict textures.

Table 1: Location, sample description of zircon morphologies and cathodoluminescence (CL) interpretations for each sample in Butana. Figure 3 shows the representative CL images.

Sample	GPS Coordinates		Area	Rock Type	Minerology	Zircon Textures
144 + 146	14°5′N	35°01′E	Butana	Granite	Megacrysts of Mc, Perthite, Qz, Pl and Bt	**Colour:** Pale yellow - orange **Size:** 100 - 200 μm **Aspect Ratio:** Dominant aspect ratio of 7:2 and 1:1. **Morphologies and textures:** Dominated by {101} forms. Rounded grains as well as pyramidal grains present. Very cracked grains, which only preserve faint oscillatory zonation or sector zoning. Convolute and disjointed boundaries between textures. Recrystallisation fronts give rise to areas of homogeneously textured zircon that replace pre-existing textures.
122+123	14°37′N	34°56′E	Butana	Gneiss	Qzt + Ksp + Pl + Bt (defines weak foliation)	**Colour:** Pale pink - colourless **Size:** 100 - 150 μm **Aspect Ratio:** Dominant aspect ratio of 7:1 and 3:1. **Morphologies and textures:** Forms are hard to detect, all grains are fragmented, or rounded. Grains have faint oscillatory zonation or sector zoning, though in places original textures have been replaced by homogeneous lobes and patches. Some grains preserve ghost/ remnants of previous zoning and some have no definable features.
2-18	14°37′N	34°56′E	Butana	Gneiss	Qz + Ksp + Pl + Bt. Oxide and Chl. Accessory: Oxide, Ep, Zr	**Colour: Pale yellow - orange** **Size:** 70 - 100 μm **Aspect Ratio:** Dominant aspect ratio of 7:1 and 3:1. **Morphologies and textures:** Grain forms are hard to define, grains are rounded and very damaged. Grains have been recrystallised and preserve transgressive recrystallisation fronts that replace any pre-existing zonation. Some preserve ghost textures in the form of faint oscillatory zonation. Fine CL - bright rims mantle the grains.

with steep foliation plains and sub-horizontal lineation. In the high-grade rocks at least three deformation phases were observed in the field. The first deformation phase is associated with northeast–southwest foliation planes. The dome–like shape of these terranes is related to D2, with high temperature folding, while D3 is a faulting phase with brittle features (Fig. 1c).

Tuareg Shield

The N–S oriented Raghane shear zone, interpreted to represent the western boundary of the Saharan Metacraton, and is situated within the Tuareg Shield. The suture of the Tuareg Shield and Saharan Metacraton is the Raghane shear zone (Henry et al., 2009; Liégeois et al., 1994), which was tectonically active from ca. 730–580 Ma. Early suturing was of the easternmost terrane of the Hoggar shield (Aïr Massif) colliding with the Sahara Metacraton between 700–670 Ma (Liégeois et al., 1994). The Tuareg shield is composed of 23 terranes that are Archaean to Neoproterozoic in age, juxtaposed by large displacements along mega-shear zones (Black et al., 1994; Liégeois et al., 1994). Most of these shear zones are N–S oriented and are associated with granitoids of several ages at 800–820 Ma, 730 Ma, 620–580 Ma and 575–545 Ma (Caby, 1987; Fezaa et al., 2010; Liégeois et al., 2005; Liégeois et al., 1994; Liégeois et al., 1986; Liegeois et al., 2003). The central part of the shield (Central Hoggar), preserves amphibolite to granulite-facies Archaean and Paleoproterozoic terranes, with evidence of Neoproterozoic reworking (Bendaoud et al., 2008; Liegeois et al., 2003; Peucat et al., 2003). The stabilisation of this region (known as LATEA), is marked by mega-shear zones, the intrusion of batholiths (Acef et al., 2003) accompanied by high-temperature metamorphism (Bendaoud et al., 2008), occurred mainly at 620–600 Ma (Acef et al., 2003; Bendaoud et al., 2008) and ended at ca.

572 Ma, when plutons such as the Temaguessine pluton intruded (Abdallah et al., 2007). Later magmatism is seen with the intrusion of alkali-calcic plutons, such as the Tioueine pluton at 524 $\pm$ 1 Ma (Azzouni-Sekkal et al., 2003; Paquette et al., 1998). The four terranes to the east of the Raghane shear zone (Djanet, Edembo, Aouzengueur and Barghot) were juxtaposed prior to 700 Ma and are assumed to be a part of the Sahara Metacraton (Liégeois et al., 1994). These metasedimentary, volcanic and plutonic assemblages are suggested to be ca. 730 Ma, with associated mafic and ultramafic complexes thought to represent ophiolites (Boullier 1991).

METHODOLOGY

U–Pb zircon geochronology

Samples from meta-igneous rocks were collected from different locations from both Chad and Sudan (see Figs. 1 and 2).

Zircon grains were extracted from crushed rocks using standard magnetic and heavy liquid techniques (Howard et al., 2009). Mineral separates were hand-picked and mounted in epoxy resin. The polished mounts were carbon coated and zircons imaged under cathodoluminescence (CL) on a Philips XL40 scanning electron microscope (SEM), operating in high-vacuum mode with a tungsten filament with attached Gatan CL at Adelaide Microscopy (The University of Adelaide). Zircon (U–Pb) analysis on twenty two plutonic samples were conducted on New Wave 213 nm Nd-YAG laser coupled with the Agilent 7500cs Inductively Coupled Plasma Mass Spectrometer (LA–ICP–MS) at the University of Adelaide. The spot size used was 30μm with a typical pit depth of 30–50μm. GEMOC GJ-1 zircon together with TIMS normalising data $^{207}Pb/^{206}Pb=607.7 \pm 4.3$ Ma, $^{206}Pb/^{238}U=600.7 \pm 1.1$ Ma and $^{207}Pb/^{235}U=602.0 \pm 1.0$ Ma (Jackson et al., 2004) was used to correct for the U–Pb

fractionation. The Plešovice zircon internal standard (ID TIMS ^{206}Pb/^{238}U age = 337.13 ± 0.37 Ma) (Sláma et al., 2008), was used to assess accuracy before and during the analysis of the unknowns. Plešovice analyses yield a weighted-mean ^{206}Pb/^{238}U age of 335.3 ± 1.3 with an MSWD of 0.41 (n=80).

Data were collected, corrected and filtered in the software package GLITTER version 3.0 (Van Achterbergh et al., 2001). Concordia diagrams and weighted averages were calculated using ISOPLOT 4.11 for Excel (Ludwig, 2009).

Zircon Lu–Hf Isotope analysis

Analytical methods for zircon Lu–Hf isotope analysis follow Payne et al. (2013). Analyses were undertaken using a New Wave UP-193 ArF excimer laser attached to a Thermo–Scientific Neptune Multi-Collector ICP–MS at the University of Adelaide. The bulk of analyses were carried out using a beam diameter of ~50 μm for large and a minimum of ca. 25 μm for smaller grains. Typical ablation times were 40–100 s using a 5 Hz repetition rate, a 4 ns pulse rate, and an intensity of ca. 10 J/cm^2. Zircons were ablated in a helium atmosphere, which was then mixed with argon upstream of the ablation cell.

Reduction of zircon data were undertaken using a macro-driven Hf isotope data reduction Excel spreadsheet, HfTRAX (Payne et al., 2013). The data were normalised to ^{179}Hf/^{177}Hf = 0.7325, using an exponential correction for mass bias. Ytterbium and Lu isobaric interferences on ^{176}Hf were corrected following the methods of Woodhead et al. (2004).

The accuracy of the Yb and Lu corrections has been demonstrated by repeated analysis of standard zircons with a range in ^{176}Yb/^{177}Hf and ^{176}Lu/^{177}Hf values (Griffin et al., 2006). Before and during the analysis of unknowns, standards were analysed to check instrument performance and stability. The primary

zircon standard used was Plešovice, which yielded a mean ^{176}Hf/^{177}Hf ratio of 0.282473 ± 0.00002. This compares to the published value of 0.282482 ± 0.000013 (2SD) by Sláma et al. (2008). Values for ε_{Hf}(t), and T_{DMc} were calculated using ^{176}Lu decay constant after Scherer et al. (2001). TDM crustal was calculated using the methods of Griffin et al. (2002) with an average crustal composition of ^{176}Lu/^{177}Hf = 0.015.

RESULTS

All petrology (Fig. 2) and sample descriptions are located in Table 1 and analytical data are presented in the Appendix 5. All results are plotted on weighted average age plots, in which analyses have been categorised into their broadly identified internal structure based on CL imaging (Fig. 3) and grains used for concordia age calculations (Fig. 4). Data are collated on a single Wetherill plot (^{207}Pb/^{206}Pb v. ^{238}U/^{206}Pb) and all individual plots are available in Supplementary Fig. 1. All age uncertainties are quoted at the two sigma level and MSWDs are quoted for each calculated age.

Butana

2–18 Orthogneiss (15°23'N 34°41'E)

Thirty–three zircons were analysed targeting both rims and cores and of these twenty–five were ≤ 10% discordant showing a range of ^{206}Pb/^{238}U ages between 867–754 Ma (Fig. 4 and Appendix 5: Fig. 1a). The ^{206}Pb/^{238}U weighted average plot highlights two distinct plateaus, suggesting two periods of zircon formation (Appendix 5: Fig. 1a). The youngest two grains are defined by rims mantling the grains and have ages of 766 ± 11 Ma and 764 ± 12 Ma respectively. The older population (23 analyses) yields a ^{206}Pb/^{238}U age of 829 ± 7 Ma, with an MSWD of 1.7 and best represents the age of crystallisation with a recrystallisation event at ca. 765 Ma.
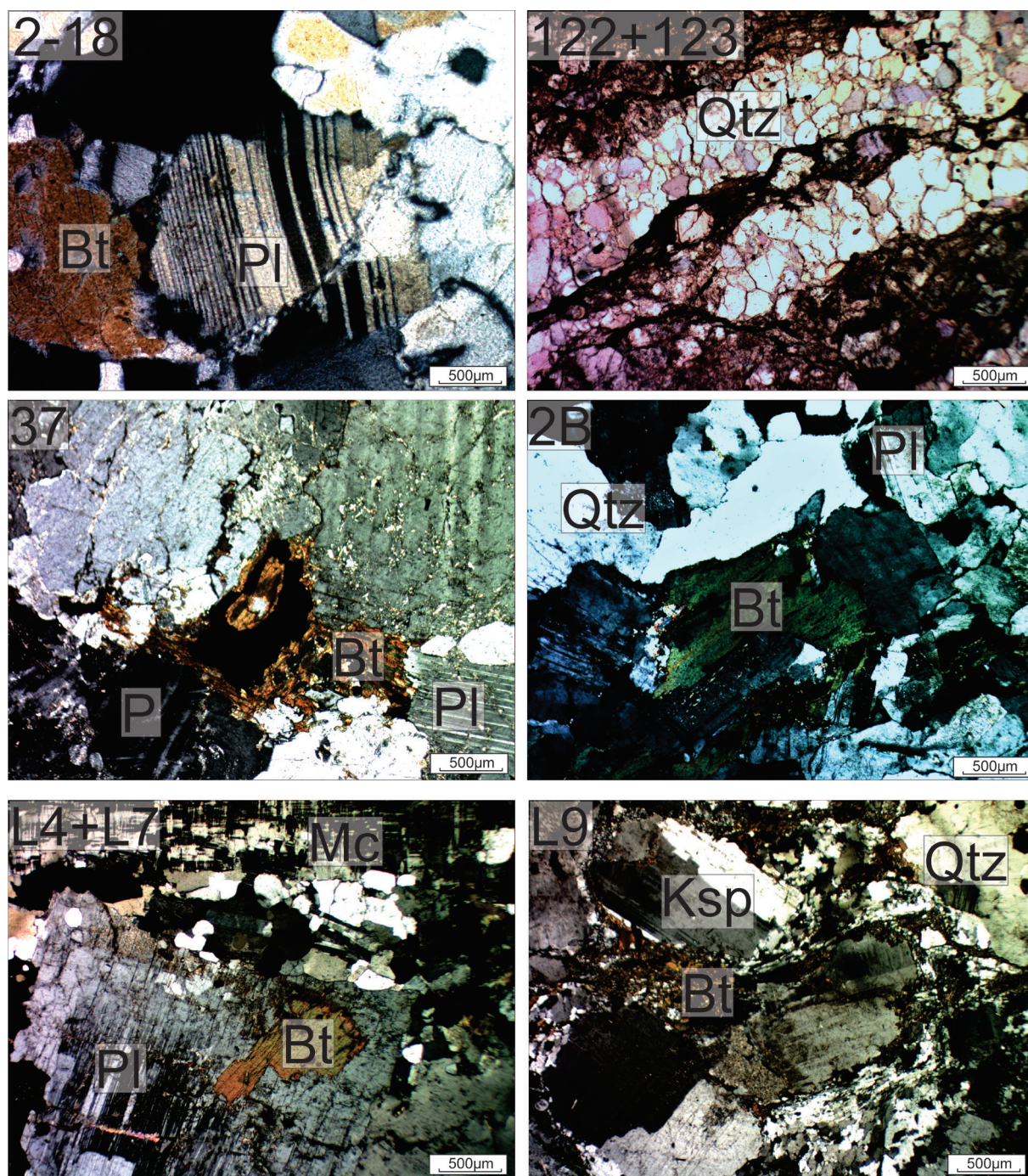
Figure 2: Representative thin section images of the igneous samples collected from Chad and Sudan, in cross polarised light. Minerals present are labelled where: Qtz is quartz; Bt is biotite; Pl is plagioclase; Mc is microcline and Ksp is K-feldspar. Minerology descriptions for each sample are availiable in Table 1.

Hafnium isotope analyses were conducted on eight zircon grains from the gneiss (2–18), yielding (ε_{Hf}(t) values between +6.59 to +9.54. This suggests juvenile sources, with minimal continental crust involvement (Fig. 5).

122 + 123 Orthogneiss (14°37'N 34°56'E and 14°38'N 34°56'E)

Of the thirty–two analyses, twenty–two are ≥ 90% concordant and show a range of $^{206}Pb/^{238}U$ ages between 1056 and 746 Ma. On the $^{206}Pb/^{238}U$ weighted average plot there are two periods of zircon formation and a discernible lead loss trend (the youngest grain from the older population has been excluded from the age calculation; Appendix 5: Fig. 1b). The youngest grain, defined by a dark lobe in CL, has a distinctly younger $^{206}Pb/^{238}U$ age of 764 ± 9 Ma. A $^{206}Pb/^{238}U$ age calculation for the oldest twenty grains yields an age of 957 ± 19 Ma with a large MSWD of 11.8, suggesting that these zircons do not form a single population. We suspect that this large MSWD is due to post–crystallisation Pb loss and recalculated these data using $^{207}Pb/^{206}Pb$ ages, which gave a robust age of 987 ± 13 Ma (MSWD = 1.12). The upper intercept calculated yields an age of 1005±37 Ma (MSWD=1.13). The upper intercept is within error of the $^{207}Pb/^{206}Pb$ weighted average and is interpreted to represent the best age for the orthogneiss, with a recrystallization event at ca. 764 Ma.

Hafnium isotope analyses on the orthogneiss (six grains) gave ε_{Hf}(t) values ranging between +6.98 and +11.25 suggesting juvenile sources, with minimal continental crust involvement (Fig. 5).

144 + 146 Granite (14°5'N 35°01'E and 14°37'N 35°01'E)

Thirty–nine analyses were conducted targeting cores and rims, though there was no discernible age difference. The $^{206}Pb/^{238}U$ weighted average plot show a spread in ages from 841–712 Ma with a perceptible lead loss trend (Appendix 5: Fig. 1c). All analyses yield a $^{206}Pb/^{238}U$ age of 753 ± 18 with a large MSWD of 16, suggesting that these analyses do not form one population and therefore was recalculated using $^{207}Pb/^{206}Pb$ ages (780 ± 14 Ma, MSWD = 0.51). These ages are within error of each other and due to the lower MSWD, ca. 780 Ma represents the closest age of crystallisation for the granite.

Hafnium isotope analyses were conducted on nine zircon grains from this granite. ε_{Hf}(t) values can be divided into two groups. One with predominately juvenile values ranging from +4.89 to +7.89, suggesting minor crustal involvement. The second group is defined by ε_{Hf}(t) values between -31.12 and -17.30. These suggest the remelting of pre–existing continental crust (Fig. 5).

Quaddai Region

S13 Coarse–grained monzogranite (12°25'N 21°26'E)

Of the thirty–four analyses, ten are ≤ 10 % discordant (targeting both rims and cores). The $^{206}Pb/^{238}U$ weighted average plot (analyses ranging between 941–576 Ma), show one main period of zircon formation with a few older grains present (Appendix 5: Fig. 1d). The older analyses (941 ± 12 Ma, 866 ± 11 Ma and 816 ± 10 Ma) are defined by cores in CL and have been interpreted to be inherited grains. All other analyses have a broadly linear slope suggesting post crystallisation lead loss trends, confirmed by the relatively large MSWD of 17 from the calculated $^{206}Pb/^{238}U$ age of 614 ± 28 Ma. Therefore, the $^{206}Pb/^{207}Pb$ age was calculated yielding 666 ± 25 Ma with a MSWD of 0.84. The $^{207}Pb/^{206}Pb$ and $206Pb/238U$ ages lie within error of each other and it is interpreted that ca. 666 Ma represents the age of crystallisation for this monzogranite.
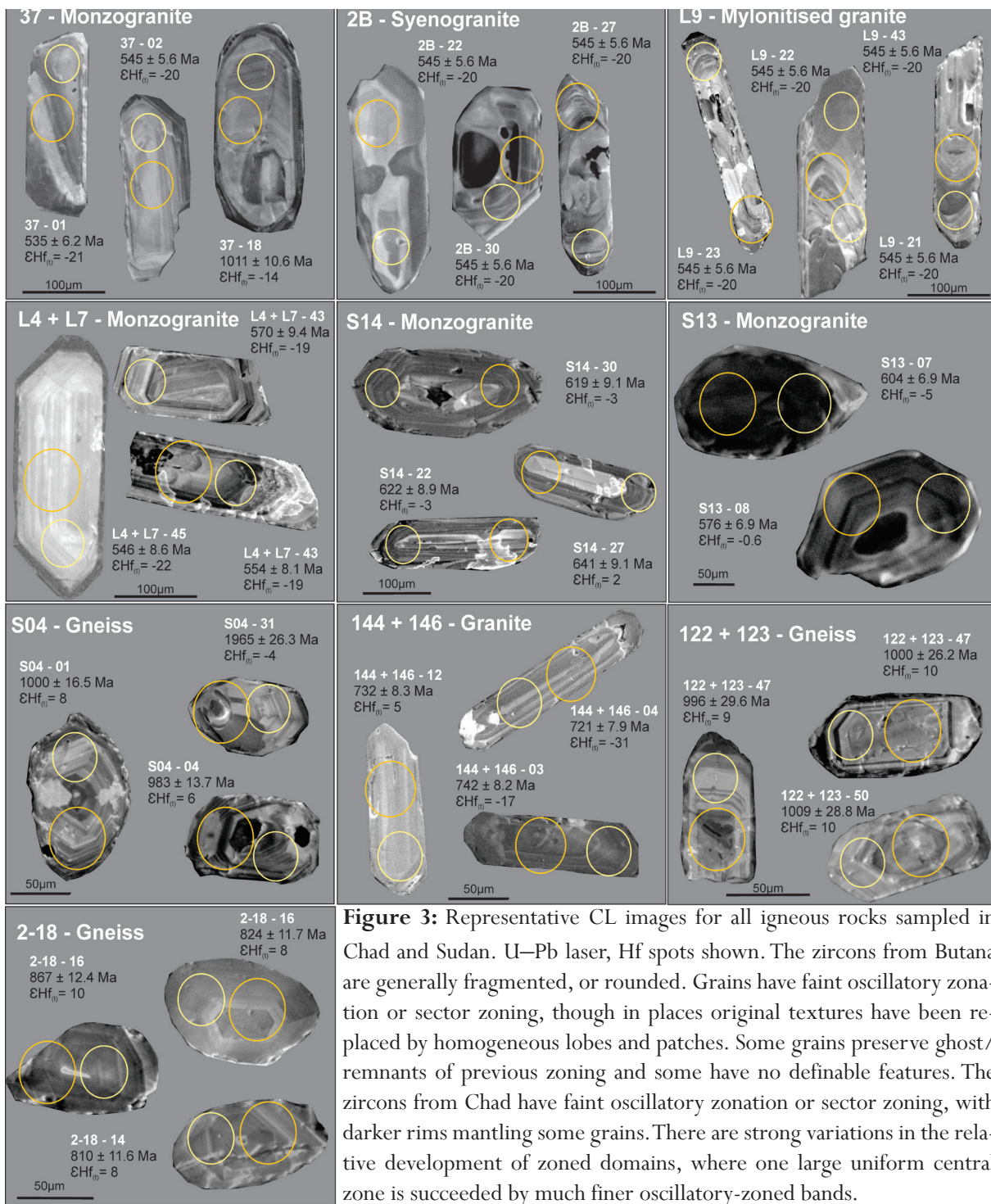
Figure 3: Representative CL images for all igneous rocks sampled in Chad and Sudan. U–Pb laser, Hf spots shown. The zircons from Butana are generally fragmented, or rounded. Grains have faint oscillatory zonation or sector zoning, though in places original textures have been replaced by homogeneous lobes and patches. Some grains preserve ghost/remnants of previous zoning and some have no definable features. The zircons from Chad have faint oscillatory zonation or sector zoning, with darker rims mantling some grains. There are strong variations in the relative development of zoned domains, where one large uniform central zone is succeeded by much finer oscillatory-zoned bands.

Hafnium isotope analyses were conducted on two zircon grains from the granite. $\varepsilon_{Hf}(t)$ values range between -0.58 and -4.96, suggesting these zircons are from a more evolved source (Fig. 5).

S14 Coarse – grained monzogranite (13°46'N 20°50'E)

Thirty one zircons were analysed, targeting rims and cores. Fourteen of these analyses were ≤ 10% discordant and show a range of $^{206}Pb/^{238}U$ ages between 963–589 Ma. The $^{206}Pb/^{238}U$ weighted average plot of analyses highlights
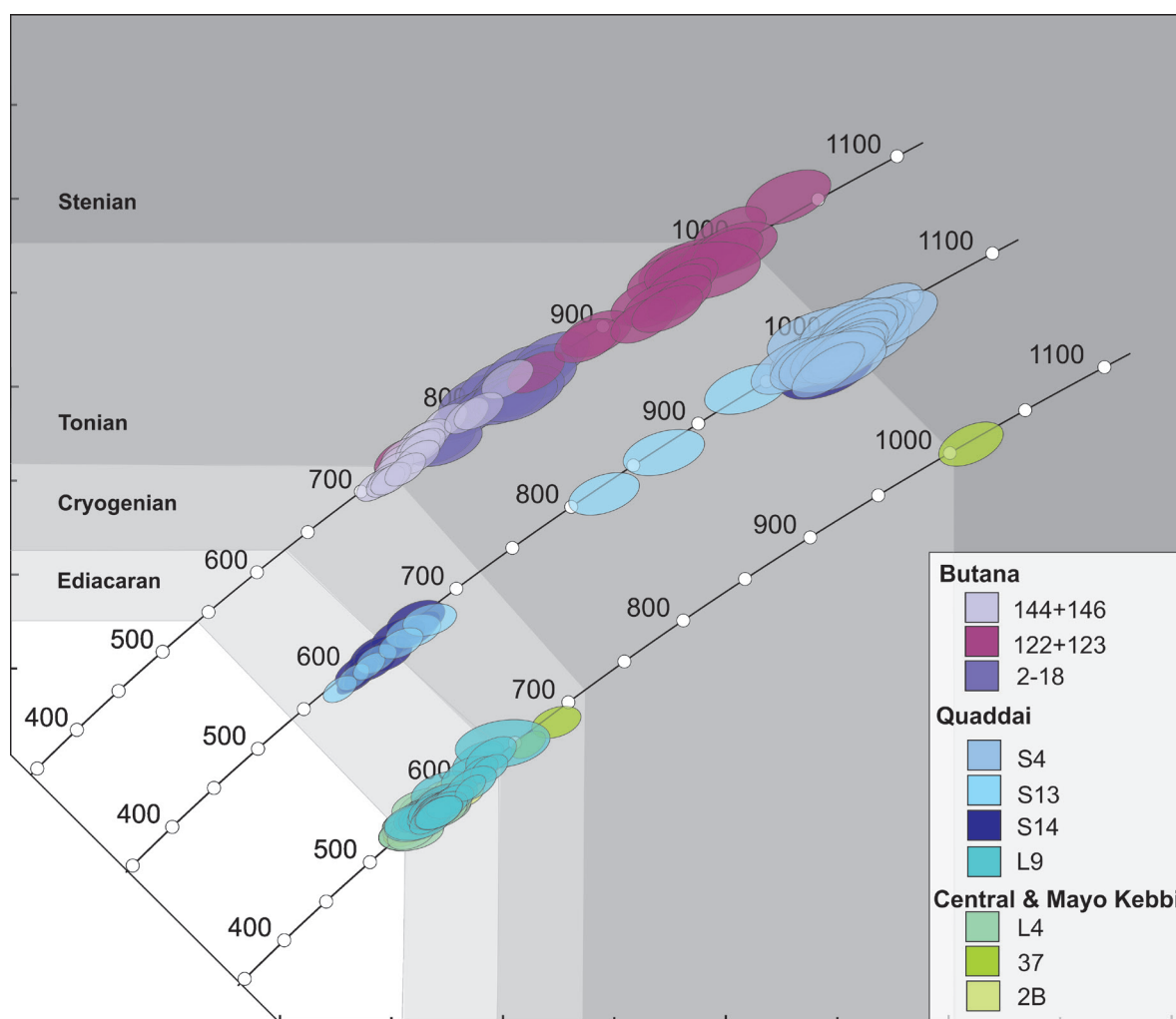
Figure 4: Samples are collated on a U-Pb Wetherill plots (^{207}Pb / ^{206}Pb v. $^{238}U/^{206}Pb$) and coloured by area. This plot was constructed with a 2 sigma data point error ellipses, only analyses within 90% concordance are shown in this figure. Each Concordia and cumulative weighted average plot, are displayed in the supplementary material. Butana is defined by three main pulses; ca. 987 Ma, 862 Ma and 764 Ma. Chad is defined by the intrusion of Neoproterozoic–late Mesoproterozoic granites (ca. 1000–1100 Ma) and Cryogenian (600–560 Ma) granites

two populations present (Appendix 5: Fig. 1e). A weighted mean 206Pb/238U age of all the concordant ($\geq$ 90%) data excluding the oldest (interpreted as an inherited grain) give an age of 614 $\pm$ 13 Ma with a large MSWD of 6, suggesting that these data do not represent one age. It is suspected that this large MSWD is due to post-crystallisation Pb loss, substantiated by the MSWD (0.54) of the $^{207}Pb/^{206}Pb$ weighted mean of the same analyses, which yields an age of 654 $\pm$ 18 Ma. Though slightly older, this is the interpreted age of the monzogranite, which

is within error of sample S13 (Appendix 5: Fig. 1d).

$\varepsilon_{Hf}(t)$ values on nine zircon grains, range between + 2.04 and -4.47 suggesting that these zircons were sourced from the remelting of pre-existing crust (Fig. 5).

S4 Orthogneiss (12°38'N 21°20'E)
Of the thirty two analyses, fourteen are within $\geq$ 90% concordance. These analyses show a range of $^{206}Pb/^{238}U$ ages from 2694–978 Ma. The $^{206}Pb/^{238}U$ weighted average plot shows

three distinct populations of zircons, with majority of the zircons defining a plateau between 1031–978 Ma (Appendix 5: Fig. 1f). The two distinctly older analyses ($^{207}Pb/^{206}Pb$ ages of 2753 ± 22 and 1967 ± 26 Ma) are defined by distinct cores and have been interpreted to represent inherited grains. The main population (defined by more prismatic, oscillatory zoned zircons), made up of twelve zircons, yields a $^{206}Pb/^{238}U$ age of 994 ± 10 Ma with an MSWD of 1.5, which we interpret to be the age of crystallisation of the protolith of this gneiss with inheritance of grains at 2694 and 1965 Ma.

Hafnium isotope analyses were conducted on eleven zircon grains from this gneiss. $\varepsilon_{Hf}(t)$ values range between +8.72 and +6.01 suggesting these zircons were from a juvenile source, with little continental crust involvement. The two inherited grains at ca. 2753 and 1957 Ma have $\varepsilon_{Hf}(t)$ values of -13.52 and -11.29 respectively, suggesting an evolved origin (Fig. 5).

Central and Mayo Kebbi Region
37 Monzogranite (12°24'N 17°20'E)
Forty–three analyses were conducted targeting cores and rims, of these fourteen are ≤ 10% discordant. The analyses show a range of $^{206}Pb/^{238}U$ ages from 1011–535 Ma. On the
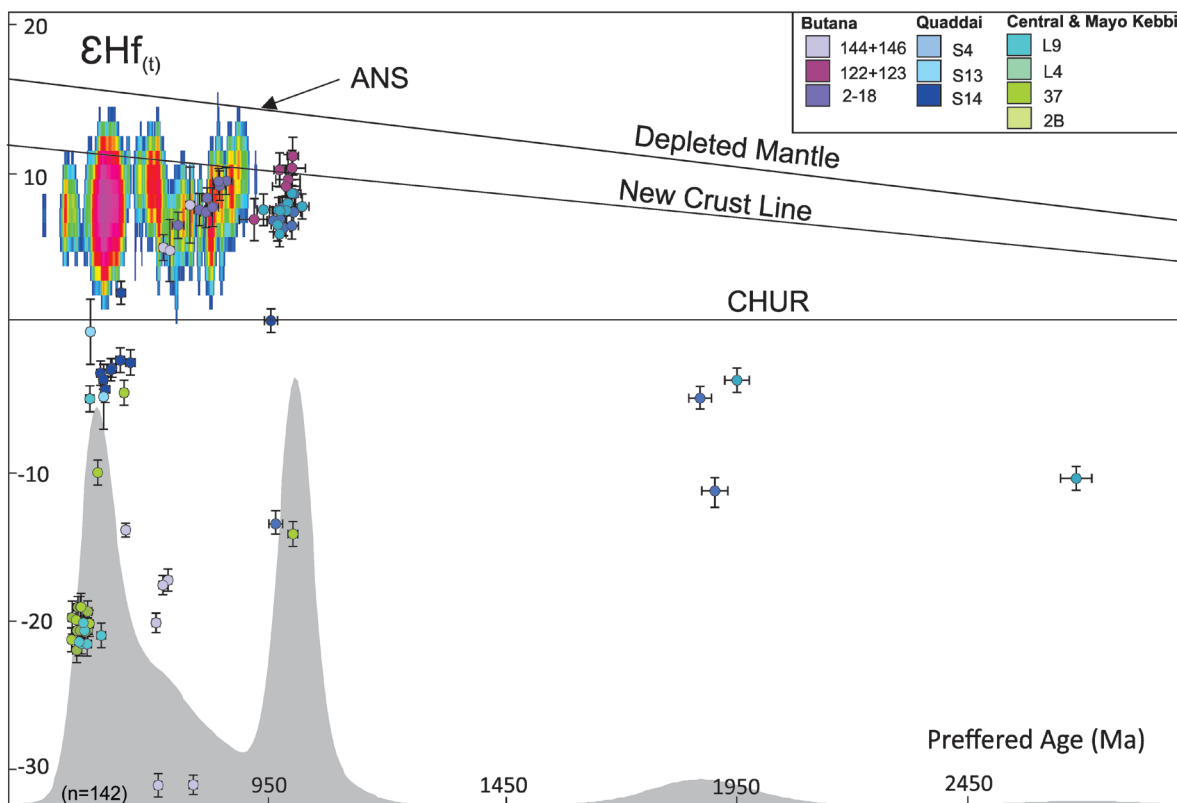
Figure 5: εHf(t) versus $^{206}Pb/^{238}U$ age plot for all igneous samples from Butana and Chad. Butana hafnium isotopic values suggest juvenile magmatism ($\varepsilon_{Hf}(t)$ of +4.89 to +7.89). The Cryogenian and Ediacaran magmatism within Chad have $\varepsilon_{Hf}(t)$ values between +2.04 and -4.07. Grey filled curve shows the density of ages within this study. Both horizontal and vertical error bars show 2σ error. Other data collated from the Arabian Nubian Shield are displayed as a grid, with red suggesting the highest concentration of data points (Alessio et al., 2017; Ali et al., 2013; Ali et al., 2016; Be'eri-Shlevin et al., 2010; Blades et al., 2015; Robinson et al., 2015; Robinson et al., 2014). New Crust line represents the best estimate for present-day compostion ($\varepsilon_{Hf}(t)$=13.2±1.1), calculated by the weighted average o the means of 13 modern island arcs world wide.

^{206}Pb/^{238}U weighted average plot the older four analyses are defined by cores and have been interpreted to represent inheritance. The other eleven form a spread along the Concordia (Supplementary Fig. 1g). A weighted average of all these zircons yields a ^{206}Pb/^{238}U age of 564 ± 9 Ma with an MSWD of 2.8. Therefore, a ^{207}Pb/^{206}Pb weighted average was calculated, giving a robust age of 604 ± 24 Ma (MSWD of 0.84), though slightly older, it provides a more accurate representation of the age of crystallisation of the deformed granite.

Hafnium isotope analyses on 6 zircon grains from this coarse grained monzogranite yielded ε_{Hf}(t) values between -4.69 and -21.32. These negative values imply formation from the reworking of continental crust. The inherited grain at 1011 Ma yields an ε_{Hf}(t) of -14.20, similar to younger ca. 550 Ma grains (Fig. 5).

2B Syenogranite (12°10'N 18°40'E)

Of the thirty three analyses, fifteen are ≤ 10% discordant and show a range of ^{206}Pb/^{238}U ages between 594–538 Ma. The youngest four analyses are located close to large cracks and have therefore been excluded from the age calculation (Appendix 5: Fig. 1h). The oldest grain (594 ± 7 Ma) is defined by a core with a younger (578 ± 7 Ma) rim. The main population of zircons is defined by ten zircons made up of differing morphologies. A weighted average of all these zircons yields a ^{206}Pb/^{238}U age of 582 ± 5 Ma with a MSWD of 0.59. The younger population (two analyses), made up of rims, give ^{206}Pb/^{238}U ages of 565 ± 6 and 565 ± 7 Ma. We interpret that the crystallisation age of this granite is best represented by 582 ± 5 Ma.

L9 Mylonitised granite (07°38'N 15°51'E)

Of the ninety–three analyses, forty–one are ≤ 10% discordance and show a range of ^{206}Pb/^{238}U ages from 649–549 Ma. The

^{206}Pb/^{238}U weighted average plot shows a distinct trend decreasing from 649 Ma with majority of the analyses at 575 Ma (Appendix 5: Fig. 1i). The older analyses are not defined by cores or differing morphologies and a weighted average of all analyses gives a ^{206}Pb/^{238}U age of 578 ± 5 Ma (MSWD of 3.6). To ensure that older analyses were not effecting the age, these were recalculated excluding the oldest six analyses, yielding an age of 571 ± 4 (MSWD of 1.6). This is within error suggesting that the array along the concordia is a result of post-formation lead loss. Therefore, in this instance, a weighted average ^{206}Pb/^{207}Pb age of 593 ± 12 Ma with an MSWD of 0.84 (within error of the ^{206}Pb/^{238}U age) provides a more accurate representation of the age of crystallisation of the deformed granite.

Hafnium isotope analyses were conducted on six zircon grains from this granite and ε_{Hf}(t) values range between -22.94 and -20.11 suggesting these zircons were formed from the reworking of continental crust (Fig. 5).

L4 + L7 Monzogranite (07°42'N 15°59'E and 07°38'N 15°53'E)

Fifty–six analyses were conducted targeting both rims and cores (with no discernible age difference). Of these fifty–six, twenty–two are ≤10% discordant and have a range of ^{206}Pb/^{238}U ages between 572–536 Ma. On the ^{206}Pb/^{238}U weighted average plot a distinct age plateau is seen (Appendix 5: Fig. 1j), suggesting one main period of zircon formation. The youngest two analyses are interpreted to represent Pb loss (analyses are within close proximity to cracks), therefore excluded from the ^{206}Pb/^{238}U age calculation. Twenty analyses give a ^{206}Pb/^{238}U age of 558 ± 4 Ma with an MSWD of 1.14 and a ^{207}Pb/^{206}Pb age of 572 ± 20 Ma (MSWD = 0.26). These ages are within error of each other and therefore interpreted that ca. 558 Ma represents the best age for the crystallisation of
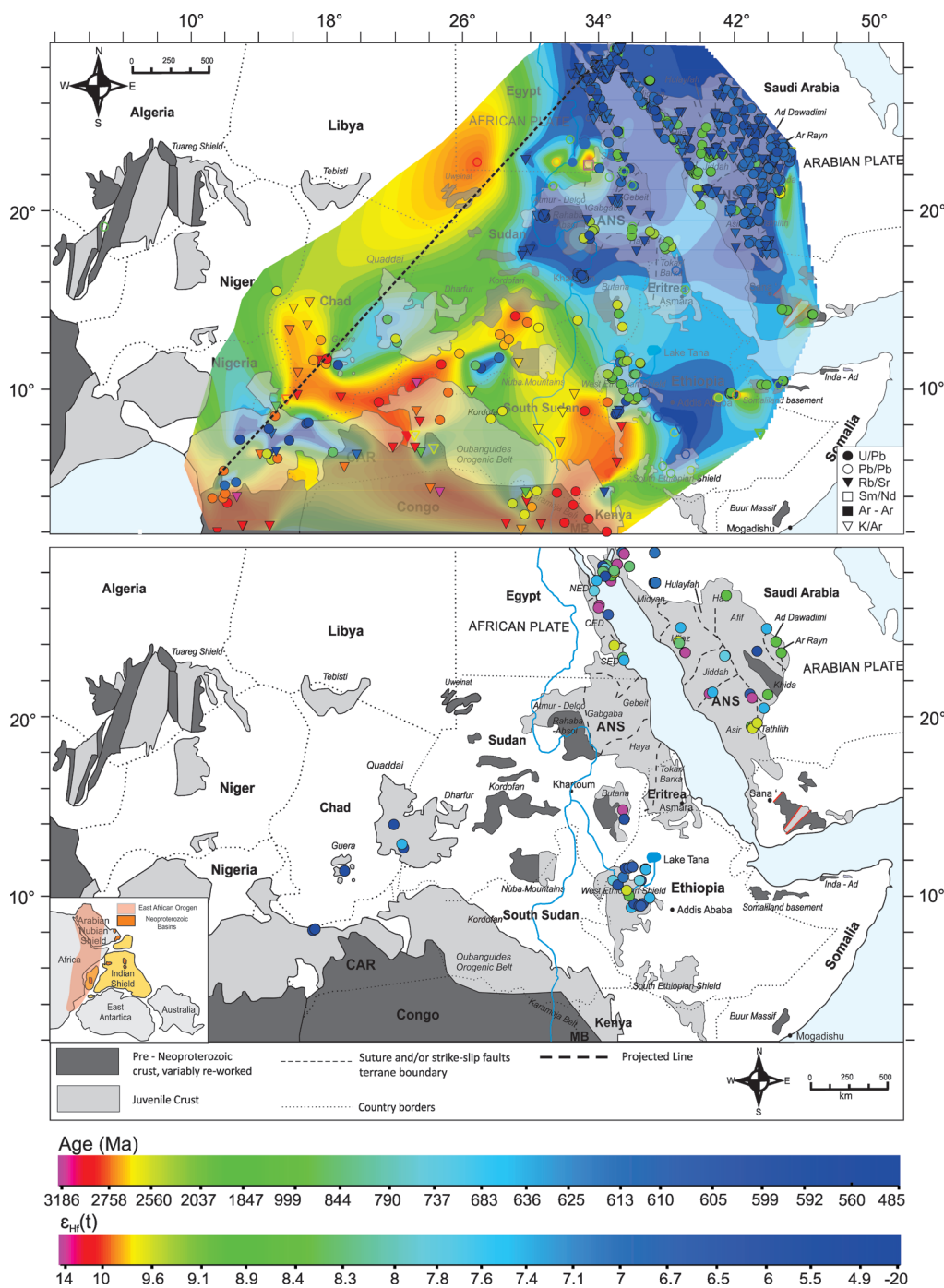
Figure 6: The top map is a collation of all available age data from northern Africa and these have been scaled by colour. Data clearly differentiates the juvenile Arabian Nubian Shield and the older mobilised Sahara Meta-craton. These ages have been gridded using ArcGIS nearest neighbour, as a visual aid (Abdelsalam et al., 2003; Abdelsalam et al., 2011; Abdelsalam et al., 2002; Be'eri-Shlevin et al., 2012; de Wit and Linol, 2015; Henry et al., 2009; Johnson et al., 2011; Johnson, 2014; Küster et al., 2008; Robinson et al., 2015; Robinson et al., 2014; Robinson et al., 2017; Whitehouse et al., 1998; Whitehouse et al., 2001; Windley et al., 1996; Yeshanew et al., 2016; Yeshanew et al., 2015). Bottom map shows a location map taken and distribution of crustal domains in the East African Orogen. SM, Sahara Metacraton; ANS, Arabian Nubian Shield. MB, Mozambique Belt. Previously published $\varepsilon_{Hf}(t)$ values (Alessio et al., 2017; Ali et al., 2013; Ali et al., 2016; Be'eri-Shlevin et al., 2010; Blades et al., 2015; Robinson et al., 2015; Robinson et al., 2014), have been collated with data from this study and are scaled by colour.
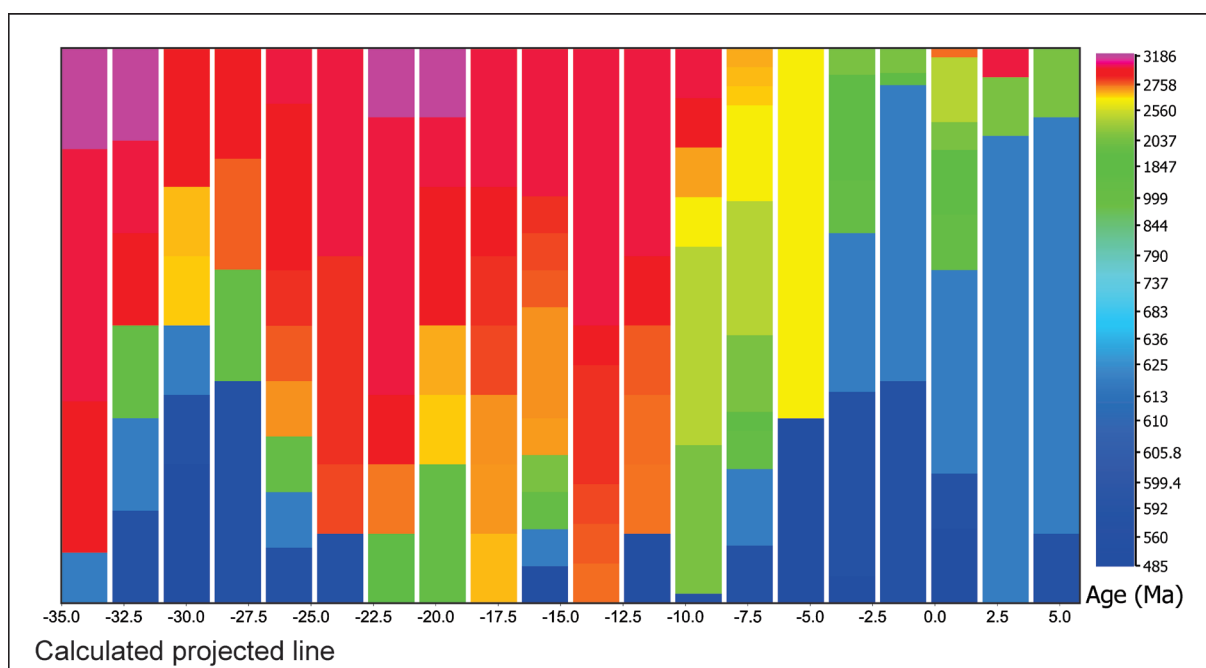
Figure 7: Histogram showing ages versus a calculated projected line, shown on figure 6. These ages have been scaled by colour. This plot shows the relative density of ages from south-west to north-east. All points have been projected onto the line. These data highlight the complex nature of the Neoproterozoic, demonstrating the continual remobilisation of the Sahara Metracraton crust during this time and the transition to the young juvenile crust of the Arabian Nubian Shield.

this granite.

Hafnium isotopes were conducted on ten zircons. These yield $\varepsilon_{Hf}(t)$ values between -19.42 and -22.02 suggesting these zircons were sourced from the remelting of continental crust (Fig. 5).

DISCUSSION

Timing and nature of magmatism in Butana

The timing and nature of magmatism in Butana is largely unknown, to date there has been little geological work done in this area. However, Butana holds an important position close to the transition between the enigmatic Sahara Metacraton and the accreted terranes of the Arabian Nubian Shield (Abdelsalam et al., 2002; Fritz et al., 2013; Johnson et al., 2011a; Johnson, 2014). The terrane is composed of low-grade meta-volcanic rocks, pre- and syn-tectonic granitic intrusions, serpentinites,

ophiolitic meta-gabbro and high-grade metamorphic rocks. This paper highlights that the magmatism in the Butana occurs at ca. 987 Ma, 829 Ma and 780 Ma. The first two pulses are seen within gneissic samples and are defined by juvenile $\varepsilon_{Hf}(t)$ values (+6.59 to +11.25), suggesting that these zircons crystallised from a melt, where older continental crust assimilation was negligible (Fig.5). Both samples are morphologically characterised by zircons with dark rims mantling the cores (ca. 765 Ma) and thus we interpret this to represent a recrystallisation event at this time. Slightly west, a granite (144 + 146) has a crystallisation age of 780 $\pm$ 14 Ma, within error of the recrystallisation rims seen within the older gneisses. $\varepsilon_{Hf}(t)$ values lie between +8 and -31, with evidence of both juvenile and reworked zircons present (Fig.5 and Fig. 6). A possible explanation for the bimodal $\varepsilon_{Hf}(t)$ signature could be that older Sahara Metacraton zircons

were entrained in the melt and reset at ca. 780 Ma but retained their original hafnium isotopic composition. These evolved $\varepsilon_{Hf}(t)$ signatures overlap with known Sahara Metacraton samples analysed in this study (S13, S14, S4 37, 2B, L9 and L4+L7). This, therefore, could provide evidence for the interpretation that Butana does indeed represent the transition between the juvenile Arabian Nubian Shield and the older, reworked Sahara Metacraton. The Uweynat massif, further west of Butana, has been suggested to contain only Archean crust that has not recorded any remobilisation within the Neoproterozoic (Harris et al., 1984; Schandelmeier and Darbyshire, 1984).

Timing and nature of magmatism in Chad

The Ouaddai region lies in the east of Chad and has basement comprised of granitoids, migmatites and gneisses (Fig. 1a). The gneiss (S4) in the Quaddia region yields an age of 1040 ± 21 Ma with inheritance of grains at 2753 ± 22 Ma and 1967 ± 26 Ma. The $\varepsilon_{Hf}(t)$ for the ca. 1040 Ma population shows a juvenile signature ($+8.72$ to $+6.55$). However, the older grains show derivation from reworked continental crust ($\varepsilon_{Hf}(t) = -13.52$ to -11.29). The samples collected from two coarse grained monzonites that intrude the older gneiss, show that magmatism occurring between 665–654 Ma, with $\varepsilon_{Hf}(t)$ values, $+2.04$ and -4.07 suggesting interaction with older continental crust (Fig. 5).

Within the Central Massif the assemblages are intruded by Precambrian alkaline granites, monzonites and syenites. The monzogranite (2B) shows magmatism at ca. 582 Ma, with a younger population, made up of rims, at ca. 565 Ma. This younger recrystallisation event is contemporaneous with the crystallisation of monzogranite (37) at ca. 550 Ma. The $\varepsilon_{Hf}(t)$

value shows significant continental crustal influence (-4.69 and -21.32), interpreted to be the melting of older Sahara Metacraton.

The southernmost exposure of Precambrian rocks in Chad, have ages coeval with the Central Massif, though younger than the Quaddai region. The deformed granite defines the oldest granites in the area at ca. 593 Ma, within error of magmatism in the Central Massif (2B ca. 582). The younger monzogranite (L4 + L7) has a crystallisation age of 558 ± 4 Ma (MSWD= 1.14), this is contemporaneous with the younger phase of magmatism in the Central Massif. The $\varepsilon_{Hf}(t)$ values are between -19.42 and -22.94 suggesting these zircons were sourced from a magma that involved the remelting of the older Sahara Metacraton.

These younger granites seen in the Quaddai region, Central Massif and the Mayo Kebbi yield similar ages to other late Neoproterozoic igneous activity (650–550 Ma) reported in the Saharan Metacraton, often interpreted as post tectonic magmatism (Ashwal and Burke, 1989; Black and Liégeois, 1993; Shang et al., 2010; Fezaa et al., 2010).

Tectonic implications of the terranes

Throughout the literature there have been numerous interpretations for the Sahara Metacraton, these are summarized in Abdelsalam et al. (2002). Briefly the main hypotheses are: 1) Data suggests the existence of a craton prior to the Neoproterozoic orogenic events, however this was decratonised. 2) There was coherent continental crust prior to the Neoproterozoic that was subjected to extension, producing rifting and subsequent opening and closing of oceanic basins, which led to the collision of continental blocks. 3) Lastly, this tract is made up of a collage of exotic terranes that were assembled during the Neoproterozoic. The presence of low grade volcano-sedimentary rocks within the medium to high grade gneissic
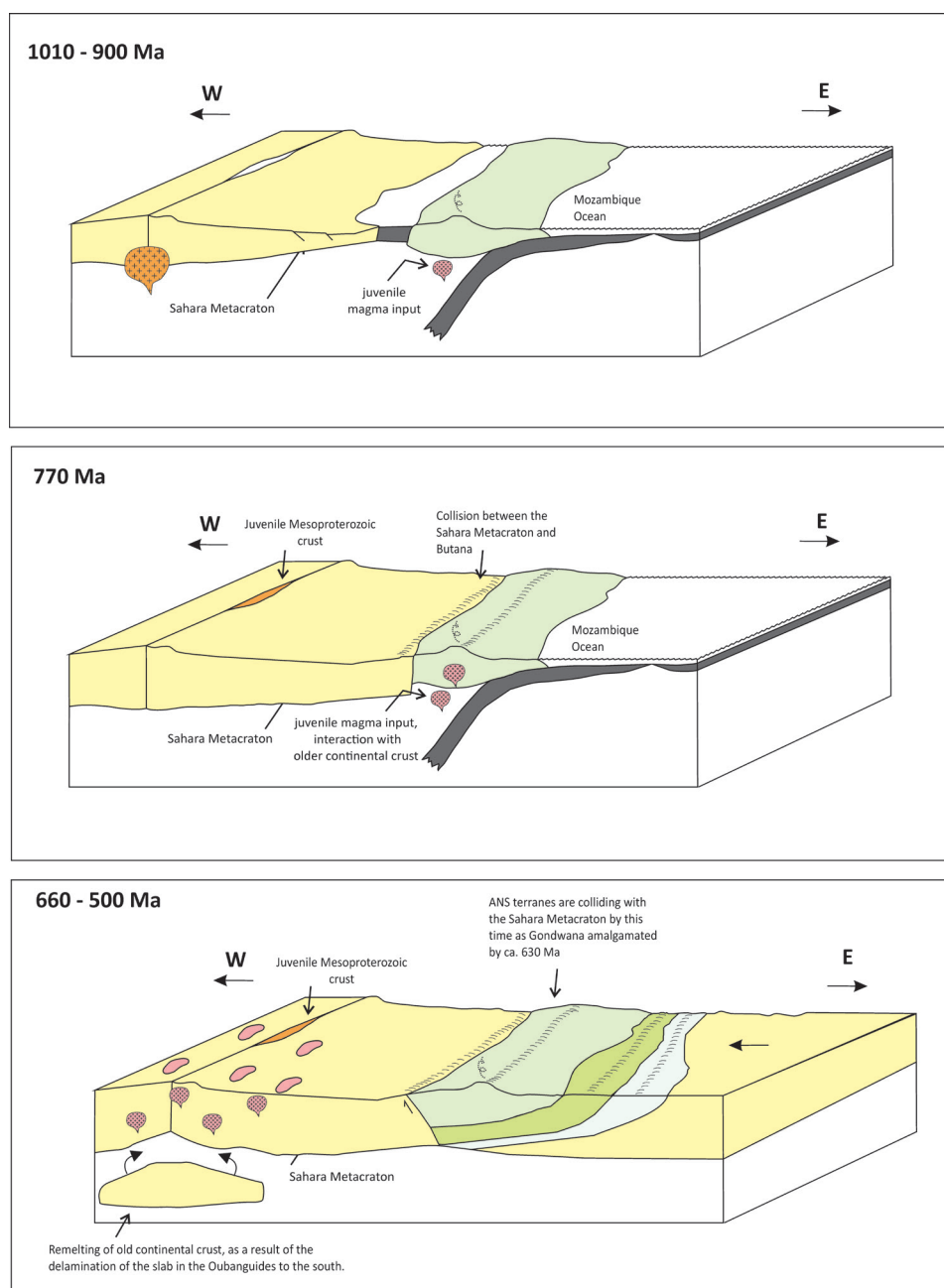
Figure 8: Three tectonic time slices for the evolution of Chad and Sudan. Neoproterozoic-late Mesoproterozoic granites seen in Chad (ca. 1000–1100 Ma), are interpreted to be related to rifting. The initiation of juvenile magamtism in Butana starts at 987 Ma. The time slice at 780 Ma represents the youngest phase of magamastim in Butana and reflects collision of Butana onto the Sahara Metacraton. The last time slice represents the amalgamation of the terranes of the Arabian Nubian Shield, Butana and the Sahara Metacraton, defined by the Keraf Suture at 650–580 Ma. The emplacement of Ediacaran–Cambrian granites were the result of the delamination of the slab to the south as the Oubanguides formed (Abdelsalam et al., 2002; Küster et al., 2008).

terranes have been considered problematic, in that the former are similar to those of the juvenile ANS. The eastern margin of the Sahara Metacraton is typically defined by the Keraf Suture, which has juxtaposed the younger, juvenile arc terranes of the Arabian Nubian Shield against Mesoproterozoic aged rocks of the eastern Sahara Metacraton (Abdelsalam et

al., 2002; Küster et al., 2008b). The variations in age data throughout northern Africa, shown in Figs. 6 and 7, highlight the remobilisation of the continental block (Sahara Metacraton) during the Neoproterozoic, as well as a definable change from juvenile younger rocks to predominantly older crust (Fig. 7). Little U–Pb data exists within the Sahara Metacraton, the majority of data being older whole rock Rb–Sr results, however recent a compilation by de Wit and Linol (2015) show that the southern parts of the region are composed of mainly late Mesoproterozoic crust (Fig. 8). In the west, geochronology suggests ages between 2629–1922 Ma (Liégeois et al., 1994; Stern, 1994a; Sultan et al., 1994). These are intruded by early Neoproterozoic – late Mesoproterozoic granites (ca. 1000–1100 Ma), which were deformed during the Neoproterozoic. Hafnium isotopes in this paper show that the Mesoproterozoic zircons in the Quaddai region were derived from mantle sources (Fig. 6 and 7) and could be explained by either rifting at this time, or the presence of an exotic Mesoproterozoic terrane, which would suggest that the 'Sahara Metacraton' was amalgamated after this time, probably during the Neoproterozoic (Fig. 8). The southernmost Precambrian exposure in Chad preserves crystallisation ages of ca. 593–580 Ma, with recrystallisation and further magmatism at ca. 565–550 Ma (Fig. 8). The $\varepsilon_{Hf}(t)$ values show significant continental crust reworking ($\varepsilon_{Hf}(t) =$ -14 to -22), suggesting the melting of the older surrounding crust, supporting rifting rather than the existence of an exotic terrane (Fig. 8). This is supported by Abdelsalam et al. (2002, 2006), who suggested that the metacraton acted as a coherent rheological entity and therefore cannot be simply interpreted as an exotic terrane with remnants of older continental crust. Seismic tomography from Abdelsalam et al. (2011) shows the Sahara

metacraton to have an upper mantle structure that can be explained by partial removal of its cratonic root, and a sub continental lithospheric mantle typical of other cratons persisting to depths of 100 km (Abdelsalam et al., 2011). Ediacaran magmatism between 600–560 Ma, seen in this study is abundant throughout the entire north-eastern Saharan metacraton, with exception of the Uweynat massif (Abdelsalam et al., 2002; Küster and Harms, 1998; Stern, 1994b), as well as on the western border of the Sahara Metacaton, in association with the Raghane shear zone (Abdallah et al., 2007; Henry et al., 2009; Liégeois et al., 1994). The emplacement of these high-K calc-alkaline granites may be due to mantle delamination during the Neoproterozoic that has resulted in the anomalously thin lithosphere beneath the region (Abdelsalam et al. 2011).

The terranes in Butana, discussed in this paper, have been interpreted to form as accreted arc terranes to the east of continental crust (Sahara Metacraton), with the oldest juvenile magmatism at ca. 987 Ma and subsequent magmatism and recrystallisation event at 780 Ma, shown by zircon core – rim relationships. The ca. 780 Ma event is believed to represent the terrane colliding or accreting on to the Sahara Metacraton. Magmatism and metamorphism at ca. 780 Ma is also seen in western Ethiopia, in the Dire Dawa Basement in eastern Ethiopia as well as the Tokar / Barka Terrane (Andersson et al., 2006; Blades et al., 2015; Teklay et al., 2003; Yeshanew et al., 2016). The bimodal $\varepsilon_{Hf}(t)$ signature and model ages, in the western most sample (144 + 146) in Butana (Fig. 5), suggest that when this granite crystallised, it was able to source older reworked zircons. This could provide the boundary between the dominantly juvenile terranes and older deformed continental crust to the west. The juvenile rocks in the Bayuda Desert reported

by Küster and Liégeois (2001) have also been interpreted to represent the eastern margin of the Sahara Metacraton. It is interpreted that the Keraf Suture was a result of a sinstral transgressive tectonic regime that was a result of the closing of the Mozambique Ocean (Fig. 8), with deformation along the shear zone ending at ca. 580 Ma and the terranes of the Arabian Nubian Shield amalgamated on the eastern margin of the Sahara Metacraton. (Abdelsalam et al., 1998; Merdith et al., 2017).

CONCLUSION

The relative timing and duration of magmatism during the Neoproterozoic within northern Africa is still slowly being unraveled and we present new U–Pb, Hf isotopic data from zircons in Butana and Chad. This paper highlights that the magmatism in the Butana is defined by three main pulses; ca. 987 Ma, 862 Ma and 764 Ma. Data suggest that accretion of the Butana terrane was initiated at ca. 987 Ma, from a mantle derived source (ε_{Hf}(t) = +6.98 to +11.25) with subsequent juvenile magmatism at ca. 864 Ma. The youngest pulse is coeval with metamorphism and hafnium isotopes suggest interaction between the juvenile terrane and older reworked continental crust. We interpret this to reflect overthrusting of Butana onto the Sahara Metacraton at this time.

Ages within the Sahara Metacraton range between 2629–1922 Ma (Liégeois et al., 1994; Stern, 1994a; Sultan et al., 1994). These are intruded by early Neoproterozoic–late Mesoproterozoic granites (ca. 1000–1100 Ma), that are here interpreted to be related to rifting. These were deformed during the Neoproterozoic and intruded by 600–560 Ma granites, which were formed by the re-melting of Mesoproterozoic terranes. These ages are abundant in the entire Saharan metacraton, with exception of the Uweynat massif (Abdelsalam

et al., 2002; Küster and Harms, 1998; Stern, 1994b) and are interpreted to reflect the Ediacaran delamination of the lithospheric root of the region.

These data highlight the complex nature of the Neoproterozoic, demonstrating the continual remobilisation of the Sahara Metracraton crust during this time, as well as that the East African Orogen represented a long lived accretionary margin through the late Mesoproterozoic to the Cambrian. Combined, the data help to better understand the Sahara Metacraton and its surrounding terranes and elucidate the nature and evolution of Neoproterozoic plate tectonics.

REFERENCES

Abdallah, N., Liégeois, J.-P., De Waele, B., Fezaa, N., Ouabadi, A., 2007. The Temaguessine Fe-cordierite orbicular granite (Central Hoggar, Algeria): U–Pb SHRIMP age, petrology, origin and geodynamical consequences for the late Pan-African magmatism of the Tuareg shield. Journal of African Earth Sciences 49, 153-178.

Abdelsalam, M., Stern, R., 1996a. Sutures and shear zones in the Arabian-Nubian Shield. Journal of African Earth Sciences 23, 289-310.

Abdelsalam, M.G., Abdel-Rahman, E., -S.M., El-Faki, E.-F.M., Al-Hur, B., El-Bashier, F.-R.M., Stern, R.J., Thurmond,

A.K., 2003. Neoproterozoic deformation in the northeastern part of the Saharan Metacraton, northern Sudan. Precambrian Research 123, 203-221.

Abdelsalam, M.G., Gao, S.S., Liégeois, J.-P., 2011. Upper mantle structure of the Saharan Metacraton. Journal of African Earth Sciences 60, 328-336.

Abdelsalam, M.G., Liégeois, J.P., Stern, R.J., 2002. The Saharan Metacraton. Journal of African Earth Sciences 34, 119-136.

Abdelsalam, M.G., Stern, R.J., 1996b. Sutures and shear zones in the Arabian-Nubian Shield. Journal Of African Earth Sciences 23, 289-310.

Abdelsalam, M.G., Stern, R.J., Copeland, P., El-Faki, E.-F.M., Al-Hur, B., Ibrahim, F.M., 1998. The Neoproterozoic Keraf Suture in NE Sudan: sinistral transpression along the eastern margin of West Gondwana. Journal of Geology 106, 133-147.

Abdelsalem, M.G., Stern, R.J., 1996. Sutures and shear zones in the Arabian-Nubian shield. Journal of African Earth Sciences 23, 289-310.

Acef, K., Liégeois, J.P., Ouabadi, A., Latouche, L., 2003. The Anfeg post-collisional Pan-African high-K calc-alkaline batholith (Central Hoggar, Algeria), result of the LATEA microcontinent metacratonization. Journal of African Earth Sciences 37, 295-311.

Allen, A., Tadesse, G., 2003. Geological setting and tectonic subdivision of the Neoproterozoic orogenic belt of Tuludimtu, western Ethiopia. Journal of African Earth Sciences 36, 329-343.

Andersson, U.B., Ghebreab, W., Teklay, M., 2006. Crustal evolution and metamorphism in east-central Eritrea, south-east Arabian-Nubian Shield. Journal of African Earth Sciences 44, 45-65.

Andresen, A., Augland, L., Boghdady, G.,

Lundmark, A., Elnady, O., Hassan, M., El-Rus, M.A., 2010. Structural constraints on the evolution of the Meatiq Gneiss Dome (Egypt), East-African Orogen. Journal of African Earth Sciences 57, 413-422.

Augland, L.E., Andresen, A., Boghdady, G.Y., 2012. U–Pb ID-TIMS dating of igneous and metaigneous rocks from the El-Sibai area: time constraints on the tectonic evolution of the Central Eastern Desert, Egypt. International Journal of Earth Sciences 101, 25-37.

Avigad, D., Stern, R., Beyth, M., Miller, N., McWilliams, M., 2007. Detrital zircon U–Pb geochronology of Cryogenian diamictites and Lower Paleozoic sandstone in Ethiopia (Tigrai): age constraints on Neoproterozoic glaciation and crustal evolution of the southern Arabian–Nubian Shield. Precambrian Research 154, 88-106.

Azzouni-Sekkal, A., Liegeois, J.P., Bechiri-Benmerzoug, F., Belaidi-Zinet, S., Bonin, B., 2003. The "Taourirt" magmatic province, a marker of the closing stage of the Pan-African orogeny in the Tuareg Shield: review of available data and Sr-Nd isotope evidence. Journal of African Earth Sciences 37, 331-350.

Be'eri-Shlevin, Y., Eyal, M., Eyal, Y., Whitehouse, M.J., Litvinovsky, B., 2012. The Sa'al volcano-sedimentary complex (Sinai, Egypt): a latest Mesoproterozoic volcanic arc in the northern Arabian Nubian Shield. Geology 40, 403-406.

Bendaoud, A., Ouzegane, K., Godard, G., Liégeois, J.-P., Kienast, J.-R., Bruguier, O., Drareni, A., 2008. Geochronology and metamorphic PTX evolution of the Eburnean granulite-facies metapelites of Tidjenouine (Central Hoggar, Algeria): witness of the LATEA metacratonic evolution. Geological Society, London, Special Publications 297, 111-146.

Black, R., Latouche, L., Liégeois, J.P., Caby, R., Bertrand, J.M., 1994. Pan-African displaced terranes in the Tuareg shiled (central Sahara). Geology 22, 641-644.

Black, R., Liegeois, J.P., 1993. Cratons, Mobile Belts, Alkaline Rocks and Continental Lithospheric Mantle - the Pan-African Testimony. Journal Of the Geological Society 150, 89-98.

Blades, M.L., Collins, A.S., Foden, J., Payne, J.L., Xu, X., Alemu, T., Woldetinsae, G., Clark, C., Taylor, R.J., 2015. Age and hafnium isotopic evolution of the Didesa and Kemashi Domains, western Ethiopia. Precambrian Research 270, 267-284.

Caby, R., 1987. The Pan-African belt of West Africa from the Sahara desert to the Gulf of Benin. Anatomy of Mountain Ranges 1, 129-170.

Cox, G.M., Lewis, C.J., Collins, A.S., Halverson, G.P., Jourdan, F., Foden, J., Nettle, D., Kattan, F., 2012. Ediacaran terrane accretion within the Arabian-Nubian Shield. Gondwana Research 21, 341-352.

de Wit, M.J., Linol, B., 2015. Precambrian Basement of the Congo Basin and Its Flanking Terrains, Geology and Resource Potential of the Congo Basin. Springer, pp. 19-37.

El Makkrouf, A.A., 1988. Tectonic interpretation of Jabal Eghei area and its regional application to Tibesti orogenic belt, south central Libya (SPLAJ). Journal of African Earth Sciences (and the Middle East) 7, 945-967.

Fezaa, N., Liégeois, J.-P., Abdallah, N., Cherfouh, E.H., De Waele, B., Bruguier, O., Ouabadi, A., 2010. Late Ediacaran geological evolution (575–555Ma) of the Djanet Terrane, Eastern Hoggar, Algeria, evidence for a Murzukian intracontinental episode. Precambrian Research 180, 299-327.

Fritz, H., Abdelsalam, M., Ali, K.A., Bingen, B., Collins, A.S., Fowler, A.R., Ghebreab, W., Hauzenberger, C.A., Johnson, P.R., Kusky, T.M., Macey, P., Muhongo, S., Stern, R.J., Viola, G., 2013. Orogen styles in the East African Orogen: A review of the Neoproterozoic to Cambrian tectonic evolution. Journal of African Earth Sciences.

Ghuma, M.A., Rogers, J.J., 1978. Geology, geochemistry, and tectonic setting of the Ben Ghnema batholith, Tibesti massif, southern Libya. Geological Society of America Bulletin 89, 1351-1358.

Griffin, W., Pearson, N., Belousova, E., Saeed, A., 2006. Comment: Hf-isotope heterogeneity in zircon 91500. Chemical Geology 233, 358-363.

Griffin, W., Wang, X., Jackson, S., Pearson, N., O'Reilly, S.Y., Xu, X., Zhou, X., 2002. Zircon chemistry and magma mixing, SE China: in-situ analysis of Hf isotopes, Tonglu and Pingtan igneous complexes. Lithos 61, 237-269.

Harris, N., Hawkesworth, C., Ries, A., 1984. Crustal evolution in north-east and east Africa from model Nd ages. Nature 309, 773-776.

Henry, B., Liégeois, J.-P., Nouar, O., Derder, M., Bayou, B., Bruguier, O., Ouabadi, A., Belhai, D., Amenna, M., Hemmi, A., 2009. Repeated granitoid intrusions during the Neoproterozoic along the western boundary of the Saharan metacraton, Eastern Hoggar, Tuareg shield, Algeria: an AMS and U–Pb zircon age study. Tectonophysics 474, 417-434.

Howard, K.E., Hand, M., Barovich, K.M., Reid, A., Wade, B.P., Belousova, E.A., 2009. Detrital zircon ages: Improving interpretation via Nd and Hf isotopic data. Chemical Geology 262, 277-292.

Jackson, S.E., Pearson, N.J., Griffin, W.L., Belousova, E.A., 2004. The application of

laser ablation-inductively coupled plasma-mass spectrometry to in-situ U/Pb zircon geochronology. Chemical Geology 211, 47-69.

Johnson, P., Andresen, A., Collins, A.S., Fowler, A., Fritz, H., Ghebreab, W., Kusky, T., Stern, R., 2011a. Late Cryogenian–Ediacaran history of the Arabian–Nubian Shield: A review of depositional, plutonic, structural, and tectonic events in the closing stages of the northern East African Orogen. Journal of African Earth Sciences 61, 167-232.

Johnson, P.R., 2014. An Expanding Arabian-Nubian Shield Geochronologic and Isotopic Dataset: Defining Limits and Confirming the Tectonic Setting of a Neoproterozoic Accretionary Orogen. Open Geology Journal 8, 3-33.

Johnson, P.R., Andresen, A., Collins, A.S., Fowler, A.R., Fritz, H., Ghebreab, W., Kusky, T., Stern, R.J., 2011b. Late Cryogenian-Ediacaran history of the Arabian-Nubian Shield: A review of depositional, plutonic, structural, and tectonic events in the closing stages of the northern East African Orogen. Journal of African Earth Sciences 61, 167-232.

Johnson, P.R., Woldehaimanot, B., 2003. Development of the Arabian-Nubian Shield: perspectives on accretion and deformation in the northern East African Orogen and the assembly of Gondwana, in: Yoshida, M., Windley, B.F., Dasgupta, S. (Eds.), Proterozoic East Gondwana: Supercontinent Assembly and Breakup. Geological Society, London, Special Publication 206, pp. 289-325.

Kennedy, W.Q., 1964. The structural differentiation of Africa in the Pan-African (+/- 500 m.y.) Tectonic Episode, Eighth Annual Report on Scientific Results of the Research Institute of African Geology,

University of Leeds., pp. 48-49.

Kröner, A., 1977. The Precambrian geotectonic evolution of Africa: plate accretion versus plate destruction. Precambrian Research 4, 163-213.

Kröner, A., Linnebacher, P., Stern, R., Reischmann, T., Manton, W., Hussein, I., 1991. Evolution of Pan-African island arc assemblages in the southern Red Sea Hills, Sudan, and in southwestern Arabia as exemplified by geochemistry and geochronology. Precambrian Research 53, 99-118.

Küster, D., Harms, U., 1998. Post-collisional potassic granitoids from the southern and northwestern parts of the Late Neoproterozoic East African Orogen: a review. Lithos 45, 177-195.

Küster, D., Liégeois, 2001. Sr, Nd isotopes and geochemistry of the Bayuda Desert high-grade metamorphic basement (Sudan): an early Pan-African oceanic convergent margin, not the edge of the East Saharan ghost craton? Precambrian Research 109, 1-23.

Küster, D., Liégeois, J.-P., Matukov, D., Sergeev, S., Lucassen, F., 2008a. Zircon geochronology and Sr, Nd, Pb isotope geochemistry of granitoids from Bayuda Desert and Sabaloka (Sudan): Evidence for a Bayudian event (920–900 Ma) preceding the Pan-African orogenic cycle (860–590 Ma) at the eastern boundary of the Saharan Metacraton. Precambrian Research 164, 16-39.

Küster, D., Liégeois, J.-P., Matukov, D., Sergeev, S., Lucassen, F., 2008b. Zircon geochronology and Sr, Nd, Pb isotope geochemistry of granitoids from Bayuda Desert and Sabaloka (Sudan): Evidence for a Bayudian event (920–900Ma) preceding the Pan-African orogenic cycle (860–590Ma) at the eastern boundary of the Saharan

Metacraton. Precambrian Research 164, 16-39.

Liégeois, J.-P., Benhallou, A., Azzouni-Sekkal, A., Yahiaoui, R., Bonin, B., 2005. The Hoggar swell and volcanism: reactivation of the Precambrian Tuareg shield during Alpine convergence and West African Cenozoic volcanism. Geological Society of America Special Papers 388, 379-400.

Liégeois, J.-P., Black, R., Navez, J., Latouche, L., 1994. Early and late Pan-African orogenies in the Air assembly of terranes (Tuareg Shield, Niger). Precambrian research 67, 59-88.

Liégeois, J., Bertrand, J., Black, R., 1986. The subduction and collision related batholith of the Adrar des Iforas (Mali): Geochemical trends and evolution in space and time, A review, African Geology Reviews J. Kinnaird, P. Bowden, and.

Liegeois, J.P., Latouche, L., Boughrara, M., Navez, J., Guiraud, M., 2003. The LATEA metacraton (Central Hoggar, Tuareg shield, Algeria): behaviour of an old passive margin during the Pan-African orogeny. Journal of African Earth Sciences 37, 161-190.

Ludwig, K.R., 2009. Isoplot 3.0.

Ludwig, W., Strunk, O., Westram, R., Richter, L., Meier, H., Buchner, A., Lai, T., Steppi, S., Jobb, G., Förster, W., 2004. ARB: a software environment for sequence data. Nucleic acids research 32, 1363-1371.

Lundmark, A.M., Andresen, A., Hassan, M.A., Augland, L.E., Boghdady, G.Y., 2012. Repeated magmatic pulses in the East African Orogen in the Eastern Desert, Egypt: an old idea supported by new evidence. Gondwana Research 22, 227-237.

Merdith, A.S., Collins, A.S., Williams, S.E., Pisarevsky, S., Foden, J.F., Archibald, D.A., Blades, M.L., Alessio, B.L., Armistead, S., Plavsa, D., Clark, C., D.R, M., 2017. A Full PLate Global Reconstruction of the Neoproterzoic Gondwana Research.

Nkoumbou, C., Barbey, P., Yonta-Ngouné, C., Paquette, J.-L., Villiéras, F., 2014. Pre-collisional geodynamic context of the southern margin of the Pan-African fold belt in Cameroon. Journal of African Earth Sciences 99, 245-260.

Owona, S., Schulz, B., Ratschbacher, L., Ondoa, J.M., Ekodeck, G.E., Tchoua, F.M., Affaton, P., 2011. Pan-African metamorphic evolution in the southern Yaounde Group (Oubanguide Complex, Cameroon) as revealed by EMP-monazite dating and thermobarometry of garnet metapelites. Journal of African Earth Sciences 59, 125-139.

Paquette, J., Caby, R., Djouadi, M., Bouchez, J., 1998. U–Pb dating of the end of the Pan-African orogeny in the Tuareg shield: the post-collisional syn-shear Tioueine pluton (Western Hoggar, Algeria). Lithos 45, 245-253.

Payne, J.L., Pearson, N.J., Grant, K., Halverson, G.P., 2013. Reassessment of relative oxide formation rates and molecular interferences on in-situ Lutetium-Hafnium analysis with Laser Ablation MC-ICP-MS. . Journal of Analytical Atomic Spectrometry 28, 1068-1079.

Penaye, J., Kröner, A., Toteu, S.F., Van Schmus, W.R., Doumnang, J.-C., 2006. Evolution of the Mayo Kebbi region as revealed by zircon dating: An early (ca. 740Ma) Pan-African magmatic arc in southwestern Chad. Journal of African Earth Sciences 44, 530-542.

Peucat, J.J., Drareni, A., Latouche, L., Deloule, E., Vidal, P., 2003. U-Pb zircon (TIMS and SIMS) and Sm-Nd whole-rock geochronology of the Gour Oumelalen granulitic basement, Hoggar massif, Tuareg shield, Algeria. Journal of African Earth Sciences 37, 229-239.

Pin, C., Poidevin, J.L., 1987. U-Pb zircon

evidence for a Pan-African granulite facies metamorphism in the Central African Republic. A new interpretation of the high-grade series of the northern border of the Congo Craton. Precambrian Research 36, 303-312.

Robinson, F., Foden, J., Collins, A., Payne, J., 2014. Arabian Shield magmatic cycles and their relationship with Gondwana assembly: Insights from zircon U–Pb and Hf isotopes. Earth and Planetary Science Letters 408, 207-225.

Rocci, G., 1965. Essai d'interpretation de mesures geochronologiques. La structure de l'Ouest africain. Sciences Terre Nancy 10, 461-479.

Schandelmeier, H., Darbyshire, F., 1984. Metamorphic an magmatic events in the Uweinat—Bir Safsaf Uplift (Western Desert/Egypt). Geologische Rundschau 73, 819-831.

Schandelmeier, H., Klitzsch, E., Hendriks, F., Wycisk, P., 1987. Structural development of north-east Africa since Precambrian times. Berliner Geowissenschaftliche Abhandlungen 75, 5-24.

Schandelmeier, H., Wipfler, E., Küster, D., Sultan, M., Becker, R., Stern, R.J., Abdelsalam, M.G., 1994. Atmur-Delgo suture: A Neoproterozoic oceanic basin extending into the interior of northeast Africa. Geology 22, 563-566.

Scherer, E., Münker, C., Mezger, K., 2001. Calibration of the lutetium-hafnium clock. Science 293, 683-687.

Schneider, J., Wolf, J., 1992. Geological map and hydrogeological maps on scale 1/500,000 of Chad Republic. Explanatory project document of BRGM.

Schoene, B., 2014. 4.10-U–Th–Pb Geochronology. Treatise on Geochemistry 4, 341-378.

Shackleton, R., 1996. The final collision zone between East and West Gondwana: where is it? Journal of African Earth Sciences 23, 271-287.

Shalaby, A., Stüwe, K., Makroum, F., Fritz, H., Kebede, T., Klötzli, U., 2005. The Wadi Mubarak belt, Eastern Desert of Egypt: a Neoproterozoic conjugate shear system in the Arabian–Nubian Shield. Precambrian Research 136, 27-50.

Sláma, J., Kosler, J., Condon, D.J., Crowley, J.L., Gerdes, A., Hanchar, J.M., Horstwood, M.S.A., Morris, G.A., Nasdala, L., Norberg, N., Schaltegger, U., Schoene, B., Tubrett, M.N., Whitehouse, M.J., 2008. Plesovice zircon - A new natural reference material for U-Pb and Hf isotopic microanalysis. . Chemical Geology 249, 1-35.

Stern, R.A., Hedge, C.E., 1985. Geochronologic and isotopic constraints on Late Precambrian crustal evolution in the Eastern Desert of Egypt. American Journal of Science 285, 97-127.

Stern, R.J., 1994a. Arc-Assembly and Continental Collision in the Neoproterozoic African Orogen: Implications for the Consolidation of Gondwanaland. Annual Review of Earth and Planetary Sciences 22, 319-351.

Stern, R.J., 1994b. Arc Assembly and continental collision in the Neoproterozoic East African orogeny - implications for the consolidation of Gondwana. Annual Review of Earth and Planetary Sciences 22, 319-351.

Stern, R.J., 2002. Crustal evolution in the East African Orogen: a neodymium isotopic perspective. Journal of African Earth Sciences 34, 109-117.

Suayah, I.B., Miller, J.S., Miller, B.V., Bayer, T.M., Rogers, J.J., 2006. Tectonic significance of Late Neoproterozoic granites from the Tibesti massif in southern Libya inferred from Sr and Nd isotopes and U–

Pb zircon data. Journal of African Earth Sciences 44, 561-570.

Sultan, M., Tucker, R., El Alfy, Z., Attia, R., Ragab, A.G., 1994. U-Pb (zircon) ages for the gneissic terrane west of the Nile, southern Egypt. Geologische Rundschau 83, 514-522.

Teklay, M., Haile, T., Kröner, A., Asmerom, Y., Watson, J., 2003. A back-arc palaeotectonic setting for the Augaro Neoproterozoic magmatic rocks of western Eritrea. Gondwana Research 6, 629-640.

Toteu, S., Michard, A., Bertrand, J., Rocci, G., 1987. U/Pb dating of Precambrian rocks from northern Cameroon, orogenic evolution and chronology of the Pan-African belt of central Africa. Precambrian Research 37, 71-87.

Toteu, S., Van Schmus, W., Penaye, J., Nyobe, J., 1994. U–Pb and Sm–Nd evidence for Eburnian and Pan-African high-grade metamorphism in cratonic rocks of southern Cameroon. Precambrian Research 67, 321-347.

Toteu, S.F., Penaye, J., Deloule, E., Van Schmus, W.R., Tchameni, R., 2006. Diachronous evolution of volcano-sedimentary basins north of the Congo craton: Insights from U-Pb ion microprobe dating of zircons from the Poli, Lom and Yaounde Groups (Cameroon). Journal of African Earth Sciences 44, 428-442.

Toteu, S.F., Penaye, J., Djomani, Y.P., 2004. Geodynamic evolution of the Pan-African belt in central Africa with special reference to Cameroon. Canadian Journal of Earth Science 41, 73-85.

Toteu, S.F., Van Schmus, W.R., Penaye, J., Michard, A., 2001. New U-Pb and Sm-Nd data from north-central Cameroon and its bearing on the pre-Pan African history of central Africa. Precambrian Research 108, 45-73.

Vail, J.R., 1973. Outline of the geology of the Nuba Mountains and vicinity, southern Kordofan Province, Sudan. Democratic Republic of the Sudan, Ministry of Industry and Mining, Geological and Mineral Resources Department.

Vail, J.R., 1983. Pan-African crustal accretion in north-east Africa. Journal of African Earth Sciences (1983) 1, 285-294.

Vail, J.R., Rex, D.C., 1971. Potassium-argon age measurements on pre-Nubian basement complex rocks from Sudan. Proc. Geol. Soc. London 1664, 205-214.

Van Achterbergh, E., Ryan, C.G., Jackson, S.E., Griffin, W.L., 2001. Data reduction software for LA-ICP-MS, in: Sylvester, P.J. (Ed.), Laser-ablation-ICPMS in the earth sciences; principles and applications. Mineralogical Association of Canada, Short Course Handbook, Ottowa, pp. 239-243.

Wendt, I., Carl, C., 1991. The statistical distribution of the mean squared weighted deviation. Chemical Geology: Isotope Geoscience Section 86, 275-285.

Woodhead, J.D., Hergt, J.M., Shelley, M., Eggins, S., Kemp, R., 2004. Zircon Hf-isotope analysis with an Excimer laser, depth profiling, ablation of complex geometries, and concomitant age estimation. . Chemical Geology 209, 121-135.

Yeshanew, F.G., Pease, V., Abdelsalam, M.G., Whitehouse, M.J., 2016. Zircon U–Pb ages, $\delta^{18}O$ and whole-rock Nd isotopic compositions of the Dire Dawa Precambrian basement, eastern Ethiopia: implications for the assembly of Gondwana. Journal of the Geological Society, jgs2016-2017.

CHAPTER 6

This chapter is written for submission to *The Journal of Geological Society of London* as:

Blades, M.L., Alessio, B.L., Collins, A.S., Foden, J., Payne, J.L., Holden, P., Glorie, S., Thorpe, B., Al-Khirbash, S. Unravelling the Neoproterozoic Accretionary History of Oman, Using an Array of Isotopic Systems in Zircon.

Statement of Authorship

Title of Paper	Unravelling the Neoproterozoic accretionary history of Oman, using an array of isotopic systems in zircon.
Publication Status	☐ Published ☐ Accepted for Publication ☐ Submitted for Publication ☑ Unpublished and Unsubmitted work written in manuscript style
Publication Details	For submission to Journal of the Geological Society of (London) as: Blades, M.L., Alessio, B.L., Collins, A.S., Foden, J., Payne, J.L., Holden, P., Glorie, S., Thorpe, B., Al-Khirbash, S. Unravelling the Neoproterozoic accretionary history of Oman, using an array of isotopic systems in zircon.

Principal Author

Name of Principal Author (Candidate)	Morgan Blades		
Contribution to the Paper	Data collection, processing and interpretation, manuscript design and composition, creation of figures		
Overall percentage (%)	80		
Certification:	This paper reports on original research I conducted during the period of my Higher Degree by Research candidature and is not subject to any obligations or contractual agreements with a third party that would constrain its inclusion in this thesis. I am the primary author of this paper.		
Signature		Date	06/09/2017

Co-Author Contributions

By signing the Statement of Authorship, each author certifies that:

    i.   the candidate's stated contribution to the publication is accurate (as detailed above);

    ii.   permission is granted for the candidate in include the publication in the thesis; and

    iii.   the sum of all co-author contributions is equal to 100% less the candidate's stated contribution.

Name of Co-Author	Brandon Alessio		
Contribution to the Paper	Guidance in fieldwork, sample preparation, data interpretation and manuscript review.		
Signature		Date	06/09/2017

Name of Co-Author	Professor Alan Collins		
Contribution to the Paper	Guidance in fieldwork, sample preparation, data interpretation and manuscript review.		
Signature		Date	06/09/2017

Name of Co-Author	Emeritus Professor John Foden

Signature		Date	06/09/2017

Name of Co-Author	Emeritus Professor John Foden
Contribution to the Paper	Guidance in fieldwork, sample preparation, data interpretation and manuscript review.

Signature		Date	06/09/2017

Name of Co-Author	Dr Justin Payne
Contribution to the Paper	Guidance in sample preparation, data collection and interpretation (Lu-Hf isotopes) and manuscript review.

Signature		Date	06/09/2017

Name of Co-Author	Dr Peter Holden
Contribution to the Paper	SHRIMP O isotope data collection and manuscript review

Signature		Date	06/09/2017

Name of Co-Author	Dr Stijn Glorie
Contribution to the Paper	Guidance in sample preparation, data interpretation and manuscript review.

Signature		Date	06/09/2017

Name of Co-Author	Ben Thorpe
Contribution to the Paper	Field work, data collection of Jebel Ja'alan metasediment

Signature		Date	06/09/2017

Name of Co-Author	Associate Professor Salah Al Khirbash
Contribution to the Paper	Fieldwork logistics and manuscript revision.

Signature		Date	06/09/2017

Please cut and paste additional co-author panels here as required.

ABSTRACT

The Neoproterozoic was a period of major plate tectonic activity, climatic extremes, the appearance of multicellular life and the accumulation of some of the first major petroleum deposits. The position of Oman during the Neoproterozoic is still relatively unconstrained. Yet, understanding it is critical to understanding the tectonic geography link between the Arabian-Nubian Shield and Neoproterozoic India. The Huqf Supergroup and basement are exposed in small inliers; in northern Oman (Jebal Akhdar), east-central Oman (Huqf area and Jebel Ja'alan) and southern Oman (Mirbat area of Dhofar). The Omani basement is located to the east of the juvenile arc terranes of the Arabian Nubian Shield (ANS). While the geology and nature of the ANS is relatively well known, the basement to the east in Oman, is far less understood. Though much of the Neoproterozoic basement is overlain by thick cover, they are critical to understanding the eastern half of the Arabian plate. Here, we provide some of the first Lu–Hf and oxygen isotope data in zircons from igneous and metasedimentary units from various basement localities in Oman. Geochronological data suggests a progressive decrease in the age of arc magmatism from present day east to west, from Jebel Ja'alan to the Huqf and Mirbat. Lu–Hf and oxygen isotopes support the progressive development of arc rocks, with a decrease in crustal influence starting from the older eastern exposures ($\delta^{18}O$ (zircon) ‰ average value of 7.57) to the more juvenile exposures in Mirbat ($\varepsilon_{Hf}(t)$ values 10.5–8.72 and $\delta^{18}O$ (zircon) ‰ of 4.3 − 5.3‰). The detritus from Mirbat preserves no evidence of older zircons, with the main age peak at ca. 777 Ma. These patterns together with the zircon Lu–Hf and oxygen isotopes are consistent local sediment derivation, and little older crustal input. In contrast the small detrital zircon age peaks (and Lu–Hf isotopes) seen in the metasedimentary rocks in Jebel Ja'alan (2706 and 1204 Ma) indicate that at this time Jebel Ja'alan was depositionally connected to a Paleoproterozoic–Neoarchean source region. These sources broadly correlate with the detritus seen in the Marwar Supergroup and Upper Vidhyan in NW India and correlate with magmatic ages seen in the Kabul Block. This therefore supports the Omani basement representing its own tectonic domain, separate from the Arabian Nubian Shield, accreting onto the Neoproterozoic accretionary margin of NW India.

INTRODUCTION:

The Oman basement underlies the Cryogenian to Ediacaran Huqf Supergroup, host to some of the oldest known petroleum source rocks and a record of basin development, climate change and biosphere evolution during the Neoproterozoic (Allen, 2007) While the geology and nature of eastern Arabia is relatively well know, the basement in eastern Arabia is far less understood (Allen, 2007; Whitehouse et al. 2016; Alessio et al. 2017). Towards the Arabian Gulf states and Oman, sedimentary cover increases to the point that much of Oman's basement is extensively overlain by Late Neoproterozoic to Phanerozoic sedimentary

and volcanic rocks (Stern and Johnson, 2010). As a result there are only a small number of windows into the basement that occur within Oman; Mirbat, the Huqf, Jebel Ja'Alan and Al Jobah (Fig. 1b). These exposures offer an insight into the palaeogeography of the region during Neoproterozoic time; a period of plate reorganisation, glacial episodes and the explosion of Ediacaran fauna (Allen, 2007; Hoffman et al., 1998; Meert and Lieberman, 2008; Merdith et al., 2017).

A number of authors have used geochemistry to interpret the tectonic setting of the igneous and metamorphic basement of Oman and suggest that it formed in an intra-oceanic volcanic-

arc setting (Alessio et al., 2017; Bowring et al., 2007; Gass et al., 1990; Mercolli et al., 2006; Rantakokko et al., 2014; Rieu et al., 2007; Whitehouse et al., 2016) within the Neoproterozoic Mozambique Ocean (Allen, 2007; Fritz et al., 2013; Johnson et al., 2011; Johnson, 2014; Johnson and Woldehaimanot, 2003; Stern and Johnson, 2010). To the west of the Omani basement is the collage of island arc terranes of the Arabian Nubian Shield (Fig. 1a) and these represent the northern extension of the vast East African Orogen, which stretches 8000 km's, forming the largest Precambrian mobile belt (Johnson et al., 2011; Johnson, 2014; Johnson and Kattan, 2012). The relationship between the Omani basement and the arc terranes of the Arabian Nubian Shield (ANS) has been addressed by several authors (Alessio et al., 2017; Allen, 2007; Collins and Pisarevsky, 2005; Fritz et al., 2013; Johnson et al., 2011; Johnson, 2014; Johnson and Woldehaimanot, 2003; Merdith et al., 2017; Rantakokko et al., 2014; Stern and Johnson, 2010; Whitehouse et al., 2016) and recent studies have concluded that the Omani basement represents its own tectonic domain separate to the ANS (Alessio et al., 2017; Merdith et al., 2017; Whitehouse et al., 2016). However, where Oman sits in the reconstruction of Gondwana, is still being unravelled. To date, one of the most widely adopted approaches is using the radiogenic decay of ^{147}Sm to ^{143}Nd, however hafnium and oxygen isotopes in zircon are increasingly being used as tools to determine the magma sources and the extent of crustal recycling. Here we present some of the first Lu–Hf and oxygen isotope data from Oman, using these geochemical fingerprints, together with previously published data, we constrain the nature of the basement rocks in Oman. These findings are used to further understand the geological evolution of Oman during a period of major tectonic plate reorganisation, and to further elucidate its location in Gondwana.

BACKGROUND

A comprehensive review of the architecture of the Arabian plate are given by Stern and Johnson (2010) and detailed accounts of the geology of the Arabian Shield and its complex geological evolution are available (Hargrove et al., 2006; Johnson et al., 2011; Johnson, 2014; Johnson and Woldehaimanot, 2003). The Arabian basement is composed of rocks formed in the Neoproterozoic, though remnants of Archaean and Palaeoproterozoic crust (2900–2000 Ma) have been identified in Yemen and Saudi Arabia (Whitehouse et al., 2001a, b; Yeshanew et al., 2015). Collins and Windley (2002), identified this as an extensive Neoproterozoic ribbon or micro-continent (Azania) that is now preserved in rocks from southern India, Madagascar, Somalia, eastern Ethiopia to Arabia (Afif Terrane). Numerous authors have recognized the similarities between the basement rocks of Oman and those of Yemen and the ANS. Many authors note the possibility that Oman represents an eastern extension of the ANS (Bowring et al., 2007; Gass et al., 1990; Immenhauser et al., 2000; Worthing, 2005), which was described by Johnson et al. (2011) as a collage of Neoproterozoic juvenile arcs, younger sedimentary and volcanic basins, granitoid intrusions and enclaves of pre-Neoproterozoic crust. However, the absence of pre-Phanerozoic outcrop between Oman and the Arabian Shield of Saudi Arabia impede any direct connection between the regions (Alessio et al., 2017; Collins and Pisarevsky, 2005; Merdith et al., 2017; Rantakokko et al., 2014; Stern and Johnson, 2010; Worthing, 2005). It is clear that due to the sparse outcrops and extensive cover, the eastern basement of Arabia is far less well known than the Arabian Shield segment in the west. Arc accretion
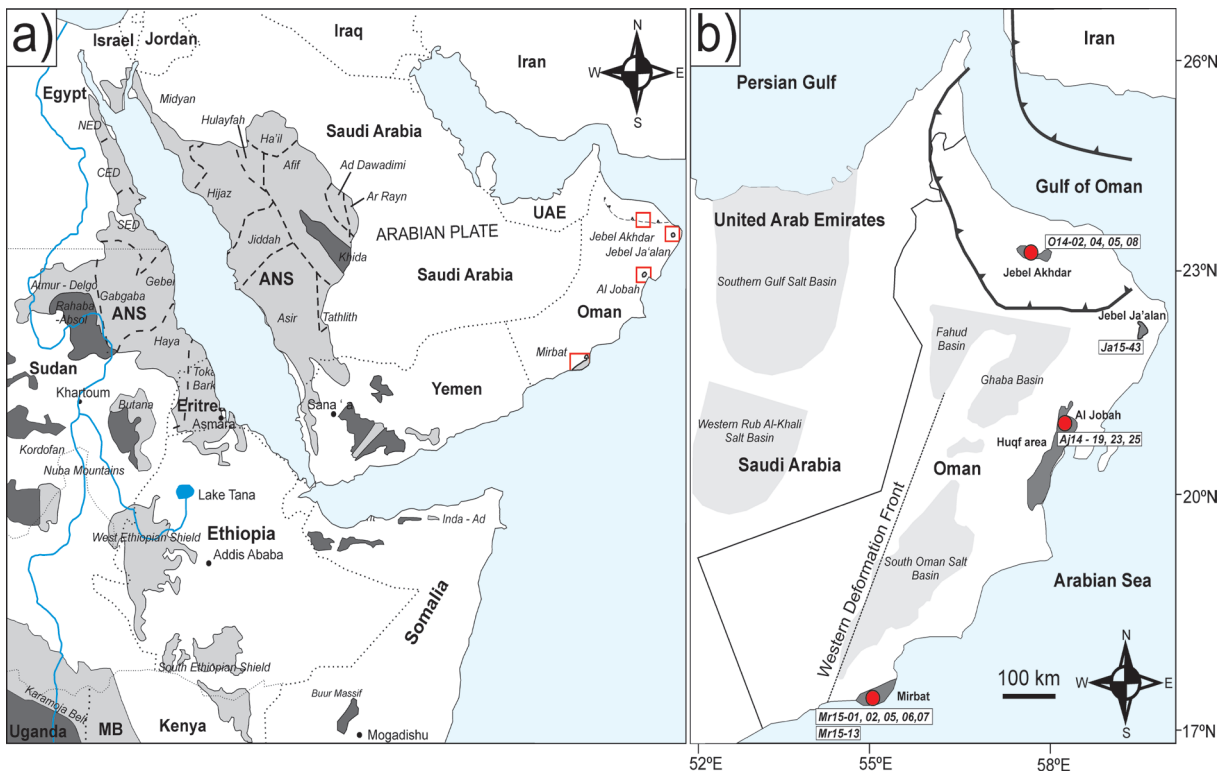
Figure 1: a) Location map of the Arabian–Nubian Shield (ANS) and Oman, red boxes indicate the areas where Neoproterozoic basement samples were taken for this study (adapted from Blades et al. 2015; Allen, 2007). b) Location map of Neoproterozoic exposures in Oman and main structural trends present (adapted from Allen, 2007).

during the Tonian (1000–850 Ma) and early Cryogenian (Alessio et al., 2017; Stern and Johnson, 2010), created the terranes that make up Oman. There are three main windows into the Neoproterozoic basement of Oman; east central Oman (Huqf area, Al Jobah and Jebel Ja'Alan) and southern Oman (Mirbat region of Dhofar; Fig 1b).

Jebel Akhdar

Jebel Akhdar, northern Oman (Fig. 1b), has no basement exposures. However, the Huqf supergroup is exposed in the core of an east–west trending anticline in the Jebel Akhdar of the Oman Mountains and includes diamictites, with granitic cobbles, that can be used as a proxy for basement lithologies. The rocks of Jebel Akhdar are deformed and exposed in a series of erosional windows namely the

Sahtan, Kharus and Mistal inliers. The Jebel Akhdar exposures belong to the Abu Mahara and Nafun groups of the Huqf Supergroup (Fig. 2a). While the base of these sequences is not seen the top is defined by an erosional, angular unconformity beneath the carbonate rocks of the Saiq Formation (Allen, 2007; Bowring et al., 2007; Rieu et al., 2007).

The Abu Mahara Group is made up of a lower diamictite-rich Ghubrah Formation (Fig. 2a) and the laterally discontinuous volcaniclastic and volcanic Saqlah Member. This separates the upper diamictite-rich Fiq Formation. Younger Cryogenian glaciogenic sedimentary rocks are found in the cyclical Fiq Formation (Allen et al., 2004; Leather et al., 2002). The older Cryogenian glaciogenic deposits are found in the much less well-understood Ghubrah Formation (Allen et al., 2004; Brasier et al.,
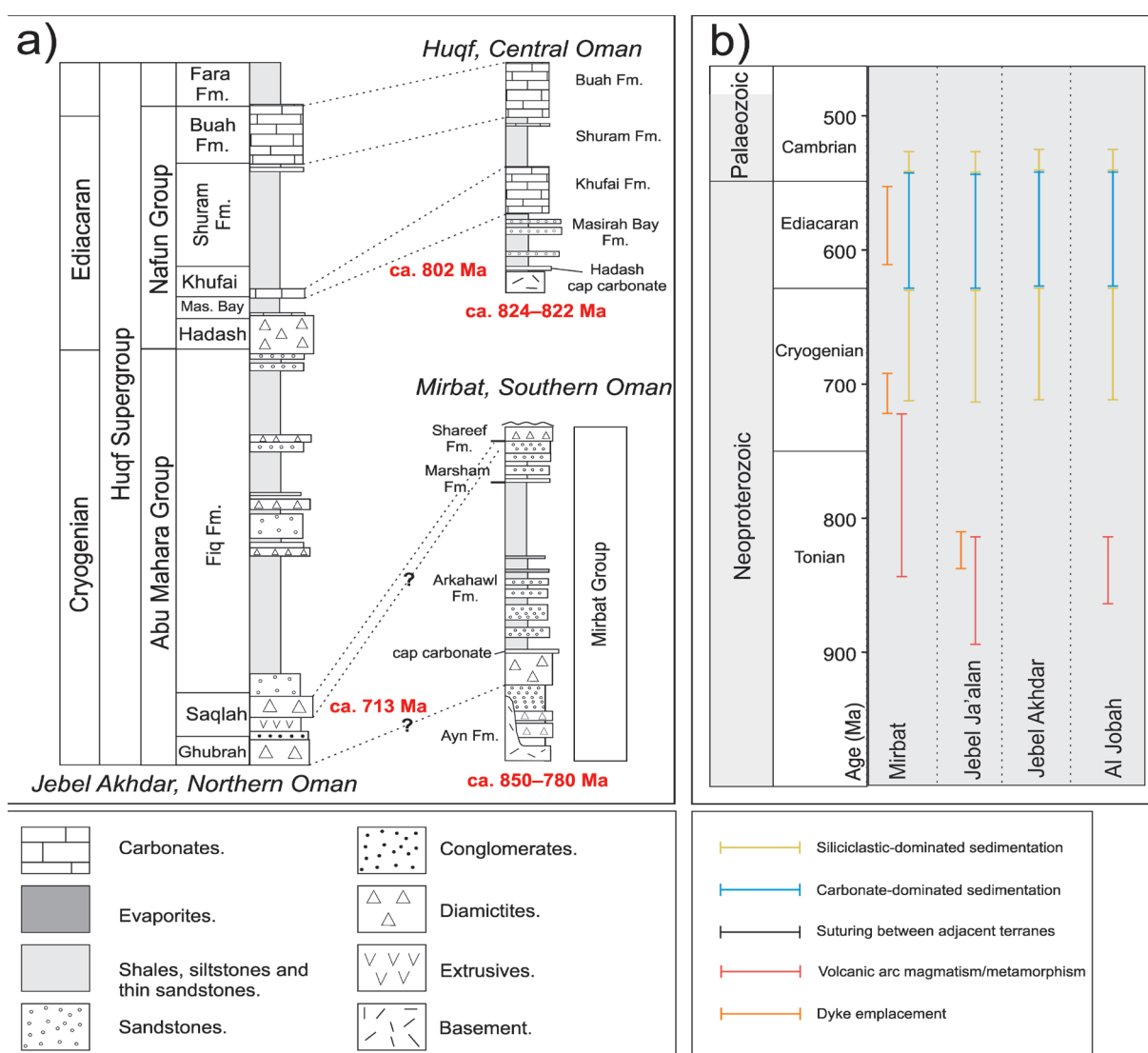
Figure 2: a) Lithostratigraphy of Neoproterozoic to early Cambrian rocks in Oman for each of the geographic regions studied, along with horizons represented by geochronology samples. b) Time-space plot for the terranes in Oman. Ages displayed for Oman are from Allen (2007), Rantakokko et al. (2014). Adapted from Alessio et al. (2017) and Bowring et al. (2007).

2000; Leather et al., 2002; Rabu et al., 1986). The Ghubrah Formation was first recognised by Kapp and Llewellyn (1965) as the lower part of the Mistal conglomerate. Rabu et al. (1986) contrasted it to the Fiq Formation as comprising of poorly stratified diamictic conglomerates (Leather et al., 2002). The diamictites appear structureless, though some striated clasts have been reported. The associated siltstones indicated quiet marine sedimentation when ice rafting was reduced either due to glacial retreat of iceberg movement. Geochronological data obtained by Brasier et al. (2000) and Bowring

et al. (2007) suggest that >713 Ma best represents the depositional age of tuffaceous ash interbedded with the interpreted glacial diamictites, providing a constraint on the age of Neoproterozoic glaciation (Fig. 2a). A dominantly Neoproterozoic source is interpreted for the Ghubrah Formation, containing detrital zircons with a reworked contribution from older sources aged ca. 826–755 Ma (Allen, 2007; Allen et al., 2004; Brasier et al., 2000; Leather et al., 2002).

Al Jobah

Basement and overlying Neoproterozoic sediments are exposed in central, eastern Oman in Al Jobah (Fig. 1b). The age of the low-grade basement to the Huqf Supergroup in this region, is based on the age of the granodiorite (Fig. 2b), volcanic rocks and the detrital zircons in the volcaniclastics rocks. Felsic volcanic and shallow marine sedimentary rocks of the Halfayn Formation overlie the penetratively deformed granodioritic rocks (ca. 824 Ma), with little evidence of any older cratonic crust (Bowring et al., 2007). Geochronology on the volcanic rocks overlying the volcaniclastic rocks suggest that these non-deformed, low-grade rocks are ca. 823 Ma and older (Allen and Leather, 2006).

Jebel Ja'Alan

Jebel Ja'Alan is located in NE Oman, approximately 30km south of Sur (Fig. 1b). Basement exposures are unconformably overlain by upper Campanian–lower Maastrichtian chert conglomerates, lithic sandstones and shales or marls of the Qahlah Formation. The mountain summits are defined by Maastrichtian limestones of the Simsina Formation (Fig. 2b). The Jebel Ja'Alan basement inlier is made up of metapelitic schists and orthogneisses, which were intruded by variably deformed granodiorite, granite, diorite and hornblendite (Alessio et al., 2017; Gass et al., 1990; Whitehouse et al., 2016). In the southern parts of the inlier an undeformed granite pluton is cross cut by several distinct generations of dykes with varying chemistry and orientation. Pressure–temperature modelling of the Al Wafi schist (Fig. 3d), indicates that the basement of Jebel Ja'Alan reached peak conditions of ~4–7.5 kbar at 650–700 °C (Alessio et al., 2017). U–Pb age data obtained from Al Wafi Schist monazite suggests that these peak metamorphic conditions occurred at 834 ± 12 Ma, with [40]Ar/[39]Ar muscovite data suggesting rapid,

exhumation-related cooling (Alessio et al., 2017). The tonalite and granodiorite plutonic suite (Jebel Ja'Alan batholith) intrudes the Al Wafi schist and has been tentatively assigned an age of 881 ± 8.3 (Whitehouse et al., 2016) Recent studies suggest that the main phases of magmatism occur between ca. 890–830 Ma, with the subsequent emplacement of three generations of dyke swarms (Alessio et al., 2017; Whitehouse et al., 2016). The magmatism leading up to orogenesis is interpreted to be arc magmatism (Alessio et al., 2017; Whitehouse et al., 2016). The main phases of magmatism, have a juvenile $\varepsilon_{Nd}(t)$ and $\varepsilon_{Hf}(t)$ signature (+0.56 to +6.78 and +2.33 to +13.3, respectively), suggesting limited input from Paleoproterozoic or older continental crust. Previous studies interpret progressive decrease in the ages of arc magmatism and metamorphism from NW India through to Jebel Ja'Alan to the Huqf and Mirbat, implying arc accretion occurred towards the modern day west (Alessio et al., 2017; Whitehouse et al., 2016).

Mirbat

The Mirbat region is located in southern Oman (Fig. 1b), with several lithologies making up the Precambrian crystalline basement (Mercolli et al., 2006; Platel et al., 1987; Rantakokko et al., 2014). The oldest of these units are the metasedimentary Juffa gneiss/schist and meta-igneous Sadh gneiss complexes. These are succeeded by the undeformed Tonalite Group and cross-cutting intrusive rocks. The latter intrusive rocks are comprised of the Mirbat granodiorite and extensive calc-alkaline dyke swarms, pegmatites and the Leger granite. The Juffa and Sadh complexes were metamorphosed to amphibolite facies with partial retrogression to greenschist facies (Mercolli et al., 2006; Platel et al., 1987; Rantakokko et al., 2014). The Sadh Complex has been previously

interpreted to represent a subduction related island arc (Mercolli et al., 2006; Platel et al., 1987; Rantakokko et al., 2014). The complex is lithologically heterogeneous, consisting predominantly of mafic and intermediate gneiss with subordinate felsic gneiss and amphibolite. Hornblende, biotite–hornblende and biotite gneiss varieties are generally considered to be of magmatic origin, although occasional small calc-silicate nodules in the biotite gneiss suggest that at least some of these may be sedimentary in origin. Sm–Nd model ages (T_{DM}) of ca. 960–910 Ma have been reported from rocks of the Sadh complex (Mercolli et al., 2006). Geochronology on the Sadh complex records Cryogenian magmatic and metamorphic events occurring in a short period at ca. 850–780 Ma (Rantakokko et al., 2014). The Mahall complex, made up of dioritic to tonalitic plutons intrude the Sadh complex and yield U–Pb zircon ages of ca. 800–780 Ma and T_{DM} ages of 950–880 Ma (Mercolli et al., 2006; Rantakokko et al., 2014). The Mirbat granodiorite cross cuts the penetrative foliation of the surrounding gneisses and contains xenoliths of dark gneiss, which are interpreted to represent fragments of the host Sadh gneiss complex (Mercolli et al., 2006). The Mirbat granodiorite is the youngest lithological unit at ca. 770–750 Ma (U–Pb zircon, Mercolli et al., 2006). Mercolli et al. (2006) reported Rb–Sr whole-rock ages plus muscovite ages of ca. 745 Ma and a K–Ar biotite age of 718 ± 12 Ma from pegmatitic complex. These were interpreted to represent the timing of retrograde greenschist facies metamorphism (Mercolli et al., 2006; Rantakokko et al., 2014). Deformation and syn-tectonic migmatisation is interpreted to have occurred between ca 815–820 Ma and related to arc accretion in the area. The Precambrian basement of the Mirbat region is unconformably overlain by the Mirbat sandstone, while the precise time of deposition for the lower member of the

Ayn formation (a member within the Mirbat Sandstone Formation) remains uncertain age peaks suggest that these are locally derived sediments, with the youngest age of ≤ 745 Ma defining the maximum depositional age (Allen, 2007; Bowring et al., 2007; Brasier et al., 2000; Rieu et al., 2007).

METHODOLOGY
U–Pb zircon geochronology

Samples from metaigneous and metasedimentary rocks were collected from a number of basement exposures (Table. 1) throughout Oman (Fig. 1b and 3). All zircon morphologies and internal textures are noted in Table 2, with representative CL images from each sample (Fig 4 and 5).

Zircon grains were extracted from crushed rocks using standard magnetic and heavy liquid techniques. Mineral separates were handpicked and mounted in epoxy resin. The polished mounts were carbon coated and zircon grains imaged using cathodoluminescence (CL) on a Philips XL40 scanning electron microscope (SEM) with attached Gatan CL detector (Adelaide Microscopy, The University of Adelaide). Zircon U–Pb isotope analysis was conducted on a New Wave 213 nm Nd-YAG laser coupled with an Agilent 7500cs Inductively Coupled Plasma Mass Spectrometer (LA–ICP–MS) at The University of Adelaide. A 30 μm spot size was used with a typical pit depth of 30–50 μm. The GEMOC GJ-1 zircon (TIMS normalising data $^{207}Pb/^{206}Pb$ = 607.7 ± 4.3 Ma, $^{206}Pb/^{238}U$ = 600.7 ± 1.1 Ma and $^{207}Pb/^{235}U$ = 602.0 ± 1.0 Ma; Jackson et al., (2004) was used to correct for U–Pb mass bias and laser induced fractionation. The Plešovice zircon internal standard (ID TIMS $^{206}Pb/^{238}U$ age = 337.13 ± 0.37 Ma; Sláma et al., (2008) was used to assess accuracy before and during analysis of the unknowns. Plešovice analyses yield a weighted average mean $^{206}Pb/^{238}U$ age

Table 1: Location, minerology and main field observations for samples from the main basement exposures in Oman

Sample	Longitude (Decimal Degrees)	Latitude (Decimal Degrees)	Minerology	Field observations
Mirbat				
Granite (MR15-01)	54.693	17.013	Qz, Pl, Ksp, Bt	Granite is not homogeneous and contains small rounded xenoliths that are Bt-rich
Tonalite (MR15-02)	55.074	17.044	Pl, Bt, Hbl, Qz	Areas of the tonalite have been foliated. Cross-cutting dykes are seen in outcrop. Mafic enclaves present in the tonalite.
Tonalite (MR15-04)	55.249	17.219	Pl, Ksp, Bt, Qz	Tonalite with granitic and mafic dykes cross-cutting. In some cases felsic dykes are classified as pegmatitic.
Monzonite (MR15-05)	55.249	17.219	Pl, Ksp, Bt, Qz	Monzonite has mafic enclaves. Cross cutting granite phase.
Gneiss (MR15-07)	55.188	17.185	Qz, Pl, Ksp, Bt	Interlayered with mafic amphibolites. Granitic layers also present.
Al Jobah				
Granite (AJ14-19)	59.360	22.128	Qz, Ksp, Bt ± Pl	Granites are slightly deformed, with evidence of magma mingling present. Thin pink granitic dykes cross-cut. Out crop is scattered and only small windows are seen.
Microgranite (AJ14-23)	58.039	20.902	Qz, Ksp, Bt ± Pl	Very fine grained granite, sitting on top of the coarser grained granite (AJ14-19). Outcrop is isolated and small.
Granite (AJ14-25)	58.042	20.908	Qz, Ksp, Bt, Pl	Homogeneous granite with mafic enclaves. No fabric present.
Jebel Akhdar				
Granitic diamictite clast (O14-05)	57.657	23.056	Pl, Ksp, Bt, Qz	Rounded to sub-rounded rocks with a fine grained matrix. Granitic clasts. Moving down the succession clasts are larger ~20cm. Coarse grained.
Granitic diamictite clast (O14-04)	57.667	23.063	Pl, Ksp, Bt, Qz	Rounded to sub-rounded clasts within a fine grained matrix. Granitic clasts about 20 cm. Coarse grained.
Granitic diamictite clast (O14-08)	58.134	20.948	Pl, Ksp, Bt, Qz	Rounded to sub-rounded rocks with a fine grained matrix. Granitic clasts present. Moving down the succession clasts are larger ~20cm. Fine grained.

GPS coordinates are based on the WGS84 datum.

of 337.3 $\pm$ 4.5 (n=15) with an MSWD of 1.4 and a ^{206}Pb/^{207}Pb age of 334 $\pm$ 15 (MSWD = 0.53 and n=15). Data were processed in the software package GLITTER version 3.0 (Van Achterbergh et al., 2001). Concordia diagrams and weighted averages were calculated using ISOPLOT 4.11 for Excel (Ludwig, 2009).

Zircon Lu–Hf Isotope analysis
Analytical methods for zircon Lu–Hf isotope analysis follow Payne et al. (2013). Analyses were undertaken using a New Wave UP-193 ArF excimer laser attached to a Thermo–Scientific Neptune Multi-Collector ICP–MS at the University of Adelaide. The bulk of analyses were carried out using a beam diameter of ~50 µm, with a beam diameter of 35µm used for smaller grains. Typical ablation times were 40–100 s using a 5 Hz repetition rate, a 4 ns pulse rate, and an intensity of ~10 J/cm2. Zircons were ablated in a helium atmosphere, which was then mixed with Ar and N2 upstream of the ablation cell. Reduction of zircon data were undertaken using a macro-driven Hf isotope data reduction Excel spreadsheet, HfTRAX (Payne et al., 2013). The data were normalised to ^{179}Hf/^{177}Hf = 0.7325, using an exponential correction for mass bias. Yb and Lu isobaric interferences on ^{176}Hf were corrected following the methods of Woodhead et al. (2004).

The accuracy of the Yb and Lu corrections has been demonstrated by repeated analysis of standard zircons with a range in ^{176}Yb/^{177}Hf and ^{176}Lu/^{177}Hf values (Griffin et al., 2006). Before and during the analysis of unknowns, standards were analysed to check instrument performance and stability. The primary zircon standard used was Plešovice, which yielded a mean ^{176}Hf/^{177}Hf ratio of 0.282466 $\pm$ 0.00003. This compares to the published value of 0.282482 $\pm$ 0.000013 (2SD) by Sláma et al. (2008). Values for ε_{Hf}(t), and T_{DMc} were calculated using ^{176}Lu decay constant after

Scherer et al. (2001). T_{DMc} was calculated using the two stage methods of Griffin et al. (2002) with an average crustal composition of ^{176}Lu/^{177}Hf = 0.015.

Zircon Oxygen Isotope analysis
Oxygen isotope data were collected from the same samples used for U–Pb geochronology. The U–Pb mounts were repolished and oxygen isotope spots were placed on the same zircon sites as those used in the Hf determination. Analyses were undertaken using the SHRIMP SI at the Research School of Earth Sciences in the Australian National University, Canberra. A 10 kV, ~3 nA Cs+ primary ion beam was focused to an ~30 µm diameter spot on an Al-coated sample. Each analysis consisted of a pre-burn of about 2 mins to allow the secondary ion isotopic composition to stabilise and remove the Aluminium coat prior to the analysis, followed by 5, ~10 seconds estimates of the ^{18}O/^{16}O ratio. A standard (Temora II) was analysed first, then again after 6 unknown samples. Sample δ^{18}O(zircon) values were determined by difference relative to the mean δ^{18}O(zircon) measured on standards following normalisation for long-term drift in its measured composition. The δ^{18}O (zircon) values for the Temora II standard analysed in this study are 8.27 $\pm$ 0.21‰. These values are comparable with the published δ^{18}O (zircon) value of 8.20 $\pm$ 0.01‰ (Valley et al., 2005).

RESULTS
U–Pb geochronology was undertaken on eight igneous rocks, three igneous clasts within diamictites and two metasedimentary rocks. A subset of these samples were then used for Lu–Hf isotope analysis and O isotope analysis. All U–Pb geochronology results are plotted on Wetherill plots with their respective cumulative weighted average plots, in which both the ^{206}Pb/^{238}U and ^{207}Pb/^{206}Pb
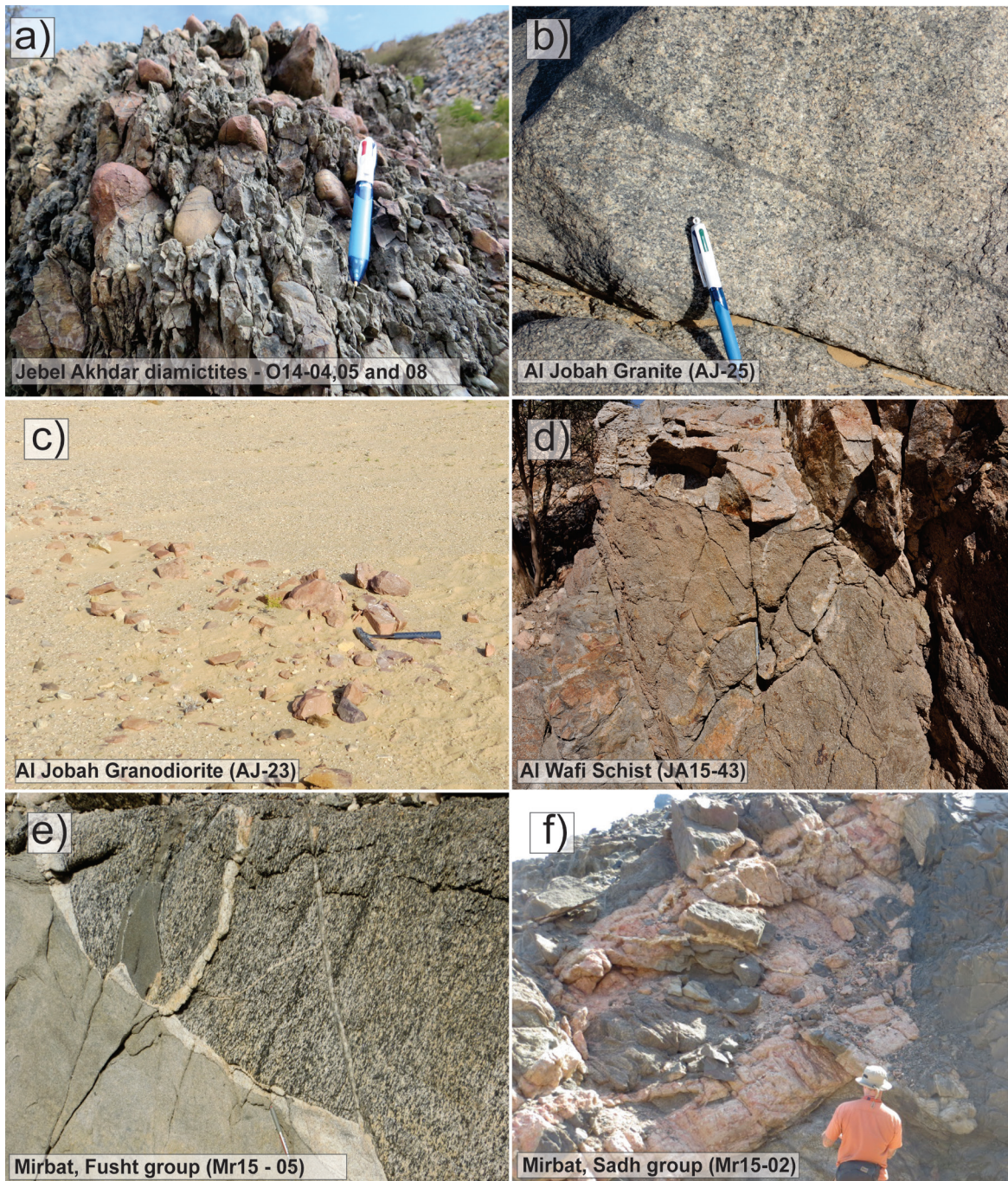
Figure 3: Field photos taken from Neoproterozoic basement exposures throughout Oman. a) Diamictites within the Ghubrah Formation, Jebel Akhdar. Some of the rounded cobbles are granitic in composition. These were sampled as a proxy into the basement as there is no basement outcrop in Jebel Akhdar. b-c) Taken from the central eastern exposures in the Huqf region (Al Jobah), basement exposures in these areas are sparse. Outcrop is variably deformed, with thin pink dykes cross cutting the main foliation. d) Al Wafi Schist, sampled in Jebel Ja'alan. This is banded biotite-sillimanite mica schist, best exposed in the north-western area of Jebel Ja'alan. This unit is intruded by granitic veins. e) Tonalite Group Mirbat – interaction between tonalite and monzonite, with cross cutting felsic and mafic phases d) This image shows three phases of magmatism oldest to youngest, based on field relationships 1) Tonalite (plag, Qtz, Bt, Hbl) 2) Pink granite (Ksp, Qtz, Plag) 3) Dolerite dyke cross cutting all three lithologies. Mafic enclaves are seen in Unit 1, interpreted to represent xenoliths of the gneiss.

Table 2: Zircon morphologies and CL characteristics from igneous samples of the Omani basement

Sample	Zircon colour	Zircon, shape, size and aspect ratio	CL characteristics
MR15-01	pale brown	**Shape:** Pyramidal {101} **Aspect ratio:** 4:1 and 2:1 **Size:** 100μm - 350 μm	Grains preserve a homogenous core, with varying development of OZ. Complex growth zoning with local intermediate resorption in some places. Most grains are not luminescent and are CL dark.
MR15-02	pale brown - colourless	**Shape:** Prismatic {100} {211} **Aspect ratio:** 3:1, 4:1 and 2:1 **Size:** 100μm - 400μm	Preserve oscillatory zoning and sector zonation present in some grains. There are strong variations in the relative development of zoned domains, where one large uniform central zone is succeeded by much finer oscillatory-zoned bands. Zircons have segments of homogeneously textured zircon appearing as transgressive (across all pre-existing textures) zircon patches and lobes
MR15-04	pale orange - colourless	**Shape:** Prismatic /pyramidal {101}, {211}. Though grains exhibit rounded edges. **Aspect ratio:** 3:1, 4:1 and 2:1 **Size:** 100μm - 400μm	Most grains have OZ, though relative development of oscillatory bands vary. Zircons have segments of homogeneously textured zircon appearing as transgressive (across all pre-existing textures) zircon patches and lobes. Areas of recrystallization occur dominantly at crystal terminations.
MR15-05	pale orange - colourless	**Shape:** Pyramidal {101} grains have mostly rounded edges **Aspect ratio:** 2:1, 1:1 **Size:** 100μm - 400μm	Sector zonation dominates. OZ is present, though faint in most grains. Recrystallisation/new growth is seen cutting well defined OZ euhedral core.
MR15-07	pale yellow/ orange	**Shape:** Prismatic {100} {110} mostly with some rounded more rounded zircons. **Aspect ratio:** 2:1, 1:1, 5:2 **Size:** 100μm - 400μm	Relative development of oscillatory zonation (OZ) varies. Some exhibit homogeneous cores, with finer OZ towards the edge of the grain. Some recrystallisation/newly grown homogeneous seen cutting the euhedral grain, though rare.
AJ14-19	pale yellow/ orange	**Shape:** Pyramidal {101} **Aspect ratio:** 2:1, 7:2, 5:2 **Size:** 50μm - 150μm	Some grains are homogeneous with a thin dark rim mantling the grain. Others preserve large homogeneous cores, with fine OZ defining the rims. Some cases have complex feathery textures. Areas of recrystallisation present, mainly at crystal terminations.
AJ14-23	pale brown - pale orange	**Shape:** Pyramidal {101} **Aspect ratio:** 2:1, 7:2, 5:2 **Size:** 70μm - 250μm	Grains are largely homogeneous with a few oscillatory growth bands defining the rims. Grains are largely featureless
AJ14-25	colourless - pale yellow	**Shape:** Pyramidal {101} **Aspect ratio:** 3:1, 4:1, 7:1 7:2 **Size:** 100μm - 200μm	Majority of the grains are homogeneous no defining features. Other grains have a large uniform central zone that is succeeded by much finer oscillatory-zoned bands.
O14-04	pale yellow/ orange	**Shape:** Pyramidal {101} **Aspect ratio:** 4:1, 2:1 **Size:** 50μm - 250μm	Grains have well defined OZ, though relative development of zones varies across the sample. Zircons have segments of homogeneously textured zircon appearing as transgressive (across all pre-existing textures) zircon patches and lobes.
O14-05	pale brown - pale orange	**Shape:** Pyramidal {101} **Aspect ratio:** 4:1, 2:1 **Size:** 50μm - 250μm	Well-developed OZ present, as well as sector zoning. Grains that have a low CL response generally have a large homogenous core, succeeded by OZ.
O14-08	pale orange - colourless	**Shape:** Pyramidal {101} and sub-rounded grains **Aspect ratio:** 4:1, 2:1 **Size:** 100μm - 200μm	OZ present, though in some grains zonation is faint. Grains contain areas of recrystallisation, evident by lobes and patches seen in the zircon.

Figure 4: Representative CL images for all igneous rocks sampled in Oman. U–Pb laser, hafnium and oxygen spots shown. Hafnium and oxygen analyses were conducted in the same pit. Generally grains are pyramidal or prismatic. The zircons from Mirbat are notably larger than other basement areas of Oman and are defined by sector zonation and oscillatory zonation. No definable cores–rim relationships are seen in the samples from Mirbat. Majority of the grains from Al Jobah are homogeneous with no defining features. Some grains have a large uniform central zone that is succeeded by much finer oscillatory-zoned bands. Grains from Jebel Akhdar are relatively small with oscillatory zonation. Some grains contain areas of recrystallisation, evident by homogeneous lobes and patches seen in the zircon.

Table 2a: Zircon morphologies and CL characteristics from metasedimentary rocks in Jebel Ja'Alan (JA15—43) and Mirbat (MR15—14)

Sample	Zircon colour	Zircon, shape, size and aspect ratio	CL characteristics
MR15-14	colour-less, pale brown, pale or-ange	**Shape:** {101} and {211} **Aspect ratio:** Dominant ratio is 2:1, with some rounded 1:1 grains. **Size:** 100μm - 300μm	Two main groups of zircon - *Group 1* is dominated by grains with prismatic forms. They are characterised by OZ of varying thickness. Few grains shows signs of recrystallisation (in the form of lobes and patches). *Group 2* Small rounded grains have a CL dark core with thin bright rims. Some of the rounded grains have well defined OZ
JA15-43	pale yellow/orange	**Shape:** Pyrami-dal {101} and {211}. Rounded grains present **Aspect ratio:** 4:1, 5:1, 2:1, 1:1 **Size:** 50μm - 200μm	Well defined OZ. Cores are present, though textures suggest they are metamict. Some grains display areas of recrystallisation, overprinting of the pre-existing tex-ture. CL bright rims are seen mantling a few grains.
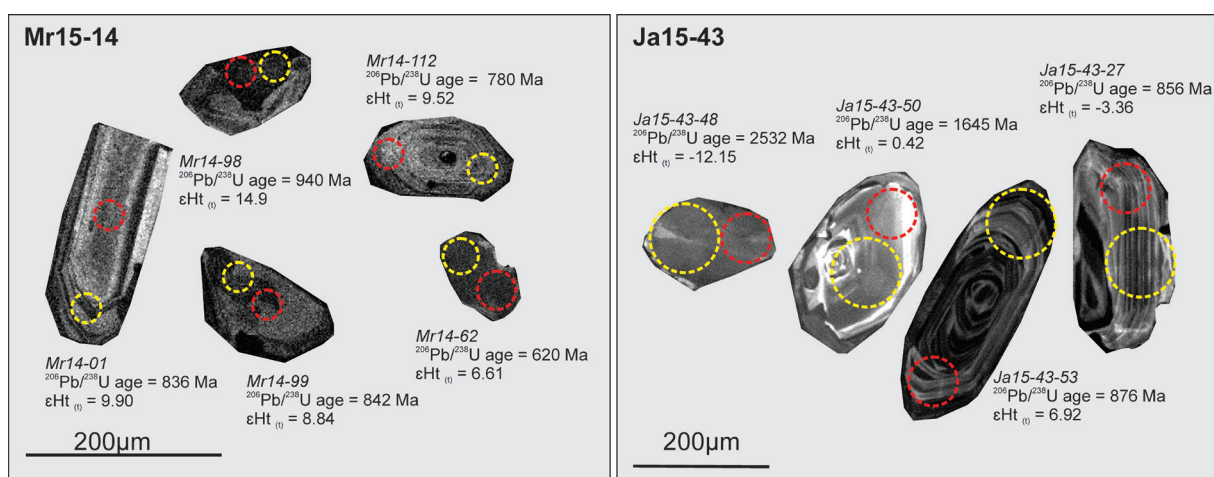
Figure 5: Representative CL images for sedimentary rocks sampled in Oman. U/Pb laser and hafnium spots shown for each grain pit. Mirbat sandstone (MR15—14) and Al Wafi schist (JA15—43). The Mirbat region is dominated by grains with prismatic forms. They are characterised by oscillatory zoning (OZ) of varying development. Few grains shows signs of recrystallisation (in the form of lobes and patches). The sample also contains smaller rounded grains have a CL dark core with thin bright rims. Some of the rounded grains have well defined zonation. The Al Wafi Schist contains zircons of variable nature. Grains contain areas of recrystallisation, overprinting of the pre-existing texture. CL bright rims are seen mantling a few grains.

analyses have been displayed. These have been categorised based upon their identified internal structure based in CL imaging (Fig. 4 and 5) and grains used for concordia age calculations. All age uncertainties are quoted at a two sigma level (Fig. 6). Calculated ages are considered statistically valid when the calculated MSWD falls within the acceptable range as determined using the formula outlined in Wendt and Carl (1991) and Schoene (2014).

Lu—Hf isotopes were undertaken on all samples and oxygen isotopes were done on a representative selection of samples. Lu—Hf data are presented as $\varepsilon_{Hf}(t)$ versus U—Pb age data (Fig 8). Oxygen isotope data are presented as $\delta^{18}O$ (zircon) values versus U—Pb age data (Fig. 9a) and $\varepsilon_{Hf}(t)$ values (Fig. 9b). Uncertainties on Lu—Hf and oxygen isotope data are quoted at the two sigma level. To assess whether the intra-sample spread represents geological or analytical variation a weighted mean $\varepsilon_{Hf}(t)$ value has

been calculated for each sample. If the MSWD of this mean is within the range considered statistically indicative of a single population, then the mean value is used as representative of the sample. This has been done in this study as the small grain size in a number of samples, and hence the required small beam diameter, has resulted in large analytical uncertainties, which may yield a large range in calculated $\varepsilon_{Hf}(t)$ values that is purely an analytical spread as opposed to a geologically meaningful spread. A lack of recognition of an analytical cause for the data spread could otherwise lead to erroneous interpretations of the geological significance of the spread in values.

Igneous Zircon geochronology, Lu–Hf and oxygen isotope analysis

Samples were taken from a diamictite within theAbu Mahara Group in Jebel Akhdar. These are rounded granitic cobbles that are characterised by quartz, feldspars and biotite. These could be differentiated based on the grain size, with both coarse (O14–04, 14–05) and fine (O14–08) grained cobbles present (Table. 1).

O14–04: Coarse grained granitic clast

Thirty one analyses were conducted and of these, fourteen are > 90% concordant and show a range between 852–697 Ma. The Concordia plot of all analyses shows a distinct Pb-loss trend, with no definable morphological differences between zircon grains (Fig. 4 and 5a). The oldest grain is considerably older and is interpreted to represent inheritance, supported by morphological characteristics of the grain. Due to the defined Pb-loss trend an upper intercept was calculated, giving an age of 801 ± 28. The $^{206}Pb/^{238}U$ weighted average of these grains was calculated giving an age of 744 ± 17 (MSWD = 5.2). Due to the defined Pb-loss trend a $^{207}Pb/^{206}Pb$ age was calculated to

provide an estimate for the age of this granitic clast. This yielded a weighted average of 779 ± 18 Ma with a MSWD of 0.61, though is interpreted to only represent an estimate.

Lu–Hf isotope analyses were conducted on eleven grains giving a range of $\varepsilon_{Hf}(t)$ values between +4.56 and +6.95 (Fig. 8a), with a weighted average of 6.29 ± 0.74 (MSWD = 0.46). The low MSWD indicates the values can be considered to represent a single population. Oxygen isotopes on these same zircons gave $\delta^{18}O$ (zircon)‰ values between 10.33 ± 0.12 ‰ and 7.73 ± 0.23 ‰ and collectively give a weighted average of 9.33 ± 0.70 ‰, suggesting some crustal input (Fig 9a).

O14–05: Coarse grained granitic clast

Forty four analyses were conducted on forty zircons, with no discernible age differences between core and rim analyses. A definable Pb-loss trend is seen in Concordia (Fig. 4 and 6b) and an upper intercept of 811 ± 15 Ma (MSWD of 1.4) was calculated, though the lower intercept obtained was younger than present day suggesting that these grains have been affected by ancient Pb-loss. All > 90% concordant data were calculated to yield a $^{206}Pb/^{238}U$ weighted average age of 736 ± 18 (MSWD = 7.5). A $^{207}Pb/^{206}Pb$ weighted average age of 767 ± 18 Ma (MSWD = 0.32) was calculated and interpreted to provide the best estimate for the age of this clast.

Hafnium isotope analysis was undertaken on eleven zircon grains giving $\varepsilon_{Hf}(t)$ values between +4.63 and +7.55 (Fig. 8). These give a calculated weighted average of 6.14 ± 0.96 (MSWD=1.8). Based on the hafnium isotope data, this sample shows a mantle signature. However, it must be noted that oxygen isotopes conducted in other granitic clasts suggest continental crust involvement.

O14–08: Fine grained granitic clast

Thirty zircons were analysed and of these

sixteen were > 90% concordant. The cumulative weighted average plot shows a range of ^{206}Pb/^{238}U ages between 781–721 Ma and the Concordia plot (Fig. 1c) show a distinct Pb-loss trend. Morphologically these zircons show no differing characteristics and therefore are treated as one population (Fig. 4 and 6c). An upper intercept was calculated for yielding an age of 795 ± 8 Ma. A ^{206}Pb/^{238}U weighted average of all grains yields an age of 749 ± 8 Ma, with an MSWD of 1.4. However, due to the defined Pb-loss trend a ^{207}Pb/^{206}Pb age was calculated to provide an estimated for the age of O14–08. This yielded an age of 794 ± 24 Ma (MSWD = 0.24) and is within error of the upper intercept. This is therefore interpreted to best represent the age of this fine grained granitic clast.

Hafnium isotopes were done on twelve zircons and these give ε_{Hf}(t) values between +1.94 and +7.84 (Fig. 7) and a calculated weighted average of 6.61 ± 0.87 (MSWD = 1.3). These same zircons were analysed for oxygen isotopes giving δ^{18}O (zircon) ‰ values between 10.25 ± 0.21 ‰ and 6.78 ± 0.16 ‰ and collectively give a weighted average of 8.67 ± 0.89 ‰ (Fig. 8). These values suggest that there were small amounts of higher vO supra-crustal material involved.

AJ14–19: Al Jobah Granite

The Al Jobah granite, only forms as sparse outcrops and shows evidence of being deformed. Mineralogically, it is characterised by quartz, feldspar (Pl and Ksp) and biotite, with thin pink dykes cross cutting the main foliation (Table 1). Fifty six grains are > 90% concordance and show a range of ^{206}Pb/^{238}U ages between 902–789 Ma. The cumulative ^{206}Pb/^{238}U weighted average plot shows one main period of zircon formation, with an older grain at 902 Ma. These zircons are morphologically characterised by a large homogeneous core and fine oscillatory rims, whereas the oldest grain differentiated from the other grains by its rounded morphology (Fig. 3 and 5d). The calculated ^{206}Pb/^{238}U weighted average for all grains (excluding the oldest analyses) yields an age of 836 ± 5 Ma with an MWSD of 2.8. These grains were recalculated using the ^{207}Pb/^{206}Pb ages, yielding an age of 855 ± 8 Ma (MSWD = 1.4). To test the validity of the ^{207}Pb/^{206}Pb age, the upper intercept was calculated giving an age of 868 ± 30 Ma (MSWD = 1.4), falling within error of the ^{207}Pb/^{206}Pb age of 855 Ma, suggesting that this provides a reliable representation of the age of the Al Jobah Granite.

Lu–Hf isotopes were analysed and have juvenile signature, with ε_{Hf}(t) values ranging between +8.07 and +11.52 (Fig. 8). A calculated weighted average of all analyses yields 10.34 ± 0.67 (MSWD=1.6). These same zircons gave δ^{18}O (zircon) ‰ values between 6.84 ± 0.15 and 11.31 ± 0.09, with a calculated weighted average of 8.2 ± 1.1 ‰ (Fig 9a).

AJ14–23: Microgranite

Exposure of the microgranite (AJ14–23) is sparse and occurs in small rounded boulders generally in isolation. However, where sampled, it is seen overlying the coarser grained Al Jobah granite. This is mineralogically similar to the Al Jobah granite (AJ14–19), however defined by a much finer grain size. Thirty analyses were conducted on largely homogeneous, featureless zircons and, of these, twenty one are ≤ 10% discordant and show a range between 863–802 Ma. The cumulative weighted average plot highlights a distinct slope in the data, suggesting that these zircons have experienced some lead loss (Fig. 4 and 6e). The youngest two analyses are significantly younger than the other grains. These are interpreted to represent grains that have not remained in a closed system and have been excluded from the age calculation.

A $^{206}Pb/^{238}U$ weighted average yielded an age of 838 $\pm$ 7 Ma (MSWD of 1.3). This was recalculated yielding $^{207}Pb/^{206}Pb$ age of 861 $\pm$ 14 Ma (MSWD of 1.04). The $^{206}Pb/^{238}U$ age is marginally younger than the corresponding $^{207}Pb/^{206}Pb$ age and is accordingly interpreted as a result of minor, recent Pb-loss. It is interpreted that ca. 861 best represents the crystallisation age of this microgranite.

Ten analyses were undertaken for Lu–Hf isotopes and these reveal a juvenile signature. $\varepsilon_{Hf}(t)$ values range between +8.89 and +12.04 (Fig. 7) and give a weighted mean of 10.44 $\pm$ 0.72 (MSWD of 1.6). Eight of these zircons gave $\delta^{18}O$ values between 7.08 and 10.43. These yielded a weighted average of 7.77 $\pm$ 0.78 ‰ (Fig. 9a), which suggests that these values are elevated and may reflect some supra-crustal input.

AJ14–25: Granite

This homogeneous granite is seen in isolation and unlike Al Jobah granite does not seem to have been deformed. The granite contains mafic enclaves, evidence of magma mingling and is primarily composed of quartz, K-feldspar, biotite and plagioclase. Thirty five analyses were undertaken and of these thirty–one are $\leq$ 10% discordant and show a range of $^{206}Pb/^{238}U$ ages between 904–813 Ma. The cumulative weighted average plot shows a perceptible lead loss trend, forming no definable plateau (Fig. 4 and 6f). A $^{206}Pb/^{238}U$ weighted average was calculated, yielding an age of 840 $\pm$ 7 Ma (MSWD = 2.2). To determine the validity of this calculated age, it was recalculated and gave a $^{207}Pb/^{206}Pb$ age of 854 $\pm$ 14, with an MSWD of 1.6. These two systems are within error of each other and therefore have been interpreted to represent a reliable age for crystallisation for this granite.

Lu–Hf isotopes were undertaken on ten grains, with $\varepsilon_{Hf}(t)$ values between +8.89 and +12.04

(Fig. 8). These give a weighted average of 10.44 $\pm$ 0.72 (MSWD = 1.6), showing these zircons were derived from melt with little crustal input.

MR15–01: Mirbat Granite

The Mirbat granite cross cuts the penetrative foliation of the surrounding gneisses and contains xenoliths of dark bt-rich gneiss, which are interpreted to represent fragments of the surrounding gneiss. Forty three zircons were analysed and, of these, twenty one are $\leq$ 10% discordant, showing a range of $^{206}Pb/^{238}U$ ages between 889–799 Ma. The cumulative $^{206}Pb/^{238}U$ age plot highlights one distinct plateau, suggesting a single period of zircon formation. The oldest grain defined by a core has a $^{206}Pb/^{238}U$ age of 889 $\pm$ 11 Ma (Fig. 4 and 6g). The other twenty two analyses yield a $^{206}Pb/^{238}U$ weighted average of 809 $\pm$ 6 Ma with an MSWD of 1.5. The $^{207}Pb/^{206}Pb$ was calculated for these analyses and gave an age of 834 $\pm$ 27 Ma (MSWD = 0.51). The $^{206}Pb/^{238}U$ and $^{207}Pb/^{206}Pb$ calculated ages lie within error of each other, therefore suggests that $^{206}Pb/^{238}U$ age of 809 $\pm$ 6 Ma (MSWD of 1.5) is taken as a reliable estimate for the crystallisation of this granite.

Eleven analyses for Lu–Hf isotopes were obtained, giving a $\varepsilon_{Hf}(t)$ range between +7.44 and +9.80 (Fig. 8). These values suggest a juvenile source magma and give a calculated weighted average of 8.72 $\pm$ 0.60 (MSWD of 1.2). These give $\delta^{18}O$ (zircon) ‰ values between 3.71 $\pm$ 0.26 ‰ and 6.67 $\pm$ 0.27 ‰ and a weighted average of 5.28 $\pm$ 0.44 ‰ (Fig. 9a), similar to $\delta^{18}O$ values from primitive mantle derived magmas with $\delta^{18}O$ values of 5.3 $\pm$ 0.6‰ (Valley, 2003).

MR15–02: Tonalite

The tonalite is lithologically heterogeneous (quartz, feldspar, hornblende and biotite) and

contain mafic xenoliths, interpreted to be from surrounding gneiss. Regions of the tonalite are foliated and felsic and mafic dykes are seen cross cutting the tonalite. Thirty four analyses (out of forty) are within 90% concordance with $^{206}Pb/^{238}U$ ages between 814–754 Ma. The cumulative weighted average plot shows a definable lead loss trend, with no visible plateau (Fig. 4 and h). A weighted average was calculated for all grains, giving a $^{206}Pb/^{238}U$ age of 781 ± 6 Ma (MSWD = 2.2). We suspect that this larger MSWD is due to post-crystallisation Pb-loss, substantiated by the MSWD (0.44) of the $^{207}Pb/^{206}Pb$ weighted mean of the same analyses, which yields an age of 795 ± 20 Ma. This is within error of the $^{206}Pb/^{238}U$ age and due to the lower MSWD provides the best estimate for the crystallisation of the granite.

Of these grains analysed, Lu–Hf data were collected on ten grains. These give a range of $\varepsilon_{Hf}(t)$ values between + 9.04 and + 10.39 (Fig. 7). These juvenile zircons gave $\delta^{18}O$ (zircon) ‰ range between 3.29 ± 0.38 ‰ and 4.89 ± 0.38 ‰ and a weighted average of 4.13 ± 0.50 ‰ (Fig. 9). The $\delta^{18}O$ values from primitive mantle derived magmas are 5.3 ± 0.6‰, suggesting these samples were exposed to low $\delta^{18}O$ meteoric waters (Valley, 2003).

MR15–04: Tonalite

The tonalite, like previous samples (MR15–02 and 01) contains mafic xenoliths, interpreted to be from the older surrounding gneiss. Cross cutting felsic pegmatites and mafic dykes are seen intruding this tonalite. Forty four zircons were analysed, targeting both rims and cores and of the analysed grains, between range from 852–720 Ma. The cumulative weighted average plot highlights two definable plateaus, with a perceptible lead loss trend (Fig. 4 and 6i). The youngest grain (ca. 721 Ma) has been interpreted to represent post crystallisation lead loss, based on morphological characteristics of the grain.

The oldest three grains (defined by cores) have a $^{206}Pb/^{238}U$ weighted average of 840 ± 28 Ma (MSWD = 1.4). The calculated age for the other seventeen grains have a $^{206}Pb/^{238}U$ weighted average of 788 ± 10 (MSWD = 3.4). This large MSWD is possibly due to post-crystallisation Pb-loss and these data were recalculated using $^{207}Pb/^{206}Pb$ ages, which gave a robust age of 804 ± 22 Ma. (MSWD = 0.27). These two systems are with error of each other and we interpret this to represent the best age for crystallisation for the tonalite.

Twelve analyses were conducted for Lu–Hf isotopes giving a $\varepsilon_{Hf}(t)$ range between +7.87 and +11.64 (Fig 7). These positive values suggest a juvenile signature and yield a weighted average of 10.44 ± 0.67. $\delta^{18}O$ (zircon) ‰ values give a range between 3.9 ± 0.29 and 6.9 ± 0.27 ‰ (Fig. 9). These gave a weighted average of 5.37 ± 0.48, similar to $\delta^{18}O$ values from primitive mantle derived magmas ($\delta^{18}O$ = 5.3 ± 0.6‰; Valley, 2003).

MR15 – 05: Monzonite

The monzonite (Fig. 3e) shows a weak foliation and intruding felsic and mafic dykes. Mafic enclaves are seen within this unit, suggesting magma mingling. Thirty five analyses were conducted targeting cores and rims, of these thirty one are ≤ 10% discordant. The analyses show a range of $^{206}Pb/^{238}U$ ages from 779–751 Ma. The cumulative $^{206}Pb/^{238}U$ age plot shows one main period of zircon formation (Fig. 3 and 5j). A $^{206}Pb/^{238}U$ weighted average of all concordant zircons yields an age of 765 ± 5 (MSWD = 1.8). To assess the validity of this age, it was recalculated using the $^{207}Pb/^{206}Pb$ ages, yielding 771 ± 18 (MSWD = 0.43). These systems are with error of each other and therefore the $^{206}Pb/^{238}U$ age ca. 765 Ma provides the best age for the formation of these zircons.

Eleven zircons were analysed for Lu–Hf isotopes
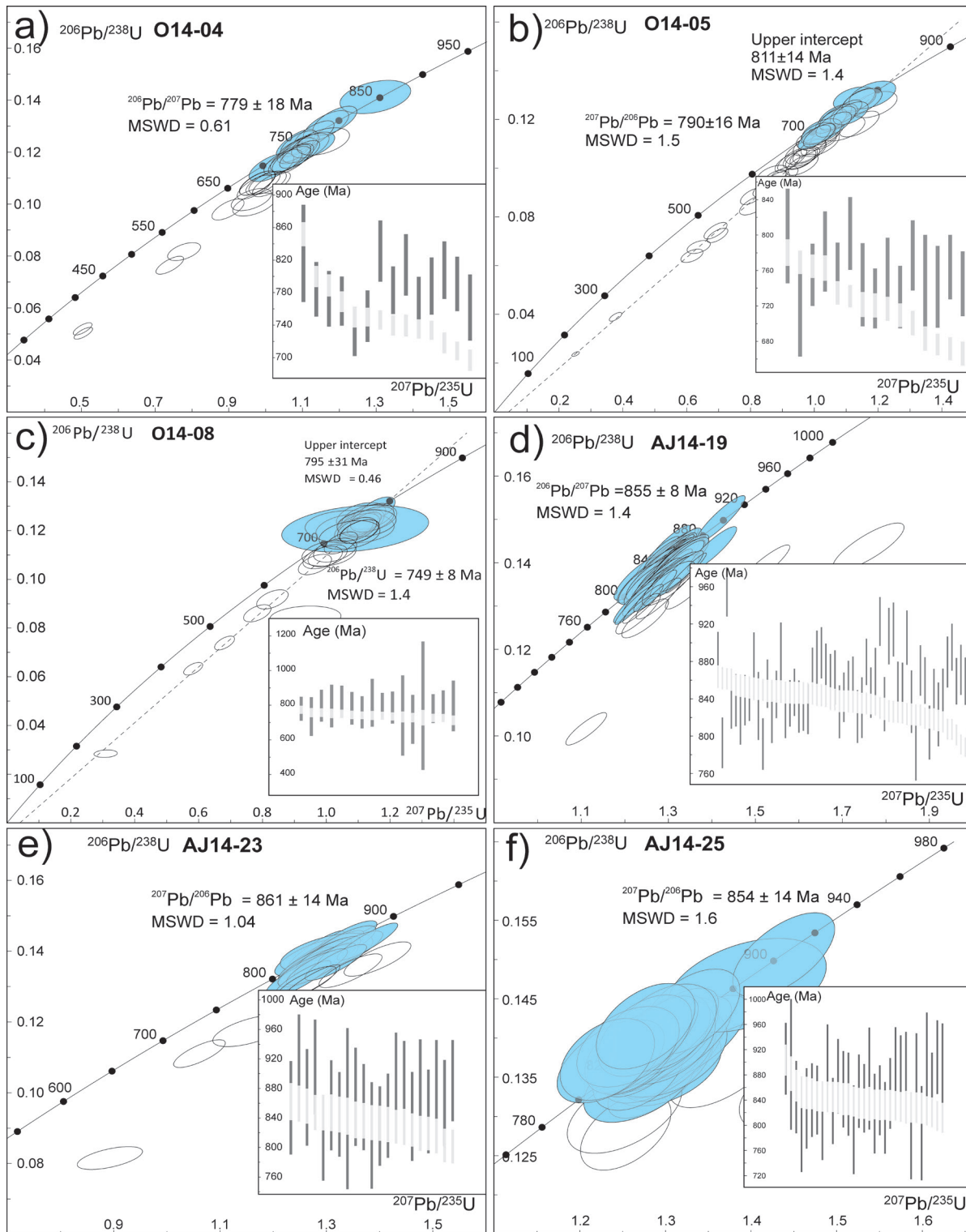
Figure 6: a-f) U–Pb Wetherill plots (^{207}Pb /^{206}Pb v. ^{238}U/^{206}Pb) constructed with a 2 sigma data point error ellipses. Filled grains represent those within 90% concordance and outlines represent all other grains present. Weighted average and calculated intercepts (where applicable) are included on the plot. Each plot has a representative cumulative weighted average plot, displaying ^{206}Pb/^{238}U (light grey) and corresponding ^{206}Pb/^{207}Pb ages (dark grey). These plots show the relationship between the two isotopic systems.
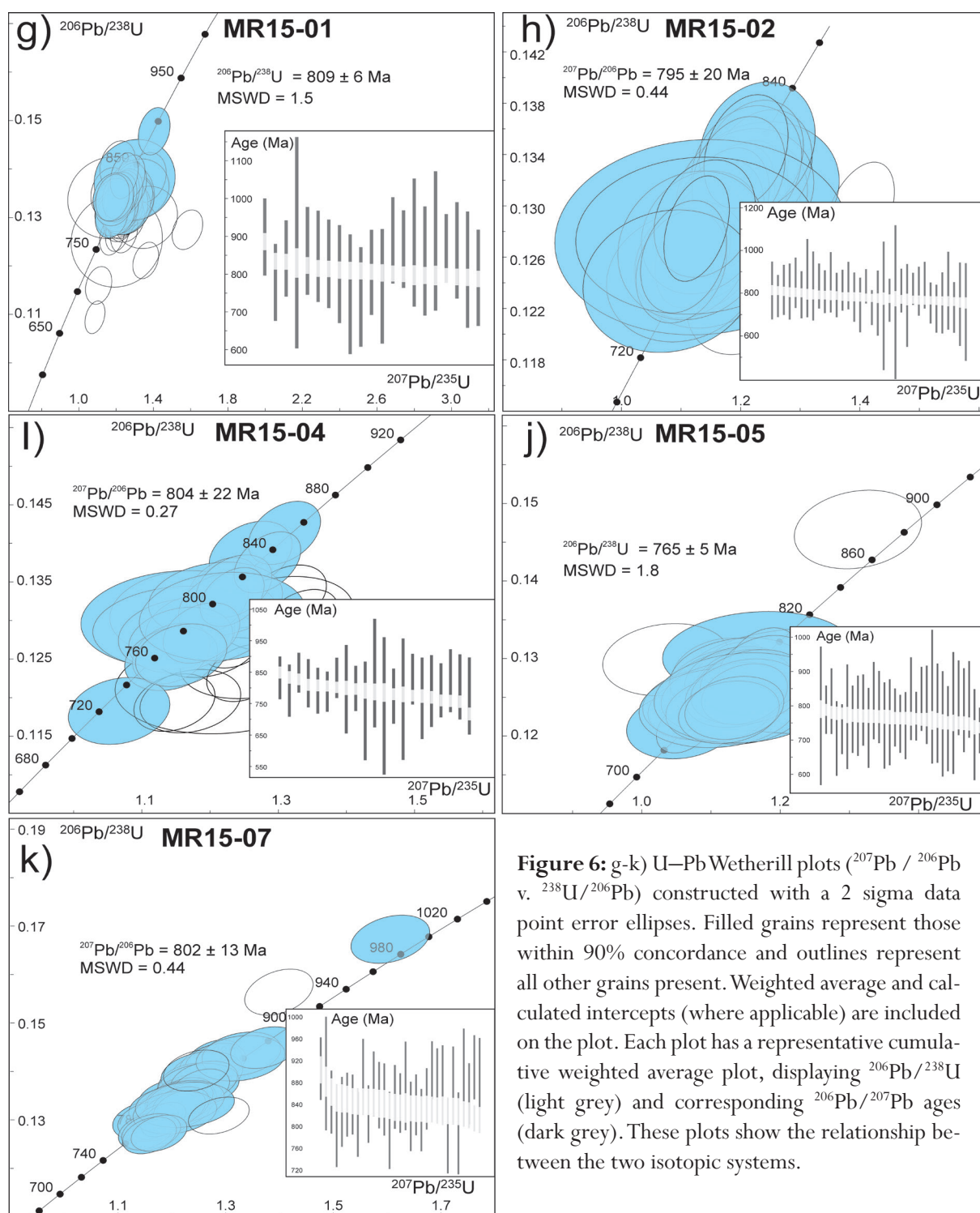
Figure 6: g-k) U–Pb Wetherill plots (^{207}Pb / ^{206}Pb v. ^{238}U / ^{206}Pb) constructed with a 2 sigma data point error ellipses. Filled grains represent those within 90% concordance and outlines represent all other grains present. Weighted average and calculated intercepts (where applicable) are included on the plot. Each plot has a representative cumulative weighted average plot, displaying ^{206}Pb/^{238}U (light grey) and corresponding ^{206}Pb/^{207}Pb ages (dark grey). These plots show the relationship between the two isotopic systems.

and yielded a ε_{Hf}(t) range between +8.21 and +10.26 (Fig. 8). The weighted average for these analyses is 9.13 ± 0.41, suggesting these zircons have a juvenile signature. The δ^{18}O (zircon) ‰ values give a range between 4.49 ± 0.24 and 5.75 ± 0.27 ‰ (Fig 9a). These

gave a weighted average of 5.09 ± 0.37 ‰ and support the positive juvenile ε_{Hf}(t) values.

MR15–07: Sadh Complex
These granodiorites are interlayered with mafic amphibolites and have a defined foliation in

areas. Granitic rich layers are also seen making this lithologically heterogeneous (quartz, feldspar and biotite). Forty three analyses were conducted on forty zircons and of these, thirty seven are within 10% discordance. Single grain analyses show a $^{206}Pb/^{238}U$ age range of 997–774 Ma and the cumulative weighted average plot defines a perceptible lead loss trend (Fig. 3 and 5k). The oldest analyses (997 ± 11) has been interpreted as an inherited grain (based on morphology) and has therefore been excluded from the main age calculation. A weighted average on all grains was calculated yielding a $^{206}Pb/^{238}U$ age of 813 ± 8.5 Ma (MSWD = 7.4). This was recalculated using $^{207}Pb/^{206}Pb$ ages, giving an age of 802 ± 13 Ma (MSWD = 0.44). This $^{207}Pb/^{206}Pb$ age is within error and is interpreted to represent a reliable age estimate for the crystallisation age of this granodiorite. Lu–Hf isotopes were done on twelve zircons showing a juvenile signature (+9.07 to +11.58). A weighted average was calculated giving an $\varepsilon_{Hf}(t)$ of 10.5 ± 0.48 (Fig. 8). Oxygen isotopes on these same zircons give $\delta^{18}O$ values ranging between 3.31 ± 0.31 ‰ to 6.67 ± 0.31 ‰ and a calculated weighted average of 5.00 ± 0.59‰ (Fig. 9a).

Metasedimentary zircon geochronology and Lu–Hf analysis

U–Hf and Lu–Hf isotopes were undertaken on two metasedimentary samples from Jebel Ja'Alan (central east) and Mirbat (south). All data are displayed on Wetherill plots ($^{207}Pb/^{206}Pb$ v. $^{238}U/^{206}Pb$; Fig. 7a and b). Multiple studies now show that the initial $^{176}Hf/^{177}Hf$ value, once incorporated into the zircon lattice during growth, is not modified by processes that may disturb or reset the U–Pb isotopic system (Halpin et al., 2007). Therefore, as U–Pb and Lu–Hf systems in zircon are decoupled, Pb-loss in zircon can be identified by horizontal trends in initial $^{176}Hf/^{177}Hf$ versus preferred

age (Fig 8e and f).

Ja15–43: AlWafi Schist

All zircon grains within this sample exhibit no definable core rim structures. Eighty nine analyses were performed on this sample with thirty five of these ≤10% discordant. These analyses yield a broad range of ages from the Tonian to the Neoarchean (818–2706 Ma). Most of the population have a $^{206}Pb/^{238}U$ age less than 1000 Ma (975–818 Ma) and are defined morphologically by larger, elongate grains with oscillatory zonation (Fig. 7b and d). The oldest grains are defined by equant to rounded shapes (Fig. 5). Peak metamorphism in the area has been temporally constrained at 834 ± 12 Ma (Alessio et al., 2017), providing a constraint for the minimum depositional age for this schist. This indicates that at least some portion of the young population must have suffered lead loss to yield a U–Pb age younger than the metamorphic age obtained for the sample. Morphology, internal textures and Th/U ratios do not allow for distinction between grains with original or reset ages. However, common initial $^{176}Hf/^{177}Hf$ values can be used for identification of Pb-loss in zircon (e.g. Halpin et al. (2007)) with lead loss not affecting the initial $^{176}Hf/^{177}Hf$ value. In this sample, all ages at or below 900 Ma can be traced back to initial $^{176}Hf/^{177}Hf$ values of ~0.282400 or 0.282100. This is consistent with the interpretation of Pb-loss in these zircons. A weighted average, using $^{207}Pb/^{206}Pb$ ages of grains < 1 Ga, yields an age of 903 ± 15 (MSWD = 0.56) and calculating an upper intercept of these same grains gives a similar age of 910 ± 16 (MSWD = 0.83). Although it is likely that the grains are not sourced from a single igneous rock (as indicated by two distinct Hf isotope compositions; Fig. 7f), and therefore an upper intercept or weighted mean age is an artificial construct, the upper intercept age
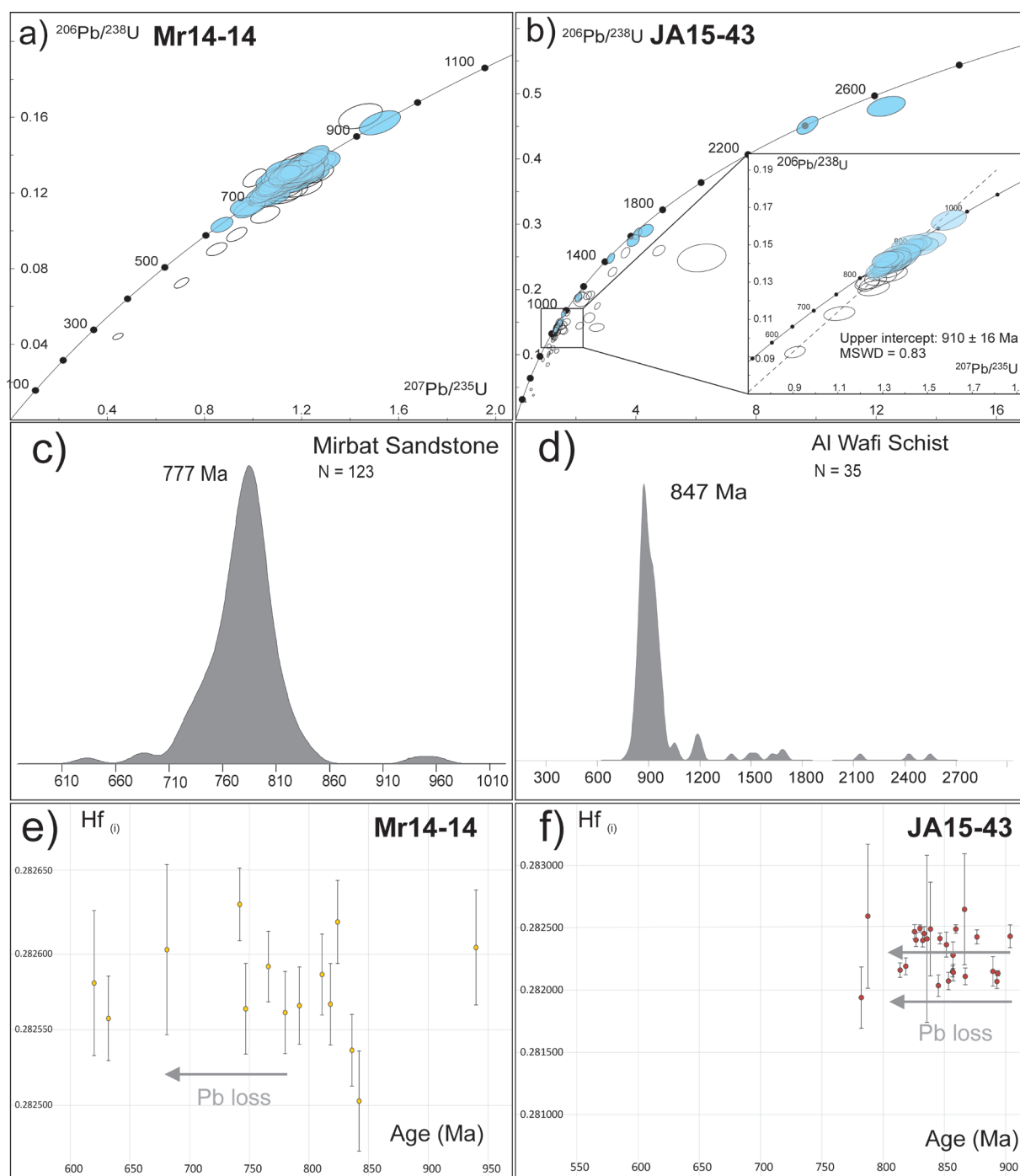
Figure 7: U-Pb Wetherill plots (^{207}Pb / ^{206}Pb v. ^{238}U/^{206}Pb) constructed with a 2 sigma data point error ellipses for two sedimentary samples Mirbat Sandstone. a) and Al Wafi Schist b). Figure 6b) contains an inset of the main population at ca. 900 Ma and the calculated upper intercept. Figure 6c– d) Kernel density plots for Mirbat and Jebel Ja'alan showing main peaks at ca. 777 Ma and ca. 847 Ma respectively. Jebel Akhdar show inheritance of older grains spaning from $1200 - 2700$ Ma. e and f) Initial ^{176}Hf/^{177}Hf versus ^{206}Pb/^{238}U age used to identify any distinct Pb-loss trends that appear as a horizontal trend on the plot. Pb-loss trends are seen in both samples, shown by the grey arrows. Al Wafi schist show two distinct Hf isotope compositions suggesting multiple sources.

(ca. 910 Ma) is used as an approximation of the maximum depositional age for this schist as it partly circumvents the issues created by Pb loss in this sample.

The older grains above 1000 Ma have $\varepsilon_{Hf}(t)$ values range between +6.81 and -12.15, suggesting that these grains were derived from multiple sources of variable natures (Fig. 7b). The younger population gives a dominantly bimodal $\varepsilon_{Hf}(t)$ range defined by two groups +14.54 to +1.28 and -2.74 to -7.66. This suggests a magmatic event (or events) that have a similar age but dramatically differing proportions of crustal input or crustal compositions.

MR15–14: Mirbat Sandstone

One hundred and twenty analyses were undertaken for this sample. Of those ninety eight were determined to be ≥ 90% concordant. No discernible age differences are observed between core and rim structures. $^{206}Pb/^{238}U$ ages for the sample range between 940 and 633 Ma. A major peak is identified in the kernel density plot at ca. 747 Ma (Fig. 7a and c). The youngest grain (633 Ma) is morphologically different to the other grains, characterised by its rounded, equant shape contrasting to the more prismatic oscillatory zoned zircons (Fig. 5a). However, using this grain to constrain the depositional age is complicated by the possibility of Pb-loss during younger events. Figure 7d, shows the younger ca. 633 Ma grain to have a similar initial $^{176}Hf/^{177}Hf$ to the older population, which could suggest that this grain merely reflects lead loss (Fig. 7e). Similarly, the single older grain at ca. 920 Ma may also reflect the incorporation of older radiogenic Pb in the analysis as it also has a similar $^{176}Hf/^{177}Hf_i$ value. The main population of grains have $\varepsilon_{Hf}(t)$ values ranging between 12.98 and 6.61 (Fig. 8b), suggesting that these zircons were derived from juvenile sources, with negligible old, continental crust input although recent crustal additions cannot be excluded.

DISCUSSION

Understanding the assembly of the ANS and the relative position of Oman in Gondwana hinges upon the ability to identify terrane boundaries, timing of accretion events and the prior crustal histories of each terrane. As the ANS and parts of Oman are recognised as being dominantly juvenile terranes, the use of Hf and O isotopic data from zircon has the potential to rapidly identify terranes with a continental affinity. This discussion focusses on using the geochemical fingerprints from the Omani basement to determine its position, whether it be as an extension of the ANS or in a separate tectonic domain.

The central exposures of basement in Oman, are defined by small exposures of the Al Jobah granite and volcanic and volcanosedimentary rocks. Data (AJ–19, 23, 25) suggests that within central exposures of the Huqf, magmatism occurs between ca. 854 and 838 Ma. Other interpretations by Bowring et al. (2007) suggest that the Al Jobah granite (AJ14–19) crystallised at ca. 824 Ma, defined by the youngest population, with the older grains representing inheritance. However, we suggest that the crystallisation of the granite occurred before this at ca. 855 Ma (AJ–19). The other granitic (AJ14–23 and 25) samples, differentiated from the Al Jobah granite by grain size, sit within error of each other (861 ± 14 Ma and 854 ± 14, respectively) and therefore have been interpreted to represent heterogeneities within the Al Jobah granite. Lu–Hf isotopes from these granites (AJ–19, 23, 25) have an average $\varepsilon_{Hf}(t)$ value of 10.44 and combined with oxygen isotopes (average $\delta^{18}O$ (zircon) ‰ value of 7.57‰), reflect a component of supra-crustal, material incorporated into the magma from which the zircon precipitated
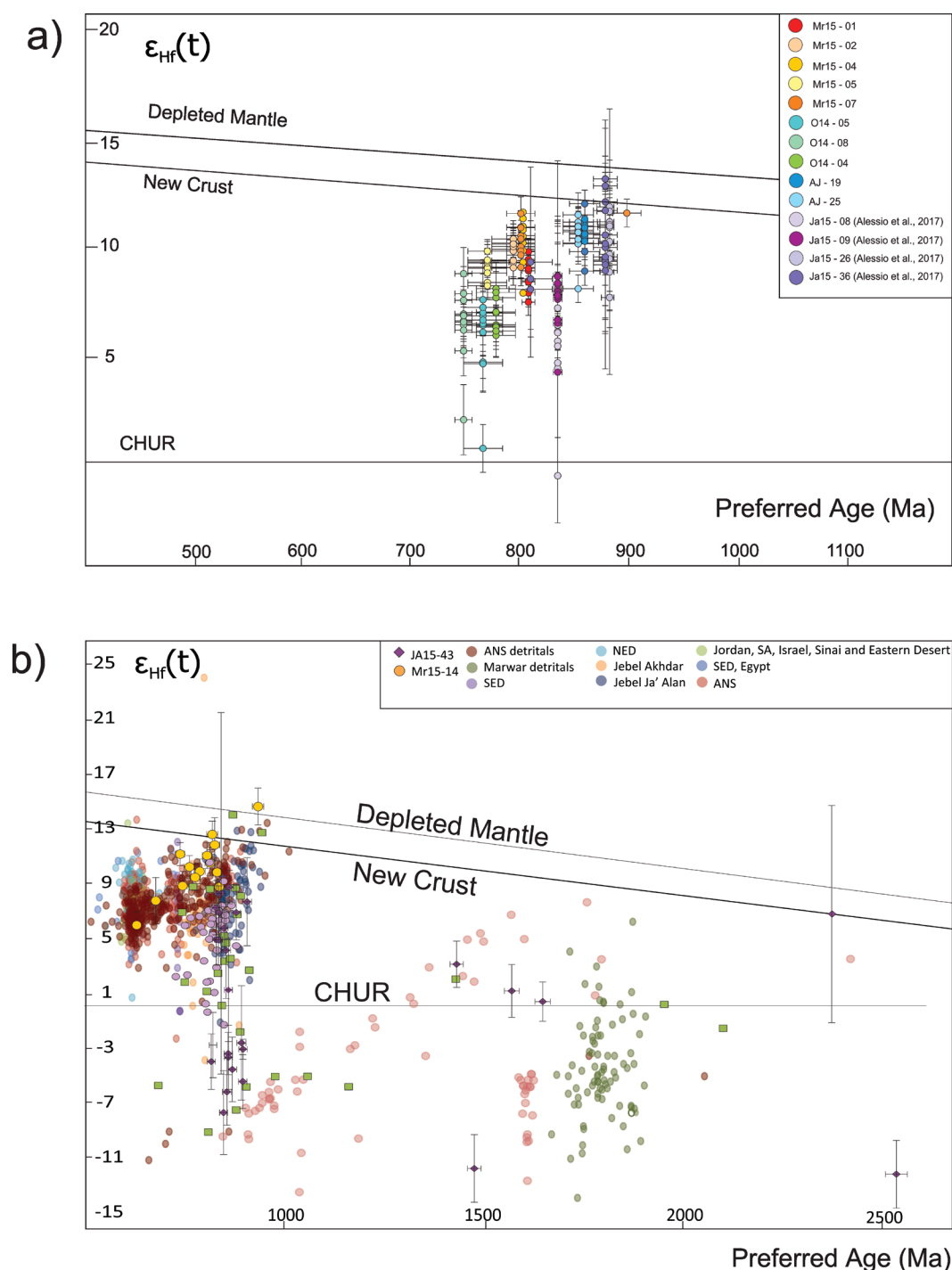
Figure 8: a) $\varepsilon_{Hf}(t)$ versus $^{206}Pb/^{238}U$ age plot for all igneous samples. Plots show that all samples are juvenile, with negligible old, continental crust input although recent crustal additions cannot be excluded. Both horizontal and vertical error bars show 2σ error. b) $\varepsilon_{Hf}(t)$ versus $^{206}Pb/^{238}U$ age plot for two sedimentary samples (MR15-14 and JA15-43). Plots (JA15-43) show grains >1000 Ma have $\varepsilon_{Hf}(t)$ values range between +6.81 and -12.15, suggesting that these grains were derived from multiple sources of variable natures. The younger population gives a dominantly bimodal $\varepsilon_{Hf}(t)$range defined by two groups + 14.54 to + 1.28 and -2.74 to -7.66. This suggests a magmatic event (or events) that have a similar age but dramatically differing proportions of crustal input or compositions of crust. MR15—14 has a dominantly juvenile signature, showing negligible older continental input. Both horizontal and vertical error bars show 2σ error.
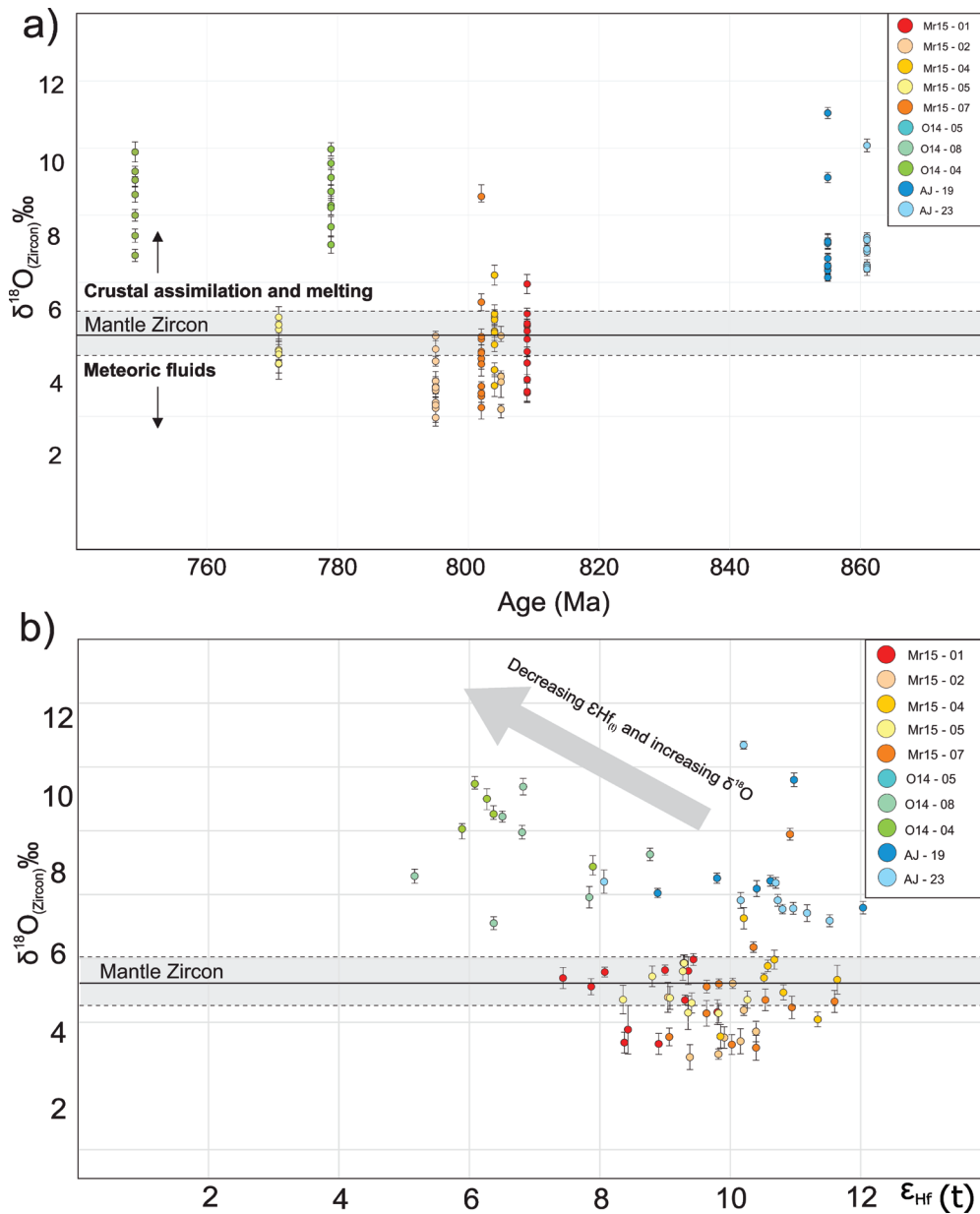
Figure 9: a) $\delta^{18}O$ plotted against the interpreted crystallisation age for analyses of Western Ethiopian Shield samples. Error bars are two sigma. Range of mantle derived $\delta^{18}O$ (zircon) values are $5.3 \pm 0.6‰$ (Valley et al., 1998). b) Plot of $\delta^{18}O$ versus $\varepsilon_{Hf}(t)$ for all zircon analysed in this study. Range of mantle derived $\delta^{18}O$ (zircon) values are $5.3 \pm 0.6‰$ (Valley et al., 1998).

(Valley, 2003; Valley et al., 2005). The southernmost exposure in Mirbat, Salalah, provides some of the best basement exposures in Oman. The Sadh gneissic complex comprises much of the basement of Mirbat and has been previously interpreted to represent subduction-related island arc, on the basis of its geochemical signature (Alessio et al., 2017; Rantakokko et al., 2014; Whitehouse et al.,

2016). Recent geochronological constraints on the gneiss have been established by Rantakokko et al. (2014) and they suggest the protolith ages of the orthogneiss are between ca. 835–831 Ma. These ages broadly correlate with basement rocks elsewhere in Oman, Saudi Arabia, Yemen and northern Somalia (Alessio et al., 2017; Fritz et al., 2013; Johnson et al., 2011; Johnson, 2014; Johnson and Kattan,
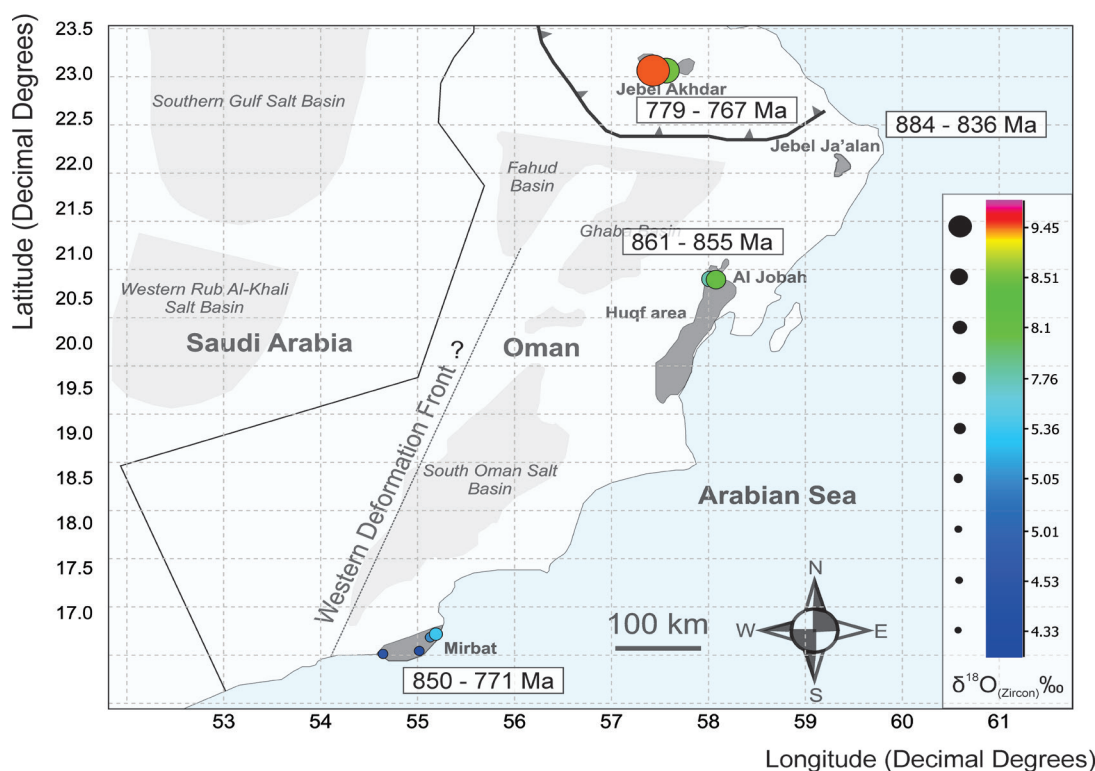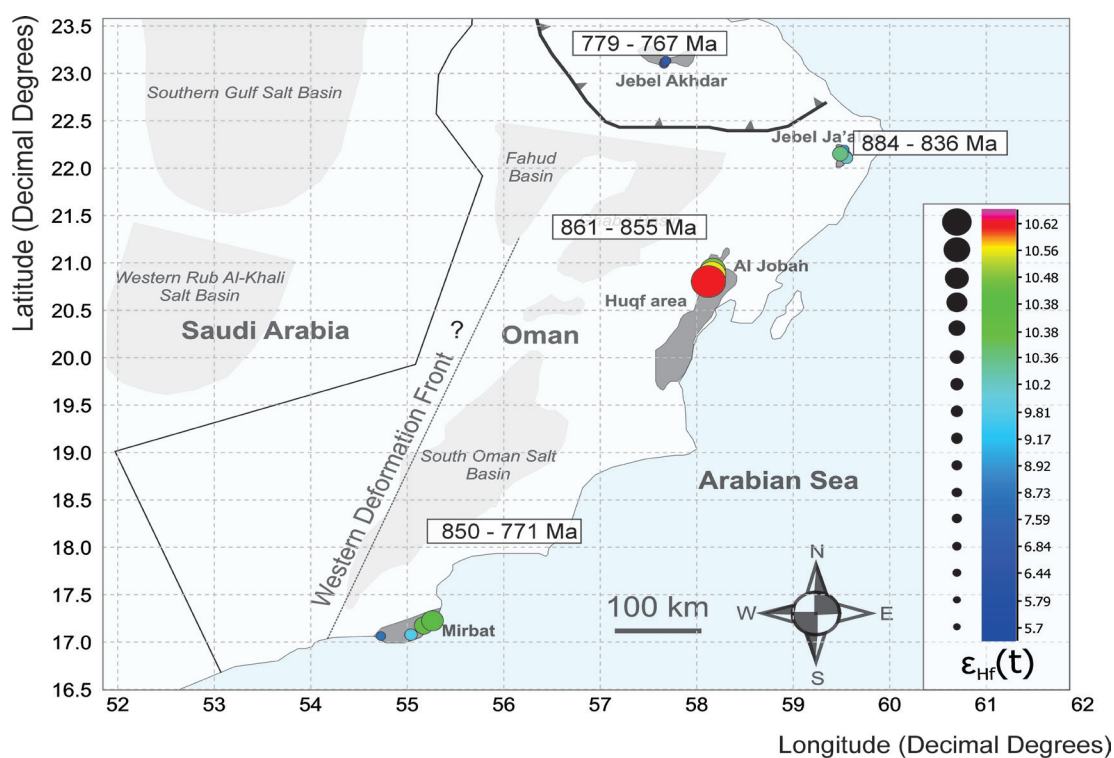
Figure 10: Geographical location (decimal degrees) of $\varepsilon_{Hf}(t)$ scaled by colour and size to represent the change across Oman. Crystallisation ages (zircon) from igneous rocks for each basement inlier, data taken from this study and other published studies (Allen et al., 2004; Brasier et al., 2000; Leather et al., 2002; Mercolli et al., 2006; Worthing, 2005, Alessio et al., 2017; Mercolli et al., 2006; Whitehouse et al., 2016). Geographical location (decimal degrees) of $\delta^{18}O$ (zircon) ‰ scaled by colour and size to represent the change across Oman. Crystallisation ages are present for each basement inlier.

2012; Johnson and Woldehaimanot, 2003; Kröner and Sassi, 1996; Rantakokko et al., 2014; Stoeser et al., 2001a; Whitehouse et al., 2016; Whitehouse et al., 2001a; Whitehouse et al., 2001c; Yeshanew et al., 2015). However, this study records a younger crystallisation age of ca. 813 Ma (MR15–07), likely dating a younger phase within the heterogeneous Sadh Gneiss (MR15–07). This interpretation is supported by previously published data, which yield zircon rim ages of 821–815 Ma (Rantakokko et al., 2014; Worthing, 2005). The lithologically younger units, the Mirbat granite (MR15–02) and tonalite (MR15–04), have crystallisation ages of ca. 809–795 Ma with inheritance of older ca. 834–840 Ma grains, interpreted to be derived from the Sadh gneiss, based on the presence of xenoliths of dark gneiss within both units. The youngest phase seen in this study is the monzonite (MR15–05), seen cross cutting the tonalitic rocks, yields an age of ca. 765 Ma. However, this unit does not preserve ca. 835–840 Ma history, as seen in the Mirbat granite and tonalite. The zircons from the basement rocks, that crop out in Mirbat, are defined by a juvenile signature (ε_{Hf}(t) values +10.5 to +8.72), suggesting continental crust input is negligible. The grains interpreted as inheritance within samples from Mirbat have similar hafnium isotopic signatures, with values between +10.9 and +8.43, supporting derivation from the Sadh Complex. Complementary oxygen isotopes data show zircons to have an average values between $\delta^{18}O$ (zircon) ‰ of 4.3 − 5.3‰. Zircons in equilibrium with pristine mantle derived melts have $\delta^{18}O$ values of 5.3‰ ± 0.6‰; (Valley, 2003). It has been inferred that zircons with $\delta^{18}O$ of less than 6.5‰ formed from melts that contained a minor to negligible sedimentary component (Valley, 2003; Valley et al., 2005). The low $\delta^{18}O$ values seen in a few samples, suggest interaction with meteoric

waters or hydrothermal fluids.

Correlation of metasedimentary sequences in Oman

There is no exposed basement in Jebel Akhdar, northern Oman. The granitic clasts in the diamictite (Abu Mahara Group) are instead used as a proxy to the basement. A Neoproterozoic source for the Abu Mahara zircons has been previously interpreted, with a syn-depositional crystallization age of 714 Ma and a reworked contribution from older sources aged ca. 755–826 Ma (Allen, 2007; Allen et al., 2004; Bowring et al., 2007; Brasier et al., 2000; Rieu et al., 2007). Within the diamictite there are two types of granitic clasts, coarser grained (O14–04 and 05) and finer grained granites (O14–08). The coarser grained clasts have crystallisation ages between ca. 779–767 Ma, whereas the younger is ca. 749 Ma. The error between these two types of granitic clast overlap making it hard to differentiate between them. The crustal component to these zircons is more recognisable through the Lu–Hf and oxygen isotopes, yielding average ε_{Hf}(t) and $\delta^{18}O$ (zircon) ‰ values of 6.42 and 8.93 ‰, respectively. The elevated $\delta^{18}O$ values suggest that the zircons within these clasts have incorporated a component of sedimentary material (Valley et al., 2005). These crystallisation ages of these granitic clasts are synonymous with the latest phase of magmatism seen in Mirbat, however, the oxygen and hafnium isotopes suggest a higher supra-crustal input into the magma, from which these zircons were precipitated. The Ayn glacial sedimentary rocks of Mirbat have been interpreted to be coeval with the Abu Mahara Group of the Jebal Akhdar, and the older Cryogenian glacial epoch is between ca. 726–714 Ma (Allen, 2007; Allen and Leather, 2006; Allen et al., 2004; Bowring et al., 2007; Leather et al., 2002; Rieu et al., 2007; Stern
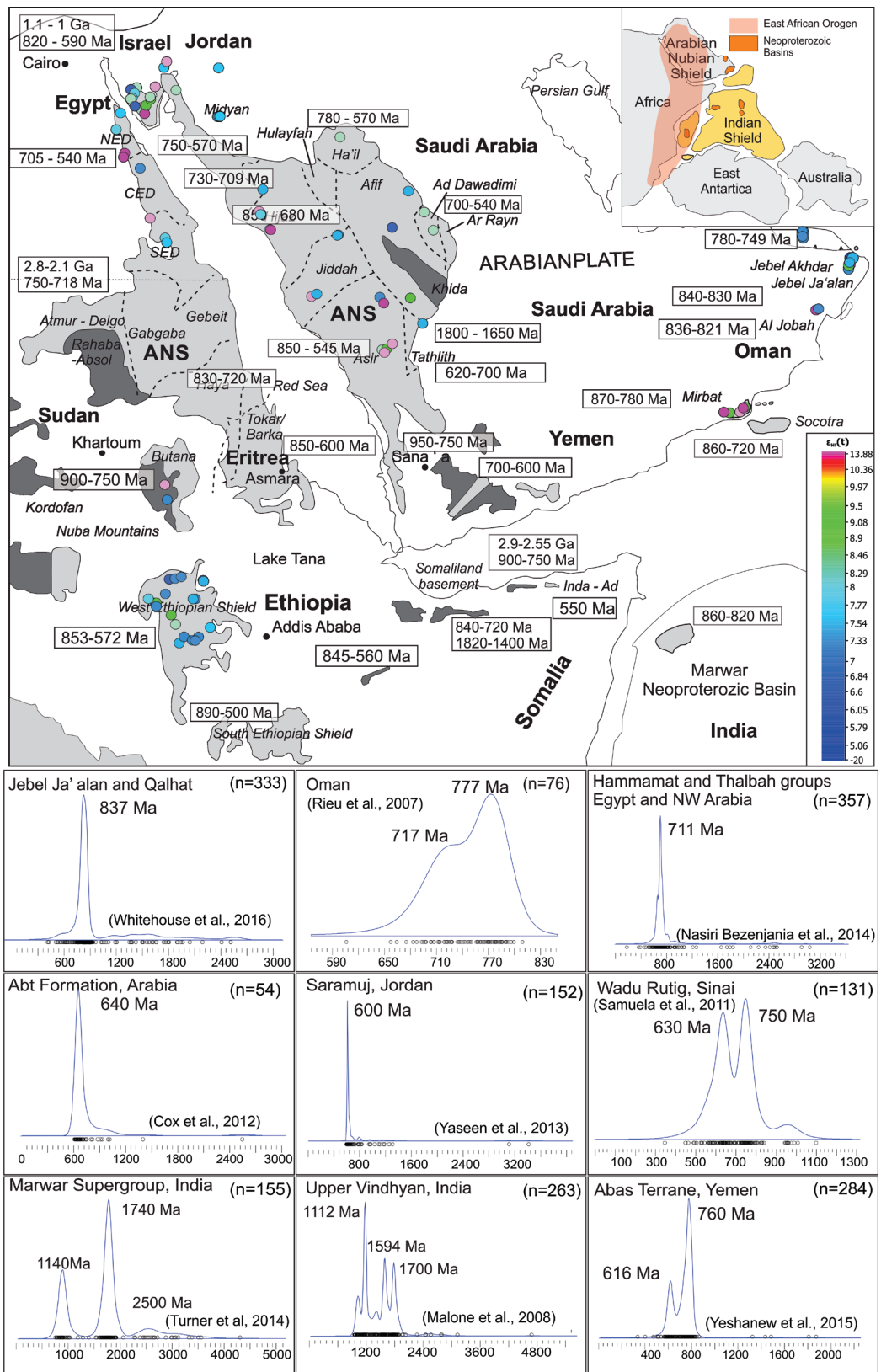
Figure 11: Comparative figure showing previously published ages and hafnium isotopic data form the northern East African Orogen. Kernel density plots from regions in the Arabian Nubian Shield and NW India are shown at the bottom of the figure (Alessio et al., 2017; Ali et al., 2013; Ali et al., 2016; Be'eri-Shlevin et al., 2010; Blades et al., 2015; Robinson et al., 2015; Robinson et al., 2014).

and Johnson, 2010). It has been suggested that the clasts from the Abu Mahara Group may correlate with the exotic clasts from salt domes in the United Arab Emirates (UAE). However, these are likely comparisons to the Shuram and Khufai Formations (640–600 Ma) with the Nafun Group (Huqf Supergroup) in Oman (Thomas et al., 2015). The diamictites of the Abu Mahara group have been interpreted to have a glaciomarine origin by fallout from suspension and rainout of ice-rafted debris (Allen, 2007; Allen et al., 2004; Bowring et al., 2007; Brasier et al., 2000; Rieu et al., 2007). Therefore, these clasts could have been significantly transported and exotic to Arabia.

Metasedimentary rocks from the southern exposures in Mirbat (Fig. 6a, c and e) have been interpreted to have a localised Neoproterozoic source region, with ages similar to that of the crystalline basement of Mirbat, supported by previously published data (Mercolli et al., 2006; Rantakokko et al., 2014). These metasedimentary rocks have no evidence of older zircons, with the main age peak at ca. 777 Ma (MR15–14; Fig. 7a, c and e). Together, the zircon Lu–Hf and oxygen isotopes are consistent local sediment derivation. In contrast, the small age peaks (and Lu–Hf isotopes) seen in the metasedimentary rocks in Jebel Ja'Alan (2706 and 1204 Ma) indicate that at this time, Jebel Ja'Alan was depositionally connected to a Paleoproterozoic–Neoarchean source region (Fig. 7b, d and f). This is of course assuming that these older zircons do not represent a recycled component.

Like the sedimentary rocks of Jebel Ja'Alan, the exotic clasts from the UAE, show derivation from the erosion of Neoproterozoic–Palaeoproterozoic and Neoarchaean sources (Thomas et al., 2015). Input of detritus from older Palaeoproterozoic to Archaean sources

(largely c. 1800–2050 Ma, and ca. 2500 Ma), are possibly from rocks of the Arabian Shield (Johnson, 2014) as exposed in southeast Saudi Arabia and Yemen (Fig. 11) (Stoeser et al., 2001b; Whitehouse and Bridgwater, 2001; Whitehouse et al., 2001b; Whitehouse et al., 1998; Whitehouse et al., 2001c; Windley et al., 1999; Yeshanew et al., 2015). However, it can be speculated that other sources such as the basement blocks such as those embedded in present-day Iran (Fig. 11) and Afghanistan (Faryad, 1999; Faryad et al., 2016), the precise whereabouts of these blocks during the Neoproterozoic remains uncertain. These ages are common to crustal blocks, such as the Dharwar Craton and Southern Granulite Terrane in India (Collins et al., 2014; Collins et al., 2007; Meert et al., 2010; Plavsa et al., 2014), as well as detritus in the Marwar Supergroup and Upper Vidhyan (Fig. 11) in NW India (Davis et al., 2014; Malone et al., 2008; Meert et al., 2010; Pradhan et al., 2010). The Sherdarwaza Formation, located on the Kabul Block, has Neoarchaean crystallisation ages of ca. 2.5–2.8 Ga, with Neoproterozoic over print at ca. 850–900 Ma (Faryad et al., 2016) and may provide the source of the detritus seen in both Oman and NW India.

Regional Implications

To the west of these terranes sits the island arc terranes of the Arabian Nubian Shield. Four discrete magmatic events have been previously identified in the eastern Arabian Nubian Shield; island arc (ca. 845 Ma), syn-collisional (ca. 710 Ma), post-tectonic (ca. 620 Ma) and anorogenic (ca. 525 Ma; Robinson et al., 2014). These are defined by juvenile magmas $\varepsilon_{Hf}(t)$ values of +4.5 to +10 regardless of their intrusive ages or spatial relationship (Ali et al., 2015; Ali et al., 2010; Ali et al., 2013; Morag et al., 2011; Robinson et al., 2015; Robinson et al., 2014). Oxygen isotope data are sparse
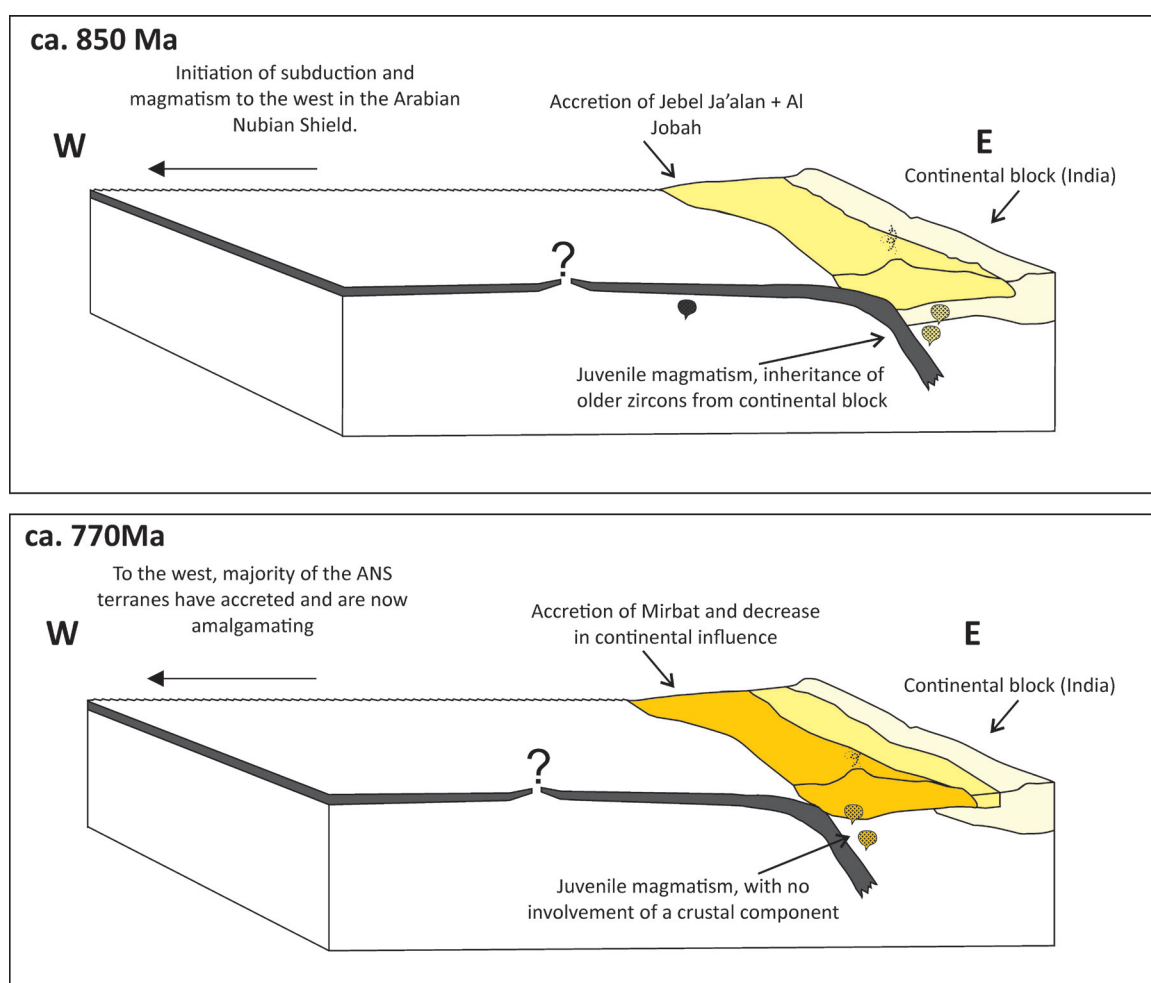
Figure 12: Schematic illustration of the stages of development in Oman. There are two main phases of subduction and arc magmatism at 850 Ma and 770 Ma. 850 Ma depicts the initiation of magmatism in the easternmost exposures of Jebel Ja'alan and Al Jobah. The time-slice at 770 Ma represents the westward accretion of the arc (Mirbat). Igneous and metamorphic activity occurred during the Tonian (1000–850 Ma) and early Cryogenian, and had concluded by ca. 700 Ma, transitioning into a passive margin.

in the ANS, however, oxygen isotopes have a range between 3.2‰ to 7.4‰ consistent with melting of a relatively juvenile crustal protolith that was formed during the Neoproterozoic (Ali et al., 2015; Ali et al., 2013; Ali et al., 2016). What is of particular importance is that geochronological data in Oman indicate that igneous and metamorphic activity occurred during the Tonian (1000–850 Ma) and early Cryogenian, and had concluded by ca. 700 Ma (Alessio et al., 2017; Stern and Johnson, 2010). This is in contrast to the prolonged period of magmatic and metamorphic events that occur during the growth of the Arabian

Shield. Subsequent Neoproterozoic activity in Oman took the form of Cryogenian–Ediacaran deposition of siliciclastic, glaciogenic, carbonate and evaporite rocks (the Huqf Supergroup) unconformable on the crystalline basement (Allen et al., 2004; Brasier et al., 2000; Leather et al., 2002; Mercolli et al., 2006; Worthing, 2005). These packages were deposited in a stable, passive margin environment (Allen, 2007), suggesting that at this time the rocks of Oman were in a different tectono-geographic position to the Arabian Nubian Shield. Geochronology from Oman shows a younging direction to the east. Previously reported Nd

isotope systematics from Jebel Ja' Alan, yield $\varepsilon_{Nd}(t)$ (ca. 840 Ma) values between +3 and +6, compared to $\varepsilon_{Nd}(t)$ (ca. 840) between +5 and +7 in Mirbat (Alessio et al., 2017; Mercolli et al., 2006; Whitehouse et al., 2016). Previous interpretations suggest that that this decrease is possibly due to the outward growth of arcs, progressing further away from a continental source (Whitehouse et al., 2016). It is difficult to unequivocally demonstrate this outward decrease in continental influence using these Sm–Nd and Lu–Hf systematics. The spread in data could represent the mixing of material from different sources or be a result of analytical uncertainty as opposed to real geological variation. However, oxygen isotopes in the east (Al Jobah) have $\delta^{18}O$ (zircon) ‰ values (Fig. 10), which show that a component of ^{18}O-enriched, supra-crustal, material was at some point incorporated into the magma from which the zircon precipitated. Assuming that the Mirbat region lies structurally to the west, $\delta^{18}O$ (zircon) ‰ values show that these zircons (Fig. 10) were in equilibrium with pristine mantle derived melts ($\delta^{18}O$ values of 5.3‰ ± 0.6‰; Valley et al., 2005).

Detrital data collected in this study, as well as by others (Bowring et al., 2007; Brasier et al., 2000; Mercolli et al., 2006; Rieu et al., 2007; Whitehouse et al., 2016) show that sediments from Jebel Ja'Alan were sourcing Palaeoproterozoic–Mesoarchaean zircons, suggesting that NE Oman was at one point depositionally connected to older crust. However, the presence of these older grains may also be the result of sedimentary recycling, though there is no definitive way to test these hypotheses and no other age populations are present in this sample (JA15–43). This is in contrast to the detrital populations seen in Mirbat, where there is no evidence for pre-existing crust. Together with the Sm–Nd and Lu–Hf isotope systems, this is consistent with

the progressive development of these arc rocks onto the western margin of an eastern Neoproterozoic continent. Data is suggested to reflect the outward growth of the related subduction zone (Fig. 12), progressing further away from a continental source (Alessio et al., 2017; Whitehouse et al., 2016). In Gondwana, Oman lay adjacent to NW India (Alessio et al., 2017; Merdith et al., 2017). Ediacaran sedimentary rocks have been correlated from Oman, across Rajasthan and Pakistan (Cozzi et al., 2012), which include similar petroleum source rocks and characteristic late Ediacaran evaporites. We suggest that this passive margin developed after Tonian accretion of the Rajasthan, Pakistan and Omani basement volcanic arcs onto NW Neoproterozoic India (Fig. 12).

Comparative magmatic ages to Mirbat exist in the island of Socotra (ca. 825–815 Ma) and Yemen (Whitehouse et al., 2001a; Whitehouse et al., 1998; Yeshanew et al., 2015), which lay close to Mirbat (Fig. 10) before the opening of the Gulf of Aden (Denèle et al., 2013). Granitoids have been dated from Rajasthan and from Nagar Parkar in eastern Sind (Pakistan) at ca. 1100 Ma (Meert et al., 2013; Raza et al., 2012), with metamorphism occurring at ca. 950–940 Ma. Evidence for Tonian granitoids and rhyolites occur in inliers through NW India and Pakistan (Fig. 11), with crystallisation ages between ca. 900–970 Ma, ca. 860–820 Ma and 775–760 Ma (Haldar & Deb, 2001; Pandit et al. 2003; Davies & Crawford, 1971; Deb et al. 2001; Van Lente et al. 2009; Just et al. 2011; Gregory et al. 2009; Van Lente et al. 2009; Ashwal et al. 2013; Meert, Pandit & Kamenov, 2013). This shows that NW India has an extensive accretionary history from the Stenian – Tonian (1100–720 Ma), overlapping with magmatism and metamorphism seen in the Omani basement. The Seychelles share similar

geology to western Rajasthan, with granites intruding between ca. 810–750 Ma (Torsvik et al., 2001; Tucker et al., 2001). Correlating with the Seychelles, the Bemarivo Belt in NW Madagascar, records juvenile magmatism between 750–705 Ma (Collins, 2006; Collins and Windley, 2002; Thomas et al., 2009; Tucker, 2014) and perhaps represents the final Mozambique Ocean volcanic arc accretion onto India before the margin evolved into a Cryogenian passive margin.

The location of the suture between the Omani basement and the Arabian Nubian Shield is still controversial. Geophysical data have been used to differentiate the Arabian shield in the east from the terranes in the west (Stern and Johnson, 2010). A major magnetic feature (Central Arabian Magnetic Anomaly) has been suggested to represent the boundary of these two crustal segments. However, this has been disputed by other authors (Cox et al., 2012), who suggest that the boundary lies further east along the 'Western Deformation Front' in the subsurface beneath the Rub Al Khali Desert (Allen, 2007). Allen (2007) argue that the Western Deformation Front represents a collisional zone during the Neoproterozoic and is supported by seismic wave anisotropy studies (Al-Lazki et al., 2012), which picked out different terranes based on their anisotropic signature and proposed a major suture directly east of Mirbat in SE Oman. The Betsimisaraka Suture Zone of Madagascar (Malagasy Orogeny) is a controversial suture in east Madagascar and has been interpreted as the result of the closure of the Mozambique Ocean and the Ediacaran–Cambrian collision of Neoproterozoic India with a continent made up of rocks now found in central Madagascar, Somalia and Arabia. This has been interpreted to continue into Palghat–Cauvery suture of southern India (Collins et al., 2007; Reeves and de Wit, 2000) and

is supported by both these belts preserving Cambrian ages of metamorphism (Collins et al., 2003). The northward continuity of the Betsimisaraka Suture zone is here suggested to form the Western Deformation Front in Oman, as it lies broadly on-strike in Gondwana and is a coeval suture. This Palghat–Betsimisaraka–Western Deformation Front suture would then extend into the final suture of the Mozambique Ocean.

CONCLUSIONS

Geochronological data in this study, combined with other published works, suggest that the basement rocks of Oman accreted during the Tonian (1000–850 Ma) and early Cryogenian. The cessation of magmatism had occurred by ca. 700 Ma, and this was followed by the deposition of passive margin sequences. This is in contrast to the prolonged period of magmatic and metamorphic events that occur during the growth of the Arabian Shield (ca. 850–600 Ma). Lu–Hf isotope data obtained in this study, suggest the progressive development of arc rocks away from a continental source, starting from the older eastern exposures (δ^{18}O (zircon) ‰ value of 7.57) to the more juvenile exposures in Mibrat (ε_{Hf}(t) values 10.5–8.72 and δ^{18}O (zircon) ‰ of 4.3–5.3‰). Detrital data collected in this study and by others, support the outward growth of Omani basement away from continental crust, with sediments from Jebel Ja'Alan sourcing Palaeoproterozoic–Neoarchaean zircons, whereas Mirbat detrital populations are wholly juvenile and interpreted to be locally derived. The sources of Palaeoproterozoic–Neoarchaean zircons broadly correlate with the detritus seen in rocks of the Marwar Supergroup and Upper Vidhyan in NW India. These Neoarchaean detrius can be correlated to the Kabul Block, Afghanistan, with crystallisation ages of 2.5–2.8 Ga and Neoproterozoic overprint. As such,

these data are used to interpret the formation of the Omani basement on the margin of Neoproterozoic India, and its outward growth thereafter. Therefore, these data support the accretion of Oman onto Neoproterozoic India, thus supporting the continuation of the Betsimisaraka Suture (Madagascar) through to the Palghat–Cauvery suture (India) and potentially the Western Deformation Front in Oman.

REFERENCES

Al-Lazki, A., Ebinger, C., Kendall, M., Helffrich, G., Leroy, S., Tiberi, C., Stuart, G., Al-Toobi, K., 2012. Upper mantle anisotropy of southeast Arabia passive margin [Gulf of Aden northern conjugate margin], Oman. Arabian Journal of Geosciences 5, 925-934.

Alessio, B.L., Blades, M.L., Murray, G., Thorpe, B., Collins, A.S., Kelsey, D.E., Foden, J.F., Payne, J.L., Al-Khirbash, S., Jourdan, F., 2017. Origin and tectonic evolution of the NE basement of Oman: a window into the Neoproterozoic accretionary growth of India? Geological Magazine, 1-25.

Ali, K.A., Kröner, A., Hegner, E., Wong, J., Li, S.-Q., Gahlan, H.A., El Ela, F.F.A., 2015. U–Pb zircon geochronology and Hf–Nd isotopic systematics of Wadi Beitan granitoid gneisses, South Eastern Desert, Egypt. Gondwana Research 27, 811-824.

Ali, K.A., Stern, R.J., Manton, W.I., Kimura, J.-I., Whitehouse, M.J., Mukherjee, S.K., Johnson, P.R., Griffin, W.R., 2010. Geochemical, U–Pb zircon, and Nd isotope

investigations of the Neoproterozoic Ghawjah Metavolcanic rocks, Northwestern Saudi Arabia. Lithos 120, 379-392.

Ali, K.A., Wilde, S.A., Stern, R.J., Moghazi, A.-K.M., Ameen, S.M., 2013. Hf isotopic composition of single zircons from Neoproterozoic arc volcanics and post-collision granites, Eastern Desert of Egypt: Implications for crustal growth and recycling in the Arabian-Nubian Shield. Precambrian Research 239, 42-55.

Ali, K.A., Zoheir, B.A., Stern, R.J., Andresen, A., Whitehouse, M.J., Bishara, W.W., 2016. Lu–Hf and O isotopic compositions on single zircons from the North Eastern Desert of Egypt, Arabian–Nubian Shield: Implications for crustal evolution. Gondwana Research 32, 181-192.

Allen, P.A., 2007. The Huqf Supergroup of Oman: Basin development and context for Neoproterozoic glaciation. Earth Science Reviews 84, 139-185.

Allen, P.A., Leather, J., 2006. Post-Marinoan marine siliciclastic sedimentation: the Masirah bay formation, Neoproterozoic Huqf supergroup of Oman. Precambrian Research 144, 167-198.

Allen, P.A., Leather, J., Brasier, M.D., 2004. The Neoproterozoic Fiq glaciation and its aftermath, Huqf supergroup of Oman. Basin Research 16, 507-534.

Bowring, S.A., Grotzinger, J.P., Condon, D.J., Ramezani, J., Newall, M.J., Allen, P.A., 2007. Geochronologic constraints on the chronostratigraphic framework of the Neoproterozoic Huqf Supergroup, Sultanate of Oman. American Journal of Science 307, 1097-1145.

Brasier, M., McCarron, G., Tucker, R., Leather, J., Allen, P., Shields, G., 2000. New U-Pb zircon dates for the Neoproterozoic Ghubrah glaciation and for the top of the Huqf Supergroup, Oman. Geology 28, 175-

178.

Collins, A., Pisarevsky, S., 2005. Amalgamating eastern Gondwana: The evolution of the Circum-Indian Orogens. Earth-Science Reviews 71, 229-270.

Collins, A.S., 2006. Madagascar and the amalgamation of Central Gondwana. Gondwana Research 9, 3-16.

Collins, A.S., Clark, C., Plavsa, D., 2014. Peninsula India in Gondwana: The Tectonothermal Evolution of the Southern Granulite Terrane and its Gondwanan Counterparts. Gondwana Research 25, 190–203.

Collins, A.S., Clark, C., Sajeev, K., Santosh, M., Kelsey, D.E., Hand, M., 2007. Passage Through India: The Mozambique Ocean Suture, High Pressure Granulites and the Palghat-Cauvery Shear System. Terra Nova 19, 141-147.

Collins, A.S., Johnson, S., Fitzsimons, I.C.W., Powell, C.M., Hulscher, B., Abello, J., Razakamanana, T., 2003. Neoproterozoic deformation in central Madagascar: a structural section through part of the East African Orogen, in: Yoshida, M., Windley, B., Dasgupta, S. (Eds.), Proterozoic East Gondwana: Supercontinent Assembly and Breakup. Special Publication of the Geological Society, London, 206, pp. 363-379.

Collins, A.S., Windley, B.F., 2002. The tectonic evolution of central and northern Madagascar and its place in the final assembly of Gondwana. Journal of Geology 110, 325-339.

Cox, G.M., Lewis, C.J., Collins, A.S., Halverson, G.P., Jourdan, F., Foden, J., Nettle, D., Kattan, F., 2012. Ediacaran terrane accretion within the Arabian-Nubian Shield. Gondwana Research 21, 341-352.

Cozzi, A., Rea, G., Craig, J., 2012. From global geology to hydrocarbon exploration: Ediacaran-Early Cambrian petroleum plays of India, Pakistan and Oman. Geological Society, London, Special Publications 366, 131-162.

Davis, J.K., Meert, J.G., Pandit, M.K., 2014. Paleomagnetic analysis of the Marwar Supergroup, Rajasthan, India and proposed interbasinal correlations. Journal of Asian Earth Sciences 91, 339-351.

Denèle, Y., Leroy, S., Pelleter, E., Pik, R., Talbot, J.-Y., Khanbarri, K., 2013. The Cryogenian arc formation and successive high-K calc-alkaline plutons of Socotra Island (Yemen), Lithosphere dynamics and sedimentary basins: The Arabian plate and analogues. Springer, pp. 335-360.

Faryad, S.W., 1999. Metamorphic evolution of the Precambrian South Badakhshan block, based on mineral reactions in metapelites adn metabasites associated with whiteschists from Sare Sang (Western Hindu Kush, Afghanistan). Precambrian Research 98, 223-241.

Faryad, S.W., Collett, S., Finger, F., Sergeev, S.A., opjaková, R., Siman, P., 2016. The Kabul Block (Afghanistan), a segment of the Columbia Supercontinent, with a Neoproterozoic metamorphic overprint. Gondwana Research 34, 221-240.

Fritz, H., Abdelsalam, M., Ali, K.A., Bingen, B., Collins, A.S., Fowler, A.R., Ghebreab, W., Hauzenberger, C.A., Johnson, P.R., Kusky, T.M., Macey, P., Muhongo, S., Stern, R.J., Viola, G., 2013. Orogen styles in the East African Orogen: A review of the Neoproterozoic to Cambrian tectonic evolution. Journal of African Earth Sciences.

Gass, I.G., Ries, A.C., Shackleton, R.M., Smewing, J.D., 1990. Tectonics, geochronology and geochemistry of the Precambrian rocks of Oman, in: Robertson, A.H.F., Searle, M.P., Ries, A.C. (Eds.), The Geology and Tectonics of the Oman Region,

pp. 585-599.

Griffin, W., Pearson, N., Belousova, E., Saeed, A., 2006. Comment: Hf-isotope heterogeneity in zircon 91500. Chemical Geology 233, 358-363.

Griffin, W., Wang, X., Jackson, S., Pearson, N., O'Reilly, S.Y., Xu, X., Zhou, X., 2002. Zircon chemistry and magma mixing, SE China: in-situ analysis of Hf isotopes, Tonglu and Pingtan igneous complexes. Lithos 61, 237-269.

Halpin, J., Clarke, G., White, R., Kelsey, D., 2007. Contrasting P–T–t paths for Neoproterozoic metamorphism in MacRobertson and Kemp Lands, east Antarctica. Journal of Metamorphic Geology 25, 683-701.

Hargrove, U.S., Stern, R.J., Kimura, J.I., Manton, W.I., Johnson, P.R., 2006. How juvenile is the Arabian-Nubian Shield? Evidence from Nd isotopes and pre-Neoproterozoic inherited zircon in the Bi'r Umq suture zone, Saudi Arabia. Earth and Planetary Science Letters 252, 308-326.

Hoffman, P.F., Kaufman, A.J., Halverson, G.P., Schrag, D.P., 1998. A Neoproterozoic Snowball Earth. Science 281, 1342-1346.

Immenhauser, A., Schreurs, G., Gnos, E., Oterdoom, H.W., Hartmann, B., 2000. Late Palaeozoic to Neogene geodynamic evolution of the northeastern Oman margin. Geological Magazine 137, 1-18.

Jackson, S.E., Pearson, N.J., Griffin, W.L., Belousova, E.A., 2004. The application of laser ablation-inductively coupled plasma-mass spectrometry to in-situ U/Pb zircon geochronology. Chemical Geology 211, 47-69.

Johnson, P., Andresen, A., Collins, A.S., Fowler, A., Fritz, H., Ghebreab, W., Kusky, T., Stern, R., 2011. Late Cryogenian–Ediacaran history of the Arabian–Nubian Shield: A review of depositional, plutonic, structural, and tectonic events in the closing stages of the northern East African Orogen. Journal of African Earth Sciences 61, 167-232.

Johnson, P.R., 2014. An Expanding Arabian-Nubian Shield Geochronologic and Isotopic Dataset: Defining Limits and Confirming the Tectonic Setting of a Neoproterozoic Accretionary Orogen. Open Geology Journal 8, 3-33.

Johnson, P.R., Kattan, F.H., 2012. Teh Geology of the Saudi Arabian Shield. Saudi Geological Survey, Jeddah.

Johnson, P.R., Woldehaimanot, B., 2003. Development of the Arabian-Nubian Shield: perspectives on accretion and deformation in the northern East African Orogen and the assembly of Gondwana, in: Yoshida, M., Windley, B.F., Dasgupta, S. (Eds.), Proterozoic East Gondwana: Supercontinent Assembly and Breakup. Geological Society, London, Special Publication 206, pp. 289-325.

Kapp, H., Llewellyn, P., 1965. The geology of the Central Oman Mountains. Report S00005-9, geological group, Petroleum Development Oman Ltd.

Kröner, A., Sassi, F.P., 1996. Evolution of the northern Somali basement: new constraints from zircon ages. Journal of African Earth Sciences 22, 1-15.

Leather, J., Allen, P.A., Brasier, M.D., Cozzi, A., 2002. Neoproterozoic snowball Earth under scrutiny: Evidence from the Fiq glaciation of Oman. Geology 30, 891-894.

Ludwig, K.R., 2009. Isoplot 3.0.

Ludwig, W., Strunk, O., Westram, R., Richter, L., Meier, H., Buchner, A., Lai, T., Steppi, S., Jobb, G., Förster, W., 2004. ARB: a software environment for sequence data. Nucleic acids research 32, 1363-1371.

Malone, S.J., Meert, J.G., Banerjee, D.M., Pandit, M.K., Tamrat, E., Kamenov,

G.D., Pradhan, V.R., Sohl, L.E., 2008. Paleomagnetism and detrital zircon geochronology of the Upper Vindhyan sequence, Son Valley and Rajasthan, India: A ca. 1000 ma closure age for the Purana Basins? Precambrian Research 164, 137-159.

Meert, J.G., Lieberman, B.S., 2008. The Neoproterozoic assembly of Gondwana and its relationship to the Ediacaran–Cambrian radiation. Gondwana Research 14, 5-21.

Meert, J.G., Pandit, M.K., Kamenov, G.D., 2013. Further geochronological and paleomagnetic constraints on Malani (and pre-Malani) magmatism in NW India. Tectonophysics 608, 1254-1267.

Meert, J.G., Pandit, M.K., Pradhan, V.R., Banks, J., Sirianni, R., Stroud, M., Newstead, B., Gifford, J., 2010. Precambrian crustal evolution of Peninsular India: A 3.0 billion year odyssey. Journal of Asian Earth Sciences 39, 483-515.

Mercolli, I., Briner, A.P., Frei, R., Schönberg, R., Nägler, T.F., Kramers, J., Peters, T., 2006. Lithostratigraphy and geochronology of the Neoproterozoic crystalline basement of Salalah, Dhofar, Sultanate of Oman. Precambrian Research 145, 182-206.

Merdith, A.S., Collins, A.S., Williams, S.E., Pisarevsky, S., Foden, J.F., Archibald, D.A., Blades, M.L., Alessio, B.L., Armistead, S., Plavsa, D., Clark, C., D.R, M., 2017. A Full PLate Global Reconstruction of the Neoproterzoic Gondwana Research.

Morag, N., Avigad, D., Gerdes, A., Belousova, E., Harlavan, Y., 2011. Crustal evolution and recycling in the northern Arabian-Nubian Shield: new perspectives from zircon Lu–Hf and U–Pb systematics. Precambrian Research 186, 101-116.

Payne, J.L., Pearson, N.J., Grant, K., Halverson, G.P., 2013. Reassessment of relative oxide formation rates and molecular interferences on in-situ Lutetium-Hafnium analysis with Laser Ablation MC-ICP-MS. . Journal of Analytical Atomic Spectrometry 28, 1068-1079.

Platel, J., Qidwai, H., Khalifa, M., 1987. Geological Map of Marbat (1: 100 000)-Explanatory notes. MOPMR, Sultanate of Oman 60.

Plavsa, D., Collins, A.S., Payne, J.L., Foden, J.D., Clark, C., Santosh, M., 2014. Detrital Zircons in Basement Metasedimentary Protoliths Unveil the Origins of Southern India. Geological Society of America, Bulletin in press.

Pradhan, V.R., Meert, J.G., Pandit, M.K., Kamenova, G., Gregory, L.C., Malone, S.J., 2010. India's changing place in global Proterozoic reconstructions: A review of geochronologic constraints and paleomagnetic poles from the Dharwar, Bundelkhand and Marwar cratons. Journal of Geodynamics 50, 224-242.

Rabu, D., Béchennec, F., Beurrier, M., Hutin, G., 1986. Explanatory notes to the geological map of the Nakhl Quadrangle, Sultanate of Oman. Geoscience map, scale 1.

Rantakokko, N.E., Whitehouse, M.J., Pease, V., Windley, B.F., 2014. Neoproterozoic evolution of the eastern Arabian basement based on a refined geochronology of the Marbat region, Sultanate of Oman. Geological Society, London, Special Publications 392, 107-127.

Raza, M., Khan, A., Bhardwaj, V., Rais, S., 2012. Geochemistry of Mesoproterozoic sedimentary rocks of upper Vindhyan Group, southeastern Rajasthan and implications for weathering history, composition and tectonic setting of continental crust in the northern part of Indian shield. Journal of Asian Earth Sciences 48, 160-172.

Reeves, C., de Wit, M.J., 2000. Making ends

meet in Gondwana: retracing the transforms of the Indian Ocean and reconnecting continental shear zones. Terra Nova 12, 272-280.

Rieu, R., Allen, P.A., Cozzi, A., Kosler, J., Bussy, F., 2007. A composite stratigraphy for the Neoproterozoic Huqf Supergroup of Oman: integrating new litho-, chemo-and chronostratigraphic data of the Mirbat area, southern Oman. Journal of the Geological Society 164, 997-1009.

Robinson, F., Foden, J., Collins, A., 2015. Geochemical and isotopic constraints on island arc, synorogenic, post-orogenic and anorogenic granitoids in the Arabian Shield, Saudi Arabia. Lithos 220, 97-115.

Robinson, F., Foden, J., Collins, A., Payne, J., 2014. Arabian Shield magmatic cycles and their relationship with Gondwana assembly: Insights from zircon U–Pb and Hf isotopes. Earth and Planetary Science Letters 408, 207-225.

Scherer, E., Münker, C., Mezger, K., 2001. Calibration of the lutetium-hafnium clock. Science 293, 683-687.

Schoene, B., 2014. 4.10-U–Th–Pb Geochronology. Treatise on Geochemistry 4, 341-378.

Sláma, J., Kosler, J., Condon, D.J., Crowley, J.L., Gerdes, A., Hanchar, J.M., Horstwood, M.S.A., Morris, G.A., Nasdala, L., Norberg, N., Schaltegger, U., Schoene, B., Tubrett, M.N., Whitehouse, M.J., 2008. Plesovice zircon - A new natural reference material for U-Pb and Hf isotopic microanalysis. . Chemical Geology 249, 1-35.

Stern, R.J., Johnson, P., 2010. Continental lithosphere of the Arabian Plate: a geologic, petrologic, and geophysical synthesis. Earth-Science Reviews 101, 29-67.

Stoeser, D.B., Whitehouse, M.J., Stacey, J.S., 2001a. The Khida Terrane -- Geology of Paleoproterozoic Rocks in the Muhayil

Area, Eastern Arabian Shield, Saudi Arabia. Gondwana Research 4, 192-194.

Stoeser, D.B., Whitehouse, M.J., Stacey, J.S., 2001b. The Khida terrane - Geology of Paleoproterozoic rocks in the Muhayil area, eastern Arabian Shield, Saudi Arabia. Gondwana Research 4, 192-194.

Thomas, R.J., De Waele, B., Schofield, D.I., Goodenough, K.M., Horstwood, M., Tucker, R.D., Bauer, W., Annells, R., Howard, K., Walsh, G., Rabarimanana, M., Rafahatelo, J.-M., Ralison, A.V., Randriamananjara, T., 2009. Geological evolution of the Neoproterozoic Bemarivo Belt, northern Madagascar. Precambrian Research 172, 279-300.

Thomas, R.J., Ellison, R.A., Goodenough, K.M., Roberts, N.M., Allen, P.A., 2015. Salt domes of the UAE and Oman: probing eastern Arabia. Precambrian Research 256, 1-16.

Torsvik, T.H., Ashwal, L.D., Tucker, R.D., Eide, E.A.P.R., 2001. Geochronology and paleomagnetism of the Seychelles microcontinent: The India link. Precambrian Research 110, 47-59.

Tucker, R., 2014. Stratigraphy, sedimentation and age of the upper Cretaceous Winton Formation, central-western Quensland, Australia: implications for regional palaeogeography, palaeoenvironments and Gondwana palaeontology. James Cook University, p. 228.

Tucker, R.D., Ashwal, L.D., Torsvik, T.H., 2001. U-Pb geochronology of Seychelles granitoids: a Neoproterozoic continental arc fragment. Earth and Planetary Science Letters 187, 27-38.

Valley, J., 2003. Oxygen Isotopes in Zircon. Reviews in Mineralogy and Geochemistry 53, 343-385.

Valley, J., Lackey, J., Cavosie, A., Clechenko, C., Spicuzza, M., Basei, M., Bindeman,

I., Ferreira, V., Sial, A., King, E., 2005. 4.4 billion years of crustal maturation: oxygen isotope ratios of magmatic zircon. Contributions to Mineralogy and Petrology 150, 561-580.

Van Achterbergh, E., Ryan, C.G., Jackson, S.E., Griffin, W.L., 2001. Data reduction software for LA-ICP-MS, in: Sylvester, P.J. (Ed.), Laser-ablation-ICPMS in the earth sciences; principles and applications. Mineralogical Association of Canada, Short Course Handbook, Ottowa, pp. 239-243.

Wendt, I., Carl, C., 1991. The statistical distribution of the mean squared weighted deviation. Chemical Geology: Isotope Geoscience Section 86, 275-285.

Whitehouse, M.J., Bridgwater, D., 2001. Geochronological constraints on Paleoproterozoic crustal evolution and regional correlations of the northern Outer Hebridean Lewisian complex, Scotland. Precambrian Research 105, 227-245.

Whitehouse, M.J., Pease, V., Al-Khirbash, S., 2016. Neoproterozoic crustal growth at the margin of the East Gondwana continent– age and isotopic constraints from the easternmost inliers of Oman. International Geology Review 58, 2046-2064.

Whitehouse, M.J., Stoeser, D.B., Stacey, J.S., 2001a. The Khida Terrane -- Geochronological and Isotopic Evidence for Paleoproterozoic and Archean Crust in the Eastern Arabian Shield of Saudi Arabia. Gondwana Research 4, 200-202.

Whitehouse, M.J., Stoeser, D.B., Stacey, J.S., 2001b. The Khida terrane - Geochronological and isotopic evidence for Paleoproterozoic and Archean crust in the eastern Arabian Shield of Saudi Arabia. Gondwana Research 4, 200-202.

Whitehouse, M.J., Windley, B.F., Ba-bttat, M.A.O., Fanning, C.M., Rex, D.C., 1998. Crustal evolution and terrane correlation in the eastern Arabian Shield, Yemen: geochronological constraints. Journal of the Geological Society, London 155, 281-295.

Whitehouse, M.J., Windley, B.F., Stoeser, D.B., Al-Khirbash, S., Ba-Bttat, M.A.O., Haider, A., 2001c. Precambrian basement character of Yemen and correlations with Saudi Arabia and Somalia. Precambrian Research 105, 357-369.

Windley, B.F., Collins, A.S., Kroner, A., Whitehouse, M., 1999. The Neoproterozoic suture zone of Eastern Gondwana from Arabia to Madagscar and india: a transect through the continental crust. Journal of Conference EUG10 4, 104.

Woodhead, J.D., Hergt, J.M., Shelley, M., Eggins, S., Kemp, R., 2004. Zircon Hf-isotope analysis with an Excimer laser, depth profiling, ablation of complex geometries, and concomitant age estimation. . Chemical Geology 209, 121-135.

Worthing, M., 2005. Petrology and geochronology of a Neoproterozoic dyke swarm from Marbat, South Oman. Journal of African Earth Sciences 41, 248-265.

Yeshanew, F.G., Pease, V., Whitehouse, M.J., Al-Khirbash, S., 2015. Zircon U–Pb geochronology and Nd isotope systematics of the Abas terrane, Yemen: Implications for Neoproterozoic crust reworking events. Precambrian Research 267, 106-120.

CHAPTER 7

Discussion and Conclusions

This thesis examines the evolution of terranes within the Arabian Nubian Shield (Fig.1); namely the Western Ethiopian Shield (Chapter 1, 2, 3 and 4), Chad and Sudan (Chapter 5) and Oman (Chapter 6). Zircon isotopic systematics and whole-rock geochemical data are used to characterise the age range and nature of subduction occurring as a result of the closure of the Mozambique Ocean, as India collided with the amalgams of Africa during the Neoproterozoic.

The Western Ethiopian Shield is located in an important position between the predominantly juvenile Arabian Nubian Shield in the north and the southern high-grade Mozambique Belt (Fig. 1). The Western Ethiopian Shield forms one of the largest tracts of exposed outcrop in the northern East African Orogen and data presented in this thesis are used to better elucidate the timing of tectonothermal events throughout the Western Ethiopian Shield and to determine its relationship with the Arabian Nubian Shield. Previously published data show that there were three main phases of magmatism in the Western Ethiopian Shield ca. 850–810 Ma, 780–700 Ma and 620–550 Ma (Ayalew et al., 1990; Ayalew and Peccerillo, 1998; Blades et al., 2015; Kebede et al., 2001a; Kebede et al., 1999; Kebede et al., 2001b). These magmatic pulses have been previously assigned to pre-, syn- and post-tectonic environments respectively (Woldemichael and Kimura, 2008; Woldemichael et al., 2010). Here, data demonstrate that these pre-, syn- and post-tectonic assignments are complicated by metamorphism and deformation occurring at both ca. 810–770 Ma and at ca. 660–655 Ma (Chapter 2b). Notably, the latest Cryogenian phase of magmatism is absent in the Sirkole Domain. Geochemical and isotopic data from igneous rocks of the Western Ethiopian Shield suggest that these are predominantly calc-alkaline sources with characteristics consistent with emplacement within a volcanic or continental arc. Steeper rare earth element (REE) patterns and enrichments of highly incompatible trace elements are also found in subduction-related environments. They show low values of high-field strength elements such as Ti, Zr, Nb and Y that are typical of sub-alkaline, island-arc volcanic rocks. Unusually, some samples are characterised by >56% SiO_2 (75.2–60.00 wt %), > 15% Al_2O_3, < 3%, MgO (0.6–0.12 wt%), low Y (5.5-3.3 ppm) and HREE (for example, Yb < 1.9 ppm), suggesting an adakite-like nature (Chapter 4). High Sr/Y ratios are observed and are commonly interpreted as reflecting melting from the deep lower crustal hot zone, rather than dehydration of the slab. The igneous rocks in the Western Ethiopian Shield have been interpreted to have been formed from the fractional crystallization and assimilation of mantle derived parental magmas. The suites in western Ethiopia contain variable but mostly high $^{143}Nd/^{144}Nd$ signatures, suggesting a juvenile source or the remelting of pre-existing juvenile rocks. However, the high $^{87}Sr/^{86}Sr$ and indicate the hydrothermal alteration of MORB (Chapter 4).

To date, one of the most widely adopted approaches to determine the nature of magmatism is using Sm–Nd whole rock isotope data, however Hf and O isotopes in zircon are increasingly being used as tools to determine the magma sources and the extent of crustal recycling (Hawkesworth and Kemp, 2006). All phases of magmatism in western Ethiopia are shown to be juvenile ($\varepsilon_{Hf}(t)$ values of +4 and +9.7, Chapter 2a and b). Oxygen isotope data in zircons from the Western Ethiopian Shield reflect values between 6.98 and 8.84 ‰ (mantle-derived melts have $\delta^{18}O$ values of 5.3‰ ± 0.6‰; (Valley et al., 2005)
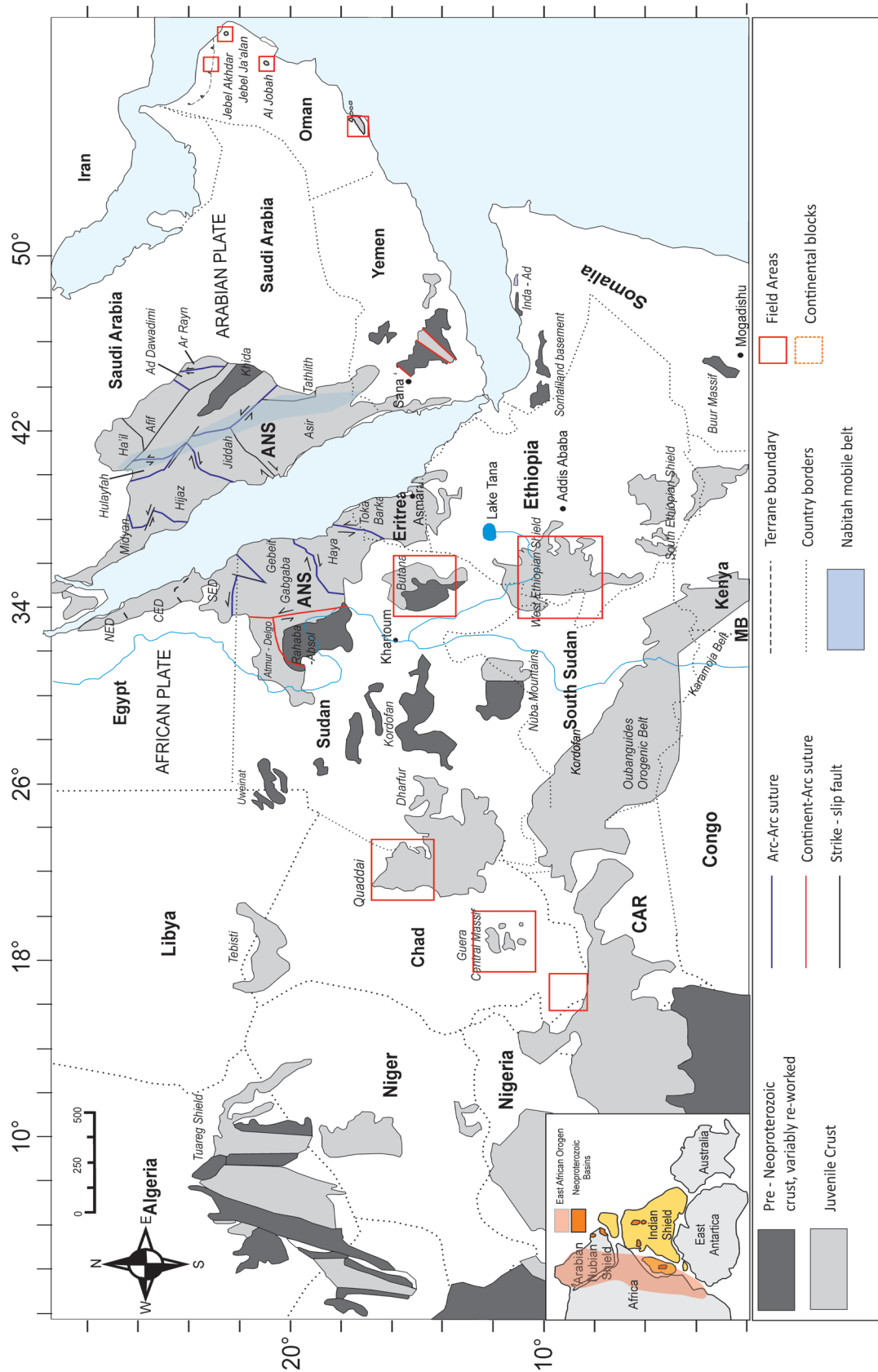
Figure 1: Location map of the Arabian–Nubian Shield (ANS), the red boxes indicate the areas where Neoproterozoic basement samples were taken for this study (adapted from Blades et al. (2015); Johnson et al., (2014) and Abdelsalam et al. (2002).

(Chapter 2b). The data from the Western Ethiopian Shield therefore reflect either a sedimentary component or the incorporation of pre-existing Neoproterozoic crust into the melt. The data collated from the Western Ethiopian Shield, can be compared to available published data from the Arabian Nubian Shield to further elucidate the relationship between the two areas. The Arabian Nubian Shield has been widely accepted over the past decade to be of juvenile character (Johnson, 2014, Morag et al., 2011, Ali et al., 2013, Ali et al., 2014, Robinson et al. 2014, 2015a, 2015b, 2017 and Ali et al., 2015) similar to data collected in this study. Data from the eastern terranes of the Arabian Nubian Shield are defined by juvenile magmas (ε_{Hf}(t) values of +4.5 to +10) regardless of their intrusive ages or spatial relationship (Morag et al., 2011, Ali et al., 2013, Ali et al., 2014, Robinson et al. 2014, 2015a, 2015b, 2017 and Ali et al., 2015).

A significant aspect of the geological evolution of the Western Ethiopian Shield is the recognition of the N–S oriented shear zone, the Baruda-Tulu Dimtu zone, which stretches through Ethiopia and connects with the Barka zone in Eritrea (Braathen et al., 2001; Stern, 1994; Tadesse and Allen, 2004, 2005). These N–S trending structures are also recognised throughout the Arabian Nubian Shield and often interpreted as ophiolite decorated sutures, representing major boundaries that separate arc terranes that accreted during the amalgamation of Gondwana (Stern, 1994; Tadesse and Allen, 2004, 2005). These 'suture zones', however, have been considered to be controversial due to their often disparate history. Ultramafic and mafic plutonic rocks within the Western Ethiopian Shield, where little metamorphism and deformation have occurred, allow for the identification of primary structures (Braathen et al., 2001). These structures do not contradict an oceanic

crust origin of the Western Ethiopian Shield. However, it has also been suggested that there is a lack of geochemical evidence to support the presence of ophiolites in the Western Ethiopian Shield and although the ultramafic complexes are concentrated along the Baruda-Tulu Dimtu shear belt, their existence outside this zone is has been considered problematic for an ophiolite suture model (Braathen et al., 2001). New chrome spinel and olivine data from the Western Ethiopian Shield (Chapter 3) has been combined with previous data to demonstrate that ultramafic rocks of Tulu Dimtu, Daleti and Yubdo are derived from a subduction-related (island-arc) environment, from sources that are enriched in the slab component in the presence of a hydrous melt. The main features of the Western Ethiopian Shield chrome spinels are their high Cr# (from 33 to 99), lower Mg# (0.117 to 0.464) and a trend towards Fe^{3+} rich compositions, which is typical of an arc trend (Chapter 3). These data highlight the variable nature of the ultramafic bodies in western Ethiopia, in particular between Yubdo and Daleti. Fresh olivine chemistry could only be obtained from Yubdo and Daleti, with forsterite contents ranging between Fo_{90}–$Fo_{93.5}$ (Chapter 3). The olivine from Daleti, in comparison to Yubdo, are more magnesium, MnO and CaO poor and extremely high in Ni concentrations. The oxygen fugacity of the peridotites from Yubdo are highly oxidised (FMQ (fayalite–magnetite–quartz) +2.71 − +3.6) from the FMQ buffer and plot in a field of known Alaskan-type intrusions. Yubdo exhibits map features that suggest a concentric nature and together with the chemistry of the spinels, it is proposed that Yubdo represents a solitary intrusion, comparable to other intrusions in the Arabian Nubian Shield (particularly Dahanib Alaskan-type intrusion). The data suggests that Daleti, Tulu Dimtu, Abshala Melange and Yubdo were formed close

to the initiation of supra-subduction and the beginning of known magmatism in the Western Ethiopian Shield. These areas originated as new ocean crust and intrusions formed due to the onset of subduction and were preserved by emplacement in suture zones (Chapter 3).

To the north–west of the Western Ethiopian Shield is the Sahara Metacraton, a piece of pre-Neoproterozoic tract of continental crust that occupies ca. 500,000 km^2 and extends from the Arabian Nubian Shield in the east and to the Tuareg Shield in the west (Abdelsalam et al., 2002). Ages within the Sahara Metacraton range between 2629–1922 Ma (Liégeois et al., 1994; Stern, 1994; Sultan et al., 1994). These are intruded by early Neoproterozoic–late Mesoproterozoic granites (ca. 1000–1100 Ma), that are interpreted here to be related to rifting. These were deformed during the Neoproterozoic and intruded by 600–560 Ma granites, which were formed by the re-melting of Mesoproterozoic terranes (Chapter 5). The data presented in this thesis emphasises the continual remobilisation of the Sahara Metracraton crust. Magmatism in Butana, Sudan, is defined by three main pulses; ca. 987 Ma, 862 Ma and 764 Ma. Accretion of the Butana terrane was initiated at ca. 987 Ma, from a mantle derived source ($\varepsilon_{Hf}(t) = +6.98$ to $+11.25$) with subsequent juvenile magmatism at ca. 864 Ma. The youngest pulse is coeval with metamorphism and Hf isotopes suggest interaction between the juvenile terrane and older reworked continental crust. This is interpreted to reflect over-thrusting of Butana onto the Sahara Metacraton (Chapter 5).

Understanding the assembly of the Arabian Nubian Shield and the relative position of Oman in Gondwana hinges upon the ability to identify terrane boundaries, timing of accretion events and the prior crustal histories of each

terrane (Chapter 6). A number of authors have used geochemistry to interpret the tectonic setting of the igneous and metamorphic basement of Oman and suggest that it formed in an intra-oceanic volcanic-arc setting (Alessio et al., 2017; Bowring et al., 2007; Gass et al., 1990; Mercolli et al., 2006; Rantakokko et al., 2014; Rieu et al., 2007; Whitehouse et al., 2016) within the Neoproterozoic Mozambique Ocean (Allen, 2007; Fritz et al., 2013; Johnson et al., 2011a; Johnson, 2014; Johnson and Woldehaimanot, 2003; Stern and Johnson, 2010). Geochronological data suggests a progressive decrease in the age of arc magmatism from present day east to west, from Jebel Ja'alan to the Huqf and Mirbat. Lutetium–Hafnium and Oxygen isotopes support the progressive development of arc rocks, with a decrease in crustal influence starting from the older eastern exposures ($\delta^{18}O$ (zircon) ‰ average value of 7.57) to the more juvenile exposures in Mirbat ($\varepsilon_{Hf}(t)$ values 10.5–8.72 and $\delta^{18}O$ (zircon) ‰ of 4.3–5.3‰). The cessation of magmatism had occurred by ca. 700 Ma, and this was followed by the deposition of passive margin sequences. This is in contrast to the prolonged period of magmatic and metamorphic events that occur during the growth of the Arabian Nubian Shield (ca. 850–600 Ma). This strongly supports the theory that during the Neoproterozoic, Oman was within its own tectonic domain, rather than an extension of the Arabian Nubian Shield. Detrital zircon (Chapter 6) data shows that the Omani basement was sourcing Palaeoproterozoic–Neoarchaean zircons (Chapter 6). The sources for the Palaeoproterozoic–Neoarchaean zircons can be correlated to the Kabul Block in Afghanistan, with crystallisation ages of 2.5–2.8 Ga and Neoproterozoic overprint. As such, these data are used to interpret the formation of the Omani basement on the margin of Neoproterozoic India, and its outward growth

thereafter. As discussed in Chapter 6, the 'Western Deformation Front' has previously been interpreted to represent a Neoproterozoic suture zone (Allen, 2007) and is supported by seismic wave anisotropy studies (Al-Lazki et al., 2012). The Western Deformation Front lies broadly on strike with the Betsimisaraka Suture Zone of Madagascar (Malagasy Orogeny), which has been interpreted to continue into southern India as the Palghat–Cauvery Suture (Collins et al., 2007; Reeves and de Wit, 2000). This continuation is supported by both these belts preserving Cambrian ages of metamorphism (Collins et al., 2003). Therefore, it is suggested that the northward continuity of the Betsimisaraka Suture zone is represented in Oman by the Western Deformation Front. This Palghat–Betsimisaraka–Western Deformation Front suture would then be the final suture of the Mozambique Ocean (Chapter 6).

How do the terranes of the Arabian Nubian Shield fit into Gondwana?

Recent topological models by Merdith et al. (2017), integrate geological and palaeomagnetic data to create the first full-plate reconstruction model that maps the evolution of tectonic plate configurations during the Neoproterozoic. Here we present a G-plates model, made in collaboration with Andrew Merdith (EarthByte group, University of Sydney), to demonstrate how these data combine to provide information on the evolution of the northern East African Orogen. The model presented in this study is based on the reconstruction proposed by Merdith et al. (2017) and a description of both geological and palaeomagnetic data used to constrain cratonic configurations, positions and motions is provided in Merdith et al. (2017). This new model integrates the terranes of northern Africa using previously published geological data, as well as data presented in this study.

Constraining the location of the plates during the Neoproterozoic is difficult as no in situ ocean crust exists before ca. 200 Ma, so before this time models rely solely on palaeomagnetic data and the geological products of past plate interactions, such as collisional zones (e.g. Himalayas), rifts (e.g. East African Rift) and subduction zones (e.g. Pacific Ring of Fire). In G-Plates, the motion of plates uses a hierarchal system, whereby a series of Euler poles describes each plate moving relative to another (Seton et al., 2012, Merdith et al, 2017). The earlier parts of the model (ca. 1000–700 Ma) have plate motions moving relative to Laurentia (central position in Rodinia), whilst the latter reconstructions (ca. 700–520) move relative to the Congo Craton (Merdith et al., 2017). As a requirement of plate tectonics, oceanic plates (without cratons or terranes) are constructed and assigned arbitrary Plate ID and artificial rotations, to demonstrate the formation of new crust. Their existence is preserved in the products of volcanic arcs at ocean–continent convergent zones.

Below is a brief summary of tectonic and magmatic events within the northern East African Orogen during the Neoproterozoic. These data are used to constrain the accretion of the island arc terranes of the Arabian Nubian Shield within the G-Plates model. However, no palaeomagnetic data exists, making it difficult to constrain the spatial position relative to the Sahara Metacraton and the Congo Craton. Geochronology and geochemistry in the northern extent of the East African Orogen demonstrate that these terranes were formed by a multiphase accretion of a number of crustal blocks.

1000–900 Ma

Early Neoproterozoic subduction follows on from late Mesoproterozoic subduction in west Sudan/Chad (de Wit and Linol, 2015) and
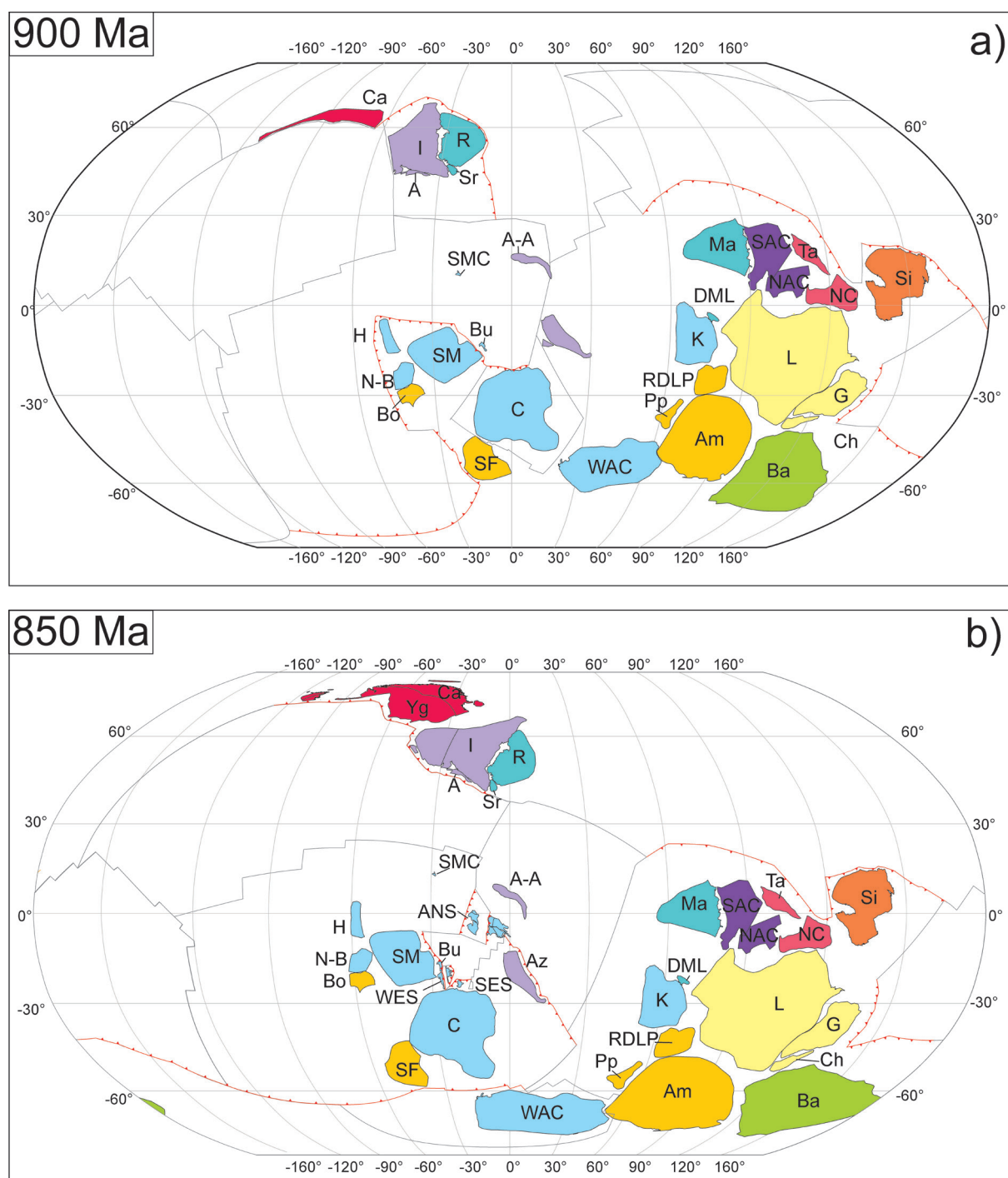
Figure 2: Tectonic geography at (a) 900 Ma and (b) 850 Ma. A-A, Afif-Abas Terrane; Am, Amazonia; Az, Azania; Ba, Baltica; Bo, Borborema; Bu, Butana; Ca, Cathaysia (South China); C, Congo; Ch, Chortis; G, Greenland; H, Hoggar; I, India; K, Kalahari; L, Laurentia; Ma, Mawson; NAC, North Australian Craton; N-B, Nigeria-Benin; NC, North China; Pp, Paranapanema; Ra, Rayner (Antarctica); RDLP, Rio de la Plata; SAC, South Australian Craton; SF, São Francisco; Si, Siberia; SM, Sahara Metacraton; WAC, West African Craton; ANS, Western Ethiopian Shield; SES, Southern Ethiopian Shield; SMC Sa'al Metamorphic Complex; O, Oman; Tr, Tarim. The longitude is arbitrary and unconstrained, and used here as a relative reference. Cratonic crust is coloured by present day geography: North America, yellow; South America, light orange; Baltica, green; Siberia, orange; India and the Middle East, light purple; China, pink; Africa, blue; Australia, dark purple; Antarctica, teal.

Figure 2: Tectonic geography at (a) 750 Ma and (b) 700 Ma. A-A, Afif-Abas Terrane; Am, Amazonia; Az, Azania; Ba, Baltica; Bo, Borborema; Bu, Butana; Ca, Cathaysia (South China); C, Congo; Ch, Chortis; G, Greenland; H, Hoggar; I, India; K, Kalahari; L, Laurentia; Ma, Mawson; NAC, North Australian Craton; N-B, Nigeria-Benin; NC, North China; Pp, Paranapanema; Ra, Rayner (Antarctica); RDLP, Rio de la Plata; SAC, South Australian Craton; SF, São Francisco; Si, Siberia; SM, Sahara Metacraton; WAC, West African Craton; ANS, Western Ethiopian Shield; SES, Southern Ethiopian Shield; SMC Sa'al Metamorphic Complex; O, Oman; Tr, Tarim. The longitude is arbitrary and unconstrained, and used here as a relative reference. Cratonic crust is coloured by present day geography: North America, yellow; South America, light orange; Baltica, green; Siberia, orange; India and the Middle East, light purple; China, pink; Africa, blue; Australia, dark purple; Antarctica, teal.

the Sinai (Fig. 2a Be'eri-Shlevin et al., 2012; Eyal et al., 2014). Late Mesoproterozoic ages (1.03–1.02 Ga) from the Sa'al Metamorphic Complex have been suggested to mark the beginning of magmatism in the northern most (Fig. 2a) Arabian Nubian Shield. Pulses of 920–900 Ma magmatism and amphibolite facies metamorphism are recorded in the Bayuda Block in North Sudan, south of the Keraf Suture (Evuk et al., 2014; Karmakar and Schenk, 2015; Küster et al., 2008). These are followed by juvenile magmatism and amphibolite metamorphism preserved in the terranes of Butana at ca. 987 Ma (Chapter 5) and northern Sudan ca. 920–900 Ma (Be'eri-Shlevin et al., 2012). These terranes have been interpreted to represent island arc terranes and therefore at this time sit adjacent to the Sahara Metacraton, in a westward dipping subduction zone. On the eastern margin of Gondwana, Oman started accreting onto the margin of NW India, which has been previously accepted to have been close to South China (Cawood et al., 2013).

900–830 Ma

Geochemical and isotopic data confirm that crust within the low and high-grade terranes of Eritrea were formed in juvenile oceanic arc systems with crystallisation ages mainly between 850–792 Ma (Andersson et al., 2006). These ages correlate to the onset of juvenile magmatism in western Ethiopia (ca. 854 Ma, Chapter 2a and b) and southern Ethiopia (890–840 Ma). The terranes that form the Arabian Nubian Shield were accreted as a chain of juvenile island arcs and it has been interpreted that the initiation of island arc magmatism (Fig. 2b) occurred in the Gebeit–Haya–Jiddah terranes (correlated within this model; ca. 870–830 Ma). These were interpreted to have been emplaced in the upper plate above the eastward-moving subduction zone formed in the preliminary phase of the

closure of the Mozambique ocean (Cox et al., 2012b; Evuk et al., 2014; Küster and Liégeois, 2001; Merdith et al., 2017; Robinson et al., 2015; Robinson et al., 2014). The Tokar/Barka Terrane consists of the high-grade Barka, Arag and Ghedem terranes that lie either side of the low-grade Hagar, Adhoba–Abi and Nacfa terranes of Eritrea and the Tsaliet Group of northern Ethiopia (Andersson et al., 2006; Avigad et al., 2007). Juvenile arc magmatism occurred between ca. 850–740 Ma (Andersson et al., 2006; Teklay et al., 2003), followed by the deposition of the Tonian-Cryogenian Tsalkiet and Tambien Groups (post ca. 820 Ma; Swanson-Hysell et al. (2015).

750–700 Ma

The amalgamation of the Jiddah–Gebeit and Haya terranes is marked by the Bi'r Umq–Nakasib suture (780–760 Ma). This defines the beginning of the amalgamation of the newly formed terranes (Fig 2c) of the Arabian Nubian Shield (Johnson and Woldehaimanot, 2003). Suturing between the Midyan-Eastern Desert and Hijaz-Gebeit terranes has been previously reported to occur between 740–700 Ma (Johnson, 2014). The timing of the suture has been since further clarified by Robinson et al (2015) at ca. 715 Ma. These sutures have been reported as south-east dipping subduction zones (Fritz et al., 2013; Johnson et al., 2011a; Johnson, 2014). Westward-moving subduction between the Gebeit and Eastern Desert has been suggested in Ali et al. (2009). However, in our model, the Eastern Desert suture has been interpreted to be dipping towards the south-east (Fig. 2c and d). The Karamoja Belt of north-east Uganda is dominated by the Karasuk Supergroup (Vail, 1983; Westerhof et al., 2014), composed of metaigneous rocks that crystallised between ca. 740 Ma and 680 Ma (Mänttäri et al., 2011; Westerhof et al., 2014). Arc magmatism is prevalent further
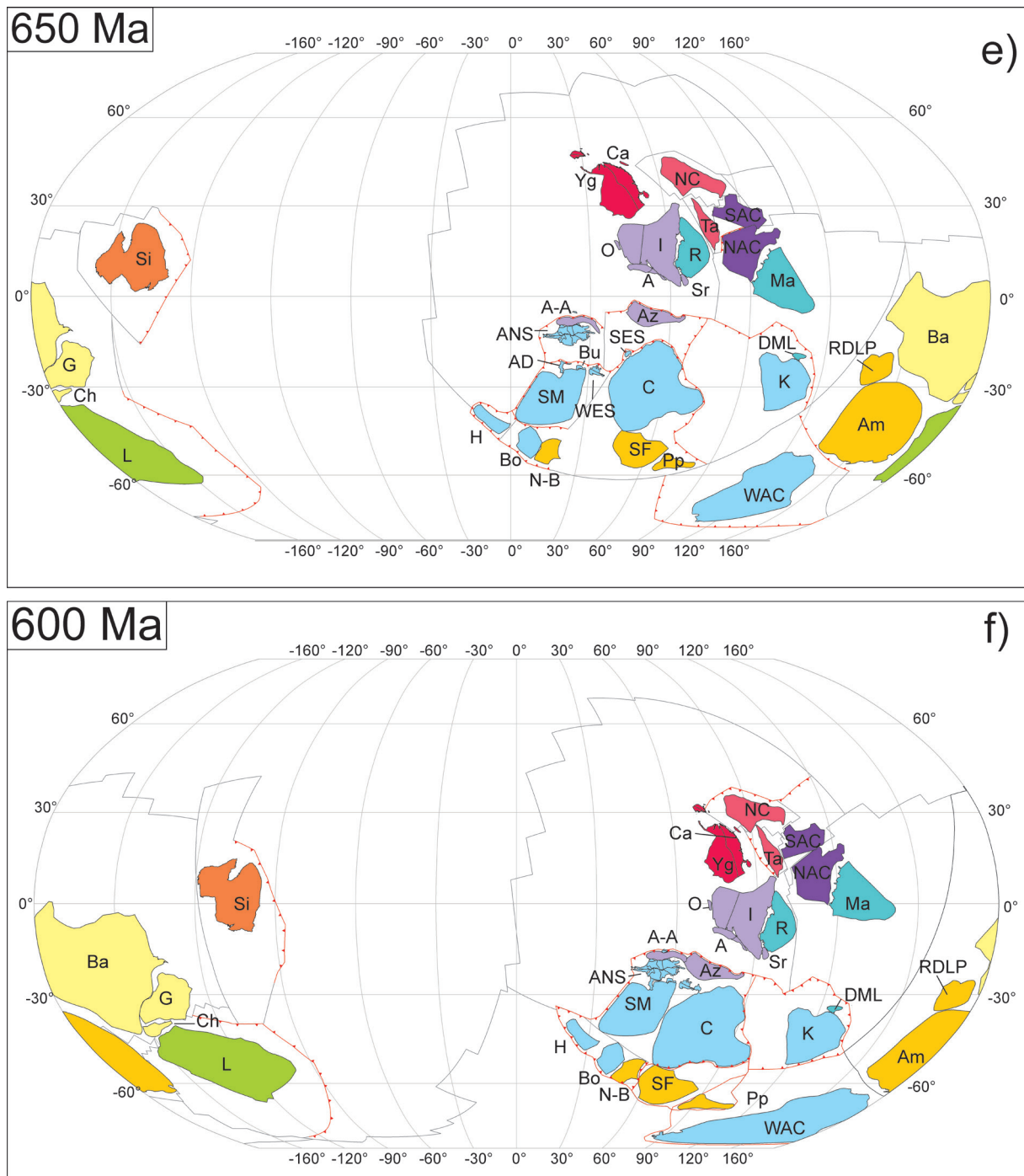
Figure 2: Tectonic geography at (a) 650 Ma and (b) 600 Ma. A-A, Afif-Abas Terrane; Am, Amazonia; Az, Azania; Ba, Baltica; Bo, Borborema; Bu, Butana; Ca, Cathaysia (South China); C, Congo; Ch, Chortis; G, Greenland; H, Hoggar; I, India; K, Kalahari; L, Laurentia; Ma, Mawson; NAC, North Australian Craton; N-B, Nigeria-Benin; NC, North China; Pp, Paranapanema; Ra, Rayner (Antarctica); RDLP, Rio de la Plata; SAC, South Australian Craton; SF, São Francisco; Si, Siberia; SM, Sahara Metacraton; WAC, West African Craton; ANS, Western Ethiopian Shield; SES, Southern Ethiopian Shield; SMC Sa'al Metamorphic Complex; O, Oman; Tr, Tarim. The longitude is arbitrary and unconstrained, and used here as a relative reference. Cratonic crust is coloured by present day geography: North America, yellow; South America, light orange; Baltica, green; Siberia, orange; India and the Middle East, light purple; China, pink; Africa, blue; Australia, dark purple; Antarctica, teal.

north in southern Ethiopia (790–700 Ma) and western Ethiopia (780–700 Ma, Chapter 2a and b) and Butana (ca. 780 Ma, Chapter 5). The magmatism in Butana has a bimodal Hf isotope signature, which suggests the interaction with older reworked continental crust and is therefore interpreted to represent the collision or accretion of Butana onto the Sahara Metacraton (Chapter 5). In Oman (Chapter 6), the cessation of magmatism had occurred by ca. 700 Ma (Fig. 2d), and this was followed by the deposition of passive margin sequences (Alessio et al., 2017; Merdith et al., 2017; Stern and Johnson, 2010).

650–600 Ma

Arc magmatism has been identified within the Eastern Desert, Egypt, and has been interpreted to indicate six pulses of magmatic/metamorphic events (ca. 705–680 Ma, 654 Ma, 630 Ma, 610–604 Ma and 590 Ma; (Augland et al., 2012; Lundmark et al., 2012; Pease et al., 2010; Shalaby et al., 2005)). High-temperature deformation and magmatism occurs at ca. 660 Ma in western Ethiopia, southern Ethiopia (Moyale Event) and eastern Ethiopia (Yeshanew et al., 2016). At this time, the Tokar–Barka Terrane and north-east Uganda have transitioned into post tectonic magmatism with the emplacement of granitoids at ca. 660 Ma and the later Mereb granites (640–600 Ma; (Avigad et al., 2007).

There is a distinct change in orientation from N–S to E–W subduction in the ANS. This change coincides with the southward migration of Neoproterozoic India, with respect to Australia. Subduction within the Arabian Nubian Shield could be interpreted to be the driving force of the migration of India (Fig. 2d and e) from South China (Cawood et al., 2013; Merdith et al., 2017). Collins and Pisarevsky (2005) suggest that ca. 650–640 Ma orogenesis

was a result of the collision of Azania with the Congo Craton (Meert and VanderVoo, 1997; Stern, 1994). Eastward subduction was also occurring under the Afif-Abas, suturing the western arc terranes of the Arabian Nubian Shield (Fig. 6f). The suturing of the youngest arcs occurs (post ca. 680 Ma) on the eastern margin (Ad Dawadimi) of the Afif Terrane (Fig. 6e and f).

600–520 Ma

The final collision between Neoproterozoic India and the Azania/Congo Craton occurred at ca. 570–540 Ma, closing the Mozambique Ocean (Collins and Pisarevsky, 2005). This has been suggested to continue into Palghat–Cauvery Suture of southern India (Collins et al., 2007; Plavsa et al., 2012; Plavsa et al., 2014; Reeves and de Wit, 2000) and northward to form the Western Deformation Front in Oman (Chapter 6). This Palghat–Betsimisaraka–Western Deformation Front suture represents the final suture of the Mozambique Ocean. On the western margin of the Arabian Nubian Shield, the Keraf Suture suggests deformation along the shear zone ends at ca. 580 Ma, with the terranes of the Arabian Nubian Shield amalgamating on the eastern margin of the Sahara Metacraton (Abdelsalam et al., 1998; Merdith et al., 2017). Metamorphic monazite ages from eastern Eritrea constrain the timing of peak collision metamorphism in Eritrea at ca. 590 Ma (Andersson et al 2006). The transition to post-tectonic magmatism within the eastern terranes of the Arabian Nubian Shield begins from 605 Ma (Cox et al., 2012a; Cox et al., 2012b; Doebrich et al., 2007; Doebrich et al., 2004; Johnson, 2014; Johnson et al., 2011b; Robinson et al., 2015; Robinson et al., 2014; Robinson et al., 2017) and in western Ethiopia at ca. 572 Ma (Blades et al., 2015).

Understanding the terranes that make up

northern Africa are critical to understanding the tectonic geography link between the Sahara Metacraton, the Arabian Nubian Shield and Neoproterozoic India. These data provide a comprehensive geochronological and geochemical investigation on basement outcrops in Ethiopia, Sudan, Chad and Oman. Some areas have been the subject of few, or no, modern geochronological studies. These terranes sit within one of the most complicated long-lived accretionary orogens and document the consumption and closure of the Mozambique Ocean. The contribution of these data and the collation of previously published data have allowed for the further development of the palaeogeographic Neoproterozoic model constructed by Merdith et al. (2017) to include the terranes of the Arabian Nubian Shield. Placing all of the terranes of the Arabian Nubian Shield into a tectonic context has not been previously attempted. Geochronology and geochemistry in the northern extent of the East African Orogen demonstrate that these terranes were formed by a multiphase accretion of a number of crustal blocks. The existence of the East African Orogen as a continuous tectonic event has been previously disputed (Collins and Pisarevsky, 2005). The complexity of the East African Orogen, and in particular the northern extent does not reflect a simple Wilson cycle of oceanic opening and closing, but instead reflects more than 400 Ma of subduction accretion.

REFERENCES

Abdelsalam, M.G., Liégeois, J.P., Stern, R.J., 2002. The Saharan Metacraton. Journal of African Earth Sciences 34, 119-136.

Abdelsalam, M.G., Stern, R.J., Copeland, P., El-Faki, E.-F.M., Al-Hur, B., Ibrahim, F.M., 1998. The Neoproterozoic Keraf Suture in NE Sudan: sinistral transpression along the eastern margin of West Gondwana. Journal of Geology 106, 133-147.

Al-Lazki, A., Ebinger, C., Kendall, M., Helffrich, G., Leroy, S., Tiberi, C., Stuart, G., Al-Toobi, K., 2012. Upper mantle anisotropy of southeast Arabia passive margin [Gulf of Aden northern conjugate margin], Oman. Arabian Journal of Geosciences 5, 925-934.

Alessio, B.L., Blades, M.L., Murray, G., Thorpe, B., Collins, A.S., Kelsey, D.E., Foden, J.F., Payne, J.L., Al-Khirbash, S., Jourdan, F., 2017. Origin and tectonic evolution of the NE basement of Oman: a window into the Neoproterozoic accretionary growth of India? Geological Magazine, 1-25.

Ali, K.A., Stern, R.J., Manton, W.I., Kimura, J.-I., Khamees, H.A., 2009. Geochemistry, Nd isotopes and U–Pb SHRIMP zircon dating of Neoproterozoic volcanic rocks from the Central Eastern Desert of Egypt: New insights into the 750Ma crust-forming event. Precambrian Research 171, 1-22.

Allen, P.A., 2007. The Huqf Supergroup of Oman: Basin development and context for Neoproterozoic glaciation. Earth Science Reviews 84, 139-185.

Andersson, U.B., Ghebreab, W., Teklay, M., 2006. Crustal evolution and metamorphism in east-central Eritrea, south-east Arabian-Nubian Shield. Journal of African Earth Sciences 44, 45-65.

Augland, L.E., Andresen, A., Boghdady, G.Y., 2012. U–Pb ID-TIMS dating of igneous and metaigneous rocks from the El-Sibai area: time constraints on the tectonic evolution of the Central Eastern Desert, Egypt. International Journal of Earth Sciences 101, 25-37.

Avigad, D., Stern, R., Beyth, M., Miller, N., McWilliams, M., 2007. Detrital zircon U–Pb geochronology of Cryogenian diamictites and Lower Paleozoic sandstone in Ethiopia (Tigrai): age constraints on Neoproterozoic glaciation and crustal

evolution of the southern Arabian–Nubian Shield. Precambrian Research 154, 88-106.

Ayalew, T., Bell, K., Moore, J.M., Parrish, R.R., 1990. U-Pb and Rb-Sr geochronology of the western Ethiopian shield. Geological Society of America Bulletin 102, 1309-1316.

Ayalew, T., Peccerillo, A., 1998. Petrology and geochemistry of the Gore-Gambella plutonic rocks: implications for magma genesis and the tectonic setting of the Pan-African Orogenic Belt of western Ethiopia. Journal of African Earth Sciences 27, 397-416.

Be'eri-Shlevin, Y., Eyal, M., Eyal, Y., Whitehouse, M.J., Litvinovsky, B., 2012. The Sa'al volcano-sedimentary complex (Sinai, Egypt): A latest Mesoproterozoic volcanic arc in the northern Arabian Nubian Shield. Geology 40, 403-406.

Blades, M.L., Collins, A.S., Foden, J., Payne, J.L., Xu, X., Alemu, T., Woldetinsae, G., Clark, C., Taylor, R.J., 2015. Age and hafnium isotopic evolution of the Didesa and Kemashi Domains, western Ethiopia. Precambrian Research 270, 267-284.

Bowring, S.A., Grotzinger, J.P., Condon, D.J., Ramezani, J., Newall, M.J., Allen, P.A., 2007. Geochronologic constraints on the chronostratigraphic framework of the Neoproterozoic Huqf Supergroup, Sultanate of Oman. American Journal of Science 307, 1097-1145.

Braathen, A., Grenne, T., Selassie, M., Worku, T., 2001. Juxtaposition of Neoproterozoic units along the Baruda–Tulu Dimtu shear-belt in the East African Orogen of western Ethiopia. Precambrian Research 107, 215-234.

Cawood, P.A., Wang, Y., Xu, Y., Zhao, G., 2013. Locating South China in Rodinia and Gondwana: A fragment of greater India lithosphere? Geology 41, 903-906.

Collins, A., Pisarevsky, S., 2005. Amalgamating eastern Gondwana: The evolution of the Circum-Indian Orogens. Earth-Science Reviews 71, 229-270.

Collins, A.S., Clark, C., Sajeev, K., Santosh, M., Kelsey, D.E., Hand, M., 2007. Passage Through India: The Mozambique Ocean Suture, High Pressure Granulites and the Palghat-Cauvery Shear System. Terra Nova 19, 141-147.

Collins, A.S., Johnson, S., Fitzsimons, I.C.W., Powell, C.M., Hulscher, B., Abello, J., Razakamanana, T., 2003. Neoproterozoic deformation in central Madagascar: a structural section through part of the East African Orogen, in: Yoshida, M., Windley, B., Dasgupta, S. (Eds.), Proterozoic East Gondwana: Supercontinent Assembly and Breakup. Special Publication of the Geological Society, London, 206, pp. 363-379.

Cox, G.M., Lewis, C.J., Collins, A.S., Halverson, G.P., Jourdan, F., Foden, J., Nettle, D., Kattan, F., 2012a. Ediacaran Terrane Accretion in the Arabian-Nubian Shield. Gondwana Research 21, 341-352.

Cox, G.M., Lewis, C.J., Collins, A.S., Halverson, G.P., Jourdan, F., Foden, J., Nettle, D., Kattan, F., 2012b. Ediacaran terrane accretion within the Arabian-Nubian Shield. Gondwana Research 21, 341-352.

Doebrich, J.L., Al-Jehani, A.M., Siddiqui, A.A., Hayes, T.S., Wooden, J.L., Johnson, P.R., 2007. Geology and metalogeny of the Ar Rayn terrane, eastern Arabian shield: Evolution of a Neoproterozoic continental-margin arc during assembly of Gondwana within the East African orogen. Precambrian Research 158, 17-50.

Doebrich, J.L., Zahony, S.G., Leavitt, J.D., Portacio, J.S., Siddiqui, A.A., Wooden, J.L., Fleck, R.J., Stein, H.J., 2004. Ad Duwayhi, Saudi Arabia: geology and geochronology

of a Neoproterozoic intrusion-related gold system in the Arabian Shield. Economic Geology 99, 713-741.

Evuk, D., Franz, G., Frei, D., Lucassen, F., 2014. The Neoproterozoic evolution of the central-eastern Bayuda Desert (Sudan). Precambrian Research 240, 108-125.

Fritz, H., Abdelsalam, M., Ali, K.A., Bingen, B., Collins, A.S., Fowler, A.R., Ghebreab, W., Hauzenberger, C.A., Johnson, P.R., Kusky, T.M., Macey, P., Muhongo, S., Stern, R.J., Viola, G., 2013. Orogen styles in the East African Orogen: A review of the Neoproterozoic to Cambrian tectonic evolution. Journal of African Earth Sciences.

Gass, I.G., Ries, A.C., Shackleton, R.M., Smewing, J.D., 1990. Tectonics, geochronology and geochemistry of the Precambrian rocks of Oman, in: Robertson, A.H.F., Searle, M.P., Ries, A.C. (Eds.), The Geology and Tectonics of the Oman Region, pp. 585-599.

Hawkesworth, C.J., Kemp, A.I.S., 2006. Using hafnium and oxygen isotopes in zircons to unravel the record of crustal evolution. Chemical Geology 226, 144-162.

Johnson, P., Andresen, A., Collins, A.S., Fowler, A., Fritz, H., Ghebreab, W., Kusky, T., Stern, R., 2011a. Late Cryogenian–Ediacaran history of the Arabian–Nubian Shield: A review of depositional, plutonic, structural, and tectonic events in the closing stages of the northern East African Orogen. Journal of African Earth Sciences 61, 167-232.

Johnson, P.R., 2014. An Expanding Arabian-Nubian Shield Geochronologic and Isotopic Dataset: Defining Limits and Confirming the Tectonic Setting of a Neoproterozoic Accretionary Orogen. Open Geology Journal 8, 3-33.

Johnson, P.R., Andresen, A., Collins, A.S., Fowler, A.R., Fritz, H., Ghebreab, W., Kusky,

T., Stern, R.J., 2011b. Late Cryogenian-Ediacaran history of the Arabian-Nubian Shield: A review of depositional, plutonic, structural, and tectonic events in the closing stages of the northern East African Orogen. Journal of African Earth Sciences 61, 167-232.

Johnson, P.R., Woldehaimanot, B., 2003. Development of the Arabian-Nubian Shield: perspectives on accretion and deformation in the northern East African Orogen and the assembly of Gondwana, in: Yoshida, M., Windley, B.F., Dasgupta, S. (Eds.), Proterozoic East Gondwana: Supercontinent Assembly and Breakup. Geological Society, London, Special Publication 206, pp. 289-325.

Kebede, T., Kloetzli, U., Koeberl, C., 2001a. U/Pb and Pb/Pb zircon ages from granitoid rocks of Wallagga area: constraints on magmatic and tectonic evolution of Precambrian rocks of western Ethiopia. Mineralogy and Petrology 71, 251-271.

Kebede, T., Koeberl, C., Koller, F., 1999. Geology, geochemistry and petrogenesis of intrusive rocks of the Wallagga area, western Ethiopia. Journal of African Earth Sciences 29, 715-734.

Kebede, T., Koeberl, C., Koller, F., 2001b. Magmatic evolution of the Suqii-Wagga garnet-bearing two-mica granite, Wallagga area, western Ethiopia. Journal of African Earth Sciences 32, 193-221.

Küster, D., Liégeois, 2001. Sr, Nd isotopes and geochemistry of the Bayuda Desert high-grade metamorphic basement (Sudan): an early Pan-African oceanic convergent margin, not the edge of the East Saharan ghost craton? Precambrian Research 109, 1-23.

Liégeois, J.-P., Black, R., Navez, J., Latouche, L., 1994. Early and late Pan-African orogenies in the Air assembly of terranes

(Tuareg Shield, Niger). Precambrian research 67, 59-88.

Lundmark, A.M., Andresen, A., Hassan, M.A., Augland, L.E., Boghdady, G.Y., 2012. Repeated magmatic pulses in the East African Orogen in the Eastern Desert, Egypt: an old idea supported by new evidence. Gondwana Research 22, 227-237.

Mänttäri, I., Kigereigu, F., Huhma, H., De Kock, G., Koistinen, T., Kuosmanen, E., Lahaye, Y., Lehtonen, M., Mäkitie, H., Manninen, T., 2011. New Precambrian rock ages from Uganda, 23rd Colloquium of African Geology (CAG23), University of Johannesburg, Republic of South Africa, Abstract Volume, p. 260.

Meert, J.G., VanderVoo, R., 1997. The assembly of Gondwana 800-550 Ma. Journal of Geodynamics 23, 223-235.

Mercolli, I., Briner, A.P., Frei, R., Schönberg, R., Nägler, T.F., Kramers, J., Peters, T., 2006. Lithostratigraphy and geochronology of the Neoproterozoic crystalline basement of Salalah, Dhofar, Sultanate of Oman. Precambrian Research 145, 182-206.

Merdith, A.S., Collins, A.S., Williams, S.E., Pisarevsky, S., Foden, J.F., Archibald, D.A., Blades, M.L., Alessio, B.L., Armistead, S., Plavsa, D., Clark, C., D.R, M., 2017. A Full PLate Global Reconstruction of the Neoproterzoic Gondwana Research.

Pease, V., Shalaby, E., Axelsson, E., Whitehouse, M., Om, M., 2010. Neoproterozoic Wadi Nabi intrusive complex, Central Eastern Desert. Saudi Geological Survey, Technical Report SGS-TR-2010 2, 56-60.

Plavsa, D., Collins, A.S., Foden, J.F., Kropinski, L., Santosh, M., Chetty, T.R.K., Clark, C., 2012. Delineating crustal domains in Peninsular India: Age and chemistry of orthopyroxene-bearing felsic gneisses in the Madurai Block. Precambrian Research 198, 77-93.

Plavsa, D., Collins, A.S., Payne, J.L., Foden, J.D., Clark, C., Santosh, M., 2014. Detrital Zircons in Basement Metasedimentary Protoliths Unveil the Origins of Southern India. Geological Society of America, Bulletin in press.

Rantakokko, N.E., Whitehouse, M.J., Pease, V., Windley, B.F., 2014. Neoproterozoic evolution of the eastern Arabian basement based on a refined geochronology of the Marbat region, Sultanate of Oman. Geological Society, London, Special Publications 392, 107-127.

Reeves, C., de Wit, M.J., 2000. Making ends meet in Gondwana: retracing the transforms of the Indian Ocean and reconnecting continental shear zones. Terra Nova 12, 272-280.

Rieu, R., Allen, P.A., Cozzi, A., Kosler, J., Bussy, F., 2007. A composite stratigraphy for the Neoproterozoic Huqf Supergroup of Oman: integrating new litho-, chemo-and chronostratigraphic data of the Mirbat area, southern Oman. Journal of the Geological Society 164, 997-1009.

Robinson, F., Foden, J., Collins, A., 2015. Geochemical and isotopic constraints on island arc, synorogenic, post-orogenic and anorogenic granitoids in the Arabian Shield, Saudi Arabia. Lithos 220, 97-115.

Robinson, F., Foden, J., Collins, A., Payne, J., 2014. Arabian Shield magmatic cycles and their relationship with Gondwana assembly: Insights from zircon U–Pb and Hf isotopes. Earth and Planetary Science Letters 408, 207-225.

Robinson, F.A., Bonin, B., Pease, V., Anderson, J., 2017. A discussion on the tectonic implications of Ediacaran late to post-orogenic A-type granite in the northeastern Arabian Shield, Saudi Arabia. Tectonics 36, 582-600.

Shalaby, A., Stüwe, K., Makroum, F., Fritz,

H., Kebede, T., Klötzli, U., 2005. The Wadi Mubarak belt, Eastern Desert of Egypt: a Neoproterozoic conjugate shear system in the Arabian–Nubian Shield. Precambrian Research 136, 27-50.

Stern, R.J., 1994. Arc-assembly and continental collision in the Neoproterozoic African orogen: implications for the consolidation of Gondwanaland. Annual Review of Earth and Planetary Sciences 22, 319-351.

Stern, R.J., Johnson, P., 2010. Continental lithosphere of the Arabian Plate: a geologic, petrologic, and geophysical synthesis. Earth-Science Reviews 101, 29-67.

Sultan, M., Tucker, R., El Alfy, Z., Attia, R., Ragab, A.G., 1994. U-Pb (zircon) ages for the gneissic terrane west of the Nile, southern Egypt. Geologische Rundschau 83, 514-522.

Swanson-Hysell, N.L., Maloof, A.C., Condon, D.J., Jenkin, G.R., Alene, M., Tremblay, M.M., Tesema, T., Rooney, A.D., Haileab, B., 2015. Stratigraphy and geochronology of the Tambien Group, Ethiopia: Evidence for globally synchronous carbon isotope change in the Neoproterozoic. Geology 43, 323-326.

Tadesse, G., Allen, A., 2004. Geochemistry of metavolcanics from the Neoproterozoic Tuludimtu orogenic belt, Western Ethiopia. Journal of African Earth Sciences 39, 177-185.

Tadesse, G., Allen, A., 2005. Geology and geochemistry of the Neoproterozoic Tuludimtu Ophiolite suite, western Ethiopia. Journal of African Earth Sciences 41, 192-211.

Teklay, M., Haile, T., Kröner, A., Asmerom, Y., Watson, J., 2003. A back-arc palaeotectonic setting for the Augaro Neoproterozoic magmatic rocks of western Eritrea. Gondwana Research 6, 629-640.

Vail, J.R., 1983. Pan-African crustal accretion in north-east Africa. Journal of African Earth Sciences (1983) 1, 285-294.

Westerhof, A., Haermae, P., Isabirye, E., Katto, E., Koistinen, T., Kuosmanen, E., Lehto, T., Lehtonen, M., Maekitie, H., Manninen, T., 2014. Geology and geodynamic development of Uganda with explanation of the 1: 1,000,000: scale geological map. Geol Surv Finland, Special Paper 55.

Whitehouse, M.J., Pease, V., Al-Khirbash, S., 2016. Neoproterozoic crustal growth at the margin of the East Gondwana continent–age and isotopic constraints from the easternmost inliers of Oman. International Geology Review 58, 2046-2064.

Woldemichael, B.W., Kimura, J.-I., 2008. Petrogenesis of the Neoproterozoic Bikilal-Ghimbi gabbro, Western Ethiopia. Journal of mineralogical and petrological sciences 103, 23-46.

Woldemichael, B.W., Kimura, J.-I., Dunkley, D.J., Tani, K., Ohira, H., 2010. SHRIMP U–Pb zircon geochronology and Sr–Nd isotopic systematic of the Neoproterozoic Ghimbi-Nedjo mafic to intermediate intrusions of Western Ethiopia: a record of passive margin magmatism at 855 Ma? International Journal of Earth Sciences 99, 1773-1790.

Yeshanew, F.G., Pease, V., Abdelsalam, M.G., Whitehouse, M.J., 2016. Zircon U–Pb ages, [18]O and whole-rock Nd isotopic compositions of the Dire Dawa Precambrian basement, eastern Ethiopia: implications for the assembly of Gondwana. Journal of the Geological Society, jgs2016-2017.

APPENDIX 2.1

Supplementary data for chapter 2:
Age and hafnium isotopic evolution of the Didesa and Kemashi Domains, western Ethiopia.

Table 1: SHRIMP U-Pb data from Western Ethiopia.

Appendix 2.1: Age and hafnium isotopic evolution of the Didesa and Kemashi Domains, western Ethiopia.-

Spot Name	U ppm	Th ppm	4-corr Pb^{206} com (%)	^{232}Th /^{238}U	4corr 238 /206*	% err	4corr 207* /206*	% err	4corr 207* /235	% err	4corr 206* /238	% err	Disc (%)	204corr ^{206}Pb /^{238}U Age (Ma)	1s err	204corr ^{207}Pb /^{206}Pb Age	1s err
K-spar rich granite																	
001-2.1	1519	679	0.44	0.46	12.83	1.56	0.06	2.85	0.68	3.24	0.08	1.6	+35	483.8	7.2	727.2	60.4
001-3.1	2867	1389	0.09	0.50	9.39	1.54	0.06	0.40	0.90	1.59	0.11	1.5	-1	652.3	9.6	647.0	8.6
001-4.1	123	65	0.25	0.54	7.60	1.87	0.06	2.19	1.17	2.88	0.13	1.9	-7	796.8	14.0	749.8	46.3
001-5.1	491	479	1.41	1.01	8.73	1.62	0.07	4.01	1.10	4.32	0.11	1.6	+25	699.4	10.8	914.7	82.4
001-6.1	2732	1946	1.37	0.74	18.16	1.54	0.06	1.38	0.45	2.07	0.06	1.5	+43	345.6	5.2	591.0	29.8
001-8.1	3837	2216	0.21	0.60	9.20	1.54	0.06	0.58	0.92	1.65	0.11	1.5	-0	665.0	9.7	664.8	12.5
001-9.1	230	81	0.75	0.36	7.96	1.71	0.06	2.40	1.12	2.95	0.13	1.7	+1	762.7	12.3	768.3	50.5
001-10.1	2231	874	0.27	0.40	9.27	3.15	0.06	2.09	0.94	3.78	0.11	3.1	+7	660.2	19.8	708.3	44.4
001-12.1	2289	1683	3.43	0.76	17.51	1.65	0.06	8.26	0.46	8.42	0.06	1.7	+34	358.1	5.8	536.1	180.7
001-13.1	2336	364	0.43	0.16	10.09	1.54	0.06	0.70	0.85	1.70	0.10	1.5	+10	609.4	9.0	673.4	15.0
001-14.1	636	253	18.65	0.41	15.73	1.75	0.07	9.19	0.58	9.36	0.06	1.7	+53	397.4	6.7	824.8	191.8
001-15.1	147	82	0.62	0.58	7.59	1.82	0.06	3.03	1.08	3.53	0.13	1.8	-38	797.6	13.6	587.6	65.6
001-17.1	3783	2356	0.28	0.64	9.65	1.54	0.06	1.62	0.88	2.23	0.10	1.5	+5	635.5	9.3	670.4	34.7
001-19.1	115	66	0.08	0.60	9.35	1.87	0.06	1.92	0.92	2.68	0.11	1.9	+5	654.9	11.6	688.4	40.9
001-20.1	54	23	-0.69	0.44	7.95	2.24	0.07	4.13	1.24	4.70	0.13	2.2	+22	763.6	16.2	966.1	84.3
001-21.1	168	20	2.02	0.12	9.58	1.90	0.06	5.88	0.90	6.18	0.10	1.9	+7	639.9	11.6	683.5	125.6
001-21.2	3746	1499	0.13	0.41	9.06	1.54	0.06	0.45	0.95	1.61	0.11	1.5	+1	675.0	9.9	680.9	9.7
001-22.1	3593	1164	1.61	0.33	11.38	1.96	0.06	1.29	0.73	2.35	0.09	2.0	+13	542.7	10.2	622.7	27.9
001-22.2	109	43	0.46	0.40	7.81	2.00	0.07	3.06	1.21	3.65	0.13	2.0	+13	776.6	14.7	889.1	63.1
001-23.1	377	169	0.26	0.46	9.46	1.71	0.06	1.81	0.87	2.49	0.11	1.7	-8	647.6	10.5	604.3	39.2

4 - corr = 204 corrected

Table 1: SHRIMP U-Pb data from Western Ethiopia.

Spot Name	U ppm	Th ppm	4-corr Pb 206 com (%)	232Th /238U	4corr 238 /206*	% err	4corr 207* /206*	% err	4corr 207* /235	% err	4corr 206* /238	% err	Disc (%)	204corr 206Pb /238U Age (Ma)	1s err	204corr 207Pb /206Pb Age	1s err
Foliated Gneiss																	
003-1.1	1949	673	1.15	0.36	11.34	1.56	0.063	1.32	0.77	2.04	0.088	1.556	+26	545.0	8.1	722.5	28.1
003-2.1	276	182	0.40	0.68	7.46	1.72	0.067	1.77	1.24	2.47	0.134	1.722	+5	811.3	13.1	847.5	36.9
003-3.1	1080	641	16.83	0.61	14.86	1.66	0.071	6.43	0.66	6.64	0.067	1.660	+57	419.7	6.7	947.3	131.7
003-4.1	258	194	1.37	0.78	10.60	1.74	0.065	3.54	0.85	3.94	0.094	1.740	+27	581.3	9.7	781.6	74.3
003-5.1	323	19	0.52	0.06	8.35	1.70	0.062	2.03	1.03	2.65	0.120	1.703	-6	729.0	11.7	689.5	43.4
003-6.1	509	327	4.03	0.66	9.15	1.66	0.067	4.18	1.01	4.50	0.109	1.664	+22	668.6	10.6	843.5	86.9
003-6.2	5486	3371	20.19	0.63	16.84	4.93	0.072	42.28	0.59	42.57	0.059	4.926	+64	372.0	17.8	993.6	859.5
003-7.1	423	116	0.51	0.28	9.17	1.67	0.063	1.83	0.95	2.47	0.109	1.665	+8	667.0	10.6	724.8	38.8
003-8.1	1365	22	0.20	0.02	9.14	1.57	0.061	0.79	0.92	1.76	0.109	1.569	-5	669.4	10.0	640.4	17.0
003-8.2	227	129	0.05	0.59	8.04	1.78	0.066	1.41	1.13	2.27	0.124	1.783	+7	755.6	12.7	806.7	29.4
003-9.1	232	183	0.83	0.81	7.58	1.77	0.062	2.92	1.12	3.41	0.132	1.770	-22	798.9	13.3	663.8	62.5
003-10.1	375	333	0.81	0.92	7.80	1.70	0.065	2.38	1.16	2.93	0.128	1.700	+1	778.0	12.5	787.1	50.0
003-10.2	322	285	-0.06	0.91	7.45	1.70	0.069	1.09	1.27	2.03	0.134	1.705	+9	811.6	13.0	883.8	22.6
003-11.1	175	91	2.25	0.53	9.28	1.90	0.065	10.28	0.96	10.45	0.108	1.897	+14	659.5	11.9	763.7	216.6
003-12.1	240	162	0.00	0.70	7.79	1.76	0.066	1.18	1.17	2.12	0.128	1.764	+3	778.8	12.9	803.8	24.8
003-12.2	144	67	0.08	0.48	8.19	1.94	0.066	1.95	1.12	2.75	0.122	1.938	+10	742.4	13.6	817.6	40.7
003-13.1	91	48	1.01	0.55	9.54	2.15	0.057	6.03	0.83	6.40	0.105	2.153	-31	642.5	13.2	495.4	132.8
003-14.1	3284	1422	0.24	0.45	9.39	1.55	0.062	1.49	0.91	2.14	0.107	1.547	+4	652.5	9.6	675.6	31.8
003-15.1	222	217	0.23	1.01	8.08	1.78	0.065	1.85	1.10	2.57	0.124	1.784	+2	751.8	12.7	765.5	39.0
003-16.1	153	70	0.48	0.47	9.94	1.94	0.060	3.51	0.83	4.01	0.101	1.939	-4	618.1	11.4	595.9	76.1
003-17.1	1903	1183	0.09	0.64	9.23	1.56	0.062	0.57	0.93	1.66	0.108	1.559	+2	662.9	9.8	677.8	12.2
003-18.1	3580	1927	9.84	0.56	25.78	2.44	0.058	27.29	0.31	27.40	0.039	2.438	+56	245.4	5.9	545.8	596.3
003-19.1	466	54	0.91	0.12	19.29	1.68	0.063	3.34	0.45	3.74	0.052	1.682	+56	325.8	5.3	711.5	70.9
003-20.1	523	981	4.27	1.94	9.73	1.66	0.070	4.26	0.99	4.57	0.103	1.662	+34	630.9	10.0	930.5	87.4
003-20.2	923	50	0.21	0.06	8.07	1.60	0.064	0.96	1.10	1.87	0.124	1.601	-1	753.4	11.4	745.1	20.4
003-21.1	571	256	1.15	0.46	9.44	1.64	0.060	2.58	0.87	3.06	0.106	1.642	-10	649.3	10.1	594.8	55.9
003-22.1	625	342	4.75	0.57	8.86	2.09	0.068	15.99	1.06	16.13	0.113	2.087	+22	689.0	13.6	869.6	331.4

4 - corr = 204 corrected

Table 1: SHRIMP U-Pb data from western Ethiopia.

Spot Name	U ppm	Th ppm	4-corr Pb²⁰⁶com (%)	²³²Th /²³⁸U	4corr 238 /206*	% err	4corr 207* /206*	% err	4corr 207* /235	% err	4corr 206* /238	% err	Disc (%)	204corr ²⁰⁶Pb /²³⁸U Age (Ma)	1s err	204corr ²⁰⁷Pb /²⁰⁶Pb Age	1s err
Hornblende, biottite gneiss																	
007-1.1	146	38	0.33	0.27	7.43	1.97	0.07	2.59	1.27	3.25	0.13	1.97	+9	814.1	15.0	886.4	53.5
007-1.2	146	52	0.81	0.37	7.86	2.02	0.06	9.34	1.13	9.56	0.13	2.02	-3	771.9	14.7	751.3	197.3
007-2.1	302	111	0.15	0.38	7.08	1.76	0.07	1.43	1.31	2.26	0.14	1.76	-0	852.0	14.0	849.8	29.6
007-3.1	91	19	0.53	0.22	7.89	2.22	0.07	3.94	1.18	4.52	0.13	2.22	+10	768.9	16.1	849.3	81.9
007-4.1	231	101	0.33	0.45	7.23	1.82	0.07	2.05	1.25	2.74	0.14	1.82	-5	834.7	14.2	797.6	43.0
007-5.1	284	158	0.23	0.58	7.09	1.77	0.07	1.66	1.30	2.42	0.14	1.77	-2	850.3	14.1	834.4	34.5
007-5.2	148	35	1.78	0.24	7.71	2.15	0.06	6.70	1.09	7.04	0.13	2.15	-25	786.5	15.9	636.1	144.3
007-6.1	457	404	0.24	0.91	7.01	1.68	0.07	1.31	1.30	2.13	0.14	1.68	-6	860.0	13.6	813.0	27.3
007-7.1	333	153	0.03	0.47	7.21	1.73	0.07	4.19	1.30	4.53	0.14	1.73	+3	836.9	13.5	862.9	86.9
007-8.1	276	129	0.32	0.48	6.99	1.77	0.07	1.82	1.32	2.54	0.14	1.77	-3	861.9	14.3	841.2	37.8
007-9.1	367	192	0.21	0.54	7.14	4.55	0.07	1.40	1.29	4.77	0.14	4.55	-1	845.0	36.1	837.8	29.2
007-10.1	238	96	0.54	0.42	7.17	1.82	0.06	2.49	1.24	3.08	0.14	1.82	-11	841.7	14.3	764.6	52.5
007-10.2	389	278	0.08	0.74	7.23	1.70	0.07	3.84	1.28	4.19	0.14	1.70	+0	835.1	13.3	838.6	79.9
007-11.1	468	368	0.14	0.81	7.11	1.68	0.07	1.15	1.29	2.03	0.14	1.68	-2	848.1	13.3	828.9	24.0
007-11.2	89	23	-0.13	0.26	7.75	2.21	0.07	2.50	1.30	3.34	0.13	2.21	+24	782.6	16.3	1011.3	50.8
007-12.1	238	93	0.43	0.40	6.91	1.82	0.06	2.24	1.28	2.89	0.14	1.82	-17	870.9	14.8	753.0	47.3
007-13.1	167	55	0.00	0.34	7.35	1.92	0.07	1.46	1.30	2.41	0.14	1.92	+11	822.4	14.8	913.1	30.1
007-14.1	95	23	0.63	0.25	7.93	2.20	0.07	14.68	1.15	14.85	0.13	2.20	+7	765.9	15.9	816.7	306.9
007-15.1	696	14	0.17	0.02	7.70	1.63	0.06	1.05	1.13	1.94	0.13	1.63	-10	787.3	12.1	718.8	22.3
007-16.1	190	75	0.61	0.41	7.77	1.90	0.06	8.85	1.11	9.05	0.13	1.90	-13	780.7	14.0	696.6	188.5
007-17.1	425	323	0.16	0.79	7.29	1.69	0.07	1.21	1.28	2.08	0.14	1.69	+3	828.7	13.2	853.1	25.2
007-18.1	606	547	0.14	0.93	7.17	1.64	0.07	1.00	1.29	1.92	0.14	1.64	-0	841.6	13.0	841.5	20.7

4 - corr = 204 corrected

Table 1: SHRIMP U-Pb data from western Ethiopia.

Appendix 2.1: Age and hafnium isotopic evolution of the Didesa and Kemashi Domains, western Ethiopia.-

Spot Name	U ppm	Th ppm	4-corr Pb206 com (%)	232Th/238U	4corr 238/206*	% err	4corr 207*/206*	% err	4corr 207*/235	% err	4corr 206*/238	% err	Disc (%)	204corr 206Pb/238U Age (Ma)	1s err	204corr 207Pb/206Pb Age	1s err
Felsic Granite																	
008A-15.1	350	185	0.16	0.55	6.84	1.27	0.07	4.87	1.38	5.03	0.15	1.27	1	880.2	10.4	886.7	100.6
008A-2.1	456	294	0.17	0.67	6.85	1.15	0.07	1.08	1.33	1.58	0.15	1.15	-10	878.4	9.4	803.3	22.6
008A-6.1	377	205	0.27	0.56	6.89	1.20	0.07	1.34	1.35	1.79	0.15	1.20	-3	874.0	9.8	847.9	27.8
008A-7.1	507	215	0.17	0.44	6.94	1.14	0.07	1.05	1.33	1.55	0.14	1.14	-4	868.3	9.3	838.3	21.8
008A-11.1	281	54	0.97	0.20	6.94	1.29	0.07	2.34	1.45	2.67	0.14	1.29	15	867.4	10.4	1013.0	47.4
008A-9.1	344	166	0.16	0.50	7.02	1.21	0.07	1.24	1.33	1.73	0.14	1.21	-1	858.6	9.8	854.3	25.7
008A-10.1	273	135	0.46	0.51	7.03	1.32	0.06	2.15	1.23	2.52	0.14	1.32	-26	857.8	10.6	689.6	45.9
008A-8.1	238	96	0.28	0.42	7.10	1.32	0.07	6.75	1.28	6.88	0.14	1.32	-6	849.1	10.5	802.5	141.3
008A-1.1	306	152	0.20	0.51	7.11	1.22	0.07	1.35	1.29	1.82	0.14	1.22	-4	848.7	9.7	821.7	28.1
008A-3.1	345	250	0.35	0.75	7.12	1.21	0.06	1.57	1.26	1.98	0.14	1.21	-11	847.4	9.6	768.8	33.1
008A-6.2	254	114	0.41	0.46	7.12	1.31	0.06	2.21	1.22	2.57	0.14	1.31	-21	847.2	10.4	705.2	47.1
008A-16.1	400	206	0.17	0.53	7.13	1.29	0.07	1.29	1.29	1.82	0.14	1.29	-1	846.2	10.2	836.3	26.8
008A-4.1	425	145	0.15	0.35	7.15	1.16	0.07	1.13	1.26	1.62	0.14	1.16	-7	843.5	9.2	791.6	23.7
008A-13.1	241	94	0.42	0.40	7.18	1.31	0.07	1.96	1.27	2.36	0.14	1.31	-4	840.4	10.3	812.5	40.9
008A-5.1	124	37	1.03	0.30	7.22	1.61	0.06	4.15	1.21	4.45	0.14	1.61	-18	836.0	12.6	713.4	88.1
008A-14.1	411	174	0.11	0.44	7.36	1.28	0.07	1.33	1.25	1.84	0.14	1.28	2	821.0	9.8	833.9	27.6
008A-17.1	353	160	0.52	0.47	7.75	10.16	0.07	2.03	1.22	10.37	0.13	10.16	12	782.6	74.9	883.7	42.1
008A-12.1	5310	278	0.56	0.05	10.10	1.56	0.06	0.59	0.87	1.67	0.10	1.56	18	608.6	9.1	738.2	12.5

4 - corr = 204 corrected

Appendix 2.1: Age and hafnium isotopic evolution of the Didesa and Kemashi Domains, western Ethiopia.-

Table 1: SHRIMP U-Pb data from western Ethiopia.

Spot Name	U ppm	Th ppm	$^{232}Th/^{238}U$	4-corr Pb^{206} com (%)	4corr 238 /206*	% err	4corr 207* /206*	% err	4corr 207* /235	% err	4corr 206* /238	% err	Disc (%)	204corr $^{206}Pb/^{238}U$ Age (Ma)	1s err	204corr $^{207}Pb/^{206}Pb$ Age	1s err
Ganjii granite																	
012-1.1	205	65	0.33	0.11	10.51	1.75	0.06	1.81	0.76	2.52	0.10	1.75	-9	585.8	9.81	538.1	39.50
012-2.1	59	22	0.39	0.23	10.27	2.29	0.06	12.80	0.78	13.01	0.10	2.29	-11	598.8	13.12	541.5	279.96
012-3.1	83	32	0.40	0.78	10.78	2.11	0.05	5.93	0.68	6.29	0.09	2.11	-70	571.9	11.55	342.8	134.20
012-4.1	51	24	0.49	-1.07	11.02	2.49	0.07	7.09	0.88	7.52	0.09	2.49	41	560.1	13.37	927.3	145.63
012-5.1	70	21	0.31	47.56	9.80	8.41	0.14	35.78	1.96	36.75	0.10	8.41	75	626.4	50.21	2217.5	620.20
012-6.1	153	49	0.33	42.66	10.39	8.12	0.09	47.95	1.15	48.63	0.10	8.12	59	592.1	45.93	1347.6	925.65
012-7.1	174	49	0.29	0.25	10.49	1.78	0.06	2.37	0.75	2.97	0.10	1.78	-18	587.0	9.99	502.7	52.24
012-8.1	46	15	0.33	0.24	10.70	2.37	0.06	4.34	0.78	4.94	0.09	2.37	9	575.8	13.04	632.5	93.44
012-9.1	29	10	0.35	0.38	11.11	2.71	0.06	16.98	0.75	17.19	0.09	2.71	11	555.4	14.44	618.9	366.42
012-9.2	67	21	0.33	-0.14	10.59	2.08	0.06	8.75	0.79	8.99	0.09	2.08	7	581.4	11.58	624.0	188.68
012-10.1	140	42	0.31	0.09	11.02	1.85	0.06	2.12	0.77	2.81	0.09	1.85	15	559.7	9.90	654.5	45.38
012-11.1	105	31	0.30	3.97	11.02	2.13	0.04	14.83	0.55	14.99	0.09	2.13	593	560.0	11.43	-119.7	365.87
012-12.1	120	39	0.33	0.00	10.63	1.86	0.06	6.72	0.76	6.97	0.09	1.86	-3	579.5	10.33	562.4	146.41
012-13.1	34	10	0.32	1.59	10.72	2.63	0.05	11.95	0.67	12.24	0.09	2.63	-113	575.2	14.48	276.2	273.68
012-14.1	37	10	0.29	2.84	10.45	2.67	0.04	19.81	0.53	19.99	0.10	2.67	298	589.0	15.05	-319.9	508.32
012-15.1	111	63	0.58	0.61	10.80	1.91	0.05	4.53	0.67	4.92	0.09	1.91	-83	570.7	10.43	318.9	102.94
012-16.1	41	14	0.35	2.57	10.71	2.57	0.04	17.43	0.54	17.61	0.09	2.57	350	575.5	14.14	-245.5	440.57
012-17.1	44	15	0.34	3.29	10.15	12.19	0.08	57.48	1.13	58.76	0.10	12.19	55	605.5	70.45	1279.8	1120.26
012-18.1	149	49	0.34	0.00	11.21	1.82	0.06	1.67	0.76	2.47	0.09	1.82	19	550.9	9.59	672.4	35.80
012-19.1	69	22	0.33	39.07	18.76	5.81	0.02	361.82	0.11	361.86	0.05	5.81	N/A	334.8	18.95		
012-19.2	189	98	0.54	10.93	11.16	2.12	0.08	12.03	0.93	12.22	0.09	2.12	51	553.3	11.25	1079.8	241.40
012-10.2	58	29	0.52	0.00	10.77	2.39	0.06	2.90	0.81	3.76	0.09	2.39	20	572.6	13.10	706.6	61.63
012-12.2	92	43	0.49	0.83	10.63	2.17	0.06	13.46	0.72	13.63	0.09	2.17	-36	579.7	12.02	432.7	299.84

Table 1: SHRIMP U-Pb data from western Ethiopia.

Spot Name	U ppm	Th ppm	4-corr Pb^{206} com (%)	^{232}Th/^{238}U	4corr 238/206*	% err	4corr 207*/206*	% err	4corr 207*/235	% err	4corr 206*/238	% err	Disc (%)	204corr ^{206}Pb/^{238}U Age (Ma)	1s err	204corr ^{207}Pb/^{206}Pb Age	1s err
Meta-quartz arenite																	
024-1.1	415.76	100.8	0.05	0.2506	2.3104965	1.638	0.173	1.4236	10.3252	2.1705	0.4328074	1.638	+12	2318.361	31.9	2587.098	23.7594
024-2.1	97.42	52.08	0.25	0.5522	5.9813646	1.969	0.072	2.0233	1.66721	2.8235	0.1671859	1.969	-0	996.58768	18.18	995.0984	41.1214
024-3.1	296.18	236.1	0.08	0.8235	3.0174931	1.697	0.113	0.5415	5.16686	1.7813	0.3314009	1.697	+0	1845.1682	27.23	1849.436	9.79172
024-4.1	706	608.4	0.20	0.8902	7.2022035	1.597	0.066	0.8551	1.26356	1.8114	0.1388464	1.597	-4	838.13581	12.55	806.453	17.8981
024-5.1	83.127	28.46	0.92	0.3536	6.4869895	2.122	0.069	10.261	1.45947	10.478	0.1541547	2.122	-4	924.21095	18.27	888.7002	212.006
024-6.1	88.98	48.43	0.15	0.5622	5.4608438	6.461	0.075	1.9307	1.88574	6.7437	0.1831219	6.461	-2	1084.0071	64.47	1060.067	38.8544
024-7.1	386.85	195.5	0.05	0.5221	3.1414419	5.766	0.114	1.8081	4.99211	6.0424	0.3183252	5.766	+5	1781.5446	89.74	1860.006	32.6563
024-8.1	1132	254.5	0.00	0.2322	3.1094887	1.573	0.113	0.2547	5.03079	1.5934	0.3215963	1.573	+4	1797.5201	24.67	1855.478	4.60207
024-9.1	520.72	153	0.03	0.3034	2.3241996	3.269	0.164	0.2958	9.73803	3.2823	0.4302556	3.269	+9	2306.8699	63.39	2498.871	4.97906
024-10.1	110.72	157.7	0.18	1.4717	3.0367528	1.972	0.111	1.0236	5.05606	2.2217	0.3292991	1.972	-1	1834.9835	31.49	1821.692	18.5723
024-11.1	91.307	45.43	0.39	0.514	5.8375142	2.057	0.073	2.5637	1.72541	3.2867	0.1713058	2.057	-0	1019.3018	19.39	1015.34	51.9434

4 - corr = Pb^{204} corrected

Table 2: LA-MC-ICP-MS Lu-Hf isotopes (zircon) from the Western Ethiopian Shield

Sample Name	Hf^{176}/Hf^{177}	2 S.E.	Lu^{176}/Hf^{177}	Yb^{176}/Hf^{177}	U/Pb AGE	Hfi	epsilon	1s	T (DM) Ga	T(DM) Crustal	Hf Chur (t)	Hf DM (t)
Ganjii Granite												
E13.12.1	0.282626944	2.137E-05	0.000790626	0.029531711	572.6	0.282618	6.88	0.7	0.88	1.07	0.282424	0.282839
E13.12.2	0.282626944	2.137E-05	0.000790626	0.029531711	572.6	0.282618	6.88	0.7	0.88	1.07	0.282424	0.282839
E13.12.3	0.282657072	2.544E-05	0.000692878	0.02559139	572.6	0.282650	7.98	0.9	0.84	1.00	0.282424	0.282839
E13.12.4	0.282628961	2.839E-05	0.001197959	0.047475324	572.6	0.282616	6.79	1.0	0.89	1.07	0.282424	0.282839
E13.12.5	0.282669157	4.402E-05	0.001577538	0.055800666	572.6	0.282652	8.07	1.5	0.84	0.99	0.282424	0.282839
E13.9.1	0.282664933	4.266E-05	0.001321719	0.051032892	572.6	0.282651	8.02	1.5	0.84	0.99	0.282424	0.282839
E13.10.1	0.282658463	2.627E-05	0.000927117	0.035928517	572.6	0.282649	7.94	0.9	0.84	1.00	0.282424	0.282839
E13.15.1	0.282653641	5.2E-05	0.002506399	0.102421166	572.6	0.282627	7.17	1.8	0.88	1.05	0.282424	0.282839
E13.18.1	0.282645965	2.858E-05	0.00067038	0.026906998	572.6	0.282639	7.60	1.0	0.85	1.02	0.282424	0.282839
Meta quartz arenite												
E13.24.1	0.281224739	3.097E-05	0.001017834	0.047365451	2587	0.281174	1.79	1.1	2.83	2.96	0.281124	0.281353
E13.24.2	0.282289313	5.534E-05	0.001871221	0.069273659	995	0.282254	3.49	1.9	1.39	1.61	0.282156	0.282532
E13.24.3	0.281528269	3.066E-05	0.001105731	0.037728543	1849	0.281489	-4.14	1.1	2.42	2.74	0.281606	0.281904
E13.24.4	0.282516827	3.956E-05	0.001282886	0.049470895	806	0.282497	7.84	1.4	1.05	1.19	0.282276	0.282669
E13.24.5	0.282286234	5.681E-05	0.001654842	0.05973369	889	0.282259	1.25	2.0	1.39	1.66	0.282223	0.282609
E13.24.6	0.282206083	7.778E-05	0.001765605	0.084304999	1060	0.282171	2.01	2.7	1.51	1.75	0.282114	0.282484
E13.24.7	0.281523972	3.459E-05	0.000859304	0.031531103	1860	0.281494	-3.74	1.2	2.41	2.72	0.281599	0.281896
E13.24.8	0.281577537	3.803E-05	0.001130074	0.04415401	1855	0.281538	-2.29	1.3	2.35	2.63	0.281602	0.281899
E13.24.9	0.281282299	3.419E-05	0.000874414	0.033348348	2499	0.281241	2.08	1.2	2.74	2.88	0.281182	0.281419
E13.24.10	0.281292257	3.452E-05	0.000524221	0.024630661	1822	0.281274	-12.41	1.2	2.70	3.21	0.281624	0.281924
13.24.11	0.282223824	5.695E-05	0.000874622	0.037479575	1015	0.282207	2.28	2.0	1.45	1.70	0.282143	0.282517

CHUR from Bouvier et al. (2008); Earth and Planetary Science Letters 273 (2008) 48–57

CHUR 176Lu/177Hf = 0.0336±1 and 176Hf/177Hf = 0.282785±11

Hfi = 176Hf/177Hf ratio - (176Lu/177Hf ratio * (EXP(0.0193 * 207Pb/206Pb ratio / 1000)-1))

Table 2: LA-MC-ICP-MS Lu-Hf isotopes (zircon) from the Western Ethiopian Shield

Appendix 2.1: Age and hafnium isotopic evolution of the Didesa and Kemashi Domains, western Ethiopia.-

Sample Name	Hf^{176}/Hf^{177}	2 S.E.	Lu^{176}/Hf^{177}	Yb^{176}/Hf^{177}	U/Pb AGE	Hfi	epsilon	1s	T (DM) Ga	T(DM) Crustal	Hf Chur (t)	Hf DM (t)
Foliated gneiss												
XX.1.4	0.282521429	4.817E-05	0.002371657	0.100105683	797	0.282486	7.23	1.7	1.07	1.22	0.282282	0.282676
XX.1.8	0.282598715	0.0001139	0.003516594	0.133691856	655	0.282555	6.50	4.0	0.99	1.15	0.282372	0.282779
XX.1.9	0.28259993	3.89E-05	0.0017076	0.071496802	763	0.282575	9.64	1.4	0.94	1.04	0.282303	0.282701
XX.1.10	0.28261055	6.478E-05	0.002429792	0.109176511	663	0.282580	7.56	2.3	0.94	1.09	0.282367	0.282773
XX.1.13	0.282554084	5.564E-05	0.003289113	0.137644854	609	0.282517	4.08	1.9	1.05	1.27	0.282401	0.282812
XX.1.15	0.282563209	3.787E-05	0.001646638	0.065963131	798	0.282539	9.12	1.3	0.99	1.10	0.282281	0.282675
XX.1.17	0.28265138	0.0001564	0.004820015	0.201733537	636	0.282594	7.43	5.5	0.95	1.08	0.282384	0.282793
XX.1.19	0.28257678	1.682E-05	0.000766015	0.027207757	655	0.282567	6.92	0.6	0.95	1.13	0.282372	0.282779
XX.1.21	0.282666174	7.228E-05	0.003024616	0.127629114	640	0.282630	8.79	2.5	0.88	1.00	0.282382	0.282790
XX.1.22	0.28253444	4.55E-05	0.002197967	0.094064995	543	0.282512	2.45	1.6	1.05	1.32	0.282443	0.282860
Homogeneous K-feldspar rich granite												
XX.3.2	0.282490593	3.39E-05	0.002094954	0.071063306	811	0.282459	6.58	1.2	1.11	1.27	0.282273	0.282666
XX.3.4	0.282511421	4.759E-05	0.002029818	0.086490759	581	0.282489	2.49	1.7	1.08	1.35	0.282419	0.282833
XX.3.6	0.282543201	2.256E-05	0.001430537	0.056546385	669	0.282525	5.74	0.8	1.02	1.21	0.282363	0.282769
XX.3.7	0.282553493	6.059E-05	0.003958277	0.151413449	667	0.282504	4.94	2.1	1.07	1.26	0.282364	0.282770
XX.3.8	0.282571315	2.072E-05	0.00140957	0.055941233	669	0.282554	6.75	0.7	0.97	1.15	0.282363	0.282769
XX.3.9	0.282542893	5.867E-05	0.001679106	0.06482438	799	0.282518	8.40	2.1	1.02	1.15	0.282281	0.282675
XX.3.10	0.282534348	7.532E-05	0.002928736	0.117050849	778	0.282492	7.00	2.6	1.07	1.22	0.282294	0.282690
XX.3.12	0.282543554	2.386E-05	0.001282646	0.04836183	779	0.282525	8.20	0.8	1.01	1.15	0.282293	0.282689
XX.3.15	0.282471753	9.36E-05	0.002262495	0.073632384	752	0.282440	4.58	3.3	1.14	1.35	0.282310	0.282709
XX.3.19	0.282508879	0.000367	0.001774447	0.067469372	326	0.282498	-2.90	12.8	1.07	1.49	0.282580	0.283017
XX.3.20	0.282484584	2.751E-05	0.001451551	0.049310768	753	0.282464	5.46	1.0	1.10	1.30	0.282310	0.282708

CHUR from Bouvier et al. (2008); Earth and Planetary Science Letters 273 (2008) 48–57

CHUR 176Lu/177Hf = 0.0336±1 and 176Hf/177Hf = 0.282785±11

Hfi = 176Hf/177Hf ratio - (176Lu/177Hf ratio * (EXP(0.0193 * 207Pb/206Pb ratio / 1000)-1))

Appendix 2.1: Age and hafnium isotopic evolution of the Didesa and Kemashi Domains, western Ethiopia.-

Table 2: LA-MC-ICP-MS Lu-Hf isotopes (zircon) from the Western Ethiopian Shield

Sample Name	Hf^{176}/Hf^{177}	2 S.E.	Lu^{176}/Hf^{177}	Yb^{176}/Hf^{177}	U/Pb AGE	Hfi	epsilon	1s	T (DM) Ga	T(DM) Crustal	Hf Chur (t)	Hf DM (t)
Hornblende, biotite gneiss												
XX.7.1.1	0.28243628	2.58E-05	0.000957825	0.031303543	814	0.282422	5.34	0.9	1.15	1.35	0.282271	0.282664
XX.7.1.2	0.282417675	3.578E-05	0.28240898	3.57948E-05	772	0.278322	-140.83	1.3	-0.18	9.76	0.282298	0.282694
XX.7.3	0.28240898	3.579E-05	0.001005257	0.037056836	769	0.282394	3.36	1.3	1.19	1.44	0.282300	0.282696
XX.7.4	0.282411798	1.963E-05	0.001080199	0.035999566	835	0.282395	4.86	0.7	1.19	1.40	0.282258	0.282648
XX.7.5	0.282431563	2.652E-05	0.001082012	0.037562649	850	0.282414	5.89	0.9	1.16	1.35	0.282248	0.282637
XX.7.6	0.282443926	4.557E-05	0.002132585	0.077304231	860	0.282409	5.94	1.6	1.18	1.35	0.282242	0.282630
XX.7.7	0.282409899	2.648E-05	0.001080113	0.036078544	837	0.282393	4.84	0.9	1.19	1.40	0.282256	0.282647
XX.7.8	0.282430778	1.836E-05	0.001109552	0.035541206	862	0.282413	6.11	0.6	1.17	1.34	0.282240	0.282629
XX.7.9	0.282419229	2.031E-05	0.000868434	0.029186982	845	0.282405	5.46	0.7	1.17	1.37	0.282251	0.282641
XX.7.10	0.282397078	2.501E-05	0.000812947	0.027840629	842	0.282384	4.64	0.9	1.20	1.42	0.282253	0.282643
XX.7.11	0.282404668	3.78E-05	0.001628592	0.060583989	848	0.282379	4.58	1.3	1.22	1.43	0.282249	0.282639
XX.7.12	0.282396648	3.301E-05	0.001140385	0.039173489	871	0.282378	5.07	1.2	1.21	1.41	0.282235	0.282622
XX.7.13	0.282414838	2.8E-05	0.000839418	0.026740797	822	0.282402	4.82	1.0	1.18	1.39	0.282266	0.282658
XX.7.14	0.282375805	3.659E-05	0.000820452	0.025212983	766	0.282364	2.21	1.3	1.23	1.51	0.282302	0.282698
XX.7.15	0.282445206	4.186E-05	0.000772671	0.023067375	787	0.282434	5.16	1.5	1.13	1.34	0.282288	0.282683
XX.7.17	0.282402212	0.000102	0.001735011	0.076854864	829	0.282375	4.03	3.6	1.23	1.45	0.282261	0.282653
Felsic granite												
XX.8.1	0.282446687	3.342E-05	0.000857399	0.028823692	849	0.282433	6.52	1.2	1.14	1.31	0.282249	0.282638
XX.8.2	0.282442493	2.422E-05	0.001058603	0.036902949	878	0.282425	6.91	0.8	1.15	1.30	0.282230	0.282617
XX.8.3	0.282446683	4.744E-05	0.000919147	0.02366147	847	0.282432	6.46	1.7	1.14	1.31	0.282250	0.282639
XX.8.4	0.282376323	3.248E-05	0.001020767	0.033700848	843	0.282360	3.82	1.1	1.24	1.47	0.282252	0.282642
XX.8.5	0.282423916	2.132E-05	0.000719081	0.022643392	836	0.282413	5.51	0.7	1.16	1.36	0.282257	0.282648
XX.8.6	0.28240093	2.528E-05	0.00111559	0.038737492	874	0.282383	5.31	0.9	1.21	1.40	0.282233	0.282620
XX.8.7	0.282406351	3.598E-05	0.001018902	0.032342869	868	0.282390	5.43	1.3	1.20	1.39	0.282236	0.282624
XX.8.9	0.282453153	3.433E-05	0.001391544	0.047255397	859	0.282431	6.66	1.2	1.14	1.30	0.282243	0.282631
XX.8.13	0.282414967	2.003E-05	0.000996157	0.032320376	840	0.282399	5.14	0.7	1.18	1.39	0.282254	0.282644
XX.8.14	0.282443946	3.828E-05	0.001239357	0.046692112	821	0.282425	5.61	1.3	1.15	1.34	0.282267	0.282658
XX.8.16	0.282455848	2.597E-05	0.000943133	0.031263463	846	0.282441	6.74	0.9	1.12	1.29	0.282251	0.282640

CHUR from Bouvier et al. (2008); Earth and Planetary Science Letters 273 (2008) 48–57

CHUR 176Lu/177Hf = 0.0336±1 and 176Hf/177Hf = 0.282785±11

Hfi = 176Hf/177Hf ratio - (176Lu/177Hf ratio * (EXP(0.0193 * 207Pb/206Pb ratio / 1000)-1))

APPENDIX 2.2

Supplementary data for chapter 2b:
The East African Orogenic Missing Link: Age, Hafnium
and Oxygen Isotopic Evolution of the Western Ethiopian
Shield.

Figure 1: U–Pb Wetherill plots (^{207}Pb / ^{206}Pb v. $^{238}U/^{206}Pb$) constructed with a 2 sigma data point error ellipses. Filled grains represent those within 90% concordance and outlines represent all other grains present. Each plot has a representative cumulative weighted average plot, with the unfilled bars representing grains that have experienced Pb-loss

Figure 1: U–Pb Wetherill plots (^{207}Pb / ^{206}Pb v. ^{238}U / ^{206}Pb) constructed with a 2 sigma data point error ellipses. Filled grains represent those within 90% concordance and outlines represent all other grains present. Each plot has a representative cumulative weighted average plot, with the unfilled bars representing grains that have experienced Pb-loss

Figure 1: U–Pb Wetherill plots (^{207}Pb / ^{206}Pb v. ^{238}U/^{206}Pb) constructed with a 2 sigma data point error ellipses. Filled grains represent those within 90% concordance and outlines represent all other grains present. Each plot has a representative cumulative weighted average plot, with the unfilled bars representing grains that have experienced Pb-loss

Figure 1: U–Pb Wetherill plots (^{207}Pb / ^{206}Pb v. ^{238}U / ^{206}Pb) constructed with a 2 sigma data point error ellipses. Filled grains represent those within 90% concordance and outlines represent all other grains present. Each plot has a representative cumulative weighted average plot, with the unfilled bars representing grains that have experienced Pb-loss

Table 1: LA-ICP-MS U–Pb data used to calculate Concordias from the Western Ethiopian Shield

Analysis	$^{207}Pb/^{235}U$		$^{206}Pb/^{238}U$		rho	Conc (%)	$^{207}Pb/^{206}Pb$		$^{206}Pb/^{238}U$	
E14-02										
02-01	0.875	0.013	0.095	0.001	0.444	69	841.9	28.69	582.1	6.44
02-02	0.747	0.010	0.088	0.001	0.494	81	668.3	26.4	541.7	5.96
02-03	0.927	0.013	0.110	0.001	0.649	104	645.4	23.79	672.4	8.22
02-04	0.716	0.009	0.078	0.001	0.536	58	833.8	24.41	482	5.39
02-05	0.810	0.011	0.092	0.001	0.685	76	744	22.91	565.9	7.31
02-06	0.880	0.011	0.100	0.001	0.601	84	735	23.73	614.8	7.16
02-07	0.634	0.010	0.069	0.001	0.710	51	835.8	23.16	428.6	5.95
02-08	0.883	0.013	0.102	0.001	0.694	88	706.6	23.67	624.9	8.39
02-09	0.931	0.014	0.110	0.002	0.706	103	653.5	24.49	672.6	9.36
02-10	0.891	0.013	0.105	0.001	0.634	96	666.4	25.12	641.1	8.07
02-11	0.990	0.014	0.109	0.001	0.604	82	810.6	25.06	664.3	8.13
02-12	0.833	0.011	0.083	0.001	0.600	50	1015	23.36	512.5	6.14
02-13	0.803	0.012	0.088	0.001	0.691	67	813.9	23.21	543.5	7.21
02-14	0.807	0.012	0.092	0.001	0.678	77	737.8	23.68	565.3	7.39
02-15	0.645	0.009	0.071	0.001	0.649	56	792.2	23.85	444.7	5.67
02-16	0.648	0.009	0.062	0.001	0.720	36	1075.2	20.9	390.3	5.27
02-17	0.908	0.013	0.106	0.002	0.731	94	685.8	22.51	647.2	8.79
02-18	0.874	0.012	0.091	0.001	0.714	61	924.3	21.44	559.9	7.35
02-19	0.900	0.013	0.102	0.001	0.713	85	736.9	22.31	627.6	8.31
02-20	0.777	0.012	0.076	0.001	0.523	46	1033.4	27.16	475.1	5.76
02-21	0.878	0.013	0.102	0.001	0.713	93	678.6	22.84	628.9	8.39
02-22	0.937	0.015	0.098	0.001	0.730	66	912	22.8	601.8	8.61
02-23	0.890	0.013	0.095	0.001	0.722	69	856.6	22.37	587.5	8.02
02-24	0.865	0.012	0.098	0.001	0.604	80	751.4	25.39	600	7.37
02-25	0.943	0.014	0.105	0.002	0.715	82	786.6	22.94	641.3	8.75
02-26	0.514	0.008	0.057	0.001	0.709	47	772.3	23.09	360.2	4.98
02-27	0.875	0.013	0.082	0.001	0.589	44	1139.5	24.82	506.4	6.33
02-28	0.987	0.015	0.083	0.001	0.710	38	1349.1	21.36	512.5	7.03
02-29	0.592	0.009	0.065	0.001	0.576	51	795.6	27.08	408.1	5.18
02-30	0.884	0.013	0.103	0.001	0.698	91	688.9	24.21	630	8.51
02-31	0.810	0.013	0.094	0.001	0.726	86	680	24.93	582	8.57
02-32	0.892	0.013	0.100	0.001	0.651	79	771.1	25.03	613	8.03
02-33	0.837	0.013	0.066	0.001	0.628	28	1470.4	23.6	411.5	5.42
02-34	0.943	0.015	0.101	0.001	0.704	71	870.2	23.78	617.5	8.63
02-35	0.820	0.014	0.099	0.001	0.642	100	606.3	29.63	608.6	8.73
E14-04										
04-01	1.134	0.017	0.123	0.002	0.684	88	841.9	24.24	744.9	10.08
04-02	0.874	0.013	0.103	0.001	0.723	95	662.8	22.99	630.7	8.66
04-03	1.362	0.026	0.143	0.002	0.604	96	899.4	32.03	862.3	12.7
04-04	0.986	0.016	0.107	0.002	0.732	78	836.8	24.26	653.6	9.74
04-05	1.559	0.024	0.114	0.002	0.708	43	1615	21.01	693.8	9.57
04-06	1.292	0.022	0.138	0.002	0.638	95	872.2	27.67	830.7	11.51
04-07	1.052	0.016	0.111	0.002	0.699	77	881.6	23.65	681.4	9.35
04-08	0.888	0.015	0.101	0.002	0.727	85	733.8	25.7	620.2	9.46
04-09	1.011	0.019	0.114	0.002	0.624	94	746	32.19	697.8	10.68
04-10	1.331	0.024	0.144	0.002	0.589	103	842.1	31.35	866.1	12.14
04-11	1.172	0.019	0.131	0.002	0.674	103	772	26.77	792.9	11.17
04-12	1.297	0.023	0.139	0.002	0.598	98	855.2	31.14	840.3	11.91
04-13	0.944	0.014	0.108	0.002	0.704	91	723.8	24.17	660.4	9.11
04-14	0.969	0.015	0.101	0.001	0.708	67	918.4	23.49	619.5	8.63
04-15	1.033	0.018	0.116	0.002	0.632	94	756.5	29.99	708.6	10.21
04-16	1.171	0.022	0.110	0.002	0.460	59	1130.9	34.6	671.1	8.98
04-17	1.342	0.023	0.141	0.002	0.688	95	897.2	25.97	851.5	12.27

Table 1: LA-ICP-MS U–Pb data used to calculate Concordias from the Western Ethiopian Shield

Analysis	$^{207}Pb/^{235}U$		$^{206}Pb/^{238}U$		rho	Conc (%)	$^{207}Pb/^{206}Pb$		$^{206}Pb/^{238}U$	
E14-04										
04-18	1.365	0.025	0.148	0.002	0.618	107	834.2	30.84	890	12.87
04-19	0.977	0.015	0.113	0.002	0.730	100	692.3	24.01	692	9.88
04-20	2.130	0.039	0.086	0.001	0.439	20	2653.9	29.39	530.5	7.57
04-21	1.211	0.020	0.118	0.002	0.728	68	1051.5	23.43	719.7	10.51
04-22	1.419	0.023	0.134	0.002	0.736	72	1121	22.74	808.7	11.66
04-23	1.349	0.023	0.144	0.002	0.680	99	873.4	26.84	864.5	12.46
04-24	0.999	0.017	0.110	0.002	0.717	85	795.4	25.28	674.7	9.99
04-25	1.322	0.025	0.136	0.002	0.623	87	947.8	31.39	820.5	12.32
04-26	1.365	0.025	0.148	0.002	0.635	106	837.7	30.26	888.4	12.96
04-27	1.243	0.020	0.138	0.002	0.687	106	783.7	26	833.8	11.69
04-28	1.269	0.025	0.131	0.002	0.571	85	933.2	34.26	794.6	11.8
04-29	1.196	0.021	0.125	0.002	0.658	83	911.6	28.56	758.8	11.2
04-30	0.937	0.015	0.109	0.002	0.721	97	689.9	24.86	665.8	9.58
04-31	1.309	0.025	0.140	0.002	0.618	98	859.5	31.48	845.7	12.55
04-32	1.051	0.017	0.115	0.002	0.750	87	810.1	23.32	703.8	10.34
04-33	1.213	0.020	0.127	0.002	0.711	86	901.9	25.15	772.9	11.32
04-34	1.380	0.024	0.146	0.002	0.656	99	884.5	28.16	878.9	12.62
04-35	2.557	0.040	0.087	0.001	0.576	18	2926.3	22.04	539	7.22
04-36	0.979	0.016	0.109	0.002	0.752	85	783.4	23.38	665.8	9.83
04-37	1.477	0.023	0.103	0.001	0.631	37	1702	23.58	630.6	8.53
04-38	1.217	0.020	0.127	0.002	0.688	85	907.5	25.23	773.2	10.94
04-39	1.238	0.022	0.123	0.002	0.678	74	1011.1	27.34	749.1	11.2
04-40	0.995	0.017	0.081	0.001	0.671	35	1415.4	24.45	499.9	7.27
04-41	0.981	0.015	0.087	0.001	0.695	43	1244.7	22.98	536.5	7.53
04-42	0.898	0.015	0.100	0.002	0.697	79	777.9	26.44	614.7	9.14
04-43	1.309	0.022	0.125	0.002	0.696	70	1090.8	25.1	760.4	11.09
04-44	1.175	0.020	0.119	0.002	0.711	75	969	25.49	727.1	10.91
04-45	1.190	0.019	0.134	0.002	0.710	106	760.3	24.95	808.9	11.46
04-46	1.269	0.023	0.139	0.002	0.608	103	813.4	31.01	839.1	11.96
04-47	1.433	0.026	0.142	0.002	0.528	84	1016.7	31.98	857.2	11.54
04-48	1.166	0.019	0.115	0.002	0.695	69	1020.9	25.08	704.3	10.13
04-49	1.274	0.020	0.142	0.002	0.684	109	782	25.39	854.1	11.65
04-50	1.337	0.026	0.141	0.002	0.625	96	887.1	31.75	852.2	12.81
04-51	0.977	0.016	0.114	0.002	0.721	104	670.5	25.11	698.5	10.1
04-52	1.209	0.021	0.129	0.002	0.666	91	861.7	27.25	784.3	11.23
04-53	1.360	0.024	0.145	0.002	0.631	100	870	29.42	872.6	12.52
E14-38										
38-01	1.344	0.021	0.147	0.002	0.679	107	822.8	25.49	881.3	12.11
38-02	1.249	0.020	0.137	0.002	0.658	102	809.5	26.38	828	11.28
38-03	1.259	0.023	0.136	0.002	0.625	99	834.6	31	824.5	12.23
38-04	1.209	0.020	0.132	0.002	0.635	97	822	27.59	798.5	10.96
38-05	1.236	0.021	0.137	0.002	0.659	104	793.9	28.04	825.8	11.89
38-06	1.242	0.022	0.132	0.002	0.653	92	871.2	29.07	801.1	11.76
38-07	1.237	0.023	0.135	0.002	0.640	99	822.7	30.11	815.5	12.07
38-08	1.434	0.026	0.137	0.002	0.646	76	1090.6	28.52	828.6	12.25
38-09	1.265	0.024	0.134	0.002	0.615	92	883.9	31.35	810.2	11.97
38-10	1.308	0.021	0.133	0.002	0.707	84	965.1	24.41	805.9	11.5
38-11	1.242	0.020	0.134	0.002	0.670	96	841.3	25.89	811.8	11.16
38-12	1.522	0.025	0.134	0.002	0.647	64	1257.7	25.15	809.3	11.14
38-13	1.237	0.021	0.135	0.002	0.675	99	825.5	26.91	815	11.7
38-14	1.287	0.022	0.135	0.002	0.531	91	900.6	31.59	817	10.76
38-15	1.225	0.021	0.133	0.002	0.671	97	833.2	26.96	804.5	11.42
38-16	1.330	0.023	0.134	0.002	0.664	82	983.9	27.33	811.4	11.71

Table 1: LA–ICP–MS U–Pb data used to calculate Concordias from the Western Ethiopian Shield

Analysis	$^{207}Pb/^{235}U$		$^{206}Pb/^{238}U$		rho	Conc (%)	$^{207}Pb/^{206}Pb$		$^{206}Pb/^{238}U$	
E14-38										
38-17	1.257	0.021	0.139	0.002	0.640	106	791.5	28.03	839.4	11.57
38-18	1.250	0.021	0.133	0.002	0.655	92	877.9	26.63	803.3	11.15
38-19	1.225	0.022	0.134	0.002	0.617	98	824.4	30.86	807.8	11.64
38-20	1.324	0.030	0.138	0.002	0.503	92	911.5	41.43	835.3	13.13
38-21	1.310	0.022	0.142	0.002	0.687	104	827.5	26.21	858.6	12.13
38-22	1.325	0.023	0.143	0.002	0.709	101	849	26	859.8	12.74
38-23	1.316	0.027	0.138	0.002	0.548	93	897.2	36.75	835.6	12.64
38-24	1.284	0.023	0.135	0.002	0.626	91	894.7	30.03	818	11.85
38-25	1.207	0.020	0.132	0.002	0.644	98	817.4	27.51	798.7	11.02
38-26	1.217	0.021	0.130	0.002	0.632	90	872.2	28.46	785.6	10.95
38-27	1.215	0.020	0.132	0.002	0.656	96	834.2	27.6	798	11.25
38-28	1.359	0.025	0.139	0.002	0.607	88	950.5	31.25	840.8	12.28
38-29	1.254	0.021	0.134	0.002	0.660	93	871.7	26.89	808.1	11.3
38-30	1.357	0.028	0.139	0.002	0.579	89	948.9	35.49	840	13.05
38-31	1.503	0.046	0.125	0.002	0.314	56	1355.8	57.16	762	12.82
E14-43										
43-1	0.772	0.013	0.095	0.001	0.586	104	561	32.33	585.8	8.1
43-2	1.050	0.016	0.089	0.001	0.646	41	1327.4	23.76	549.9	7.27
43-3	1.280	0.019	0.092	0.001	0.693	35	1640.1	20.88	567.7	7.62
43-4	1.697	0.033	0.082	0.001	0.636	21	2355.8	26.25	506.1	8.01
43-5	1.146	0.018	0.127	0.002	0.669	97	793.8	25.96	769	10.55
43-6	0.814	0.015	0.042	0.001	0.441	12	2226.1	30.26	266.5	3.65
43-7	0.306	0.005	0.028	0.000	0.642	15	1192.3	25.65	176.7	2.53
43-8	1.411	0.023	0.124	0.002	0.659	60	1254.1	24.96	755.3	10.53
43-9	1.152	0.020	0.125	0.002	0.677	90	838.3	27.9	757.6	11.27
43-10	1.126	0.019	0.120	0.002	0.623	83	875.9	28.3	729	9.98
43-11	0.970	0.020	0.070	0.001	0.439	27	1622.3	35.91	438.8	6.14
43-12	1.180	0.022	0.130	0.002	0.638	98	801.1	30.29	787.7	11.53
43-13	1.100	0.020	0.080	0.001	0.656	30	1626.8	26.28	494.2	7.54
E14-50										
50-1	1.291	0.022	0.125	0.002	0.680	72	1060.3	25.55	761.2	10.94
50-2	1.300	0.021	0.140	0.002	0.629	99	853.7	27.19	843.2	11.27
50-3	0.755	0.012	0.075	0.001	0.720	46	1015.9	22.47	465.7	6.57
50-4	1.355	0.021	0.143	0.002	0.684	98	884.7	24.54	864.3	11.69
50-5	1.326	0.023	0.140	0.002	0.604	95	891	29.45	844.2	11.63
50-6	0.993	0.015	0.098	0.001	0.717	59	1020	22.63	605.2	8.4
50-7	1.303	0.021	0.139	0.002	0.637	97	865.2	27.04	840.2	11.33
50-8	1.294	0.020	0.139	0.002	0.670	99	847.5	24.69	841.6	11.22
50-9	1.227	0.020	0.132	0.002	0.590	93	857.9	28.95	796.8	10.57
50-10	1.234	0.020	0.132	0.002	0.564	93	862.4	28.63	799.6	10.09
50-11	1.315	0.021	0.136	0.002	0.671	89	928.8	25.22	823.6	11.27
50-12	1.299	0.020	0.137	0.002	0.677	93	887.2	24.8	829.4	11.2
50-13	1.212	0.019	0.128	0.002	0.585	87	888.1	27.15	776.9	9.83
50-14	1.246	0.020	0.136	0.002	0.605	99	827	27.99	820.2	10.8
50-15	1.219	0.019	0.131	0.002	0.628	92	858.9	26.17	792	10.34
50-16	1.254	0.023	0.124	0.002	0.496	74	1021.4	33.04	754.4	10.07
50-17	1.222	0.022	0.120	0.002	0.607	70	1045.6	29.3	728	10.4
50-18	1.479	0.023	0.131	0.002	0.550	64	1241.5	26.97	794.2	9.98
50-19	1.249	0.020	0.136	0.002	0.620	100	825	27.14	822.2	10.8
E14-53										
53-01	1.379	0.022	0.142	0.002	0.681	90	945.3	24.39	854.1	11.53
53-02	1.333	0.023	0.134	0.002	0.643	82	986.3	27.62	812.7	11.48
53-03	1.427	0.021	0.149	0.002	0.704	99	907.1	22.6	897.7	11.81

Table 1: LA–ICP–MS U–Pb data used to calculate Concordias from the Western Ethiopian Shield

Analysis	$^{207}Pb/^{235}U$		$^{206}Pb/^{238}U$		rho	Conc (%)	$^{207}Pb/^{206}Pb$		$^{206}Pb/^{238}U$	
					E14-53					
53-04	1.369	0.023	0.142	0.002	0.705	91	933.8	24.82	853.4	12.18
53-05	1.364	0.021	0.143	0.002	0.695	95	906.1	24.19	860.9	11.76
53-06	1.331	0.021	0.137	0.002	0.698	89	936	23.71	830.2	11.29
53-07	1.387	0.021	0.139	0.002	0.597	85	994	26.41	840	10.68
53-08	1.306	0.020	0.139	0.002	0.650	95	880.3	25.46	836.4	11.02
53-09	1.362	0.021	0.132	0.002	0.593	75	1064.7	26.52	799.2	10.27
53-10	2.378	0.052	0.145	0.002	0.491	45	1943	35.12	872	13.69
53-11	1.457	0.024	0.153	0.002	0.682	102	901.4	25.61	917.6	12.78
53-12	2.611	0.061	0.155	0.003	0.441	47	1983.5	38.53	931.3	14.76
53-13	1.314	0.024	0.139	0.002	0.588	95	882.8	31.29	840.2	11.82
53-14	1.286	0.019	0.136	0.002	0.647	92	892	24.74	819.8	10.51
53-15	1.341	0.022	0.141	0.002	0.657	94	902.5	26.25	848.7	11.59
53-16	1.433	0.024	0.152	0.002	0.674	104	880.9	26.47	912.2	12.74
53-17	1.199	0.019	0.129	0.002	0.621	92	852.5	27.38	781.5	10.43
53-18	1.330	0.021	0.140	0.002	0.672	95	890.7	25.31	847.1	11.53
53-19	1.216	0.020	0.132	0.002	0.668	97	827.1	26.7	801.5	11.24
53-20	1.329	0.023	0.141	0.002	0.674	97	874.4	27.42	852.1	12.38
53-21	1.344	0.022	0.143	0.002	0.656	99	873.4	26.4	861.7	11.79
53-22	1.350	0.022	0.144	0.002	0.677	99	874	25.94	865.1	12.01
53-23	1.301	0.023	0.133	0.002	0.664	84	961.5	27.44	803.1	11.55
53-24	1.362	0.023	0.144	0.002	0.670	98	887	27.01	867.1	12.24
E14-58										
58-01	1.343	0.021	0.137	0.002	0.682	86	959.3	24.8	828.4	11.39
58-02	1.412	0.024	0.143	0.002	0.670	88	981.1	26.88	859.1	12.41
58-03	1.279	0.021	0.129	0.002	0.683	79	984.8	25.5	781.9	11.09
58-04	1.689	0.030	0.167	0.002	0.540	97	1022.5	31.52	996.4	13.3
58-05	1.311	0.020	0.135	0.002	0.681	86	944.9	24.35	814.9	11.07
58-06	1.305	0.020	0.135	0.002	0.657	88	927.3	24.93	818.2	10.85
58-07	1.322	0.022	0.139	0.002	0.641	93	903.3	27.3	836.9	11.45
58-08	1.315	0.023	0.137	0.002	0.632	90	918.4	29.1	827.1	11.75
58-09	1.580	0.027	0.132	0.002	0.656	59	1353.6	25.35	800.2	11.26
58-10	1.293	0.021	0.137	0.002	0.667	93	890	25.75	825	11.23
58-11	1.284	0.023	0.138	0.002	0.543	97	856.6	32.28	832	11.14
58-12	1.335	0.022	0.112	0.002	0.674	51	1349	24.19	684.2	9.59
58-13	1.176	0.022	0.098	0.002	0.624	44	1360.9	28.63	602.7	9.04
58-14	1.306	0.022	0.137	0.002	0.638	92	902.8	27.46	827.8	11.38
58-15	1.264	0.021	0.131	0.002	0.639	86	920.6	27.38	796	11.01
58-16	1.563	0.027	0.141	0.002	0.646	71	1203.7	26.42	851.8	12.01
58-17	1.282	0.022	0.138	0.002	0.649	99	844.1	27.62	835.4	11.65
58-18	1.339	0.022	0.139	0.002	0.687	91	924.2	25.24	839.3	11.8
58-19	1.319	0.020	0.135	0.002	0.659	85	957.2	24.69	814.9	10.7
58-20	1.815	0.031	0.171	0.003	0.682	91	1118.1	25.72	1018.7	14.49
58-21	1.112	0.018	0.111	0.002	0.670	67	1012.8	25.63	675.8	9.52
58-22	1.283	0.021	0.138	0.002	0.663	98	850.2	26.11	833.9	11.35
58-23	1.311	0.020	0.086	0.001	0.695	29	1819	20.84	528.9	7.31
58-24	1.324	0.023	0.142	0.002	0.638	100	854.6	28.47	856.8	11.98
58-25	1.743	0.030	0.173	0.003	0.616	101	1016.8	28.42	1028.2	13.96
58-26	1.260	0.021	0.122	0.002	0.658	69	1071.7	26.73	739.9	10.62
58-27	1.315	0.021	0.137	0.002	0.661	90	918.7	25.86	827.3	11.24
58-28	1.356	0.025	0.141	0.002	0.622	92	921.4	30.46	850.3	12.34
58-29	1.784	0.030	0.121	0.002	0.659	42	1750.4	23.83	735.4	10.44
58-30	1.328	0.024	0.128	0.002	0.638	73	1070.9	28.27	778.1	11.29

Table 1: LA–ICP–MS U–Pb data used to calculate Concordias from the Western Ethiopian Shield

Analysis	$^{207}Pb/^{235}U$		$^{206}Pb/^{238}U$		rho	Conc (%)	$^{207}Pb/^{206}Pb$		$^{206}Pb/^{238}U$	
E14-70										
70-01	1.252	0.020	0.133	0.002	0.646	91	881.8	26.67	803.6	10.98
70-02	1.217	0.019	0.133	0.002	0.687	98	818.2	24.73	805.1	10.97
70-03	1.281	0.020	0.135	0.002	0.661	90	900.1	25.35	813.8	11.02
70-04	1.269	0.020	0.133	0.002	0.657	90	899.8	25.83	807.2	10.93
70-05	1.280	0.020	0.135	0.002	0.670	91	898.2	24.88	814.4	10.99
70-06	1.251	0.019	0.135	0.002	0.661	96	850.9	25.07	814	10.78
70-07	1.240	0.020	0.133	0.002	0.641	94	858.5	26.54	804.4	10.78
70-08	1.232	0.020	0.133	0.002	0.648	96	842.2	26.82	805.3	10.98
70-09	1.209	0.020	0.133	0.002	0.638	101	798	28.22	807.3	11.19
70-10	1.236	0.020	0.136	0.002	0.658	101	810.9	25.97	819.5	11.07
70-11	1.306	0.024	0.135	0.002	0.598	87	936.9	30.96	814.9	11.67
70-12	1.267	0.022	0.136	0.002	0.609	97	852.8	29.23	823.3	11.36
70-13	1.198	0.019	0.130	0.002	0.645	94	837.3	26.8	786.7	10.71
70-14	1.223	0.020	0.131	0.002	0.658	92	859.7	26.87	793.9	11.02
70-15	1.222	0.022	0.132	0.002	0.578	94	847.3	31.71	797.9	11.2
70-16	1.264	0.020	0.136	0.002	0.674	97	845.8	25.51	823.6	11.27
70-17	1.250	0.021	0.134	0.002	0.677	94	858.4	26.34	810.4	11.55
70-18	1.261	0.021	0.129	0.002	0.678	81	961.3	26.34	779.9	11.18
70-19	1.214	0.021	0.131	0.002	0.680	94	843.8	26.79	793.9	11.43
70-20	1.189	0.031	0.133	0.002	0.309	105	766.6	52.99	806.2	11.66
70-21	1.231	0.021	0.131	0.002	0.607	90	878.9	29.48	791.6	10.97
70-22	1.220	0.019	0.134	0.002	0.624	99	815.1	27.25	808.1	10.72
70-23	1.239	0.020	0.134	0.002	0.658	96	841.1	25.97	810.4	10.9
70-24	1.235	0.020	0.135	0.002	0.656	101	811.5	26.6	818.5	11.23
70-25	1.202	0.019	0.129	0.002	0.647	92	849.3	26.3	784.3	10.59
70-26	1.235	0.020	0.133	0.002	0.659	94	855.6	26.24	802.4	10.99
70-27	1.190	0.019	0.131	0.002	0.663	100	798.1	26.58	795.4	11
70-28	1.286	0.024	0.137	0.002	0.568	96	865.2	32.75	829.6	11.67
70-29	1.280	0.021	0.137	0.002	0.634	97	858.7	28.01	828.7	11.46
70-30	1.234	0.020	0.134	0.002	0.642	97	831.6	27.45	810.8	11.2
70-31	1.206	0.022	0.128	0.002	0.559	89	877	32.75	777.3	10.87
E14-77										
77-01	1.192	0.019	0.131	0.002	0.570	97	813.6	28.39	791.2	10.12
77-02	1.172	0.020	0.131	0.002	0.502	100	795	32.69	795	10.35
77-03	1.218	0.019	0.130	0.002	0.575	90	871.1	27.98	786.4	10.06
77-04	1.376	0.022	0.130	0.002	0.550	71	1108.4	28.39	790.4	10.23
77-05	1.151	0.023	0.127	0.002	0.450	96	804.2	38.95	768.4	10.47
77-06	1.318	0.022	0.115	0.002	0.514	55	1278.7	29.27	699.2	9.16
77-07	1.801	0.028	0.129	0.002	0.575	48	1643.4	25.24	783.9	10.15
77-08	1.224	0.019	0.132	0.002	0.596	95	841.5	26.79	800.8	10.04
77-09	1.240	0.019	0.133	0.002	0.601	93	862.6	26.38	803.1	10.07
77-10	1.318	0.022	0.135	0.002	0.545	85	956	29.55	814.9	10.55
77-11	5.659	0.083	0.148	0.002	0.634	26	3352.9	18.79	887.1	11.18
77-12	1.908	0.030	0.131	0.002	0.564	46	1720.7	25.64	795.5	10.36
77-13	1.287	0.021	0.136	0.002	0.561	91	895.8	28.62	819.4	10.27
77-14	1.228	0.020	0.130	0.002	0.556	89	884.8	29.5	787.4	10.21
77-15	1.197	0.025	0.131	0.002	0.427	98	812	39.96	794.6	10.62
77-16	1.081	0.018	0.110	0.001	0.539	69	968.4	29.64	671.9	8.64
77-17	1.204	0.020	0.134	0.002	0.542	103	786	30.84	808.3	10.39
77-18	1.318	0.020	0.136	0.002	0.589	88	931.4	26.6	824.1	10.32
77-19	1.374	0.026	0.134	0.002	0.476	77	1052.3	34.46	810.1	10.91
77-20	1.377	0.028	0.135	0.002	0.442	79	1036.5	37.89	818.2	11.06
77-21	1.200	0.022	0.130	0.002	0.507	94	835.7	33.54	788.4	10.38

Table 1: LA–ICP–MS U–Pb data used to calculate Concordias from the Western Ethiopian Shield

Analysis	$^{207}Pb/^{235}U$		$^{206}Pb/^{238}U$		rho	Conc (%)	$^{207}Pb/^{206}Pb$		$^{206}Pb/^{238}U$	
E14-77										
77-22	1.241	0.026	0.132	0.002	0.403	91	877.8	41.1	798.3	10.67
77-23	1.354	0.023	0.132	0.002	0.497	76	1048.1	31.09	801.3	10.1
77-24	1.236	0.022	0.136	0.002	0.499	102	805.9	33.07	821.8	10.44
77-25	2.281	0.038	0.136	0.002	0.562	42	1975.7	25.63	824	10.72
77-26	1.236	0.019	0.126	0.002	0.586	79	965.5	26.58	763.6	9.64
77-27	1.264	0.020	0.135	0.002	0.577	94	867.7	27.82	815.6	10.29
77-28	1.342	0.024	0.132	0.002	0.515	78	1028.1	32.52	801.3	10.62
77-29	1.245	0.020	0.136	0.002	0.554	101	814.4	29.32	824	10.4
77-30	1.223	0.020	0.131	0.002	0.547	91	865.2	29.61	791.5	10.05
77-31	1.216	0.021	0.133	0.002	0.541	98	818.6	31.11	804	10.43
77-32	1.254	0.022	0.135	0.002	0.526	97	843.9	31.73	818.4	10.6
77-33	1.247	0.021	0.135	0.002	0.546	98	831.3	30.02	818.7	10.37
77-34	1.276	0.022	0.138	0.002	0.530	100	836.8	31.21	834.5	10.62
77-35	2.778	0.053	0.139	0.002	0.491	37	2288.8	29.57	838	11.38
77-36	1.236	0.021	0.135	0.002	0.543	99	822.1	30.61	815.3	10.37
77-37	0.956	0.018	0.100	0.001	0.504	67	917.8	33.94	612.2	8.18
77-38	1.286	0.027	0.136	0.002	0.444	93	886.1	40	822.3	11.25
77-39	1.288	0.030	0.136	0.002	0.360	91	897	45.88	819.2	11.34
77-40	1.261	0.028	0.133	0.002	0.401	89	897.7	43.38	802.8	11.18
77-41	1.369	0.023	0.129	0.002	0.546	70	1118.3	28.85	783	9.97
77-42	1.209	0.026	0.127	0.002	0.398	86	895.8	42.2	773	10.55
77-43	1.422	0.024	0.136	0.002	0.523	76	1084.4	30.08	824.6	10.53
77-44	1.784	0.039	0.139	0.002	0.424	57	1483.3	38.78	841.3	11.93
77-45	1.247	0.022	0.134	0.002	0.515	95	850.3	32.07	811.6	10.39
E14-78										
78-01	0.840	0.019	0.099	0.001	0.354	92	661.4	45.56	607.6	8.09
78-02	0.849	0.017	0.099	0.001	0.390	89	683.7	41.19	607.7	7.93
78-03	0.434	0.009	0.043	0.001	0.395	26	1043	38.91	269	3.7
78-06	0.835	0.021	0.095	0.001	0.280	81	723.6	53.49	587.6	8.19
78-07	0.795	0.017	0.096	0.001	0.373	95	619	45.07	588	7.92
78-08	0.784	0.022	0.088	0.001	0.274	71	761.9	57.52	543.9	8.05
78-09	0.712	0.016	0.083	0.001	0.357	74	690	46.47	512.3	7.04
78-10	0.626	0.017	0.061	0.001	0.249	37	1044.3	53.65	383.1	5.58
78-11	0.795	0.020	0.094	0.001	0.309	88	654.8	52.08	578.5	8.12
78-12	0.733	0.014	0.081	0.001	0.433	63	793.8	36.79	502.2	6.49
78-13	0.481	0.009	0.058	0.001	0.435	59	618.4	39.22	362.1	4.89
78-14	0.568	0.012	0.058	0.001	0.374	38	959.2	42.73	363.2	5.09
78-15	0.526	0.009	0.051	0.001	0.449	31	1047.6	33.19	323.2	4.19
78-16	0.834	0.031	0.099	0.002	0.175	94	648.2	79.77	607	9.82
78-17	0.703	0.017	0.074	0.001	0.334	51	900.8	48.51	459.3	6.61
78-18	0.751	0.015	0.076	0.001	0.403	48	976.9	37.92	472	6.2
78-19	0.774	0.016	0.083	0.001	0.375	61	851.7	40.96	515.7	6.79
78-20	0.613	0.013	0.077	0.001	0.369	90	529.6	46.23	476	6.42
78-21	0.571	0.010	0.057	0.001	0.464	35	1009.8	33.13	356.7	4.58
78-22	0.551	0.012	0.065	0.001	0.365	60	670.1	43.51	403.5	5.4
E14-79										
79-02	0.536	0.008	0.048	0.001	0.525	25	1205.6	26.85	304.8	3.79
79-03	0.841	0.015	0.100	0.001	0.443	95	646.3	36.42	612.3	7.79
79-04	1.326	0.021	0.141	0.002	0.493	97	874.5	30.25	850.7	10.2
79-05	1.297	0.022	0.138	0.002	0.452	95	876.5	32.61	832.4	10.02
79-06	0.827	0.013	0.099	0.001	0.491	96	633.4	31.84	606.1	7.42
79-08	1.298	0.021	0.138	0.002	0.480	96	869.4	31.24	835.7	10.11
79-09	1.306	0.021	0.134	0.002	0.494	86	946.8	30.5	811.2	9.88

Table 1: LA–ICP–MS U–Pb data used to calculate Concordias from the Western Ethiopian Shield

Analysis	$^{207}Pb/^{235}U$		$^{206}Pb/^{238}U$		rho	Conc (%)	$^{207}Pb/^{206}Pb$		$^{206}Pb/^{238}U$	
E14-79										
79-10	1.328	0.028	0.141	0.002	0.375	97	879.5	42.35	849.8	11.22
79-11	1.258	0.020	0.131	0.002	0.514	85	925.8	29.35	791	9.63
79-12	0.935	0.016	0.089	0.001	0.468	49	1107	32.24	547.7	7.02
79-13	1.297	0.021	0.139	0.002	0.485	98	854.3	30.98	840.6	10.15
79-14	27.542	4.433	0.300	0.051	0.198	36	4674.4	272.1	1692.8	252.14
79-15	0.707	0.016	0.079	0.001	0.343	63	774.3	46.04	489.6	6.65
79-16	0.367	0.006	0.033	0.000	0.520	17	1219.2	26.81	208.9	2.58
79-17	1.267	0.026	0.133	0.002	0.371	89	903.7	40.12	804.1	10.16
79-18	1.288	0.028	0.139	0.002	0.348	99	848.1	44.45	837.6	11.13
79-19	1.340	0.025	0.141	0.002	0.409	95	896.8	36.64	850.3	10.55
79-20	1.326	0.022	0.143	0.002	0.484	102	843.3	31.4	862.7	10.36
79-21	0.469	0.010	0.047	0.001	0.354	29	1009.7	42.32	294	4.03
79-22	0.489	0.009	0.047	0.001	0.438	27	1095.5	33.79	294.2	3.82
79-23	0.753	0.017	0.091	0.001	0.334	92	607.8	48.32	560.6	7.54
79-24	0.684	0.015	0.080	0.001	0.328	74	668.3	46.93	497.4	6.74
79-25	0.452	0.010	0.050	0.001	0.344	39	799.6	44.16	314	4.24
79-26	1.139	0.024	0.118	0.002	0.343	78	926.6	42.36	720.3	9.22
79-27	0.223	0.008	0.023	0.000	0.200	16	917.3	70.47	148.2	2.47
79-28	0.472	0.010	0.051	0.001	0.349	37	857	44.19	318.3	4.34
79-29	1.108	0.019	0.116	0.002	0.458	79	902.8	32.4	708.7	8.65
79-30	1.083	0.022	0.105	0.001	0.371	61	1056.8	40.19	645.8	8.4
79-31	1.328	0.025	0.141	0.002	0.409	96	883.7	36.28	848.1	10.46
79-32	1.354	0.027	0.140	0.002	0.393	91	930.9	38.74	845.4	10.72
79-33	1.272	0.025	0.139	0.002	0.389	101	824.7	38.62	836.4	10.45
79-34	1.009	0.019	0.094	0.001	0.414	51	1139.4	34.7	580.3	7.3
79-35	1.211	0.022	0.116	0.002	0.413	65	1087.9	35.08	707.6	8.81
79-36	1.275	0.034	0.136	0.002	0.277	94	873.4	53.82	819.8	11.55
79-37	1.293	0.031	0.138	0.002	0.314	96	868.3	48.39	832.9	11.24
E14-83										
83-01	1.250	0.022	0.132	0.002	0.448	91	882.7	33.95	801.7	9.96
83-02	1.190	0.022	0.121	0.002	0.399	76	970.9	36.11	734.8	9.09
83-03	1.261	0.024	0.136	0.002	0.410	97	848.5	37.66	821	10.31
83-04	1.088	0.016	0.107	0.001	0.543	64	1030.1	25.98	656.9	7.79
83-05	1.293	0.021	0.139	0.002	0.472	99	850.5	31.38	839.8	10.07
83-06	1.271	0.023	0.138	0.002	0.407	101	824	36.12	836.1	10.26
83-07	1.282	0.022	0.138	0.002	0.449	98	851.8	33.57	832.5	10.14
83-08	1.019	0.015	0.095	0.001	0.528	52	1133.7	26.36	587.3	7.02
83-09	1.260	0.022	0.129	0.002	0.463	82	949.7	33.03	783.5	9.72
83-10	1.224	0.021	0.129	0.002	0.440	87	894.3	33.42	782.2	9.55
83-11	1.288	0.022	0.138	0.002	0.470	98	853.3	32.71	835.6	10.23
83-12	1.245	0.021	0.136	0.002	0.471	99	824.6	31.93	819.7	9.93
83-13	1.308	0.024	0.140	0.002	0.392	98	864.8	37.02	843.5	10.33
83-14	1.237	0.022	0.136	0.002	0.448	101	812	34.36	819.5	10.14
83-15	1.292	0.031	0.139	0.002	0.288	99	846.6	49.92	840.4	11.23
83-16	1.176	0.018	0.120	0.002	0.524	76	960.9	27.95	730.1	8.73
83-17	1.302	0.022	0.132	0.002	0.468	82	977.7	32.43	797.9	9.86
83-18	1.253	0.035	0.137	0.002	0.235	101	821.2	58.27	826.1	11.69
83-19	1.322	0.026	0.140	0.002	0.363	96	881.9	40.05	845.3	10.53
83-20	1.299	0.025	0.132	0.002	0.377	83	965.8	38.56	800.1	10.03
83-21	1.353	0.027	0.146	0.002	0.371	103	849.9	39.3	876.3	10.82
83-22	1.303	0.024	0.141	0.002	0.412	102	835.7	36.57	851.3	10.5
83-23	1.227	0.022	0.130	0.002	0.435	90	876.1	35.08	790	9.78
83-24	1.353	0.022	0.140	0.002	0.477	90	938.9	31.22	842	10.12

Table 1: LA–ICP–MS U–Pb data used to calculate Concordias from the Western Ethiopian Shield

Analysis	207Pb/235U		206Pb/238U		rho	Conc (%)	207Pb/206Pb		206Pb/238U	
E14-83										
83-25	1.281	0.025	0.137	0.002	0.395	97	857.8	37.8	829.9	10.34
83-26	1.304	0.023	0.135	0.002	0.438	88	928	34.17	817.1	10.05
83-27	1.301	0.025	0.140	0.002	0.407	98	857.2	37.38	842	10.45
83-28	1.323	0.025	0.142	0.002	0.384	99	860.7	38.11	854	10.5
83-29	1.339	0.024	0.141	0.002	0.424	95	897.3	35.32	849.8	10.38
83-30	1.323	0.023	0.142	0.002	0.454	99	861.7	33.46	853.6	10.34
83-31	1.249	0.024	0.134	0.002	0.398	94	860.1	37.79	809.7	10.1
83-32	1.292	0.024	0.139	0.002	0.420	98	852.8	35.82	838.1	10.32
83-33	1.288	0.026	0.139	0.002	0.367	100	841.4	40.71	840	10.58
83-34	1.327	0.024	0.137	0.002	0.430	89	932.4	35.13	828.7	10.19
83-35	1.307	0.022	0.140	0.002	0.472	99	855.1	31.98	846.5	10.18
83-36	1.314	0.024	0.139	0.002	0.419	94	889.2	36.07	838	10.32
83-37	1.274	0.024	0.136	0.002	0.411	95	865.2	36.86	822.4	10.19
83-38	1.312	0.023	0.138	0.002	0.448	93	898.1	33.04	833.1	10.07
83-39	1.117	0.019	0.098	0.001	0.443	48	1253.6	31.27	604.9	7.4
83-40	1.397	0.024	0.139	0.002	0.450	82	1017.6	33.02	836.3	10.14
83-41	1.385	0.035	0.143	0.002	0.297	93	929.6	50.64	864.1	11.89
83-42	1.315	0.024	0.141	0.002	0.425	98	865	35.77	847.6	10.36
83-43	1.268	0.033	0.138	0.002	0.254	100	830.3	53.41	832.2	11.19
83-44	1.441	0.032	0.130	0.002	0.327	65	1204.5	42.66	788.5	10.19
83-45	1.253	0.043	0.133	0.002	0.168	90	889.3	72.22	802.1	12.54
83-46	1.339	0.027	0.141	0.002	0.384	95	896	38.9	849.9	10.64
83-47	1.310	0.025	0.140	0.002	0.399	98	861.1	37.39	846.1	10.43
83-48	1.334	0.024	0.137	0.002	0.419	88	939.3	35.46	830.3	10.14
83-49	1.360	0.026	0.141	0.002	0.397	92	927.2	37.58	850.6	10.59
83-50	1.123	0.022	0.109	0.001	0.370	63	1064.5	37.89	666.1	8.32
83_44	1.332	0.025	0.143	0.002	0.399	100	856.9	37.04	860.9	10.48
83_45	1.288	0.030	0.139	0.002	0.299	98	849.9	48.26	836.9	10.99
83_46	1.304	0.026	0.138	0.002	0.367	95	882	39.27	834.6	10.34
83_47	1.307	0.028	0.140	0.002	0.354	99	856	42.82	846.5	10.8
83_48	1.260	0.029	0.137	0.002	0.311	100	830.7	46.32	827.1	10.73
83_49	1.661	0.035	0.099	0.001	0.353	31	1977.7	36.16	609.8	8.15
83_50	1.278	0.026	0.138	0.002	0.353	98	846.5	41.42	832.6	10.46
E14-86										
86_01	1.327	0.023	0.141	0.002	0.438	98	872.8	33.44	851.7	10.19
86_02	1.324	0.025	0.140	0.002	0.381	95	887.5	38.06	844.6	10.41
86_03	1.488	0.030	0.136	0.002	0.356	69	1184.5	38.94	821.1	10.58
86_04	1.226	0.024	0.136	0.002	0.367	104	789.1	40.1	821.3	10.24
86_05	1.145	0.020	0.123	0.002	0.437	87	856	33.68	747.2	9.11
86_06	1.184	0.023	0.130	0.002	0.390	97	811.9	38.12	787	9.74
86_07	1.273	0.024	0.134	0.002	0.397	90	898.2	37.14	809.6	10.08
86_08	1.256	0.022	0.135	0.002	0.411	97	847.3	35.32	818.7	9.92
86_09	1.281	0.024	0.135	0.002	0.394	92	889.4	37.26	818	10.04
86_10	1.300	0.027	0.135	0.002	0.354	89	918.7	41.6	818.1	10.54
86_11	1.313	0.028	0.138	0.002	0.330	92	902.7	43.18	832.4	10.61
86_12	1.222	0.026	0.132	0.002	0.347	96	837.5	42.78	801.4	10.17
86_13	1.264	0.021	0.135	0.002	0.468	95	858.5	31.35	819	9.7
86_14	1.177	0.018	0.130	0.002	0.488	99	796.8	30.07	787.7	9.25
86_15	1.240	0.023	0.134	0.002	0.402	96	841.7	36.19	810.5	9.82
86_16	1.231	0.028	0.132	0.002	0.316	92	863.4	45.45	797.2	10.31
86_17	1.239	0.025	0.133	0.002	0.366	95	852.4	40.2	806.1	10.07
86_18	1.212	0.023	0.133	0.002	0.374	100	809.1	38.36	805.2	9.86
86_19	1.264	0.020	0.136	0.002	0.473	97	848.3	31.26	822.7	9.81

Table 1: LA–ICP–MS U–Pb data used to calculate Concordias from the Western Ethiopian Shield

Analysis	$^{207}Pb/^{235}U$		$^{206}Pb/^{238}U$		rho	Conc (%)	$^{207}Pb/^{206}Pb$		$^{206}Pb/^{238}U$	
E14-86										
86_20	1.250	0.022	0.136	0.002	0.414	99	828.4	35.47	821.9	9.98
86_21	1.318	0.027	0.141	0.002	0.344	98	868.7	41.18	848	10.56
86_22	1.299	0.026	0.140	0.002	0.377	99	850	40.26	843.7	10.64
86_23	1.267	0.034	0.135	0.002	0.251	95	865.4	54.81	818.4	11.32
86_24	1.271	0.025	0.134	0.002	0.380	91	893.9	38.44	810.4	10.08
86_25	1.283	0.025	0.137	0.002	0.380	97	859.1	38.42	830.4	10.24
86_26	1.289	0.024	0.138	0.002	0.391	96	868.6	36.92	830.7	10.15
86_27	1.268	0.024	0.137	0.002	0.401	97	848.7	37.04	825.5	10.09
86_28	1.232	0.027	0.133	0.002	0.340	96	837.4	43.61	807.5	10.33
86_29	1.287	0.026	0.135	0.002	0.377	91	901.7	40.75	816.6	10.5
86_30	1.287	0.022	0.139	0.002	0.432	101	837	34.24	841.3	10.08
86_31	1.268	0.024	0.135	0.002	0.392	93	875.9	36.83	815	9.92
86_32	1.301	0.024	0.137	0.002	0.404	93	894	36.56	828.3	10.14
86_33	1.233	0.023	0.131	0.002	0.391	91	873.4	37.54	795.2	9.79
86_34	1.270	0.024	0.136	0.002	0.398	95	867.3	37.18	819.7	10.04
86_35	1.203	0.032	0.133	0.002	0.262	103	787.1	55.86	807.4	11.22
86_36	1.239	0.025	0.134	0.002	0.360	97	835.7	40.9	812.5	10.18
86_37	1.301	0.025	0.138	0.002	0.382	94	886.1	37.7	831.2	10.21
86_38	1.635	0.064	0.128	0.003	0.163	53	1478.5	75.43	777.3	14.27
86_39	1.263	0.035	0.140	0.002	0.278	108	784.8	56.39	845.8	12.07
86_40	1.217	0.032	0.135	0.002	0.265	103	789	54.58	815.5	11.1
86_41	1.238	0.023	0.136	0.002	0.391	101	813.9	37.3	819.9	10.01
86_42	1.291	0.028	0.136	0.002	0.329	92	891.1	43.64	823.4	10.43
86_43	1.277	0.028	0.136	0.002	0.320	93	880.7	44.98	819.2	10.57
E14-87										
87_01	1.232	0.027	0.137	0.002	0.337	105	786.5	44.43	826.4	10.57
87_02	1.218	0.026	0.131	0.002	0.351	92	856.9	42.24	791.9	10.05
87_03	1.202	0.031	0.132	0.002	0.254	98	813.8	54.18	797.3	10.91
87_04	1.189	0.022	0.130	0.002	0.411	96	820.6	35.96	786.7	9.65
87_05	1.060	0.021	0.112	0.002	0.374	77	885.7	38.86	685.3	8.69
87_06	1.181	0.023	0.129	0.002	0.397	96	816.1	38.13	783.6	9.73
87_07	1.240	0.024	0.129	0.002	0.380	86	914.7	38.96	784.6	9.87
87_08	1.210	0.022	0.129	0.002	0.410	91	864.8	36.69	783.9	9.68
87_09	1.244	0.036	0.134	0.002	0.224	95	853.3	59.71	808.7	11.57
87_10	1.225	0.028	0.132	0.002	0.298	95	840.9	47	801.9	10.42
87_11	1.222	0.033	0.132	0.002	0.247	96	835.7	56.31	801.5	11.13
87_12	1.263	0.028	0.135	0.002	0.313	94	868	45.62	815.1	10.54
87_13	1.188	0.029	0.134	0.002	0.287	108	751.3	50.22	810.7	10.67
87_14	1.223	0.035	0.129	0.002	0.227	88	888.8	59.99	783.3	11.28
87_15	1.231	0.039	0.130	0.002	0.201	88	893.2	65.86	786.4	11.82
87_16	1.199	0.032	0.128	0.002	0.242	89	870.1	55.53	775.2	10.75
87_17	1.142	0.021	0.121	0.002	0.420	84	876.6	36.09	738.5	9.17
87_18	1.240	0.026	0.134	0.002	0.359	96	846.5	42.53	809.2	10.41
87_19	1.206	0.023	0.131	0.002	0.391	95	832	37.49	793.4	9.81
87_20	1.255	0.024	0.131	0.002	0.382	88	908.3	37.76	795.4	9.86
87_21	1.168	0.024	0.129	0.002	0.354	99	790.5	41.6	784.3	9.91
87_22	1.234	0.029	0.128	0.002	0.291	84	922.5	48.31	778.3	10.34
87_23	1.273	0.027	0.139	0.002	0.339	104	812.8	43.71	841.7	10.71
87_24	1.270	0.026	0.134	0.002	0.350	91	894	41.84	810	10.29
87_25	1.270	0.020	0.139	0.002	0.495	103	813	29.33	840.1	9.79
87_26	1.235	0.024	0.135	0.002	0.376	100	818.1	39.6	816.1	10.13
87_27	1.197	0.035	0.132	0.002	0.226	100	798.9	60.82	799.7	11.45
87_28	1.051	0.021	0.116	0.002	0.380	88	802.8	39.34	706	8.81

Table 1: LA–ICP–MS U–Pb data used to calculate Concordias from the Western Ethiopian Shield

Analysis	$^{207}Pb/^{235}U$		$^{206}Pb/^{238}U$		rho	Conc (%)	$^{207}Pb/^{206}Pb$		$^{206}Pb/^{238}U$	
E14-87										
87_29	0.983	0.018	0.105	0.001	0.424	75	863.7	35.47	644.4	8
87_30	1.225	0.025	0.133	0.002	0.361	97	830.7	40.75	805.4	10.06
87_31	1.164	0.027	0.128	0.002	0.305	96	809	48.45	775.2	10.2
87_32	1.245	0.023	0.136	0.002	0.397	100	824.2	37.15	820.1	10.05
87_33	1.234	0.024	0.133	0.002	0.382	94	851.9	38.7	803.2	9.96
87_34	1.041	0.022	0.112	0.002	0.345	80	857.9	41.94	682.2	8.73
87_35	1.209	0.025	0.130	0.002	0.356	93	846.3	41.58	790	9.98
87_36	1.119	0.019	0.114	0.001	0.439	72	961.6	32.91	696.5	8.46
87_37	1.192	0.026	0.131	0.002	0.332	98	807.8	44.79	793.3	10.2
87_38	1.240	0.025	0.132	0.002	0.356	91	874.3	41.13	798.5	10.09
87_39	1.109	0.033	0.124	0.002	0.214	98	769.8	63.02	753.9	10.93
87_40	1.205	0.024	0.130	0.002	0.361	93	844.2	39.91	788.4	9.82
87_41	1.196	0.028	0.132	0.002	0.295	100	798.5	48.82	798.8	10.52
87_42	1.308	0.033	0.128	0.002	0.272	74	1043.7	50.53	776.7	10.66
87_43	1.227	0.028	0.133	0.002	0.301	97	834.1	47.33	805.6	10.46
87_44	1.227	0.030	0.132	0.002	0.289	94	853.4	49.35	798.4	10.56
87_45	1.181	0.033	0.129	0.002	0.233	95	822.3	58.99	781.3	11.02
87_46	1.209	0.025	0.130	0.002	0.343	92	853	41.27	787.4	9.83
87_47	1.275	0.030	0.137	0.002	0.290	96	861.4	48.7	825	10.86
87_48	1.275	0.026	0.140	0.002	0.357	104	808.4	40.89	844.7	10.5
87_49	1.264	0.028	0.138	0.002	0.317	102	820.6	45.11	833.5	10.66
87_50	1.229	0.028	0.132	0.002	0.310	94	850.8	46.5	800.5	10.39
E14-96										
96-01	1.262	0.022	0.136	0.002	0.496	98	842.8	32.15	823.5	10.32
96-02	1.267	0.022	0.137	0.002	0.518	98	846	31.54	825.7	10.47
96-03	1.314	0.021	0.140	0.002	0.542	96	876.5	29.06	842.5	10.46
96-04	1.273	0.021	0.135	0.002	0.523	93	877.4	30.55	817.7	10.27
96-05	0.957	0.017	0.085	0.001	0.517	43	1227.5	30.43	528.5	6.93
96-06	1.024	0.017	0.098	0.001	0.527	56	1083.5	29.45	604.5	7.75
96-07	1.234	0.020	0.118	0.002	0.531	65	1097.7	29.07	716.8	9.07
96-08	1.471	0.027	0.152	0.002	0.484	97	935.3	33.93	911.8	11.63
96-09	1.435	0.025	0.149	0.002	0.513	97	925.6	31.3	894.9	11.28
96-10	1.231	0.026	0.129	0.002	0.394	85	913	40.94	779.4	10.18
96-11	1.340	0.027	0.133	0.002	0.410	79	1013.7	38.54	805.8	10.44
96-12	1.095	0.025	0.108	0.002	0.379	64	1033.5	43.96	659.8	9.42
96-13	1.132	0.021	0.117	0.002	0.473	77	932	34.59	713.8	9.29
96-14	0.936	0.019	0.103	0.001	0.446	78	809.7	39.15	629.9	8.68
96-15	1.096	0.021	0.117	0.002	0.455	83	860.3	37.24	715.6	9.43
96-16	1.274	0.032	0.133	0.002	0.336	89	908	49.84	806.8	11.2
96-17	0.953	0.041	0.080	0.002	0.222	37	1341.9	82.27	497.4	9.68
96-18	0.399	0.010	0.030	0.000	0.327	12	1564.7	47	190	2.89
E14-97										
97-01	0.917	0.015	0.106	0.001	0.557	92	705.7	29.36	647.6	8.33
97-02	0.909	0.014	0.105	0.001	0.555	93	696.1	28.91	645.1	8.08
97-03	0.459	0.007	0.028	0.000	0.581	9	1917.3	22.77	180.2	2.32
97-04	0.933	0.021	0.110	0.002	0.365	102	657.3	45.43	672.7	8.99
97-05	0.778	0.013	0.093	0.001	0.514	90	633.3	31.77	572.1	7.49
97-06	1.251	0.020	0.086	0.001	0.540	31	1724.5	26.31	531.5	7.06
97-07	0.884	0.014	0.101	0.001	0.526	85	729.3	30.78	619	7.8
97-08	0.583	0.011	0.054	0.001	0.491	30	1145.2	32.46	340.5	4.66
97-09	0.894	0.015	0.100	0.001	0.490	81	760.6	32.91	616.7	7.86
97-10	0.883	0.017	0.106	0.002	0.435	106	613.1	39.51	651.2	8.8
97-11	0.886	0.018	0.105	0.001	0.405	99	648.6	41.64	643.2	8.5

Table 1: LA–ICP–MS U–Pb data used to calculate Concordias from the Western Ethiopian Shield

Analysis	$^{207}Pb/^{235}U$		$^{206}Pb/^{238}U$		rho	Conc (%)	$^{207}Pb/^{206}Pb$		$^{206}Pb/^{238}U$	
E14-97										
97-12	0.840	0.019	0.097	0.001	0.359	84	710.6	46.86	594.3	8.26
97-13	0.905	0.017	0.103	0.001	0.474	85	738.1	35.44	630.5	8.23
97-14	0.894	0.018	0.099	0.001	0.433	76	798.6	38.66	605.9	8.14
97-15	0.239	0.009	0.011	0.000	0.171	3	2493.5	64.41	68.1	1.51
97-16	0.770	0.013	0.092	0.001	0.523	90	630.6	31.45	567	7.37
97-17	0.918	0.020	0.106	0.002	0.393	93	696.5	42.78	651.1	8.85
97-18	0.939	0.026	0.109	0.002	0.291	96	692.9	58.69	666.3	10
97-19	0.921	0.020	0.108	0.002	0.391	98	671.5	44.12	660.5	8.99
97-20	0.726	0.015	0.079	0.001	0.381	59	828	41.26	490.2	6.56
97-21	0.721	0.013	0.082	0.001	0.470	68	740.6	34.99	506.5	6.74
97-22	0.747	0.014	0.084	0.001	0.439	70	745.9	36.17	522.6	6.77
97-23	0.903	0.021	0.108	0.002	0.323	104	632.6	49.19	659.6	8.86
97-24	0.942	0.016	0.107	0.001	0.487	90	732.5	32.82	656.8	8.27
97-25	0.890	0.026	0.109	0.002	0.250	118	568.5	62.42	668.7	9.79
97-26	0.935	0.019	0.108	0.001	0.403	94	703.1	40.47	660.8	8.62
97-27	0.651	0.011	0.069	0.001	0.512	49	879.6	30.3	430.2	5.46
97-28	0.918	0.020	0.106	0.001	0.357	91	708.5	44.12	647.7	8.54
97-29	0.792	0.023	0.093	0.001	0.246	85	673.4	61.4	571.2	8.3
97-30	0.897	0.017	0.106	0.001	0.425	98	659.4	38.53	647.6	8.35
97-31	0.761	0.016	0.079	0.001	0.350	52	931.9	42.42	488.4	6.48
97-32	0.901	0.015	0.105	0.001	0.501	95	676.4	31.9	645.2	8.08
97-33	0.910	0.017	0.104	0.001	0.444	87	733.6	36.25	635.1	8.12
97-34	0.983	0.017	0.111	0.001	0.465	91	743.5	33.82	680.3	8.56
97-35	0.791	0.013	0.087	0.001	0.493	66	808	31.78	537.2	6.72
97-36	0.948	0.017	0.113	0.002	0.443	110	629	36.82	691.4	8.79
97-37	0.896	0.017	0.105	0.001	0.431	98	661.8	37.16	646	8.15
97-38	0.926	0.021	0.110	0.002	0.340	105	641.1	47.39	672.5	9.14
97-39	0.503	0.008	0.039	0.001	0.479	16	1500.7	28.99	246.5	3.2
97-40	0.775	0.019	0.089	0.001	0.302	76	722.5	51.17	547.1	8
97-41	0.932	0.018	0.109	0.001	0.419	99	676.5	38.51	666.7	8.56
97-42	0.935	0.022	0.110	0.002	0.323	103	653.7	48.26	675	8.96
97-43	0.947	0.027	0.111	0.002	0.244	103	662.8	60.34	681.3	9.68
97-44	0.950	0.022	0.109	0.002	0.341	95	707	46.59	669.2	8.94
E14-100										
100-01	0.925	0.017	0.108	0.001	0.383	97	678.9	38.22	661	8.15
100-02	0.878	0.017	0.106	0.001	0.382	107	606.7	39.54	649.3	8.08
100-03	0.876	0.018	0.107	0.002	0.318	113	580.6	45.42	655.6	8.71
100-04	0.878	0.018	0.103	0.001	0.334	96	661.2	44.08	634.1	8.38
100-05	0.857	0.015	0.101	0.001	0.444	93	662.6	34.09	618.8	7.51
100-06	0.906	0.017	0.109	0.001	0.391	108	618.4	39.13	665.9	8.27
100-07	0.874	0.018	0.104	0.001	0.354	98	645.3	43.8	635.3	8.15
100-08	0.390	0.008	0.027	0.000	0.367	10	1721	35.15	170.6	2.2
100-09	0.908	0.019	0.103	0.001	0.368	86	738.4	41.64	632.6	7.99
100-11	0.902	0.017	0.107	0.001	0.390	103	636	39.66	658.1	8.28
100-12	1.018	0.027	0.037	0.001	0.293	8	2826.9	42.97	233.7	3.61
E14-113										
113-01	1.072	0.020	0.119	0.002	0.367	93	778.2	38.17	727.3	8.84
113-02	0.976	0.017	0.100	0.001	0.402	65	945.7	34.02	616.5	7.53
113-03	1.042	0.019	0.116	0.002	0.388	91	780	37.71	707.4	8.69
113-04	0.936	0.017	0.107	0.001	0.390	90	728.3	36.77	654.2	8.03
113-05	0.947	0.020	0.106	0.001	0.305	83	776.3	43.55	647.6	8.05
113-06	1.063	0.019	0.119	0.002	0.408	94	771.4	36.36	723.7	8.82
113-07	1.008	0.023	0.117	0.002	0.280	102	696.4	48.1	711.9	9.04

Table 1: LA–ICP–MS U–Pb data used to calculate Concordias from the Western Ethiopian Shield

Analysis	$^{207}Pb/^{235}U$		$^{206}Pb/^{238}U$		rho	Conc (%)	$^{207}Pb/^{206}Pb$		$^{206}Pb/^{238}U$	
E14-113										
113-08	0.958	0.019	0.107	0.001	0.339	84	781.5	41.17	653.1	8.01
113-09	0.896	0.019	0.064	0.001	0.297	24	1645.9	40.34	401.3	5.51
113-10	0.787	0.015	0.078	0.001	0.372	48	1016.2	37.18	484.9	6.26
113-11	1.004	0.019	0.112	0.001	0.381	89	772.7	39.18	684.9	8.54
113-12	0.994	0.022	0.115	0.002	0.309	101	696.7	46.5	702.7	9.24
113-13	1.047	0.021	0.116	0.002	0.358	91	782.4	40.41	709.7	8.8
113-14	1.036	0.018	0.120	0.002	0.403	105	697.7	35.81	730.1	8.78
113-15	1.044	0.019	0.116	0.002	0.378	90	783.3	37.71	707.7	8.66
113-16	0.937	0.030	0.108	0.002	0.219	92	714.7	66.7	659	10.09
113-17	1.031	0.024	0.113	0.002	0.305	85	813.3	47.7	689.7	9.05
113-18	1.063	0.021	0.115	0.002	0.368	83	844.5	39.83	700	8.71
113-19	1.049	0.021	0.111	0.001	0.359	76	889.5	39.36	677	8.42
113-20	1.034	0.021	0.111	0.001	0.346	79	859.4	41.02	677.5	8.47
113-21	1.192	0.026	0.127	0.002	0.329	87	878.7	43.88	768.4	9.82
113-22	1.178	0.027	0.128	0.002	0.303	92	837.7	47.33	773.9	10.13
113-23	1.122	0.025	0.127	0.002	0.318	104	742.3	47	771.3	9.93
113-24	1.178	0.028	0.128	0.002	0.303	92	838.1	47.7	773.9	10.09
113-25	1.115	0.021	0.122	0.002	0.405	91	814.7	37.12	742.3	9.14
113-26	1.041	0.022	0.121	0.002	0.357	107	689.9	44.25	735.8	9.63
113-27	0.892	0.033	0.086	0.002	0.175	50	1069	74.97	533.6	9.17
113-28	1.104	0.024	0.122	0.002	0.341	94	793.5	44.56	742.8	9.51
113-29	1.011	0.027	0.118	0.002	0.279	107	672.9	56.2	721	10.3
113-30	1.045	0.023	0.108	0.002	0.353	70	938.9	43.78	659.4	8.86
113-31	1.083	0.026	0.118	0.002	0.323	88	816	48.16	721.4	9.85
113-32	1.043	0.024	0.107	0.001	0.321	69	948.6	44.95	655.1	8.61
113-33	1.099	0.023	0.123	0.002	0.353	97	770.5	43.23	746.9	9.49
113-34	1.297	0.024	0.121	0.002	0.415	65	1132.2	35.45	739	9.2
113-35	0.815	0.019	0.088	0.001	0.347	66	833.3	47.06	546.4	7.49
113-36	1.027	0.022	0.116	0.002	0.351	95	743.6	44.46	709.3	9.41
E14-115										
115-01	0.796	0.013	0.085	0.001	0.432	61	859.8	31.58	527.8	6.25
115-02	0.929	0.017	0.094	0.001	0.368	58	987.2	35.31	576.6	7.03
115-03	0.755	0.012	0.065	0.001	0.437	31	1304.6	29.5	405	4.9
115-04	0.910	0.019	0.098	0.001	0.328	71	845.3	42.52	604.1	7.62
115-05	0.820	0.022	0.092	0.001	0.239	76	752.4	56.73	569.6	8.16
115-06	0.842	0.014	0.070	0.001	0.423	32	1364.5	29.99	436.6	5.25
115-07	1.138	0.020	0.095	0.001	0.391	43	1361.1	33.02	584.4	7.2
115-08	0.885	0.017	0.095	0.001	0.350	69	852.4	39.97	585.7	7.31
115-09	0.695	0.012	0.079	0.001	0.383	65	747.9	35.81	487.6	5.78
115-10	0.814	0.015	0.094	0.001	0.381	82	706.9	36.72	577.5	6.91
115-11	0.869	0.019	0.084	0.001	0.303	48	1075.4	43.31	518.1	6.98
115-12	0.922	0.017	0.094	0.001	0.367	60	968.9	35.9	576.9	6.87
115-13	1.049	0.025	0.079	0.001	0.266	32	1556.1	45.52	490.3	6.94
115-14	0.805	0.019	0.093	0.001	0.273	81	708.5	49.43	571.2	7.74
115-15	0.815	0.019	0.085	0.001	0.269	58	904.4	49.52	527.8	7.38
115-16	0.869	0.017	0.082	0.001	0.354	45	1129.5	38.43	505.6	6.44
115-17	0.856	0.014	0.097	0.001	0.430	80	747.7	33.59	595.4	7.08
115-18	0.820	0.015	0.097	0.001	0.362	91	655.5	39.16	595.7	7.25
115-19	0.708	0.017	0.084	0.001	0.288	81	641.3	50.32	520.8	7.04
115-20	1.158	0.026	0.100	0.001	0.297	48	1291.8	43.66	614.3	8.49
115-21	0.834	0.016	0.101	0.001	0.371	103	601.6	39.67	619.5	7.51
115-22	0.812	0.015	0.097	0.001	0.400	94	631.2	36.89	596.1	7.16
115-23	0.846	0.018	0.098	0.001	0.334	88	688.2	43.7	604.5	7.67

Table 1: LA–ICP–MS U–Pb data used to calculate Concordias from the Western Ethiopian Shield

Analysis	$^{207}Pb/^{235}U$		$^{206}Pb/^{238}U$		rho	Conc (%)	$^{207}Pb/^{206}Pb$		$^{206}Pb/^{238}U$	
E14-115										
115-24	1.101	0.018	0.092	0.001	0.448	41	1366.1	29.06	564.5	6.69
115-25	0.815	0.013	0.079	0.001	0.449	46	1057.6	30.38	491.5	5.84
115-26	0.823	0.017	0.081	0.001	0.317	49	1032.8	42.25	501.9	6.37
115-27	0.779	0.018	0.089	0.001	0.296	75	730.8	49.62	548.2	7.53
115-28	0.486	0.008	0.048	0.001	0.419	30	1012.9	32.69	304.4	3.71
115-29	0.811	0.015	0.096	0.001	0.395	93	640.8	37.73	593.4	7.18
115-30	0.841	0.019	0.097	0.001	0.306	85	704.7	48.24	597	7.92
115-31	0.815	0.014	0.098	0.001	0.410	96	623.4	35.8	600.7	7.2
115-32	0.801	0.020	0.090	0.001	0.283	73	762.9	52.59	555.1	7.81
115-33	0.832	0.015	0.088	0.001	0.411	60	895.4	34.27	541.6	6.59
115-34	0.859	0.022	0.101	0.002	0.264	94	661.7	54.84	620.6	8.79
115-35	0.897	0.019	0.092	0.001	0.351	61	939.8	42.2	570.2	7.48
115-36	0.943	0.019	0.100	0.001	0.358	69	886.3	40.17	612.7	7.62
115-37	0.851	0.029	0.082	0.001	0.199	48	1065.5	68.94	510.5	8.8
115-38	0.833	0.015	0.087	0.001	0.430	59	909	33.87	538.8	6.56
115-39	0.857	0.017	0.102	0.001	0.363	99	632.3	41.09	627.3	7.76
115-40	0.894	0.020	0.102	0.001	0.336	85	735.4	45.44	623.8	8.22
115-41	0.868	0.019	0.102	0.001	0.336	96	655.3	46.35	628.8	8.2
115-42	1.042	0.026	0.098	0.001	0.296	54	1120.9	48.02	603.9	8.14
115-43	0.822	0.015	0.093	0.001	0.414	78	736.8	35.91	575.6	7.03
115-44	0.870	0.020	0.102	0.001	0.323	96	658.4	47.54	629	8.39

Table 2: LA–MC–ICP-MS Lu–Hf isotopes (zircon) from the Western Ethiopian Shield

Sample Name	Hf^{176}/Hf^{177}	2 S.E.	Lu^{176}/Hf^{177}	Yb^{176}/Hf^{177}	U/Pb AGE	Hfi	epsilon	1s	T (DM) Ga	T(DM) Crustal	Hf Chur (t)	Hf DM (t)
E14-02												
02_01	0.28256	2.00E-05	0.00086	0.02575	618	0.28255	5.58	0.7	0.97	1.18	0.28240	0.28281
02_03	0.28258	1.67E-05	0.00080	0.02215	645	0.28257	6.73	0.6	0.95	1.13	0.28238	0.28279
02_09	0.28257	1.51E-05	0.00086	0.02557	654	0.28256	6.65	0.5	0.96	1.14	0.28237	0.28278
02_17	0.28256	2.60E-05	0.00113	0.03915	686	0.28254	6.71	0.9	0.99	1.17	0.28235	0.28276
02_21	0.28255	3.07E-05	0.00094	0.02495	679	0.28253	6.26	1.1	1.00	1.19	0.28236	0.28276
02_30	0.28260	1.97E-05	0.00251	0.06736	689	0.28257	7.76	0.7	0.96	1.10	0.28235	0.28275
E14-04												
04_02	0.28243	2.88E-05	0.00076	0.01806	663	0.28242	1.94	1.0	1.15	1.45	0.28237	0.28277
04_06	0.28243	2.32E-05	0.00065	0.01920	872	0.28242	6.71	0.8	1.15	1.31	0.28223	0.28262
04_10	0.28245	2.28E-05	0.00054	0.01511	842	0.28244	6.49	0.8	1.13	1.30	0.28225	0.28264
04_12	0.28242	1.88E-05	0.00064	0.01837	855	0.28241	5.86	0.7	1.17	1.35	0.28224	0.28263
04_17	0.28249	2.28E-05	0.00075	0.01713	897	0.28248	9.20	0.8	1.07	1.18	0.28222	0.28260
04_18	0.28245	2.36E-05	0.00065	0.01939	834	0.28244	6.51	0.8	1.12	1.29	0.28226	0.28265
04_19	0.28246	2.38E-05	0.00056	0.01239	692	0.28245	3.54	0.8	1.11	1.37	0.28235	0.28275
04_23	0.28244	2.36E-05	0.00055	0.01661	873	0.28243	6.92	0.8	1.14	1.30	0.28223	0.28262
04_26	0.28244	2.40E-05	0.00074	0.02219	838	0.28243	6.22	0.8	1.14	1.32	0.28226	0.28265
04_27	0.28245	2.30E-05	0.00049	0.01065	784	0.28245	5.51	0.8	1.12	1.32	0.28229	0.28269
04_31	0.28246	2.22E-05	0.00054	0.01510	860	0.28245	7.42	0.8	1.11	1.26	0.28224	0.28263
04_34	0.28251	2.01E-05	0.00052	0.01077	885	0.28250	9.71	0.7	1.04	1.13	0.28223	0.28261
E13-38												
38_01	0.28250	2.97E-05	0.00048	0.01116	881	0.28249	9.34	1.0	1.05	1.15	0.28223	0.28261
38_03	0.28246	4.12E-05	0.00117	0.02206	826	0.28245	6.48	1.4	1.12	1.29	0.28226	0.28266
38_06	0.28252	2.02E-05	0.00055	0.01525	812	0.28251	8.52	0.7	1.02	1.15	0.28227	0.28267
38_09	0.28252	2.65E-05	0.00072	0.01858	803	0.28250	8.02	0.9	1.04	1.18	0.28228	0.28267
38_13	0.28252	2.83E-05	0.00086	0.02458	799	0.28251	8.09	1.0	1.03	1.17	0.28228	0.28267
38_16	0.28251	2.40E-05	0.00079	0.02329	810	0.28250	8.03	0.8	1.04	1.18	0.28227	0.28267
38_18	0.28253	2.65E-05	0.00080	0.02471	871	0.28252	10.00	0.9	1.02	1.11	0.28223	0.28262
38_22	0.28254	2.76E-05	0.00078	0.01726	826	0.28252	9.22	1.0	1.01	1.12	0.28226	0.28266

CHUR from Bouvier et al. (2008); Earth and Planetary Science Letters 273 (2008) 48–57

CHUR 176Lu/177Hf = 0.0336±1 and 176Hf/177Hf = 0.282785±11

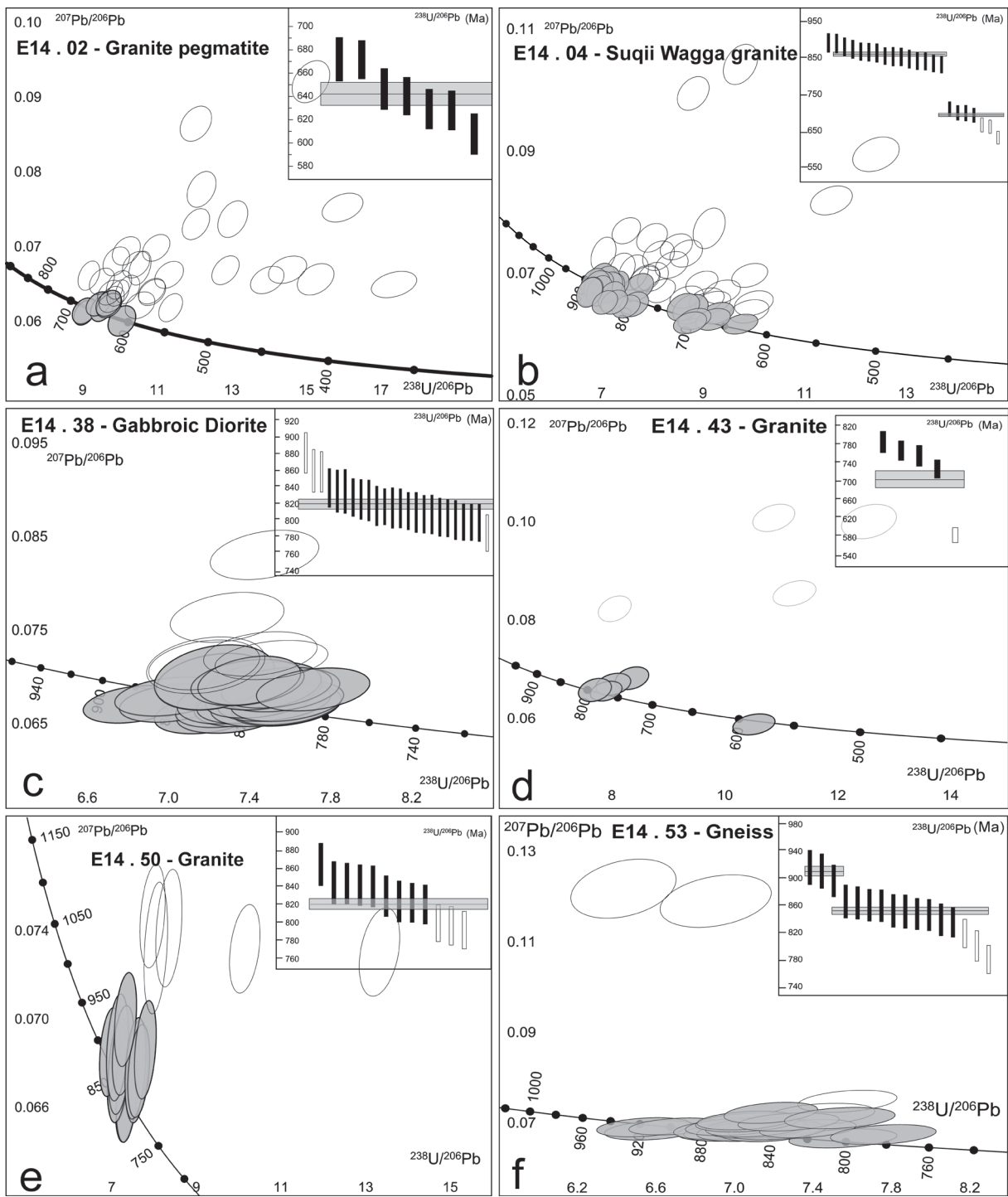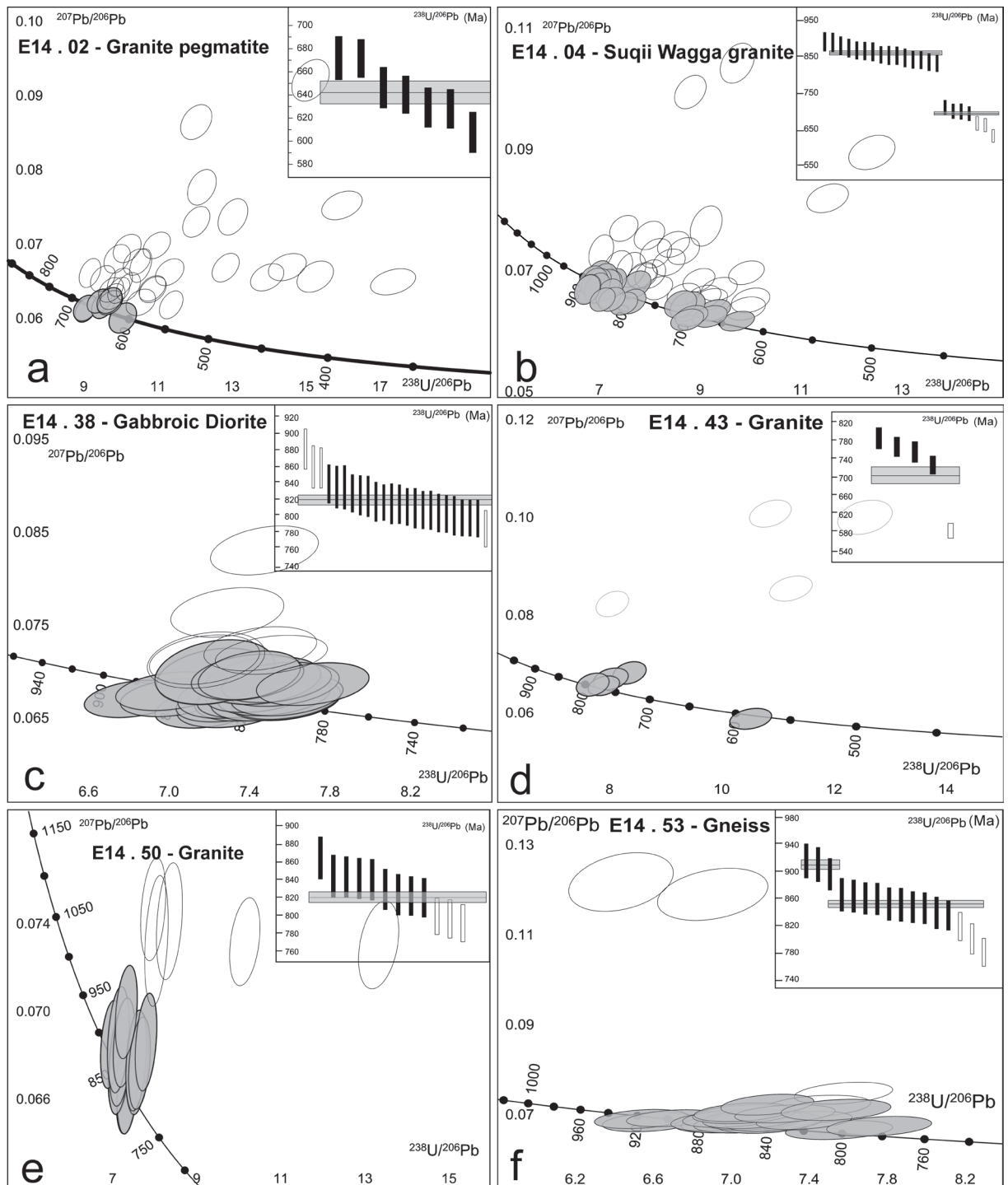**Hfi = 176Hf/177Hf ratio - (176Lu/177Hf ratio * (EXP(0.0193 * 207Pb/206Pb ratio / 1000)-1))**

Table 2: LA–MC–ICP-MS Lu–Hf isotopes (zircon) from the Western Ethiopian Shield

Sample Name	Hf^{176}/Hf^{177}	2 S.E.	Lu^{176}/Hf^{177}	Yb^{176}/Hf^{177}	U/Pb AGE	Hfi	epsilon	1s	T (DM) Ga	T(DM) Crustal	Hf Chur (t)	Hf DM (t)
E14-43												
43_05	0.28254	3.22E-05	0.00194	0.07022	794	0.28251	7.89	1.1	1.04	1.18	0.28228	0.28268
43_08	0.28261	4.70E-05	0.00271	0.11207	838	0.28256	10.92	1.6	0.96	1.02	0.28226	0.28265
43_10	0.28254	3.06E-05	0.00164	0.05889	876	0.28251	9.97	1.1	1.03	1.11	0.28223	0.28262
43_12	0.28253	2.95E-05	0.00160	0.05812	801	0.28251	8.04	1.0	1.04	1.17	0.28228	0.28267
E14-50												
50_02	0.28247	2.28E-05	0.00033	0.01408	854	0.28247	7.82	0.8	1.08	1.23	0.28225	0.28263
50_04	0.28248	3.08E-05	0.00135	0.05503	885	0.28246	8.19	1.1	1.10	1.23	0.28223	0.28261
50_07	0.28245	2.90E-05	0.00069	0.02339	865	0.28244	7.01	1.0	1.13	1.29	0.28224	0.28263
50_08	0.28250	2.86E-05	0.00154	0.05621	848	0.28247	7.84	1.0	1.09	1.22	0.28225	0.28264
50_09	0.28247	2.64E-05	0.00054	0.01894	858	0.28246	7.69	0.9	1.10	1.24	0.28224	0.28263
50_10	0.28245	2.22E-05	0.00042	0.01617	862	0.28245	7.35	0.8	1.11	1.26	0.28224	0.28263
50_12	0.28251	4.26E-05	0.00209	0.07390	887	0.28247	8.74	1.5	1.09	1.20	0.28222	0.28261
50_13	0.28248	2.34E-05	0.00084	0.03345	888	0.28247	8.60	0.8	1.09	1.21	0.28222	0.28261
50_14	0.28249	2.86E-05	0.00072	0.02781	827	0.28248	7.80	1.0	1.06	1.21	0.28226	0.28265
50_19	0.28252	2.27E-05	0.00064	0.01819	825	0.28251	8.58	0.8	1.03	1.16	0.28226	0.28266
E14-63												
63_01	0.28244	3.80E-05	0.00292	0.11200	764	0.28240	3.43	1.3	1.21	1.43	0.28230	0.28270
63_03	0.28244	2.81E-05	0.00154	0.05697	797	0.28241	4.70	1.0	1.17	1.38	0.28228	0.28268
63_06	0.28244	3.98E-05	0.00212	0.06829	765	0.28241	3.64	1.4	1.19	1.42	0.28230	0.28270
63_09	0.28247	1.04E-04	0.00281	0.07910	778	0.28243	4.85	3.6	1.16	1.35	0.28229	0.28269
63_11	0.28252	5.68E-05	0.00306	0.13825	762	0.28248	6.09	2.0	1.10	1.26	0.28230	0.28270
63_13	0.28246	5.61E-05	0.00148	0.05044	761	0.28244	4.87	2.0	1.13	1.34	0.28230	0.28270
63_15	0.28251	3.90E-05	0.00228	0.07478	795	0.28247	6.79	1.4	1.09	1.25	0.28228	0.28268
63_19	0.28251	4.53E-05	0.00139	0.04462	703	0.28249	5.17	1.6	1.07	1.28	0.28234	0.28274
63_20	0.28245	4.91E-05	0.00141	0.04502	770	0.28242	4.46	1.7	1.15	1.37	0.28230	0.28270
63_25	0.28245	5.49E-05	0.00177	0.04710	783	0.28242	4.61	1.9	1.16	1.37	0.28229	0.28269

CHUR from Bouvier et al. (2008); Earth and Planetary Science Letters 273 (2008) 48–57

CHUR 176Lu/177Hf = 0.0336±1 and 176Hf/177Hf = 0.282785±11

*Hfi = 176Hf/177Hf ratio - (176Lu/177Hf ratio * (EXP(0.0193 * 207Pb/206Pb ratio / 1000)-1))*

Table 2: LA–MC–ICP-MS Lu–Hf isotopes (zircon) from the Western Ethiopian Shield

Sample Name	Hf^{176}/Hf^{177}	2 S.E.	Lu^{176}/Hf^{177}	Yb^{176}/Hf^{177}	U/Pb AGE	Hfi	epsilon	1s	T (DM) Ga	T(DM) Crustal	Hf Chur (t)	Hf DM (t)
E14-64												
64_04	0.282555	0.000028	0.001239	0.045224	782	0.28254	8.70	1.0	0.99	1.12	0.28229	0.28269
64_05	0.282527	0.000032	0.001401	0.055409	834	0.28251	8.75	1.1	1.04	1.15	0.28226	0.28265
64_07	0.282583	0.000279	0.001693	0.068939	792	0.28256	9.67	9.8	0.97	1.06	0.28229	0.28268
64_11	0.282575	0.000046	0.003012	0.128323	850	0.28253	9.87	1.6	1.01	1.10	0.28225	0.28264
64_16	0.282525	0.000049	0.001535	0.050139	811	0.28250	8.11	1.7	1.04	1.18	0.28227	0.28267
64_18	0.282520	0.000050	0.001746	0.061841	845	0.28249	8.55	1.8	1.06	1.18	0.28225	0.28264
64_27	0.282526	0.000042	0.001265	0.052471	812	0.28251	8.31	1.5	1.04	1.16	0.28227	0.28267
64_33	0.282490	0.000040	0.002985	0.121196	853	0.28244	6.94	1.4	1.14	1.28	0.28225	0.28264
64_34	0.282557	0.000040	0.002262	0.091245	791	0.28252	8.40	1.4	1.02	1.14	0.28229	0.28268
E14-68												
68_01	0.282482	0.000034	0.001641	0.056236	835	0.28246	7.02	1.2	1.11	1.26	0.28226	0.28265
68_02	0.282482	0.000034	0.001641	0.056236	835	0.28246	7.02	1.2	1.11	1.26	0.28226	0.28265
68_08	0.282458	0.000033	0.001311	0.047826	835	0.28244	6.36	1.2	1.13	1.30	0.28226	0.28265
68_04	0.282461	0.000042	0.001078	0.040169	835	0.28244	6.61	1.5	1.12	1.29	0.28226	0.28265
68_05	0.282407	0.000049	0.001233	0.036539	835	0.28239	4.61	1.7	1.20	1.41	0.28226	0.28265
68_06	0.282484	0.000045	0.001496	0.055729	835	0.28246	7.20	1.6	1.10	1.25	0.28226	0.28265
68_07	0.282484	0.000045	0.001496	0.055729	835	0.28246	7.20	1.6	1.10	1.25	0.28226	0.28265
68_08	0.282447	0.000034	0.001384	0.039197	835	0.28243	5.93	1.2	1.15	1.33	0.28226	0.28265
68_09	0.282498	0.000032	0.001321	0.040354	835	0.28248	7.77	1.1	1.08	1.22	0.28226	0.28265
68_10	0.282484	0.000030	0.001208	0.041990	835	0.28247	7.36	1.0	1.09	1.24	0.28226	0.28265
68_11	0.282452	0.000020	0.001083	0.039154	835	0.28243	6.28	0.7	1.13	1.31	0.28226	0.28265
68_12	0.282441	0.000038	0.002917	0.112002	835	0.28240	4.88	1.3	1.21	1.40	0.28226	0.28265
E14-69												
69_05	0.282520	0.000067	0.002555	0.107001	832	0.28248	7.81	2.34	1.08	1.21	0.28226	0.28265
69_11	0.282539	0.000034	0.001112	0.046538	853	0.28252	9.75	1.21	1.01	1.11	0.28225	0.28264
69_12	0.282530	0.000046	0.001137	0.037901	843	0.28251	9.20	1.63	1.03	1.13	0.28225	0.28264
69_13	0.282579	0.000050	0.001496	0.057737	831	0.28256	10.46	1.76	0.97	1.04	0.28226	0.28265
69_14	0.282549	0.000025	0.000924	0.035495	824	0.28253	9.57	0.87	0.99	1.09	0.28226	0.28266
69_15	0.282509	0.000030	0.001425	0.051816	815	0.28249	7.68	1.04	1.06	1.21	0.28227	0.28266
69_16	0.282520	0.000036	0.001230	0.047963	855	0.28250	9.03	1.25	1.04	1.15	0.28224	0.28263
69_19	0.282541	0.000039	0.001454	0.058640	804	0.28252	8.57	1.38	1.02	1.14	0.28228	0.28267

CHUR from Bouvier et al. (2008); Earth and Planetary Science Letters 273 (2008) 48–57

CHUR 176Lu/177Hf = 0.0336±1 and 176Hf/177Hf = 0.282785±11

Hfi = 176Hf/177Hf ratio - (176Lu/177Hf ratio * (EXP(0.0193 * 207Pb/206Pb ratio / 1000)-1))

Table 2: LA–MC–ICP-MS Lu–Hf isotopes (zircon) from the Western Ethiopian Shield

Sample Name	Hf^{176}/Hf^{177}	2 S.E.	Lu^{176}/Hf^{177}	Yb^{176}/Hf^{177}	U/Pb AGE	Hfi	epsilon	1s	T (DM) Ga	T(DM) Crustal	Hf Chur (t)	Hf DM (t)
E14-69												
69_20	0.282568	0.000060	0.001266	0.043072	790	0.28255	9.31	2.10	0.98	1.08	0.28229	0.28268
69_21	0.282493	0.000034	0.000853	0.031843	843	0.28248	8.05	1.17	1.07	1.21	0.28225	0.28264
69_25	0.282485	0.000055	0.001967	0.066813	837	0.28245	6.99	1.94	1.11	1.27	0.28226	0.28265
69_26	0.282579	0.000046	0.001140	0.037839	818	0.28256	10.40	1.60	0.96	1.04	0.28227	0.28266
69_27	0.282597	0.000036	0.001181	0.046283	828	0.28258	11.19	1.26	0.93	1.00	0.28226	0.28265
E14-70												
70_04	0.282444	0.000035	0.001094	0.041077	807	0.28243	5.40	1.2	1.15	1.34	0.28228	0.28267
70_05	0.282458	0.000041	0.001443	0.049395	814	0.28244	5.86	1.4	1.14	1.32	0.28227	0.28266
70_07	0.282457	0.000033	0.001353	0.044110	804	0.28244	5.66	1.1	1.14	1.32	0.28228	0.28267
70_11	0.282495	0.000044	0.001319	0.041265	815	0.28248	7.25	1.5	1.08	1.23	0.28227	0.28266
70_14	0.282491	0.000039	0.001575	0.049365	794	0.28247	6.51	1.4	1.09	1.26	0.28228	0.28268
70_15	0.282438	0.000033	0.001082	0.034152	798	0.28242	4.99	1.2	1.15	1.36	0.28228	0.28268
70_19	0.282451	0.000345	0.001527	0.043016	794	0.28243	5.11	12.1	1.15	1.35	0.28228	0.28268
70_20	0.282436	0.000037	0.001322	0.049330	806	0.28242	4.96	1.3	1.16	1.37	0.28228	0.28267
70_21	0.282482	0.000033	0.001055	0.037163	792	0.28247	6.40	1.2	1.09	1.27	0.28229	0.28268
70_22	0.282475	0.000049	0.002073	0.079866	808	0.28244	5.96	1.7	1.13	1.31	0.28227	0.28267
70_26	0.282445	0.000036	0.001325	0.047887	802	0.28243	5.20	1.3	1.15	1.35	0.28228	0.28267
70_27	0.282454	0.000052	0.001992	0.067108	795	0.28242	5.00	1.8	1.16	1.36	0.28228	0.28268
70_28	0.282465	0.000035	0.001991	0.058401	830	0.28243	6.14	1.2	1.14	1.31	0.28226	0.28265
70_29	0.282469	0.000037	0.001096	0.043357	829	0.28245	6.74	1.3	1.11	1.28	0.28226	0.28265

CHUR from Bouvier et al. (2008); Earth and Planetary Science Letters 273 (2008) 48–57

CHUR 176Lu/177Hf = 0.0336±1 and 176Hf/177Hf = 0.282785±11

Hfi = 176Hf/177Hf ratio - (176Lu/177Hf ratio * (EXP(0.0193 * 207Pb/206Pb ratio / 1000)-1))

Table 2: LA–MC–ICP-MS Lu–Hf isotopes (zircon) from the Western Ethiopian Shield

Sample Name	Hf^{176}/Hf^{177}	2 S.E.	Lu^{176}/Hf^{177}	Yb^{176}/Hf^{177}	U/Pb AGE	Hfi	epsilon	1s	T (DM) Ga	T(DM) Crustal	Hf Chur (t)	Hf DM (t)
E14-77												
MB_77_01	0.28096	0.00004	0.00177	0.05000	791.2	0.28093	-47.9	1.4	3.3	4.6	0.28229	0.28268
MB_77_08	0.28059	0.00005	0.00254	0.06813	800.8	0.28055	-61.3	1.9	3.8	5.4	0.28228	0.28267
MB_77_13	0.27940	0.00006	0.00159	0.04813	819.4	0.27938	-102.4	2.0	5.3	7.7	0.28227	0.28266
MB_77_21	0.28251	0.00005	0.00187	0.05939	788.4	0.28248	7.0	1.6	1.1	1.2	0.28229	0.28268
MB_77_22	0.28246	0.00003	0.00110	0.03421	798.3	0.28245	5.9	1.0	1.1	1.3	0.28228	0.28268
MB_77_24	0.28246	0.00004	0.00162	0.04631	821.8	0.28244	6.1	1.4	1.1	1.3	0.28227	0.28266
MB_77_27	0.28248	0.00003	0.00160	0.05292	815.6	0.28246	6.7	1.0	1.1	1.3	0.28227	0.28266
MB_77_29	0.28248	0.00004	0.00176	0.05611	824	0.28245	6.7	1.3	1.1	1.3	0.28226	0.28266
MB_77_30	0.28251	0.00003	0.00238	0.08156	791.5	0.28247	6.7	1.2	1.1	1.3	0.28229	0.28268
MB_77_32	0.28250	0.00003	0.00193	0.05905	818.4	0.28247	7.0	1.0	1.1	1.2	0.28227	0.28266
MB_77_33	0.28252	0.00005	0.00262	0.09343	818.7	0.28248	7.5	1.6	1.1	1.2	0.28227	0.28266
MB_77_34	0.28254	0.00004	0.00217	0.07423	834.5	0.28251	8.8	1.4	1.0	1.2	0.28226	0.28265
MB_77_36	0.28249	0.00002	0.00121	0.03652	815.3	0.28247	7.2	0.9	1.1	1.2	0.28227	0.28266
E14-78												
MB_78_01	0.28254	0.00003	0.00069	0.02029	607.6	0.28253	4.4	1.1	1.0	1.2	0.28240	0.28281
MB_78_02	0.28253	0.00004	0.00074	0.02131	607.7	0.28252	4.1	1.3	1.0	1.3	0.28240	0.28281
MB_78_05	0.28251	0.00003	0.00123	0.03005	808.9	0.28249	7.6	1.1	1.1	1.2	0.28227	0.28267
MB_78_07	0.28254	0.00005	0.00068	0.02222	588	0.28253	4.0	1.9	1.0	1.3	0.28241	0.28283
MB_78_16	0.28255	0.00004	0.00061	0.01747	607	0.28255	5.1	1.3	1.0	1.2	0.28240	0.28281
E14-78												
MB_79_03	0.28255	0.00004	0.00071	0.02275	612.3	0.28254	5.2	1.2	1.0	1.2	0.28240	0.28281
MB_79_05	0.29613	0.01646	0.00013	-0.00018	832.4	0.29613	491.4	576.2	-22.0	-43.4	0.28226	0.28265
MB_79_06	0.28258	0.00002	0.00057	0.01845	606.1	0.28257	6.1	0.8	0.9	1.1	0.28240	0.28281
MB_79_08	0.28246	0.00007	0.00111	0.02625	835.7	0.28245	6.7	2.3	1.1	1.3	0.28226	0.28265
MB_79_13	0.28244	0.00006	0.00138	0.03434	840.6	0.28242	5.9	2.0	1.2	1.3	0.28225	0.28264
MB_79_19	0.28248	0.00003	0.00060	0.01700	850.3	0.28247	7.9	1.0	1.1	1.2	0.28225	0.28264
MB_79_20	0.28246	0.00004	0.00071	0.01718	862.7	0.28244	7.3	1.3	1.1	1.3	0.28224	0.28263
MB_79_23	0.28266	0.00007	0.00456	0.18109	560.6	0.28261	6.3	2.5	0.9	1.1	0.28243	0.28285
MB_79_31	0.28248	0.00003	0.00057	0.01432	848.1	0.28247	7.7	1.2	1.1	1.2	0.28225	0.28264
MB_79_32	0.28029	0.00261	0.00147	0.04671	845.4	0.28027	-70.3	91.4	4.1	5.9	0.28225	0.28264

CHUR from Bouvier et al. (2008); Earth and Planetary Science Letters 273 (2008) 48–57

CHUR 176Lu/177Hf = 0.0336±1 and 176Hf/177Hf = 0.282785±11

Hfi = 176Hf/177Hf ratio - (176Lu/177Hf ratio * (EXP(0.0193 * 207Pb/206Pb ratio / 1000)-1))

Table 2: LA–MC–ICP-MS Lu–Hf isotopes (zircon) from the Western Ethiopian Shield

Sample Name	Hf^{176}/Hf^{177}	2 S.E.	Lu^{176}/Hf^{177}	Yb^{176}/Hf^{177}	U/Pb AGE	Hfi	epsilon	1s	T (DM) Ga	T(DM) Crustal	Hf Chur (t)	Hf DM (t)
E14-83												
MB_83_01	0.28250	0.00002	0.00074	0.02090	801.7	0.28249	7.6	0.8	1.1	1.2	0.28228	0.28267
MB_83_05	0.28248	0.00004	0.00073	0.02373	839.8	0.28247	7.5	1.3	1.1	1.2	0.28225	0.28264
MB_83_07	0.28245	0.00003	0.00057	0.01485	832.5	0.28245	6.6	0.9	1.1	1.3	0.28226	0.28265
MB_83_13	0.28246	0.00002	0.00056	0.01496	843.5	0.28245	7.2	0.7	1.1	1.3	0.28225	0.28264
MB_83_14	0.28245	0.00002	0.00064	0.01649	819.5	0.28244	6.1	0.7	1.1	1.3	0.28227	0.28266
MB_83_15	0.28245	0.00002	0.00101	0.02991	840.4	0.28243	6.4	0.9	1.1	1.3	0.28225	0.28264
MB_83_21	0.28242	0.00003	0.00093	0.02559	876.3	0.28240	6.1	1.0	1.2	1.4	0.28223	0.28262
MB_83_27	0.28247	0.00002	0.00091	0.02648	842	0.28245	7.0	0.8	1.1	1.3	0.28225	0.28264
MB_83_31	0.28246	0.00002	0.00075	0.01971	809.7	0.28245	6.2	0.8	1.1	1.3	0.28227	0.28267
E14-86												
MB_86_01	0.28246	0.00003	0.00109	0.03367	851.7	0.28244	7.0	0.9	1.1	1.3	0.28225	0.28264
MB_86_02	0.28250	0.00003	0.00145	0.04318	844.6	0.28247	7.9	1.1	1.1	1.2	0.28225	0.28264
MB_86_04	0.28242	0.00004	0.00140	0.04386	821.3	0.28240	4.6	1.2	1.2	1.4	0.28227	0.28266
MB_86_08	0.28244	0.00003	0.00126	0.03532	818.7	0.28242	5.2	1.1	1.2	1.4	0.28227	0.28266
MB_86_09	0.28242	0.00002	0.00080	0.02570	818	0.28240	4.8	0.7	1.2	1.4	0.28227	0.28266
MB_86_13	0.28244	0.00003	0.00167	0.05066	801.4	0.28241	4.6	1.0	1.2	1.4	0.28228	0.28267
MB_86_15	0.28245	0.00004	0.00168	0.04243	810.5	0.28243	5.5	1.3	1.1	1.3	0.28227	0.28267
MB_86_16	0.28246	0.00003	0.00092	0.02774	797.2	0.28245	5.9	1.1	1.1	1.3	0.28228	0.28268
MB_86_17	0.28240	0.00003	0.00140	0.04295	806.1	0.28238	3.6	1.1	1.2	1.5	0.28228	0.28267
E14-87												
MB_87_06	0.28251	0.00002	0.00064	0.01673	783.6	0.28250	7.5	0.9	1.0	1.2	0.28229	0.28269
MB_87_08	0.28251	0.00004	0.00115	0.03603	783.9	0.28250	7.3	1.4	1.1	1.2	0.28229	0.28269
MB_87_12	0.28251	0.00003	0.00104	0.03046	815.1	0.28249	7.9	1.1	1.1	1.2	0.28227	0.28266
MB_87_13	0.28250	0.00003	0.00084	0.02353	810.7	0.28249	7.6	1.2	1.1	1.2	0.28227	0.28267
MB_87_18	0.28250	0.00003	0.00087	0.02724	809.2	0.28249	7.5	1.1	1.1	1.2	0.28227	0.28267
MB_87_23	0.28249	0.00003	0.00068	0.02089	841.7	0.28247	7.8	1.1	1.1	1.2	0.28225	0.28264
MB_87_24	0.28250	0.00003	0.00097	0.02594	810	0.28249	7.5	1.0	1.1	1.2	0.28227	0.28267
MB_87_25	0.28252	0.00002	0.00193	0.05865	840.1	0.28249	8.3	0.9	1.1	1.2	0.28225	0.28264
MB_87_39	0.28249	0.00004	0.00173	0.05053	753.9	0.28247	5.5	1.4	1.1	1.3	0.28231	0.28271
MB_87_48	0.28250	0.00002	0.00063	0.01713	844.7	0.28249	8.5	0.8	1.1	1.2	0.28225	0.28264

CHUR from Bouvier et al. (2008); *Earth and Planetary Science Letters 273 (2008) 48–57*

CHUR 176Lu/177Hf = 0.0336±1 and 176Hf/177Hf = 0.282785±11

Hfi = 176Hf/177Hf ratio - (176Lu/177Hf ratio * (EXP(0.0193 * 207Pb/206Pb ratio / 1000)-1))

Table 2: LA–MC–ICP–MS Lu–Hf isotopes (zircon) from the Western Ethiopian Shield

Sample Name	Hf^{176}/Hf^{177}	2 S.E.	Lu^{176}/Hf^{177}	Yb^{176}/Hf^{177}	U/Pb AGE	Hfi	epsilon	1s	T (DM) Ga	T(DM) Crustal	Hf Chur (t)	Hf DM (t)
E14-96												
MB_96_01	0.28246	0.00002	0.00048	0.01211	823.5	0.28246	6.7	0.6	1.1	1.3	0.28226	0.28266
MB_96_04	0.28247	0.00002	0.00060	0.01448	817.7	0.28246	6.6	0.8	1.1	1.3	0.28227	0.28266
MB_96_08	0.28247	0.00003	0.00176	0.05072	911.8	0.28244	8.1	1.1	1.1	1.3	0.28221	0.28259
MB_96_09	0.28249	0.00005	0.00272	0.08713	894.9	0.28245	8.1	1.6	1.1	1.2	0.28222	0.28260
MB_96_16	0.28247	0.00003	0.00092	0.02692	806.8	0.28246	6.6	1.2	1.1	1.3	0.28228	0.28267
E14-97												
MB_97_01	0.28257	0.00006	0.00077	0.02565	647.6	0.28256	6.5	2.2	1.0	1.1	0.28238	0.28278
MB_97_04	0.28250	0.00005	0.00056	0.01672	672.7	0.28249	4.5	1.7	1.1	1.3	0.28236	0.28277
MB_97_10	0.28145	0.00606	0.00077	0.02539	651.2	0.28144	-33.1	212.1	2.5	3.6	0.28237	0.28278
MB_97_11	0.28257	0.00004	0.00182	0.06764	643.2	0.28255	6.1	1.3	1.0	1.2	0.28238	0.28279
MB_97_16	0.28258	0.00008	0.00108	0.03789	567	0.28257	5.1	2.8	1.0	1.2	0.28243	0.28284
MB_97_23	0.28256	0.00003	0.00042	0.01471	659.6	0.28255	6.4	0.9	1.0	1.2	0.28237	0.28278
MB_97_24	0.28258	0.00003	0.00087	0.02961	656.8	0.28257	7.2	1.2	0.9	1.1	0.28237	0.28278
MB_97_28	0.28254	0.00003	0.00082	0.03143	647.7	0.28253	5.4	1.1	1.0	1.2	0.28238	0.28278
MB_97_30	0.28259	0.00003	0.00054	0.01718	647.6	0.28258	7.2	0.9	0.9	1.1	0.28238	0.28278
E14-100												
MB_100_01	0.28251	0.00002	0.00037	0.01197	661	0.28251	5.0	0.7	1.0	1.3	0.28237	0.28277
MB_100_04	0.28251	0.00004	0.00085	0.02462	634.1	0.28250	4.1	1.6	1.0	1.3	0.28239	0.28279
MB_100_06	0.28254	0.00002	0.00054	0.01848	665.9	0.28254	6.1	0.7	1.0	1.2	0.28237	0.28277
MB_100_07	0.28252	0.00002	0.00062	0.02207	635.3	0.28252	4.7	0.8	1.0	1.3	0.28238	0.28279
E14-113												
MB_113_01	0.28254	0.00003	0.00058	0.01808	727.3	0.28253	7.3	0.9	1.0	1.2	0.28233	0.28273
MB_113_04	0.28256	0.00003	0.00065	0.01893	654.2	0.28255	6.3	0.9	1.0	1.2	0.28237	0.28278
MB_113_07	0.28252	0.00002	0.00079	0.02132	711.9	0.28251	6.3	0.9	1.0	1.2	0.28234	0.28274
MB_113_13	0.28260	0.00004	0.00080	0.02522	709.7	0.28259	8.8	1.3	0.9	1.1	0.28234	0.28274
MB_113_14	0.28255	0.00004	0.00090	0.02923	730.1	0.28254	7.7	1.4	1.0	1.1	0.28232	0.28272
MB_113_15	0.28254	0.00003	0.00058	0.01526	707.7	0.28254	7.0	1.2	1.0	1.2	0.28234	0.28274
MB_113_22	0.28256	0.00002	0.00024	0.00689	773.9	0.28256	9.4	0.6	1.0	1.1	0.28230	0.28269
MB_113_24	0.28253	0.00003	0.00096	0.02722	773.9	0.28252	7.7	1.2	1.0	1.2	0.28230	0.28269
MB_113_25	0.28252	0.00011	0.00089	0.03257	742.3	0.28251	6.9	3.8	1.0	1.2	0.28232	0.28272
MB_113_33	0.28257	0.00005	0.00058	0.01686	746.9	0.28256	8.9	1.7	1.0	1.1	0.28231	0.28271

CHUR from Bouvier et al. (2008); Earth and Planetary Science Letters 273 (2008) 48–57
CHUR 176Lu/177Hf = 0.0336±1 and 176Hf/177Hf = 0.282785±11
Hfi = 176Hf/177Hf ratio - (176Lu/177Hf ratio * (EXP(0.0193 * 207Pb/206Pb ratio / 1000)-1))

Table 2: LA–MC–ICP-MS Lu–Hf isotopes (zircon) from the Western Ethiopian Shield

Sample Name	Hf^{176}/Hf^{177}	2 S.E.	Lu^{176}/Hf^{177}	Yb^{176}/Hf^{177}	U/Pb AGE	Hfi	epsilon	1s	T (DM) Ga	T(DM) Crustal	Hf Chur (t)	Hf DM (t)
E14-115												
MB_115_22	0.28263	0.00003	0.00086	0.02426	596.1	0.28262	7.5	0.9	0.9	1.0	0.28241	0.28282
MB_115_29	0.28260	0.00002	0.00054	0.01386	593.4	0.28259	6.5	0.9	0.9	1.1	0.28241	0.28282
MB_115_31	0.28262	0.00002	0.00092	0.01904	600.7	0.28261	7.2	0.8	0.9	1.1	0.28241	0.28282
MB_115_39	0.28260	0.00003	0.00082	0.01824	627.3	0.28259	7.1	1.0	0.9	1.1	0.28239	0.28280
MB_115_41	0.28260	0.00005	0.00065	0.01504	628.8	0.28259	7.2	1.7	0.9	1.1	0.28239	0.28280
MB_115_44	0.28261	0.00002	0.00093	0.02199	629	0.28260	7.6	0.8	0.9	1.1	0.28239	0.28280

CHUR from Bouvier et al. (2008); Earth and Planetary Science Letters 273 (2008) 48–57

CHUR 176Lu/177Hf = 0.0336±1 and 176Hf/177Hf = 0.282785±11

Hfi = 176Hf/177Hf ratio - (176Lu/177Hf ratio * (EXP(0.0193 * 207Pb/206Pb ratio / 1000)-1))

Table 2: SHRIMP SI O isotopes (zircon) from the Western Ethiopian Shield

Spot Number	Zircon Age ^{206}Pb/^{238}U	± 1s	^{18}O/^{16}O	1s	^{18}O/^{16}O (‰)	Error T 95%	External error 2s
E14-77							
077-21	798	10.67	0.002033	0.00000038	6.98	0.1868	0.6093
077-22	788	10.38	0.002033	0.00000042	7.19	0.2065	0.6157
077-24	821	10.4	0.002034	0.000000392	7.55	0.1928	0.6112
077-27	816	10.29	0.002032	0.000000409	6.63	0.2012	0.6139
077-31	804	10.43	0.002033	0.000000369	7.03	0.1814	0.6077
077-34	835	10.62	0.002034	0.000000398	7.36	0.1956	0.6121
E14-78							
078-01	607	8.09	0.002035	0.000000366	8.19	0.1800	0.6073
078-07	588	7.92	0.002036	0.000000418	8.33	0.2055	0.6153
078-16	607	9.82	0.002035	0.000000383	8.12	0.1883	0.6098
E14-79							
079-03	612	7.79	0.002034	0.000000342	7.63	0.1681	0.6039
079-06	606	7.42	0.002034	0.000000385	7.66	0.1892	0.6101
079-08	836	10.11	0.002037	0.000000462	9.24	0.2267	0.6227
079-20	863	10.36	0.002039	0.000000441	10.22	0.2161	0.6189
079-19	850	10.36	0.002035	0.000000396	8.02	0.1948	0.6118
E14-83							
083-01	802	9.96	0.002039	0.000000401	10.11	0.1967	0.6124
083-05	840	10	0.002039	0.000000415	9.80	0.2033	0.6146
083-07	833	10.14	0.002038	0.000000368	9.36	0.1804	0.6074
083-11	835	10.23	0.002038	0.000000544	9.44	0.2671	0.6385
083-13	844	10.33	0.002039	0.000000413	10.21	0.2024	0.6143
083-14	819	10.14	0.002038	0.00000041	9.67	0.2013	0.6139
E14-86							
086-02	845	10.41	0.002038	0.000000387	9.33	0.1897	0.6102
086-01	851	10.19	0.002037	0.000000385	9.07	0.1891	0.6100
086-04	821	10.24	0.002037	0.00000039	9.26	0.1916	0.6108
086-06	787	9.74	0.002042	0.000000332	11.37	0.1627	0.6024
086-08	819	9.92	0.002038	0.000000347	9.38	0.1704	0.6045
086-16	797	10.31	0.002033	0.00000039	6.98	0.1920	0.6110
086-42	823	10.43	0.002037	0.000000361	8.89	0.1771	0.6064
086-44	860	10.48	0.002042	0.000000414	11.71	0.2025	0.6143
E14-87							
087-01	826	10.51	0.002031	0.000000471	5.88	0.2321	0.6247
087-06	784	9.73	0.002031	0.000000378	5.95	0.1864	0.6092
087-08	784	9.68	0.002031	0.000000429	6.17	0.2112	0.6172
087-12	815	10.54	0.002031	0.000000357	5.94	0.1759	0.6061
087-13	810	10.67	0.00203	0.000000342	5.81	0.1682	0.6039
087-25	840	9.79	0.00203	0.000000425	5.73	0.2092	0.6166
087-30	805	10.06	0.002031	0.000000347	5.96	0.1710	0.6047
087-39	754	10.93	0.002031	0.000000362	6.30	0.1783	0.6068
087-48	845	10.5	0.002031	0.000000373	6.13	0.1837	0.6084
E14-96							
096-01	824	10.32	0.002039	0.000000379	10.00	0.1858	0.6090
096-03	843	10.46	0.002039	0.00000031	10.19	0.1521	0.5996
096-08	912	11.63	0.002034	0.000000345	7.52	0.1698	0.6043
096-16	807	11.2	0.002036	0.000000386	8.28	0.1895	0.6102

Table 2: SHRIMP SI O isotopes (zircon) from the Western Ethiopian Shield

Spot Number	Zircon Age $^{206}Pb/^{238}U$	± 1s	$^{18}O/^{16}O$	1s	$^{18}O/^{16}O$ (‰)	Error T 95%	External error 2s
E14-99							
099-03	645	8.08	0.002031	0.000000326	6.03	0.1607	0.6019
099-10	651	8.8	0.002033	0.000000373	6.99	0.1835	0.6083
099-11	643	8.5	0.002033	0.000000451	7.19	0.2219	0.6210
099-17	651	8.85	0.002031	0.00000045	5.98	0.2216	0.6209
099-23	659	8.86	0.002032	0.000000477	6.80	0.2347	0.6257
E14-100							
100-01	661	8.15	0.002039	0.000000427	10.08	0.2096	0.6167
100-05	618	7.51	0.002036	0.000000393	8.71	0.1929	0.6112
100-06	666	8.27	0.002036	0.000000382	8.58	0.1878	0.6096
100-07	635	8.15	0.002035	0.000000345	8.00	0.1698	0.6043
E14-113							
113-01	727	8.84	0.002033	0.000000431	7.23	0.2121	0.6176
113-04	654	8.03	0.002033	0.000000409	6.94	0.2010	0.6139
113-07	712	9.04	0.002033	0.000000433	7.08	0.2132	0.6179
113-13	710	8.8	0.002034	0.000000426	7.35	0.2096	0.6167
113-22	774	10.13	0.002032	0.000000371	6.71	0.1828	0.6081
E14-115							
115-18	595	7.25	0.002033	0.000000451	6.95	0.2221	0.6211
115-21	620	7.51	0.002033	0.000000417	7.10	0.2053	0.6153
115-29	593	7.18	0.002032	0.000000382	6.65	0.1880	0.6097

APPENDIX 3

Supplementary data for chapter 3:
Age, Hafnium and Oxygen Isotopic Evolution of the
Western Ethiopian Shield. The Origin of Ultramafic
rocks of the Tulu Dimtu Belt, western Ethiopia – Do
they represent remnants of the Mozambique Ocean?

Table 1: Chrome spinel microprobe analyses from ultramafic rocks of the Western Ethiopian Shield

Tulu Dimtu Hill (9° 27' 60.9"N 35° 44' 19.8"E)

ID number	E13-26-01	E13-26-02	E13-26-03	E13-26-04	E13-26-05	E13-26-06	E13-26-07	E13-26-08	E13-26-09	E13-26-10	E13-26-11	E13-26-12	E13-26-13
SiO_2	<0.01	<0.01	0.01	0.03	0.03	0.03	0.03	0.01	0.03	0.02	<0.1	0.01	0.010
TiO_2	0.02	<0.01	<0.01	0.02	<0.01	<0.01	0.02	<0.01	<0.01	0.01	0.02	0.01	0.019
Al_2O_3	6.72	6.64	6.63	6.76	6.65	6.42	6.37	6.83	6.76	6.57	6.71	5.22	5.192
Cr_2O_3	64.09	64.18	64.79	64.33	63.90	63.54	62.67	63.87	63.99	62.62	62.89	64.90	65.535
Fe_2O_3	0.00	0.00	0.00	0.00	0.00	0.00	0.11	0.13	0.06	0.33	0.17	0.00	0.000
FeO	21.58	21.85	20.06	20.91	21.87	23.50	25.71	21.40	21.25	24.81	24.23	24.67	23.538
MnO	0.37	0.44	0.44	0.45	0.45	0.54	0.57	0.47	0.44	0.54	0.55	0.54	0.486
MgO	7.03	6.70	7.79	7.31	6.77	5.53	4.31	6.91	6.93	4.69	5.05	4.40	4.880
ZnO	0.11	0.12	0.20	0.16	0.28	0.40	0.15	0.19	0.35	0.32	0.27	0.15	0.298
CaO	<0.01	<0.01	<0.01	<0.01	<0.01	<0.01	<0.01	<0.01	0.02	0.02	<0.01	<0.01	<0.01
Na_2O	0.02	<0.02	0.02	<0.02	<0.02	<0.02	0.02	0.12	0.12	0.07	0.09	0.04	0.023
K_2O	0.00	0.00	0.00	0.00	0.00	0.00	0.00	0.00	0.00	0.00	0.00	0.00	0.000
NiO	0.05	0.04	0.05	0.03	0.02	0.02	0.03	0.06	0.03	<0.03	<0.03	0.04	0.010
Cations to 32 oxygens													
Si	0.00	0.00	0.00	0.00	0.00	0.00	0.00	0.00	0.00	0.00	0.00	0.00	0.00
Ti	0.00	0.00	0.00	0.00	0.00	0.00	0.00	0.00	0.00	0.00	0.00	0.00	0.00
Al	0.27	0.27	0.27	0.27	0.27	0.26	0.26	0.28	0.27	0.27	0.27	0.22	0.21
Cr	1.74	1.74	1.75	1.74	1.73	1.74	1.73	1.73	1.73	1.72	1.73	1.80	1.82
Fe^{3+}	0.00	0.00	0.00	0.00	0.00	0.00	0.00	0.00	0.00	0.01	0.00	0.00	0.00
Fe^{2+}	0.62	0.63	0.57	0.60	0.63	0.68	0.75	0.61	0.61	0.72	0.70	0.72	0.69
Mn^{2+}	0.01	0.01	0.01	0.01	0.01	0.02	0.02	0.01	0.01	0.02	0.02	0.02	0.01
Mg	0.36	0.34	0.40	0.37	0.35	0.29	0.22	0.35	0.35	0.24	0.26	0.23	0.25
Zn	0.00	0.00	0.00	0.00	0.00	0.01	0.00	0.00	0.01	0.01	0.01	0.00	0.01
Ca	0.00	0.00	0.00	0.00	0.00	0.00	0.00	0.00	0.00	0.00	0.00	0.00	0.00
Na	0.00	0.00	0.00	0.00	0.00	0.00	0.00	0.01	0.01	0.00	0.01	0.00	0.00
K	0.00	0.00	0.00	0.00	0.00	0.00	0.00	0.00	0.00	0.00	0.00	0.00	0.00
Ni	0.00	0.00	0.00	0.00	0.00	0.00	0.00	0.00	0.00	0.00	0.00	0.00	0.00
Mg #	0.37	0.35	0.41	0.38	0.36	0.30	0.23	0.37	0.37	0.25	0.27	0.24	0.27
Fe #	0.63	0.65	0.59	0.62	0.64	0.70	0.77	0.63	0.63	0.75	0.73	0.76	0.73
Cr #	0.86	0.87	0.87	0.86	0.87	0.87	0.87	0.86	0.86	0.86	0.86	0.89	0.89
Fe^{3+} #	0.00	0.00	0.00	0.00	0.00	0.00	0.00	0.00	0.00	0.00	0.00	0.00	0.00

Table 1: Chrome spinel microprobe analyses from ultramafic rocks of the Western Ethiopian Shield

ID number	E13-26-14	E13-26-15	E13-26-16	E13-26-17	E13-26-18	E13-26-19	E13-26-20	E13-26-21	E13-26-22	E13-26-23	E13-26-24	E13-26-25	E13-26-26
Tulu Dimtu Hill (9° 27' 60.9"N 35° 44' 19,8"E)													
SiO_2	0.02	0.04	0.02	0.13	0.05	0.02	0.03	0.02	0.03	<0.01	0.04	0.04	0.07
TiO_2	0.01	0.01	<0.01	<0.01	0.02	0.01	0.01	<0.01	0.02	0.01	0.02	0.00	0.01
$Al2O_3$	5.16	0.65	6.07	4.65	6.56	6.54	6.56	6.69	6.78	6.69	6.54	6.52	6.28
Cr_2O_3	64.45	60.27	62.58	62.29	64.35	64.33	64.93	64.38	65.33	65.74	63.97	63.38	62.53
Fe_2O_3	0.00	7.93	0.23	1.47	0.00	0.00	0.00	0.00	0.00	0.00	0.00	0.00	0.19
FeO	25.05	27.18	25.96	27.54	21.50	21.81	20.13	21.17	18.57	18.26	21.91	23.53	26.06
MnO	0.54	0.87	0.60	0.74	0.40	0.41	0.42	0.41	0.42	0.34	0.44	0.52	0.64
MgO	4.15	2.04	3.83	2.87	6.92	6.75	7.74	7.21	8.73	8.75	6.73	5.54	4.08
ZnO	0.57	0.85	0.68	0.23	0.13	0.13	0.14	0.06	0.08	0.15	0.30	0.45	0.11
CaO	0.02	0.02	<0.01	0.02	<0.01	<0.01	<0.01	<0.01	<0.01	<0.01	<0.01	<0.01	0.02
Na_2O	0.02	<0.02	<0.02	<0.02	<0.02	<0.02	<0.02	0.02	<0.02	<0.02	0.02	0.02	0.02
K_2O	0.00	0.00	0.00	0.00	0.00	0.00	0.00	0.00	0.00	0.00	0.00	0.00	0.00
NiO	<0.03	0.15	<0.03	0.05	0.05	<0.03	0.04	0.03	0.03	0.04	0.02	<0.03	<0.03
Cations to 32 oxygens													
Si	0.00	0.00	0.00	0.00	0.00	0.00	0.00	0.00	0.00	0.00	0.00	0.00	0.00
Ti	0.00	0.00	0.00	0.00	0.00	0.00	0.00	0.00	0.00	0.00	0.00	0.00	0.00
Al	0.21	0.03	0.25	0.20	0.27	0.26	0.26	0.27	0.27	0.27	0.26	0.27	0.26
Cr	1.80	1.75	1.74	1.76	1.75	1.75	1.75	1.74	1.75	1.76	1.74	1.74	1.73
Fe^{3+}	0.00	0.22	0.01	0.04	0.00	0.00	0.00	0.00	0.00	0.00	0.00	0.00	0.00
Fe^{2+}	0.74	0.83	0.76	0.82	0.62	0.63	0.57	0.61	0.53	0.52	0.63	0.68	0.76
Mn^{2+}	0.02	0.03	0.02	0.02	0.01	0.01	0.01	0.01	0.01	0.01	0.01	0.02	0.02
Mg	0.22	0.11	0.20	0.15	0.35	0.35	0.39	0.37	0.44	0.44	0.34	0.29	0.21
Zn	0.01	0.02	0.02	0.01	0.00	0.00	0.00	0.00	0.00	0.00	0.01	0.01	0.00
Ca	0.00	0.00	0.00	0.00	0.00	0.00	0.00	0.00	0.00	0.00	0.00	0.00	0.00
Na	0.00	0.00	0.00	0.00	0.00	0.00	0.00	0.00	0.00	0.00	0.00	0.00	0.00
K	0.00	0.00	0.00	0.00	0.00	0.00	0.00	0.00	0.00	0.00	0.00	0.00	0.00
Ni	0.00	0.00	0.00	0.00	0.00	0.00	0.00	0.00	0.00	0.00	0.00	0.00	0.00
Mg #	0.23	0.12	0.21	0.16	0.36	0.36	0.41	0.38	0.46	0.46	0.35	0.30	0.22
Fe #	0.77	0.88	0.79	0.84	0.64	0.64	0.59	0.62	0.54	0.54	0.65	0.70	0.78
Cr #	0.89	0.88	0.87	0.88	0.87	0.87	0.87	0.87	0.87	0.87	0.87	0.87	0.87
Fe^{3+}#	0.00	0.11	0.00	0.02	0.00	0.00	0.00	0.00	0.00	0.00	0.00	0.00	0.00

Table 1: Chrome spinel microprobe analyses from ultramafic rocks of the Western Ethiopian Shield

ID number	E13-26 - 27	E13-26 - 28	E13-26 - 29	E13-26 - 30	E13-26 - 31	E13-26 - 32	E13-26 - 33	E13-26 - 34	E13-26 - 35	E13-26 - 36	E13-26 - 37
Tulu Dimtu Hill (9° 27' 60.9"N 35° 44' 19.8"E)											
SiO_2	0.06	0.01	0.05	0.03	0.03	0.03	0.02	<0.01	0.02	0.95	0.04
TiO_2	0.01	0.01	0.03	<0.01	0.02	0.03	0.02	0.01	0.01	0.03	0.02
$Al2O_3$	6.59	6.67	6.34	6.69	2.65	5.19	5.22	5.19	7.22	3.97	6.78
Cr_2O_3	64.03	64.01	62.34	62.89	63.39	65.03	65.48	64.59	63.15	63.46	62.94
Fe_2O_3	0.10	0.00	0.42	0.25	2.59	0.00	0.00	0.00	0.00	0.19	0.00
FeO	21.56	21.45	25.71	23.66	28.05	24.55	23.59	25.38	22.61	26.05	23.64
MnO	0.49	0.42	0.56	0.58	0.79	0.53	0.45	0.56	0.52	0.55	0.53
MgO	6.86	6.85	4.21	5.30	2.14	4.44	4.89	4.01	6.24	4.45	5.64
ZnO	0.17	0.44	0.28	0.46	0.26	0.13	0.26	0.23	0.16	0.22	0.34
CaO	0.02	0.02	0.01	0.03	0.02	0.01	0.02	0.01	0.00	0.06	0.03
Na_2O	0.12	0.08	0.05	0.08	0.02	0.06	<0.02	0.02	0.02	0.06	<0.02
K_2O	0.00	0.00	0.00	0.00	0.00	0.00	0.00	0.00	0.00	0.00	0.00
NiO	<0.03	0.03	<0.03	0.03	0.04	<0.03	0.04	<0.03	0.03	<0.03	0.03
Cations to 32 oxygens											
Si	0.00	0.00	0.00	0.00	0.00	0.00	0.00	0.00	0.00	0.03	0.00
Ti	0.00	0.00	0.00	0.00	0.00	0.00	0.00	0.00	0.00	0.00	0.00
Al	0.27	0.27	0.26	0.27	0.11	0.21	0.22	0.22	0.29	0.16	0.28
Cr	1.73	1.73	1.73	1.72	1.82	1.81	1.81	1.80	1.72	1.77	1.72
Fe^{3+}	0.00	0.00	0.01	0.01	0.07	0.00	0.00	0.00	0.00	0.01	0.00
Fe^{2+}	0.62	0.61	0.75	0.69	0.85	0.72	0.69	0.75	0.65	0.77	0.68
Mn^{2+}	0.01	0.01	0.02	0.02	0.02	0.02	0.01	0.02	0.02	0.02	0.02
Mg	0.35	0.35	0.22	0.27	0.12	0.23	0.26	0.21	0.32	0.23	0.29
Zn	0.00	0.01	0.01	0.01	0.01	0.00	0.01	0.01	0.00	0.01	0.01
Ca	0.00	0.00	0.00	0.00	0.00	0.00	0.00	0.00	0.00	0.00	0.00
Na	0.01	0.01	0.00	0.01	0.00	0.00	0.00	0.00	0.00	0.00	0.00
K	0.00	0.00	0.00	0.00	0.00	0.00	0.00	0.00	0.00	0.00	0.00
Ni	0.00	0.00	0.00	0.00	0.00	0.00	0.00	0.00	0.00	0.00	0.00
Mg #	0.36	0.36	0.23	0.29	0.12	0.24	0.27	0.22	0.33	0.23	0.30
Fe #	0.64	0.64	0.77	0.71	0.88	0.76	0.73	0.78	0.67	0.77	0.70
Cr #	0.87	0.87	0.86	0.86	0.91	0.89	0.89	0.89	0.85	0.91	0.86
Fe^{3+}#	0.00	0.00	0.01	0.00	0.04	0.00	0.00	0.00	0.00	0.00	0.00

Table 1: Chrome spinel microprobe analyses from ultramafic rocks of the Western Ethiopian Shield

ID number	E14-10-01	E14-10-02	E14-10-03	E14-10-04	E14-10-05	E14-10-06	E14-10-07	E14-10-08	E14-10-09	E14-10-10	E14-10-11	E14-10-12	E14-10-13
Yubdo E14.10 (8° 57'37.4" N, 35° 27' 18.2'													
SiO_2	<0.01	0.08	0.04	0.05	<0.01	0.03	<0.01	0.38	0.02	0.05	0.14	0.16	0.09
TiO_2	0.45	0.38	0.49	0.41	0.46	0.40	0.46	0.48	0.47	0.48	0.44	0.42	0.35
$Al2O_3$	10.38	9.65	9.94	10.39	9.31	10.90	10.22	9.92	10.70	10.50	10.40	9.80	9.12
Cr_2O_3	41.67	42.45	44.32	42.34	42.52	36.57	43.49	43.19	39.07	37.33	40.82	39.58	39.34
Fe_2O_3	16.43	17.56	14.70	17.14	16.59	20.97	15.69	17.78	18.29	20.18	18.35	19.18	20.41
FeO	24.83	21.65	23.15	21.29	25.32	25.50	23.03	19.63	25.62	25.55	21.56	24.64	24.51
MnO	0.72	0.52	0.56	0.45	0.71	0.78	0.55	0.51	0.85	0.70	0.50	0.70	0.56
MgO	5.26	7.40	6.54	7.66	4.70	3.99	6.20	7.19	4.55	4.92	7.48	5.11	5.38
ZnO	0.21	0.28	0.20	0.17	0.30	0.58	0.15	0.19	0.35	0.22	0.19	0.17	0.11
CaO	<0.01	<0.01	<0.01	<0.01	<0.01	<0.01	<0.01	0.02	<0.01	<0.01	<0.01	0.02	0.00
Na_2O	<0.02	<0.02	0.02	0.05	0.04	0.21	0.14	0.69	0.03	0.04	0.06	0.11	0.03
K_2O	0.00	0.00	0.00	0.00	0.00	0.00	0.00	0.00	0.00	0.00	0.00	0.00	0.00
NiO	0.04	0.03	0.07	0.06	0.05	0.08	0.06	0.03	0.06	0.10	0.05	0.10	0.10
Cations to 32 oxygens													
Si	0.00	0.00	0.00	0.00	0.00	0.00	0.00	0.01	0.00	0.00	0.00	0.01	0.00
Ti	0.01	0.01	0.01	0.01	0.01	0.01	0.01	0.01	0.01	0.01	0.01	0.01	0.01
Al	0.42	0.39	0.40	0.41	0.38	0.44	0.41	0.39	0.44	0.43	0.41	0.40	0.37
Cr	1.13	1.14	1.19	1.13	1.17	1.00	1.17	1.15	1.07	1.02	1.09	1.08	1.08
Fe^{3+}	0.42	0.45	0.38	0.44	0.43	0.55	0.40	0.45	0.47	0.52	0.47	0.50	0.53
Fe^{2+}	0.71	0.61	0.66	0.60	0.73	0.74	0.66	0.55	0.74	0.74	0.61	0.71	0.71
Mn^{2+}	0.02	0.02	0.02	0.01	0.02	0.02	0.02	0.01	0.02	0.02	0.01	0.02	0.02
Mg	0.27	0.37	0.33	0.39	0.24	0.21	0.32	0.36	0.23	0.25	0.38	0.26	0.28
Zn	0.01	0.01	0.01	0.00	0.01	0.01	0.00	0.00	0.01	0.01	0.00	0.00	0.00
Ca	0.00	0.00	0.00	0.00	0.00	0.00	0.00	0.00	0.00	0.00	0.00	0.00	0.00
Na	0.00	0.00	0.00	0.00	0.00	0.01	0.00	0.04	0.00	0.00	0.00	0.01	0.00
K	0.00	0.00	0.00	0.00	0.00	0.00	0.00	0.00	0.00	0.00	0.00	0.00	0.00
Ni	0.00	0.00	0.00	0.00	0.00	0.00	0.00	0.00	0.00	0.00	0.00	0.00	0.00
Mg #	0.27	0.38	0.34	0.39	0.25	0.22	0.32	0.40	0.24	0.26	0.38	0.27	0.28
Fe #	0.73	0.62	0.66	0.61	0.75	0.78	0.68	0.60	0.76	0.74	0.62	0.73	0.72
Cr #	0.57	0.58	0.61	0.57	0.59	0.50	0.59	0.58	0.54	0.52	0.55	0.55	0.54
Fe^{3+}#	0.21	0.23	0.19	0.22	0.22	0.27	0.20	0.23	0.24	0.27	0.24	0.25	0.27

Table 1: Chrome spinel microprobe analyses from ultramafic rocks of the Western Ethiopian Shield

ID number	E14-10-14	E14-10-15	E14-10-16	E14-10-17	E14-10-18	E14-10-19	E14-10-20	E14-10-21	E14-10-22	E14-10-23	E14-10-24	E14-10-25
Yubdo E14.10 (8° 57'37.4" N, 35° 27' 18.2"E)												
SiO_2	0.00	0.03	<0.01	0.06	0.57	0.13	0.02	0.06	0.04	0.06	0.02	0.05
TiO_2	0.51	0.42	0.40	0.49	0.42	0.45	0.46	0.42	0.44	0.40	0.36	0.40
$Al2O3$	9.08	10.31	8.93	10.52	12.99	10.26	10.88	10.20	10.77	9.83	9.12	10.12
Cr_2O_3	41.81	40.90	37.84	37.11	39.48	43.59	43.23	41.97	40.18	40.11	40.82	38.69
Fe_2O_3	17.81	18.43	21.77	20.67	16.18	15.25	15.55	17.30	18.32	19.24	18.71	19.06
FeO	24.45	21.96	25.30	24.92	21.78	22.54	21.36	21.83	22.37	23.04	24.98	26.45
MnO	0.70	0.52	0.77	0.61	0.39	0.55	0.46	0.57	0.61	0.54	0.68	0.92
MgO	5.24	7.18	4.66	5.26	7.57	6.87	7.78	7.40	7.06	6.63	5.04	3.92
ZnO	0.21	0.18	0.20	0.21	0.18	0.27	0.18	0.14	0.20	0.11	0.15	0.31
CaO	0.02	<0.01	0.02	<0.01	0.14	<0.01	<0.01	<0.01	<0.01	<0.01	0.02	<0.01
Na_2O	0.05	0.04	<0.02	<0.02	0.19	0.03	<0.02	0.03	<0.02	0.03	<0.02	0.03
K_2O	0.00	0.00	0.00	0.00	0.00	0.00	0.00	0.00	0.00	0.00	0.00	0.00
NiO	0.12	0.05	0.12	0.11	0.10	0.07	0.07	0.14	0.03	0.06	0.10	0.04
Cations to 32 oxygens												
Si	0.00	0.00	0.00	0.00	0.02	0.00	0.00	0.00	0.00	0.00	0.00	0.00
Ti	0.01	0.01	0.01	0.01	0.01	0.01	0.01	0.01	0.01	0.01	0.01	0.01
Al	0.37	0.41	0.37	0.43	0.51	0.41	0.43	0.41	0.43	0.40	0.37	0.41
Cr	1.14	1.10	1.04	1.01	1.04	1.17	1.15	1.12	1.08	1.08	1.12	1.06
Fe^{3+}	0.46	0.47	0.57	0.53	0.41	0.39	0.39	0.44	0.47	0.49	0.49	0.50
Fe^{2+}	0.71	0.62	0.74	0.72	0.61	0.64	0.60	0.62	0.63	0.66	0.72	0.77
Mn^{2+}	0.02	0.01	0.02	0.02	0.01	0.02	0.01	0.02	0.02	0.02	0.02	0.03
Mg	0.27	0.36	0.24	0.27	0.38	0.35	0.39	0.37	0.36	0.34	0.26	0.20
Zn	0.01	0.00	0.01	0.01	0.00	0.01	0.00	0.00	0.00	0.00	0.00	0.01
Ca	0.00	0.00	0.00	0.00	0.01	0.00	0.00	0.00	0.00	0.00	0.00	0.00
Na	0.00	0.00	0.00	0.00	0.01	0.00	0.00	0.00	0.00	0.00	0.00	0.00
K	0.00	0.00	0.00	0.00	0.00	0.00	0.00	0.00	0.00	0.00	0.00	0.00
Ni	0.00	0.00	0.00	0.00	0.00	0.00	0.00	0.00	0.00	0.00	0.00	0.00
Mg #	0.28	0.37	0.25	0.27	0.38	0.35	0.39	0.38	0.36	0.34	0.26	0.21
Fe #	0.72	0.63	0.75	0.73	0.62	0.65	0.61	0.62	0.64	0.66	0.74	0.79
Cr #	0.58	0.55	0.53	0.51	0.53	0.59	0.58	0.57	0.55	0.55	0.57	0.54
Fe^{3+}#	0.23	0.24	0.29	0.27	0.21	0.20	0.20	0.22	0.24	0.25	0.25	0.25

Table 1: Chrome spinel microprobe analyses from ultramafic rocks of the Western Ethiopian Shield

ID number	E14-19-02	E14-19-03	E14-19-04	E14-19-05	E14-19-06	E14-19-07	E14-19-08	E14-19-09	E14-19-10	E14-19-11	E14-19-12	E14-19-13	E14-19-14	E14-19-15
Abshala Melange E14.19 (09° 23' 16.0" N 035° 43' 15.9" E)														
SiO_2	0.21	<0.01	<0.01	0.04	0.02	<0.01	<0.01	0.03	0.04	0.09	<0.01	<0.01	0.02	0.06
TiO_2	<0.01	0.03	<0.01	0.01	<0.01	0.02	<0.01	0.06	0.01	0.01	<0.01	0.01	0.04	0.02
Al_2O_3	7.24	7.51	7.37	8.11	8.01	8.31	7.80	7.00	7.16	8.20	8.15	6.99	7.13	7.10
Cr_2O_3	62.62	58.94	56.72	64.27	59.33	62.18	59.30	57.63	56.74	65.46	55.40	65.72	60.35	61.68
Fe_2O_3	0.00	1.41	6.71	0.00	2.33	0.00	0.29	4.19	7.48	0.00	7.03	0.00	1.29	0.00
FeO	26.72	28.75	21.43	22.53	23.72	26.28	30.10	26.70	19.76	22.12	21.27	22.71	26.78	28.49
MnO	0.29	0.34	0.37	0.42	0.39	0.36	0.38	0.34	0.37	0.38	0.44	0.34	0.35	0.42
MgO	2.57	2.21	7.18	4.24	5.81	2.25	1.33	3.76	8.12	3.55	7.42	3.85	3.74	1.22
ZnO	0.31	0.75	0.17	0.35	0.35	0.58	0.67	0.27	0.19	0.23	0.23	0.29	0.25	0.87
CaO	<0.01	<0.01	<0.01	<0.01	<0.01	<0.01	<0.01	<0.01	<0.01	<0.01	<0.01	0.02	<0.01	0.03
Na_2O	0.04	0.02	0.04	<0.02	<0.02	<0.02	0.02	<0.02	0.09	<0.02	<0.02	0.04	0.04	0.04
K_2O	0.00	0.00	0.00	0.00	0.00	0.00	0.00	0.00	0.00	0.00	0.00	0.00	0.00	0.00
NiO	<0.03	<0.03	<0.03	0.03	0.03	<0.03	0.10	0.07	0.03	<0.03	0.07	0.05	<0.03	0.07
Cations to 32 oxygens														
Si	0.01	0.00	0.00	0.00	0.00	0.00	0.00	0.00	0.00	0.00	0.00	0.00	0.00	0.00
Ti	0.00	0.00	0.00	0.00	0.00	0.00	0.00	0.00	0.00	0.00	0.00	0.00	0.00	0.00
Al	0.30	0.31	0.30	0.33	0.32	0.35	0.33	0.29	0.29	0.34	0.33	0.29	0.29	0.30
Cr	1.75	1.65	1.53	1.77	1.61	1.73	1.67	1.60	1.52	1.81	1.49	1.82	1.67	1.74
Fe^{3+}	0.00	0.04	0.17	0.00	0.06	0.00	0.01	0.11	0.19	0.00	0.18	0.00	0.03	0.00
Fe^{2+}	0.79	0.85	0.61	0.66	0.68	0.78	0.89	0.78	0.56	0.65	0.61	0.67	0.78	0.85
Mn^{2+}	0.01	0.01	0.01	0.01	0.01	0.01	0.01	0.01	0.01	0.01	0.01	0.01	0.01	0.01
Mg	0.14	0.12	0.37	0.22	0.30	0.12	0.07	0.20	0.41	0.19	0.38	0.20	0.20	0.06
Zn	0.01	0.02	0.00	0.01	0.01	0.02	0.02	0.01	0.00	0.01	0.01	0.01	0.01	0.02
Ca	0.00	0.00	0.00	0.00	0.00	0.00	0.00	0.00	0.00	0.00	0.00	0.00	0.00	0.00
Na	0.00	0.00	0.00	0.00	0.00	0.00	0.00	0.00	0.01	0.00	0.00	0.00	0.00	0.00
K	0.00	0.00	0.00	0.00	0.00	0.00	0.00	0.00	0.00	0.00	0.00	0.00	0.00	0.00
Ni	0.00	0.00	0.00	0.00	0.00	0.00	0.00	0.00	0.00	0.00	0.00	0.00	0.00	0.00
Mg #	0.15	0.12	0.37	0.25	0.30	0.13	0.07	0.20	0.42	0.22	0.38	0.23	0.20	0.07
Fe #	0.85	0.88	0.63	0.75	0.70	0.87	0.93	0.80	0.58	0.78	0.62	0.77	0.80	0.93
Cr #	0.85	0.82	0.77	0.84	0.81	0.83	0.83	0.80	0.76	0.84	0.75	0.86	0.84	0.85
Fe^{3+} #	0.00	0.02	0.09	0.00	0.03	0.00	0.00	0.06	0.10	0.00	0.09	0.00	0.02	0.00

Table 1: Chrome spinel microprobe analyses from ultramafic rocks of the Western Ethiopian Shield

ID number	E14-19-16	E14-19-17	E14-19-18	E14-19-19	E14-19-20	E14-19-21	E14-19-22	E14-19-23	E14-19-24	E14-19-25	E14-19-26	E14-19-27	E14-19-28 E
Abshala Melange E14.19 (09° 23' 16.0" N 035° 43' 15.9" E)													
SiO_2	0.09	0.03	0.08	0.04	0.06	0.04	0.03	0.03	0.05	0.06	<0.01	0.13	0.49
TiO_2	<0.01	0.01	<0.01	0.01	<0.01	<0.01	0.01	<0.01	0.01	<0.01	<0.01	<0.01	<0.01
$Al2O_3$	6.78	7.07	9.84	10.29	10.57	9.78	10.06	6.89	7.59	6.77	7.31	6.37	9.43
Cr_2O_3	60.59	58.00	53.02	60.42	63.30	56.39	55.06	64.32	60.66	63.87	64.81	61.58	60.52
Fe_2O_3	0.00	3.23	7.96	0.13	0.00	2.99	6.01	0.00	3.22	0.98	0.00	2.55	0.00
FeO	30.09	27.78	19.88	19.85	21.72	25.09	19.28	20.31	18.77	18.65	20.80	21.90	21.80
MnO	0.36	0.24	0.48	0.42	0.26	0.34	0.41	0.46	0.39	0.43	0.37	0.29	0.33
MgO	1.23	2.88	8.50	8.57	3.41	5.05	8.90	7.71	9.14	9.02	6.37	6.90	7.14
ZnO	0.78	0.68	0.17	0.18	0.68	0.22	0.19	0.16	0.15	0.09	0.24	0.12	0.27
CaO	<0.01	<0.01	<0.01	<0.01	<0.01	0.02	<0.01	<0.01	<0.01	<0.01	<0.01	0.06	0.02
Na_2O	0.04	0.02	<0.02	0.04	0.03	0.05	0.03	0.05	<0.02	0.04	<0.02	0.05	<0.02
K_2O	0.00	0.00	0.00	0.00	0.00	0.00	0.00	0.00	0.00	0.00	0.00	0.00	0.00
NiO	0.05	0.04	0.07	0.05	<0.03	<0.03	0.02	0.08	<0.03	0.07	0.07	0.06	0.01
Cations to 32 oxygens													
Si	0.00	0.00	0.00	0.00	0.00	0.00	0.00	0.00	0.00	0.00	0.00	0.00	0.02
Ti	0.00	0.00	0.00	0.00	0.00	0.00	0.00	0.00	0.00	0.00	0.00	0.00	0.00
Al	0.29	0.29	0.39	0.40	0.43	0.40	0.40	0.28	0.30	0.27	0.30	0.26	0.38
Cr	1.71	1.62	1.41	1.59	1.73	1.53	1.45	1.73	1.61	1.70	1.76	1.67	1.62
Fe^{3+}	0.00	0.09	0.20	0.00	0.00	0.08	0.15	0.00	0.08	0.02	0.00	0.07	0.00
Fe^{2+}	0.90	0.82	0.56	0.55	0.63	0.72	0.54	0.58	0.53	0.53	0.60	0.63	0.62
Mn^{2+}	0.01	0.01	0.01	0.01	0.01	0.01	0.01	0.01	0.01	0.01	0.01	0.01	0.01
Mg	0.07	0.15	0.42	0.43	0.18	0.26	0.44	0.39	0.46	0.45	0.33	0.35	0.36
Zn	0.02	0.02	0.00	0.00	0.02	0.01	0.00	0.00	0.00	0.00	0.01	0.00	0.01
Ca	0.00	0.00	0.00	0.00	0.00	0.00	0.00	0.00	0.00	0.00	0.00	0.00	0.00
Na	0.00	0.00	0.00	0.00	0.00	0.00	0.00	0.00	0.00	0.00	0.00	0.00	0.00
K	0.00	0.00	0.00	0.00	0.00	0.00	0.00	0.00	0.00	0.00	0.00	0.00	0.00
Ni	0.00	0.00	0.00	0.00	0.00	0.00	0.00	0.00	0.00	0.00	0.00	0.00	0.00
Mg #	0.07	0.16	0.43	0.43	0.22	0.26	0.45	0.40	0.46	0.46	0.35	0.36	0.37
Fe #	0.93	0.84	0.57	0.57	0.78	0.74	0.55	0.60	0.54	0.54	0.65	0.64	0.63
Cr #	0.86	0.81	0.70	0.80	0.80	0.76	0.73	0.86	0.81	0.85	0.86	0.84	0.81
Fe^{3+} #	0.00	0.04	0.10	0.00	0.00	0.04	0.08	0.00	0.04	0.01	0.00	0.03	0.00

Table 1: Chrome spinel microprobe analyses from ultramafic rocks of the Western Ethiopian Shield

ID number	E13-22-01	E13-22-02	E13-22-03	E13-22-04	E13-22-05	E13-22-06	E13-22-07	E13-22-08	E13-22-09	E13-22-10	E13-22-11	E13-22-12	E13-22-13
Tulu Dimtu Hill (9° 27' 60.9"N 35° 44' 19.8"E)													
SiO_2	<0.01	<0.01	<0.01	<0.01	<0.01	<0.01	0.06	<0.01	<0.01	<0.01	<0.01	<0.01	0.01
TiO_2	0.39	0.37	0.08	0.42	0.20	0.25	0.24	0.37	0.38	0.30	0.37	0.38	0.37
$Al2O3$	10.85	10.68	5.86	0.20	10.56	10.02	0.07	10.67	10.59	9.00	11.03	10.84	10.56
Cr_2O_3	53.16	53.48	50.12	34.65	52.40	51.78	17.92	53.11	53.48	51.12	52.75	53.02	53.99
Fe_2O_3	3.56	3.47	12.16	33.26	4.61	5.68	50.36	3.63	3.56	7.24	3.63	3.54	3.15
FeO	27.26	27.04	28.37	29.67	27.85	28.04	30.25	27.42	27.13	28.44	27.31	27.44	26.97
MnO	0.47	0.56	0.72	0.63	0.68	0.67	0.32	0.65	0.52	0.69	0.65	0.57	0.51
MgO	3.90	3.96	2.20	0.78	3.09	2.84	0.45	3.53	3.94	2.57	3.67	3.65	4.07
ZnO	0.34	0.40	0.44	0.26	0.57	0.63	0.16	0.57	0.38	0.62	0.51	0.47	0.35
CaO	<0.01	<0.01	<0.01	0.03	0.03	0.02	0.09	0.03	<0.01	<0.01	<0.01	<0.01	<0.01
Na_2O	<0.02	<0.02	<0.02	0.04	<0.02	0.02	<0.02	<0.02	<0.02	<0.02	<0.02	<0.02	<0.02
K_2O	0.00	0.00	0.00	0.00	0.00	0.00	0.00	0.00	0.00	0.00	0.00	0.00	0.00
NiO	0.04	0.03	<0.03	0.06	<0.03	0.03	0.08	<0.03	<0.03	<0.03	0.04	0.07	<0.03
Cations to 32 oxygens													
Si	0.00	0.00	0.00	0.00	0.00	0.00	0.00	0.00	0.00	0.00	0.00	0.00	0.00
Ti	0.01	0.01	0.00	0.01	0.01	0.01	0.01	0.01	0.01	0.01	0.01	0.01	0.01
Al	0.44	0.43	0.25	0.01	0.43	0.41	0.00	0.43	0.43	0.37	0.45	0.44	0.43
Cr	1.45	1.46	1.42	1.03	1.44	1.43	0.54	1.45	1.46	1.42	1.44	1.45	1.47
Fe^{3+}	0.09	0.09	0.33	0.94	0.12	0.15	1.44	0.09	0.09	0.19	0.09	0.09	0.08
Fe^{2+}	0.78	0.78	0.85	0.93	0.81	0.82	0.96	0.79	0.78	0.84	0.79	0.79	0.78
Mn^{2+}	0.01	0.02	0.02	0.02	0.02	0.02	0.01	0.02	0.02	0.02	0.02	0.02	0.01
Mg	0.20	0.20	0.12	0.04	0.16	0.15	0.03	0.18	0.20	0.13	0.19	0.19	0.21
Zn	0.01	0.01	0.01	0.01	0.01	0.02	0.00	0.01	0.01	0.02	0.01	0.01	0.01
Ca	0.00	0.00	0.00	0.00	0.00	0.00	0.00	0.00	0.00	0.00	0.00	0.00	0.00
Na	0.00	0.00	0.00	0.00	0.00	0.00	0.00	0.00	0.00	0.00	0.00	0.00	0.00
K	0.00	0.00	0.00	0.00	0.00	0.00	0.00	0.00	0.00	0.00	0.00	0.00	0.00
Ni	0.00	0.00	0.00	0.00	0.00	0.00	0.00	0.00	0.00	0.00	0.00	0.00	0.00
Mg #	0.20	0.21	0.12	0.04	0.17	0.15	0.03	0.19	0.21	0.14	0.19	0.19	0.21
Fe #	0.80	0.79	0.88	0.96	0.83	0.85	0.97	0.81	0.79	0.86	0.81	0.81	0.79
Cr #	0.73	0.74	0.71	0.52	0.72	0.72	0.27	0.73	0.74	0.72	0.73	0.73	0.74
Fe^{3+} #	0.05	0.05	0.16	0.48	0.06	0.08	0.73	0.05	0.05	0.10	0.05	0.05	0.04

Table 1: Chrome spinel microprobe analyses from ultramafic rocks of the Western Ethiopian Shield

ID number	E13-22-14	E13-22-15	E13-22-16	E13-22-17	E13-22-18	E13-22-19	E13-22-20	E13-22-21	E13-22-22	E13-22-23	E13-22-24	E13-22-25	E1
Tulu Dimtu Hill (9° 27' 60.9"N 35° 44' 19.8"E)													
SiO_2	0.02	<0.01	<0.01	<0.01	0.04	0.02	<0.01	<0.01	<0.01	<0.01	0.02	<0.01	<0.01
TiO_2	0.34	0.31	0.36	0.34	0.33	0.31	0.41	0.26	0.26	0.17	0.23	0.26	
$Al2O_3$	10.40	9.20	10.41	10.03	9.58	10.76	0.21	8.71	8.83	0.20	8.57	8.16	
Cr_2O_3	53.96	52.46	53.68	54.05	52.48	53.28	33.32	56.42	56.55	13.08	55.25	56.80	
Fe_2O_3	3.23	5.66	3.45	3.44	5.25	3.53	35.03	3.06	2.94	55.47	3.95	3.23	
FeO	27.29	28.38	27.31	27.62	27.97	27.41	29.09	26.70	26.33	29.84	27.64	27.05	
MnO	0.58	0.72	0.61	0.61	0.65	0.63	0.56	0.57	0.45	0.21	0.63	0.48	
MgO	3.74	2.68	3.65	3.43	3.01	3.47	0.90	3.96	4.31	0.59	3.10	3.66	
ZnO	0.42	0.53	0.50	0.47	0.66	0.50	0.18	0.26	0.27	0.14	0.54	0.31	
CaO	<0.01	<0.01	<0.01	<0.01	0.02	<0.01	0.02	<0.01	<0.01	<0.01	<0.01	<0.01	
Na_2O	<0.02	<0.02	<0.02	<0.02	<0.02	0.04	0.14	<0.02	<0.02	0.01	0.01	0.03	
K_2O	0.00	0.00	0.00	0.00	0.00	0.00	0.00	0.00	0.00	0.00	0.00	0.00	
NiO	<0.03	0.03	<0.03	<0.03	<0.03	0.03	0.14	0.05	0.03	0.27	0.03	<0.03	
Cations to 32 oxygens													
Si	0.00	0.00	0.00	0.00	0.00	0.00	0.00	0.00	0.00	0.00	0.00	0.00	
Ti	0.01	0.01	0.01	0.01	0.01	0.01	0.01	0.01	0.01	0.00	0.01	0.01	
Al	0.42	0.38	0.42	0.41	0.39	0.44	0.01	0.36	0.36	0.01	0.35	0.34	
Cr	1.47	1.45	1.47	1.48	1.45	1.46	0.99	1.55	1.55	0.39	1.53	1.57	
Fe^{3+}	0.08	0.15	0.09	0.09	0.14	0.09	0.99	0.08	0.08	1.59	0.10	0.08	
Fe^{2+}	0.79	0.83	0.79	0.80	0.82	0.79	0.91	0.78	0.76	0.95	0.81	0.79	
Mn^{2+}	0.02	0.02	0.02	0.02	0.02	0.02	0.02	0.02	0.01	0.01	0.02	0.01	
Mg	0.19	0.14	0.19	0.18	0.16	0.18	0.05	0.21	0.22	0.03	0.16	0.19	
Zn	0.01	0.01	0.01	0.01	0.02	0.01	0.00	0.01	0.01	0.00	0.01	0.01	
Ca	0.00	0.00	0.00	0.00	0.00	0.00	0.00	0.00	0.00	0.00	0.00	0.00	
Na	0.00	0.00	0.00	0.00	0.00	0.00	0.01	0.00	0.00	0.00	0.00	0.00	
K	0.00	0.00	0.00	0.00	0.00	0.00	0.00	0.00	0.00	0.00	0.00	0.00	
Ni	0.00	0.00	0.00	0.00	0.00	0.00	0.00	0.00	0.00	0.01	0.00	0.00	
Mg #	0.20	0.14	0.19	0.18	0.16	0.18	0.05	0.21	0.23	0.03	0.17	0.19	
Fe #	0.80	0.86	0.81	0.82	0.84	0.82	0.95	0.79	0.77	0.97	0.83	0.81	
Cr #	0.74	0.73	0.74	0.75	0.73	0.73	0.50	0.78	0.78	0.20	0.77	0.79	
Fe^{3+}#	0.04	0.08	0.05	0.05	0.07	0.05	0.50	0.04	0.04	0.80	0.05	0.04	

Table 1: Chrome spinel microprobe analyses from ultramafic rocks of the Western Ethiopian Shield

ID number	E13-22-27	E13-22-28	E13-22-29	E13-22-30	E13-22-31	E13-22-32	E13-22-33	E13-22-34	E13-22-35	E13-22-36	E13-22-37	E13-22-38	E13-22-39
Tulu Dimtu Hill (9° 27' 60.9"N 35° 44' 19.8"E)													
SiO_2	<0.01	0.02	<0.01	<0.01	0.02	<0.01	<0.01	0.02	<0.01	<0.01	0.05	0.02	0.01
TiO_2	0.24	0.05	0.11	0.10	0.20	0.23	0.41	0.36	0.23	0.21	0.23	0.07	0.24
Al_2O_3	8.19	4.36	3.99	7.54	1.38	8.25	0.61	1.12	7.95	8.06	7.54	7.89	7.72
Cr_2O_3	56.67	53.07	51.86	55.55	50.11	56.85	43.89	35.91	57.10	57.19	56.97	50.76	57.63
Fe_2O_3	3.10	10.79	12.38	5.03	16.75	2.98	23.57	31.09	2.90	2.70	3.29	9.28	2.71
FeO	27.55	28.60	28.74	27.70	28.91	27.14	29.05	29.34	27.51	27.43	27.70	28.24	27.34
MnO	0.60	0.77	0.76	0.70	0.76	0.59	0.83	0.64	0.72	0.66	0.65	0.74	0.68
MgO	3.34	1.90	1.79	2.89	1.42	3.53	1.29	1.23	3.14	3.24	2.85	2.46	3.34
ZnO	0.29	0.43	0.31	0.47	0.38	0.37	0.26	0.14	0.38	0.47	0.61	0.46	0.29
CaO	0.02	<0.01	<0.01	<0.01	<0.01	0.02	<0.01	<0.01	<0.01	<0.01	0.05	<0.01	<0.01
Na_2O	<0.02	<0.02	0.02	<0.02	<0.02	<0.02	<0.02	<0.02	0.02	<0.02	0.03	0.01	0.02
K_2O	0.00	0.00	0.00	0.00	0.00	0.00	0.00	0.00	0.00	0.00	0.00	0.00	0.00
NiO	<0.03	<0.03	0.03	<0.03	0.06	0.03	0.09	0.14	0.03	0.02	0.04	0.04	<0.03
Cations to 32 oxygens													
Si	0.00	0.00	0.00	0.00	0.00	0.00	0.00	0.00	0.00	0.00	0.00	0.00	0.00
Ti	0.01	0.00	0.00	0.00	0.01	0.01	0.01	0.01	0.01	0.01	0.01	0.00	0.01
Al	0.34	0.19	0.17	0.31	0.06	0.34	0.03	0.05	0.33	0.33	0.31	0.33	0.32
Cr	1.57	1.52	1.49	1.55	1.46	1.57	1.29	1.06	1.58	1.58	1.59	1.42	1.60
Fe^{3+}	0.08	0.29	0.34	0.13	0.47	0.08	0.66	0.87	0.08	0.07	0.09	0.25	0.07
Fe^{2+}	0.81	0.86	0.87	0.82	0.89	0.79	0.90	0.91	0.81	0.80	0.82	0.84	0.80
Mn^{2+}	0.02	0.02	0.02	0.02	0.02	0.02	0.03	0.02	0.02	0.02	0.02	0.02	0.02
Mg	0.17	0.10	0.10	0.15	0.08	0.18	0.07	0.07	0.16	0.17	0.15	0.13	0.17
Zn	0.01	0.01	0.01	0.01	0.01	0.01	0.01	0.00	0.01	0.01	0.02	0.01	0.01
Ca	0.00	0.00	0.00	0.00	0.00	0.00	0.00	0.00	0.00	0.00	0.00	0.00	0.00
Na	0.00	0.00	0.00	0.00	0.00	0.00	0.00	0.00	0.00	0.00	0.00	0.00	0.00
K	0.00	0.00	0.00	0.00	0.00	0.00	0.00	0.00	0.00	0.00	0.00	0.00	0.00
Ni	0.00	0.00	0.00	0.00	0.00	0.00	0.00	0.00	0.00	0.00	0.00	0.00	0.00
Mg #	0.18	0.11	0.10	0.16	0.08	0.19	0.07	0.07	0.17	0.17	0.15	0.13	0.18
Fe #	0.82	0.89	0.90	0.84	0.92	0.81	0.93	0.93	0.83	0.83	0.85	0.87	0.82
Cr #	0.79	0.76	0.75	0.78	0.74	0.79	0.65	0.53	0.80	0.80	0.80	0.71	0.80
Fe^{3+} #	0.04	0.15	0.17	0.07	0.23	0.04	0.33	0.44	0.04	0.04	0.04	0.12	0.04

Table 1: Chrome spinel microprobe analyses from ultramafic rocks of the Western Ethiopian Shield

ID number	E13-22-40	E13-22-41	E13-22-42	E13-22-43	E13-22-44	E13-22-45	E13-22-46	E13-22-47	E13-22-48	E13-22-49	E13-22-50	E13-22-51
Tulu Dimtu Hill (9° 27′ 60.9″N 35° 44′ 19.8″E)												
SiO_2	0.04	<0.01	<0.01	<0.01	<0.01	<0.01	<0.01	0.02	0.02	0.03	<0.01	<0.01
TiO_2	0.22	0.22	0.09	0.21	0.17	0.24	0.09	0.24	0.30	0.29	0.23	0.24
$Al2O_3$	7.67	7.78	3.88	7.77	5.78	7.78	3.24	7.81	0.18	0.63	7.74	7.81
Cr_2O_3	56.90	57.18	54.37	57.47	55.94	57.06	53.81	57.20	22.91	29.56	56.84	57.35
Fe_2O_3	3.29	3.04	10.00	2.86	6.41	3.13	11.18	2.99	45.30	38.14	3.36	2.84
FeO	27.67	27.39	28.61	27.32	27.87	27.38	28.59	27.34	29.80	29.63	27.59	27.52
MnO	0.67	0.72	0.75	0.66	0.69	0.71	0.80	0.69	0.41	0.50	0.70	0.60
MgO	3.06	3.17	1.89	3.33	2.62	3.24	1.69	3.28	0.72	0.93	2.98	3.15
ZnO	0.46	0.45	0.38	0.31	0.46	0.46	0.55	0.37	0.09	0.14	0.51	0.38
CaO	<0.01	0.02	<0.01	0.02	<0.01	<0.01	0.02	0.02	0.03	<0.01	0.02	0.02
Na_2O	<0.02	<0.02	<0.02	<0.02	<0.02	<0.02	<0.02	0.03	<0.02	0.02	0.03	0.03
K_2O	0.00	0.00	0.00	0.00	0.00	0.00	0.00	0.00	0.00	0.00	0.00	0.00
NiO	<0.03	0.03	<0.03	0.04	0.05	<0.03	0.03	<0.03	0.22	0.13	<0.03	0.05
ons to 32 oxygens												
Si	0.00	0.00	0.00	0.00	0.00	0.00	0.00	0.00	0.00	0.00	0.00	0.00
Ti	0.01	0.01	0.00	0.01	0.00	0.01	0.00	0.01	0.01	0.01	0.01	0.01
Al	0.32	0.32	0.17	0.32	0.24	0.32	0.14	0.32	0.01	0.03	0.32	0.32
Cr	1.58	1.59	1.56	1.59	1.58	1.58	1.55	1.59	0.69	0.88	1.58	1.59
Fe^{3+}	0.09	0.08	0.27	0.08	0.17	0.08	0.31	0.08	1.29	1.08	0.09	0.08
Fe^{2+}	0.81	0.80	0.87	0.80	0.83	0.80	0.87	0.80	0.94	0.93	0.81	0.81
Mn^{2+}	0.02	0.02	0.02	0.02	0.02	0.02	0.02	0.02	0.01	0.02	0.02	0.02
Mg	0.16	0.17	0.10	0.17	0.14	0.17	0.09	0.17	0.04	0.05	0.16	0.16
Zn	0.01	0.01	0.01	0.01	0.01	0.01	0.01	0.01	0.00	0.00	0.01	0.01
Ca	0.00	0.00	0.00	0.00	0.00	0.00	0.00	0.00	0.00	0.00	0.00	0.00
Na	0.00	0.00	0.00	0.00	0.00	0.00	0.00	0.00	0.00	0.00	0.00	0.00
K	0.00	0.00	0.00	0.00	0.00	0.00	0.00	0.00	0.00	0.00	0.00	0.00
Ni	0.00	0.00	0.00	0.00	0.00	0.00	0.00	0.00	0.01	0.00	0.00	0.00
Mg #	0.16	0.17	0.11	0.18	0.14	0.17	0.10	0.18	0.04	0.05	0.16	0.17
Fe #	0.84	0.83	0.89	0.82	0.86	0.83	0.90	0.82	0.96	0.95	0.84	0.83
Cr #	0.80	0.80	0.78	0.80	0.79	0.80	0.78	0.80	0.35	0.44	0.79	0.80
Fe^{3+}#	0.04	0.04	0.14	0.04	0.09	0.04	0.15	0.04	0.65	0.54	0.04	0.04

Table 1: Chrome spinel microprobe analyses from ultramafic rocks of the Western Ethiopian Shield

Daleti Quarry – E13.11 (09° 09' 56.4" N, 35° 37' 30.0" E)

ID number	E13 - 11 - 01	E13 - 11 - 02	E13 - 11 - 03	E13 - 11 - 04	E13 - 11 - 05	E13 - 11 - 06	E13 - 11 - 07	E13 - 11 - 08	E13 - 11 - 09	E13 - 11 - 10	E13 - 11 - 11	E13 - 11 - 12	E13 - 11 - 13
SiO_2	<0.01	<0.01	<0.01	0.02	0.02	0.04	<0.01	<0.01	0.02	0.02	<0.01	0.02	0.02
TiO_2	<0.01	<0.01	<0.01	0.02	<0.01	<0.01	<0.01	0.01	<0.01	<0.01	<0.01	<0.01	<0.01
Al_2O_3	0.60	0.76	0.67	1.88	0.93	0.81	2.47	1.66	2.06	1.20	2.11	1.63	1.94
Cr_2O_3	30.82	31.58	31.46	35.80	32.55	31.50	44.68	37.65	39.38	36.54	36.91	36.28	37.37
Fe_2O_3	37.19	36.36	36.53	30.65	35.07	36.22	21.12	29.15	27.06	30.84	29.39	30.61	29.09
FeO	28.01	27.72	27.87	27.23	27.57	27.58	27.10	27.57	27.21	27.52	27.08	27.20	27.08
MnO	2.26	2.30	2.29	3.08	2.70	2.65	3.24	2.76	2.94	2.56	3.20	3.07	3.26
MgO	0.47	0.54	0.52	0.61	0.54	0.53	0.67	0.60	0.58	0.63	0.61	0.58	0.58
ZnO	0.16	0.21	0.18	0.30	0.16	0.17	0.46	0.18	0.31	0.24	0.30	0.16	0.25
CaO	<0.01	<0.01	<0.01	<0.01	<0.01	<0.01	<0.01	<0.01	<0.01	<0.01	<0.01	<0.01	<0.01
Na_2O	<0.02	0.03	<0.02	<0.02	<0.02	<0.02	0.03	0.03	0.07	0.03	0.02	0.04	0.03
K_2O	0.00	0.00	0.00	0.00	0.00	0.00	0.00	0.00	0.00	0.00	0.00	0.00	0.00
NiO	0.47	0.48	0.47	0.41	0.43	0.49	0.24	0.37	0.36	0.41	0.36	0.41	0.37
Cations to 32 oxygens													
Si	0.00	0.00	0.00	0.00	0.00	0.00	0.00	0.00	0.00	0.00	0.00	0.00	0.00
Ti	0.00	0.00	0.00	0.00	0.00	0.00	0.00	0.00	0.00	0.00	0.00	0.00	0.00
Al	0.03	0.03	0.03	0.08	0.04	0.04	0.11	0.07	0.09	0.05	0.09	0.07	0.09
Cr	0.92	0.94	0.94	1.06	0.97	0.94	1.31	1.11	1.16	1.08	1.09	1.07	1.10
Fe^{3+}	1.05	1.03	1.03	0.86	0.99	1.02	0.59	0.82	0.76	0.87	0.82	0.86	0.82
Fe^{2+}	0.88	0.87	0.88	0.85	0.87	0.87	0.84	0.86	0.85	0.86	0.84	0.85	0.84
Mn^{2+}	0.07	0.07	0.07	0.10	0.09	0.08	0.10	0.09	0.09	0.08	0.10	0.10	0.10
Mg	0.03	0.03	0.03	0.03	0.03	0.03	0.04	0.03	0.03	0.03	0.03	0.03	0.03
Zn	0.00	0.01	0.01	0.01	0.00	0.00	0.01	0.01	0.01	0.01	0.01	0.00	0.01
Ca	0.00	0.00	0.00	0.00	0.00	0.00	0.00	0.00	0.00	0.00	0.00	0.00	0.00
Na	0.00	0.00	0.00	0.00	0.00	0.00	0.00	0.00	0.00	0.00	0.00	0.00	0.00
K	0.00	0.00	0.00	0.00	0.00	0.00	0.00	0.00	0.00	0.00	0.00	0.00	0.00
Ni	0.01	0.01	0.01	0.01	0.01	0.01	0.01	0.01	0.01	0.01	0.01	0.01	0.01
Mg #	0.03	0.03	0.03	0.04	0.03	0.03	0.04	0.04	0.04	0.04	0.04	0.04	0.04
Fe #	0.97	0.97	0.97	0.96	0.97	0.97	0.96	0.96	0.96	0.96	0.96	0.96	0.96
Cr #	0.46	0.47	0.47	0.53	0.48	0.47	0.65	0.55	0.58	0.54	0.54	0.53	0.55
Fe^{3+}#	0.53	0.51	0.52	0.43	0.50	0.51	0.29	0.41	0.38	0.43	0.41	0.43	0.41

Table 1: Chrome spinel microprobe analyses from ultramafic rocks of the Western Ethiopian Shield

Daleti Quarry – E13.11 (09° 09' 56.4" N, 35° 37' 30.0" E)

ID number	E13-11-14	E13-11-15	E13-11-16	E13-11-17	E13-11-18	E13-11-19	E13-11-20	E13-11-21	E13-11-22	E13-11-23	E13-11-24	E13-11-25	E13-11-26
SiO_2	<0.01	<0.01	<0.01	0.03	<0.01	<0.01	<0.01	<0.01	0.02	<0.01	<0.01	<0.01	0.015
TiO_2	0.01	0.01	<0.01	0.01	<0.01	0.01	0.02	<0.01	<0.01	0.01	0.01	0.02	0.010
$Al2O_3$	1.26	1.68	1.70	1.38	1.48	1.18	1.55	2.78	2.72	2.36	2.33	1.40	0.603
Cr_2O_3	35.65	37.81	36.85	36.24	36.62	35.72	37.03	45.08	47.61	39.18	39.35	36.62	32.549
Fe_2O_3	31.63	28.92	29.88	30.97	30.36	31.68	29.82	20.30	17.82	26.72	26.63	30.51	35.502
FeO	27.29	27.17	27.30	27.14	27.37	27.24	27.43	26.97	26.95	27.13	27.12	27.36	27.668
MnO	3.02	3.24	3.00	2.86	2.90	2.86	2.90	3.62	3.70	3.31	3.30	2.86	2.416
MgO	0.53	0.59	0.55	0.65	0.59	0.56	0.60	0.67	0.66	0.62	0.60	0.58	0.568
ZnO	0.19	0.23	0.31	0.27	0.24	0.27	0.26	0.38	0.32	0.31	0.33	0.23	0.217
CaO	<0.01	<0.01	<0.01	<0.01	<0.01	<0.01	<0.01	<0.01	<0.01	<0.01	<0.01	0.02	<0.01
Na_2O	0.02	<0.02	0.02	0.05	<0.02	0.03	<0.02	<0.02	0.03	<0.02	0.02	0.03	<0.02
K_2O	0.00	0.00	0.00	0.00	0.00	0.00	0.00	0.00	0.00	0.00	0.00	0.00	0.000
NiO	0.38	0.35	0.37	0.39	0.40	0.43	0.38	0.19	0.17	0.34	0.30	0.37	0.434
Cations to 32 oxygens													
Si	0.00	0.00	0.00	0.00	0.00	0.00	0.00	0.00	0.00	0.00	0.00	0.00	0.001
Ti	0.00	0.00	0.00	0.00	0.00	0.00	0.00	0.00	0.00	0.00	0.00	0.00	0.000
Al	0.06	0.07	0.07	0.06	0.07	0.05	0.07	0.12	0.12	0.10	0.10	0.06	0.027
Cr	1.05	1.11	1.09	1.07	1.08	1.06	1.09	1.32	1.39	1.15	1.15	1.08	0.968
Fe^{3+}	0.89	0.81	0.84	0.87	0.85	0.89	0.84	0.56	0.49	0.75	0.74	0.86	1.005
Fe^{2+}	0.85	0.85	0.85	0.85	0.85	0.85	0.86	0.83	0.83	0.84	0.84	0.85	0.870
Mn^{2+}	0.10	0.10	0.09	0.09	0.09	0.09	0.09	0.11	0.12	0.10	0.10	0.09	0.077
Mg	0.03	0.03	0.03	0.04	0.03	0.03	0.03	0.04	0.04	0.03	0.03	0.03	0.032
Zn	0.01	0.01	0.01	0.01	0.01	0.01	0.01	0.01	0.01	0.01	0.01	0.01	0.006
Ca	0.00	0.00	0.00	0.00	0.00	0.00	0.00	0.00	0.00	0.00	0.00	0.00	0.000
Na	0.00	0.00	0.00	0.00	0.00	0.00	0.00	0.00	0.00	0.00	0.00	0.00	0.001
K	0.00	0.00	0.00	0.00	0.00	0.00	0.00	0.00	0.00	0.00	0.00	0.00	0.000
Ni	0.01	0.01	0.01	0.01	0.01	0.01	0.01	0.01	0.01	0.01	0.01	0.01	0.013
Mg #	0.03	0.04	0.03	0.04	0.04	0.04	0.04	0.04	0.04	0.04	0.04	0.04	0.035
Fe #	0.97	0.96	0.97	0.96	0.96	0.96	0.96	0.96	0.96	0.96	0.96	0.96	0.965
Cr #	0.53	0.56	0.54	0.53	0.54	0.53	0.55	0.66	0.69	0.58	0.58	0.54	0.484
Fe^{3+}#	0.45	0.41	0.42	0.43	0.43	0.45	0.42	0.28	0.25	0.37	0.37	0.43	0.503

Table 1: Chrome spinel microprobe analyses from ultramafic rocks of the Western Ethiopian Shield

ID number	E13-11-27	E13-11-28	E13-11-29	E13-11-30	E13-11-31	E13-11-32	E13-11-33	E13-11-34	E13-11-35	E13-11-36	E13-11-37	E13-11-38	E13-11-39
Daleti Quarry – E13.11 (09° 09' 56.4" N, 35° 37' 30.0" E)													
SiO_2	<0.01	<0.01	<0.01	<0.01	<0.01	<0.01	<0.01	<0.01	<0.01	<0.01	<0.01	<0.01	0.02
TiO_2	0.01	<0.01	0.01	0.01	0.01	0.01	0.01	0.01	<0.01	0.02	0.01	0.01	<0.01
$Al2O_3$	0.57	0.78	0.90	0.78	0.95	0.66	1.84	1.26	2.34	1.36	0.91	0.60	0.60
Cr_2O_3	32.62	33.25	32.36	33.45	33.42	33.61	34.13	33.37	59.72	33.23	31.78	32.35	32.76
Fe_2O_3	35.42	34.59	35.31	34.32	34.16	34.39	32.48	34.02	5.95	33.94	35.92	35.76	35.30
FeO	27.93	27.75	27.80	27.72	27.76	27.65	26.86	27.35	26.45	27.39	27.63	27.63	27.70
MnO	2.38	2.46	2.49	2.50	2.48	2.48	3.50	2.90	4.36	2.90	2.52	2.47	2.49
MgO	0.51	0.55	0.45	0.51	0.57	0.57	0.57	0.57	0.71	0.53	0.54	0.55	0.54
ZnO	0.16	0.17	0.20	0.26	0.25	0.20	0.19	<0.07	0.44	0.18	0.20	0.17	0.15
CaO	<0.01	<0.01	<0.01	<0.01	<0.01	<0.01	<0.01	<0.01	<0.01	<0.01	<0.01	<0.01	<0.01
Na_2O	<0.02	<0.02	0.02	<0.02	<0.02	0.02	0.02	0.05	<0.02	0.03	<0.02	0.03	0.02
K_2O	0.00	0.00	0.00	0.00	0.00	0.00	0.00	0.00	0.00	0.00	0.00	0.00	0.00
NiO	0.39	0.44	0.44	0.42	0.38	0.41	0.37	0.39	<0.03	0.40	0.46	0.44	0.42
Cations to 32 oxygens													
Si	0.00	0.00	0.00	0.00	0.00	0.00	0.00	0.00	0.00	0.00	0.00	0.00	0.00
Ti	0.00	0.00	0.00	0.00	0.00	0.00	0.00	0.00	0.00	0.00	0.00	0.00	0.00
Al	0.03	0.03	0.04	0.03	0.04	0.03	0.08	0.06	0.10	0.06	0.04	0.03	0.03
Cr	0.97	0.99	0.96	0.99	0.99	1.00	1.01	0.99	1.73	0.98	0.94	0.96	0.97
Fe^{3+}	1.00	0.98	1.00	0.97	0.96	0.97	0.91	0.96	0.16	0.96	1.02	1.01	1.00
Fe^{2+}	0.88	0.87	0.87	0.87	0.87	0.87	0.84	0.86	0.81	0.86	0.87	0.87	0.87
Mn^{2+}	0.08	0.08	0.08	0.08	0.08	0.08	0.11	0.09	0.14	0.09	0.08	0.08	0.08
Mg	0.03	0.03	0.03	0.03	0.03	0.03	0.03	0.03	0.04	0.03	0.03	0.03	0.03
Zn	0.00	0.00	0.01	0.01	0.01	0.01	0.01	0.00	0.01	0.00	0.01	0.00	0.00
Ca	0.00	0.00	0.00	0.00	0.00	0.00	0.00	0.00	0.00	0.00	0.00	0.00	0.00
Na	0.00	0.00	0.00	0.00	0.00	0.00	0.00	0.00	0.00	0.00	0.00	0.00	0.00
K	0.00	0.00	0.00	0.00	0.00	0.00	0.00	0.00	0.00	0.00	0.00	0.00	0.00
Ni	0.01	0.01	0.01	0.01	0.01	0.01	0.01	0.01	0.00	0.01	0.01	0.01	0.01
$Mg\#$	0.03	0.03	0.03	0.03	0.04	0.04	0.04	0.04	0.05	0.03	0.03	0.03	0.03
$Fe\#$	0.97	0.97	0.97	0.97	0.96	0.96	0.96	0.96	0.95	0.97	0.97	0.97	0.97
$Cr\#$	0.49	0.49	0.48	0.50	0.50	0.50	0.50	0.49	0.87	0.49	0.47	0.48	0.49
$Fe^{3+}\#$	0.50	0.49	0.50	0.49	0.48	0.49	0.46	0.48	0.08	0.48	0.51	0.51	0.50

Table 1: Chrome spinel microprobe analyses from ultramafic rocks of the Western Ethiopian Shield

ID number	E13 - 11 - 40	E13 - 11 - 41	E13 - 11 - 42	E13 - 11 - 43	E13 - 11 - 44	E13 - 11 - 45	E13 - 11 - 46	E13 - 11 - 47
Daleti Quarry – E13.11 (09° 09' 56.4" N, 35° 37' 30.0" E)								
SiO_2	0.02	<0.01	0.02	<0.01	<0.01	<0.01	0.02	0.04
TiO_2	<0.01	0.01	<0.01	0.01	<0.01	0.02	0.01	<0.01
$Al2O_3$	1.03	0.63	2.39	2.44	1.88	0.88	2.53	0.02
Cr_2O_3	33.14	32.25	37.63	38.28	38.98	33.12	36.70	22.53
Fe_2O_3	34.38	35.72	28.25	27.68	27.58	34.62	28.98	47.77
FeO	27.62	27.87	25.54	27.05	27.21	27.46	27.27	21.84
MnO	2.63	2.38	5.01	3.25	3.09	2.72	3.29	2.34
MgO	0.52	0.52	0.59	0.63	0.62	0.54	0.60	3.49
ZnO	0.25	0.19	0.22	0.26	0.25	0.16	0.24	0.60
CaO	<0.01	<0.01	<0.01	<0.01	<0.01	<0.01	<0.01	0.03
Na_2O	0.02	<0.02	<0.02	0.04	0.03	0.02	<0.02	<0.02
K_2O	0.00	0.00	0.00	0.00	0.00	0.00	0.00	0.00
NiO	0.39	0.41	0.33	0.33	0.35	0.47	0.37	1.33
Cations to 32 oxygens								
Si	0.00	0.00	0.00	0.00	0.00	0.00	0.00	0.00
Ti	0.00	0.00	0.00	0.00	0.00	0.00	0.00	0.00
Al	0.05	0.03	0.10	0.11	0.08	0.04	0.11	0.00
Cr	0.98	0.96	1.10	1.12	1.15	0.98	1.08	0.66
Fe^{3+}	0.97	1.01	0.79	0.77	0.77	0.98	0.81	1.33
Fe^{2+}	0.87	0.88	0.79	0.84	0.85	0.86	0.85	0.68
Mn^{2+}	0.08	0.08	0.16	0.10	0.10	0.09	0.10	0.07
Mg	0.03	0.03	0.03	0.04	0.03	0.03	0.03	0.19
Zn	0.01	0.01	0.01	0.01	0.01	0.00	0.01	0.02
Ca	0.00	0.00	0.00	0.00	0.00	0.00	0.00	0.00
Na	0.00	0.00	0.00	0.00	0.00	0.00	0.00	0.00
K	0.00	0.00	0.00	0.00	0.00	0.00	0.00	0.00
Ni	0.01	0.01	0.01	0.01	0.01	0.01	0.01	0.04
Mg #	0.03	0.03	0.04	0.04	0.04	0.03	0.04	0.22
Fe #	0.97	0.97	0.96	0.96	0.96	0.97	0.96	0.78
Cr #	0.49	0.48	0.55	0.56	0.57	0.49	0.54	0.33
Fe^{3+}#	0.49	0.51	0.39	0.39	0.39	0.49	0.41	0.67

Table 1: Chrome spinel microprobe analyses from ultramafic rocks of the Western Ethiopian Shield

ID number	E13-20-01	E13-20-02	E13-20-03	E13-20-04	E13-20-05	E13-20-06	E13-20-07	E13-20-08	E13-20-09	E13-20-10	E13-20-11	E13-20-12	E13-20-13
Tulu Dimtu Hill (9° 27' 60.9"N 35° 44' 19.8"E)													
SiO_2	0.05	0.06	0.05	<0.01	0.02	0.05	<0.01	0.08	0.23	0.04	0.02	0.14	0.02
TiO_2	<0.01	<0.01	<0.01	<0.01	0.02	<0.01	0.01	0.01	<0.01	<0.01	<0.01	<0.01	<0.01
$Al2O_3$	<0.007	<0.007	<0.007	11.05	11.53	12.22	12.35	11.97	<0.007	12.40	11.81	30.56	10.54
Cr_2O_3	0.34	2.84	3.04	58.88	59.60	58.05	57.26	58.38	1.54	57.57	56.54	<0.03	60.25
Fe_2O_3	68.76	66.19	66.02	0.00	0.00	0.00	0.00	0.00	67.14	0.00	0.00	33.57	0.00
FeO	27.71	27.80	27.79	20.30	19.16	20.42	21.04	20.45	27.75	20.36	22.13	15.58	20.72
MnO	0.84	1.35	1.37	7.45	9.05	8.53	8.83	8.40	1.11	8.83	8.59	18.96	7.90
MgO	0.30	0.45	0.49	1.56	0.33	0.42	0.40	0.40	0.46	0.45	0.62	0.98	0.36
ZnO	<0.07	0.03	0.02	0.69	0.20	0.22	0.22	0.20	<0.07	0.27	0.24	<0.07	0.20
CaO	<0.01	0.04	0.02	<0.01	<0.01	<0.01	<0.01	<0.01	0.03	<0.01	<0.01	<0.01	<0.01
Na_2O	0.04	<0.02	<0.02	0.02	0.02	0.03	<0.02	<0.02	0.02	0.04	<0.02	0.05	<0.02
K_2O	0.00	0.00	0.00	0.00	0.00	0.00	0.00	0.00	0.00	0.00	0.00	0.00	0.00
NiO	1.88	1.22	1.20	<0.03	0.06	0.05	0.03	0.07	1.73	0.03	0.04	0.17	<0.03
Cations to 32 oxygens													
Si	0.00	0.00	0.00	0.00	0.00	0.00	0.00	0.00	0.01	0.00	0.00	0.00	0.00
Ti	0.00	0.00	0.00	0.00	0.00	0.00	0.00	0.00	0.00	0.00	0.00	0.00	0.00
Al	0.00	0.00	0.00	0.46	0.48	0.51	0.51	0.50	0.00	0.51	0.49	1.17	0.44
Cr	0.01	0.09	0.09	1.63	1.66	1.61	1.59	1.62	0.05	1.59	1.57	0.00	1.69
Fe^{3+}	1.99	1.91	1.90	0.00	0.00	0.00	0.00	0.00	1.94	0.00	0.00	0.82	0.00
Fe^{2+}	0.89	0.89	0.89	0.59	0.56	0.60	0.62	0.60	0.89	0.60	0.65	0.42	0.61
Mn^{2+}	0.03	0.04	0.04	0.22	0.27	0.25	0.26	0.25	0.04	0.26	0.25	0.52	0.24
Mg	0.02	0.03	0.03	0.08	0.02	0.02	0.02	0.02	0.03	0.02	0.03	0.05	0.02
Zn	0.00	0.00	0.00	0.02	0.01	0.01	0.01	0.01	0.00	0.01	0.01	0.00	0.01
Ca	0.00	0.00	0.00	0.00	0.00	0.00	0.00	0.00	0.00	0.00	0.00	0.00	0.00
Na	0.00	0.00	0.00	0.00	0.00	0.00	0.00	0.00	0.00	0.00	0.00	0.00	0.00
K	0.00	0.00	0.00	0.00	0.00	0.00	0.00	0.00	0.05	0.00	0.00	0.00	0.00
Ni	0.06	0.04	0.04	0.00	0.00	0.00	0.00	0.00	0.05	0.00	0.00	0.00	0.00
Mg #	0.02	0.03	0.03	0.12	0.03	0.04	0.03	0.03	0.03	0.04	0.05	0.10	0.03
Fe #	0.98	0.97	0.97	0.88	0.97	0.96	0.97	0.97	0.97	0.96	0.95	0.90	0.97
Cr #	0.01	0.04	0.05	0.78	0.78	0.76	0.76	0.77	0.02	0.76	0.76	0.00	0.79
Fe^{3+}#	0.99	0.96	0.95	0.00	0.00	0.00	0.00	0.00	0.98	0.00	0.00	0.41	0.00

Table 2: Olivine microprobe analyses from ultramafic rocks of the Western Ethiopian Shield

ID number	E14-10-01	E14-10-02	E14-10-03	E14-10-04	E14-10-05	E14-10-06	E14-10-07	E14-10-08	E14-10-09	E14-10-10
SiO_2	39.77	40.13	39.83	40.57	40.35	40.77	40.28	40.40	40.82	40.06
TiO_2	0.05	0.01	<0.01	<0.01	0.02	<0.01	0.02	0.01	0.01	0.01
Al_2O_3	0.03	0.01	0.20	<0.01	0.01	0.11	<0.01	0.01	0.02	0.15
Cr_2O_3	0.04	0.03	0.03	<0.03	<0.03	0.03	0.01	<0.03	0.03	<0.03
FeO	9.60	9.70	9.58	9.63	9.85	9.91	9.71	9.57	9.55	9.44
MnO	0.19	0.21	0.14	0.20	0.22	0.22	0.21	0.19	0.18	0.19
MgO	49.00	49.99	49.68	50.43	50.11	49.62	50.12	50.66	50.55	49.77
ZnO	0.02	<0.02	0.08	0.02	<0.02	0.10	0.03	0.05	<0.02	0.05
CaO	0.17	0.16	0.18	0.14	0.09	0.08	0.09	0.10	0.07	0.16
Na_2O	0.46	<0.02	0.18	<0.02	<0.02	0.04	<0.02	0.05	0.04	0.10
K_2O	0.00	0.00	0.00	0.00	0.00	0.00	0.00	0.00	0.00	0.00
NiO	0.12	0.13	0.12	0.13	0.09	0.09	0.08	0.10	0.13	0.10
Cl	0.00	0.00	0.00	0.00	0.00	0.00	0.00	0.00	0.00	0.00
F	0.00	0.00	0.00	0.00	0.00	0.00	0.00	0.00	0.00	0.00
Total	99.35	100.37	99.85	101.08	100.70	100.87	100.51	101.14	101.40	99.93
No. Oxygens	4.00	4.00	4.00	4.00	4.00	4.00	4.00	4.00	4.00	4.00
Si	0.98	0.98	0.98	0.98	0.98	0.99	0.98	0.98	0.99	0.98
Ti	0.00	0.00	0.00	0.00	0.00	0.00	0.00	0.00	0.00	0.00
Al	0.00	0.00	0.01	0.00	0.00	0.00	0.00	0.00	0.00	0.00
Cr	0.00	0.00	0.00	0.00	0.00	0.00	0.00	0.00	0.00	0.00
Fe^{2+}	0.20	0.20	0.20	0.20	0.20	0.20	0.20	0.19	0.19	0.19
Mn^{2+}	0.00	0.00	0.00	0.00	0.00	0.00	0.00	0.00	0.00	0.00
Mg	1.81	1.82	1.82	1.82	1.82	1.80	1.83	1.83	1.82	1.82
Zn	0.00	0.00	0.00	0.00	0.00	0.00	0.00	0.00	0.00	0.00
Ca	0.00	0.00	0.00	0.00	0.00	0.00	0.00	0.00	0.00	0.00
Na	0.02	0.00	0.01	0.00	0.00	0.00	0.00	0.00	0.00	0.00
K	0.00	0.00	0.00	0.00	0.00	0.00	0.00	0.00	0.00	0.00
Ni	0.00	0.00	0.00	0.00	0.00	0.00	0.00	0.00	0.00	0.00
Cl	0.00	0.00	0.00	0.00	0.00	0.00	0.00	0.00	0.00	0.00
F	0.00	0.00	0.00	0.00	0.00	0.00	0.00	0.00	0.00	0.00
Total Cations (S)	3.03	3.02	3.02	3.01	3.02	3.01	3.02	3.02	3.01	3.02
Xmg (mg/(fe+mg))	0.90	0.90	0.90	0.90	0.90	0.90	0.90	0.90	0.90	0.90
Xmg(divalent)	0.90	0.90	0.90	0.90	0.90	0.89	0.90	0.90	0.90	0.90
XFe^{2+}	0.10	0.10	0.10	0.10	0.10	0.10	0.10	0.10	0.10	0.10

Table 2: Olivine microprobe analyses from ultramafic rocks of the Western Ethiopian Shield

ID number	E14-10-11	E14-10-12	E14-10-13	E14-10-14	E13-11-01	E13-11-02	E13-11-03	E13-11-04	E13-11-05	E13-11-06
	Yubdo ultra mafic				Daleti Dunite					
SiO_2	40.65	40.47	39.85	39.85	42.08	41.68	42.05	42.12	41.64	41.03
TiO_2	0.01	0.01	0.01	<0.01	<0.01	0.01	<0.01	<0.01	<0.01	<0.01
Al_2O_3	1.56	<0.01	0.01	0.02	<0.01	<0.01	<0.01	0.01	<0.01	<0.01
Cr_2O_3	0.03	<0.03	<0.03	0.02	<0.03	<0.03	<0.03	0.03	<0.03	<0.03
FeO	9.52	9.62	9.83	9.56	5.99	5.60	5.54	5.58	5.50	5.77
MnO	0.18	0.23	0.15	0.17	0.11	0.10	0.16	0.11	0.11	0.13
MgO	50.32	50.28	50.07	50.03	49.26	52.87	52.80	52.24	52.90	53.43
ZnO	<0.02	0.06	0.03	0.04	0.03	0.06	<0.02	0.04	0.03	<0.02
CaO	0.17	0.12	0.16	0.17	0.01	0.03	0.01	0.02	<0.01	0.01
Na_2O	0.07	<0.02	0.02	0.02	<0.02	<0.02	<0.02	<0.02	0.03	<0.02
K_2O	0.00	0.00	0.00	0.00	0.00	0.00	0.00	0.00	0.00	0.00
NiO	0.12	0.18	0.12	0.09	0.41	0.37	0.37	0.37	0.40	0.41
Cl	0.00	0.00	0.00	0.00	0.00	0.00	0.00	0.00	0.00	0.00
F	0.00	0.00	0.00	0.00	0.00	0.00	0.00	0.00	0.00	0.00
Total	102.64	100.96	100.24	99.90	97.90	100.74	100.95	100.51	100.62	100.82
No. Oxygens	4.00	4.00	4.00	4.00	4.00	4.00	4.00	4.00	4.00	4.00
Si	0.97	0.98	0.98	0.98	1.03	1.00	1.00	1.01	1.00	0.98
Ti	0.00	0.00	0.00	0.00	0.00	0.00	0.00	0.00	0.00	0.00
Al	0.04	0.00	0.00	0.00	0.00	0.00	0.00	0.00	0.00	0.00
Cr	0.00	0.00	0.00	0.00	0.00	0.00	0.00	0.00	0.00	0.00
Fe^{2+}	0.19	0.20	0.20	0.20	0.12	0.11	0.11	0.11	0.11	0.12
Mn^{2+}	0.00	0.00	0.00	0.00	0.00	0.00	0.00	0.00	0.00	0.00
Mg	1.79	1.82	1.83	1.83	1.80	1.88	1.87	1.86	1.89	1.91
Zn	0.00	0.00	0.00	0.00	0.00	0.00	0.00	0.00	0.00	0.00
Ca	0.00	0.00	0.00	0.00	0.00	0.00	0.00	0.00	0.00	0.00
Na	0.00	0.00	0.00	0.00	0.00	0.00	0.00	0.00	0.00	0.00
K	0.00	0.00	0.00	0.00	0.00	0.00	0.00	0.00	0.00	0.00
Ni	0.00	0.00	0.00	0.00	0.01	0.01	0.01	0.01	0.01	0.01
Cl	0.00	0.00	0.00	0.00	0.00	0.00	0.00	0.00	0.00	0.00
F	0.00	0.00	0.00	0.00	0.00	0.00	0.00	0.00	0.00	0.00
Total Cations (S)	3.01	3.02	3.02	3.02	2.97	3.00	3.00	2.99	3.00	3.02
Xmg (mg/(fe+mg))	0.90	0.90	0.90	0.90	0.94	0.94	0.94	0.94	0.94	0.94
Xmg(divalent)	0.90	0.90	0.90	0.90	0.93	0.94	0.94	0.94	0.94	0.94
XFe^{2+}	0.10	0.10	0.10	0.10	0.06	0.06	0.06	0.06	0.06	0.06

Table 2: Olivine microprobe analyses from ultramafic rocks of the Western Ethiopian Shield

ID number	E13-11-07	E13-11-08	E13-11-09	E13-11-10	E13-11-11	E13-11-12	E13-11-13	E13-11-14	E13-11-15	E13-11-16
	Daleti Dunite									
SiO_2	40.42	39.86	36.28	41.18	41.25	42.37	42.27	44.26	42.25	41.87
TiO_2	<0.01	0.01	<0.01	0.01	0.01	0.01	0.01	<0.01	<0.01	<0.01
Al_2O_3	<0.01	<0.01	<0.01	<0.01	<0.01	0.01	<0.01	0.02	<0.01	<0.01
Cr_2O_3	<0.03	<0.03	0.03	<0.03	<0.03	<0.03	<0.03	<0.03	<0.03	<0.03
FeO	5.76	5.78	5.59	5.84	6.00	6.12	6.10	5.96	6.04	6.16
MnO	0.10	0.10	0.09	0.12	0.13	0.10	0.11	0.11	0.15	0.14
MgO	53.89	53.86	54.29	53.29	53.42	50.33	50.22	49.29	50.77	48.65
ZnO	0.02	<0.02	0.01	<0.02	0.03	<0.02	0.02	<0.02	0.01	0.03
CaO	0.01	<0.01	0.02	<0.01	<0.01	<0.01	<0.01	<0.01	0.01	<0.01
Na_2O	<0.02	<0.02	<0.02	<0.02	<0.02	<0.02	<0.02	<0.02	<0.02	<0.02
K_2O	0.00	0.00	0.00	0.00	0.00	0.00	0.00	0.00	0.00	0.00
NiO	0.39	0.34	0.34	0.34	0.32	0.40	0.42	0.37	0.45	0.38
Cl	0.00	0.00	0.00	0.00	0.00	0.00	0.00	0.00	0.00	0.00
F	0.00	0.00	0.00	0.00	0.00	0.00	0.00	0.00	0.00	0.00
Total	100.60	99.95	96.66	100.79	101.15	99.34	99.14	100.02	99.68	97.24
No. Oxygens	4.00	4.00	4.00	4.00	4.00	4.00	4.00	4.00	4.00	4.00
Si	0.97	0.96	0.92	0.99	0.98	1.03	1.02	1.06	1.02	1.03
Ti	0.00	0.00	0.00	0.00	0.00	0.00	0.00	0.00	0.00	0.00
Al	0.00	0.00	0.00	0.00	0.00	0.00	0.00	0.00	0.00	0.00
Cr	0.00	0.00	0.00	0.00	0.00	0.00	0.00	0.00	0.00	0.00
Fe^{2+}	0.12	0.12	0.12	0.12	0.12	0.12	0.12	0.12	0.12	0.13
Mn^{2+}	0.00	0.00	0.00	0.00	0.00	0.00	0.00	0.00	0.00	0.00
Mg	1.93	1.94	2.04	1.90	1.90	1.82	1.82	1.76	1.83	1.79
Zn	0.00	0.00	0.00	0.00	0.00	0.00	0.00	0.00	0.00	0.00
Ca	0.00	0.00	0.00	0.00	0.00	0.00	0.00	0.00	0.00	0.00
Na	0.00	0.00	0.00	0.00	0.00	0.00	0.00	0.00	0.00	0.00
K	0.00	0.00	0.00	0.00	0.00	0.00	0.00	0.00	0.00	0.00
Ni	0.01	0.01	0.01	0.01	0.01	0.01	0.01	0.01	0.01	0.01
Cl	0.00	0.00	0.00	0.00	0.00	0.00	0.00	0.00	0.00	0.00
F	0.00	0.00	0.00	0.00	0.00	0.00	0.00	0.00	0.00	0.00
Total Cations (S)	3.03	3.03	3.08	3.01	3.02	2.97	2.98	2.94	2.98	2.97
Xmg (mg/(fe+mg))	0.94	0.94	0.95	0.94	0.94	0.94	0.94	0.94	0.94	0.93
Xmg(divalent)	0.94	0.94	0.94	0.94	0.94	0.93	0.93	0.93	0.93	0.93
XFe^{2+}	0.06	0.06	0.05	0.06	0.06	0.06	0.06	0.06	0.06	0.07

Table 3: Olivine spinel geothermometer

Yubdo E14.10 (8° 57'37.4" N, 35° 27' 18.2"E)

Xsp Ti	XOlvMg	XolFe	XspFe^{2+}	Xsp Mg	P	XspCr	KD (ol-Sp Mg - Fe)	Temp (K)	Fe^{3+}	KD (ol-Sp Mg - Fe)	Temp in °C
0.011587	1.808	0.199	0.714	0.270	1	1.132	24.077	1236.4	0.425	24.077	963.4
0.009734	1.808	0.199	0.615	0.375	1	1.140	14.940	1427.2	0.449	14.940	1154.2
0.012544	1.808	0.199	0.660	0.333	1	1.195	18.060	1325.4	0.377	18.060	1052.4
0.010297	1.808	0.199	0.601	0.385	1	1.131	14.193	1430.4	0.435	14.193	1157.4
0.011905	1.808	0.199	0.734	0.243	1	1.165	27.485	1220.0	0.433	27.485	947.0
0.010323	1.808	0.199	0.738	0.206	1	1.001	32.644	1175.2	0.546	32.644	902.2
0.011852	1.808	0.199	0.657	0.315	1	1.172	18.967	1316.9	0.403	18.967	1043.9
0.012131	1.808	0.199	0.553	0.361	1	1.150	13.931	1465.1	0.451	13.931	1192.1
0.012182	1.808	0.199	0.739	0.234	1	1.066	28.763	1190.4	0.475	28.763	917.4
0.012426	1.808	0.199	0.737	0.253	1	1.018	26.507	1228.9	0.524	26.507	955.9
0.011219	1.808	0.199	0.610	0.377	1	1.091	14.703	1422.6	0.467	14.703	1149.6
0.011013	1.808	0.199	0.710	0.263	1	1.079	24.603	1259.9	0.498	24.603	986.9
0.009163	1.808	0.199	0.708	0.277	1	1.075	23.252	1302.0	0.531	23.252	1029.0
0.013199	1.808	0.199	0.707	0.270	1	1.143	23.806	1277.8	0.463	23.806	1004.8
0.010667	1.808	0.199	0.623	0.363	1	1.097	15.617	1404.9	0.471	15.617	1131.9
0.010355	1.808	0.199	0.737	0.242	1	1.042	27.715	1261.9	0.570	27.715	988.9
0.012795	1.808	0.199	0.717	0.270	1	1.009	24.181	1261.2	0.535	24.181	988.2
0.010448	1.808	0.199	0.606	0.375	1	1.039	14.691	1333.5	0.405	14.691	1060.5
0.011457	1.808	0.199	0.640	0.348	1	1.170	16.737	1348.6	0.389	16.737	1075.6
0.011749	1.808	0.199	0.601	0.390	1	1.150	14.020	1409.7	0.394	14.020	1136.7
0.01063	1.808	0.199	0.619	0.374	1	1.125	15.059	1408.6	0.441	15.059	1135.6
0.011149	1.808	0.199	0.634	0.357	1	1.077	16.170	1377.2	0.467	16.170	1104.2
0.010	1.808	0.199	0.658	0.337	1	1.083	17.746	1370.0	0.494	17.746	1097.0
0.009	1.808	0.199	0.724	0.260	1	1.119	25.303	1263.0	0.488	25.303	990.0
0.010	1.808	0.199	0.769	0.203	1	1.064	34.465	1156.5	0.499	34.465	883.5
Average Values E14 - 10											
0.009734	1.808	0.198708	0.614919	0.375	1	1.140	14.940	1427.2	0.449	14.940	1154.2

Ballhaus et al. (1991) and Ballhaus et al. (1994)

Table 3: Olivine spinel geothermometer

Daleti Quarry – E13.11 (09° 09' 56.4" N, 35° 37' 30.0" E)

Xsp Ti	XOlvMg	XolFe	XspFe²⁺	Xsp Mg	P	XspCr	KD (ol-Sp Mg - Fe)	Temp (K)	Fe³⁺	KD (ol-Sp Mg - Fe)	Temp in °C
0.00	1.87	0.12	0.88	0.03	1	0.92	523.62	945	1.05	523.62	672
0.00	1.87	0.12	0.87	0.03	1	0.94	454.15	959	1.03	454.15	686
0.00	1.87	0.12	0.88	0.03	1	0.94	475.27	955	1.03	475.27	682
0.00	1.87	0.12	0.85	0.03	1	1.06	395.26	935	0.86	395.26	662
0.00	1.87	0.12	0.87	0.03	1	0.97	452.20	951	0.99	452.20	678
0.00	1.87	0.12	0.87	0.03	1	0.94	457.53	955	1.02	457.53	682
0.00	1.87	0.12	0.84	0.04	1	1.31	358.16	897	0.59	358.16	624
0.00	1.87	0.12	0.86	0.03	1	1.11	403.43	930	0.82	403.43	657
0.00	1.87	0.12	0.85	0.03	1	1.16	411.71	912	0.76	411.71	639
0.00	1.87	0.12	0.86	0.03	1	1.08	388.92	949	0.87	388.92	676
0.00	1.87	0.12	0.84	0.03	1	1.09	391.66	928	0.82	391.66	655
0.00	1.87	0.12	0.85	0.03	1	1.07	413.55	933	0.86	413.55	660
0.00	1.87	0.12	0.84	0.03	1	1.10	415.07	921	0.82	415.07	648
0.00	1.87	0.12	0.85	0.03	1	1.05	451.70	931	0.89	451.70	658
0.00	1.87	0.12	0.85	0.03	1	1.11	410.74	925	0.81	410.74	652
0.00	1.87	0.12	0.85	0.03	1	1.09	437.88	921	0.84	437.88	648
0.00	1.87	0.12	0.85	0.04	1	1.07	372.20	953	0.87	372.20	680
0.00	1.87	0.12	0.85	0.03	1	1.08	410.22	935	0.85	410.22	662
0.00	1.87	0.12	0.85	0.03	1	1.06	428.59	939	0.89	428.59	666
0.00	1.87	0.12	0.86	0.03	1	1.09	401.36	934	0.84	401.36	661
0.00	1.87	0.12	0.83	0.04	1	1.32	357.54	889	0.56	357.54	616
0.00	1.87	0.12	0.83	0.04	1	1.39	363.04	876	0.49	363.04	603
0.00	1.87	0.12	0.84	0.03	1	1.15	384.77	914	0.75	384.77	641
0.00	1.87	0.12	0.84	0.03	1	1.15	401.75	909	0.74	401.75	636
0.00	1.87	0.12	0.85	0.03	1	1.08	413.95	936	0.86	413.95	663
0.00	1.87	0.12	0.87	0.03	1	0.97	430.93	964	1.00	430.93	691
0.00	1.87	0.12	0.88	0.03	1	0.97	483.41	949	1.00	483.41	676
0.00	1.87	0.12	0.87	0.03	1	0.99	443.28	954	0.98	443.28	681
0.00	1.87	0.12	0.87	0.03	1	0.96	550.10	926	1.00	550.10	653
0.00	1.87	0.12	0.87	0.03	1	0.99	476.60	942	0.97	476.60	669

Ballhaus et al. (1991) and Ballhaus et al. (1994)

Table 3: Olivine spinel geothermometer

Xsp Ti	XOlvMg	XolFe	XspFe^{2+}	Xsp Mg	P	XspCr	KD (ol-Sp Mg - Fe)	Temp (K)	Fe^{3+}	KD (ol-Sp Mg - Fe)	Temp in °C
Daleti Quarry – E13.11 (09° 09′ 56.4″ N, 35° 37′ 30.0″ E)											
0.00	1.87	0.12	0.87	0.03	1	0.99	428.02	954	0.96	428.02	681
0.00	1.87	0.12	0.87	0.03	1	1.00	429.25	959	0.97	429.25	686
0.00	1.87	0.12	0.84	0.03	1	1.01	413.88	938	0.91	413.88	665
0.00	1.87	0.12	0.86	0.03	1	0.99	423.87	951	0.96	423.87	678
0.00	1.87	0.12	0.81	0.04	1	1.73	329.29	837	0.16	329.29	564
0.00	1.87	0.12	0.86	0.03	1	0.98	455.45	939	0.96	455.45	666
0.00	1.87	0.12	0.87	0.03	1	0.94	449.53	956	1.02	449.53	683
0.00	1.87	0.12	0.87	0.03	1	0.96	445.83	961	1.01	445.83	688
0.00	1.87	0.12	0.87	0.03	1	0.97	455.54	956	1.00	455.54	683
0.00	1.87	0.12	0.87	0.03	1	0.98	470.43	941	0.97	470.43	668
0.00	1.87	0.12	0.88	0.03	1	0.96	469.78	953	1.01	469.78	680
0.00	1.87	0.12	0.79	0.03	1	1.10	382.08	920	0.79	382.08	647
0.00	1.87	0.12	0.84	0.04	1	1.12	377.98	921	0.77	377.98	648
0.00	1.87	0.12	0.85	0.03	1	1.15	388.94	924	0.77	388.94	651
0.00	1.87	0.12	0.86	0.03	1	0.98	448.85	951	0.98	448.85	678
0.00	1.87	0.12	0.85	0.03	1	1.08	404.05	916	0.81	404.05	643
Average Values - E13 - 11											
0.00	1.87	0.12	0.85	0.04	1	1.06	378.76	951	0.88	378.76	678

Ballhaus et al. (1991) and Ballhaus et al. (1994)

Table 4: Oxygen fugacity $\Delta f O2$ (FMQ) calculations for spinel and olivine

Sample	Temperature (K)	Pressure (Gpa)	Xolfe	Xspfe^{2+}	Xspfe^{3+}	Xspal	$\Delta f O_{2\,(FMQ)}$
Daleti Quarry – E13.11 (09° 09' 56.4" N, 35° 37' 30.0" E)							
E13 - 11	945.3	1	0.06	0.46	0.53	0.01	5.06
E13 - 11	959.3	1	0.06	0.46	0.51	0.02	5.03
E13 - 11	954.9	1	0.06	0.46	0.52	0.01	5.04
E13 - 11	935.4	1	0.06	0.50	0.43	0.04	4.78
E13 - 11	950.6	1	0.06	0.47	0.50	0.02	4.97
E13 - 11	955.5	1	0.06	0.46	0.51	0.02	5.02
E13 - 11	896.9	1	0.06	0.59	0.29	0.05	4.23
E13 - 11	929.5	1	0.06	0.51	0.41	0.04	4.71
E13 - 11	911.9	1	0.06	0.53	0.38	0.04	4.58
E13 - 11	949.1	1	0.06	0.50	0.43	0.03	4.80
E13 - 11	928.2	1	0.06	0.51	0.41	0.05	4.71
E13 - 11	933.1	1	0.06	0.50	0.43	0.04	4.77
E13 - 11	920.8	1	0.06	0.51	0.41	0.04	4.69
E13 - 11	930.7	1	0.06	0.49	0.45	0.03	4.81
E13 - 11	925.1	1	0.06	0.51	0.41	0.04	4.69
E13 - 11	920.7	1	0.06	0.50	0.42	0.04	4.73
E13 - 11	953.2	1	0.06	0.49	0.43	0.03	4.80
E13 - 11	934.8	1	0.06	0.50	0.43	0.03	4.76
E13 - 11	939.4	1	0.06	0.49	0.45	0.03	4.82
E13 - 11	934.2	1	0.06	0.51	0.42	0.03	4.74
E13 - 11	888.6	1	0.06	0.60	0.28	0.06	4.16
E13 - 11	875.6	1	0.06	0.63	0.25	0.06	3.97
E13 - 11	914.4	1	0.06	0.53	0.37	0.05	4.57
E13 - 11	908.8	1	0.06	0.53	0.37	0.05	4.56
E13 - 11	935.9	1	0.06	0.50	0.43	0.03	4.77
E13 - 11	964.5	1	0.06	0.46	0.50	0.01	5.00
E13 - 11	948.6	1	0.06	0.47	0.50	0.01	4.99
E13 - 11	953.8	1	0.06	0.47	0.49	0.02	4.96
E13 - 11	926.1	1	0.06	0.47	0.50	0.02	4.97
E13 - 11	942.2	1	0.06	0.47	0.49	0.02	4.94
E13 - 11	954.2	1	0.06	0.47	0.48	0.02	4.95
E13 - 11	959.2	1	0.06	0.47	0.49	0.01	4.96
E13 - 11	938.2	1	0.06	0.48	0.46	0.04	4.85
E13 - 11	951.0	1	0.06	0.47	0.48	0.03	4.93
E13 - 11	837.1	1	0.06	0.83	0.08	0.05	2.26
E13 - 11	938.8	1	0.06	0.47	0.48	0.03	4.92
E13 - 11	956.2	1	0.06	0.46	0.51	0.02	5.01
E13 - 11	961.2	1	0.06	0.46	0.51	0.01	5.01
E13 - 11	955.7	1	0.06	0.47	0.50	0.01	4.99
E13 - 11	940.9	1	0.06	0.47	0.49	0.02	4.94
E13 - 11	953.0	1	0.06	0.46	0.51	0.01	5.01
E13 - 11	920.1	1	0.06	0.50	0.39	0.05	4.62
E13 - 11	920.9	1	0.06	0.52	0.39	0.05	4.62
E13 - 11	924.0	1	0.06	0.52	0.39	0.04	4.62
E13 - 11	950.8	1	0.06	0.47	0.49	0.02	4.96
Average E13 -	951.3	1	0.06	0.49	0.44	0.03	4.81

Ballhaus et al. (1991) and Ballhaus et al. (1994)

Table 4: Oxygen fugacity $\Delta f O2$ (FMQ) calculations for spinel and olivine

Sample	Temperature (K)	Pressure (Gpa)	Xolfe	Xspfe^{2+}	Xspfe^{3+}	Xspal	$\Delta fO_{2\ (FMQ)}$
Yubdo E14.10 (8° 57'37.4" N, 35° 27' 18.2"E)							
E14 - 10	1236.4	1	0.10	0.63	0.21	0.21	2.92
E14 - 10	1427.2	1	0.10	0.58	0.23	0.20	2.97
E14 - 10	1325.4	1	0.10	0.64	0.19	0.20	2.74
E14 - 10	1430.4	1	0.10	0.58	0.22	0.21	2.93
E14 - 10	1220.0	1	0.10	0.63	0.22	0.19	2.93
E14 - 10	1175.2	1	0.10	0.57	0.27	0.22	3.26
E14 - 10	1316.9	1	0.10	0.62	0.20	0.21	2.82
E14 - 10	1465.1	1	0.10	0.55	0.23	0.20	2.93
E14 - 10	1190.4	1	0.10	0.61	0.24	0.22	3.08
E14 - 10	1228.9	1	0.10	0.58	0.27	0.22	3.23
E14 - 10	1422.6	1	0.10	0.57	0.24	0.21	3.03
E14 - 10	1259.9	1	0.10	0.59	0.25	0.20	3.13
E14 - 10	1302.0	1	0.10	0.57	0.27	0.19	3.22
E14 - 10	1277.8	1	0.10	0.60	0.23	0.19	3.03
E14 - 10	1404.9	1	0.10	0.57	0.24	0.21	3.04
E14 - 10	1261.9	1	0.10	0.56	0.29	0.19	3.32
E14 - 10	1261.2	1	0.10	0.57	0.27	0.22	3.25
E14 - 10	1333.5	1	0.10	0.60	0.21	0.26	2.88
E14 - 10	1348.6	1	0.10	0.62	0.20	0.21	2.79
E14 - 10	1409.7	1	0.10	0.60	0.20	0.22	2.80
E14 - 10	1408.6	1	0.10	0.58	0.22	0.21	2.96
E14 - 10	1377.2	1	0.10	0.58	0.24	0.22	3.05
E14 - 10	1370.0	1	0.10	0.57	0.25	0.20	3.12
E14 - 10	1263.0	1	0.10	0.60	0.25	0.19	3.10
E14 - 10	1156.5	1	0.10	0.61	0.25	0.21	3.14
Average E14 - 10	1427.0	1	0.10	0.62	0.23	0.20	3.03

APPENDIX 4

Supplementary data for chapter 4:
The Geochemical Evolution of the Western Ethiopian
Shield

Table 1: Whole-rock major and trace element data for the Western Ethiopian Shield

Sample No.	E14 - 02	E14 - 03	E14 - 04	E14 - 06	E14 - 09	E14 - 10	E14 - 13	E14 - 14	E14 - 15	E14 - 16	E14 - 17	E14 - 18	E14 - 19
SiO$_2$	75.34	69.73	75.20	47.32	78.95	36.41	29.93	30.49	29.06	30.18	32.68	28.58	45.38
Al$_2$O$_3$	13.87	15.62	13.89	15.70	0.12	0.13	18.51	19.57	20.66	19.66	12.60	20.08	0.15
Fe$_2$O$_3$	0.57	2.75	0.29	9.54	7.77	10.08	13.84	12.37	14.07	13.02	12.57	14.84	7.31
MgO	0.12	0.79	0.04	10.63	8.94	42.74	23.61	24.60	22.83	23.61	27.45	23.03	32.76
CaO	1.58	3.67	0.97	12.30	0.01	0.07	0.35	0.04	0.01	0.01	0.02	0.02	0.02
Na$_2$O	3.53	4.64	3.80	2.26	0.01	0.01	0.01	0.01	0.01	0.01	0.01	0.01	0.01
K$_2$O	4.24	1.57	4.75	0.16	0.01	0.01	0.01	0.01	0.01	0.01	0.01	0.01	0.01
TiO$_2$	0.03	0.29	0.04	0.60	0.01	0.01	1.39	1.05	1.25	1.22	2.05	1.08	0.01
P$_2$O$_5$	0.01	0.10	0.01	0.03	0.01	0.01	0.39	0.08	0.01	0.03	0.05	0.12	0.01
MnO	0.01	0.06	0.01	0.16	0.07	0.19	0.14	0.12	0.29	0.13	0.04	0.12	0.06
Cr$_2$O$_3$	0.002	0.002	0.002	0.061	0.360	0.368	0.041	0.009	0.067	0.048	0.180	0.071	0.389
Rb	9.23	5.31	25.98	0.06	0.06	0.00	0.00	0.00	0.03	0.03	0.01	0.03	0.03
Ba	171.84	52.65	7.87	12.16	0.86	2.58	10.30	6.87	2.29	1.72	1.14	16.88	1.57
Th	20.00	30.59	101.18	2.35	2.35	2.35	56.47	20.00	25.88	31.76	14.12	23.53	2.35
U	119.05	76.19	219.05	0.00	19.05	0.00	61.90	33.33	42.86	42.86	23.81	28.57	0.00
Nb	0.42	9.26	19.78	0.00	0.00	0.00	16.41	11.92	6.87	6.87	21.88	14.59	0.56
Ta	0.00	0.60	1.70	0.00	0.00	0.00	0.60	0.50	0.30	0.40	1.00	0.60	0.00
K	140.78	52.13	157.72	5.31	0.33	0.33	0.33	0.33	0.33	0.33	0.33	0.33	0.33
La	4.80	15.43	4.95	2.47	1.16	0.29	118.34	117.90	27.51	208.59	17.61	93.60	1.60
Ce	2.87	10.76	3.77	2.31	0.17	0.17	55.38	28.51	16.28	27.04	12.79	34.99	0.00
Pb	7.57	7.03	9.19	0.54	1.08	0.54	4.32	1.08	1.62	3.24	2.16	7.03	1.62
Sr	18.64	24.70	2.33	15.78	0.03	0.07	3.50	2.39	0.49	0.16	0.08	5.34	0.05
P	0.46	4.59	0.46	1.38	0.46	0.46	17.91	3.67	0.46	1.38	2.30	5.51	0.46
Nd	1.48	6.94	2.07	2.95	0.37	0.22	56.20	58.12	12.41	110.78	9.08	35.60	0.37
Zr	7.55	9.64	3.35	1.42	0.04	0.02	13.21	11.88	13.60	14.18	10.58	12.89	0.09
Sm	0.63	4.71	2.32	3.18	0.18	0.11	32.30	32.70	7.75	58.78	5.83	18.81	0.41
Eu	1.25	3.81	1.79	5.24	0.18	0.12	17.68	25.42	7.74	41.85	0.89	12.26	0.42
Ti	0.14	1.34	0.18	2.77	0.05	0.05	6.41	4.84	5.76	5.63	9.45	4.98	0.05
Dy	0.46	1.97	1.74	2.17	0.15	0.07	11.38	9.10	5.88	12.67	3.35	6.50	0.42
Y	0.48	2.11	1.54	1.85	0.15	0.00	8.07	5.60	4.92	8.40	2.99	4.42	0.26
Yb	0.59	1.93	1.46	1.28	0.12	0.10	6.09	3.61	5.48	6.73	2.56	2.88	0.22
Pr	0.56	2.40	0.80	0.71	0.16	0.02	18.70	19.19	4.25	38.03	2.78	12.57	0.06
Gd	0.32	1.92	0.96	1.84	0.11	0.05	12.79	11.93	3.82	18.13	3.16	7.56	0.22
Tb	0.04	0.27	0.19	0.29	0.02	0.01	1.66	1.42	0.67	2.04	0.45	0.99	0.04
Ho	0.07	0.28	0.25	0.31	0.02	0.02	1.4	1.01	0.86	1.56	0.52	0.8	0.06
Er	0.21	0.89	0.75	0.88	0.07	0.03	3.45	2.25	2.74	3.65	1.36	2.12	0.17
Tm	0.04	0.13	0.12	0.12	0.01	0.01	0.46	0.3	0.4	0.54	0.22	0.26	0.02
Lu	0.07	0.18	0.13	0.1	0.01	0.01	0.42	0.25	0.4	0.49	0.19	0.23	0.02

Table 1: Whole-rock major and trace element data for the Western Ethiopian Shield

Sample No.	E14-20	E14-21	E14-22	E14-23	E14-24	E14-27	E14-28	E14-29	E14-30	E14-36	E14-37	E14-38	E14-39
SiO_2	31.02	28.49	52.70	28.52	46.94	62.21	56.83	48.40	48.74	48.37	73.47	53.43	50.05
Al_2O_3	21.73	17.35	12.65	18.50	14.34	15.12	18.57	15.02	15.45	18.13	14.55	17.94	17.43
Fe_2O_3	22.04	18.90	11.62	16.68	13.18	7.73	6.84	10.95	9.72	12.24	0.95	9.39	9.85
MgO	5.84	20.04	6.90	21.87	6.92	2.39	2.20	6.45	9.36	5.49	0.18	4.00	5.64
CaO	2.75	0.05	9.17	0.23	9.51	1.84	2.73	9.34	8.68	10.96	2.46	8.06	9.60
Na_2O	0.01	0.01	3.60	0.01	3.35	4.10	6.43	3.58	2.69	2.69	3.77	3.36	3.61
K_2O	0.50	0.01	0.13	0.01	0.28	1.74	1.56	1.64	0.67	0.20	3.10	0.97	0.70
TiO_2	2.94	2.46	1.32	2.57	2.50	1.21	1.28	1.51	0.80	0.77	0.06	0.63	0.91
P_2O_5	0.12	0.03	0.15	0.16	0.21	0.35	0.31	0.63	0.25	0.17	0.02	0.23	0.40
MnO	0.26	0.13	0.74	0.18	0.25	0.09	0.11	0.15	0.08	0.23	0.03	0.17	0.17
Cr_2O_3	0.043	0.052	0.058	0.022	0.028	0.003	0.002	0.012	0.033	0.006	0.002	0.003	0.011
Rb	1.33	0.03	0.29	0.03	1.16	5.21	4.05	5.01	2.12	0.17	6.34	2.45	1.39
Ba	42.07	4.29	30.91	28.76	28.04	98.73	91.14	98.01	38.49	32.19	142.22	65.96	67.82
Th	16.47	10.59	23.53	11.76	14.12	52.94	38.82	48.24	69.41	2.35	57.65	16.47	17.65
U	14.29	14.29	28.57	14.29	14.29	119.05	80.95	76.19	90.48	0.00	66.67	28.57	38.10
Nb	25.53	20.20	10.38	22.44	19.64	33.94	25.11	18.37	14.73	1.12	6.03	3.51	4.91
Ta	1.20	0.80	0.60	0.80	0.80	1.40	1.00	0.90	0.40	0.00	0.20	0.10	0.20
K	16.60	0.33	4.32	0.33	9.30	57.77	51.80	54.45	22.25	6.64	102.93	32.21	23.24
La	18.92	32.02	18.63	21.11	18.49	48.76	37.55	43.09	45.71	9.32	18.92	20.52	30.28
Ce	10.37	15.72	16.34	14.76	16.96	37.75	29.07	35.32	35.66	7.89	13.07	15.89	28.39
Pb	14.59	2.16	10.27	1.62	3.78	17.30	169.19	3.78	4.32	7.57	22.16	9.19	10.27
Sr	16.09	0.11	16.57	0.27	15.78	15.52	24.88	49.74	40.23	34.21	20.52	33.45	49.11
P	5.51	1.38	6.89	7.35	9.65	16.08	14.24	28.94	11.48	7.81	0.92	10.56	18.37
Nd	13.74	16.69	11.60	13.96	13.81	21.27	17.28	22.90	18.39	7.24	6.72	11.08	21.79
Zr	14.29	10.80	9.08	12.06	12.43	23.08	16.09	11.97	5.98	1.01	5.29	3.85	6.22
Sm	11.60	11.17	8.90	11.26	9.44	12.55	10.41	14.12	9.01	5.41	3.40	7.43	12.39
Eu	11.19	4.35	6.37	2.56	9.46	8.99	8.33	11.85	6.01	5.83	2.32	6.01	10.06
Ti	13.56	11.34	6.09	11.85	11.53	5.58	5.90	6.96	3.69	3.55	0.28	2.90	4.20
Dy	11.76	7.73	5.67	7.64	6.35	6.76	5.56	6.07	3.80	3.66	2.27	3.49	4.44
Y	8.22	7.16	4.57	6.73	4.90	5.30	5.19	5.03	3.12	3.12	2.40	3.45	3.58
Yb	10.14	5.96	3.71	6.49	4.38	5.29	4.16	4.34	2.92	3.20	2.29	3.23	3.29
Pr	4.06	5.25	3.48	4.11	3.87	7.33	5.80	7.51	7.21	1.95	2.46	3.38	6.43
Gd	6.61	5.56	4.22	5.93	5.12	5.33	4.62	5.84	3.31	2.92	1.73	3.14	4.67
Tb	1.25	0.89	0.67	0.96	0.8	0.86	0.7	0.83	0.47	0.47	0.24	0.49	0.65
Ho	1.73	1.21	0.78	1.29	0.89	0.95	0.81	0.96	0.52	0.58	0.34	0.59	0.6
Er	4.95	3.47	2.33	3.5	2.33	2.74	2.44	2.44	1.59	1.81	1.06	1.49	1.83
Tm	0.75	0.46	0.31	0.51	0.31	0.36	0.33	0.37	0.21	0.27	0.16	0.24	0.25
Lu	0.76	0.48	0.29	0.56	0.29	0.42	0.31	0.34	0.22	0.24	0.17	0.25	0.2

Table 1: Whole-rock major and trace element data for the Western Ethiopian Shield

Sample No.	E14-41	E14-42	E14-43	E14-44	E14-46	E14-47	E14-48	E14-50	E14-51	E14-53	E14-53a	E14-54	E14-55
SiO2	50.04	53.42	70.15	74.17	37.93	46.55	47.37	74.54	72.53	72.13	48.10	50.68	46.71
Al2O3	17.39	18.41	14.52	13.77	12.66	12.70	13.44	15.34	16.43	13.30	8.27	14.79	14.21
Fe2O3	9.91	8.99	3.08	1.72	13.41	16.27	16.61	0.50	0.71	3.63	9.60	10.04	7.72
MgO	5.29	3.76	0.43	0.19	17.66	6.12	5.97	0.17	0.28	0.65	18.71	6.99	9.21
CaO	9.35	7.96	1.70	0.68	7.35	10.14	7.55	1.23	2.75	1.51	9.35	10.40	5.28
Na2O	3.59	3.39	4.39	4.20	0.66	2.76	4.03	5.66	5.72	3.43	0.76	3.30	4.50
K2O	0.95	0.99	3.71	4.26	0.05	0.18	0.17	1.23	0.72	2.92	0.07	0.01	0.02
TiO2	0.92	0.73	0.30	0.17	3.19	3.07	3.05	0.05	0.09	0.44	0.41	0.63	0.44
P2O5	0.49	0.22	0.14	0.05	0.40	0.36	0.32	0.01	0.03	0.08	0.12	0.04	0.04
MnO	0.18	0.17	0.07	0.03	0.13	0.24	0.25	0.03	0.01	0.14	0.15	0.16	0.10
Cr2O3	0.008	0.002	0.002	0.002	0.025	0.023	0.023	0.002	0.002	0.002	0.210	0.025	0.009
Rb	1.92	2.75	8.56	7.50	0.03	0.14	0.29	2.49	2.89	8.03	0.10	0.00	0.10
Ba	77.26	80.56	117.18	141.51	4.15	8.58	16.17	159.39	83.70	218.92	16.17	1.72	1.72
Th	22.35	10.59	71.76	138.82	14.12	17.65	10.59	22.35	22.35	45.88	2.35	2.35	5.88
U	42.86	19.05	57.14	157.14	23.81	19.05	9.52	28.57	28.57	28.57	0.00	0.00	0.00
Nb	5.05	4.35	20.90	14.17	19.50	19.35	16.83	3.93	3.79	6.17	1.68	0.70	0.56
Ta	0.20	0.10	0.70	1.00	0.90	0.70	0.80	0.40	0.30	0.30	0.00	0.00	0.00
K	31.54	32.87	123.19	141.45	1.66	5.98	5.64	40.84	23.91	96.96	2.32	0.33	0.66
La	44.25	19.51	55.17	36.68	22.42	21.83	19.07	5.24	14.56	14.99	4.51	3.20	3.06
Ce	38.37	15.89	45.01	21.13	23.15	21.35	19.61	6.25	10.59	22.76	4.68	3.21	2.82
Pb	9.73	11.35	31.35	40.00	5.95	4.32	2.16	8.65	8.11	10.81	0.54	0.54	4.86
Sr	50.93	34.05	10.37	6.62	1.33	11.83	10.95	24.48	48.76	18.07	4.16	2.32	18.60
P	22.51	10.11	6.43	2.30	18.37	16.54	14.70	0.46	1.38	3.67	5.51	1.84	1.84
Nd	27.40	10.19	22.82	10.12	21.34	18.83	18.61	2.66	4.06	9.08	3.32	3.25	2.51
Zr	7.19	4.00	24.12	13.70	21.54	20.55	18.33	3.06	6.11	8.88	2.31	2.64	2.60
Sm	15.63	6.35	12.84	4.82	18.27	16.62	15.14	1.73	2.39	5.92	3.02	3.33	2.52
Eu	11.61	6.25	7.98	3.33	14.76	12.68	12.38	1.25	1.85	5.06	2.50	3.45	2.26
Ti	4.24	3.37	1.38	0.78	14.71	14.16	14.06	0.23	0.41	2.03	1.89	2.90	2.03
Dy	4.74	3.49	4.86	2.65	13.68	13.16	11.55	0.76	0.49	4.33	2.35	3.95	3.09
Y	4.15	3.21	4.40	3.10	12.35	11.36	9.93	0.86	0.57	3.74	2.24	3.89	3.12
Yb	3.33	2.90	3.73	3.31	10.41	10.10	9.25	0.99	0.75	4.79	2.35	3.98	3.43
Pr	8.68	3.35	8.53	4.12	5.94	5.32	4.82	0.91	1.70	2.88	0.99	0.84	0.70
Gd	5.98	2.93	4.73	1.99	9.87	9.27	8.58	0.62	0.63	2.79	1.59	2.25	1.70
Tb	0.73	0.42	0.73	0.34	1.65	1.53	1.42	0.12	0.08	0.5	0.28	0.44	0.32
Ho	0.64	0.51	0.74	0.45	2.03	1.86	1.68	0.15	0.07	0.68	0.35	0.63	0.46
Er	1.85	1.59	1.99	1.28	5.51	5.51	4.73	0.35	0.24	2.02	0.91	1.8	1.45
Tm	0.27	0.22	0.29	0.24	0.82	0.78	0.66	0.06	0.04	0.38	0.13	0.29	0.23
Lu	0.26	0.24	0.28	0.26	0.8	0.74	0.66	0.08	0.04	0.39	0.17	0.32	0.25

Table 1: Whole-rock major and trace element data for the Western Ethiopian Shield

Sample No.	E14-56	E14-57	E14-58	E14-60	E14-63	E14-64	E14-65	E14-67	E14-68	E14-69	E14-70
SiO_2	60.00	52.35	70.36	64.71	69.54	67.43	77.93	59.19	58.65	75.69	66.05
Al_2O_3	15.86	14.76	16.13	11.65	14.44	15.64	11.63	16.73	17.30	12.72	15.44
Fe_2O_3	2.89	7.27	1.22	5.74	3.31	4.04	0.99	6.55	6.59	1.60	4.36
MgO	2.37	8.85	0.60	1.66	0.61	0.67	0.04	3.37	3.06	0.22	1.67
CaO	4.06	4.29	2.31	4.97	1.86	1.88	0.28	4.97	5.63	0.89	4.10
Na_2O	4.12	3.94	5.29	1.97	4.00	5.35	3.39	3.89	4.27	3.17	4.62
K_2O	2.90	0.06	2.22	0.34	4.55	3.03	4.81	2.21	2.09	4.72	1.46
TiO_2	0.36	0.42	0.14	0.31	0.46	0.60	0.09	1.08	1.09	0.15	0.84
P_2O_5	0.23	0.06	0.05	0.09	0.14	0.18	0.01	0.35	0.35	0.02	0.26
MnO	0.04	0.12	0.02	0.06	0.08	0.11	0.05	0.12	0.14	0.02	0.08
Cr_2O_3	0.008	0.058	0.002	0.002	0.002	0.002	0.002	0.006	0.007	0.002	0.004
Rb	5.67	0.29	4.92	1.22	18.84	9.21	6.54	8.08	8.53	9.43	5.47
Ba	155.10	9.30	167.26	51.08	192.30	127.49	4.15	106.31	95.72	227.36	61.38
Th	24.71	2.35	23.53	18.82	134.12	128.24	94.12	40.00	32.94	103.53	74.12
U	38.10	4.76	57.14	47.62	152.38	114.29	28.57	61.90	66.67	66.67	109.52
Nb	6.73	1.12	7.99	2.24	29.45	51.61	5.89	19.64	29.03	10.10	47.41
Ta	0.20	0.00	0.30	0.00	1.40	1.90	0.20	0.70	1.20	0.20	2.20
K	96.29	1.99	73.71	11.29	151.08	100.61	159.71	73.38	69.40	156.72	48.48
La	45.85	4.80	13.83	26.35	88.06	79.33	92.87	46.29	32.31	91.41	44.69
Ce	33.35	2.76	9.92	18.14	65.35	57.86	76.23	35.94	29.24	67.55	39.77
Pb	8.65	9.19	13.51	3.24	28.65	25.41	41.08	4.86	3.24	17.84	8.11
Sr	37.67	14.47	60.69	11.93	11.51	11.73	0.23	27.99	26.93	9.55	20.23
P	10.56	2.76	2.30	4.13	6.43	8.27	0.46	16.08	16.08	0.92	11.94
Nd	16.25	3.18	5.24	9.90	29.84	29.39	29.76	21.86	24.82	30.80	25.18
Zr	9.74	3.04	6.25	4.65	37.82	39.75	8.48	20.18	29.14	18.06	26.11
Sm	7.48	2.50	2.23	6.24	14.77	16.42	11.13	11.67	16.62	14.86	16.01
Eu	5.12	1.79	1.43	4.11	7.20	9.88	0.89	9.23	10.95	4.52	8.45
Ti	1.66	1.94	0.65	1.43	2.12	2.77	0.41	4.98	5.03	0.69	3.87
Dy	1.57	2.77	0.68	3.51	6.57	9.15	1.80	6.00	8.51	3.84	9.82
Y	1.21	2.66	0.51	3.47	6.66	8.99	1.54	5.54	7.54	3.01	9.05
Yb	0.83	3.06	0.45	3.59	6.92	9.21	1.32	4.30	6.71	2.56	9.19
Pr	6.09	0.82	1.76	3.28	11.65	10.90	12.30	7.63	7.55	12.67	8.95
Gd	2.10	1.73	0.70	2.66	5.85	7.38	2.69	5.11	7.00	4.80	6.65
Tb	0.24	0.3	0.08	0.44	0.89	1.11	0.29	0.79	1.06	0.6	1.12
Ho	0.18	0.48	0.08	0.55	1.03	1.36	0.24	0.82	1.14	0.5	1.35
Er	0.4	1.65	0.21	1.69	2.93	3.89	0.6	2.28	3.39	1.4	4.41
Tm	0.05	0.24	0.03	0.25	0.46	0.63	0.11	0.35	0.51	0.22	0.72
Lu	0.06	0.22	0.04	0.31	0.47	0.71	0.11	0.34	0.47	0.19	0.68

Whole-Rock Geochemistry

Whole-rock geochemical analyses for major, minor, and trace elements were collected at ACME Labs in Vancouver, British Columbia, Canada. Major-element oxide data collection procedure involved the crushed rock pulp being mixed with $LiBO_2/Li_2B_4O_7$ flux. Graphite crucibles were fused in a muffle furnace for 30 min at 980°C. The cooled bead was then dissolved in American Chemical Society–grade nitric acid and analysed with a SPECTRO AS500 ICP-OES (inductively coupled plasma–optical emission spectroscopy) instrument. Loss-on-ignition values were determined by igniting a sample split and then measuring the weight lost. For trace-element analyses, the crushed rock pulp was digested with a modified Aqua Regia solution of equal parts concentrated HCl, HNO_3, and deionized H_2O for 1 h in a heating block or hot water bath. Samples were made up to volume with dilute HCl and analysed with a Perkin-Elmer ELAN 9000 ICP-MS. The quality-control protocol involved analysing pulp duplicates to monitor analytical precision and a reagent blank to measure background. In addition, interspersed analyses of reference materials SO-18, OREAS45EA, GS311-1, and GS910-4 monitored the accuracy of results. Total sulphur and carbon values were determined by adding an induction flux to the prepared sample and igniting the sample in a LECO CS230 Carbon/Sulphur Series induction furnace. A carrier gas transports the released carbon and sulphur to be measured by adsorption in an infrared spectrometric cell. Results are total carbon or sulphur.

Sm-Nd and Sr Isotope Geochemistry

Nd, Sm, and Sr isotopes were measured with an Isotopx Phoenix thermal ionization mass spectrometer (TIMS) at the University of Adelaide. Sample powder weight (grams) was calculated on the basis of a nominal 2 μg of Nd (optimum TIMS accuracy and recovery value). Isotope dilution mass spectrometry was determined by the addition of a nominal 0.4 g of $^{150}Nd/^{147}Sm$-enriched spike. This allowed the concentration of Sm/Nd (μg g−1) and hence the correction factor for the measured $^{143}Nd/^{144}Nd$ and $^{147}Sm/^{149}Sm$ isotopic ratios to be determined. The addition of a strontium spike (~0.12 g) allowed $^{87}Sr/^{86}Sr$ to be simultaneously determined. All milled-powder and spike weights were accurately recorded (five decimal places) on a Mettler-Toledo AT201 balance. The 0.05–0.2-g rock powder was dissolved together with the University of Adelaide mixed spike "H" (concentrations: ^{150}Nd = 283.9797 ng g−1; ^{147}Sm = 573.5484 ng g−1) in cleaned Teflon bombs with an approximate ratio of 2 ng sample Nd/0.4 g spike H, based on whole-rock Nd values. Samples were then dissolved on a hotplate at 140°C in 2 mL of 7 M HNO_3 and 4 mL of 48% HF to dissolve silicate minerals. An additional 2 mL of 15 M HNO_3 was added before complete dryness to prevent the precipitation of insoluble silica fluorides. Next, 2 mL of 7 M HNO_3 and 4 mL of 48% HF were added to each sample. The capped and sealed bombs were then placed in an oven for 96 h at 190°C. The Teflon bombs were removed from the oven and allowed to cool before the samples were evaporated on a hotplate at 140°C. An additional 2 mL of 15 M HNO3 was added before complete evaporation of the sample to prevent the precipitation of fluorides. Once each sample was evaporated, 6 mL of 6 M HCL was added to each sample, and the bombs were placed in an oven for 24 h at 190°C. Samples were then evaporated on a hotplate. To redissolve each sample, 1.5 mL of 2 M HCl was added, and samples were placed into 2-mL centrifuge tubes for centrifuging. Element (Sr, Sm, Nd) purification was achieved by conventional ion chromatography procedures. The first pass to separate Sr from Sm–Nd was completed in 2 mL

AGW X8 200–400 mesh resin in Polyprep columns. Sm was separated from Nd with 1 mL of Eichrom Ln resin SPS in quartz glass columns.

Nd measurement involved multidynamic measurements of at least five blocks of 20 cycles (>100 ratios). Normalization to $^{146}Nd/^{144}Nd = 0.7219$ was done with exponential mass fractionation correction. Nd concentrations were corrected for a 100-pg blank. Static Sm isotopic measurements involved three blocks of 20 cycles (60 ratios). Sm concentrations were corrected for a 50-pg blank. Procedural blanks (n = 2), international standards G-2 (n= 1) and BCR-2 (n = 3), and internal standards JNdi1 (n = 2) and SRM987 (n = 5) were analysed before and during sample analysis to measure machine accuracy and precision. Procedural blanks registered values of <61 pg Nd, <6 pg Sm, and <761 pg Sr, indicating negligible contamination or procedural error. .International Nd reference material JNdi (Tanaka et al. 2000; $^{143}Nd/^{144}Nd = 0.512115 \pm 7$) yielded a mean value of 0.512107 ± 3 (n = 49), based on a 400-ng standard loading weight. Based on a 500-ng load, internal Sr standard SRM9878 ($^{87}Sr/^{86}Sr = 0.710268 \pm 17$; n > 700) yielded a mean value of 0.710245 ± 5 (n = 103) over the same time period. G-2 (Weis et al. 2006; 87Sr/86Sr =0.709770 ± 16) and BCR-2 (Balcaen et al. 2005; $^{87}Sr/^{86}Sr = 0.705015 \pm 13$) yielded $^{87}Sr/^{86}Sr$ ratios of 0.709755 ± 3 (G-2), 0.709732 ± 3 (G-2), and 0.705004 ± 3 (BCR-2). Overall, the analysed standards were within accepted values.

Present-day $\varepsilon_{Nd}(t)$ values were obtained with CHUR values for $^{143}Nd/^{144}Nd$ (0.512638) and $^{147}Sm/^{144}Nd$ (0.1966) and depleted-mantle $^{143}Nd/^{144}Nd$ (0.513150) and $^{147}Sm/^{144}Nd$ (0.2145) ratios taken from Goldstein et al. (1984). Depleted-mantle model ages (T_{DM}) were calculated on the basis of these ratios. Some samples were assigned crystallisation ages directly dated by U–Pb zircon geochronology (Chapter 2a and b). Although not directly dated, the other samples are considered to be part of the suite, on the basis of field relationships and other data. These samples are assigned an age of 700 Ma for $\varepsilon_{Nd}(t)$ and TDM model age calculations.

APPENDIX 5

Supplementary data for chapter 5:
Hafnium Isotope Evolution of Butana and Chad – Does
Butana Represent the Eastern Margin of the Sahara
Metacraton.

Figure 1: U–Pb Wetherill plots (^{207}Pb / ^{206}Pb v. ^{238}U / ^{206}Pb) constructed with a 2 sigma data point error ellipses. from Butana and Chad. Filled grains represent those within 90% concordance and outlines represent all other grains present. Each plot has a representative cumulative weighted average plot. Age (Ma) is on the y-axis. Dark grey bars represent ^{238}U / ^{206}Pb ages and light grey represent ^{207}Pb / ^{206}Pb ages. Weighted average and error are shown by light and dark grey shaded areas.

Figure 1: U–Pb Wetherill plots (^{207}Pb / ^{206}Pb v. ^{238}U/^{206}Pb) constructed with a 2 sigma data point error ellipses. from Butana and Chad. Filled grains represent those within 90% concordance and outlines represent all other grains present. Each plot has a representative cumulative weighted average plot. Age (Ma) is on the y-axis. Dark grey bars represent ^{238}U/^{206}Pb ages and light grey represent ^{207}Pb / ^{206}Pb ages. Weighted average and error are shown by light and dark grey shaded areas.

Table 1: LA–ICP–MS U–Pb data used to calculate Concordias from Butana and Chad

Analysis	$^{207}Pb/^{235}U$		$^{206}Pb/^{238}U$		rho	Conc (%)	$^{207}Pb/^{206}Pb$		$^{206}Pb/^{238}U$	
Butana										
2-18										
5_2-1801	1.289	0.026	0.137	0.002	0.523	95	875	36.41	828.1	12
5_2-1802	1.222	0.028	0.118	0.002	0.450	67	1076	41.63	717.7	10.96
5_2-1803	1.311	0.030	0.136	0.002	0.445	89	924.5	42.51	822.4	12.38
5_2-1804	1.275	0.025	0.138	0.002	0.525	98	845.5	36.44	830.9	12.06
5_2-1805	1.260	0.027	0.138	0.002	0.469	103	811.8	40.92	834.3	12.19
5_2-1806	0.783	0.015	0.079	0.001	0.550	49	992.4	33.3	488.1	7.23
5_2-1807	1.281	0.026	0.136	0.002	0.518	92	886.3	36.65	819.3	11.91
5_2-1808	1.287	0.027	0.130	0.002	0.498	81	975.7	37.97	789.8	11.71
5_2-1809	1.225	0.022	0.133	0.002	0.598	97	829.5	30.51	805.7	11.37
5_2-1810	1.219	0.025	0.135	0.002	0.501	104	786.4	38.75	817.6	11.95
5_2-1811	1.165	0.024	0.126	0.002	0.508	91	838	37.8	765.8	11.22
5_2-1812	1.300	0.034	0.137	0.002	0.380	92	896.4	50.8	826.8	12.93
5_2-1813	1.287	0.029	0.134	0.002	0.443	87	924.3	42.8	808.7	12.18
5_2-1814	1.244	0.025	0.134	0.002	0.521	95	849.8	36.53	810.1	11.79
5_2-1815	1.278	0.030	0.135	0.002	0.442	92	887.8	44.03	816.6	12.35
5_2-1816	1.292	0.022	0.136	0.002	0.613	93	890.5	29.44	824.2	11.6
5_2-1817	1.166	0.028	0.126	0.002	0.410	91	844	47.29	764.1	11.72
5_2-1818	1.204	0.025	0.132	0.002	0.493	97	819.2	39.03	796.6	11.73
5_2-1819	1.277	0.025	0.136	0.002	0.544	94	870.9	34.49	822.6	11.84
5_2-1820	1.358	0.028	0.144	0.002	0.496	99	880.6	38.6	867.4	12.61
5_2-1821	1.295	0.024	0.139	0.002	0.563	98	857.2	33.37	838.2	11.98
5_2-1822	1.340	0.027	0.142	0.002	0.514	96	888.1	37.19	853.5	12.44
5_2-1823	1.296	0.027	0.139	0.002	0.513	97	863.7	37.48	836.9	12.21
5_2-1824	1.331	0.030	0.140	0.002	0.455	93	903.3	42.7	842.4	12.67
5_2-1825	1.218	0.024	0.124	0.002	0.543	79	956.6	34.46	756.2	10.99
5_2-1826	1.289	0.026	0.139	0.002	0.533	99	849.1	36.03	838.2	12.15
5_2-1827	1.275	0.026	0.132	0.002	0.508	86	930	37.25	799.5	11.73
5_2-1828	1.291	0.025	0.138	0.002	0.536	96	868.3	35.56	831.6	12.04
5_2-1829	1.300	0.029	0.136	0.002	0.461	90	915.6	41.63	819.5	12.28
5_2-1830	1.283	0.028	0.136	0.002	0.472	94	876.3	40.88	824	12.28
5_2-1831	1.287	0.026	0.139	0.002	0.510	99	848.8	37.73	836.9	12.24
5_2-1832	1.338	0.031	0.137	0.002	0.452	87	954.7	42.74	827.1	12.5
5_2-1833	1.307	0.029	0.141	0.002	0.473	101	842.5	41.65	851.5	12.69
122 + 123										
122_21	1.564	0.026	0.152	0.002	0.501	86	1061.9	30.02	911.4	11.32
122_22	1.525	0.024	0.152	0.002	0.531	90	1009.2	28.82	912	11.26
122_23	1.112	0.017	0.114	0.002	0.554	72	960.5	27.5	693.2	8.68
122_24	1.631	0.043	0.162	0.003	0.302	96	1010.8	51.97	970.2	14.13
122_25	1.144	0.016	0.123	0.002	0.608	89	846.2	24.66	750	9.09
122_26	1.568	0.026	0.154	0.002	0.512	90	1032.4	30.27	925.6	11.55
122_27	1.528	0.025	0.156	0.002	0.487	97	960.8	30.7	933.5	11.35
122_28	1.655	0.026	0.157	0.002	0.514	85	1105.7	28.59	941	11.53
122_29	1.601	0.024	0.160	0.002	0.568	96	1000.4	26.17	957.8	11.5
122_30	1.132	0.016	0.115	0.001	0.591	72	972.4	24.82	700.4	8.55
122_31	1.601	0.027	0.164	0.002	0.492	102	954.7	31.56	977.9	12.2
122_32	1.423	0.021	0.133	0.002	0.570	70	1144.1	25.63	802.2	9.79
122_33	1.589	0.023	0.157	0.002	0.563	91	1031.6	25.84	937.6	11.27
122_34	1.589	0.023	0.161	0.002	0.568	99	970.5	25.97	964.2	11.53
122_35	1.661	0.029	0.166	0.002	0.481	99	1003.7	32.9	989.8	12.52
122_36	1.567	0.029	0.161	0.002	0.439	101	949.4	35.57	960.7	12.14
122_37	1.121	0.021	0.121	0.002	0.431	88	838.6	37.17	738.4	9.6
122_38	1.080	0.016	0.123	0.002	0.569	101	736.9	26.87	746.2	9.05

Table 1: LA–ICP–MS U–Pb data used to calculate Concordias from Butana and Chad

Analysis	$^{207}Pb/^{235}U$		$^{206}Pb/^{238}U$		rho	Conc (%)	$^{207}Pb/^{206}Pb$		$^{206}Pb/^{238}U$	
Butana										
122 + 123										
122_39	1.550	0.025	0.155	0.002	0.514	93	996.7	29.58	930.7	11.39
122_40	1.424	0.024	0.148	0.002	0.463	96	928	32.21	887.4	10.8
122_41	1.594	0.025	0.152	0.002	0.534	84	1091.4	27.73	914.3	11.12
122_42	1.440	0.026	0.149	0.002	0.476	96	931.8	33.9	895.4	11.46
122_43	1.636	0.026	0.165	0.002	0.528	99	988.8	28.87	982.4	11.98
122_44	1.586	0.024	0.159	0.002	0.529	95	997.5	27.97	950.7	11.47
122_45	1.680	0.027	0.171	0.002	0.515	105	968.6	29.08	1016.2	12.27
122_46	1.580	0.026	0.163	0.002	0.496	104	936.7	31.03	974	11.92
122_47	1.785	0.031	0.178	0.002	0.457	105	1005	33.06	1056.7	13.05
122_48	1.674	0.027	0.166	0.002	0.507	98	1014.3	29.28	991.8	12.02
122_49	2.168	0.033	0.145	0.002	0.535	49	1778.7	24.98	870.5	10.55
122_50	1.332	0.021	0.141	0.002	0.522	96	886.1	29.38	849.6	10.36
122_51	1.586	0.025	0.152	0.002	0.516	84	1084.2	28.68	913.2	11.09
122_52	1.690	0.031	0.167	0.002	0.436	98	1019.8	34.39	997.8	12.5
144 + 146										
144_01	1.118	0.015	0.106	0.001	0.520	59	1099.9	24.14	651.7	7.23
144_02	1.207	0.016	0.132	0.002	0.536	97	822.9	25.19	796.9	8.87
144_03	1.083	0.014	0.122	0.001	0.531	99	753	25.01	742.5	8.15
144_04	1.068	0.015	0.118	0.001	0.466	92	788.1	28.14	721.4	7.89
144_05	1.097	0.015	0.120	0.001	0.542	90	813	25.79	731.5	8.34
144_06	1.094	0.014	0.114	0.001	0.529	75	924.3	24.79	693.9	7.71
144_07	1.064	0.014	0.117	0.001	0.504	89	800.6	26.07	714.4	7.89
144_08	1.111	0.014	0.113	0.001	0.551	71	967.6	23.51	689.7	7.64
144_09	1.062	0.014	0.118	0.001	0.521	91	789.3	25.74	716.9	7.96
144_10	1.067	0.014	0.115	0.001	0.552	84	838.4	23.98	704.4	7.82
144_11	1.071	0.015	0.117	0.001	0.487	87	822	26.87	712.5	7.78
144_12	1.076	0.015	0.120	0.001	0.538	95	768.7	26.18	732.7	8.34
144_13	1.083	0.015	0.118	0.001	0.521	86	830.4	26.23	716.8	8.13
144_14	1.189	0.015	0.127	0.002	0.553	89	865.9	24.29	770.8	8.56
144_15	1.357	0.018	0.121	0.001	0.548	60	1230.7	23.29	735.9	8.22
144_16	1.006	0.018	0.113	0.001	0.398	89	769.8	36.05	687.3	8.27
144_17	1.062	0.016	0.114	0.001	0.500	81	856.9	28.34	695.5	8.07
144_18	1.196	0.016	0.119	0.001	0.493	71	1020.1	25.79	721.9	7.9
144_19	1.145	0.015	0.120	0.001	0.551	80	912.8	24.05	727.8	8.14
144_20	1.071	0.015	0.118	0.001	0.541	90	798.5	26.06	720.2	8.19
144_21	1.168	0.016	0.130	0.002	0.530	102	774.4	26.58	789.9	8.98
144_22	1.159	0.018	0.124	0.002	0.453	87	864.2	30.2	752.8	8.6
144_23	1.222	0.017	0.113	0.001	0.532	60	1153.3	24.89	691.6	7.87
144_24	1.120	0.016	0.123	0.001	0.509	92	810.8	27.3	746.6	8.42
144_25	1.046	0.015	0.117	0.001	0.530	92	771.3	26.67	712.4	8.11
144_26	1.086	0.018	0.117	0.002	0.483	85	839.2	31.02	715.9	8.64
144_27	1.166	0.016	0.125	0.002	0.526	89	854.2	26.46	760.7	8.65
144_28	1.132	0.018	0.122	0.001	0.468	88	847.7	30.26	741.8	8.57
144_29	1.084	0.016	0.119	0.001	0.509	89	811.3	28.67	723.6	8.56
144_30	1.120	0.016	0.125	0.002	0.512	98	775.4	27.79	758.9	8.7
144_31	1.128	0.017	0.125	0.002	0.506	97	786.5	28.27	760.3	8.74
144_32	1.140	0.017	0.123	0.002	0.512	89	842.2	28.1	748.5	8.63
144_33	1.229	0.018	0.133	0.002	0.510	95	845.3	27.81	802.7	9.22
144_34	1.280	0.019	0.139	0.002	0.514	102	826.9	27.93	841	9.65
144_35	1.209	0.018	0.127	0.002	0.509	85	902.5	28.16	769.8	8.9
144_36	1.127	0.017	0.127	0.002	0.506	101	760.9	28.73	768	8.9
144_37	1.095	0.017	0.123	0.002	0.495	100	753	29.51	750.3	8.73

Table 1: LA–ICP–MS U–Pb data used to calculate Concordias from Butana and Chad

Analysis	[207]Pb/[235]U		[206]Pb/[238]U		rho	Conc (%)	[207]Pb/[206]Pb		[206]Pb/[238]U
Butana									
144 + 146									
144_38	1.116	0.153	0.132	0.007	0.264	113	703.5	261.2	797.7
144_39	1.137	0.018	0.127	0.002	0.497	100	770.6	29.55	771.3
Quaddai Region									
S13									
S13_01	0.859	0.017	0.093	0.001	0.373	68	840.4	39.66	572.7
S13_02	0.970	0.031	0.098	0.002	0.206	61	981.4	66.08	601.9
S13_03	0.789	0.015	0.075	0.001	0.389	42	1106.4	35.55	465.7
S13_04	0.807	0.011	0.096	0.001	0.497	92	639.7	28.16	590.9
S13_05	0.944	0.020	0.108	0.001	0.302	92	719.4	43.82	662
S13_06	0.827	0.013	0.088	0.001	0.420	63	866.3	32.4	545.3
S13_07	0.836	0.012	0.098	0.001	0.514	91	663.5	27.48	604
S13_08	0.783	0.012	0.093	0.001	0.476	91	632.8	31.62	575.8
S13_09	0.860	0.017	0.100	0.001	0.368	89	690.7	41.27	613.5
S13_10	1.295	0.028	0.097	0.001	0.304	38	1559.7	41.2	598
S13_11	0.830	0.014	0.093	0.001	0.426	75	763.3	33.07	574.1
S13_12	0.848	0.015	0.098	0.001	0.410	85	709.4	36.23	600.2
S13_13	0.853	0.014	0.098	0.001	0.456	83	722	32.06	600
S13_14	0.901	0.014	0.095	0.001	0.487	66	884.9	29.99	587.1
S13_15	0.902	0.014	0.098	0.001	0.513	73	824.1	28.54	604.1
S13_16	0.892	0.014	0.103	0.001	0.488	88	711.9	31.04	629.5
S13_17	0.925	0.016	0.105	0.001	0.451	89	729.3	34.08	646.5
S13_18	0.976	0.023	0.092	0.001	0.347	50	1124.1	44.84	566.2
S13_19	1.166	0.023	0.116	0.002	0.379	70	1015.6	37.64	706.4
S13_20	0.915	0.020	0.106	0.001	0.347	92	701.4	45.16	647.9
S13_21	0.849	0.015	0.100	0.001	0.453	93	662.1	33.92	613.6
S13_22	0.832	0.019	0.096	0.001	0.336	84	701.6	46.2	591.8
S13_23	1.732	0.029	0.097	0.001	0.465	29	2087.4	27.62	598
S13_24	0.893	0.016	0.100	0.001	0.446	81	761.9	34.85	615.7
S13_25	0.893	0.016	0.103	0.001	0.443	90	700.7	35.97	633
S13_26	1.038	0.025	0.103	0.002	0.358	62	1018.6	46.43	631.3
S13_27	0.947	0.019	0.100	0.001	0.387	70	882.2	39.94	616.5
S13_28	1.061	0.023	0.100	0.001	0.349	55	1123.6	42.55	613.6
S13_29	0.817	0.020	0.093	0.001	0.343	78	731.8	49.92	573.6
S13_30	0.784	0.028	0.092	0.002	0.208	85	665.2	76.29	568.7
S13_31	1.979	0.093	0.164	0.004	0.157	71	1371.5	90.95	979.1
S13_32	1.514	0.031	0.157	0.002	0.423	102	923.9	39.31	941.6
S13_33	1.365	0.030	0.144	0.002	0.374	97	895	42.96	866
S13_34	1.258	0.026	0.135	0.002	0.399	95	856.1	40.25	816.2
S14									
5_S1430	0.840	0.016	0.101	0.002	0.577	101	616.5	34.29	619.9
5_S1424	0.919	0.021	0.108	0.002	0.436	100	662	46.01	661.8
5_S1428	0.888	0.020	0.105	0.002	0.466	97	658.7	43.67	641.4
5_S1425	0.837	0.015	0.100	0.002	0.627	96	639	30.47	611.5
5_S1415	0.813	0.016	0.097	0.001	0.541	95	627.1	35.87	597.7
5_S1411	0.822	0.013	0.098	0.001	0.663	95	633.6	27.3	602.4
5_S1431	0.838	0.019	0.099	0.002	0.457	93	656.3	44.29	607.8
5_S1404	0.861	0.021	0.101	0.002	0.390	93	669.6	49.91	619.6
5_S1422	0.866	0.015	0.101	0.002	0.624	93	672.7	30	622.4
5_S1429	0.923	0.016	0.106	0.002	0.609	92	710	30.89	650.3
5_S1420	1.657	0.035	0.161	0.003	0.481	91	1054.7	38.62	963.9
5_S1402	0.808	0.013	0.096	0.001	0.694	91	647.1	25.31	589.6
5_S1413	0.816	0.014	0.096	0.001	0.625	90	656.1	30.9	592.7
5_S1405	0.822	0.013	0.097	0.001	0.666	90	659.4	26.77	595.4

Table 1: LA–ICP–MS U–Pb data used to calculate Concordias from Butana and Chad

Analysis	$^{207}Pb/^{235}U$		$^{206}Pb/^{238}U$		rho	Conc (%)	$^{207}Pb/^{206}Pb$		$^{206}Pb/^{238}U$	
Quaddai Region										
S14										
5_S1416	0.807	0.014	0.095	0.001	0.608	88	661.6	30.63	584.9	8.3
5_S1426	1.169	0.022	0.124	0.002	0.575	86	879	32.57	753.6	10.91
5_S1409	0.912	0.016	0.103	0.002	0.587	85	745.4	31.66	632.8	9.01
5_S1403	0.872	0.015	0.099	0.001	0.636	84	726.9	28.28	611.3	8.65
5_S1401	0.829	0.017	0.095	0.002	0.507	83	710.8	38.9	587.1	8.97
5_S1421	0.869	0.015	0.098	0.001	0.627	80	750	29.77	603.4	8.68
5_S1406	0.876	0.017	0.098	0.001	0.532	79	764.8	35.83	603.3	8.75
5_S1408	0.999	0.022	0.107	0.002	0.443	75	869.4	42.4	652.9	10.1
5_S1427	0.898	0.016	0.099	0.001	0.621	75	809.5	29.72	605.6	8.75
5_S1407	0.906	0.017	0.099	0.002	0.573	74	818	32.92	608.9	8.94
5_S1414	0.830	0.014	0.093	0.001	0.627	74	773.1	29.25	571.5	8.2
5_S1419	0.918	0.016	0.100	0.002	0.613	73	833.5	29.81	611.7	8.81
5_S1410	0.917	0.017	0.097	0.001	0.558	68	877.2	33.57	599.3	8.75
5_S1412	0.822	0.017	0.087	0.001	0.499	61	879.4	39.06	539.2	8.25
5_S1418	1.213	0.021	0.104	0.002	0.633	49	1299	26.77	639.8	9.18
5_S1423	2.033	0.036	0.117	0.002	0.613	35	2045	25.72	712.5	10.38
5_S1417	0.782	0.018	0.066	0.001	0.427	31	1335.8	41.47	411.9	6.37
S4										
5_S401	1.67814	0.052	0.168	0.003	0.282	100	1000.1	62.07	1000.3	16.54
5_S402	0.80669	0.015	0.079	0.001	0.553	47	1042.8	31.51	490.4	7.01
5_S403	1.74901	0.041	0.166	0.003	0.409	89	1109.3	43.62	988.7	14.75
5_S404	1.63977	0.032	0.165	0.002	0.496	99	992.2	35.84	982.5	13.67
5_S405	0.8304	0.020	0.097	0.002	0.412	87	683	47.09	595.3	8.99
5_S406	6.63327	0.108	0.175	0.003	0.627	31	3334.6	21.3	1039.7	14.74
5_S407	1.68171	0.028	0.164	0.002	0.629	94	1047	27.17	981.1	13.41
5_S408	1.73395	0.031	0.169	0.003	0.569	96	1048.2	31.3	1008.7	14
5_S409	1.66217	0.030	0.158	0.002	0.580	86	1097.2	30.52	948.3	13.3
5_S410	1.67945	0.030	0.164	0.002	0.583	94	1043.1	30.17	981.6	13.62
5_S411	1.68988	0.029	0.164	0.002	0.605	93	1059	29.26	979.9	13.53
5_S412	1.79206	0.043	0.163	0.003	0.402	82	1190.2	44.5	973.7	14.62
5_S413	1.67911	0.032	0.167	0.003	0.542	99	1009.4	33.21	996.7	14
5_S414	1.32173	0.026	0.120	0.002	0.519	62	1188.3	33.84	732.6	10.52
5_S415	1.73056	0.031	0.165	0.002	0.598	89	1102.4	29.42	982	13.67
5_S416	1.62662	0.029	0.165	0.002	0.589	101	974.2	30.36	983.4	13.71
5_S417	1.87456	0.038	0.165	0.003	0.513	78	1256.2	35.25	984	14.39
5_S418	1.77747	0.032	0.172	0.003	0.596	96	1067.3	30.29	1023.1	14.42
5_S419	1.72582	0.036	0.170	0.003	0.499	99	1028.4	37.64	1013.5	14.84
5_S420	1.7955	0.032	0.166	0.003	0.620	85	1163.1	28.78	987.9	14.02
5_S421	1.65933	0.030	0.164	0.003	0.598	95	1026.7	30.17	978.1	13.93
5_S422	1.89864	0.037	0.173	0.003	0.558	87	1187.4	32.69	1028.5	14.78
5_S423	1.67919	0.030	0.158	0.002	0.617	84	1124.9	29.01	945	13.39
5_S424	1.28835	0.026	0.120	0.002	0.542	65	1136.5	34.26	733.1	10.86
5_S425	1.7525	0.032	0.173	0.003	0.595	101	1022.4	30.92	1030.9	14.63
5_S426	1.63571	0.030	0.158	0.002	0.609	89	1066.2	29.8	947.7	13.48
5_S427	13.6753	0.232	0.519	0.008	0.657	98	2752.2	21.8	2694.5	33.39
5_S428	1.3468	0.025	0.123	0.002	0.574	63	1180.7	31.48	748.5	10.93
5_S429	1.61987	0.031	0.129	0.002	0.583	54	1450.1	30.23	781.4	11.47
5_S430	0.92306	0.022	0.100	0.002	0.436	73	843.6	46.12	612.4	9.62
5_S431	5.93179	0.107	0.356	0.006	0.616	100	1966.6	26.4	1965.5	26.26
5_S432	4.24099	0.077	0.273	0.004	0.617	84	1846.2	26.71	1553.7	21.36

Table 1: LA–ICP–MS U–Pb data used to calculate Concordias from Butana and Chad

Analysis	$^{207}Pb/^{235}U$		$^{206}Pb/^{238}U$		rho	Conc (%)	$^{207}Pb/^{206}Pb$		$^{206}Pb/^{238}U$	
Central and Mayo Kebbi Region										
37										
37_01	0.69768	0.015	0.087	0.001	0.229	97	550.5	46.52	535.3	6.21
37_02	0.71657	0.010	0.088	0.001	0.377	96	569.4	29.85	544.7	5.64
37_03	0.75153	0.012	0.088	0.001	0.334	82	665.5	33.54	546.2	5.86
37_04	0.72812	0.015	0.087	0.001	0.245	84	637.7	45.05	536.4	6.2
37_05	0.911	0.011	0.085	0.001	0.427	47	1132.1	24.3	528.5	5.32
37_06	0.73181	0.012	0.088	0.001	0.298	87	623.6	36.44	542.3	5.89
37_07	0.7322	0.009	0.090	0.001	0.427	98	569.6	27.52	555.7	5.68
37_08	0.84781	0.013	0.080	0.001	0.337	44	1122.5	30.08	495	5.17
37_09	1.02586	0.016	0.089	0.001	0.346	42	1296	30.72	547	6.04
37_10	0.74451	0.014	0.089	0.001	0.273	88	626.4	41.93	550	6.29
37_11	0.76757	0.016	0.093	0.001	0.293	96	598.5	43.69	573.5	6.78
37_12	0.79357	0.015	0.087	0.001	0.305	67	804.9	40.19	539.5	6.35
37_13	0.86033	0.011	0.092	0.001	0.474	65	870.4	25.33	565.6	5.98
37_14	0.79328	0.010	0.091	0.001	0.489	79	715	25.79	561.7	5.94
37_15	1.29107	0.022	0.097	0.001	0.352	39	1550.2	31.85	599.2	6.99
37_16	1.53574	0.025	0.082	0.001	0.376	23	2171	27.96	509.3	6.01
37_17	1.6121	0.027	0.136	0.002	0.395	61	1343.1	31.62	819.8	9.46
37_18	1.71745	0.024	0.170	0.002	0.459	99	1023.3	26.49	1011	10.55
37_19	0.92222	0.013	0.106	0.001	0.481	90	716.1	27.43	647.9	6.97
37_20	0.86711	0.013	0.074	0.001	0.438	35	1324.8	28.35	458	5.23
37_21	0.68537	0.011	0.080	0.001	0.415	73	676.9	31.72	496.3	5.52
37_22	0.74426	0.013	0.090	0.001	0.369	90	611.7	36.8	553.1	6.41
37_23	0.75259	0.013	0.090	0.001	0.380	91	614.4	35.03	558.2	6.31
37_24	0.77295	0.015	0.091	0.001	0.337	86	656.5	40.11	562	6.59
37_25	0.80818	0.020	0.092	0.001	0.270	78	730.4	51.67	567.5	7.52
37_26	0.77851	0.011	0.090	0.001	0.474	81	689.4	28.09	557.4	6.11
37_27	0.80226	0.011	0.096	0.001	0.462	95	620.3	28.91	591.7	6.48
37_44	0.77782	0.020	0.092	0.001	0.217	85	661.1	56.77	564.9	7.64
37_45	0.90113	0.017	0.096	0.001	0.323	68	869.6	39.45	591.6	7.16
37_46	0.87435	0.015	0.095	0.001	0.370	70	838.7	34.66	583	6.81
37_47	0.7735	0.012	0.094	0.001	0.440	97	595.2	32.22	578.4	6.64
37_48	0.8234	0.015	0.091	0.001	0.352	72	786.3	38.82	563.7	6.89
37_49	0.79754	0.013	0.091	0.001	0.404	79	718.2	33.99	563.9	6.6
37_50	0.7706	0.016	0.091	0.001	0.299	86	653.4	44.46	561.7	7
37_51	0.96915	0.017	0.093	0.001	0.374	53	1078.2	33.63	575	6.85
37_52	0.77357	0.013	0.093	0.001	0.392	92	623	35.35	571.5	6.7
37_53	1.26302	0.021	0.123	0.002	0.392	71	1058.8	33.02	746.5	8.8
37_54	0.73926	0.012	0.089	0.001	0.402	92	602.1	34.35	552.3	6.43
37_55	0.76072	0.014	0.090	0.001	0.327	87	643	40.46	557.4	6.68
37_56	0.75583	0.014	0.090	0.001	0.347	87	635.4	38.63	555.9	6.66
37_57	0.80855	0.015	0.092	0.001	0.348	76	741.3	38.05	565.4	6.73
37_58	0.78214	0.012	0.093	0.001	0.414	90	637.6	32.95	573.8	6.61
37_59	0.97261	0.018	0.111	0.001	0.341	92	735.8	38.73	676	8.04
2B										
28_08	0.75312	0.011	0.092	0.001	0.360	96	589.1	31.22	565.3	5.93
28_09	0.77875	0.012	0.094	0.001	0.342	94	612.7	33.75	577.6	6.19
28_10	0.88482	0.013	0.093	0.001	0.347	64	896.5	31.16	573.9	6.1
28_11	0.78243	0.018	0.088	0.001	0.192	73	748.6	50.05	546	6.63
28_12	0.96729	0.014	0.090	0.001	0.390	49	1138.5	27.71	557.5	5.92
28_13	0.75527	0.011	0.091	0.001	0.362	90	621.5	32.1	558.8	5.97
28_14	0.74232	0.011	0.089	0.001	0.360	87	629	32.79	547.8	5.89

Table 1: LA–ICP–MS U–Pb data used to calculate Concordias from Butana and Chad

Analysis	$^{207}Pb/^{235}U$		$^{206}Pb/^{238}U$		rho	Conc (%)	$^{207}Pb/^{206}Pb$		$^{206}Pb/^{238}U$	
Central and Mayo Kebbi Region										
28										
28_15	0.76422	0.013	0.095	0.001	0.325	110	534.3	38.28	587.1	6.51
28_16	0.74294	0.011	0.091	0.001	0.360	96	584	32.4	559.3	5.99
28_17	1.19884	0.020	0.112	0.001	0.349	60	1134.2	33.25	685.8	7.73
28_18	3.2216	0.071	0.190	0.003	0.291	56	2003.9	39.1	1120.3	14.02
28_19	1.13273	0.022	0.108	0.001	0.303	60	1100.2	38.19	660.4	7.68
28_20	1.91742	0.038	0.101	0.001	0.310	28	2202.8	34.9	619.4	7.83
28_21	0.95499	0.016	0.095	0.001	0.343	58	1011.9	34.58	585.2	6.66
28_22	0.76069	0.014	0.092	0.001	0.337	92	612.8	39.2	565.3	6.6
28_23	0.87531	0.020	0.091	0.001	0.269	61	919	47.11	562.6	7.23
28_24	0.75608	0.016	0.094	0.001	0.279	104	555.3	46.14	576.2	6.89
28_25	0.75029	0.022	0.088	0.001	0.218	80	677.9	62.04	542	7.72
28_26	0.74433	0.016	0.089	0.001	0.293	89	618.8	44.89	552.1	6.65
28_27	0.75647	0.016	0.094	0.001	0.300	106	547.1	45.69	578.7	6.93
28_28	0.79153	0.016	0.097	0.001	0.308	102	584.9	43.64	594.3	7.07
28_29	3.18326	0.062	0.111	0.001	0.309	24	2884.6	31.99	681.1	8.54
28_30	0.77677	0.016	0.094	0.001	0.311	94	613.8	43.52	576.5	6.91
28_31	0.79937	0.017	0.095	0.001	0.299	92	640.1	45.38	585.7	7.21
28_32	0.78901	0.016	0.095	0.001	0.325	94	619.1	42.77	583.7	6.97
28_33	0.78903	0.025	0.091	0.001	0.226	80	704.5	67.25	562.2	8.5
28_34	0.9014	0.019	0.094	0.001	0.315	63	921.5	41.54	578	7.04
28_35	0.73109	0.010	0.087	0.001	0.355	85	633.4	30.9	539.7	5.58
28_36	0.73078	0.010	0.089	0.001	0.375	91	600.4	29.77	547.4	5.62
28_37	0.7054	0.010	0.087	0.001	0.386	96	559.1	29.57	538.9	5.52
28_38	0.80053	0.012	0.096	0.001	0.352	93	634	31.61	588.5	6.12
28_39	0.79002	0.011	0.087	0.001	0.351	68	797.3	30.19	539.9	5.65
28_40	0.74805	0.012	0.087	0.001	0.324	80	678.6	33.22	540.6	5.74
L9										
5_L901	0.7524	0.016	0.091	0.001	0.492	94	596.5	41.93	563	8.57
5_L902	0.76428	0.019	0.094	0.002	0.424	100	574.8	49.96	577	9.16
5_L903	0.76391	0.017	0.090	0.001	0.484	85	653.4	42.42	557	8.57
5_L904	0.74828	0.025	0.089	0.002	0.289	88	628.6	69.04	552.1	9.7
5_L905	0.72852	0.016	0.091	0.001	0.505	104	537.2	42.28	560.1	8.55
5_L906	0.827	0.022	0.092	0.002	0.387	73	776.5	51.92	568.6	
5_L907	0.72259	0.024	0.089	0.002	0.287	100	554	70.91	551.9	9.68
5_L908	0.75585	0.016	0.092	0.001	0.510	97	585.2	40.73	568.3	8.66
5_L909	0.75685	0.014	0.090	0.001	0.599	86	643.5	32.6	554.5	8.23
5_L910	0.76908	0.029	0.089	0.002	0.236	78	704.9	80.37	547.8	10.47
5_L911	0.71787	0.022	0.089	0.002	0.316	100	549.1	65.34	549.6	9.39
5_L912	0.73204	0.015	0.092	0.001	0.546	107	530	38.03	564.6	8.48
5_L913	0.75791	0.016	0.093	0.001	0.515	101	566.7	39.95	574.5	8.71
5_L914	0.73331	0.015	0.091	0.001	0.517	100	557.8	40.38	558.8	8.49
5_L915	1.01226	0.031	0.089	0.002	0.306	43	1263.8	58.95	548.1	10
5_L916	0.75522	0.016	0.089	0.001	0.504	85	652	40.87	551.4	8.39
5_L917	0.74283	0.016	0.091	0.001	0.514	99	567.6	39.93	563.3	8.51
5_L918	0.82035	0.018	0.097	0.002	0.484	93	643.3	42.77	599	9.18
5_L919	0.76091	0.018	0.091	0.001	0.455	91	621.2	46.1	562.9	8.79
5_L920	0.76121	0.015	0.092	0.001	0.544	96	593.3	37.41	570.2	8.58
5_L921	0.76148	0.017	0.091	0.001	0.475	90	622.5	44.06	563	8.7
5_L922	0.79077	0.017	0.091	0.001	0.508	79	712.9	39.93	560.7	8.52
5_L923	0.72935	0.017	0.091	0.001	0.469	106	532.6	45.82	562	8.72
5_L924	0.73036	0.017	0.091	0.001	0.472	104	539.9	45.28	560.9	8.68
5_L925	0.74614	0.015	0.090	0.001	0.538	92	605.6	38	556.3	8.42

Table 1: LA–ICP–MS U–Pb data used to calculate Concordias from Butana and Chad

Analysis	$^{207}Pb/^{235}U$		$^{206}Pb/^{238}U$		rho	Conc (%)	$^{207}Pb/^{206}Pb$		$^{206}Pb/^{238}U$	
Central and Mayo Kebbi Region										
L9										
5_L926	0.77161	0.019	0.092	0.002	0.426	89	638	48.52	566.3	8.94
5_L927	0.72183	0.017	0.091	0.001	0.466	108	518.7	46.45	559.8	8.72
5_L928	0.84765	0.027	0.090	0.002	0.318	63	884.9	62.94	553.9	9.83
5_L929	0.84831	0.019	0.094	0.002	0.467	74	784.7	43.29	580.4	9.06
5_L930	0.78766	0.021	0.092	0.002	0.391	82	685.7	53.88	565.4	9.35
5_L931	0.77019	0.022	0.091	0.002	0.354	87	649	58.79	562.6	9.45
5_L932	0.77193	0.023	0.091	0.002	0.332	86	653.7	62.04	562.6	9.49
5_L933	0.76614	0.018	0.091	0.002	0.447	89	635.9	46.55	563	8.87
5_L934	0.75205	0.015	0.093	0.001	0.540	101	565.7	38.14	570.4	8.63
5_L935	0.77308	0.016	0.093	0.001	0.536	94	609.2	38.71	574.6	8.73
5_L936	1.19898	0.030	0.117	0.002	0.421	68	1047.4	47.17	714.3	11.39
5_L937	0.76403	0.017	0.092	0.001	0.488	94	605.8	42.87	569	8.8
5_L938	0.75223	0.019	0.092	0.002	0.430	98	578.6	49.25	567.4	9.01
5_L939	0.76081	0.017	0.092	0.001	0.497	96	594	42.09	569.7	8.78
5_L940	0.75805	0.017	0.094	0.002	0.501	103	559.9	42.44	576.3	8.88
5_L941	0.80458	0.020	0.095	0.002	0.429	88	664.8	48.72	582.5	9.27
5_L942	0.76917	0.024	0.096	0.002	0.337	110	536.3	64.39	590.4	10.06
5_L943	0.85528	0.019	0.103	0.002	0.503	105	603.5	41.53	634.4	9.71
5_L944	0.9796	0.042	0.108	0.002	0.212	83	796.2	88.1	662.6	13.49
5_L945	0.87589	0.035	0.106	0.002	0.244	108	603.4	84.06	649.1	12.27
5_L946	0.832	0.019	0.103	0.002	0.484	112	561.5	44.23	629.4	9.72
5_L947	0.91045	0.026	0.104	0.002	0.366	86	736.1	58.06	634.9	10.58
5_L948	1.05971	0.024	0.103	0.002	0.481	59	1062	40.89	631	9.86
5_L949	0.81071	0.018	0.099	0.002	0.489	106	573.8	44.03	610.8	9.45
L9_01	0.80659	0.012	0.091	0.001	0.457	76	744.1	30.16	563.3	6.49
L9_02	1.22508	0.019	0.096	0.001	0.430	40	1473.9	28.64	592.5	7
L9_03	0.76579	0.013	0.092	0.001	0.414	93	609.8	34.2	569.3	6.67
L9_04	0.79945	0.013	0.091	0.001	0.415	77	733.2	33.33	561.3	6.59
L9_05	0.78256	0.014	0.092	0.001	0.379	85	664.2	37.17	567.3	6.8
L9_06	0.77566	0.015	0.093	0.001	0.338	92	623.8	41.56	572.7	7.02
L9_07	0.79443	0.014	0.094	0.001	0.375	88	658.4	37.2	577	6.92
L9_08	0.99246	0.016	0.096	0.001	0.408	56	1064.7	31.84	592	7.02
L9_09	1.09218	0.025	0.104	0.001	0.265	57	1106.3	46.5	635.9	8.45
L9_10	0.98644	0.017	0.090	0.001	0.387	47	1186	32.88	555.2	6.7
L9_11	2.32604	0.035	0.107	0.001	0.447	27	2432.6	24.7	654.8	7.89
L9_12	0.82318	0.014	0.093	0.001	0.395	76	752.3	34.01	572.3	6.7
L9_13	0.87763	0.018	0.097	0.001	0.332	75	796.7	42.99	596.4	7.74
L9_14	0.82532	0.015	0.092	0.001	0.369	74	768	37.21	569.6	6.89
L9_15	0.82018	0.015	0.094	0.001	0.355	80	721.4	38.92	578.3	7.08
L9_16	0.78846	0.015	0.094	0.001	0.357	93	627.1	39.41	580.9	7
L9_17	0.93783	0.022	0.098	0.001	0.280	67	907.5	48.77	603.7	8.2
L9_18	0.79749	0.014	0.095	0.001	0.392	93	628.3	36.58	586.9	7.01
L9_19	0.79971	0.015	0.095	0.001	0.364	89	652.4	38.96	582.2	7.1
L9_20	0.75438	0.014	0.092	0.001	0.380	99	574.4	38.56	569.9	6.93
L9_21	0.77513	0.013	0.093	0.001	0.411	92	622.2	34.92	572.7	6.8
L9_22	0.75147	0.012	0.093	0.001	0.433	105	548.7	33.45	574.3	6.78
L9_23	0.851	0.012	0.077	0.001	0.527	40	1192.4	24.79	480.2	5.55
L9_24	0.80758	0.016	0.091	0.001	0.325	75	751.1	41.6	562.2	6.9
L9_25	0.85534	0.015	0.094	0.001	0.415	70	817.6	34.29	576.2	6.97
L9_26	1.08707	0.017	0.101	0.001	0.451	54	1148.5	29.55	620.3	7.3
L9_27	0.85205	0.014	0.101	0.001	0.458	94	654.1	32.19	618	7.34
L9_28	0.84668	0.015	0.098	0.001	0.418	86	701.8	34.97	601.4	7.25

Table 1: LA–ICP–MS U–Pb data used to calculate Concordias from Butana and Chad

Analysis	$^{207}Pb/^{235}U$		$^{206}Pb/^{238}U$		rho	Conc (%)	$^{207}Pb/^{206}Pb$		$^{206}Pb/^{238}U$	
Central and Mayo Kebbi										
L9										
L9_29	1.04583	0.017	0.101	0.001	0.439	58	1075.8	30.61	619	7.33
L9_30	0.82892	0.013	0.088	0.001	0.444	63	869	31.52	546.1	6.44
L9_31	0.89314	0.016	0.099	0.001	0.407	78	785.3	36.86	609.4	7.6
L9_32	1.00724	0.021	0.112	0.001	0.315	89	774.5	42.63	686.6	8.53
L9_33	0.81808	0.011	0.097	0.001	0.528	91	656.2	26.48	593.9	6.78
L9_34	0.90477	0.017	0.098	0.001	0.424	71	846.2	36.48	599.9	7.65
L9_35	0.83619	0.013	0.100	0.001	0.462	99	621.5	31.36	615.9	7.18
L9_36	0.92177	0.017	0.099	0.001	0.414	72	843.7	37.11	611.4	7.77
L9_37	0.77445	0.013	0.094	0.001	0.442	95	604.8	33.16	576.6	6.82
L9_38	0.85254	0.013	0.090	0.001	0.520	63	883.1	28.28	557.2	6.66
L9_39	0.87447	0.014	0.087	0.001	0.471	53	1020	29.88	535.5	6.42
L9_40	0.9998	0.019	0.093	0.001	0.350	51	1136.9	37.88	575.8	7.26
L9_41	0.85588	0.022	0.091	0.001	0.248	64	876.8	52.86	561	7.64
L9_42	1.25851	0.031	0.092	0.001	0.242	35	1607.2	46.85	568	7.87
L9_43	0.75878	0.017	0.093	0.001	0.318	101	571	46.93	573.9	7.35
L9_44	0.84727	0.018	0.091	0.001	0.362	65	856.4	41.81	560.6	7.31
L4 + L7										
5_L401	1.46327	0.027	0.074	0.001	0.497	21	2257.7	29.95	463	7.08
5_L402	0.74786	0.029	0.092	0.002	0.211	102	556.5	83.72	569.6	10.3
5_L403	0.67199	0.012	0.074	0.001	0.512	58	799.2	34.71	460.6	6.65
5_L404	0.73362	0.012	0.086	0.001	0.634	80	667.3	28.14	532.4	7.48
5_L405	0.76858	0.014	0.091	0.001	0.562	88	638.2	33.17	564	7.98
5_L406	0.7115	0.024	0.087	0.002	0.261	92	581.5	71.28	537.2	9.09
5_L407	0.73244	0.015	0.089	0.001	0.463	94	585	41.36	551.5	8
5_L408	0.92388	0.017	0.084	0.001	0.550	43	1203.3	31.35	517	7.44
5_L409	0.69529	0.011	0.059	0.001	0.665	28	1325.4	23.28	369.7	5.14
5_L410	0.93535	0.015	0.072	0.001	0.642	30	1503.6	24.25	450.3	6.3
5_L411	0.73216	0.015	0.089	0.001	0.499	94	585.6	38.69	551.1	7.91
5_L412	0.74585	0.021	0.088	0.001	0.330	83	657.9	57.02	543.2	8.67
5_L413	0.76559	0.018	0.089	0.001	0.402	81	680	46.96	551.5	8.27
5_L414	0.73667	0.015	0.087	0.001	0.467	82	657.5	40.6	536.9	7.8
5_L415	0.73605	0.021	0.087	0.001	0.319	84	640.3	58.36	540.6	8.6
5_L416	0.75584	0.012	0.092	0.001	0.669	97	584.5	26.02	568.4	7.78
5_L417	0.92562	0.014	0.071	0.001	0.657	29	1513.4	23.3	443.5	6.16
5_L418	0.74623	0.020	0.089	0.001	0.353	85	644.2	53.85	546.8	8.52
5_L419	0.75026	0.017	0.088	0.001	0.427	81	673	44.96	542.6	8.1
5_L420	0.74938	0.022	0.089	0.002	0.300	84	652.3	62.42	547.1	8.93
5_L421	0.72281	0.014	0.089	0.001	0.540	98	563.2	35.53	549.7	7.84
5_L422	0.982	0.032	0.090	0.002	0.255	47	1177.2	63.99	555.1	9.92
5_L423	1.15245	0.023	0.093	0.001	0.495	40	1419.4	34.8	574.3	8.54
5_L424	0.8689	0.029	0.089	0.002	0.250	57	955.1	67.36	548.9	9.61
5_L425	0.71413	0.016	0.089	0.001	0.432	100	546.5	44.86	547.4	8.08
5_L426	0.7813	0.018	0.086	0.001	0.436	66	806.8	43.59	531	7.98
5_L427	0.82812	0.013	0.086	0.001	0.623	57	926.6	27.29	531.2	7.37
5_L428	0.79645	0.019	0.086	0.001	0.394	62	850.8	47.11	530	8.1
5_L429	0.71213	0.018	0.087	0.001	0.383	91	586.4	50.79	536.4	8.22
5_L430	0.73894	0.016	0.090	0.001	0.429	94	589.1	44.68	555.1	8.2
5_L431	0.81201	0.031	0.076	0.002	0.223	41	1144.4	74.78	470	9.14
5_L432	0.72239	0.019	0.089	0.001	0.345	96	571.9	55.56	547.3	8.53
5_L433	0.74394	0.016	0.090	0.001	0.458	91	607.7	42.31	554.2	8.1
5_L434	0.74432	0.018	0.089	0.001	0.407	87	632.1	47.96	548.5	8.27
5_L435	0.90265	0.015	0.075	0.001	0.599	34	1360.3	26.99	467.8	6.56

Table 1: LA–ICP–MS U–Pb data used to calculate Concordias from Butana and Chad

Analysis	$^{207}Pb/^{235}U$		$^{206}Pb/^{238}U$		rho	Conc (%)	$^{207}Pb/^{206}Pb$		$^{206}Pb/^{238}U$	
Central and Mayo Kebbi Region										
L4 + L7										
5_L436	1.41049	0.025	0.084	0.001	0.562	26	1983.1	27.69	519.8	7.56
5_L437	0.71664	0.023	0.089	0.002	0.274	100	547.1	69.19	549.1	9.19
5_L438	0.83149	0.015	0.094	0.001	0.551	79	739.8	33.33	581	8.24
5_L439	0.77606	0.015	0.089	0.001	0.508	78	710.8	36.93	551.1	7.95
5_L440	0.74318	0.014	0.091	0.001	0.545	99	570.5	35.04	562.8	7.98
5_L441	0.73586	0.018	0.091	0.001	0.402	101	556.2	49.18	561	8.47
5_L442	0.73579	0.019	0.092	0.002	0.366	110	518.5	54.4	570.2	8.86
5_L443	0.73428	0.015	0.091	0.001	0.476	104	543.8	41.12	562.9	8.18
5_L444	0.81886	0.016	0.082	0.001	0.512	50	1005.3	35.15	506.3	7.34
5_L445	0.70736	0.020	0.088	0.001	0.335	103	530	58.64	546.3	8.62
5_L446	0.70143	0.026	0.091	0.002	0.229	128	439.2	79.91	563.7	9.8
5_L447	0.75967	0.023	0.092	0.002	0.308	97	589.9	63.2	569.8	9.35
5_L448	0.88209	0.030	0.092	0.002	0.246	62	915.6	70.19	567.2	10.14
5_L449	0.76278	0.023	0.093	0.002	0.295	97	589.1	65.04	572.3	9.43
5_L450	0.75553	0.019	0.089	0.001	0.374	83	664.2	51.66	548.4	8.45
5_L451	0.76108	0.021	0.092	0.002	0.340	92	614.9	56.76	564.6	8.86
5_L452	0.75022	0.014	0.092	0.001	0.532	99	573.4	35.98	567.2	8.07
5_L453	1.12973	0.018	0.086	0.001	0.637	35	1528	24.64	533.4	7.42
5_L454	0.93967	0.016	0.070	0.001	0.610	28	1577.6	25.78	435.4	6.15
5_L455	0.85312	0.015	0.076	0.001	0.588	39	1224.6	28.43	473.9	6.71
5_L456	0.82863	0.019	0.097	0.002	0.427	88	675.2	44.7	596.2	8.88

Table 2: LA–ICP–MS Lu–Hf isotopes (zircon) from the Western Ethiopian Shield

Sample Name	Hf^{176}/Hf^{177}	2 S.E.	Lu^{176}/Hf^{177}	Yb^{176}/Hf^{177}	U/Pb AGE	Hfi	epsilon	1s	T (DM) Ga	T(DM) Crustal	Hf Chur (t)	Hf DM (t)
2-18												
MB_2-18_12	0.28253	1.94E-05	0.00220	0.07213	827	0.2825008	8.43	0.68	1.05	1.17	0.28226	0.28265
MB_2-18_14	0.28254	3.10E-05	0.00305	0.09697	810	0.2824892	7.64	1.09	1.07	1.20	0.28227	0.28267
MB_2-18_16	0.28252	2.99E-05	0.00268	0.08539	824	0.2824755	7.47	1.05	1.09	1.23	0.28226	0.28266
MB_2-18_17	0.28252	2.54E-05	0.00234	0.07494	764	0.2824887	6.59	0.89	1.07	1.23	0.28230	0.28270
MB_2-18_20	0.28255	2.57E-05	0.00243	0.07805	867	0.282507	9.57	0.90	1.04	1.13	0.28224	0.28262
MB_2-18_22	0.28255	2.83E-05	0.00257	0.08110	854	0.2825072	9.26	0.99	1.04	1.14	0.28225	0.28263
MB_2-18_26	0.28253	3.73E-05	0.00329	0.10882	838	0.2824759	7.81	1.30	1.09	1.22	0.28226	0.28265
MB_2-18_33	0.28256	2.49E-05	0.00249	0.07482	852	0.2825165	9.54	0.87	1.03	1.12	0.28225	0.28264
122 + 123												
MB_122_42	0.28251	3.64E-05	0.00242	0.06716	1011	0.28246	11.25	1.27	1.09	1.14	0.282146	0.282520
MB_122_43	0.28249	3.27E-05	0.00195	0.06096	982	0.28245	10.32	1.15	1.11	1.17	0.282164	0.282541
MB_122_44	0.28250	4.86E-05	0.00422	0.13482	1000	0.28242	9.66	1.70	1.16	1.23	0.282152	0.282528
MB_122_45	0.28246	4.05E-05	0.00395	0.13562	928	0.28240	6.98	1.42	1.21	1.34	0.282198	0.282581
MB_122_47	0.28246	4.08E-05	0.00256	0.07400	997	0.28241	9.20	1.43	1.17	1.25	0.282155	0.282531
MB_122_50	0.28248	3.35E-05	0.00203	0.06714	1009	0.28244	10.44	1.17	1.12	1.19	0.282147	0.282521
144 + 146												
MB_144_01	0.28198	1.31E-05	0.00023	0.00673	652	0.28198	-13.93	0.46	1.75	2.42	0.282374	0.282781
MB_144_02	0.28141	1.87E-05	0.00071	0.01976	797	0.28140	-31.09	0.65	2.55	3.57	0.282282	0.282676
MB_144_03	0.28183	2.12E-05	0.00049	0.01581	743	0.28183	-17.30	0.74	1.97	2.69	0.282316	0.282716
MB_144_04	0.28147	2.25E-05	0.00118	0.03239	721	0.28145	-31.12	0.79	2.51	3.52	0.282330	0.282731
MB_144_05	0.28183	1.85E-05	0.00050	0.01673	732	0.28183	-17.64	0.65	1.97	2.71	0.282323	0.282724
MB_144_09	0.28177	1.87E-05	0.00028	0.00868	717	0.28176	-20.18	0.65	2.05	2.85	0.282333	0.282734
MB_144_12	0.28249	2.46E-05	0.00140	0.04203	733	0.28247	5.09	0.86	1.10	1.30	0.282323	0.282723
MB_144_21	0.28255	7.31E-05	0.00279	0.07587	790	0.28251	7.95	2.56	1.04	1.17	0.282286	0.282681
MB_144_24	0.28249	5.96E-05	0.00236	0.06768	747	0.28245	4.89	2.09	1.13	1.33	0.282314	0.282713

CHUR from Bouvier et al. (2008); Earth and Planetary Science Letters 273 (2008) 48–57
CHUR 176Lu/177Hf = 0.0336±1 and 176Hf/177Hf = 0.282785±11
Hfi = 176Hf/177Hf ratio - (176Lu/177Hf ratio * (EXP(0.0193 * 207Pb/206Pb ratio / 1000)-1))

Table 2: LA–ICP–MS Lu–Hf isotopes (zircon) from the Western Ethiopian Shield

Sample Name	Hf^{176}/Hf^{177}	2 S.E.	Lu^{176}/Hf^{177}	Yb^{176}/Hf^{177}	U/Pb AGE	Hfi	epsilon	1s	T (DM) Ga	T(DM) Crustal	Hf Chur (t)	Hf DM (t)
S4												
MB_S4_01	0.28240	0.00002	0.00099	0.02694	1000	0.28238	8.08	0.84	1.21	1.33	0.28215	0.28253
MB_S4_04	0.28235	0.00002	0.00101	0.02852	983	0.28233	6.00	0.86	1.27	1.44	0.28216	0.28254
MB_S4_08	0.28241	0.00003	0.00087	0.02196	1009	0.28239	8.74	0.91	1.19	1.29	0.28215	0.28252
MB_S4_11	0.28240	0.00002	0.00090	0.02461	980	0.28238	7.61	0.85	1.21	1.34	0.28217	0.28254
MB_S4_14	0.28238	0.00003	0.00076	0.01839	997	0.28237	7.57	0.99	1.22	1.36	0.28215	0.28253
MB_S4_16	0.28239	0.00003	0.00097	0.02641	983	0.28238	7.58	0.89	1.21	1.35	0.28216	0.28254
MB_S4_21	0.28238	0.00003	0.00149	0.04271	978	0.28235	6.63	1.09	1.25	1.40	0.28217	0.28254
MB_S4_24	0.28237	0.00002	0.00076	0.02143	1031	0.28235	7.86	0.84	1.24	1.37	0.28213	0.28251
MB_S4_26	0.28245	0.00003	0.00284	0.09143	948	0.28240	7.63	1.06	1.19	1.31	0.28219	0.28257
MB_S4_27	0.28078	0.00002	0.00040	0.01259	2695	0.28076	-10.46	0.81	3.38	3.77	0.28105	0.28127
MB_S4_31	0.28145	0.00002	0.00068	0.02203	1966	0.28142	-3.85	0.82	2.50	2.81	0.28153	0.28182
S13												
MB_S13_07	0.28227	0.00003	0.00051	0.01340	604	0.28226	-4.96	1.14	1.37	1.83	0.28240	0.28282
MB_S13_08	0.28242	0.00003	0.00114	0.03427	576	0.28241	-0.58	0.97	1.18	1.54	0.28242	0.28284
S14												
MB_S14_15	0.28232	0.00002	0.00073	0.02100	598	0.28231	-3.37	0.82	1.31	1.73	0.28241	0.28282
MB_S14_18	0.28232	0.00002	0.00092	0.02335	640	0.28231	-2.49	0.83	1.31	1.71	0.28238	0.28279
MB_S14_20	0.28219	0.00002	0.00076	0.02091	964	0.28218	0.17	0.79	1.48	1.79	0.28218	0.28255
MB_S14_21	0.28231	0.00002	0.00078	0.01917	603	0.28230	-3.78	0.67	1.33	1.76	0.28240	0.28282
MB_S14_22	0.28231	0.00002	0.00059	0.01577	622	0.28231	-3.02	0.63	1.31	1.72	0.28239	0.28280
MB_S14_24	0.28230	0.00002	0.00093	0.02833	662	0.28229	-2.65	0.85	1.34	1.73	0.28237	0.28277
MB_S14_27	0.28245	0.00002	0.00079	0.02535	641	0.28244	2.04	0.78	1.13	1.42	0.28238	0.28279
MB_S14_30	0.28232	0.00002	0.00084	0.02258	620	0.28231	-3.13	0.75	1.32	1.73	0.28239	0.28280
MB_S14_31	0.28229	0.00003	0.00121	0.03549	608	0.28228	-4.47	0.88	1.37	1.80	0.28240	0.28281

CHUR from Bouvier et al. (2008); Earth and Planetary Science Letters 273 (2008) 48–57

CHUR 176Lu/177Hf = 0.0336±1 and 176Hf/177Hf = 0.282785±11

Hfi = 176Hf/177Hf ratio - (176Lu/177Hf ratio * (EXP(0.0193 * 207Pb/206Pb ratio / 1000)-1))

Table 2: LA–ICP–MS Lu–Hf isotopes (zircon) from the Western Ethiopian Shield

Sample Name	Hf^{176}/Hf^{177}	2 S.E.	Lu^{176}/Hf^{177}	Yb^{176}/Hf^{177}	U/Pb AGE	Hfi	epsilon	1s	T (DM) Ga	T(DM) Crustal	Hf Chur (t)	Hf DM (t)
37												
MB_37_05	0.28185	0.00002	0.00060	0.02092	535	0.28185	-21.32	0.80	1.95	2.79	0.28245	0.28287
MB_37_02	0.28189	0.00002	0.00077	0.02507	545	0.28188	-19.99	0.77	1.91	2.71	0.28244	0.28286
MB_37_07	0.28190	0.00003	0.00085	0.02423	556	0.28189	-19.12	0.92	1.89	2.67	0.28243	0.28285
MB_37_11	0.28186	0.00003	0.00079	0.02446	574	0.28185	-20.22	0.89	1.94	2.75	0.28242	0.28284
MB_37_18	0.28176	0.00002	0.00075	0.02270	1011	0.28174	-14.20	0.84	2.08	2.71	0.28215	0.28252
MB_37_19	0.28226	0.00002	0.00094	0.02868	648	0.28224	-4.69	0.84	1.41	1.85	0.28238	0.28278
MB_37_27	0.28214	0.00002	0.00103	0.03262	592	0.28213	-10.06	0.84	1.57	2.14	0.28241	0.28282
L9												
MB_L9_03	0.28183	0.00002	0.00052	0.01502	557	0.28182	-21.58	0.69	1.97	2.82	0.28243	0.28285
MB_L9_6	0.28182	0.00002	0.00073	0.02081	569	0.28182	-21.61	0.80	1.99	2.83	0.28243	0.28284
MB_L9_16	0.28184	0.00003	0.00103	0.03253	551	0.28183	-21.46	0.95	1.98	2.81	0.28244	0.28285
MB_L9_18	0.28182	0.00002	0.00051	0.01632	599	0.28181	-21.03	0.83	1.99	2.82	0.28241	0.28282
MB_L9_21	0.28185	0.00003	0.00039	0.01225	563	0.28185	-20.71	1.01	1.94	2.77	0.28243	0.28285
MB_L9_22	0.28187	0.00003	0.00089	0.02823	561	0.28186	-20.17	0.94	1.94	2.74	0.28243	0.28285
MB_L9_35	0.28229	0.00003	0.00079	0.02279	575	0.28228	-5.10	0.88	1.35	1.82	0.28242	0.28284
L4 + L7												
MB-L4-29	0.28190	0.00003	0.00109	0.03650	536	0.28189	-19.83	1.10	1.91	2.70	0.28245	0.28286
MB-L4-32	0.28186	0.00002	0.00063	0.02076	547	0.28186	-20.69	0.79	1.93	2.76	0.28244	0.28286
MB-L4-33	0.28185	0.00002	0.00037	0.01152	554	0.28185	-20.71	0.66	1.93	2.76	0.28244	0.28285
MB-L4-37	0.28190	0.00002	0.00041	0.01295	549	0.28190	-19.14	0.73	1.87	2.66	0.28244	0.28286
MB-L4-42	0.28185	0.00002	0.00063	0.02095	570	0.28184	-20.63	0.79	1.95	2.77	0.28243	0.28284
MB-L4-43	0.28190	0.00002	0.00081	0.02644	554	0.28190	-19.12	0.71	1.89	2.67	0.28244	0.28285
MB-L4-45	0.28183	0.00002	0.00081	0.02804	546	0.28182	-22.02	0.83	1.99	2.84	0.28244	0.28286
MB-L4-47	0.28188	0.00002	0.00045	0.01505	570	0.28188	-19.42	0.71	1.90	2.70	0.28243	0.28284
MB-L4-49	0.28186	0.00002	0.00053	0.01855	572	0.28185	-20.26	0.72	1.94	2.75	0.28242	0.28284
MB-L4-51	0.28185	0.00002	0.00072	0.02395	565	0.28184	-20.78	0.69	1.96	2.78	0.28243	0.28284

CHUR from Bouvier et al. (2008); Earth and Planetary Science Letters 273 (2008) 48–57

CHUR 176Lu/177Hf = 0.0336±1 and 176Hf/177Hf = 0.282785±11

Hfi = 176Hf/177Hf ratio - (176Lu/177Hf ratio * (EXP(0.0193 * 207Pb/206Pb ratio / 1000)-1))

APPENDIX 6

Supplementary data for chapter 6:
Unravelling the Neoproterozoic accretionary history of
Oman, using an array of isotopic systems in zircon.

Table 1: LA–ICP–MS U–Pb data used to calculate Concordias from igneous samples Oman

Analysis	$^{207}Pb/^{235}U$		$^{206}Pb/^{238}U$		rho	Conc (%)	$^{207}Pb/^{206}Pb$		$^{206}Pb/^{238}U$	
Jebel Akhdar										
O14-04										
1	1.094	0.021	0.123	0.002	0.643	100	751.5	31.56	750.3	11.48
2	1.083	0.020	0.121	0.002	0.740	95	773.1	26.82	735.8	11.77
3	1.131	0.024	0.123	0.002	0.557	90	831.5	37.6	746.8	11.65
4	1.074	0.024	0.118	0.002	0.670	89	808	35.36	718.6	12.84
5	0.995	0.019	0.108	0.002	0.660	80	830.2	30.66	661.7	10.34
6	1.049	0.021	0.116	0.002	0.644	90	791.1	33.41	708.7	11.41
7	1.088	0.022	0.121	0.002	0.606	93	788.5	35.06	734.1	11.67
8	1.007	0.021	0.108	0.002	0.603	78	851.7	34.97	663.2	10.56
9	1.158	0.029	0.124	0.002	0.453	88	857.7	47.34	754.6	12.32
10	1.190	0.024	0.132	0.002	0.651	102	784.5	33.55	800.2	13
11	0.972	0.020	0.107	0.002	0.706	80	812.4	30.35	652.9	11.01
12	1.166	0.025	0.130	0.002	0.669	102	772.8	34.16	789.3	13.58
13	1.133	0.022	0.127	0.002	0.705	100	770	30.15	769.2	12.7
14	0.979	0.020	0.108	0.002	0.684	83	795.2	31.53	662.2	11.06
15	0.780	0.018	0.082	0.001	0.526	56	904.8	41.6	506.8	8.43
16	1.170	0.027	0.111	0.002	0.676	62	1102.1	33.99	680	12.4
17	0.971	0.024	0.100	0.002	0.527	65	942.3	43.18	614	10.61
18	0.742	0.015	0.077	0.001	0.719	51	936.3	30.03	475.5	8.46
19	0.505	0.010	0.052	0.001	0.715	35	937.9	30.23	327	5.88
20	1.095	0.021	0.122	0.002	0.718	94	783.3	29.23	740.1	12.34
21	0.900	0.018	0.098	0.002	0.648	73	824.8	32.38	602.7	9.69
22	1.085	0.022	0.123	0.002	0.732	102	732.3	29.8	750.4	12.88
23	1.072	0.022	0.118	0.002	0.747	89	807.6	28.59	717.7	12.5
24	1.095	0.022	0.119	0.002	0.721	88	824.5	30.02	726.2	12.53
25	0.507	0.010	0.050	0.001	0.738	31	1013.6	28.31	316.7	5.69
26	1.018	0.021	0.108	0.002	0.694	75	884.3	31.3	659.6	11.34
27	1.018	0.025	0.114	0.002	0.627	91	762.1	40.62	697.3	12.98
28	1.111	0.026	0.122	0.002	0.645	91	814.5	37.66	740	13.43
29	0.963	0.022	0.102	0.002	0.520	70	886.9	41.73	625.1	10.18
30	1.300	0.039	0.141	0.003	0.368	103	828.6	59.65	852.1	14.79
31	1.067	0.023	0.117	0.002	0.693	88	813.7	33.6	712.4	12.85
O14-05										
1	1.069	0.021	0.121	0.002	0.700	99	743.6	29.71	736.7	11.97
2	0.379	0.008	0.039	0.001	0.700	26	940.8	31.83	247.2	4.51
3	0.807	0.015	0.089	0.001	0.619	68	809.9	30.96	547	8.17
4	0.815	0.019	0.085	0.002	0.649	57	917.2	37.45	525.7	9.88
5	1.003	0.021	0.113	0.002	0.698	91	758.3	32.15	688.8	11.95
6	0.987	0.021	0.107	0.002	0.693	79	831.7	32.72	656.5	11.63
7	1.092	0.028	0.117	0.002	0.482	82	866.4	48.16	710.6	12.38
8	0.975	0.026	0.107	0.002	0.551	81	811.6	47.54	654.9	12.49
9	1.055	0.020	0.119	0.002	0.672	98	745	30.97	727	11.64
10	0.962	0.020	0.104	0.002	0.611	76	841.4	35.75	638	10.62
11	0.989	0.022	0.110	0.002	0.621	86	780.8	36.86	673.5	11.56
12	1.077	0.025	0.121	0.002	0.556	97	757.2	41.27	737.7	12.42
13	1.018	0.020	0.114	0.002	0.664	90	774.8	31.98	693.7	11.35
14	1.027	0.026	0.115	0.002	0.500	93	760.4	46.43	703.8	11.99
15	1.009	0.026	0.112	0.002	0.339	87	789.3	51.84	683	10.39
16	0.693	0.015	0.074	0.001	0.700	54	854.1	32.26	462.9	8.32
17	1.015	0.022	0.114	0.002	0.504	92	755.2	40.67	698	10.7
18	0.933	0.019	0.104	0.002	0.731	81	785.2	29.33	635.7	10.95
19	1.021	0.025	0.110	0.002	0.587	79	848.1	41.17	672.9	12.01
20	0.850	0.016	0.092	0.002	0.711	68	831.5	28.61	569.3	9.4

Table 1: LA–ICP–MS U–Pb data used to calculate Concordias from igneous samples Oman

Analysis	$^{207}Pb/^{235}U$		$^{206}Pb/^{238}U$		rho	Conc (%)	$^{207}Pb/^{206}Pb$		$^{206}Pb/^{238}U$	
Jebel Akhdar										
O14-05										
21	1.035	0.020	0.113	0.002	0.659	84	824.3	30.54	689.1	10.65
22	1.064	0.023	0.118	0.002	0.646	91	786.4	34.8	719.2	12.17
23	1.044	0.021	0.114	0.002	0.685	86	811.6	31.19	698.7	11.61
24	0.905	0.019	0.097	0.002	0.602	69	861.8	35.83	595.9	9.67
25	0.873	0.020	0.097	0.002	0.469	78	773.4	43.54	599.6	9.14
26	0.964	0.021	0.102	0.002	0.619	70	895.7	35.21	623.4	10.33
27	1.144	0.025	0.118	0.002	0.647	77	933.2	35.22	720.5	12.53
28	0.956	0.021	0.104	0.002	0.532	77	829	39.52	637.7	9.97
29	0.640	0.015	0.068	0.001	0.468	48	885.1	43.16	422.5	6.6
30	1.102	0.020	0.123	0.002	0.679	97	769.9	29.16	749.2	11.55
31	0.973	0.019	0.105	0.002	0.563	76	845.5	34.65	643.7	9.55
32	0.883	0.017	0.095	0.002	0.653	69	852.3	30.97	584.5	9.28
33	0.699	0.013	0.073	0.001	0.664	49	925.7	30.26	451.2	7.26
34	1.152	0.026	0.128	0.002	0.556	98	790.3	39.73	773.8	12.58
35	0.875	0.016	0.096	0.002	0.661	72	816.4	29.52	589.1	9.05
36	1.185	0.030	0.130	0.002	0.483	98	805.7	46.95	789.2	13.17
37	0.619	0.014	0.064	0.001	0.550	43	928.9	39.95	400.7	6.79
38	1.076	0.023	0.120	0.002	0.586	96	766.3	37.66	733.4	11.88
39	1.142	0.021	0.128	0.002	0.637	101	767.1	30.9	775.7	11.62
40	0.254	0.005	0.024	0.000	0.636	13	1134.5	30.48	151.5	2.46
41	1.190	0.029	0.126	0.002	0.481	87	880.9	45.58	766.3	12.66
42	0.918	0.016	0.102	0.002	0.657	81	778.4	28.57	627.7	9.19
43	1.129	0.027	0.129	0.002	0.386	106	734.4	48.37	779.5	11.58
44	1.117	0.022	0.123	0.002	0.545	92	808.2	36.1	745.9	11.01
O14-08										
1	0.311	0.015	0.029	0.001	0.132	15	1174.5	96.45	181.2	3.97
2	1.048	0.021	0.115	0.002	0.568	87	809.1	35.93	702.1	10.77
3	0.937	0.046	0.084	0.002	0.140	43	1209.2	96.84	522.5	11.45
4	1.162	0.023	0.129	0.002	0.592	99	787.4	34.39	781.5	11.79
5	0.684	0.013	0.074	0.001	0.609	55	839.5	31.97	459.9	6.95
6	1.121	0.022	0.123	0.002	0.616	92	812.7	32.96	747	11.36
7	0.834	0.020	0.092	0.002	0.508	71	800.3	44.42	566.5	9.53
8	1.105	0.027	0.122	0.002	0.451	94	793.7	45.87	743.2	11.69
9	1.105	0.025	0.120	0.002	0.502	87	836.3	41.82	729.2	11.42
10	0.585	0.012	0.063	0.001	0.584	47	837.1	35.89	396.2	6.36
11	0.967	0.021	0.106	0.002	0.497	80	808.2	41.08	650.5	9.95
12	1.089	0.025	0.121	0.002	0.522	93	788.2	41.46	734.7	11.67
13	1.075	0.039	0.118	0.002	0.315	90	803.5	72.77	720.9	13.82
14	1.007	0.025	0.110	0.002	0.440	82	821.6	47.56	671.9	10.73
15	1.099	0.025	0.121	0.002	0.488	91	808.1	42.47	734.5	11.36
16	1.112	0.032	0.126	0.002	0.402	103	742.2	55.75	765	13.11
17	1.129	0.038	0.123	0.002	0.271	91	821.5	68.75	748.4	13.05
18	1.101	0.026	0.123	0.002	0.400	98	766.8	46.09	749.2	11.09
19	1.076	0.057	0.122	0.003	0.036	99	748.4	115.63	739.9	15.85
20	1.145	0.028	0.126	0.002	0.483	95	804.8	45.76	764.6	12.46
21	1.030	0.028	0.112	0.002	0.428	83	827.6	51.39	684.9	11.58
22	1.120	0.030	0.121	0.002	0.437	87	847.1	50.45	734.8	12.33
23	0.786	0.018	0.086	0.001	0.526	66	812.1	40.66	532.8	8.57
24	0.991	0.025	0.109	0.002	0.447	83	803.7	48.6	667.2	10.94
25	1.093	0.094	0.121	0.004	0.271	91	804.6	184.97	735.9	22.55
26	1.116	0.028	0.124	0.002	0.465	95	790	46.98	751.4	12.22
27	1.137	0.035	0.125	0.002	0.359	95	803	61.4	760.2	13.43

Table 1: LA–ICP–MS U–Pb data used to calculate Concordias from igneous samples Oman

Analysis	$^{207}Pb/^{235}U$		$^{206}Pb/^{238}U$		rho	Conc (%)	$^{207}Pb/^{206}Pb$		$^{206}Pb/^{238}U$	
Jebel Akhdar										
O14-08										
28	1.147	0.028	0.125	0.002	0.454	92	827	46.64	758	12.17
29	1.011	0.035	0.111	0.002	0.286	83	814.4	69.61	677.1	12.34
30	1.060	0.037	0.121	0.002	0.321	101	726.3	70.47	736.3	13.56
Al Jobah										
AJ14-19										
19-01	1.246	0.022	0.127	0.002	0.566	80	959.4	30.87	772	10.55
19-02	1.317	0.020	0.140	0.002	0.647	97	870.2	25.39	846.8	11.08
19-03	1.330	0.021	0.138	0.002	0.629	90	923.6	26.08	834	10.85
19-04	1.341	0.019	0.138	0.002	0.688	88	946.6	22.44	831.7	10.68
19-05	1.259	0.019	0.136	0.002	0.657	97	848.2	24.63	819.7	10.57
19-06	1.221	0.018	0.130	0.002	0.678	91	869.1	23.7	789.1	10.27
19-07	1.334	0.024	0.141	0.002	0.595	95	891.5	30.87	848.9	11.97
19-08	1.319	0.020	0.143	0.002	0.663	103	833.9	24.91	862.3	11.41
19-09	1.298	0.020	0.142	0.002	0.663	105	817.4	25.43	855.4	11.35
19-10	1.297	0.020	0.138	0.002	0.637	96	869.1	26.28	835.4	11.05
19-11	1.242	0.019	0.131	0.002	0.666	88	898.2	24.74	791.1	10.48
19-12	1.220	0.019	0.131	0.002	0.666	92	859.7	25.34	792.1	10.64
19-13	1.306	0.020	0.138	0.002	0.675	95	880.4	24.76	836.1	11.17
19-14	1.304	0.023	0.139	0.002	0.638	97	863.8	28.98	841.1	12.08
19-15	1.306	0.022	0.140	0.002	0.638	98	860.8	28.02	843.9	11.68
19-16	1.276	0.021	0.141	0.002	0.634	107	792.5	27.45	851.2	11.51
19-17	1.294	0.022	0.140	0.002	0.643	102	832.6	27.81	847.3	11.74
19-18	1.327	0.022	0.140	0.002	0.655	95	890.1	27.39	845.1	11.88
19-19	1.321	0.022	0.143	0.002	0.634	103	839.3	28.02	861.4	11.81
19-20	1.347	0.022	0.134	0.002	0.654	80	1008.5	26.29	811.7	11.18
19-21	1.310	0.020	0.142	0.002	0.712	102	840.8	23.51	853.8	11.62
19-22	1.304	0.021	0.141	0.002	0.682	100	847.8	25.19	847.5	11.61
19-23	1.294	0.021	0.140	0.002	0.681	102	832.2	25.5	847.2	11.62
19-24	1.401	0.023	0.143	0.002	0.657	90	955.3	26.34	862.9	11.9
19-25	1.272	0.020	0.136	0.002	0.687	96	860.5	24.96	823.4	11.32
19-26	1.306	0.021	0.141	0.002	0.678	100	845.6	25.32	849.4	11.68
19-27	1.269	0.020	0.134	0.002	0.685	90	896.1	25.06	808.4	11.16
19-28	1.315	0.021	0.141	0.002	0.671	99	857.1	25.77	850.4	11.73
19-29	1.297	0.020	0.141	0.002	0.693	101	836	24.79	847.6	11.66
19-30	1.298	0.021	0.144	0.002	0.662	109	793.8	27.08	864.6	11.97
19-31	1.305	0.023	0.137	0.002	0.624	91	906.3	28.95	826.1	11.58
19-32	1.292	0.021	0.140	0.002	0.663	102	829.8	26.52	847	11.75
19-33	1.311	0.022	0.142	0.002	0.662	102	839.5	26.89	855.1	11.88
19-34	1.420	0.023	0.150	0.002	0.677	102	886.7	25.81	901.7	12.46
19-35	1.296	0.022	0.139	0.002	0.659	98	858.8	27.18	838.2	11.7
19-36	1.272	0.022	0.139	0.002	0.640	102	822.1	28.23	837.8	11.73
19-37	1.274	0.021	0.137	0.002	0.652	97	853.3	27.43	827	11.58
19-38	1.111	0.019	0.102	0.002	0.632	53	1177.6	27.51	624.4	8.95
19-39	1.286	0.021	0.139	0.002	0.671	100	842.6	26.41	838.4	11.7
19-40	1.315	0.022	0.140	0.002	0.652	97	872.6	27.34	844.7	11.84
19-41	1.285	0.021	0.138	0.002	0.652	99	847.5	26.89	836	11.51
19-42	1.274	0.020	0.137	0.002	0.691	97	854.7	24.83	826.6	11.32
19-43	1.279	0.022	0.139	0.002	0.635	102	827	28.24	840	11.62
19-44	1.295	0.020	0.139	0.002	0.690	98	856.9	24.71	838.4	11.47
19-45	1.244	0.021	0.133	0.002	0.654	92	871.9	26.83	802.2	11.1
19-46	1.314	0.023	0.137	0.002	0.616	90	915	28.88	827.8	11.53
19-47	1.335	0.023	0.141	0.002	0.610	97	882.3	29.58	853.1	11.88
19-48	1.247	0.020	0.134	0.002	0.685	94	859.7	24.86	808.2	11.11

Table 1: LA–ICP–MS U–Pb data used to calculate Concordias from igneous samples Oman

Analysis	$^{207}Pb/^{235}U$		$^{206}Pb/^{238}U$		rho	Conc (%)	$^{207}Pb/^{206}Pb$		$^{206}Pb/^{238}U$	
Al Jobah										
JA14-19										
19-49	1.277	0.021	0.132	0.002	0.649	85	936.8	26.87	798.1	11.07
19-50	1.292	0.023	0.141	0.002	0.608	103	823.8	30.07	849.4	11.85
19-51	1.270	0.022	0.138	0.002	0.625	100	835.2	28.99	831.1	11.57
19-52	1.234	0.021	0.136	0.002	0.627	102	804.8	28.85	820.1	11.42
19-53	1.519	0.025	0.139	0.002	0.670	71	1176.2	24.83	839.8	11.59
19-54	1.279	0.021	0.136	0.002	0.657	95	871.3	26.94	823.6	11.41
19-55	1.228	0.022	0.136	0.002	0.608	105	784.2	30.71	824.4	11.55
19-56	1.277	0.024	0.139	0.002	0.577	101	831.4	32.42	837.4	11.82
19-57	1.252	0.022	0.135	0.002	0.605	97	842.8	30.32	817.7	11.48
19-58	1.273	0.021	0.135	0.002	0.649	93	880.3	27.24	816.2	11.34
19-59	1.230	0.021	0.128	0.002	0.634	85	914.9	28.15	778.2	10.89
19-60	1.302	0.026	0.141	0.002	0.528	102	833.2	36.31	851.5	12.2
19-61	1.323	0.025	0.140	0.002	0.567	96	880.5	33.35	846.6	12.02
19-62	1.261	0.024	0.136	0.002	0.562	98	837.9	33.37	824.7	11.72
19-63	1.243	0.024	0.135	0.002	0.556	99	824.3	34.04	819	11.67
19-64	1.300	0.025	0.135	0.002	0.585	89	919.4	32.59	818	11.89
19-65	1.760	0.033	0.144	0.002	0.588	62	1400	30.21	865.9	12.61
19-66	1.294	0.023	0.141	0.002	0.642	103	827.9	29	848.6	12.14
19-67	1.313	0.024	0.137	0.002	0.621	91	907.9	30.22	830.1	11.97
JA14-23										
23-01	1.281	0.021	0.141	0.002	0.685	105	809	26.47	848.2	12.02
23-02	1.300	0.023	0.140	0.002	0.650	100	845.7	28.64	845.5	12.07
23-03	1.273	0.022	0.131	0.002	0.666	85	935.5	26.86	796	11.36
23-04	1.277	0.022	0.138	0.002	0.648	99	844	28.44	832.1	11.89
23-05	1.334	0.025	0.143	0.002	0.608	101	854.7	31.63	863	12.52
23-06	1.377	0.023	0.143	0.002	0.667	93	927.4	26.76	860.4	12.13
23-07	1.345	0.025	0.141	0.002	0.576	93	910.1	32	848.3	11.88
23-08	1.264	0.025	0.138	0.002	0.524	102	817.2	36.02	834.6	11.8
23-09	1.263	0.023	0.131	0.002	0.563	86	923.7	31.77	794.4	10.89
23-10	1.345	0.024	0.135	0.002	0.559	81	1000.9	31.18	813.8	11.09
23-11	1.318	0.024	0.137	0.002	0.623	90	923	29.74	827.2	11.8
23-13	1.158	0.029	0.118	0.002	0.359	74	971.2	49.09	716.7	10.57
23-14	0.892	0.025	0.082	0.001	0.319	43	1180.4	53.7	505.9	7.84
23-15	1.240	0.022	0.133	0.002	0.632	93	861.1	29.1	803.6	11.36
23-16	1.396	0.026	0.138	0.002	0.527	81	1026.9	32.73	832.6	11.23
23-17	1.296	0.024	0.137	0.002	0.635	94	884.7	30.2	828.9	12.19
23-18	1.061	0.020	0.111	0.002	0.515	75	906.6	34.12	679.4	9.26
23-19	1.256	0.021	0.133	0.002	0.660	90	891.5	27.47	802.1	11.39
23-20	1.292	0.023	0.139	0.002	0.638	98	855.6	29.17	837.1	12.02
23-21	1.271	0.021	0.138	0.002	0.673	100	829.9	26.89	833.7	11.85
23-22	1.300	0.036	0.140	0.002	0.333	99	853.5	54.54	843.3	12.49
23-23	1.264	0.022	0.136	0.002	0.593	98	843	30.08	824.6	11.23
23-24	1.303	0.025	0.139	0.002	0.595	96	869.6	33.24	838.3	12.42
23-25	1.270	0.025	0.135	0.002	0.535	93	875.7	35.37	816.5	11.7
23-26	1.300	0.024	0.137	0.002	0.538	93	889	33.76	829.1	11.37
23-27	1.311	0.024	0.141	0.002	0.631	99	858	30.43	847.9	12.37
23-28	1.333	0.025	0.142	0.002	0.559	99	868.7	32.69	856.9	11.8
23-29	1.282	0.024	0.136	0.002	0.608	93	885.3	30.93	820.1	11.84
23-30	1.260	0.021	0.136	0.002	0.630	96	849.8	28.3	819.8	11.37

Table 1: LA–ICP–MS U–Pb data used to calculate Concordias from igneous samples Oman

Analysis	$^{207}Pb/^{235}U$		$^{206}Pb/^{238}U$		rho	Conc (%)	$^{207}Pb/^{206}Pb$		$^{206}Pb/^{238}U$	
Al Jobah										
JA14-25										
25-01	1.330	0.023	0.143	0.002	0.501	102.152	845.6	28.66	863.8	12.51
25-02	1.254	0.022	0.128	0.002	0.493	81.1827	957.1	26.17	777	11.5
25-03	1.302	0.023	0.137	0.002	0.485	92.8108	893	26.88	828.8	12.19
25-04	1.299	0.022	0.140	0.002	0.476	100.713	841	27.3	847	11.87
25-05	1.276	0.022	0.140	0.002	0.468	105.207	804.7	29.44	846.6	12
25-06	1.277	0.024	0.142	0.002	0.460	108.204	788.6	30.89	853.3	12.57
25-07	1.269	0.022	0.136	0.002	0.452	95.4783	860.3	27.92	821.4	11.79
25-08	1.475	0.036	0.133	0.002	0.443	67.1798	1201.7	43.41	807.3	13.35
25-09	1.259	0.022	0.138	0.002	0.435	102.486	812.7	28.36	832.9	11.7
25-10	1.299	0.027	0.136	0.002	0.427	91.3313	902.1	38.78	823.9	11.55
25-11	1.299	0.025	0.141	0.002	0.419	102.972	827.7	31.84	852.3	12.81
25-12	1.256	0.024	0.139	0.002	0.411	105.631	793.8	35.13	838.5	11.86
25-13	1.297	0.025	0.140	0.002	0.402	99.0708	850.2	32.88	842.3	12.61
25-14	1.232	0.022	0.137	0.002	0.394	106.675	777.5	31.01	829.4	12.06
25-15	1.300	0.029	0.138	0.002	0.386	95.4171	875	40.41	834.9	13.39
25-16	1.438	0.024	0.151	0.002	0.613	99.7683	906.5	28.46	904.4	12.3
25-17	1.276	0.022	0.138	0.002	0.670	99.1434	840.5	27.7	833.3	12.07
25-18	1.286	0.021	0.140	0.002	0.684	102.708	823.6	26.19	845.9	11.96
25-19	1.301	0.022	0.137	0.002	0.662	93.4384	888.5	27.51	830.2	11.85
25-20	1.281	0.022	0.138	0.002	0.678	98.9807	843.7	27.12	835.1	12.01
25-21	1.270	0.027	0.134	0.002	0.502	91.8003	885.4	38.49	812.8	11.84
25-22	1.281	0.023	0.138	0.002	0.672	97.7684	851.4	27.96	832.4	12.31
25-23	1.319	0.024	0.140	0.002	0.645	96.1425	878.8	29.53	844.9	12.33
25-24	1.265	0.023	0.138	0.002	0.593	101.794	819.4	31.59	834.1	11.74
25-25	1.313	0.022	0.138	0.002	0.673	92.0549	903.7	26.4	831.9	11.69
25-26	1.302	0.024	0.140	0.002	0.648	98.182	858.1	30.26	842.5	12.7
25-27	1.293	0.027	0.137	0.002	0.588	94.5413	877.5	35.79	829.6	12.95
25-28	1.341	0.022	0.140	0.002	0.697	93.0284	909.4	25.73	846	12.14
25-29	1.395	0.038	0.147	0.002	0.400	98.3512	897.6	51.78	882.8	13.71
25-30	1.252	0.027	0.131	0.002	0.522	86.2689	916.9	38.98	791	12.16
25-31	1.236	0.026	0.137	0.002	0.539	105.023	788.4	37.3	828	12.31
25-32	1.289	0.023	0.135	0.002	0.643	89.736	909	29.22	815.7	11.81
25-33	1.305	0.023	0.141	0.002	0.643	101.201	840.8	29.15	850.9	12.22
25-34	1.370	0.027	0.137	0.002	0.624	81.9907	1006.7	31.65	825.4	12.63
25-35	1.289	0.023	0.138	0.002	0.658	97.7544	855	29.06	835.8	12.24
Mirbat										
Mr15-01										
MR01-30	1.211	0.027	0.127	0.002	0.278	85.3254	903.6	44.85	771	9.38
MR01-31	1.246	0.030	0.127	0.002	0.254	80.1164	962.1	49.07	770.8	10.04
MR01-32	1.587	0.034	0.128	0.002	0.292	54.0563	1431.1	40.18	773.6	9.57
MR01-33	1.219	0.042	0.132	0.002	0.171	95.4388	837.5	72.05	799.3	11.26
MR01-34	1.207	0.100	0.125	0.004	0.053	82.6436	920.7	169.57	760.9	22.52
MR01-35	1.198	0.044	0.131	0.002	0.151	97.5083	814.7	76.83	794.4	11.43
MR01-36	1.323	0.067	0.136	0.003	0.101	86.7948	946.6	103.09	821.6	14.37
MR01-37	1.325	0.031	0.134	0.002	0.264	82.9004	977.8	47.23	810.6	10.11
MR01-38	1.090	0.022	0.109	0.001	0.317	67.4152	993.1	40.38	669.5	8.01
MR01-39	2.567	0.052	0.138	0.002	0.297	38.5263	2163.2	35.63	833.4	10.11
MR01-40	1.363	0.028	0.121	0.002	0.293	59.6666	1235.7	40.27	737.3	8.88
MR01-41	1.191	0.043	0.133	0.002	0.157	104.607	770.6	75.74	806.1	11.39
MR01-42	1.182	0.027	0.126	0.002	0.264	88.6768	864.6	47.64	766.7	9.45
MR01-43	1.110	0.029	0.116	0.002	0.225	77.7302	910.2	53.69	707.5	9.2
MR1-21a	1.303	0.089	0.138	0.003	0.078	93.9596	885.7	139.66	832.2	19.37

Table 1: LA–ICP–MS U–Pb data used to calculate Concordias from igneous samples Oman

Analysis	$^{207}Pb/^{235}U$		$^{206}Pb/^{238}U$		rho	Conc (%)	$^{207}Pb/^{206}Pb$		$^{206}Pb/^{238}U$	
Mirbat										
Mr15-01										
MR01-14	0.918	0.139	0.137	0.003	0.033	662.72	125	324.05	828.4	18.53
MR01-15	1.171	0.042	0.135	0.002	0.160	116.164	703.4	76.52	817.1	12.04
MR01-16	1.230	0.038	0.131	0.002	0.199	91.891	865.7	63.69	795.5	10.99
MR01-01	1.247	0.031	0.139	0.002	0.283	107.17	781	50.86	837	10.99
MR01-02	1.279	0.036	0.137	0.002	0.235	95.5566	864.2	57.98	825.8	10.93
MR01-03	1.257	0.036	0.135	0.002	0.216	96.2122	850.1	60.21	817.9	11.17
MR01-04	1.250	0.051	0.132	0.002	0.149	90.2516	886.3	84.53	799.9	13.1
MR01-05	1.184	0.037	0.134	0.002	0.207	109.294	742.4	65.73	811.4	11.22
MR01-17	1.239	0.031	0.130	0.002	0.255	87.1418	903.7	51.01	787.5	10.12
MR01-06	1.222	0.038	0.135	0.002	0.204	101.333	802.8	64.73	813.5	11.36
MR01-07	1.243	0.035	0.135	0.002	0.223	98.3857	830.1	58.45	816.7	10.82
MR01-08	1.223	0.036	0.130	0.002	0.208	89.1524	881.3	60.63	785.7	10.68
MR01-09	1.251	0.056	0.132	0.002	0.132	89.7373	890.6	92.03	799.2	12.9
MR01-10	1.212	0.039	0.141	0.002	0.196	123.373	688.4	68.25	849.3	11.66
MR01-11	1.366	0.044	0.138	0.002	0.188	85.5708	975.8	65.26	835	12.01
MR01-12	1.243	0.031	0.133	0.002	0.257	92.3475	869	51.19	802.5	10.32
MR01-18	1.217	0.033	0.134	0.002	0.235	100.161	807.5	56.15	808.8	10.57
MR01-19	1.362	0.070	0.130	0.003	0.099	72.0871	1093.4	103.17	788.2	14.98
MR01-20	1.280	0.051	0.133	0.002	0.147	87.9974	917.3	81.83	807.2	12.21
MR01-22	1.189	0.045	0.134	0.002	0.159	108.296	749.8	79.01	812	11.6
MR01-23	1.408	0.035	0.148	0.002	0.251	98.657	901	50.94	888.9	11.26
MR01-24	1.241	0.026	0.132	0.002	0.303	91.3685	874.7	43.39	799.2	9.67
MR01-25	1.260	0.035	0.133	0.002	0.224	90.1906	892	56.93	804.5	10.54
MR01-26	1.179	0.036	0.130	0.002	0.192	99.6343	793.1	63.6	790.2	10.74
MR01-27	1.177	0.095	0.134	0.003	0.063	111.213	729.5	167.36	811.3	19.58
MR01-28	1.257	0.041	0.130	0.002	0.187	83.7348	938.2	66.31	785.6	10.88
MR01-29	1.257	0.036	0.131	0.002	0.210	87.4259	910.6	59.16	796.1	10.5
MR01-21a	1.282	0.031	0.138	0.002	0.249	98.9696	844.3	50.43	835.6	10.51
MR15-02										
MR02-03	1.105	0.029	0.126	0.002	0.262	105.196	727.5	55.76	765.3	10.24
MR02-04	1.210	0.038	0.133	0.002	0.208	99.6285	807.6	65.33	804.6	11.37
MR02-05	1.127	0.022	0.128	0.002	0.360	106.212	732.4	40.66	777.9	9.61
MR02-06	1.197	0.032	0.132	0.002	0.253	101.161	792.5	54.89	801.7	10.57
MR02-07	1.400	0.024	0.129	0.002	0.426	67.7634	1158	32.05	784.7	9.31
MR02-08	1.120	0.051	0.127	0.002	0.131	103.758	742.5	96.59	770.4	13.56
MR02-09	1.100	0.056	0.128	0.002	0.122	114.664	679.2	106.44	778.8	13.04
MR02-10	1.161	0.022	0.127	0.002	0.387	93.83	820.1	37.32	769.5	9.3
MR02-11	1.166	0.031	0.126	0.002	0.257	91.5453	837.4	54.48	766.6	10.08
MR02-12	1.205	0.031	0.131	0.002	0.266	95.0432	833.2	52.46	791.9	10.25
MR02-13	1.117	0.038	0.126	0.002	0.194	101.286	754.3	71.25	764	10.64
MR02-14	1.121	0.026	0.126	0.002	0.299	101.604	754.3	47.84	766.4	9.73
MR02-15	1.234	0.035	0.133	0.002	0.235	94.7449	848.7	58.86	804.1	10.81
MR02-16	1.101	0.031	0.125	0.002	0.239	103.764	733.2	59.1	760.8	10.23
MR02-17	1.139	0.028	0.128	0.002	0.277	101.004	766.6	50.12	774.3	10
MR02-18	1.415	0.027	0.124	0.002	0.378	59.6675	1263	35.49	753.6	9.12
MR02-19	1.231	0.055	0.131	0.002	0.137	91.3468	870.2	91.37	794.9	12.42
MR02-20	1.080	0.059	0.124	0.002	0.107	105.97	711.9	114.05	754.4	13.01
MR02-21	1.210	0.029	0.134	0.002	0.281	103.281	786.3	49.22	812.1	10.29
MR02-22	1.208	0.047	0.131	0.002	0.161	95.249	833.5	80.45	793.9	11.63
MR02-23	1.211	0.041	0.130	0.002	0.192	92.8521	850.6	70.3	789.8	11.21
MR02-24	1.221	0.035	0.134	0.002	0.234	99.1174	815.8	58.38	808.6	10.76
MR02-25	1.161	0.032	0.129	0.002	0.239	100.166	781.7	57.46	783	10.58

Table 1: LA–ICP–MS U–Pb data used to calculate Concordias from igneous samples Oman

Analysis	$^{207}Pb/^{235}U$		$^{206}Pb/^{238}U$		rho	Conc (%)	$^{207}Pb/^{206}Pb$		$^{206}Pb/^{238}U$	
Mirbat										
MR15-02										
MR02-26	1.188	0.032	0.129	0.002	0.259	88.2884	886.3	54.29	782.5	10.9
MR02-27	1.188	0.029	0.131	0.002	0.279	98.0171	806.9	49.92	790.9	10.07
MR02-28	1.135	0.041	0.128	0.002	0.174	103.026	753.4	76.21	776.2	11.22
MR02-29	1.192	0.032	0.129	0.002	0.247	93.7986	835.3	55.46	783.5	10.39
MR02-30	1.126	0.083	0.128	0.003	0.075	104.619	740.5	149.98	774.7	14.27
MR02-31	1.176	0.030	0.130	0.002	0.266	99.722	791.3	51.92	789.1	10.12
MR02-32	1.204	0.038	0.123	0.002	0.202	77.8878	959.2	64.74	747.1	10.43
MR02-33	1.134	0.100	0.128	0.003	0.060	102.164	757.7	179.72	774.1	17.76
MR02-34	1.183	0.024	0.129	0.002	0.356	93.6771	831.9	40.16	779.3	9.41
MR02-35	1.145	0.050	0.126	0.002	0.133	93.9256	811.6	91.02	762.3	11.82
MR02-36	1.160	0.029	0.127	0.002	0.277	94.952	812.2	51.1	771.2	10.12
MR02-37	1.181	0.027	0.129	0.002	0.296	96.3632	813.9	47.69	784.3	9.9
MR02-38	1.102	0.052	0.124	0.002	0.125	101.069	748.3	97.49	756.3	11.85
MR02-39	1.153	0.032	0.126	0.002	0.245	94.8721	809.3	57.03	767.8	10.42
MR02-40	1.229	0.040	0.135	0.002	0.193	100.209	812.5	67.5	814.2	11.75
MR02-41	1.140	0.035	0.129	0.002	0.217	105.035	744.8	63.74	782.3	10.67
MR15-04										
MR04-01	1.304	0.022	0.141	0.002	0.368	102.072	835.1	33.92	852.4	9.46
MR04-02	1.230	0.023	0.134	0.002	0.329	99.4132	818	38.2	813.2	9.41
MR04-03	1.138	0.023	0.126	0.002	0.293	95.9286	795.8	42.9	763.4	9.22
MR04-04	1.138	0.028	0.125	0.002	0.238	94.1847	806.5	51.6	759.6	9.69
MR04-05	1.188	0.032	0.127	0.002	0.203	88.9595	865.9	56.81	770.3	10.06
MR04-06	1.279	0.020	0.138	0.002	0.407	97.5229	851.8	31.55	830.7	9.18
MR04-07	1.254	0.025	0.139	0.002	0.306	105.298	794.7	41.32	836.8	9.83
MR04-08	1.182	0.023	0.128	0.002	0.306	93.6605	831.3	40.23	778.6	9.13
MR04-09	1.307	0.024	0.133	0.002	0.334	83.7299	962.5	37.09	805.9	9.33
MR04-10	1.213	0.021	0.134	0.002	0.350	102.102	794.6	36.28	811.3	9.35
MR04-11	1.200	0.021	0.132	0.002	0.355	99.7631	801.9	35.76	800	9.1
MR04-12	1.448	0.025	0.118	0.001	0.365	51.6427	1397.1	32.38	721.5	8.41
MR04-13	1.328	0.022	0.130	0.002	0.373	75.7491	1041.2	33.48	788.7	9.03
MR04-14	1.062	0.030	0.118	0.002	0.195	92.6698	777.6	61.23	720.6	10.18
MR04-15	1.213	0.050	0.131	0.002	0.130	92.9915	850.4	86.19	790.8	13.35
MR04-16	1.203	0.040	0.133	0.002	0.167	100.526	799.2	70.2	803.4	11.21
MR04-17	1.152	0.031	0.127	0.002	0.203	97.5038	793.2	57.06	773.4	9.97
MR04-18	1.146	0.035	0.128	0.002	0.174	100.922	770.4	64.7	777.5	10.69
MR04-19	1.303	0.042	0.131	0.002	0.168	79.7384	994	65.18	792.6	11.35
MR04-20	1.153	0.053	0.129	0.002	0.109	102.007	767.4	96.35	782.8	12.42
MR04-21	1.211	0.063	0.122	0.003	0.091	74.4739	993.1	107.34	739.6	14.65
MR04-22	1.227	0.019	0.133	0.002	0.384	96.385	835.4	31.95	805.2	8.87
MR04-23	1.209	0.019	0.134	0.002	0.388	102.287	791.5	31.95	809.6	8.87
MR04-24	1.159	0.024	0.129	0.002	0.287	100.798	777.2	43.75	783.4	9.34
MR04-25	1.166	0.030	0.120	0.002	0.213	76.5566	950.8	53.77	727.9	9.65
MR04-26	1.247	0.023	0.123	0.002	0.316	73.0304	1025.6	37.55	749	8.74
MR04-27	1.233	0.022	0.128	0.002	0.331	83.0687	932	36.09	774.2	8.8
MR04-28	1.151	0.059	0.130	0.003	0.095	105.695	746.3	109.12	788.8	14.64
MR04-29	1.385	0.024	0.127	0.002	0.341	65.8532	1172	34.56	771.8	8.76
MR04-30	1.153	0.027	0.126	0.002	0.236	92.2649	826.1	49.88	762.2	9.53
MR04-31	1.143	0.024	0.119	0.002	0.261	79.7214	911.8	44.18	726.9	8.75
MR04-32	1.252	0.041	0.125	0.002	0.163	74.7432	1012.4	67.77	756.7	10.93
MR04-33	1.364	0.028	0.120	0.002	0.276	57.9416	1259.2	40.02	729.6	8.88
MR04-34	1.151	0.042	0.131	0.002	0.144	108.736	730.3	78.32	794.1	12.46

Table 1: LA–ICP–MS U–Pb data used to calculate Concordias from igneous samples Oman

Analysis	$^{207}Pb/^{235}U$		$^{206}Pb/^{238}U$		rho	Conc (%)	$^{207}Pb/^{206}Pb$		$^{206}Pb/^{238}U$	
Mirbat										
MR15-05										
MR05-01	1.176	0.020	0.130	0.002	0.339	100	790	35.17	789.4	8.67
MR05-02	1.161	0.031	0.127	0.002	0.192	94	816.3	56.21	770.8	9.7
MR05-03	1.140	0.031	0.127	0.002	0.189	100	772.3	58.5	772.7	9.89
MR05-04	1.178	0.027	0.129	0.002	0.236	96	814.9	47.77	782	9.34
MR05-05	1.112	0.026	0.126	0.002	0.242	103	743.5	48.9	765	9.26
MR05-06	1.152	0.033	0.126	0.002	0.176	93	821.9	60.22	763.5	9.93
MR05-07	1.149	0.029	0.127	0.002	0.217	97	797.6	52.47	769.7	9.42
MR05-08	1.147	0.028	0.127	0.002	0.223	98	789	51.87	771.6	9.48
MR05-09	1.119	0.033	0.127	0.002	0.176	103	743.9	62.78	769.3	10.2
MR05-10	1.135	0.026	0.127	0.002	0.240	101	762.1	48.95	773	9.26
MR05-11	1.118	0.030	0.127	0.002	0.189	105	737	58.13	770.9	9.84
MR05-12	1.111	0.047	0.124	0.002	0.114	96	780.5	88.7	751.5	11.97
MR05-13	1.036	0.037	0.130	0.002	0.142	150	524.5	79.43	787.2	10.86
MR05-14	1.122	0.038	0.125	0.002	0.147	97	779.8	72.23	758.7	10.85
MR05-15	1.099	0.040	0.124	0.002	0.138	101	748.6	76.74	754.6	10.94
MR05-16	1.135	0.029	0.124	0.002	0.199	91	824.7	54.39	751.5	9.51
MR05-17	1.149	0.025	0.125	0.002	0.241	93	821.5	46.67	761.7	9.15
MR05-18	1.126	0.022	0.126	0.002	0.280	100	767.1	42.16	765.4	8.82
MR05-19	1.087	0.032	0.124	0.002	0.180	102	734.5	61.95	751.5	9.63
MR05-20	1.148	0.037	0.124	0.002	0.152	88	849.9	68.2	750.8	10.69
MR05-21	1.313	0.038	0.147	0.002	0.178	114	773.2	61.01	882.3	11.63
MR05-22	1.129	0.019	0.128	0.001	0.324	106	733.3	36.21	779.1	8.53
MR05-23	1.127	0.030	0.123	0.002	0.190	91	819.7	55.78	748.3	9.47
MR05-24	1.114	0.032	0.123	0.002	0.177	95	788.6	61	750.5	9.94
MR05-25	1.124	0.019	0.126	0.001	0.338	99	771	35.43	763.3	8.34
MR05-26	1.149	0.053	0.125	0.002	0.102	92	827.8	97.43	758.9	13.63
MR05-27	1.063	0.017	0.121	0.001	0.359	101	729.4	33.17	737.6	7.97
MR05-28	1.239	0.075	0.127	0.003	0.078	81	948.7	124.13	771.6	15.89
MR05-29	1.059	0.033	0.121	0.002	0.169	103	717.2	66.27	738.8	10.25
MR05-30	1.169	0.056	0.131	0.002	0.108	103	771.9	100.9	791.5	12.74
MR05-31	1.115	0.028	0.129	0.002	0.214	110	706.1	54.38	779.4	9.66
MR05-32	1.116	0.022	0.126	0.002	0.290	102	748.7	42.18	765.1	8.87
MR05-33	1.139	0.031	0.125	0.002	0.208	95	804.3	57.11	761.2	9.83
MR05-34	1.142	0.041	0.128	0.002	0.158	101	769.3	76.16	774.6	11.78
MR05-35	1.123	0.033	0.127	0.002	0.188	102	753.2	62.63	768.2	10.21
MR15-07										
MR07-01	1.400	0.026	0.156	0.002	0.339	121	772.6	38.39	936.8	10.8
MR07-02	1.278	0.021	0.142	0.002	0.363	110	815.9	42.24	833.2	9.69
MR07-03	1.226	0.038	0.133	0.002	0.184	96	784	52.39	841.9	10.71
MR07-04	1.331	0.030	0.144	0.002	0.244	102	810.8	52.06	828.7	10.44
MR07-05	1.255	0.022	0.137	0.002	0.337	100	822.1	50.51	809.7	10.14
MR07-06	1.274	0.024	0.141	0.002	0.315	109	758.1	42.21	845.9	9.76
MR07-07	1.198	0.019	0.133	0.002	0.384	103	793.9	55.78	801.8	10.44
MR07-08	1.329	0.034	0.143	0.002	0.195	101	802.3	35.92	810	8.98
MR07-09	1.221	0.022	0.135	0.002	0.314	104	825.7	33.62	801.4	8.72
MR07-10	1.171	0.017	0.130	0.002	0.402	98	822.2	33.66	811	8.85
MR07-11	1.196	0.024	0.133	0.002	0.278	102	782.6	50.1	786.9	9.74
MR07-12	1.178	0.021	0.127	0.002	0.313	91	810.6	29.23	788.5	8.32
MR07-13	1.160	0.020	0.127	0.002	0.326	93	786.8	34.49	816.1	8.9
MR07-14	1.282	0.023	0.142	0.002	0.294	108	765.9	51.25	787	9.86
MR07-15	1.207	0.021	0.134	0.002	0.316	104	891.8	39.16	872.6	9.89
MR07-16	1.218	0.022	0.133	0.002	0.296	98	802.8	38.08	815.2	9.19

Table 1: LA–ICP–MS U–Pb data used to calculate Concordias from igneous samples Oman

Analysis	$^{207}Pb/^{235}U$		$^{206}Pb/^{238}U$		rho	Conc (%)	$^{207}Pb/^{206}Pb$		$^{206}Pb/^{238}U$	
Mirbat										
MR15-07										
MR07-17	1.207	0.032	0.132	0.002	0.206	97	790.5	38.04	774.3	8.73
MR07-18	1.218	0.027	0.134	0.002	0.238	101	799.2	30.92	795.4	8.47
MR07-19	1.232	0.023	0.138	0.002	0.277	108	968.9	36.66	793.2	8.89
MR07-20	1.163	0.022	0.128	0.002	0.280	95	811.1	38.96	797.6	8.96
MR07-21	1.608	0.030	0.167	0.002	0.298	109	754.7	39.78	812.7	9.14
MR07-22	1.249	0.021	0.140	0.002	0.344	110	767.7	34.83	843.4	9.16
MR07-23	1.193	0.022	0.134	0.002	0.294	108	918.6	38.45	997.5	11.18
MR07-24	1.201	0.022	0.132	0.002	0.295	98	811.2	40.7	773.7	8.87
MR07-25	1.289	0.023	0.131	0.002	0.308	82	772.9	40.63	831.1	9.44
MR07-26	1.191	0.018	0.131	0.001	0.384	100	804.9	47.35	810.5	9.72
MR07-27	1.153	0.021	0.128	0.002	0.313	98	823.6	55.61	796.8	10.29
MR07-28	1.225	0.022	0.135	0.002	0.315	102	819.6	37.59	805.1	8.93
MR07-29	1.374	0.026	0.145	0.002	0.298	98	778.3	36.24	813.2	8.98
MR07-30	1.159	0.028	0.130	0.002	0.222	103	793.8	38.17	854.8	9.49
MR07-31	1.217	0.020	0.135	0.002	0.341	104	827.3	36.72	769.8	8.86
MR07-32	1.186	0.017	0.130	0.001	0.412	97	848	37.51	772.4	8.78
MR07-33	1.168	0.028	0.130	0.002	0.232	101	785.4	42.1	803.7	9.29
MR07-34	1.229	0.020	0.134	0.002	0.361	99	801.2	30.18	786	8.56
MR07-35	1.216	0.020	0.132	0.002	0.360	97	789.6	37.85	817.8	9.23
MR07-36	1.216	0.021	0.134	0.002	0.338	101	855.5	53.83	860.2	10.86
MR07-37	1.198	0.031	0.132	0.002	0.198	101	783.7	32.62	805.6	8.82
MR07-38	1.247	0.025	0.140	0.002	0.284	112	785.5	39.66	852.5	9.88
MR07-39	1.227	0.029	0.134	0.002	0.234	98	827.3	36.37	824.9	9.35
MR07-40	1.251	0.031	0.137	0.002	0.229	102	844.1	47.13	865.2	10.43
MR07-41	1.257	0.031	0.140	0.002	0.218	107	843.1	64.1	805.8	10.84
MR07-42	1.261	0.025	0.138	0.002	0.282	102	777.2	34.42	858.3	9.54

Table 1: LA–ICP–MS U–Pb data used to calculate Concordias from igneous samples Oman

Analysis	$^{207}Pb/^{235}U$		$^{206}Pb/^{238}U$		rho	Conc (%)	$^{207}Pb/^{206}Pb$		$^{206}Pb/^{238}U$	
MR15-14										
MR14-01	1.261	0.029	0.130	0.002	0.436	84	934.6	43.81	789	11.93
MR14-02	1.257	0.020	0.139	0.002	0.678	104	801.1	25.91	836.4	11.67
MR14-03	1.198	0.040	0.132	0.002	0.278	101	795.1	68.51	801.8	13.8
MR14-04	1.193	0.042	0.131	0.002	0.258	98	810.4	72.64	792.4	14
MR14-05	1.198	0.024	0.131	0.002	0.546	97	818.3	35.73	793	11.66
MR14-06	1.062	0.037	0.118	0.002	0.268	93	776.5	71.28	721.4	12.87
MR14-07	1.040	0.022	0.119	0.002	0.498	101	717	40.52	726.2	11.1
MR14-08	1.165	0.032	0.132	0.002	0.369	107	746.4	55.42	798.1	12.78
MR14-09	1.261	0.040	0.136	0.002	0.316	98	840.6	63.67	824.2	14.07
MR14-10	0.850	0.017	0.090	0.001	0.527	63	878.6	36.89	557	8.36
MR14-11	0.933	0.017	0.098	0.002	0.599	67	899.1	31.35	603	8.85
MR14-12	1.159	0.023	0.130	0.002	0.560	103	762.7	35.11	788	11.55
MR14-13	1.054	0.019	0.117	0.002	0.611	92	780.3	31.42	714.7	10.38
MR14-14	1.188	0.023	0.131	0.002	0.565	99	800.7	34.95	792.9	11.72
MR14-15	1.174	0.030	0.128	0.002	0.404	94	824.3	50.16	776	12.46
MR14-16	1.219	0.026	0.134	0.002	0.492	101	803.8	40.57	811.2	12.12
MR14-17	1.185	0.022	0.131	0.002	0.573	100	792.2	33.44	794	11.51
MR14-18	1.188	0.022	0.130	0.002	0.594	98	808.9	31.88	789.9	11.39
MR14-19	1.141	0.026	0.127	0.002	0.465	100	773.8	42.68	772.8	11.6
MR14-20	0.978	0.029	0.113	0.002	0.296	98	701.4	62.76	689.6	11.76
MR14-21	1.140	0.021	0.126	0.002	0.589	97	790.7	32.37	766.3	11.02
MR14-22	1.007	0.020	0.128	0.002	0.546	157	494.7	37.46	775.8	11.15
MR14-23	1.142	0.025	0.127	0.002	0.487	99	779.6	40.33	771.4	11.46
MR14-24	1.189	0.023	0.130	0.002	0.550	97	814.4	34.9	789	11.42
MR14-25	1.190	0.024	0.127	0.002	0.522	89	865.6	37.26	771.2	11.29
MR14-26	1.216	0.027	0.132	0.002	0.465	96	833.1	42.07	798.7	11.91
MR14-27	0.444	0.009	0.044	0.001	0.538	28	1007.9	34.79	278.8	4.2
MR14-28	1.211	0.026	0.129	0.002	0.492	90	867.6	39.54	783.4	11.54
MR14-29	0.872	0.019	0.103	0.002	0.439	97	649.1	42.81	632.8	9.51
MR14-30	1.197	0.025	0.128	0.002	0.507	91	856.3	37.86	778.8	11.36
MR14-31	1.174	0.050	0.132	0.003	0.207	105	760.8	87.9	798.4	15.19
MR14-32	1.203	0.028	0.133	0.002	0.449	102	791.3	44.1	805.6	12.16
MR14-33	1.191	0.022	0.132	0.002	0.587	101	792.8	32.73	797.5	11.46
MR14-34	1.156	0.023	0.128	0.002	0.539	99	786.3	36.09	778.2	11.39
MR14-35	1.169	0.024	0.132	0.002	0.525	107	745.9	37.77	800.9	11.82
MR14-36	1.185	0.024	0.131	0.002	0.545	99	799.8	35.96	791.8	11.66
MR14-37	1.185	0.023	0.131	0.002	0.571	101	787.6	34.2	796	11.61
MR14-38	1.075	0.022	0.123	0.002	0.531	105	713.7	37.77	750.5	11.09
MR14-39	1.140	0.043	0.129	0.002	0.246	104	749.3	78.9	780.4	14.2
MR14-40	1.212	0.026	0.131	0.002	0.510	94	844.4	39.43	792.4	11.86
MR14-41	1.213	0.032	0.129	0.002	0.414	89	875.9	50.26	782	12.85
MR14-42	1.167	0.027	0.130	0.002	0.491	100	785.3	42.61	785.2	12.15
MR14-43	1.152	0.024	0.129	0.002	0.548	103	761.9	37.4	784.2	11.86
MR14-44	1.055	0.023	0.120	0.002	0.511	99	738.2	40.39	729.5	11.24
MR14-45	1.135	0.028	0.128	0.002	0.455	103	751.7	46.52	776.6	12.29
MR14-46	1.192	0.023	0.136	0.002	0.572	113	728.5	35.14	821.8	12.4
MR14-47	1.132	0.022	0.128	0.002	0.572	105	742.7	34.79	777.9	11.69
MR14-48	1.206	0.031	0.135	0.002	0.430	106	768.4	49.7	816.4	13.11
MR14-49	1.130	0.028	0.126	0.002	0.454	98	777.4	47.24	764.5	12.25
MR14-50	1.137	0.036	0.121	0.002	0.326	85	870.7	63.32	737.5	13.01
MR14-51	1.187	0.024	0.129	0.002	0.557	93	837	36.37	779.7	11.94
MR14-52	1.160	0.034	0.125	0.002	0.355	90	843.5	58.31	760.6	12.78
MR14-53	1.139	0.023	0.126	0.002	0.562	96	793.1	36.06	764.9	11.56

Table 1: LA–ICP–MS U–Pb data used to calculate Concordias from igneous samples Oman

Analysis	$^{207}Pb/^{235}U$		$^{206}Pb/^{238}U$		rho	Conc (%)	$^{207}Pb/^{206}Pb$		$^{206}Pb/^{238}U$	
MR15-14										
MR14-54	1.071	0.030	0.122	0.002	0.382	101	735.4	55.49	740.5	12.14
MR14-55	1.165	0.029	0.127	0.002	0.430	94	819	48.21	772.1	12.33
MR14-56	1.111	0.020	0.123	0.002	0.634	95	788.4	30.5	749.1	11.09
MR14-57	1.140	0.028	0.122	0.002	0.448	87	857.5	46.45	743.9	11.96
MR14-58	1.161	0.025	0.127	0.002	0.500	95	813.9	39.88	771.5	11.94
MR14-59	1.050	0.024	0.108	0.002	0.479	71	935.5	42.87	663.8	10.62
MR14-60	1.108	0.020	0.121	0.002	0.643	90	820.1	29.52	736.4	10.91
MR14-61	1.209	0.025	0.133	0.002	0.560	100	807.7	36.31	803.7	12.25
MR14-62	0.978	0.024	0.111	0.002	0.446	93	730.4	46.92	681.1	11.01
MR14-63	1.190	0.034	0.135	0.002	0.378	112	732.7	56.5	818.6	13.44
MR14-64	1.239	0.023	0.136	0.002	0.612	101	813.6	32.16	820.6	12.23
MR14-65	1.160	0.027	0.131	0.002	0.477	105	755.3	43.53	791.4	12.22
MR14-66	1.173	0.023	0.129	0.002	0.572	97	807.5	35.24	781.5	11.69
MR14-67	1.181	0.042	0.124	0.002	0.278	83	905.3	71.94	752.1	14.07
MR14-68	1.171	0.026	0.129	0.002	0.488	98	799.6	41.96	782.6	12.04
MR14-69	1.177	0.026	0.128	0.002	0.507	95	822.1	41.26	778.6	12.12
MR14-70	1.284	0.024	0.135	0.002	0.621	92	891.9	31.07	818.6	12.05
MR14-71	1.071	0.020	0.117	0.002	0.625	88	811.8	31.12	715.4	10.58
MR14-72	1.227	0.023	0.132	0.002	0.599	94	847.3	32.82	800.4	11.85
MR14-73	1.157	0.030	0.130	0.002	0.419	104	758.4	51.19	788.5	12.82
MR14-74	1.164	0.025	0.130	0.002	0.514	102	774.6	40.2	787.2	12.05
MR14-75	1.212	0.032	0.132	0.002	0.414	98	820.9	50.83	800.9	12.86
MR14-76	1.189	0.024	0.127	0.002	0.566	88	869.3	35.38	769.3	11.56
MR14-77	1.166	0.023	0.130	0.002	0.588	101	778.8	33.86	786.7	11.7
MR14-78	1.159	0.024	0.131	0.002	0.533	107	741.6	38.43	795.6	12.01
MR14-79	1.137	0.021	0.125	0.002	0.618	94	803.9	31.46	759.6	11.21
MR14-80	1.164	0.021	0.130	0.002	0.637	102	772.4	30.17	788.1	11.52
MR14-81	1.168	0.025	0.129	0.002	0.532	99	793.6	38.16	782.9	11.82
MR14-82	0.705	0.012	0.072	0.001	0.649	48	947.2	28.1	450.7	6.75
MR14-83	1.149	0.023	0.125	0.002	0.555	92	823.6	35.84	760.3	11.4
MR14-84	1.157	0.032	0.130	0.002	0.378	105	755.3	55.59	789.3	13.04
MR14-85	1.156	0.023	0.129	0.002	0.582	101	776.5	34.63	781.3	11.68
MR14-86	1.221	0.024	0.134	0.002	0.583	99	815.1	34.43	808.2	12.07
MR14-87	1.200	0.023	0.132	0.002	0.602	99	809.1	32.66	797.8	11.79
MR14-88	1.132	0.028	0.129	0.002	0.439	108	724.5	47.64	783.9	12.29
MR14-89	1.114	0.028	0.129	0.002	0.437	112	699	48.07	781.2	12.25
MR14-91	1.230	0.033	0.135	0.002	0.413	100	816.7	51.52	813.5	13.37
MR14-93	1.119	0.021	0.126	0.002	0.593	100	763.8	33.39	762.2	11.57
MR14-94	1.224	0.024	0.134	0.002	0.603	100	813.5	33.01	810.9	12.19
MR14-95	1.220	0.023	0.134	0.002	0.610	100	807.8	32.03	810.6	12.16
MR14-96	1.221	0.028	0.127	0.002	0.477	84	914.9	43.04	772.8	12.28
MR14-97	1.236	0.029	0.137	0.002	0.476	106	781	44.57	830.2	12.96
MR14-98	1.522	0.035	0.157	0.003	0.490	100	937.1	41.63	940.4	14.53
MR14-99	1.251	0.025	0.140	0.002	0.579	109	774.7	35.31	842	12.73
MR14-100	1.237	0.025	0.135	0.002	0.567	100	815.8	35.43	818.5	12.42
MR14-101	1.159	0.030	0.129	0.002	0.427	100	781.9	49.79	781.1	12.68
MR14-102	1.156	0.030	0.127	0.002	0.419	94	814.6	50.39	768.1	12.54
MR14-103	1.123	0.026	0.126	0.002	0.486	100	762.3	44.21	765.4	12.02
MR14-104	1.156	0.023	0.127	0.002	0.581	95	811	34.69	769.5	11.66
MR14-105	1.169	0.028	0.130	0.002	0.461	102	774.8	45.46	790	12.49
MR14-106	1.141	0.025	0.128	0.002	0.526	101	765.3	39.41	775.5	11.91
MR14-107	1.160	0.024	0.129	0.002	0.542	100	781.1	37.76	782.5	11.96
MR14-108	1.443	0.037	0.161	0.003	0.415	123	779.6	49.71	959.9	15.05

Table 1: LA–ICP–MS U–Pb data used to calculate Concordias from igneous samples Oman

Analysis	^{207}Pb/^{235}U		^{206}Pb/^{238}U		rho	Conc (%)	^{207}Pb/^{206}Pb		^{206}Pb/^{238}U	
MR15-14										
MR14-109	1.073	0.025	0.123	0.002	0.442	104	720.7	46.03	747.1	11.67
MR14-110	1.135	0.025	0.123	0.002	0.471	90	830.8	41.76	749.3	11.52
MR14-111	1.131	0.029	0.119	0.002	0.416	81	894.8	48.81	725.8	11.46
MR14-112	1.142	0.032	0.129	0.002	0.376	104	752.7	56.22	780.9	12.94
MR14-113	1.099	0.024	0.122	0.002	0.496	95	783.3	41.68	742.8	11.47
MR14-114	1.213	0.041	0.130	0.002	0.290	93	851.8	68.51	790.3	13.66
MR14-115	1.114	0.042	0.126	0.002	0.245	103	741.6	77.71	766.4	13.81
MR14-116	1.103	0.026	0.123	0.002	0.465	96	777.8	44.25	746.8	11.56
MR14-117	1.152	0.035	0.126	0.002	0.323	93	823	61.73	762.5	13.06
MR14-118	1.161	0.034	0.128	0.002	0.355	98	794.6	57.99	778.2	12.94
MR14-119	1.203	0.027	0.131	0.002	0.490	95	832.3	41.05	791.4	11.91
MR14-120	1.093	0.022	0.120	0.002	0.540	90	809.1	36.63	730.1	10.81
JA15-43										
JA43_01A	2.446	0.075	0.157	0.003	0.195	51	1848.2	58.69	940	17.12
JA43_02A	1.353	0.028	0.141	0.002	0.360	93	913.1	41.11	851.6	11.09
JA43_02B	1.101	0.019	0.102	0.001	0.424	54	1154.1	33.28	626.3	7.82
JA43_03A	4.048	0.061	0.286	0.004	0.510	97	1673.2	25.59	1621.1	18.13
JA43_05A	0.516	0.018	0.047	0.001	0.177	25	1180.9	69.84	296.9	5.06
JA43_06A	1.442	0.023	0.149	0.002	0.470	95	940.2	30.48	892.8	10.56
JA43_07A	1.364	0.024	0.144	0.002	0.426	97	890.2	34.1	867	10.5
JA43_08A	3.166	0.052	0.248	0.003	0.468	97	1477.5	28.94	1429.3	16.5
JA43_09A	3.654	0.060	0.257	0.003	0.465	88	1682.7	28.43	1473.5	17.01
JA43_10A	2.187	0.106	0.185	0.004	0.125	82	1332.3	96.56	1094.5	24.24
JA43_11A	2.179	0.045	0.192	0.003	0.367	90	1256.6	38.44	1130.6	14.26
JA43_12A	1.179	0.023	0.105	0.001	0.377	52	1233.9	37.22	643.1	8.27
JA43_13A	0.590	0.014	0.038	0.001	0.314	13	1827.3	41.05	242.4	3.41
JA43_14A	1.556	0.060	0.139	0.003	0.161	68	1231.2	76.52	836.9	14.74
JA43_15A	1.301	0.026	0.125	0.002	0.356	70	1080.1	39.53	759.8	9.7
JA43_16A	1.346	0.029	0.142	0.002	0.348	95	899.1	42.42	853.3	10.99
JA43_17A	0.908	0.019	0.093	0.001	0.362	59	963.4	41.12	570.5	7.5
JA43_17B	1.284	0.024	0.137	0.002	0.398	95	870.6	37.23	826.8	10.26
JA43_19A	2.133	0.053	0.145	0.002	0.280	50	1746.6	45.7	871.7	12.63
JA43_20A	1.596	0.032	0.163	0.002	0.370	102	954.3	39.81	975	12.27
JA43_21A	1.393	0.033	0.145	0.002	0.329	95	919.5	46.16	872.9	10.89
JA43_22A	3.912	0.083	0.275	0.004	0.370	93	1679.9	37.32	1567.6	18.57
JA43_23A	8.773	0.156	0.386	0.005	0.449	84	2505.2	27.69	2105	23.01
JA43_24A	4.764	0.084	0.260	0.003	0.456	70	2137.5	28.24	1489.1	16.88
JA43_25A	2.090	0.047	0.189	0.003	0.347	93	1204	42.33	1115.1	13.64
JA43_27A	1.378	0.031	0.142	0.002	0.344	91	937.4	44.23	856.7	10.61
JA43_28A	1.465	0.035	0.149	0.002	0.330	92	967.9	46.59	894.9	11.2
JA43_30A	1.396	0.030	0.144	0.002	0.368	93	933.9	41.13	868.8	10.61
JA43_31A	2.488	0.056	0.192	0.003	0.343	75	1511.4	40.91	1130.3	13.95
JA43_32A	1.260	0.029	0.127	0.002	0.338	78	986	44.52	770.2	9.63
JA43_33A	1.496	0.036	0.152	0.002	0.319	94	970.6	47.15	911.2	11.42
JA43_34A	2.091	0.044	0.187	0.002	0.381	90	1228.8	38.97	1102.8	13.27
JA43_35A	2.393	0.053	0.191	0.003	0.353	78	1443.9	40.59	1127	13.82
JA43_36A	1.250	0.025	0.123	0.002	0.386	72	1032.1	38.66	748.2	9.15
JA43_38A	1.725	0.036	0.165	0.002	0.378	90	1092.6	39.21	983.6	11.88
JA43_39A	1.291	0.029	0.133	0.002	0.345	85	945.6	44.67	803.1	10
JA43_41A	2.698	0.100	0.142	0.002	0.182	39	2198.2	64.54	856.9	13.98
JA43_43A	1.487	0.038	0.148	0.002	0.298	88	1010.9	50.25	889.6	11.33
JA43_44A	1.326	0.029	0.128	0.002	0.357	72	1078.6	41.92	774.2	9.58
JA43_45A	1.316	0.030	0.139	0.002	0.345	94	892.8	44.97	837.7	10.38

Table 2: LA–MC–ICP–MS Lu–Hf isotopes (zircon) from igneous samples in Oman

Sample Name	Hf^{176}/Hf^{177}	2 S.E.	Lu^{176}/Hf^{177}	U/Pb AGE	Hfi	epsilon	2s	Hf DM (t) (Crustal)	T(NC) (Crustal)
O14-04									
MB_O1_02-01	0.28249	0.00002	0.00107	752	0.28247	5.77	0.79	1.27	1.09
MB_O1_02-02	0.28254	0.00004	0.00160	773	0.28252	7.94	1.23	1.15	0.97
MB_O1_02-03	0.28251	0.00003	0.00160	832	0.28249	8.05	0.95	1.19	1.01
MB_O1_02-04	0.28254	0.00004	0.00229	808	0.28251	8.25	1.23	1.16	0.98
MB_O1_02-06	0.28254	0.00003	0.00152	791	0.28252	8.15	0.92	1.16	0.97
MB_O1_02-07	0.28249	0.00003	0.00155	789	0.28247	6.51	0.90	1.26	1.07
MB_O1_02-12	0.28249	0.00003	0.00142	773	0.28247	6.13	1.04	1.27	1.08
MB_O1_02-13	0.28249	0.00003	0.00207	770	0.28246	5.70	1.03	1.29	1.11
MB_O1_02-20	0.28250	0.00003	0.00271	783	0.28246	6.17	1.19	1.27	1.09
MB_O1_02-27	0.28252	0.00003	0.00222	762	0.28249	6.62	1.08	1.23	1.04
O14-08									
MB_O1_04-04	0.28252	0.00003	0.00165	782	0.28249	7.07	0.97	1.22	1.03
MB_O1_04-07	0.28252	0.00003	0.00117	747	0.28251	6.84	1.05	1.20	1.02
MB_O1_04-08	0.28254	0.00004	0.00276	743	0.28250	6.44	1.24	1.23	1.04
MB_O1_04-12	0.28256	0.00004	0.00175	735	0.28253	7.53	1.26	1.15	0.96
MB_O1_04-13	0.28255	0.00003	0.00211	721	0.28253	6.93	1.12	1.18	0.99
MB_O1_04-15	0.28253	0.00003	0.00206	735	0.28251	6.52	1.11	1.21	1.03
MB_O1_04-17	0.28251	0.00003	0.00168	748	0.28249	6.12	1.07	1.25	1.06
MB_O1_04-18	0.28254	0.00003	0.00259	749	0.28250	6.81	1.21	1.21	1.02
MB_O1_04-20	0.28253	0.00005	0.00223	765	0.28250	6.83	1.67	1.22	1.03
MB_O1_04-25	0.28249	0.00003	0.00220	736	0.28246	4.89	1.17	1.32	1.13
MB_O1_04-27	0.28258	0.00003	0.00160	760	0.28256	9.01	1.22	1.08	0.89
MB_O1_04-29	0.28241	0.00005	0.00277	758	0.28237	2.12	1.64	1.51	1.32
O14-05									
MB-O1-01	0.28246	0.00004	0.00198	744	0.28243	4.14	1.35	1.37	1.18
MB-O1-05	0.28255	0.00005	0.00224	758	0.28251	7.37	1.70	1.18	0.99
MB-O1-09	0.28252	0.00004	0.00201	745	0.28249	6.34	1.36	1.23	1.05
MB-O1-12	0.28235	0.00003	0.00197	757	0.28232	0.39	1.12	1.61	1.43
MB-O1-13	0.28251	0.00003	0.00172	775	0.28248	6.52	1.22	1.25	1.06
MB-O1-17	0.28252	0.00004	0.00231	755	0.28248	6.18	1.51	1.25	1.07
MB-O1-30	0.28251	0.00006	0.00267	770	0.28247	6.09	2.16	1.27	1.08
MB-O1-34	0.28245	0.00004	0.00119	790	0.28243	5.07	1.33	1.35	1.16
MB-O1-36	0.28254	0.00005	0.00291	806	0.28249	7.74	1.81	1.19	1.01
MB-O1-39	0.28253	0.00006	0.00163	767	0.28250	7.19	2.24	1.20	1.01
MB-O1-44	0.28250	0.00005	0.00102	808	0.28249	7.50	1.68	1.21	1.03
AJ14-19									
MB_AJ19_22	0.28248	0.00002	0.00020	842	0.28247	7.78	0.62	1.22	1.04
MB_AJ19_30	0.28260	0.00003	0.00255	842	0.28256	10.91	1.22	1.02	0.84
MB_AJ19_31	0.28257	0.00002	0.00119	842	0.28255	10.52	0.84	1.05	0.86
MB_AJ19_33	0.28257	0.00002	0.00097	842	0.28256	10.71	0.83	1.04	0.85
MB_AJ19_34	0.28256	0.00002	0.00067	842	0.28255	10.44	0.68	1.05	0.87
MB_AJ19_36	0.28256	0.00002	0.00143	842	0.28253	9.92	0.85	1.08	0.90
MB_AJ19_39	0.28260	0.00003	0.00189	842	0.28257	11.25	1.05	1.00	0.82
MB_AJ19_47	0.28258	0.00003	0.00183	842	0.28256	10.72	0.88	1.03	0.85
MB_AJ19_55	0.28258	0.00002	0.00136	842	0.28255	10.68	0.82	1.04	0.85
MB_AJ19_56	0.28256	0.00002	0.00145	842	0.28253	9.88	0.81	1.09	0.90
MB_AJ19_57	0.28257	0.00002	0.00158	842	0.28255	10.42	0.86	1.05	0.87
MB_AJ19_63	0.28256	0.00003	0.00160	842	0.28254	10.09	1.01	1.07	0.89

CHUR from Bouvier et al. (2008); Earth and Planetary Science Letters 273 (2008) 48–57
CHUR 176Lu/177Hf = 0.0336±1 and 176Hf/177Hf = 0.282785±11
Hfi = 176Hf/177Hf ratio - (176Lu/177Hf ratio * (EXP(0.0193 * 207Pb/206Pb ratio / 1000)-1))

Table 2: LA–MC–ICP–MS Lu–Hf isotopes (zircon) from igneous samples in Oman

Sample Name	Hf^{176}/Hf^{177}	2 S.E.	Lu^{176}/Hf^{177}	U/Pb AGE	Hfi	epsilon	2s	Hf DM (t) (Crustal)	T(NC) (Crustal
AJ14-23									
MB_AJ25_01	0.28256	0.00002	0.00262	842	0.28252	9.40	0.65	1.12	0.93
MB_AJ25_04	0.28260	0.00002	0.00115	842	0.28258	11.62	0.64	0.98	0.79
MB_AJ25_09	0.28252	0.00002	0.00181	842	0.28249	8.48	0.66	1.18	0.99
MB_AJ25_11	0.28256	0.00003	0.00102	842	0.28254	10.20	0.89	1.07	0.88
MB_AJ25_12	0.28256	0.00003	0.00070	842	0.28255	10.56	1.18	1.04	0.86
MB_AJ25_13	0.28255	0.00003	0.00098	842	0.28254	9.99	0.98	1.08	0.90
MB_AJ25_16	0.28256	0.00003	0.00139	842	0.28254	10.02	1.02	1.08	0.89
MB_AJ25_17	0.28254	0.00002	0.00144	842	0.28252	9.39	0.83	1.12	0.93
MB_AJ25_20	0.28257	0.00002	0.00144	842	0.28254	10.26	0.72	1.06	0.88
MB_AJ25_24	0.28257	0.00002	0.00053	842	0.28256	10.77	0.82	1.03	0.85
AJ14-25									
MB_AJ25_02	0.28258	0.00003	0.00174	834	0.28255	10.44	1.03	1.05	0.86
MB_AJ25_08	0.28256	0.00003	0.00169	834	0.28254	9.82	0.91	1.08	0.90
MB_AJ25_09	0.28259	0.00003	0.00166	834	0.28256	10.74	0.92	1.03	0.84
MB_AJ25_12	0.28256	0.00002	0.00150	834	0.28253	9.75	0.84	1.09	0.91
MB_AJ25_15	0.28256	0.00002	0.00144	834	0.28254	10.03	0.82	1.07	0.89
MB_AJ25_19	0.28257	0.00002	0.00193	834	0.28254	9.83	0.85	1.08	0.90
MB_AJ25_20	0.28257	0.00003	0.00245	834	0.28253	9.80	1.17	1.09	0.90
MB_AJ25_21	0.28256	0.00003	0.00130	834	0.28254	9.93	0.90	1.08	0.89
MB_AJ25_25	0.28257	0.00003	0.00179	834	0.28254	10.04	0.90	1.07	0.89
MB_AJ25_26	0.28258	0.00003	0.00176	834	0.28255	10.34	0.96	1.05	0.87
MB_AJ25_28	0.28256	0.00003	0.00149	834	0.28253	9.70	1.02	1.09	0.91
MR15-01									
MB_MR1_01	0.28253	0.00003	0.00046	809	0.28253	8.90	0.92	1.12	0.94
MB_MR1_02	0.28253	0.00003	0.00137	809	0.28251	8.43	0.98	1.15	0.97
MB_MR1_03	0.28255	0.00003	0.00083	809	0.28254	9.36	0.98	1.09	0.91
MB_MR1_06	0.28256	0.00002	0.00050	809	0.28255	9.80	0.61	1.07	0.88
MB_MR1_07	0.28255	0.00002	0.00050	809	0.28254	9.44	0.78	1.09	0.90
MB_MR1_11	0.28255	0.00003	0.00074	809	0.28254	9.30	1.07	1.10	0.91
MB_MR1_12	0.28254	0.00002	0.00191	809	0.28251	8.38	0.78	1.16	0.97
MB_MR1_13	0.28254	0.00002	0.00068	809	0.28253	9.00	0.62	1.12	0.93
MB_MR1_15	0.28249	0.00002	0.00068	809	0.28248	7.44	0.62	1.21	1.03
MB_MR1_18	0.28251	0.00002	0.00066	809	0.28250	7.87	0.65	1.19	1.00
MB_MR1_25	0.28251	0.00002	0.00052	809	0.28250	8.08	0.77	1.17	0.99
MR15-02									
MB_MR2_11	0.28257	0.00003	0.00047	781	0.28256	9.59	0.91	1.06	0.87
MB_MR2_16	0.28257	0.00002	0.00138	781	0.28255	8.98	0.66	1.10	0.91
MB_MR2_21	0.28256	0.00002	0.00097	781	0.28255	9.07	0.83	1.09	0.90
MB_MR2_24	0.28257	0.00002	0.00080	781	0.28256	9.60	0.66	1.06	0.87
MB_MR2_25	0.28259	0.00002	0.00107	781	0.28257	9.90	0.68	1.04	0.85
MB_MR2_28	0.28257	0.00002	0.00094	781	0.28256	9.51	0.85	1.06	0.88
MB_MR2_30	0.28259	0.00002	0.00078	781	0.28258	10.09	0.86	1.03	0.84
MB_MR2_35	0.28258	0.00002	0.00061	781	0.28257	9.73	0.75	1.05	0.86
MB_MR2_38	0.28258	0.00003	0.00075	781	0.28257	9.85	0.94	1.04	0.86
MB_MR2_39	0.28258	0.00002	0.00256	781	0.28254	8.75	0.81	1.11	0.92

CHUR from Bouvier et al. (2008); Earth and Planetary Science Letters 273 (2008) 48–57
CHUR 176Lu/177Hf = 0.0336±1 and 176Hf/177Hf = 0.282785±11
Hfi = 176Hf/177Hf ratio - (176Lu/177Hf ratio * (EXP(0.0193 * 207Pb/206Pb ratio / 1000)-1))

Table 2: LA–MC–ICP–MS Lu–Hf isotopes (zircon) from igneous samples in Oman

Sample Name	Hf^{176}/Hf^{177}	2 S.E.	Lu^{176}/Hf^{177}	U/Pb AGE	Hfi	epsilon	2s	Hf DM (t) (Crustal)	T(NC) (Crustal)
MR15-04									
MB_MR4_01	0.28261	0.00002	0.00155	810	0.28258	10.96	0.71	0.99	0.81
MB_MR4_03	0.28260	0.00002	0.00085	810	0.28259	11.11	0.68	0.98	0.80
MB_MR4_06	0.28252	0.00002	0.00107	810	0.28250	8.00	0.86	1.18	1.00
MB_MR4_11	0.28259	0.00003	0.00356	810	0.28254	9.42	1.16	1.09	0.91
MB_MR4_15	0.28259	0.00003	0.00183	810	0.28257	10.34	0.95	1.03	0.85
MB_MR4_18	0.28258	0.00002	0.00164	810	0.28256	9.98	0.86	1.06	0.87
MB_MR4_19	0.28262	0.00002	0.00100	810	0.28261	11.77	0.80	0.94	0.76
MB_MR4_20	0.28260	0.00005	0.00154	810	0.28257	10.65	1.81	1.01	0.83
MB_MR4_23	0.28263	0.00003	0.00199	810	0.28260	11.47	1.04	0.96	0.78
MB_MR4_24	0.28260	0.00003	0.00094	810	0.28258	10.95	1.09	1.00	0.81
MB_MR4_28	0.28260	0.00003	0.00119	810	0.28258	10.81	0.91	1.00	0.82
MB_MR4_31	0.28258	0.00003	0.00028	810	0.28258	10.71	1.00	1.01	0.83
MR15-05									
MB_MR5_04	0.28257	0.00003	0.00033	810	0.28256	10.26	1.04	1.04	0.85
MB_MR5_05	0.28256	0.00003	0.00032	764	0.28255	8.92	0.99	1.09	0.90
MB_MR5_06	0.28257	0.00002	0.00041	764	0.28256	9.14	0.65	1.07	0.89
MB_MR5_07	0.28256	0.00002	0.00031	764	0.28255	8.87	0.67	1.09	0.90
MB_MR5_08	0.28255	0.00002	0.00033	764	0.28255	8.65	0.55	1.10	0.92
MB_MR5_10	0.28258	0.00002	0.00022	764	0.28258	9.66	0.68	1.04	0.85
MB_MR5_11	0.28256	0.00002	0.00026	764	0.28256	9.12	0.57	1.07	0.89
MB_MR5_12	0.28257	0.00002	0.00019	764	0.28256	9.20	0.70	1.07	0.88
MB_MR5_14	0.28254	0.00002	0.00061	764	0.28253	8.20	0.73	1.13	0.95
MB_MR5_17	0.28257	0.00002	0.00049	764	0.28256	9.25	0.64	1.07	0.88
MB_MR5_18	0.28256	0.00002	0.00234	764	0.28253	8.06	0.75	1.14	0.95
MR15-07									
MB_MR7_05	0.28261	0.00003	0.00194	802	0.28258	10.54	1.14	1.01	0.83
MB_MR7_06	0.28260	0.00002	0.00082	802	0.28259	10.95	0.77	0.99	0.80
MB_MR7_11	0.28258	0.00002	0.00115	802	0.28256	10.02	0.76	1.05	0.86
MB_MR7_12	0.28258	0.00004	0.00088	802	0.28257	10.36	1.24	1.03	0.84
MB_MR7_16	0.28257	0.00003	0.00118	802	0.28255	9.64	1.06	1.07	0.89
MB_MR7_18	0.28257	0.00002	0.00153	900	0.28254	11.60	0.65	1.03	0.84
MB_MR7_19	0.28256	0.00002	0.00187	802	0.28253	9.07	0.86	1.11	0.92
MB_MR7_22	0.28257	0.00002	0.00071	802	0.28256	9.83	0.73	1.06	0.87
MB_MR7_23	0.28260	0.00002	0.00105	802	0.28259	10.92	0.78	0.99	0.81
MB_MR7_24	0.28258	0.00002	0.00068	802	0.28257	10.40	0.87	1.02	0.84
MB_MR7_32	0.28257	0.00003	0.00108	802	0.28255	9.64	1.09	1.07	0.89
MB_MR7_36	0.28261	0.00002	0.00000	802	0.28261	11.58	0.79	0.95	0.76

CHUR from Bouvier et al. (2008); Earth and Planetary Science Letters 273 (2008) 48–57
CHUR 176Lu/177Hf = 0.0336±1 and 176Hf/177Hf = 0.282785±11
Hfi = 176Hf/177Hf ratio - (176Lu/177Hf ratio * (EXP(0.0193 * 207Pb/206Pb ratio / 1000)-1))

Table 2: LA–MC–ICP–MS Lu–Hf isotopes (zircon) from igneous samples in Oman

Sample Name	Hf[176]/Hf[177]	2 S.E.	Lu[176]/Hf[177]	U/Pb AGE	Hfi	epsilon	2s	Hf DM (t) (Crustal)	T(NC) (Crustal)
MR15-14									
MB_MR14_01	0.28257	0.00002	0.00195	840	0.28254	9.98	0.83	1.08	0.90
MB_MR14_04	0.28259	0.00003	0.00184	840	0.28256	10.98	0.90	1.02	0.83
MB_MR14_09	0.28264	0.00003	0.00152	840	0.28262	12.98	0.96	0.89	0.71
MB_MR14_100	0.28258	0.00003	0.00077	840	0.28257	11.06	0.94	1.01	0.83
MB_MR14_110	0.28259	0.00003	0.00207	840	0.28256	10.83	1.05	1.03	0.84
MB_MR14_112	0.28258	0.00003	0.00138	840	0.28256	10.82	0.95	1.03	0.84
MB_MR14_113	0.28265	0.00002	0.00104	840	0.28263	13.34	0.84	0.87	0.68
MB_MR14_115	0.28260	0.00002	0.00055	840	0.28259	11.93	0.82	0.96	0.77
MB_MR14_16	0.28261	0.00003	0.00186	840	0.28259	11.73	0.94	0.97	0.79
MB_MR14_29	0.28258	0.00003	0.00159	840	0.28255	10.52	0.98	1.05	0.86
MB_MR14_62	0.28262	0.00005	0.00354	620	0.28258	6.61	1.68	1.12	0.93
MB_MR14_97	0.28263	0.00006	0.00239	649	0.28260	8.10	1.97	1.05	0.86
MB_MR14_98	0.28264	0.00004	0.00191	840	0.28261	12.53	1.33	0.92	0.74
JA15-43									
Ja1543-2a	0.28238	0.00010	0.00098	852	0.28236	4.16	3.51	1.45	1.27
Ja1543-3a	0.28140	0.00064	0.00093	1621	0.28137	-13.65	22.31	3.13	2.98
Ja1543-6a	0.28208	0.00006	0.00074	893	0.28207	-5.40	1.96	2.08	1.90
Ja1543-7a	0.28212	0.00007	0.00051	867	0.28211	-4.51	2.35	2.00	1.82
Ja1543-8a	0.28199	0.00005	0.00102	1429	0.28197	3.15	1.69	1.97	1.80
Ja1543-9a	0.28155	0.00007	0.00117	1474	0.28152	-11.73	2.46	2.90	2.74
Ja1543-16a	0.28209	0.00007	0.00126	853	0.28207	-6.15	2.43	2.09	1.91
Ja1543-17b	0.28241	0.00005	0.00079	827	0.28240	4.93	1.85	1.39	1.20
Ja1543-22a	0.28185	0.00005	0.00085	1568	0.28182	1.21	1.92	2.19	2.03
Ja1543-27a	0.28216	0.00004	0.00078	857	0.28215	-3.36	1.54	1.92	1.74
Ja1543-43a	0.28217	0.00012	0.00127	890	0.28215	-2.58	4.17	1.90	1.72
Ja1543-48a	0.28088	0.00007	0.00131	2532	0.28082	-12.15	2.47	3.74	3.61
Ja1543-50a	0.28177	0.00004	0.00078	1645	0.28175	0.42	1.43	2.30	2.14
Ja1543-52a	0.28250	0.00003	0.00067	859	0.28249	8.77	1.22	1.17	0.99
Ja1543-53a	0.28244	0.00006	0.00084	877	0.28243	6.92	1.99	1.30	1.12
Ja1543-54a	0.28247	0.00009	0.00201	904	0.28243	7.71	3.21	1.27	1.09
Ja1543-55a	0.28217	0.00006	0.00063	814	0.28216	-3.94	2.02	1.93	1.74
Ja1543-56a	0.28250	0.00006	0.00191	826	0.28247	7.27	1.97	1.24	1.05
Ja1543-57a	0.28243	0.00004	0.00074	846	0.28241	5.78	1.54	1.35	1.16
Ja1543-58a	0.28197	0.00025	0.00198	782	0.28194	-12.47	8.61	2.43	2.25
Ja1543-61a	0.28268	0.00045	0.00214	866	0.28265	14.54	15.59	0.81	0.63
Ja1543-62a	0.28249	0.00006	0.00220	833	0.28245	6.90	1.97	1.27	1.08
Ja1543-63a	0.28242	0.00005	0.00104	832	0.28240	4.94	1.84	1.39	1.21
Ja1543-65a	0.28251	0.00038	0.00109	839	0.28249	8.32	13.17	1.18	1.00
Ja1543-67a	0.28244	0.00067	0.00164	836	0.28241	5.44	23.47	1.36	1.18
Ja1543-69a	0.28261	0.00058	0.00150	788	0.28259	10.80	20.25	0.99	0.80
Ja1543-71a	0.28147	0.00023	0.00085	2404	0.28144	6.81	7.91	2.52	2.38
Ja1543-72a	0.28214	0.00002	0.00041	894	0.28213	-3.04	0.73	1.93	1.75
Ja1543-73a	0.28251	0.00003	0.00106	830	0.28249	8.29	1.02	1.18	0.99
Ja1543-75a	0.28205	0.00009	0.00123	845	0.28204	-7.66	3.06	2.18	2.00
Ja1543-76a	0.28216	0.00007	0.00127	857	0.28214	-3.63	2.33	1.94	1.76
Ja1543-77a	0.28222	0.00007	0.00199	818	0.28219	-2.74	2.38	1.86	1.67
Ja1543-78a	0.28232	0.00011	0.00243	857	0.28228	1.28	3.75	1.64	1.45

Table 3: SHRIMP SI O isotopes (zircon) from igneous samples in Oman

Spot Number	Zircon Age $^{206}Pb/^{238}U$	$^{18}O/^{16}O$	1s	$^{18}O/^{16}O$ (‰)	Error T 95%	External error 2s
Jebel Akhdar						
O14-04						
O14-04-01	779	0.002044	0.000000436	9.558106	0.21	1.0127
O14-04-07	779	0.002041	0.000000569	8.220604	0.28	1.0285
O14-04-10	779	0.002042	0.000000519	8.80175	0.25	1.0221
O14-04-13	779	0.002044	0.000000277	9.944936	0.14	0.9992
O14-04-20	779	0.002043	0.000000377	9.179444	0.18	1.0070
O14-04-28	779	0.002045	0.000000362	10.32642	0.18	1.0057
O14-04-30	779	0.002042	0.000000407	8.738109	0.20	1.0098
O14-04-32	779	0.00204	0.000000478	7.735557	0.23	1.0173
O14-08						
O14-08-06	749	0.002038	0.000000335	6.78195	0.16	1.0035
O14-08-13	749	0.002039	0.000000559	7.441	0.27	1.0272
O14-08-16	749	0.002045	0.00000043	10.25269	0.21	1.0121
O14-08-19	749	0.002043	0.000000352	9.093777	0.17	1.0049
O14-08-25	749	0.002044	0.000000289	9.492701	0.14	1.0000
O14-08-26	749	0.002044	0.000000366	9.722336	0.18	1.0061
O14-08-27	749	0.00204	0.000000326	7.978802	0.16	1.0028
O14-08-28	749	0.002042	0.000000226	8.530763	0.11	0.9962
Al Jobah						
AJ14-19						
19.1	855	0.00204	0.000000415	7.661325	0.20	1.0107
19-22	855	0.00204	0.000000605	7.83751	0.30	1.0335
19-30	855	0.002039	0.000000434	7.037443	0.21	1.0126
19-33	855	0.002039	0.000000246	7.14126	0.12	0.9973
19-36	855	0.002039	0.000000307	7.362485	0.15	1.0014
19-39	855	0.002047	0.000000204	11.31162	0.10	0.9950
19-47	855	0.002038	0.000000313	6.843754	0.15	1.0018
19-55	855	0.002039	0.000000307	7.158885	0.15	1.0014
19-56	855	0.00204	0.000000279	7.773573	0.14	0.9994
19-57	855	0.002039	0.000000406	7.362102	0.20	1.0098
19-63	855	0.00204	0.000000282	7.80865	0.14	0.9996
AJ14-23						
23-01	861	0.00204	0.000000263	7.92520	0.12902	0.99837
23-04	861	0.002039	0.000000322	7.174556	0.16	1.0025
23-08	861	0.00204	0.000000241	7.546724	0.12	0.9970
23-10	861	0.002039	0.000000279	7.123718	0.14	0.9994
23-11	861	0.00204	0.000000281	7.859056	0.14	0.9995
23-12	861	0.002045	0.000000353	10.42799	0.17	1.0049
23-13	861	0.002039	0.000000373	7.077258	0.18	1.0067
23-17	861	0.00204	0.000000291	7.61879	0.14	1.0002

Table 3: SHRIMP SI O isotopes (zircon) from igneous samples in Oman

Spot Number	Zircon Age $^{206}Pb/^{238}U$	$^{18}O/^{16}O$	1s	$^{18}O/^{16}O$ (‰)	Error T 95%	External error 2s
Mirbat						
MR15-01						
MR1501_01	809	0.002032	0.000001	3.71	0.27	1.02
MR1501_10	809	0.002035	0.000000	5.16	0.21	1.01
MR1501_11	809	0.002038	0.000001	6.66	0.26	1.02
MR1501_12	809	0.002035	0.000000	5.54	0.12	1.00
MR1501_2	809	0.002032	0.000001	4.07	0.62	1.17
MR1501_3	809	0.002036	0.000001	5.57	0.35	1.05
MR1501_4	809	0.002033	0.000001	4.52	0.31	1.04
MR1501_5	809	0.002036	0.000000	5.86	0.15	1.00
MR1501_6	809	0.002034	0.000000	4.83	0.13	1.00
MR1501_7	809	0.002032	0.000001	3.74	0.26	1.02
MR1501_8	809	0.002036	0.000000	5.59	0.13	1.00
MR1501_9	809	0.002035	0.000001	5.39	0.27	1.03
MR15-02						
MR1502-1	795	0.002034	0.000001	4.90	0.38	1.06
MR1502-10	795	0.002031	0.000001	3.29	0.38	1.06
MR1502-11	795	0.002022	0.000000	-0.87	0.23	1.02
MR1502-12	795	0.002032	0.000001	3.78	0.32	1.04
MR1502-2	795	0.002035	0.000000	5.25	0.13	1.00
MR1502-3	795	0.00203	0.000000	3.03	0.23	1.02
MR1502-4	795	0.002032	0.000001	4.02	0.26	1.02
MR1502-5	795	0.002031	0.000000	3.45	0.13	1.00
MR1502-6	795	0.002033	0.000000	4.57	0.13	1.00
MR1502-7	795	0.002032	0.000001	3.87	0.27	1.03
MR1502-8	795	0.002031	0.000001	3.37	0.32	1.04
MR1502-9	795	0.002032	0.000000	3.85	0.14	1.00
MR15-04						
MR1504_10	804	0.002036	0.000000	5.77	0.20	1.01
MR1504_5	804	0.002035	0.000000	5.39	0.12	1.00
MR1504_6	804	0.002035	0.000001	5.39	0.25	1.02
MR1504_7	804	0.002035	0.000001	5.34	0.37	1.06
MR1504_8	804	0.002032	0.000001	3.90	0.30	1.03
MR1504_9	804	0.002038	0.000001	6.91	0.27	1.03
MR1504-1	804	0.002036	0.000000	5.69	0.15	1.00
MR1504-2	804	0.002036	0.000000	5.86	0.24	1.02
MR1504-3	804	0.002034	0.000000	5.02	0.19	1.01
MR1504-4	804	0.002033	0.000000	4.33	0.19	1.01
MR15-05						
MR1505-01	771	0.002034	0.000000	4.83	0.22	1.01
MR1505-2	771	0.002034	0.000001	4.88	0.29	1.03
MR1505-3	771	0.002036	0.000000	5.76	0.22	1.01
MR1505-4	771	0.002035	0.000001	5.43	0.26	1.02
MR1505-5	771	0.002033	0.000000	4.49	0.24	1.02
MR1505-6	771	0.002035	0.000000	5.56	0.23	1.02
MR1505-7	771	0.002033	0.000001	4.50	0.43	1.08
MR1505-8	771	0.002034	0.000001	4.84	0.36	1.05
MR1505-9	771	0.002034	0.000001	4.76	0.25	1.02

Table 3: SHRIMP SI O isotopes (zircon) from igneous samples in Oman

Spot Number	Zircon Age $^{206}Pb/^{238}U$	$^{18}O/^{16}O$	1s	$^{18}O/^{16}O$ (‰)	Error T 95%	External error 2s
Mirbat						
MR15-07						
MR1507-01	802	0.002031	0.000001	3.31	0.31	1.04
MR1507-10	802	0.002043	0.000000	9.04	0.15	1.00
MR1507-11	802	0.002032	0.000001	3.62	0.32	1.04
MR1507-12	802	0.002035	0.000000	5.17	0.16	1.00
MR1507-2	802	0.002034	0.000001	4.83	0.27	1.03
MR1507-3	802	0.002034	0.000001	4.64	0.28	1.03
MR1507-4	802	0.002032	0.000001	3.69	0.25	1.02
MR1507-5	802	0.002037	0.000000	6.17	0.13	1.00
MR1507-6	802	0.002033	0.000001	4.49	0.33	1.04
MR1507-7	802	0.002034	0.000001	4.79	0.28	1.03
MR1507-8	802	0.002032	0.000000	3.89	0.23	1.02
MR1507-9	802	0.002035	0.000000	5.24	0.12	1.00